

APRIL 2019

AJNR

VOLUME 40 • PP 583-756

AJNR

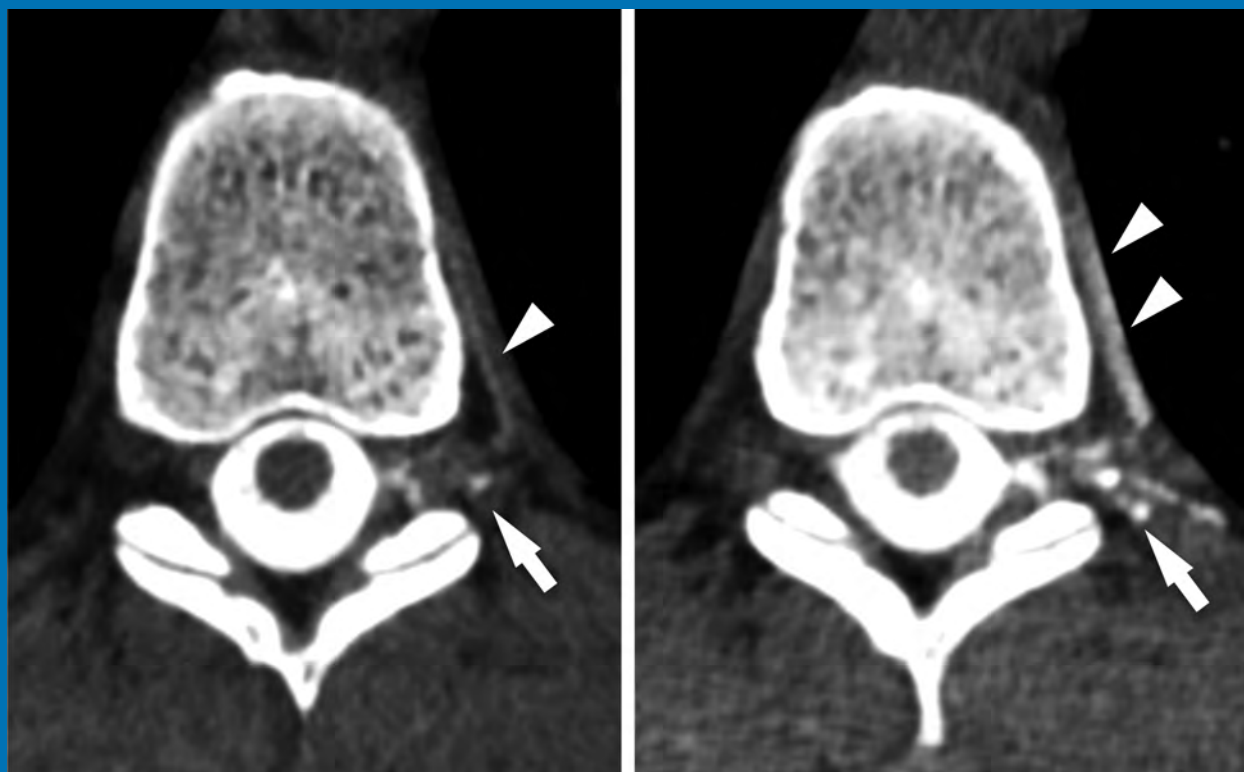
AMERICAN JOURNAL OF NEURORADIOLOGY

APRIL 2019
VOLUME 40
NUMBER 4
WWW.AJNR.ORG

THE JOURNAL OF DIAGNOSTIC AND
INTERVENTIONAL NEURORADIOLOGY

Systematic approach for spinal CSF leak localization and management
Gadolinium-enhanced susceptibility-weighted imaging in MS
Prevalence of superior semicircular canal dehiscence

Official Journal ASNR • ASFNR • ASHNR • ASPNR • ASSR





ONE AND DONE

INDICATIONS FOR USE:

The WEB Aneurysm Embolization System is indicated for use at the middle cerebral artery (MCA) bifurcation, internal carotid artery (ICA) terminus, anterior communicating artery (AComm) complex, or basilar artery apex for the endovascular treatment of adult patients with saccular, wide neck bifurcation intracranial aneurysms with dome diameter from 3 mm to 10 mm and either neck size 4 mm or greater or the dome-to-neck ratio is greater than 1 and less than 2.

The WEB Aneurysm Embolization System is contraindicated for patients with known bacterial infection that may interfere with or negatively affect the implantation procedure and patients with known hypersensitivity to nickel. For complete indications, contraindications, potential complications, warnings, precautions, and instructions, see instructions for use (IFU provided with the device).

The VIA® Catheter is intended for the introduction of non-liquid interventional devices (such as stents/_ow diverters) and infusion of diagnostic (such as contrast media) or non-liquid therapeutic agents into the neuro, peripheral, and coronary vasculature. The VIA Catheter is contraindicated for use with liquid embolic materials, such as n-butyl 2-cyanoacrylate or ethylene vinyl alcohol & DMSO (dimethyl sulfoxide). The VIA Catheter is contraindicated for use in the pediatric population (<22 yrs of age).

Caution: Federal law restricts these devices to sale by or on the order of a physician.

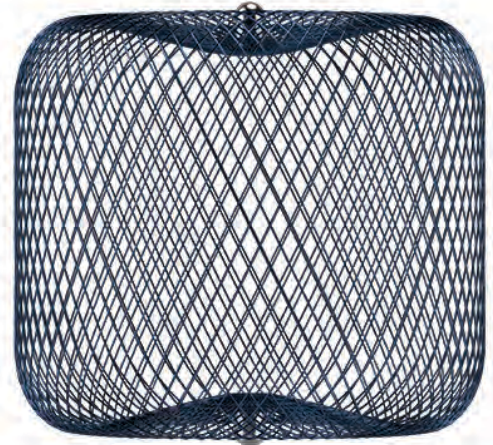
WEB[®]

Aneurysm Embolization System

MicroVention[®] delivers the first intrasaccular solution for wide neck bifurcation aneurysms.

The **world leader**
and **first**
PMA - approved
device in an
important new
category of
intrasaccular
flow disruptors.

The WEB[®] System is a safe
and effective single-device
solution for treating wide
neck bifurcation aneurysms.



SL Device



SLS Device

Contact a MicroVention sales associate to learn more about integrating the WEB[®] device into your practice.



**MicroVention Worldwide
Innovation Center**

35 Enterprise
Aliso Viejo, CA 92656 USA

MicroVention UK Limited

MicroVention Europe, S.A.R.L.

MicroVention Deutschland GmbH

microvention.com

PH +1.714.247.8000

PH +44 (0) 191 258 6777

PH +33 (1) 39 21 77 46

PH +49 211 210 798-0

Upgrade to elite status



An expanding portfolio

When partnered with products from our comprehensive vertebral compression fracture (VCF) portfolio, the iVAS Elite balloon system gives you total control over your procedural approach. Offered in 11g, 10g and 8g with bipedicular, unipedicular and à la carte packaging, we deliver the efficiency and performance you can trust.

A material difference

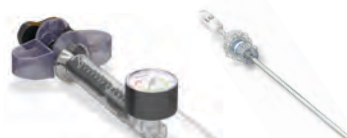
Confidently create the void you imagined. Optimized material compliance and balloon shape enable you to inflate with unmatched puncture resistance and strength you can control—up to **808psi**.^{1,2}

The system of choice

Customize your procedure with the approach and gauge size you see fit. With the addition of the iVAS Elite balloon, you now have a high-pressure balloon available in 11g, 10g and 8g kits.

Effortlessly efficient

Our user-centric features include an inflator with a weighted distal tip—for seamless contrast filling—and a locking coaxial cement tube that prevents backing out during injection.



Discover more at strykerIVS.com/iVAS-Elite

¹As compared to iVAS 1.0, Medtronic Express, and Express II balloons

²Performance of a new vertebral augmentation balloon: A comparative study. Stryker April 2018, 1000-025-893

Stryker Corporation or its affiliates own, use, or have applied for the following trademarks or service marks: iVAS and Stryker.

All other trademarks are trademarks of their respective owners or holders.

D0000003496

We're Inside Every Great Neuroradiologist!

ASNR MEMBERS RECEIVE

American Journal of Neuroradiology (AJNR)

The leading neuroradiology research journal, published monthly

Neurographics

Bimonthly educational journal with CME for members

ASNR Annual Meeting

Discounts for members on the field's premier conference

eCME

Online collection of lectures and articles with SA-CME and Category 1 credit

Advocacy

Coding/reimbursement, quality standards and practice guidelines; demonstrating neuroradiology's value!

Networking

Access to 5,000 peers

... And More!

Join the leaders in neuroradiology today!

Learn more at www.asnr.org/join

ASNR

American Society of Neuroradiology

800 Enterprise Dr., Suite 205, Oak Brook, IL 60523 • (630)574-0220 • membership@asnr.org • www.asnr.org

AJNR *go green*

***AJNR* urges American Society of Neuroradiology members to reduce their environmental footprint by voluntarily suspending their print subscription.**

The savings in paper, printing, transportation, and postage directly fund new electronic enhancements and expanded content.

The digital edition of *AJNR* presents the print version in its entirety, along with extra features including:

- Publication Preview
- Case Collection
- Podcasts
- The *AJNR* News Digest
- The *AJNR* Blog

It also reaches subscribers much faster than print. An electronic table of contents will be sent directly to your mailbox to notify you as soon as it publishes.

Readers can search, reference, and bookmark current and archived content 24 hours a day on www.ajnr.org.

ASNR members who wish to opt out of print can do so by using the *AJNR* Go Green link on the *AJNR* Website (<http://www.ajnr.org/content/subscriber-help-and-services>). Just type your name in the email form to stop print and spare our ecosystem.

stryker

Now you have **24 hours** to make a lifetime of difference in stroke patients like Nora



The Trevo Retriever is the only device cleared to **reduce disability in stroke patients up to 24 hours** from time last seen well.

For more information, visit strykerneurovascular.com/trevo24hours

Trevo[®] XP
PROVUE RETRIEVER

Copyright © 2018 Stryker
AP002078 v1.0



Simplify the MOC Process



Manage your CME Credits Online

CMEgateway.org

Available to Members of Participating Societies

American Board of Radiology (ABR)
American College of Radiology (ACR)
American Roentgen Ray Society (ARRS)
American Society of Neuroradiology (ASNR)
Commission on Accreditation of Medical
Physics Educational Programs, Inc. (CAMPEP)
Radiological Society of North America (RSNA)
Society of Interventional Radiology (SIR)
SNM
The Society for Pediatric Radiology (SPR)

It's Easy and Free!

Log on to CME Gateway to:

- View or print reports of your CME credits from multiple societies from a single access point.
- Print an aggregated report or certificate from each participating organization.
- Link to SAMs and other tools to help with maintenance of certification.

American Board of Radiology (ABR) participation!

By activating ABR in your organizational profile, your MOC-fulfilling CME and SAM credits can be transferred to your own personalized database on the ABR Web site.

Sign Up Today!

go to CMEgateway.org

AXS Vecta™ Aspiration Catheter RX ONLY

Caution: Federal Law (USA) restricts this device to sale by or on the order of a physician.

See package insert for complete indications, contraindications, warnings and instructions for use.

INTENDED USE/INDICATIONS FOR USE

The AXS Vecta Aspiration System, including the AXS Vecta Aspiration Catheter, Aspiration Tubing Set, and VC-701 Cliq Aspirator Pump, is indicated in the revascularization of patients with acute ischemic stroke secondary to intracranial large vessel occlusive disease (within the internal carotid, middle cerebral – M1 and M2 segments, basilar, and vertebral arteries) within 8 hours of symptom onset. Patients who are ineligible for intravenous tissue plasminogen activator (IV t-PA) or who failed IV t-PA therapy are candidates for treatment.

DEVICE DESCRIPTION

The AXS Vecta Aspiration System consist of the AXS Vecta Aspiration Catheter, the Aspiration Tubing Set, and the VC-701 Cliq Aspirator Pump.

The AXS Vecta Aspiration Catheter is a single lumen, flexible, variable stiffness catheter. It has a radiopaque marker band on the distal end and a Luer hub at the proximal end. The AXS Vecta Aspiration Catheter shaft has a lubricious hydrophilic coating at the distal end (distal 25 cm) to reduce friction during use. The Scout Introducer may be used in conjunction with the AXS Vecta Aspiration Catheter to facilitate in the introduction of the AXS Vecta Aspiration Catheter into distal vasculature and aid in navigation to distal anatomy. The Scout Introducer has a lubricious hydrophilic coating at the distal end to reduce friction during use. The inner lumen of the AXS Vecta Aspiration Catheters is compatible with the Scout Introducer, guide wires and micro catheters. The inner lumen of the Scout Introducer is compatible with guide wires and micro catheters of an outer diameter of less than 0.044in.

Each package includes one AXS Vecta Aspiration Catheter, one Scout Introducer, one hemostasis valve, and two peel-away introducers. Dimensions of the AXS Vecta Aspiration Catheter and Scout Introducer are included on the individual device label. The AXS Vecta Aspiration Catheters are available in 3 different lengths, the device configurations including the length of the Scout packaged with each catheter and the recommended Microcatheter length is presented in the table 1.0 below.

Catheter part number	INC-11129-115	INC-11129-125	INC-11129-132	INC-11597-115	INC-11597-125	INC-11597-132
Catheter inner diameter (in)	0.071	0.071	0.071	0.074	0.074	0.074
Distal catheter outer diameter (in)	0.082	0.082	0.082	0.083	0.083	0.083
Catheter working length (cm)	115	125	132	115	125	132
Scout Introducer length (cm)	133	143	150	133	143	150
Recommended compatible microcatheter length (cm)	150	160	160	150	160	160
Recommended compatible microcatheter outer diameter (in)	0.044 max	0.044 max	0.044 max	0.044 max	0.044 max	0.044 max
Recommended compatible guidewire outer diameter (in)	0.038 max	0.038 max	0.038 max	0.038 max	0.038 max	0.038 max

The AXS Vecta Aspiration System is recommended for use in the following vessel size ranges based on non-clinical testing. Refer to Table 2.0 below.

AXS Vecta Aspiration Catheter	Catheter part number	Vessel size in mm (Vessel size in inches)
AXS Vecta 71	INC-11129-115	2.1-4mm (0.083in – 0.157in)
	INC-11129-125	2.1-4 mm (0.083in – 0.157in)
	INC-11129-132	2.1-4 mm (0.083in – 0.157in)
AXS Vecta 74	INC-11597-115	2.2-4 mm (0.087in – 0.157in)
	INC-11597-125	2.2-4 mm (0.087in – 0.157in)
	INC-11597-132	2.2-4 mm (0.087in – 0.157in)

CONTRAINDICATIONS

The AXS Vecta Aspiration Catheter has not been evaluated for use in the coronary vasculature. Do not use automated high-pressure contrast injection equipment with the AXS Vecta Aspiration Catheter because it may damage the device.

ADVERSE EVENTS

- Acute vessel occlusion
- Air embolism
- Allergic reaction and anaphylaxis from contrast media
- Arteriovenous fistula
- Death
- Device malfunction
- Distal embolization
- Emboli
- False aneurysm formation
- Hematoma or hemorrhage at the puncture site
- Inability to completely remove thrombus
- Infection
- Intracranial hemorrhage
- Ischemia
- Kidney damage from contrast media
- Neurological deficit including stroke
- Risks associated with angiographic and fluoroscopic radiation including but not limited to: alopecia, burns ranging in severity from skin reddening to ulcers, cataracts, and delayed neoplasia
- Sterile inflammation or granulomas at the access site
- Tissue necrosis
- Vessel spasm, thrombosis, dissection or perforation

WARNING

Contents supplied STERILE using an ethylene oxide (EO) process. Do not use if sterile barrier is damaged. If damage is found, call your Stryker Neurovascular representative. For single use only. Do not reuse, reprocess or resterilize. Reuse, reprocessing or resterilization may compromise the structural integrity of the device and/or lead to device failure which, in turn, may result in patient injury, illness or death. Reuse, reprocessing or resterilization may also create a risk of contamination of the device and/or cause patient infection or cross-infection, including, but not limited to, the transmission of infectious disease(s) from one patient to another. Contamination of the device may lead to injury, illness or death of the patient. After use, dispose of product and packaging in accordance with hospital, administrative and/or local government policy.

WARNINGS

- The AXS Vecta Aspiration Catheter has not been evaluated for more than one (1) clot retrieval attempt.
- The AXS Vecta Aspiration Catheter was evaluated for an average duration of direct aspiration of 4 minutes.
- This product is intended for single use only, do not re-sterilize or reuse. Re-sterilization and/or reuse may result in cross contamination and/or reduced performance.

COMPATIBILITY

3x20mm retrievers are compatible with Trevo® Pro 14 Microcatheters (REF 90231) and Trevo® Pro 18 Microcatheters (REF 90238). 4x20mm retrievers are compatible with Trevo® Pro 18 Microcatheters (REF 90238). 4x30mm retrievers are compatible with Excelsior® XT-27® Microcatheters (150cm x 6cm straight REF 275081) and Trevo® Pro 18 Microcatheters (REF 90238). 6x25mm retrievers are compatible with Excelsior® XT-27® Microcatheters (150cm x 6cm straight REF 275081). Recommended minimum vessel ID for all Retriever sizes is 2.5mm. Compatibility of the Retriever with other microcatheters has not been established. Performance of the Retriever device may be impacted if a different microcatheter is used. Balloon Guide Catheters (such as Merc® Balloon Guide Catheter and FlowGate® Balloon Guide Catheter) are recommended for use during thrombus removal procedures. Retrievers are compatible with the Abbott Vascular DOC® Guide Wire Extension (REF 22260). Retrievers are compatible with Boston Scientific Rotating Hemostatic Valve (Ref 421242).

SPECIFIC WARNINGS FOR INDICATION 1

- The safety and effectiveness of the Trevo Retrievers in reducing disability has not been established in patients with large core infarcts (i.e. ASPECTS ≤ 7). There may be increased risks, such as intracerebral hemorrhage, in these patients.
- The safety and effectiveness of the Trevo Retrievers in reducing disability has not been established or evaluated in patients with occlusions in the posterior circulation (e.g., basilar or vertebral arteries) or for more distal occlusions in the anterior circulation.

SPECIFIC WARNINGS FOR INDICATION 2

- To reduce risk of vessel damage, take care to appropriately size Retriever to vessel diameter at intended site of deployment.

SPECIFIC WARNINGS FOR INDICATION 3

- The safety and effectiveness of the Trevo Retrievers in reducing disability has not been established in patients with large core infarcts (i.e., ASPECTS ≤ 7). There may be increased risks, such as intracerebral hemorrhage, in these patients.
- The safety and effectiveness of the Trevo Retrievers in reducing disability has not been established or evaluated in patients with occlusions in the posterior circulation (e.g., basilar or vertebral arteries) or for more distal occlusions in the anterior circulation.

- Users should validate their imaging software analysis techniques to ensure robust and consistent results for assessing core infarct size.

WARNINGS APPLIED TO ALL INDICATIONS

- Administration of IV t-PA should be within the FDA-approved window (within 3 hours of stroke symptom onset).
- To reduce risk of vessel damage, adhere to the following recommendations:
 - Do not perform more than six (6) retrieval attempts in same vessel using Retriever devices.
 - Maintain Retriever position in vessel when removing or exchanging Microcatheter.
- To reduce risk of kinking/fracture, adhere to the following recommendations:
 - Immediately after unsheathing Retriever, position Microcatheter tip marker just proximal to shaped section. Maintain Microcatheter tip marker just proximal to shaped section of Retriever during manipulation and withdrawal.
 - Do not rotate or torque Retriever.
 - Use caution when passing Retriever through stented arteries.
- The Retriever is a delicate instrument and should be handled carefully. Before use and when possible during procedure, inspect device carefully for damage. Do not use a device that shows signs of damage. Damage may prevent device from functioning and may cause complications.
- Do not advance or withdraw Retriever against resistance or significant vasospasm. Moving or torquing device against resistance or significant vasospasm may result in damage to vessel or device. Assess cause of resistance using fluoroscopy and if needed resheat the device to withdraw.
- If Retriever is difficult to withdraw from the vessel, do not torque Retriever. Advance Microcatheter distally, gently pull Retriever back into Microcatheter, and remove Retriever and Microcatheter as a unit. If undue resistance is met when withdrawing the Retriever into the Microcatheter, consider extending the Retriever using the Abbott Vascular DOC guidewire extension (REF 22260) so that the Microcatheter can be exchanged for a larger diameter catheter such as a DAC® Catheter. Gently withdraw the Retriever into the larger diameter catheter.

- When the catheter is exposed to the vascular system, it should be manipulated while under high-quality fluoroscopic observation. Do not advance or retract the catheter if resistance is met during manipulation; determine the cause of the resistance before proceeding.
 - Operators should take all necessary precautions to limit X-Radiation doses to patients and themselves by using sufficient shielding, reducing fluoroscopy times, and modifying X-Ray technical factors where possible.
 - This device is coated with a hydrophilic coating at the proximal end of the device for a length of 25 cm. Please refer to the Device Preparation Section for further information on how to prepare and use this device to ensure it performs as intended. Failure to abide by the warnings in this labeling might result in damage to the device coating, which may necessitate intervention or result in serious adverse events.
- ### PRECAUTIONS
- Store in a cool, dry, dark place.
 - Do not use kinked, damaged, or opened devices.
 - Use the device prior to the "Use By" date specified on the package.
 - Exposure to temperatures above 54°C (130°F) may damage device. Do not autoclave.
 - Torquing or moving the device against resistance may result in damage to the vessel or device.
 - Maintain a constant infusion of appropriate flush solution.
 - If flow through the device becomes restricted, do not attempt to clear the lumen by infusion. Remove and replace the device.
 - Examine the device to verify functionality and to ensure that its size and shape are suitable for the specific procedure for which it is to be used.
 - The AXS Vecta Aspiration Catheter should be used only by physicians trained in percutaneous procedures and/or interventional techniques.
 - The Scout Introducer should be used with a guidewire and microcatheter inserted when in vasculature.
 - If using the AXS Vecta Aspiration Catheter for thrombectomy, monitor the canister fluid level and replace the canister if the fill level reaches 75% of the canister volume.
 - Administration of anticoagulants and antiplatelets should be suspended until 24 hours post-treatment. Medical management and acute post stroke care should follow the ASA guidelines.
 - Any neurological determination should be evaluated by urgent CT scan and other evaluations as indicated according to investigator/hospital best practice.
 - As in all surgical interventions, monitoring of intra-procedural blood loss is recommended so that appropriate management may be instituted.
 - Limit the usage of the AXS Vecta Aspiration Catheter to arteries greater than the catheter's outer diameter.
 - Excessive aspiration with the distal tip of the AXS Vecta Aspiration Catheter covered by the vessel wall may cause vessel injury. Carefully investigate location of the distal tip under fluoroscopy prior to aspiration.
 - There is an inherent risk with the use of angiography and fluoroscopy.
 - When transporting the VC-701 Cliq pump, utilize the pump handle.



Stryker Neurovascular
47900 Bayside Parkway
Fremont, CA 94538

strykerneurovascular.com

Date of Release: FEB/2019

EX_EN_US

Copyright © 2019 Stryker
AP002427 v1.0 | Page 2 of 2

Trevo® XP ProVue Retrievers

See package insert for complete indications, contraindications, warnings and instructions for use.

INDICATIONS FOR USE

- The Trevo Retriever is indicated for use to restore blood flow in the neurovasculature by removing thrombus for the treatment of acute ischemic stroke to reduce disability in patients with a persistent, proximal anterior circulation, large vessel occlusion, and smaller core infarcts who have first received intravenous tissue plasminogen activator (IV t-PA). Endovascular therapy with the device should start within 6 hours of symptom onset.
- The Trevo Retriever is intended to restore blood flow in the neurovasculature by removing thrombus in patients experiencing ischemic stroke within 8 hours of symptom onset. Patients who are ineligible for intravenous tissue plasminogen activator (IV t-PA) or who fail IV t-PA therapy are candidates for treatment.
- The Trevo Retriever is indicated for use to restore blood flow in the neurovasculature by removing thrombus for the treatment of acute ischemic stroke to reduce disability in patients with a persistent, proximal anterior circulation, large vessel occlusion of the internal carotid artery (ICA) or middle cerebral artery (MCA)-M1 segments with smaller core infarcts (0-50cc for age < 80 years, 0-20cc for age ≥ 80 years). Endovascular therapy with the device should start within 6-24 hours of time last seen well in patients who are ineligible for intravenous tissue plasminogen activator (IV t-PA) or who fail IV t-PA therapy.

COMPLICATIONS

Procedures requiring percutaneous catheter introduction should not be attempted by physicians unfamiliar with possible complications which may occur during or after the procedure. Possible complications include, but are not limited to, the following: air embolism; hematoma or hemorrhage at puncture site; infection; distal embolization; pain/headache; vessel spasm, thrombosis, dissection, or perforation; emboli; acute occlusion; ischemia; intracranial hemorrhage; false aneurysm formation; neurological deficits including stroke; and death.

Copyright © 2018 Stryker
AP002078 v1.0 | Page 2 of 2



Stryker Neurovascular
47900 Bayside Parkway
Fremont, CA 94538

strykerneurovascular.com

Date of Release: APR/2018

EX_EN_US

REGISTER TODAY

<https://2019.asnr.org>

CONNECTION SCIENCE & PRACTICE

ASNR

American Society of Neuroradiology

May 18-23, 2019 | Boston

ASFNR | ASHNR | ASPNR | ASSR | SNIS

*Join us to be inspired by
neuroradiology's leaders and legends;
connect with colleagues and friends; and
prepare to innovate on behalf of patients
and neuroradiology.*



Ingest more.

The AXS Vecta 74 Aspiration Catheter is the first **extra-large bore aspiration catheter** on the market, providing a 0.074in lumen designed to ingest the clot.

Redefine aspiration.

AXS Vecta™ 74
ASPIRATION CATHETER

AJNR



AMERICAN JOURNAL OF NEURORADIOLOGY

APRIL 2019
VOLUME 40
NUMBER 4
WWW.AJNR.ORG


















Publication Preview at www.ajnr.org features articles released in advance of print. Visit www.ajnrblog.org to comment on AJNR content and chat with colleagues and AJNR's News Digest at <http://ajnrndigest.org> to read the stories behind the latest research in neuroimaging.

583 PERSPECTIVES *I. Ikuta*

REVIEW ARTICLES

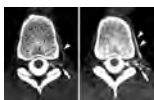
-   584 **Imaging Review of New and Emerging Sinonasal Tumors and Tumor-Like Entities from the Fourth Edition of the *World Health Organization Classification of Head and Neck Tumors*** *K.E. Dean, et al.* **HEAD & NECK**
-   591 **On Flow Diversion: The Changing Landscape of Intracerebral Aneurysm Management** *A.A. Dmytriv, et al.* **INTERVENTIONAL**

GENERAL CONTENTS

-    601 **Behavioral and Structural Effects of Single and Repeat Closed-Head Injury** *Y.-C.J. Kao, et al.* **ADULT BRAIN**
-   609 **Periventricular White Matter Abnormalities on Diffusion Tensor Imaging of Postural Instability Gait Disorder Parkinsonism** *S.Y.Z. Tan, et al.* **ADULT BRAIN**
-   614 **Gadolinium-Enhanced Susceptibility-Weighted Imaging in Multiple Sclerosis: Optimizing the Recognition of Active Plaques for Different MR Imaging Sequences** *L.L.F. do Amaral, et al.* **ADULT BRAIN**
-  620 **Leptomeningeal Contrast Enhancement Is Related to Focal Cortical Thinning in Relapsing-Remitting Multiple Sclerosis: A Cross-Sectional MRI Study** *N. Bergsland, et al.* **ADULT BRAIN**
-   626 **Moving Toward a Consensus DSC-MRI Protocol: Validation of a Low-Flip Angle Single-Dose Option as a Reference Standard for Brain Tumors** *K.M. Schmainda, et al.* **ADULT BRAIN**
-   634 **Morphologic Features on MR Imaging Classify Multifocal Glioblastomas in Different Prognostic Groups** *J. Pérez-Beteta, et al.* **ADULT BRAIN**
-   641 **Effects of Acute Alcohol Consumption on the Human Brain: Diffusional Kurtosis Imaging and Arterial Spin-Labeling Study** *L.M. Kong, et al.* **ADULT BRAIN**
-  648 **Measuring Glymphatic Flow in Man Using Quantitative Contrast-Enhanced MRI** *R. Watts, et al.* **ADULT BRAIN**
-  652 **Risk of Acute Kidney Injury with Consecutive, Multidose Use of Iodinated Contrast in Patients with Acute Ischemic Stroke** *Z.Y. Jia, et al.* **ADULT BRAIN
PATIENT SAFETY**
-  655 **Clot Burden Score and Early Ischemia Predict Intracranial Hemorrhage following Endovascular Therapy** *V. Yogendrakumar, et al.* **INTERVENTIONAL**

AJNR (Am J Neuroradiol ISSN 0195-6108) is a journal published monthly, owned and published by the American Society of Neuroradiology (ASNR), 800 Enterprise Drive, Suite 205, Oak Brook, IL 60523. Annual dues for the ASNR include \$170.00 for journal subscription. The journal is printed by Cadmus Journal Services, 5457 Twin Knolls Road, Suite 200, Columbia, MD 21045; Periodicals postage paid at Oak Brook, IL and additional mailing offices. Printed in the U.S.A. POSTMASTER: Please send address changes to American Journal of Neuroradiology, P.O. Box 3000, Denville, NJ 07834, U.S.A. Subscription rates: nonmember \$410 (\$480 foreign) print and online, \$320 online only; institutions \$470 (\$540 foreign) print and basic online, \$935 (\$1000 foreign) print and extended online, \$380 online only (basic), extended online \$825; single copies are \$35 each (\$40 foreign). Indexed by PubMed/Medline, BIOSIS Previews, Current Contents (Clinical Medicine and Life Sciences), EMBASE, Google Scholar, HighWire Press, Q-Sensei, RefSeek, Science Citation Index, SCI Expanded, Meta/CZI and ReadCube. Copyright © American Society of Neuroradiology.

-   661 **Metallic Hyperdensity Sign on Noncontrast CT Immediately after Mechanical Thrombectomy Predicts Parenchymal Hemorrhage in Patients with Acute Large-Artery Occlusion** *C. Xu, et al.* **INTERVENTIONAL**
- 668 **Endovascular Treatment for Low-Grade (Spetzler-Martin I–II) Brain Arteriovenous Malformations** *H. Baharvahdat, et al.* **INTERVENTIONAL**
- 673 **Commentary**
Curing Low-Grade Brain AVMs with Embolization? *J.L. Brisman* **INTERVENTIONAL**
- 675 **Morphologic Change of Flow-Related Aneurysms in Brain Arteriovenous Malformations after Stereotactic Radiosurgery** *Y.-S. Tsuei, et al.* **INTERVENTIONAL**
-   681 **Comparison of Prasugrel and Clopidogrel Used as Antiplatelet Medication for Endovascular Treatment of Unruptured Intracranial Aneurysms: A Meta-Analysis** *F. Cagnazzo, et al.* **INTERVENTIONAL**
-   687 **Treatment of Unruptured Distal Anterior Circulation Aneurysms with Flow-Diverter Stents: A Meta-Analysis** *F. Cagnazzo, et al.* **INTERVENTIONAL**
- 694 **Aneurysm Remnants after Flow Diversion: Clinical and Angiographic Outcomes** *T.P. Madaelil, et al.* **INTERVENTIONAL**
-  699 **Imaging-Guided Superior Ophthalmic Vein Access for Embolization of Dural Carotid Cavernous Fistulas: Report of 20 Cases and Review of the Literature** *M.K.S. Heran, et al.* **INTERVENTIONAL**
-   703 **Flow Patterns in Carotid Webs: A Patient-Based Computational Fluid Dynamics Study** *K.C.J. Compagne, et al.* **EXTRACRANIAL VASCULAR**
- 709 **Prevalence of Superior Semicircular Canal Dehiscence on High-Resolution CT Imaging in Patients without Vestibular or Auditory Abnormalities** *A.W. Berning, et al.* **HEAD & NECK**
-  713 **Determinants of Radiation Dose in Selective Ophthalmic Artery Chemosurgery for Retinoblastoma** *A.M. Qureshi, et al.* **PEDIATRICS PATIENT SAFETY**
-  718 **Morphologic Evolution and Coordinated Development of the Fetal Lateral Ventricles in the Second and Third Trimesters** *Z. Li, et al.* **PEDIATRICS**
- 726 **Brain MRI Findings in Pediatric-Onset Neuromyelitis Optica Spectrum Disorder: Challenges in Differentiation from Acute Disseminated Encephalomyelitis** *E. Bulut, et al.* **PEDIATRICS**
-   732 **CT and Multimodal MR Imaging Features of Embryonal Tumors with Multilayered Rosettes in Children** *V. Dangouloff-Ros, et al.* **PEDIATRICS**
-    737 **Convolutional Neural Network–Based Automated Segmentation of the Spinal Cord and Contusion Injury: Deep Learning Biomarker Correlates of Motor Impairment in Acute Spinal Cord Injury** *D.B. McCoy, et al.* **SPINE**
-   745 **Spontaneous Intracranial Hypotension: A Systematic Imaging Approach for CSF Leak Localization and Management Based on MRI and Digital Subtraction Myelography** *R.I. Farb, et al.* **SPINE**
- 754 **Decubitus CT Myelography for Detecting Subtle CSF Leaks in Spontaneous Intracranial Hypotension** *P.G. Kranz, et al.* **SPINE**



Axial prone CT myelogram (left) shows vague filling of a network of paraspinal veins lateral to the nerve root. Axial image (right) from a decubitus CTM performed after dynamic myelography on a subsequent day shows increased filling of the lateral veins from the CSF-venous fistula.

- E19** **Paranasal Sinus CT Is of Variable Value in Patients with Pediatric Cancer with Neutropenic Fever** *C.M. Pfeifer*

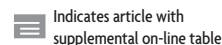
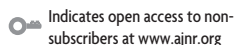
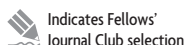
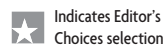
ONLINE FEATURES

LETTERS

BOOK REVIEWS

R.M. Quencer, Section Editor

Please visit www.ajnrblog.org to read and comment on Book Reviews.



Official Journal:

American Society of Neuroradiology
 American Society of Functional Neuroradiology
 American Society of Head and Neck Radiology
 American Society of Pediatric Neuroradiology
 American Society of Spine Radiology

EDITOR-IN-CHIEF

Jeffrey S. Ross, MD

Professor of Radiology, Department of Radiology,
 Mayo Clinic College of Medicine, Phoenix, AZ

SENIOR EDITORS

Harry J. Cloft, MD, PhD

Professor of Radiology and Neurosurgery,
 Department of Radiology, Mayo Clinic College of
 Medicine, Rochester, MN

Thierry A.G.M. Huisman, MD

Radiologist-in-Chief, Texas Children's Hospital,
 Houston, TX

Yvonne W. Lui, MD

Associate Professor of Radiology,
 Chief of Neuroradiology,
 New York University School of Medicine,
 New York, NY

C.D. Phillips, MD, FACR

Professor of Radiology, Weill Cornell Medical
 College, Director of Head and Neck Imaging,
 New York-Presbyterian Hospital, New York, NY

Pamela W. Schaefer, MD

Clinical Director of MRI and Associate Director of
 Neuroradiology, Massachusetts General Hospital,
 Boston, Massachusetts, Associate Professor,
 Radiology, Harvard Medical School, Cambridge, MA

Charles M. Strother, MD

Professor of Radiology, Emeritus, University of
 Wisconsin, Madison, WI

STATISTICAL SENIOR EDITOR

Bryan A. Comstock, MS

Senior Biostatistician,
 Department of Biostatistics,
 University of Washington, Seattle, WA

ARTIFICIAL INTELLIGENCE DEPUTY EDITOR

Christopher G. Filippi, MD

Professor and Vice Chair of Biomedical and
 Translational Science,
 Donald and Barbara Zucker School of Medicine at
 Hofstra/Northwell,
 Lenox Hill Hospital and Greenwich Village
 Healthplex, New York, NY

EDITORIAL BOARD

Ashley H. Aiken, Atlanta, GA
 Lea M. Alhilali, Phoenix, AZ
 Kubilay Aydin, Istanbul, Turkey
 John D. Barr, Dallas, TX
 Ari Blitz, Baltimore, MD
 Barton F. Branstetter IV, Pittsburgh, PA
 Jonathan L. Brisman, Lake Success, NY
 Keith Cauley, Danville, PA
 James Y. Chen, San Diego, CA
 Asim F. Choudhri, Memphis, TN
 Daniel Chow, Irvine, CA
 J. Matthew Debnam, Houston, TX
 Seena Dehkharghani, New York, NY
 Yonghong Ding, Rochester, MN
 Clifford J. Eskey, Hanover, NH
 Saeed Fakhraan, Phoenix, AZ
 Massimo Filippi, Milan, Italy
 Reza Forghani, Montreal, Quebec, Canada
 Nils D. Forkert, Calgary, Alberta, Canada
 Wende N. Gibbs, Los Angeles, CA
 Christine M. Glastonbury, San Francisco, CA
 John L. Go, Los Angeles, CA
 Philipp Götz, Erlangen, Germany
 Allison Grayev, Madison, WI
 Brent Griffith, Detroit, MI
 Ajay Gupta, New York, NY
 Rakesh Kumar Gupta, Haryana, India
 Lotfi Hacein-Bey, Sacramento, CA
 Christopher P. Hess, San Francisco, CA
 Andrei Holodny, New York, NY
 Benjamin Huang, Chapel Hill, NC
 Mahesh V. Jayaraman, Providence, RI
 Valerie Jewells, Chapel Hill, NC
 Christof Karmonik, Houston, TX
 Timothy J. Kaufmann, Rochester, MN
 Hillary R. Kelly, Boston, MA
 Toshihumi Kinoshita, Akita, Japan
 Kenneth F. Layton, Dallas, TX
 Alexander Lerner, Los Angeles, CA
 Michael Lev, Boston, MA
 Karl-Olof Lovblad, Geneva, Switzerland
 Franklin A. Marden, Chicago, IL
 Joseph C. McGowan, Merion Station, PA
 Stephan Meckel, Freiburg, Germany
 Christopher J. Moran, St. Louis, MO
 Takahisa Mori, Kamakura City, Japan
 Suresh Mukherji, Ann Arbor, MI
 Alexander J. Nemeth, Chicago, IL
 Renato Hoffmann Nunes, Sao Paulo, Brazil
 Sasan Partovi, Cleveland, OH
 Laurent Pierot, Reims, France
 Jay J. Pillai, Baltimore, MD
 Whitney B. Pope, Los Angeles, CA
 Joana Ramalho, Lisbon, Portugal
 Otto Rapalino, Boston, MA

Álex Rovira-Cañellas, Barcelona, Spain
 Paul M. Ruggieri, Cleveland, OH
 Amit M. Saindane, Atlanta, GA
 Erin Simon Schwartz, Philadelphia, PA
 Lubdha M. Shah, Salt Lake City, UT
 Maksim Shapiro, New York, NY
 Timothy Shepherd, New York, NY
 Mark S. Shiroishi, Los Angeles, CA
 Bruno P. Soares, Baltimore, MD
 Maria Vittoria Spampinato, Charleston, SC
 Khin Khin Tha, Sapporo, Hokkaido, Japan
 Krishnamoorthy Thamburaj, Hershey, PA
 Cheng Hong Toh, Taipei, Taiwan
 Aquilla S. Turk, Charleston, SC
 Anja G. van der Kolk, Utrecht, the Netherlands
 Willem Jan van Rooij, Tilburg, the Netherlands
 Arastoo Vossough, Philadelphia, PA
 Elysa Widjaja, Toronto, Ontario, Canada
 Max Wintermark, Stanford, CA
 Ronald L. Wolf, Philadelphia, PA
 Kei Yamada, Kyoto, Japan
 Carlos Zamora, Chapel Hill, NC
 Vahe M. Zohrabian, New Haven, CT

EDITORIAL FELLOW

Alireza Radmanesh, New York, NY

SPECIAL CONSULTANTS TO THE EDITOR

AJNR Blog Editor

Neil Lall, Denver, CO

Case of the Month Editor

Nicholas Stence, Aurora, CO

Case of the Week Editors

Juan Pablo Cruz, Santiago, Chile

Sapna Rawal, Toronto, Ontario, Canada

Classic Case Editor

Sandy Cheng-Yu Chen, Taipei, Taiwan

Health Care and Socioeconomics Editor

Pina C. Sanelli, New York, NY

Physics Editor

Greg Zaharchuk, Stanford, CA

Podcast Editor

Wende N. Gibbs, Los Angeles, CA

Twitter Editor

Jennifer McCarty, Houston, TX

Founding Editor
 Juan M. Taveras

Editors Emeriti

Mauricio Castillo, Robert I. Grossman,
 Michael S. Huckman, Robert M. Quencer

Managing Editor
 Karen Halm

Assistant Managing Editor

Laura Wilhelm

Communications Coordinator

Rebecca Artz

Executive Director, ASNR

Mary Beth Hepp



Title: A panoramic view from Lydgate State Park on the Hawaiian island of Kauai. This photo was taken during the 49th Annual Meeting of the Western Neuroradiological Society in October 2017.

Ichiro Ikuta, MD, MMSc, Neuroradiology Clinical Instructor, Yale University, New Haven, Connecticut

Imaging Review of New and Emerging Sinonasal Tumors and Tumor-Like Entities from the Fourth Edition of the *World Health Organization Classification of Head and Neck Tumors*

K.E. Dean, D. Shatzkes, and C.D. Phillips



ABSTRACT

SUMMARY: The sinonasal tract is an environment diverse with neoplasia. Given the continued discovery of entities generally specific to the sinonasal tract, the fourth edition of the *World Health Organization Classification of Head and Neck Tumors* was released in 2017. It describes 3 new, well-defined entities and several less-defined, emerging entities. The new entities are seromucinous hamartomas, nuclear protein in testis carcinomas, and biphenotypic sinonasal sarcomas. Emerging entities include human papillomavirus–related sinonasal carcinomas, SWI/SNF-related matrix-associated actin-dependent regulator of chromatin subfamily B member 1–deficient sinonasal carcinomas, renal cell-like adenocarcinomas, and chondromesenchymal hamartomas. The literature thus far largely focuses on the pathology of these entities. Our goal in this report was to familiarize radiologists with these new diagnoses and to provide available information regarding their imaging appearances.

ABBREVIATIONS: HPV = human papillomavirus; NUT = nuclear protein in testis; NMC = nuclear protein in testis midline carcinomas; SCC = squamous cell carcinoma; SH = seromucinous hamartoma; SWI/SNF = SWItch/Sucrose Non-Fermentable; SMARCB1 = SWI/SNF-related matrix-associated actin-dependent regulator of chromatin subfamily B member 1; SNUC = sinonasal undifferentiated carcinoma; REAH = respiratory epithelial adenomatoid hamartoma; WHO = World Health Organization

The complex anatomy and histology, numerous potential carcinogenic exposures, and vast cancer genomics cause the aerodigestive tract to be affected by a diverse range of tumors and tumor-like entities. To stay current, the classification of head and neck tumors is frequently redefined. The fourth edition of the *World Health Organization Classification of Head and Neck Tumors*, released in 2017, includes 3 new, well-defined entities and several less-defined, emerging entities within the sinonasal tract. The emerging entities are provisional diagnoses or are only described in the context of differential diagnoses.^{1,2}

The new sinonasal entities are seromucinous hamartomas, nuclear protein in testis (NUT) carcinomas, and biphenotypic sinonasal sarcomas. Emerging entities include SWI/SNF-related matrix-associated actin-dependent regulator of chromatin subfamily B member 1 (SMARCB1)–deficient sinonasal carcinomas, renal cell-like adenocarcinomas, and chondromesenchymal

hamartomas. Human papillomavirus (HPV)-related sinonasal carcinoma with adenoid cystic features is described as an emerging entity within the World Health Organization (WHO) update. A subsequently published, expanded series suggests that this entity may be a distinct one, termed “HPV-related multiphenotypic sinonasal carcinoma.”³

To date, the literature regarding these updates largely concerns the histopathologic features.^{2,4,5} A radiologist may see these rare entities reported as pathologic diagnoses, and some familiarity with the nomenclature, pathology, and imaging features is important. This article aims to briefly review the histopathologic classifications of sinonasal tumors as well as provide imaging examples and reported imaging characteristics of these new and emerging entities. While there are no true pathognomonic imaging features and biopsy remains the criterion standard, there are findings that may be useful to characterize these lesions.

REVIEW OF HISTOLOGIC TYPES OF SINONASAL TUMORS

Accurate interpretation of sinonasal tumor imaging by neuroradiologists necessitates a fundamental understanding of the histologic subtypes. Basic classification groups include squamous cell carcinomas (SCCs), adenocarcinomas, sarcomatous/mesenchymal tumors, neuroectodermal tumors, salivary neoplasms, papillomas, respiratory epithelial lesions, hematolymphoid tumors, and tumor-like entities (On-line Table).

Received October 26, 2018; accepted after revision December 20.

From the Department of Radiology (K.E.D., C.D.P.), New York-Presbyterian/Weill Cornell Medical Center, New York, New York; and Department of Radiology (D.S.), Lenox Hill Hospital, Northwell Health, New York, New York.

Please address correspondence to Kathryn E. Dean, New York-Presbyterian/Weill Cornell Medical Center, Department of Radiology, 525 E 68th St, New York, NY 10065; e-mail: ked9042@med.cornell.edu; @kateedean

Indicates open access to non-subscribers at www.ajnr.org

Indicates article with supplemental on-line table.

<http://dx.doi.org/10.3174/ajnr.A5978>

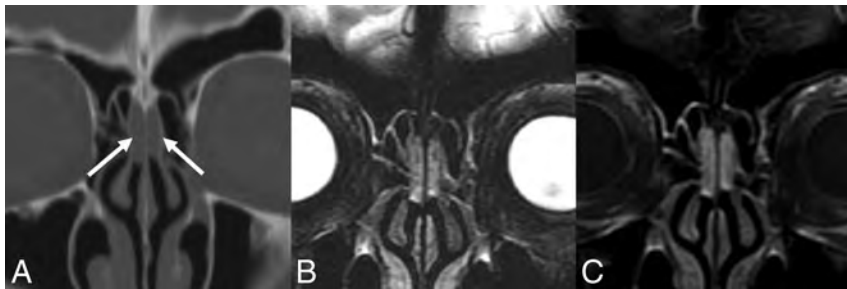


FIG 1. REAH. A, Coronal noncontrast CT shows mildly expansile soft tissue in the bilateral olfactory clefts without adjacent bony erosion or destruction (*white arrows*). Coronal T2 fat-saturated (B) and coronal T1 postcontrast, fat-saturated (C) MR images in the same patient show the lesions to be heterogeneous and hyperintense to the cortex on T2WI and enhancing.

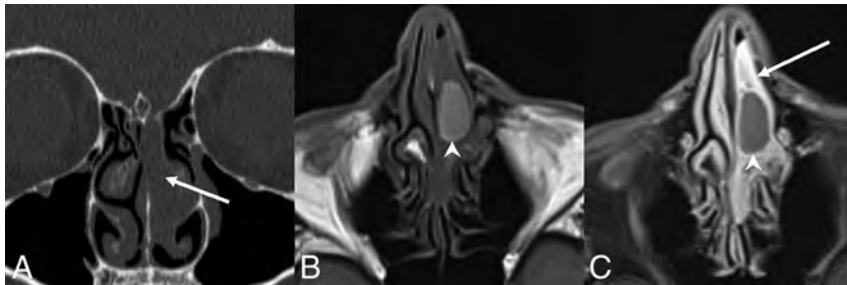


FIG 2. SH. A, Coronal noncontrast CT shows expansile soft tissue in the left olfactory recess extending inferiorly into the superior nasal cavity (*white arrows*) without erosive or destructive bony changes, similar to an REAH. Axial T1 precontrast (B) and axial T1 postcontrast, fat-saturated (C) images demonstrate predominantly homogeneous enhancement. The relatively hyperintense, nonenhancing central component on T1WI suggests proteinaceous content (*white arrowheads*), possibly reflecting glandular secretions. Areas of relative central hyperintense signal on precontrast T1WI are not described in other published examples.

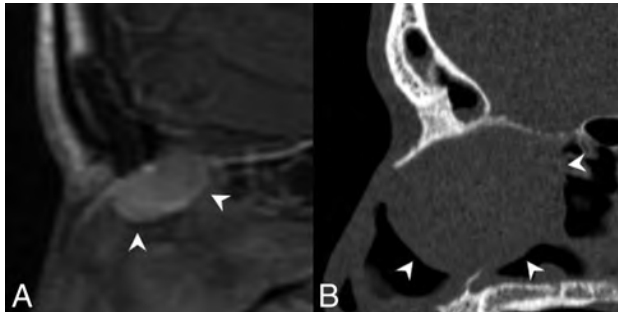


FIG 3. Crescent sign. A, Sagittal T1 postcontrast MR image of an REAH. B, Sagittal noncontrast CT image of a seromucinous hamartoma demonstrates a characteristic half-moon morphology (*white arrowheads*), which we have termed a “crescent sign” when the lesions arise in the olfactory recess.

Squamous cell carcinomas are defined as keratinizing and nonkeratinizing subtypes.⁶ Nonkeratinizing SCCs account for about 15%–20% of sinonasal SCCs.⁴ Under the umbrella of nonkeratinizing SCC is the emerging subgroup of HPV-related sinonasal carcinoma.^{1,7}

Sinonasal adenocarcinomas are classified as either intestinal or nonintestinal subtypes.⁸ Nonintestinal types are either high- or low-grade.^{9,10} Emerging within the subgroup of low-grade nonintestinal is one that resembles conventional clear cell adenocarcinoma, thus termed “renal cell-like adenocarcinoma.”^{1,2}

Other histologic carcinoma groups include neuroendocrine tumor, lymphoepithelial carcinoma, sinonasal undiffer-

entiated carcinoma (SNUC) including the emerging subtype of SMARCB1-deficient sinonasal carcinoma, and the newly defined NUT carcinoma.^{1,2,11} Biphenotypic sinonasal sarcoma is a newly defined sinonasal sarcomatous/mesenchymal tumor. New tumor-like entities include seromucinous hamartomas and chondromesenchymal hamartomas.¹

NEW ENTITIES

Seromucinous Hamartoma

Clinical and Histopathologic Review.

Sinonasal epithelial hamartomas are benign lesions that contain components of normal ciliated respiratory epithelium. Subtypes include respiratory epithelial adenomatoid hamartoma (REAH) and the newly defined seromucinous hamartoma (SH).^{12–15} SH has increased seromucinous glandular components compared with REAH, akin to adenosis.¹⁶

Both lesions affect adults with a male predilection, 7:1 for REAH and 5:2 for SH. Presenting symptoms for both include nasal congestion, anosmia, and rhinorrhea.^{15,17} REAHs have been described in isolation and in the

setting of concomitant sinonasal disease from inflammatory polyposis to malignancy, an association that suggests a potential reactive etiology of these lesions.^{18,19} Recurrence of REAHs and SHs after resection is rare.¹⁶

Imaging Features. Just as there is histologic overlap of REAH and SH, their imaging features are similar. REAHs classically arise in the olfactory clefts. Other described sites for both lesions include the nasal septum, middle turbinate, and uncinate process. The lesions may be bilateral.^{16,17,20}

REAHs are well-defined, near muscle density, and homogeneous on CT. The olfactory cleft is often expanded and smoothly remodeled without erosive changes.¹⁸ REAHs are heterogeneous on T2WI and isointense on T1WI relative to the cortex and enhance uniformly (Fig 1).²¹ To our knowledge, no substantial dedicated literature regarding the appearance of SHs on imaging exists to date. Published CT images in the pathology literature show an appearance similar to that of REAH.²⁰ MR images of a proved SH published here show similar signal on T2WI and enhancement patterns (Fig 2). On the sagittal images, both often have a characteristic half-moon appearance when situated in the olfactory cleft, here described as a “crescent sign” (Fig 3).

Diagnostic Tips and Differentials. Differentiating REAH from SH is not possible by imaging alone. The presence of frank bony erosion or skull base defects would favor encephalocele, carcinoma, or esthesioneuroblastoma (other soft-tissue lesions typical of the olfactory cleft) over REAH, SH, or benign inflammatory polyp.²² The

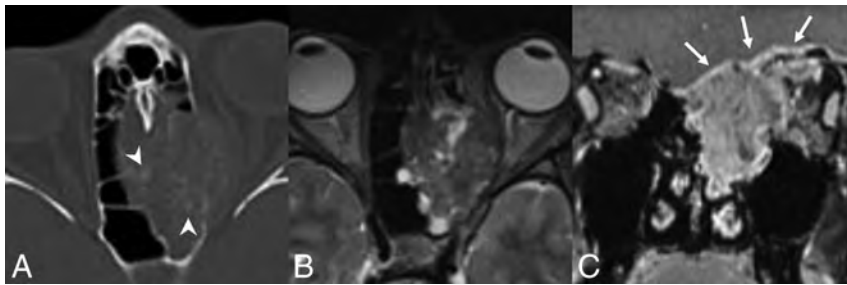


FIG 4. NUT carcinoma. A, Axial noncontrast CT image shows a locally destructive mass centered within the left ethmoid sinus extending into the left orbit and laterally displacing the medial rectus muscle. There is faint mineralization within the mass (white arrowheads). Axial T2 fat-saturated (B) and coronal T1 postcontrast, fat-saturated (C) MR images from the same patient show the mass to be heterogeneous but predominantly hypointense to the cortex on T2WI and avidly enhancing. The mass extends into the anterior cranial fossa with dural involvement (white arrows). Images are courtesy of Dr Nafi Aygun, Johns Hopkins Hospital.

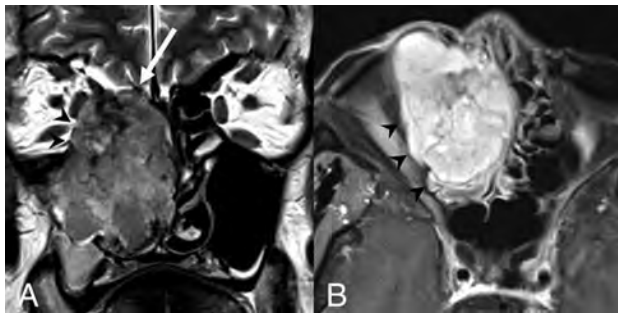


FIG 5. Biphenotypic sinonasal sarcoma. Coronal T2 (A) and axial T1 postcontrast, fat-saturated (B) MR images show a well-margined but locally aggressive right nasoethmoid mass involving the right maxillary sinus. The mass extends through the right lamina papyracea to involve the right orbit (black arrowheads) and through the right lateral lamella and fovea ethmoidalis into the right anterior cranial fossa (white arrow). Heterogeneous but predominantly isointense signal relative to the cortex and avid contrast enhancement are noted.

“crescent sign” morphology on sagittal images, in our experience, is suggestive of REAH and SH within the olfactory cleft.

NUT Carcinoma

Clinical and Histopathologic Review. Nuclear protein in testis midline carcinomas (NMCs) were initially described in the mediastinum and more recently in the sinonasal cavity. Although there are <100 cases reported, the clear genomics and histology allow the sinonasal NMCs to be included as a new entity in the latest WHO release.²³⁻²⁵ NMCs show undifferentiated round blue cells growing in the submucosa abruptly juxtaposed to mature keratinizing squamous cells.^{26,27} The diagnosis requires identification of the *NUTM1* gene rearrangement, often with *BRD4*.²⁸

Sinonasal nuclear protein in testis midline carcinoma is highly aggressive and infiltrative, with a poor prognosis and a median progression-free survival of 6.6 months and an overall median survival of 9.7 months.²⁹ Presenting symptoms include nasal obstruction, epistaxis, and orbital pain with a wide age range at presentation and a slight female predominance.^{25,30}

Imaging Features. While no substantial literature regarding imaging of sinonasal NMCs exists, case reports and images here published show aggressive features similar to those within the chest, where there is often airway and vascular invasion.³¹ In the sinonasal

cavity, rapid growth and infiltration may result in orbital or cranial involvement. Nearly half have regional or distant metastases at presentation.^{25,27,32}

On CT, the mass is near muscle density. Bony hyperostosis is described.^{31,32} In the case published here, there are internal mineralizations but no dystrophic calcifications as seen in thoracic NMCs.³¹ On MR imaging, the tumors are hypointense on T1WI and heterogeneous on T2WI relative to the cortex and enhancing (Fig 4).³³ Published cases are FDG-avid.³⁴

Diagnostic Tips and Differentials. The locally aggressive imaging characteristics of sinonasal NMCs are almost entirely nonspecific, with a multitude of potential differentials, including other carcinomas, lymphomas, and sarcomas. PET/CT may play an important role in staging, given the propensity for distant metastases at presentation.³³

Biphenotypic Sinonasal Sarcoma

Clinical and Histopathologic Review. Biphenotypic sinonasal sarcomas are histologically similar to cellular schwannomas or malignant peripheral nerve sheath tumors, with infiltrating spindle cells and entrapped invaginations of normal sinonasal epithelium.³⁴⁻³⁶ Diagnosis requires the rearrangement of the *PAX3* gene, often with *MAML3*.^{35,37,38}

With about 50 reported cases, there is a suggested female predominance (2–3:1), often occurring in the sixth decade.^{2,35} Described throughout the sinonasal tract, the most common locations of tumors include the superior nasal cavity and ethmoid sinuses, and they present with facial pressure and nasal obstruction.⁴⁰ The tumors are slow growing with no published cases with metastases to date. Local recurrence, however, is reported in about half of the cases.^{35,39}

Imaging Features. The masses are well-margined but locally aggressive and can erode through the skull base or into the orbit. Associated hyperostotic bone formation is described on CT.^{35,40} The masses avidly enhance and are isointense-to-hypointense to the cortex on T2WI (Fig 5).

Diagnostic Tips and Differentials. Exceedingly rare with nonspecific imaging findings, biphenotypic sinonasal sarcomas have imaging findings similar to those of many other primary sinonasal carcinomas and sarcomas. Hyperostotic bone formation is described in several of the published cases but is again nonspecific.³⁵

EMERGING ENTITIES: PROVISIONAL & DIFFERENTIAL DIAGNOSES

HPV-Related Sinonasal Carcinoma

Clinical and Histopathologic Review. The sinonasal cavity is a common location within the aerodigestive tract for HPV-related carcinomas. Twenty-to-thirty percent of sinonasal carcinomas

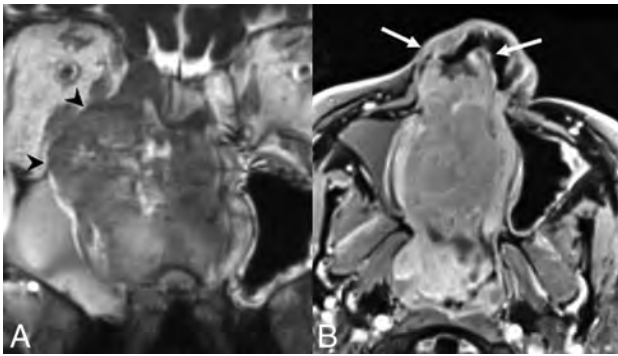


FIG 6. HPV-related sinonasal carcinoma, a nonmultiphenotypic variant. Coronal T2 (A) and axial T1 postcontrast, fat-saturated (B) MR images show a right nasoethmoid mass with extension to the right maxillary sinus and orbit (*black arrowheads*) as well as the left nasal cavity. There is anterior extension into the right nasal vestibule (*white arrows*). The mass demonstrates heterogeneous hyperintensity relative to the cortex on T2WI and avidly enhances. Images are courtesy of Dr Nafi Aygun, Johns Hopkins Hospital.

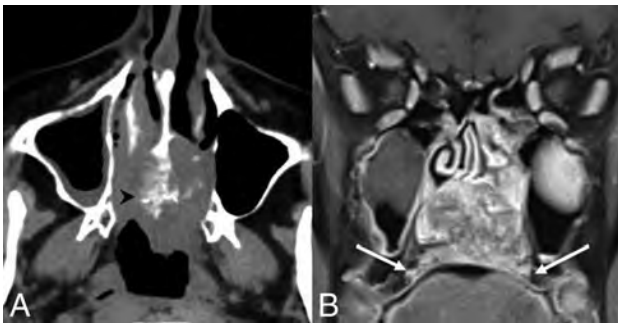


FIG 7. HPV-related multiphenotypic sinonasal carcinoma. Axial non-contrast CT (A) and coronal T1 postcontrast, fat-saturated (B) MR images show an aggressive mass centered in the inferior nasal cavity. The mass is isodense to muscle with an aggressive periosteal reaction along the nasal septum (*black arrowhead*). The mass is enhancing and locally destructive, invading the marrow of the hard palate (*white arrows*).

have associated high-risk HPV subtypes.^{2,7,41} Sinonasal HPV-related carcinoma remains an emerging entity because the histopathology is less clear and no definitive prognostic benefit to HPV association is known as in the oropharynx. Preliminary evidence is at least suggestive of improved disease-free and overall survival.^{7,41,42}

There are several known HPV-related sinonasal carcinoma variants (squamous, papillary, small-cell, adenosquamous, basaloid). One particular variant is only described in the sinonasal tract: HPV-related multiphenotypic sinonasal carcinoma.^{3,7} At the time of the WHO update publication, this variant was called HPV-related carcinoma with adenoid cystic-like features, given the associated microcystic pseudoductal spaces. It was a provisional entity with only 9 documented cases.⁷ A recent expanded series of 49 cases describes a more complex histopathology with multiple subphenotypes and proposes a change from a provisional diagnosis to a distinct entity renamed “HPV-related multiphenotypic sinonasal carcinoma.”³

Arising in adults, the multiphenotypic variant commonly presents with nasal congestion and epistaxis. Around 90% of the documented cases originate in the nasal cavity. Distant metastases

are described in 2 patients, 1 to the lung and 1 to a finger. Approximately 25% have local recurrence.⁴³

Imaging Features. Little is published on the imaging findings of HPV-related sinonasal carcinomas as a group. Pathology-proved cases here published are similar to those of other sinonasal SCCs destroying, remodeling, and/or invading bone. They have variable signal relative to the cortex on T2WI and enhance on MR imaging (Figs 6 and 7). The multiphenotypic variant case shown here was FDG-avid.

Perineural tumor spread is uncommon in the multiphenotypic variant, unlike true adenoid cystic carcinoma.^{2,3} No cystic nodal metastases have yet been described.⁴³

Diagnostic Tips and Differentials. HPV-related sinonasal carcinoma variants, including the multiphenotypic type, share many imaging characteristics with one another and with other primary sinonasal carcinomas (SCC, adenocarcinoma, and so forth). Cystic nodal metastases common in HPV-related carcinomas elsewhere in the aerodigestive tract and perineural spread common to true adenoid cystic carcinomas have not yet been described.^{2,3,43}

SMARCB1-Deficient Sinonasal Carcinoma

Clinical and Histopathologic Review. SMARCB1-deficient sinonasal carcinomas are composed of mitotically active epithelioid nests with basaloid features and necrosis similar to SNUC and nonkeratinizing SCC.⁴⁴⁻⁴⁶ Given this histologic overlap, SMARCB1-deficient sinonasal carcinomas may represent a distinct entity or a histologic pattern seen in various other tumors.^{11,47} Diagnosis is by immunohistochemical analysis demonstrating complete loss of SMARCB1 expression, a tumor-suppressor gene implicated in several tumors with rhabdoid features.^{44,45,47,48} SMARCB1-deficient sinonasal carcinoma is an emerging entity currently classified as a SNUC subtype.

SMARCB1-deficient sinonasal carcinomas are more common in women, with a wide age range from young adult to elderly.^{11,48} Local recurrence is common. Frequently with local or distant metastases at diagnosis, approximately 40% of cases are lethal.²

Imaging Features. In an imaging analysis of 17 cases, 8 were centered within the nasoethmoid region.⁴⁹ The tumors are highly aggressive and infiltrative, many demonstrating local skull/brain invasion. Eight cases had dural involvement, with extension through the dura in 3 cases.⁴⁹

On CT, the tumors are isodense to muscle, with calcifications in half of the reported cases. Both expansile and erosive patterns of bony involvement along the skull base are described with a “hair on end” pattern of periosteal reaction in several cases.⁴⁹ On MR imaging, most lesions are isointense on T1WI and variable on T2WI relative to the cortex, predominantly avidly enhancing with moderately restricted diffusion (Fig 8).⁴⁹ All cases were FDG-avid.⁴⁹

Diagnostic Tips and Differentials. Within the broad differential for locally aggressive sinonasal tumors, including SNUC and other carcinomas, SMARCB1-deficient sinonasal carcinoma di-

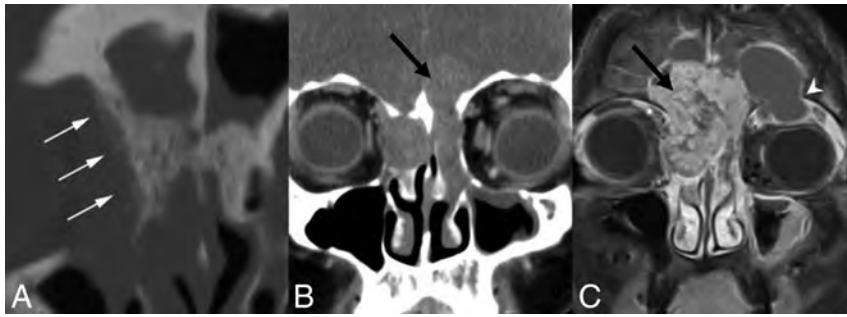


FIG 8. SMARCB1-deficient sinonasal carcinoma. A, Coronal noncontrast CT shows the “hair on end” pattern of calcification/periosteal reaction (*white arrows*) described in several published cases. Coronal postcontrast CT (B) and coronal T1 postcontrast, fat-saturated (C) MR images in a second patient demonstrate an enhancing nasoethmoid mass eroding the floor of the anterior cranial fossa (*black arrows*). There is also erosion of the right lamina papyracea with extraconal orbital extension. A secondary mucocele extends through the left orbital roof (*white arrowhead*).

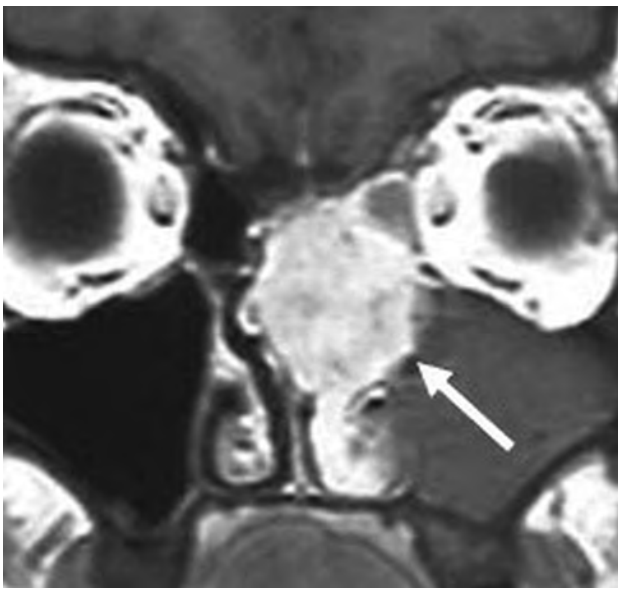


FIG 9. Renal cell-like adenocarcinoma. Coronal T1 postcontrast MR image shows an avidly enhancing, locally destructive, left nasoethmoid mass. The pronounced enhancement is akin to that of a renal cell carcinoma metastasis (*white arrow*). Images are courtesy of Dr Margie Brandwein, Mount Sinai Hospital.

agnosis is dependent on tissue sampling. Calcifications are a commonly found imaging feature.

Renal Cell-Like Adenocarcinoma

Clinical and Histopathologic Review. Renal cell-like adenocarcinoma is a variant of low-grade nonintestinal sinonasal adenocarcinoma with uniform cuboidal/columnar cells with glycogen-rich cytoplasm, akin to clear-cell renal cell carcinoma.^{4,50} With approximately 16 reported cases, it is an emerging entity in the latest WHO edition. The key differential diagnosis is renal cell carcinoma metastasis. In fact, the most common carcinoma to metastasize to the sinonasal tract is renal cell carcinoma.⁵¹ The distinguishing features are immunohistochemical, with renal cell-like adenocarcinoma negative for *PAX8*, a renal cell carcinoma marker, and vimentin.^{4,51,52}

Renal cell-like adenocarcinoma commonly presents with epi-

staxis, with ages ranging from early adulthood to elderly and a female predominance (11:5).^{51,53} The tumor demonstrates indolent growth, and no local recurrence has yet been described.⁵¹

Imaging Features. Published cases show expansile, locally destructive masses with intracranial extension and dural involvement described. On MR imaging, the tumors are heterogeneous to the cortex on T2WI and enhance avidly, similar to renal cell carcinoma.⁵⁴⁻⁵⁶ A key diagnostic criterion is the lack of a concomitant suspicious renal mass (Fig 9).

Diagnostic Tips and Differentials. There are no pathognomonic imaging findings, and the differential is broad, including other aggressive primary and secondary lesions. The absence of a concomitant renal mass is key to diagnosing renal cell-like adenocarcinoma when tissue sampling is suggestive.

Chondromesenchymal Hamartoma

Clinical and Histopathologic Review. Chondromesenchymal hamartoma is an emerging tumor-like entity in children. There is a link to germline or somatic *DICER1* gene mutations, which are also associated with pleuropulmonary blastoma tumor predisposition disorder.⁵⁷ Histology demonstrates nodules of hyaline cartilage within the stromal components of spindle cells.^{58,59}

The tumor is benign but locally aggressive, involving the paranasal sinuses, nasal cavities, and orbits. It is more common in male children with a mean age of 9 years. Nine of 42 cases in 1 series had local recurrence. One documented case had malignant transformation.⁵⁹

Imaging Features. The masses are smoothly margined and expansile, commonly with cystic components and calcifications on CT. Erosion of the skull base is often demonstrated. Half of the cases have internal calcifications. On MR imaging, solid components strongly enhance (Fig 10).^{60,61}

Diagnostic Tips and Differentials. Overlapping imaging findings with other expansile benign-appearing pathology make chondromesenchymal hamartoma a histologic diagnosis but it should be considered in a mixed cystic and calcified sinonasal mass in a child.

CONCLUSIONS

The fourth edition of the *World Health Organization Classification of Head and Neck Tumors* defines several new well-defined and other emerging sinonasal tumor and tumor-like entities. While some of these lesions, including NMCs, biphenotypic sinonasal sarcomas, HPV-related multiphenotypic sinonasal carcinomas, and seromucinous hamartomas, are considered distinct, many others lack clearly defined histopathology and genomics and are thus considered emerging or provisional diagnoses.¹⁻³

In the olfactory cleft, REAH and SH often take on the herein described “crescent sign” morphology on sagittal images. Other-



FIG 10. Chondromesenchymal hamartoma. A, Coronal noncontrast CT in a pediatric patient shows polypoid soft tissue in the bilateral nasal cavities with mild erosive changes focally along the left margin of the nasal septum (white arrow). B, Axial T1 postcontrast, fat-saturated MR image demonstrates heterogeneous enhancement. No cystic or calcified components, frequently described in these lesions, are seen in this case. Images are courtesy of Dr Nafi Aygun, Johns Hopkins Hospital.

wise, these new and emerging entities have similar, locally destructive appearances on imaging. Certain entities have more typical features, such as calcifications with SMARCB1-deficient sinonasal carcinomas and cystic and calcified components in chondromesenchymal hamartomas, but no pathognomonic findings exist. These entities are rare, many exceedingly so, and should generally not be standard in a typical sinonasal mass differential. However, familiarity with these diagnoses is warranted. As more imaging examples of these entities are analyzed, further clarification of any specific imaging characteristics may be useful in refining these differentials.

ACKNOWLEDGMENTS

We would like to thank Dr Nafi Aygun, Johns Hopkins Hospital; Dr Caroline Robson, Boston Children's Hospital; Dr Christine Glastonbury, University of California, San Francisco; and Dr Margaret Brandwein-Weber, Mount Sinai Hospital, for providing excellent sample images.

REFERENCES

1. El-Naggar AK, Chan JKC, Grandis JR, et al, eds. *WHO Classification of Head and Neck Tumours: WHO Classification of Tumours*. Vol 9. 4th ed. Geneva: International Agency for Research on Cancer; 2017
2. Stelow EB, Bishop JA. Update from the 4th edition of the World Health Organization classification of head and neck tumours: tumors of the nasal cavity, paranasal sinuses and skull base. *Head Neck Pathol* 2017;11:3–15 CrossRef Medline
3. Bishop JA, Andreasen S, Hang JF, et al. HPV-related multiphenotypic sinonasal carcinoma: an expanded series of 49 cases of the tumor formerly known as HPV-related carcinoma with adenoid cystic carcinoma-like features. *Am J Surg Pathol* 2017;41:1690–701 CrossRef Medline
4. Thompson LD, Frachi A. New tumor entities in the 4th edition of the World Health Organization classification of head and neck tumors: nasal cavity, paranasal sinuses and skull base. *Virchows Arch* 2018; 472:315–30. CrossRef Medline
5. Bishop AJ. Newly described tumor entities in the sinonasal tract pathology. *Head Neck Pathol* 2016;10:23–31 CrossRef Medline
6. Lewis JS Jr. Sinonasal squamous cell carcinoma: a review with emphasis on emerging histologic subtypes and the role of human papillomavirus. *Head Neck Pathol* 2016;10:60–67 CrossRef Medline
7. Bishop JA, Ogawa T, Stelow EB, et al. Human papillomavirus-re-

- lated carcinoma with adenoid cystic-like features: a peculiar variant of head and neck cancer restricted to the sinonasal tract. *Am J Surg Pathol* 2013;37:836–44 CrossRef Medline
8. Barnes L. Intestinal-type adenocarcinoma of the nasal cavity and paranasal sinuses. *Am J Surg Pathol* 1986;10:192–202 CrossRef Medline
9. Stelow EB, Jo VY, Mills SE, et al. A histologic and immunohistochemical study describing the diversity of tumors classified as sinonasal high-grade nonintestinal adenocarcinomas. *Am J Surg Pathol* 2011;35:971–80 CrossRef Medline
10. Leivo I. Sinonasal adenocarcinoma: update on classification, immunophenotype and molecular features. *Head Neck Pathol* 2016;10: 68–74 CrossRef Medline
11. Bishop JA, Antonescu CR, Westra WH. SMARCB1 (INI1)-deficient carcinomas of the sinonasal tract. *Am J Surg Pathol* 2014;38:1282–89 CrossRef Medline
12. Seol JG, Livolsi VA, O'Malley BW, et al. Respiratory epithelial adenomatoid hamartoma of the bilateral olfactory recesses: a neoplastic mimic? *AJNR Am J Neuroradiol* 2010;31:277–79 CrossRef Medline
13. Kossai M, El Zein S, Wassef M, et al. Olfactory epithelial hamartoma: a new subtype of sinonasal hamartoma. *Am J Surg Pathol* 2018;42: 9–17 CrossRef Medline
14. Wenig BM, Heffner DK. Respiratory epithelial adenomatoid hamartomas of the sinonasal tract and nasopharynx: a clinicopathologic study of 31 cases. *Ann Otol Rhinol Laryngol* 1995;104:639–45 CrossRef Medline
15. Huang YW, Kuo YJ, Ho CT, et al. Sinonasal seromucinous hamartoma. *Eur Arch Otorhinolaryngol* 2018;275:743–49 CrossRef Medline
16. Weinreb I, Gnepp DR, Laver NM, et al. Seromucinous hamartomas: a clinicopathological study of a sinonasal glandular lesion lacking myoepithelial cells. *Histopathology* 2009;54:205–13 CrossRef Medline
17. Tatekawa H, Shimono T, Ohsawa M, et al. Imaging features of benign mass lesions in the nasal cavity and paranasal sinuses according to the 2017 WHO classification. *Jpn J Radiol* 2018;36:361–81 CrossRef Medline
18. Hawley KA, Ahmed M, Sindwani R. CT findings of sinonasal respiratory epithelial adenomatoid hamartomas: a closer look at the olfactory clefts. *AJNR Am J Neuroradiol* 2013;34:1086–90 CrossRef Medline
19. Jo VY, Mills SE, Cathro HP, et al. Low-grade sinonasal adenocarcinomas: the association with and distinction from respiratory epithelial adenomatoid hamartomas and other glandular lesions. *Am J Surg Pathol* 2009;33:401–08 CrossRef Medline
20. Fleming KE, Perez-Ordoñez B, Nasser JG, et al. Sinonasal seromucinous hamartoma: a review of the literature and a case report with focal myoepithelial cells. *Head Neck Pathol* 2012;6:395–99 CrossRef Medline
21. Seol JG, Livolsi VA, O'Malley BW Jr, et al. Respiratory epithelial adenomatoid hamartoma of the bilateral olfactory recesses: a neoplastic mimic? *AJNR Am J Neuroradiol* 2010; 31:277–79 CrossRef Medline
22. Hoxworth JM, Glastonbury CM, Fischbein NJ, et al. Focal opacification of the olfactory recess on sinus CT: just an incidental finding? *AJNR Am J Neuroradiol* 2008;29:895–97 CrossRef Medline
23. French CA. The importance of diagnosing NUT midline carcinoma. *Head Neck Pathol* 2013;7:11–16 CrossRef Medline
24. Stelow EB. A review of NUT midline carcinoma. *Head Neck Pathol* 2011;5:31–35 CrossRef Medline
25. Bauer DE, Mitchell CM, Strait KM, et al. Clinicopathologic features and long-term outcomes of NUT midline carcinoma. *Clin Cancer Res* 2012;18:5773–79 CrossRef Medline
26. Bishop JA, Westra WH. NUT midline carcinomas of the sinonasal tract. *Am J Surg Pathol* 2012;36:1216–21 CrossRef Medline
27. Bellizzi AM, Bruzzi C, French CA, et al. The cytologic features of NUT midline carcinoma. *Cancer* 2009;117:508–15 Medline
28. French CA, Ramirez CL, Kolmakova J, et al. BRD-NUT oncoproteins: a family of closely related nuclear proteins that block

- epithelial differentiation and maintain the growth of carcinoma cells. *Oncogene* 2008;27:2237–42 CrossRef Medline
29. Chau NG, Hurqitz S, Mitchell CM, et al. **Intensive treatment and survival outcomes in NUT midline carcinoma of the head and neck.** *Cancer* 2016;122:3632–40 CrossRef Medline
 30. Kakkar A, Anotony VM, Irugu DV, et al. **NUT midline carcinoma: a series of five cases, including one with unusual clinical course.** *Head Neck Pathol* 2018;12:230–36 CrossRef Medline
 31. Bair RJ, Chick JF, Chauhan NR, et al. **Demystifying NUT midline carcinoma: radiologic and pathologic correlations of an aggressive malignancy.** *AJR Am J Roentgenol* 2014;203:W391–99 CrossRef Medline
 32. Edgar M, Caruso AM, Kim E, et al. **NUT midline carcinoma of the nasal cavity.** *Head Neck Pathol* 2017;11:389–92 CrossRef Medline
 33. Shaikh F, Pagedar N, Awan O, et al. **Sinonasal NUT-midline carcinoma: a multimodality approach to diagnosis, staging, and post-surgical restaging.** *Cuereus* 2015;7:e288 CrossRef Medline
 34. Lewis JT, Oliveira AM, Nascimento AG, et al. **Low-grade sinonasal sarcoma and neural and myogenic features: a clinicopathologic analysis of 28 cases.** *Am J Surg Pathol* 2012;36:517–25 CrossRef Medline
 35. Hellquist HB, Lungren J. **Neurogenic sarcoma of the sinonasal tract.** *J Laryngol Otol* 1991;105:186–90 CrossRef Medline
 36. Wang X, Bledsoe KL, Graham RP, et al. **Recurrent PAX3-MAML3 fusion in biphenotypic sinonasal sarcoma.** *Nat Genet* 2014;46:666–68 CrossRef Medline
 37. Wong WJ, Lauria A, Hornick JL, et al. **Alternate PAX3-FOXO1 oncogenic fusion in biphenotypic sinonasal sarcoma.** *Genes Chromosomes Cancer* 2016;55:25–29 CrossRef Medline
 38. Cannon RB, Wiggins RH 3rd, Witt BL, et al. **Imaging and outcomes for a new entity: low-grade sinonasal sarcoma with neural and myogenic features.** *J Neurol Surg Rep* 2017;78:e15–19 CrossRef Medline
 39. Rooper LM, Huang SC, Antonescu CR, et al. **Biphenotypic sinonasal sarcoma: an expanded immunoprofile including consistent nuclear β -catenin positivity and absence of SOX10 expression.** *Hum Pathol* 2016;55:44–50 CrossRef Medline
 40. Lin Y, Liao B, Han A. **Biphenotypic sinonasal sarcoma with diffuse infiltration and intracranial extension: a case report.** *Int J Clin Exp Pathol* 2017;10:11743–46
 41. Larque AB, Hakim S, Ordi J, et al. **High-risk human papillomavirus is transcriptionally active in a subset of sinonasal squamous cell carcinomas.** *Mod Pathol* 2014;27:343–51 CrossRef Medline
 42. Alos L, Moyano S, Nadal A, et al. **Human papillomaviruses are identified in a subgroup of sinonasal squamous cell carcinomas with favorable outcomes.** *Cancer* 2009;115:2701–09 CrossRef Medline
 43. Ruangritchankul K, Jitpasutham T, Kitkumthorn N, et al. **Human papillomavirus-related multiphenotypic sinonasal carcinoma: first case report associated with intermediate-risk HPV type and literatures review.** *Hum Pathol: Case Reports* 2018;14:20–24 CrossRef
 44. Biegel JA, Zhou JY, Rorke LB, et al. **Germ-line and acquired mutations of INI1 in atypical teratoid and rhabdoid tumors.** *Cancer Res* 1999;59:74–79 Medline
 45. Modena P, Lualdi E, Facchinette F, et al. **SMARCB1/INI1 tumor suppressor gene is frequently inactivated in epithelioid sarcomas.** *Cancer Res* 2005;65:4012–19 CrossRef Medline
 46. Hornick JL, Dal Cin P, Fletcher CD. **Loss of INI1 expression is characteristic of both conventional and proximal-type epithelioid sarcoma.** *Am J Surg Pathol* 2009;33:542–50 CrossRef Medline
 47. Agaimy A, Koch M, Lell M, et al. **SMARCB1(INI1)-deficient sinonasal basaloid carcinoma: a novel member of the expanding family of SMARCB1-deficient neoplasms.** *Am J Surg Pathol* 2014;38:1274–81 CrossRef Medline
 48. Bell D, Hanna EY, Agaimy A, et al. **Reappraisal of sinonasal undifferentiated carcinoma: SMARCB1 (INI1)-deficient sinonasal carcinoma—a single-institution experience.** *Virchows Arch* 2015;467:649–56 CrossRef Medline
 49. Shatzkes DR, Ginsberg LE, Wong M, et al. **Imaging appearance of SMARCB1 (INI1)-deficient sinonasal carcinoma: a newly described sinonasal malignancy.** *AJNR Am J Neuroradiol* 2016;37:1925–29 CrossRef Medline
 50. Zur KB, Branwein M, Wang B, et al. **Primary description of a new entity, renal cell-like carcinoma of the nasal cavity: van Meergeren in the house of Vermeer.** *Arch Otolaryngol Head Neck Surg* 2002;128:441–47 CrossRef 11926922
 51. Storck K, Hadi UM, Simpson R, et al. **Sinonasal renal cell-like adenocarcinoma: a report on four patients.** *Head Neck Pathol* 2008;2:75–80 CrossRef Medline
 52. Lee HM, Kang HJ, Lee SH. **Metastatic renal cell carcinoma presenting as epistaxis.** *Eur Arch Otorhinolaryngol* 2005;262:69–71 CrossRef Medline
 53. Brandwein-Gensler M, Wei S. **Envisioning the next WHO head and neck classification.** *Head Neck Pathol* 2014;8:1–15 CrossRef Medline
 54. Kim NI, Yang JI, Kim SS, et al. **Sinonasal renal-cell like adenocarcinoma, a unique variant of primary clear cell carcinoma of the head and neck: the first reported case in Korea.** *Medicine* 2017;96:e7711 CrossRef Medline
 55. Zhenwei-Chen, Zhaoming-Wang, Hongqi-Shi, et al. **Renal cell-like adenocarcinoma of the nasal cavity: a case report and review of the literature.** *Diag Pathol* 2017;12:75 CrossRef Medline
 56. Wu CN, Chuang IC, Chuang MJ, et al. **Sinonasal renal cell-like adenocarcinoma: easily misdiagnosed sinonasal tumor.** *Head Neck* 2018;40:e91–95 CrossRef Medline
 57. Mason KA, Navaratnam A, Theodorakopoulou E, et al. **Nasal chondromesenchymal hamartoma (NCMH): a systematic review of the literature with a new case report.** *J Otolaryngol Head Neck Surg* 2015;44:28 CrossRef Medline
 58. Stewart DR, Messinger Y, Williams GM, et al. **Nasal chondromesenchymal hamartomas arise secondary to germline and somatic mutations of DICER1 in the pleuropulmonary blastoma tumor predisposition disorder.** *Hum Genet* 2014;133:1443–50 CrossRef Medline
 59. Ozolek JA, Carrau R, Barnes EL, et al. **Nasal chondromesenchymal hamartoma in older children and adults: series and immunohistochemical analysis.** *Arch Pathol Lab Med* 2005;129:1444–50 Medline
 60. Wang T, Li W, Xu X, et al. **Nasal chondromesenchymal hamartoma in young children: CT and MRI findings and review of literature.** *World J Surg Oncol* 2014;12:257 CrossRef Medline
 61. Yao-Lee A, Ryan M, Rajaram V. **Nasal chondromesenchymal hamartoma: correlation of typical MR, CT and pathological findings.** *Pediatr Radiol* 2011;41:675–77 CrossRef Medline

On Flow Diversion: The Changing Landscape of Intracerebral Aneurysm Management

 A.A. Dmytriw,  K. Phan,  J.M. Moore,  V.M. Pereira,  T. Krings, and  A.J. Thomas



ABSTRACT

SUMMARY: Uptake of flow-diverting technology is rapidly outpacing the availability of clinical evidence. Most current usage is off-label, and the endovascular community is nearer the beginning than the end of the learning curve, given the number of devices in development. A comprehensive overview of technical specifications alongside key outcome data is essential both for clinical decision-making and to direct further investigations. Most-studied has been the Pipeline Embolization Device, which has undergone a transition to the Pipeline Flex for which outcome data are sparse or heterogeneous. Alternative endoluminal devices do not appear to be outperforming the Pipeline Embolization Device to date, though prospective studies and long-term data mostly are lacking, and between-study comparisons must be treated with caution. Nominal technical specifications may be unrelated to in situ performance, emphasizing the importance of correct radiologic sizing and device placement. Devices designed specifically for bifurcation aneurysms also lack long-term outcome data or have only recently become available for clinical use. There are no major studies directly comparing a flow-diverting device with standard coiling or microsurgical clipping. Data on flow-diverting stents are too limited in terms of long-term outcomes to reliably inform clinical decision-making. The best available evidence supports using a single endoluminal device for most indications. Recommendations on the suitability and choice of a device for bifurcation or ruptured aneurysms or for anatomically complex lesions cannot be made on the basis of current evidence. The appropriateness of flow-diverting treatment must be decided on a case-by-case basis, considering experience and the relative risks against standard approaches or observation.

ABBREVIATION: MCR = metal coverage ratio

The Pipeline Embolization Device (PED; Covidien, Irvine, California) was approved by the FDA in 2011 and by the European Medicines Agency (EMA) in 2008 for the treatment of large or giant, wide-neck intracranial aneurysms of the internal carotid artery from the petrous to the superior hypophyseal segments.¹ Currently, this is the only device approved in the United States. In Europe, there are additional options, including the PED, Silk flow diverter (Balt Extrusion, Montmorency, France), Flow-Redirection Endoluminal Device (FRED; MicroVention, Tustin, California), p64 (phenox, Bochum, Germany), Surpass Streamline (Stryker Neuro-


vascular, Kalamazoo, Michigan), and Derivo (Acandis, Pforzheim, Germany). Multiple other endovascular flow diverters are commercially available or in late-stage development, including the endovascular devices Pipeline Flex and Pipeline Shield (Covidien), Tubridge (MicroPort Medical Company, Shanghai, China), and the Endovascular Clip System (eCLIPs; Evasc, Vancouver, Canada). No flow-diverting stent has been approved for use in the posterior circulation, treatment of aneurysmal subarachnoid hemorrhage, or in the anterior circulation beyond the internal carotid artery superior hypophyseal segment.² The term “flow diverter” is arguably a misnomer because it is endothelialization that eventually sequesters the aneurysm.


Flow-diversion technology has relatively few studies reporting long-term outcomes, though available data suggest that complications beyond 6 months postprocedure are rare. Meanwhile, device technology is evolving rapidly, encompassing advances in the control and precision of device placement as well as growing operator experience and skill, all contributing to greater procedural safety.¹ As a result, off-label humanitarian usage is increasing well ahead of long-term outcome data or regulatory approval. Challenging indications such as distal anterior or vertebrobasilar aneurysms are increasingly considered for flow diversion, against a

Received October 26, 2018; accepted after revision January 25, 2019.

From the Department of Medical Imaging (A.A.D., V.M.P., T.K.), Toronto Western Hospital, University of Toronto, Toronto, Ontario, Canada; Neurosurgical Service (A.A.D., K.P., J.M.M., A.J.T.), Beth Israel Deaconess Medical Center, Harvard Medical School, Boston, Massachusetts; and NeuroSpine Surgery Research Group (K.P.), Prince of Wales Private Hospital, Sydney, Australia.

Please address correspondence to Adam A. Dmytriw, MD, MSc, Department of Medical Imaging, University of Toronto, 263 McCaul St, Toronto, ON M5G 0A6, Canada; e-mail: adam.dmytriw@uhn.ca

 Indicates open access to non-subscribers at www.ajnr.org

 Indicates article with supplemental on-line tables.

<http://dx.doi.org/10.3174/ajnr.A6006>

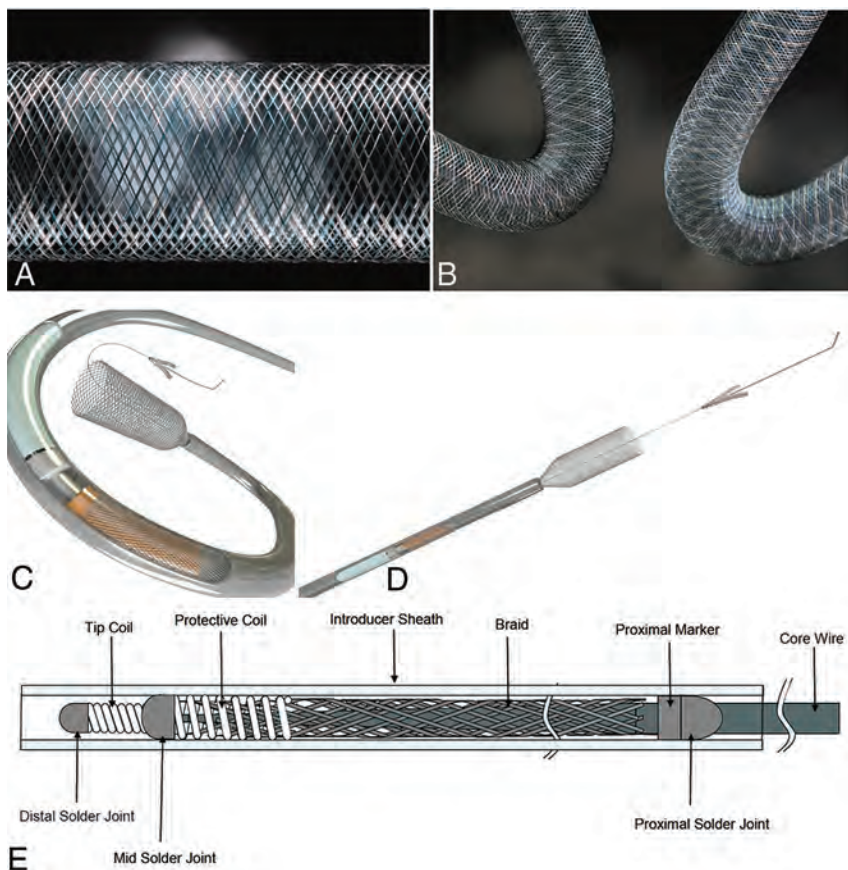


FIG 1. Magnified (A) and flexed (B) views of the Pipeline Embolization Device classic cobalt chromium and platinum tungsten composition. C and D, Deployment views of the Pipeline Flex model with a detailed assembly schematic (E). Courtesy of Medtronic/Covidien, Irvine, CA.

backdrop of sparse clinical evidence and few guidelines, which make recommendations only for licensed indications.³ For some rarer types of aneurysms, obtaining clinical evidence from prospective trials is not feasible. Thus, operators are reliant mostly on empiric medicine. To our knowledge, this represents the most comprehensive review of technical specifications and representative outcome data for flow-diverting stents to inform this fast-moving field.

Conventional Braided Mesh Devices

The Pipeline Embolization Device comprises a flexible, braided mesh tube of 48 interwoven microfilaments consisting of 25% platinum-tungsten and 75% cobalt-chromium-nickel alloy. Porosity approaches the optimal percentage of 70%, depending on sizing and configuration relative to the aneurysm (On-line Table 1).^{4,5} Studies have shown a predictable parabolic variability in PED porosity based on the parameters of device size, recipient artery size, and device curvature; even modest oversizing led to a marked increase in porosity with a reduction in the metal coverage ratio (MCR), which potentially compromises aneurysm occlusion.^{6,7}

Device oversizing and deformation during deployment in patients with ICA aneurysms have been shown to markedly reduce local MCR by 5%–7%, correlating with a lower occlusion rate at 6 months.⁷ For identical porosities, a higher pore attenuation is associated with more efficient flow diversion. Because the PED

design does not vary in terms of pore attenuation, its performance is determined by the MCR alone. In this study, the threshold MCR for better 6-month occlusion rates was 23%, markedly less than the nominal value of approximately 30%.⁷ Use of multiple, shorter devices of differing sizes may minimize transitional zone effects arising from vessel-size mismatch, especially when considering tortuous vessel anatomies⁶; however, this use may also increase complications.⁸ Relatively limited data show that a single device results in complete or near-complete occlusion of most aneurysms, including those at bifurcations, without delayed complications or mortality.^{9,10}

A second-generation version, the Pipeline Flex, was approved in Europe in 2014 and the United States in 2015. While the device itself is identical to the original, the delivery system was enhanced to improve device deployment and provide additional safety by incorporating a resheathing feature (Fig 1 and On-line Table 1).¹¹ The device is mounted over a stainless steel delivery wire, the distal part being covered by two 3-mm polytetrafluoroethylene protective sleeves, replacing the capture coil of

the original version to reduce foreshortening and enable more precise device placement.^{12,13} The distal tip is a soft hydrophilic 0.012-inch wire, with an angle of 55° and a proximal platinum marker for visibility. The proximal part of the device lies on a silicone elastomer resheathing pad with a profile of 0.023 inches that is located between 2 platinum markers; the most anterior marker is for resheathing. The pusher wire is a thicker, longer hypotube than that used for the parent device. These modifications are intended to provide multiple and technically less challenging options for precise deployment in different anatomies.¹²

A third-generation version called the Pipeline Flex Embolization Device with Shield Technology (Pipeline Shield) was approved in Europe in 2015. This latest device features the same implant and delivery system as the Pipeline Flex, with the addition of a surface modification comprising a layer of phosphorylcholine covalently bound onto the bare metal strands, with the aim of reducing unwanted thrombogenicity.^{14,15} Similar to most other available endoluminal devices, the PED, Pipeline Flex, and Pipeline Shield are delivered via a 0.027-inch microcatheter and typically use a 6F or 7F guide catheter; however, 5F intermediate catheters are also used.^{11,15}

The first-generation PED is the most studied device to date. The 2 most prominent prospective studies, the Pipeline for the Intracranial Treatment of Aneurysms (PITA) and Pipeline for Uncoilable or Failed Aneurysms (PUFS) trials (registration stud-

ies for Europe and United States, respectively), showed occlusion rates of approximately 75%–95% at 6 months to 5 years in patients with unruptured wide-neck aneurysms of the ICA (On-line Table 2). Patients in the PUPS study also had excellent neuro-ophthalmologic outcomes at 6 months. Morbidity (in terms of permanent neurologic disability) and mortality were low, at approximately 0%–3% each.^{16–19} A prospective observational study (Aneurysm Study of Pipeline in an Observational Registry [ASPIRe]) confirmed that the PED in a heterogeneous patient population with unruptured large/giant aneurysms of the ICA was safe, with low rates of neurologic morbidity and mortality (On-line Table 2).²⁰

These outcomes were consistent with a large, retrospective, safety series (International Retrospective Study of Pipeline Embolization Device [IntrePED]).²¹ In this series, further analysis showed that neurologic morbidity and mortality increased with age (though only the former was statistically marked), but both were still acceptably low in elderly patients.²² Of 793 patients, 20 (2.5%) had intraparenchymal hemorrhage (unrelated to the index aneurysm rupture); risk factors included treatment of ruptured aneurysms and use of multiple devices.²³ The fusiform aneurysm was the only variable independently associated with postoperative stroke.²⁴

The PED is being used increasingly for off-label indications. For posterior circulation aneurysms, subgroup analysis from the IntrePED safety series showed neurologic morbidity and mortality comparable with reported rates after clipping or coiling. Nevertheless, rates of morbidity and mortality after flow-diversion treatment were higher among posterior circulation (16.5%) compared with anterior circulation (5%–9%) lesions.²⁵ In this and other series, flow diversion in the posterior circulation has been shown to be associated with ischemic complications related to perforator infarcts, which are not negligible.^{26,27} Use in fusiform aneurysms (especially basilar) or use of ≥ 3 devices was associated with a higher risk.²⁵ Occlusion rates for posterior circulation aneurysms have been reported separately at approximately 80%, within the range for anterior circulation aneurysms (On-line Table 2).²⁸ Regarding off-label use for MCA aneurysms, a 2017 meta-analysis suggested that the treatment is feasible but should be considered as an alternative given a non-negligible rate of complications.^{29,30} The same group responsible for this meta-analysis also used a similar technique to analyze multiple small retrospective series of acutely ruptured aneurysms in 2018 and reported high rates of long-term occlusion but with a complication rate of 18% in the anterior and 27% in the posterior circulation.³¹

Last, a 2018 meta-analysis of distal aneurysms also suggested reasonably high rates of occlusion (70%) with marked complication rates (20%).³² Limited studies of dissecting and fusiform aneurysms demonstrate comparable outcomes to vessel sacrifice in the long term, with potentially greater short-term complications.³³ The PED has been shown to be safe and effective for many off-label uses, though these require ongoing evaluation. The forthcoming Prospective Study on Embolization of Intracranial Aneurysms with Pipeline Embolization Device (PREMIER) trial data suggest that small aneurysms may be treated safely in an off-label fashion in many situations as well. 3D rotational angiography studies of virtual stent placement have shown utility in

simulating vessel geometry and, in particular, show that delivery manipulation and vessel radius have a marked effect on PED apposition.³⁴ In the context of braided stents, local porosity and filament position have been modeled with conebeam CT, which may provide critical information to the diagnostic and interventional neuroradiologist about deployment prediction.³⁵

Outcome data for the Pipeline Flex are still limited, but initial results support its safety and short-term efficacy.³⁶ High rates of occlusion with low rates of short- and long-term disability have been reported from several selected small studies, as follows: in 10 patients with 11 anterior saccular aneurysms,¹² in 42 patients with 44 predominantly anterior saccular aneurysms,³⁷ and in 30 patients with 30 predominantly anterior saccular aneurysms.³⁸ The Pipeline Flex device has been shown to reduce total procedure and fluoroscopy times and the rate of deployment failure compared with the original PED.³⁹ It remains to be seen whether the design modifications of the Pipeline Flex will translate into improved long-term outcomes and/or use of this technology in a wider range of indications. Regarding the Pipeline Shield, a prospective single-arm study evaluating its use in 50 patients with 50 unruptured, predominantly saccular internal carotid aneurysms achieved complete wall apposition in 96% of cases, with no major strokes or neurologic mortality during 30 days postprocedure.¹⁴

The next conventional braided mesh device to debut was the original Silk device, also a flexible mesh stent made from 48 braided nitinol and 4 platinum microfilaments, which was approved in Europe in 2008—the first such device to enter clinical use for intracranial aneurysm management.^{40,41} The platinum strands with 2 flared ends act as radiopaque markers. A new-generation Silk+ device has flared ends, lower porosity, higher radial force, greater slide capacity, an extrasupple and shorter (9 mm) distal radiopaque tip, and 8 platinum markers (Fig 2).⁴² Like its predecessor, the Silk+ device requires a smaller delivery microcatheter than other similar endovascular devices, 0.023 inches, though like others, it uses a 6F or 7F guide catheter.⁴ Tapered options are available for use in irregular anatomies.

Of note is the observation from *in vitro* modeling studies that the MCR for the original Silk device had been reported as only 21% when stent and vessel were matched in a straight model segment versus a nominal MCR of 40%–55% (On-line Table 1).⁴³ The MCR was decreased at oversizing (for straight segments and on the convexity of a curved segment) and for matched stent and segment diameters on the concavity because of dynamic wire repositioning. These results are clinically relevant because of the requirement to maximize and minimize the MCR across the aneurysm ostium and branch vessel orifice, respectively. The original device was withdrawn from the market.

Most outcome data were generated from small studies of the original Silk device, which was intended for use in complex intracranial aneurysms. This feature may partly explain why occlusion rates were as low as approximately 50% at 4 months' follow-up, benchmarking poorly compared with PED data (On-line Table 2).^{44–49} Morbidity and mortality were also higher than for PED studies, consistent with more challenging indications, including a high proportion of patients with fusiform aneurysms in some

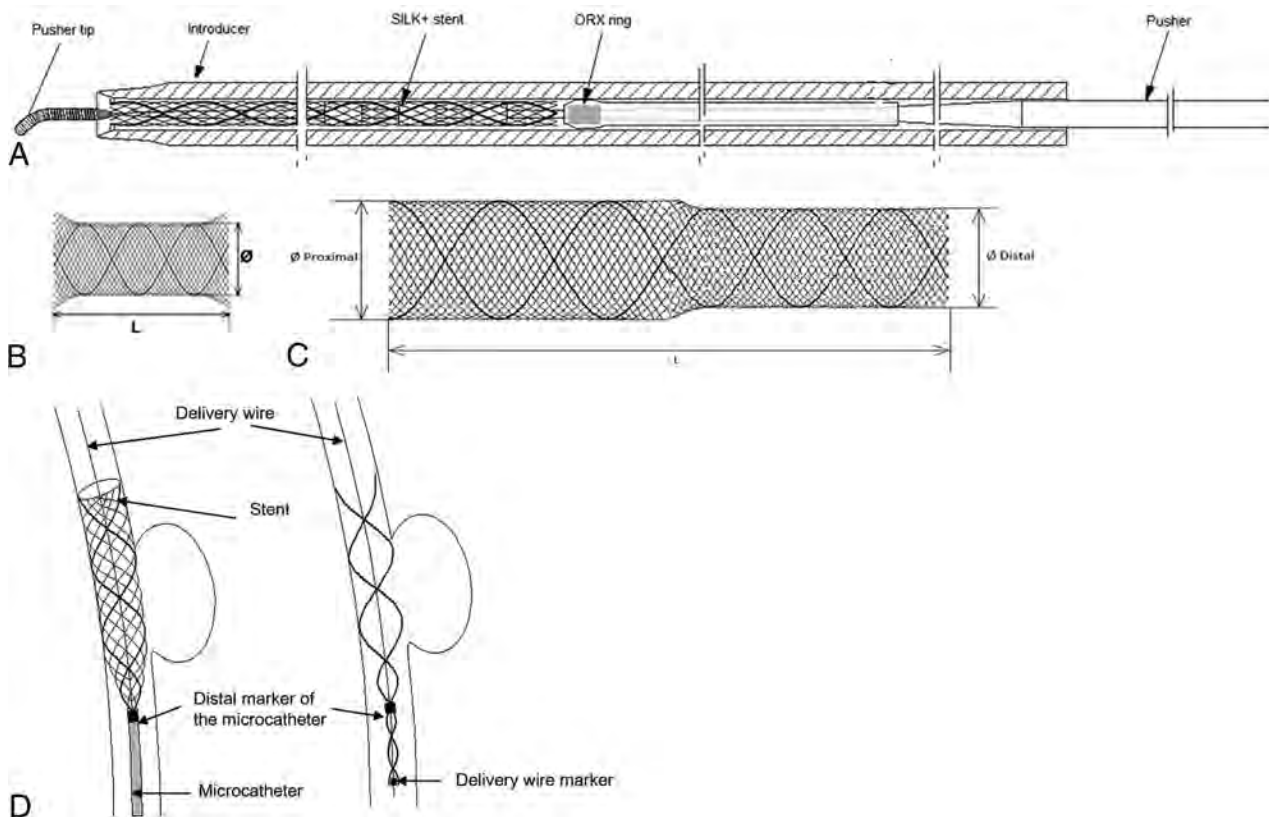


FIG 2. A, Silk+ assembly schematic with the placement system and pusher. The mono- (B) and bidiameter (C) Silk+ model as well as illustration of the position and deployment of the stent and radiopaque markers (D). Courtesy of Balt Extrusion, Montmorency, France.

studies. For studies that included patients with presentations similar to those in the initial PED studies (ie, unruptured large- or wide-neck lesions of the petrous to the superior hypophyseal ICA), the Silk seems to benchmark well compared with the PED, achieving occlusion rates approaching 90% at approximately 18 months' follow-up, though complication rates were still higher, suggesting that the device had shortcomings irrespective of aneurysm complexity.⁴⁹ One study with a very challenging patient population, however, reported 1-year occlusion rates of 84%, alongside morbidity and mortality comparable with that in the IntrePED trial.^{21,48}

Despite being first to market among flow-diverting stents, the Silk has a relatively sparse evidence base compared with the PED, and caution must be exercised when making comparisons among studies because variables differ. The Silk has been studied with computational flow dynamics showing predictable decreases in wall shear stress and intra-aneurysmal flow velocities. Flow-pattern change is less consistently demonstrated, and this feature may relate to porosity.⁵⁰ In PED studies, it has been seen that when particle imaging velocimetry shows marked reductions, computational flow dynamics velocity fields do not always predictably change in a linear manner to particle imaging velocimetry, which may be relevant in transition hemodynamic regimes.^{51,52} Mean aneurysmal flow amplitude assessment of the Silk and PED using DSA has predicted thrombosis at certain thresholds for these braided devices.⁵³

Regarding the Silk+, evidence is lacking. One small retrospective study of 58 patients with 70 aneurysms (including patients

with prior or current SAH) compared outcomes for patients who received the original Silk device with those treated with Silk+ during nearly 1 year. Most patients did not undergo concomitant coiling. Delayed thromboembolic complications were seen in 10.6% of patients, and permanent neurologic morbidity, in 5.5%, all cases occurring in patients treated with the first-generation device; there was no procedure-related mortality. The overall occlusion rate across both devices was 73%, and there were no recanalizations.⁴⁴ It can be inferred, albeit tentatively, that the second-generation Silk+ is safer than its predecessor, but more studies and data are needed to make definitive conclusions.

Dual-Porosity and Fixed-Porosity

The FRED is a self-expanding nickel titanium paired stent comprising integrated dual-layer coverage provided by a low-porosity inner mesh of higher pore attenuation (48 nitinol wires) and an outer stent with high porosity (16 nitinol wires with 4 interwoven marker strands), as well as proximal and distal markers. The dual layer is restricted to the midsection, covering approximately 80% of the length of the device with the aim of increasing coverage across the aneurysm ostium. It can be deployed and partially resheathed by a single operator using a 0.027-inch microcatheter (On-line Table 1).^{11,54,55} The FRED, Silk, and PED have been studied with 4D flow MR imaging for the detection of intrastent streamline changes and velocity reductions. Regarding animal studies, the FRED is the most comprehensively tested in complex canine aneurysm models as opposed to rabbits. This may be im-

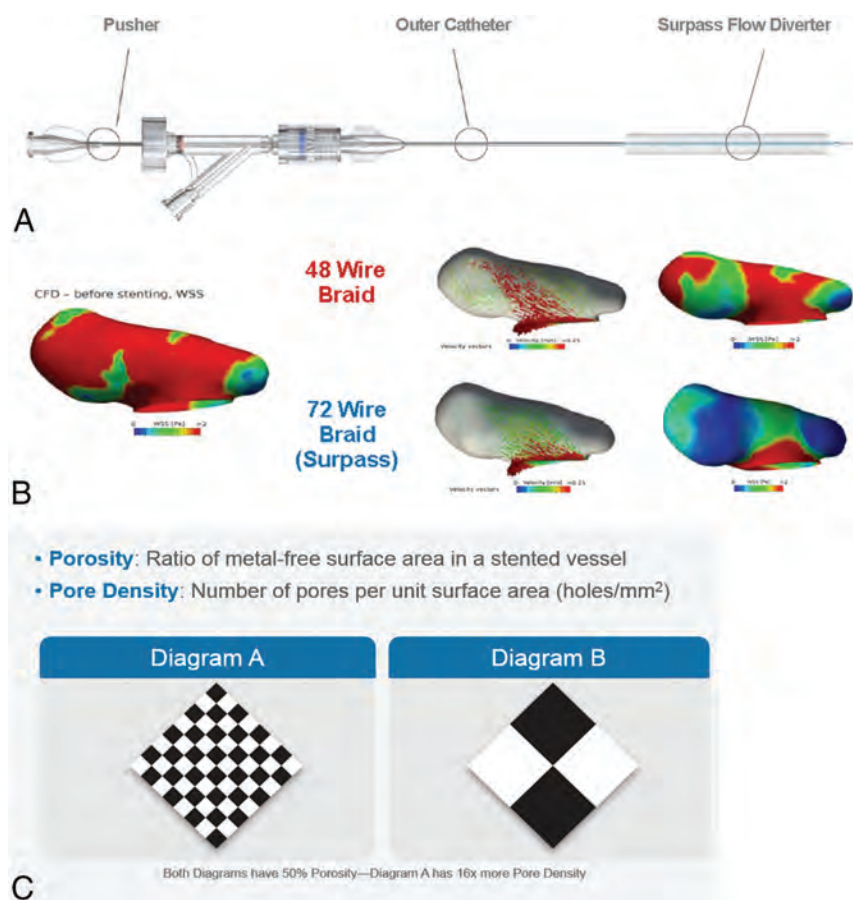


FIG 3. A, Surpass deployment system schematic. B, By increasing the number of wires while decreasing the size of the wire, the Surpass stent hypothetically creates more flow diversion while maintaining a consistent porosity. C, Computational flow dynamics shows the relationship between porosity and pore attenuation and how porosity may be maintained while increasing pore attenuation. Courtesy of Stryker Neurovascular, Kalamazoo, MI.

important because wide-neck and bifurcation aneurysms have been tested as well as porosity variations at anatomic tortuosities.⁵⁶

Data from studies evaluating the FRED are still relatively sparse, with the European Multicenter Study for the Evaluation of a Dual-Layer Flow-Diverting Stent for Treatment of Wide-Neck Intracranial Aneurysms study representing the only large multicenter study (On-line Table 2).⁵⁷ In several small studies, including studies that included patients with complex aneurysm morphologies, the FRED appeared to benchmark similar to the PED and better than the Silk (especially in terms of safety).^{40,55,58–60} As mentioned previously, however, cross-study comparisons must be interpreted with caution. The FRED has been approved and has been available in Europe for several years and is in late-stage evaluation in a Phase III multicenter US trial in patients with wide-neck aneurysms of the ICA (Pivotal Study of the FRED Stent System in the Treatment of Intracranial Aneurysms; NCT01801007). The FRED offers higher radial force and, in our experience, excellent performance in paraclinoid aneurysms. The device may twist, and we have noted occasional unexplained acute or subacute thrombosis unrelated to antiaggregation activity. A smaller form factor, Fred Jr, may be used in bifurcation aneurysms and in aneurysms on small-sized vessels.

The Surpass Streamline flow diverter is a cobalt-chromium alloy stent with 12 platinum wires to aid radiopacity. The Surpass stent was designed to optimize the flow-diversion profile, with

approximately 70% porosity and a pore attenuation of at least 20 pores/mm². The design operates on the premise that flow diversion is related not just to the metal-to-artery ratio but also to the number of pores (Fig 3). To maintain a consistent pore attenuation of >20 pores/mm², the Surpass has more wires than the other flow diverters and has a different number of metal struts, ranging from 48 in the 2-mm-diameter devices to 96 for 5 mm.⁵⁴

The other unique attribute of the Surpass is that it is an over-the-wire system, with the stent preloaded at the tip of the catheter. The system was designed this way to maintain wire access in case the stent needed to be re-crossed postdeployment, an advantage the Pipeline Flex also offers. The other benefit is the stability an over-the-wire system provides during stent deployment, even for long lengths. The downside is that the system is larger in nature, with a delivery microcatheter with a 0.040-inch inner diameter.⁶¹ Clinical data are limited but outcomes are predictable. For less challenging indications, occlusion rates and complications were favorable, while for more high-risk presentations, occlusion rates were lower and mortality was high (On-line Table 2).^{62,63} The Surpass is under evaluation for FDA approval in the Surpass Intracranial Aneurysm Embolization System Pivotal Trial to Treat Large or Giant Wide Neck Aneurysms (SCENT; NCT01716117), which reached primary end point completion in July 2017. The Surpass Flow Diverter for Intracranial Aneurysms (SURMOUNT registry; <https://www.centerwatch.com/clinical-trials/listings/66634/cerebral-aneurysm-surpass-flow-diverter-intracranial/>), a prospective multicenter postmarket surveillance study in Europe, is ongoing. This self-expandable stent mounted into the delivery catheter comprises up to 96 wires, thus providing more coverage. The Surpass is comparatively stiff and may be best navigated over a 5F distal access catheter across the aneurysm neck.

Next-Generation Nitinol Devices

The Tubridge is a braided, self-expanding device with flared ends that is approved in China. To minimize the shortening rate after full opening, large versions (diameter, ≥ 3.5 mm) comprise a braid of 62 nickel-titanium microfilaments and 2 platinum-iridium microfilaments, while small versions (diameter, <3.5 mm) comprise 46 nitinol and 2 platinum-iridium microfilaments. The MCR is comparable with that in the PED and with the limited outcome data, with the most marked being the Parent Artery Reconstruction for Large or Giant Cerebral Aneurysms Using the Tubridge Flow Diverter (PARAT) trial of large and giant aneurysms (On-line

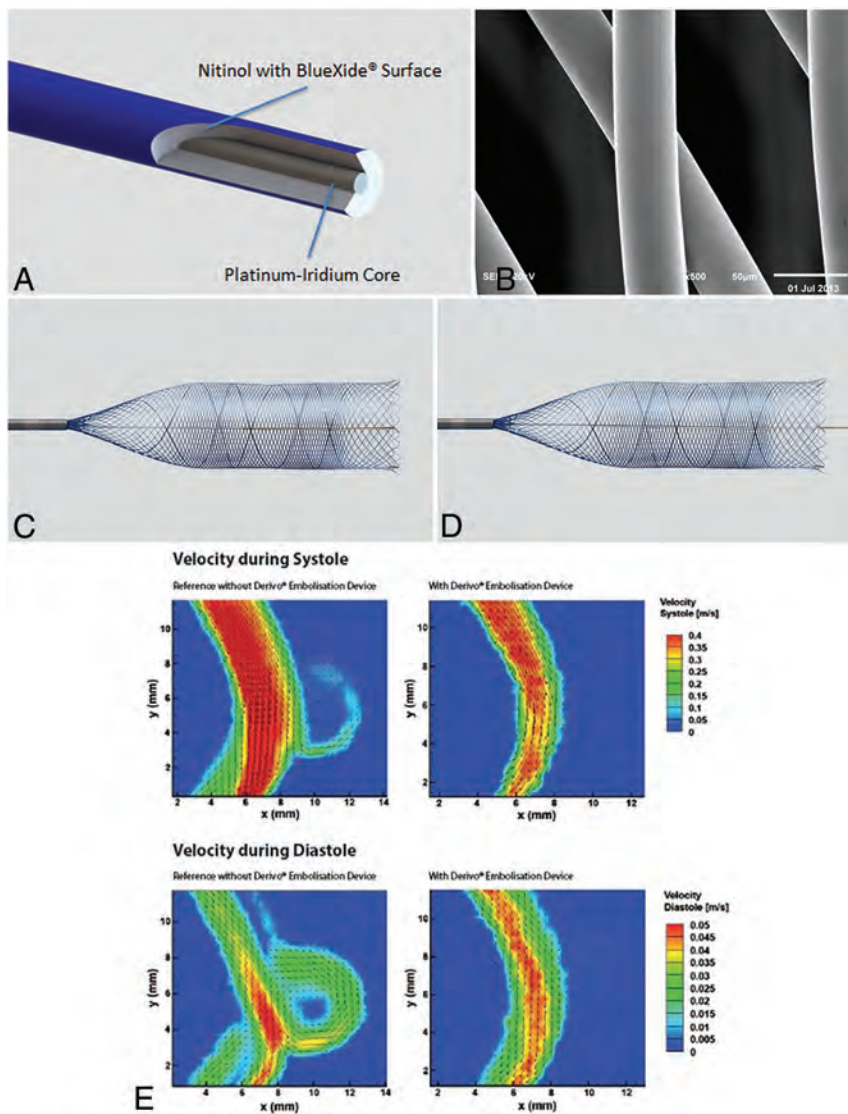


FIG 4. A, Unconstrained view of the Derivo Embolization Device (A) and magnified view of the BlueXide (B) surface of the Derivo Embolization Device acquired with a scanning electron microscope. The Derivo has closed, flared ends and may be used without a tip for increased flexibility (C) and with a tip for distal support and retention after release (D). E, Particle image velocimetry demonstrates effective flow diversion in an in vitro setting. Courtesy of Department of Cardiovascular Engineering, RWTH Aachen University in Aachen, North Rhine-Westphalia, Germany.

Tables 1 and 2).^{64,65} The Tubridge, Surpass, FRED, Silk, and PED have been tested in rabbit elastase models with acceptable occlusion rates. While this model is commonly used and favored, it is not universally standardized.⁶⁶

By comparison, the Derivo comprises 48 braiding nitinol wires with a radiopaque platinum core (Fig 4), which has undergone laboratory testing including particle image velocimetry. The device has flared ends with the goal of improved apposition. Only very preliminary data are available from 1 small study, which showed improving occlusion rates with time and no obvious safety flags (On-line Table 2).⁶⁷ The Derivo, Silk, and PED have undergone same-parameter particle imaging velocimetry testing showing that for all 3, the inflow-outflow is reversed from the proximal-to-distal aneurysm neck, after which a low-flow eddy predominates. There was a slightly higher susceptibility to inflow waveform/transient backflow with the Silk only.⁶⁸ In our experi-

ence, the device is useful for supraclinoid aneurysms, and its latest iteration is similar in characteristics to the p64.

Finally, the p64 device is a flexible, meshlike tube of 64 interwoven nitinol microfilaments grouped into 8 proximal radiopaque bundle markers, deployed using an 0.027-inch microcatheter. The p64 is completely recoverable—even after complete deployment—because of its controlled mechanical detachment (On-line Table 1).^{4,54} Data are limited, but several retrospective studies have shown midterm occlusion rates of at least 85% with low morbidity/mortality (On-line Table 2).^{11,69,70} As with all new devices, there will be a learning curve to consider. For noncontrolled descriptive studies, there is the potential for publication bias with this and all subsequent devices discussed herein. In our experience, this nitinol device is best used on small-neck or smaller overall aneurysms. The p64 does not have a distal wire for support, which may be an issue for telescoping or overly wide-neck aneurysms. The device is fully recoverable after full deployment; however, some proximal opening issues have occurred.

Bifurcation Hybrids

The second-generation eCLIPs is a novel, self-expanding, nitinol, non-circumferential, hybrid device with flow diverter properties, specifically designed for bifurcation aneurysms (Fig 5 and On-line Table 1). It has platinum radiopaque markers and comprises two discrete sections: an anchor segment designed to conform to vessel walls beside the aneurysm ostium, and a leaf segment with flow-diverter properties which has moveable ribs to allow trans-device coil delivery. Data from numerous challenging presentations are shown in On-line Table 2.⁷¹ eCLIPs is potentially unique as it is the only device to date which shows endothelialization as a bifurcation hybrid device. The European eCLIPs Safety, Feasibility and Efficacy Study (EESIS) is a prospective, multicenter cohort/registry study which is ongoing.

Like the eCLIPs, the Sphere (Minimally Invasive New Technologies [MINT]; Weill Cornell Medicine, New York, New York) was designed specifically for bifurcation aneurysms. It is constructed from a single loop of nitinol wire and reduces aneurysm inflow via a high-attenuation, patterned, elliptic surface that partially occludes the ostium (Fig 6 and On-line Table 1). The device is secured by multiple open hoops deployed in the parent vessel distal to the aneurysm, leaving daughter vessels unobstructed

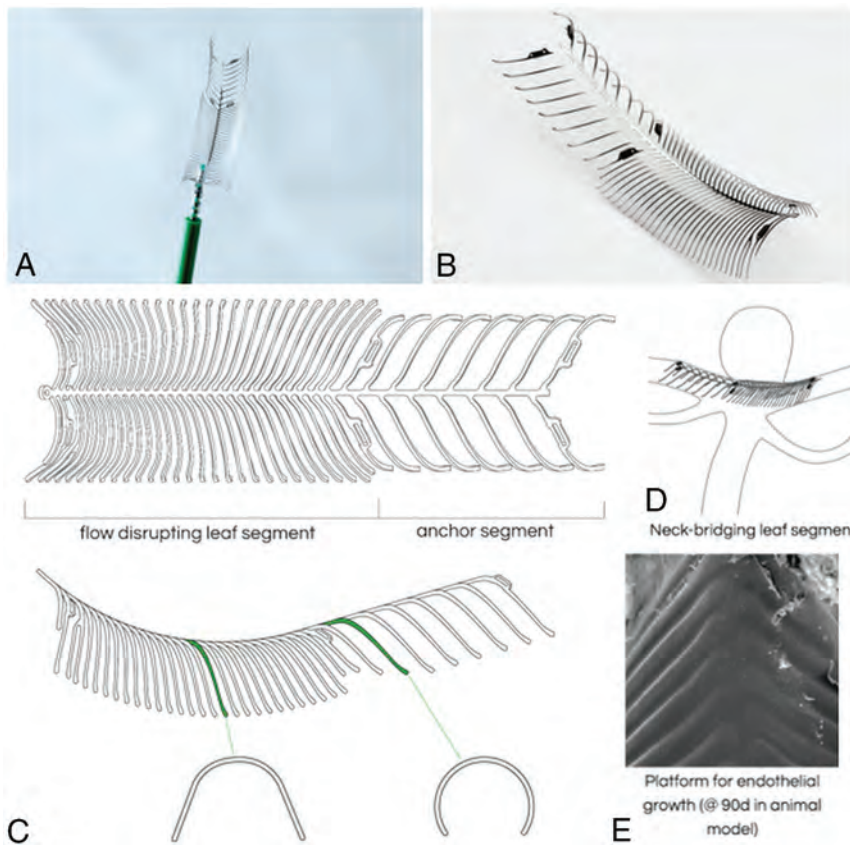


FIG 5. The bifurcation device eCLIPs (A) with a self-aligning spine rib design (B) having flow-disrupting and anchor segments (C) to enable repositioning but no migration/shortening following deployment. D, Noncircumferential morphology designed for wall apposition, which does not reside in the parent vessel or impede side branches. E, Scanning electron micrograph demonstrates neoendothelialization in vivo. Courtesy of the CV Path Institute, Gaithersburg, Maryland.

while not protruding into the delicate aneurysm dome. As yet, no clinical data are available.⁷²

CONCLUSIONS

For many types of aneurysms, flow diversion has rapidly become the treatment of choice because cure rates are high and complications rates are reasonably low. Unlike traditional stents, which require a high radial opening force, flow-diverting stents are designed to have a low radial opening force to facilitate navigability. Moreover, flow-diverting stents require greater metal coverage and decreased porosity while maintaining pore attenuation; this has been achieved using a braided metallic design for many devices. Early preclinical experiments suggested that the optimal porosity for aneurysm occlusion is 70%, but this may vary in practice according to vessel configuration and device sizing. Oversizing generally should be avoided, and the number of devices used per aneurysm should be minimized to reduce the risk of complications. There are too few data to make definitive recommendations on the choice of a device for bifurcation or ruptured aneurysms.

There are minimal data on the PED Flex alone; however, given that the device is similar to its forerunner, we may

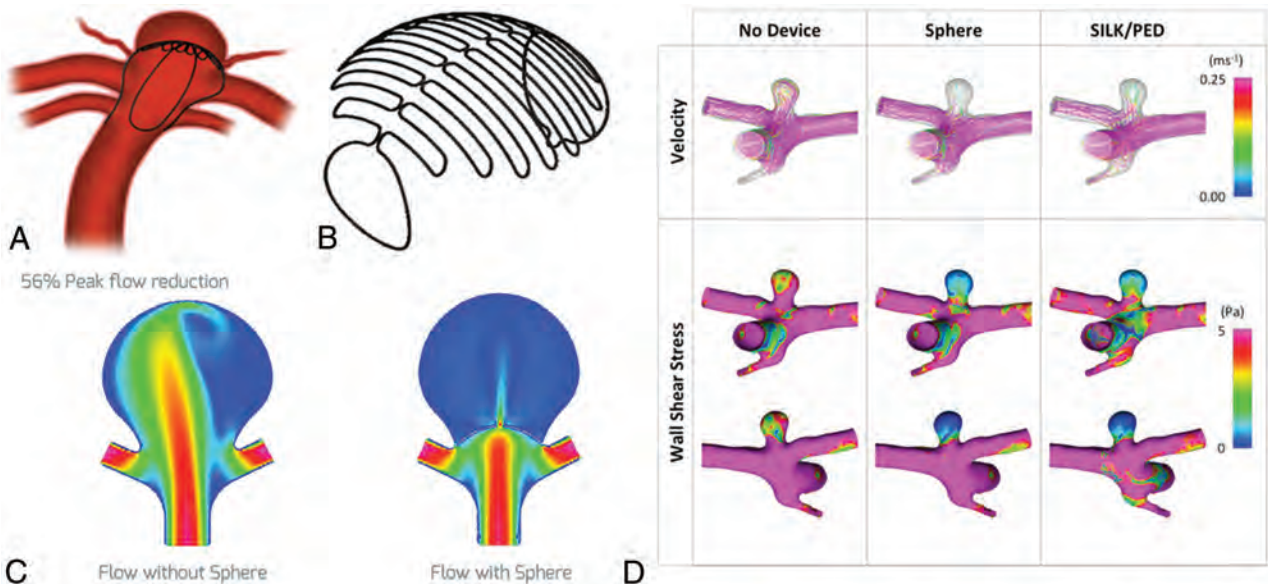


FIG 6. A, Sphere device with a high-attenuation nitinol face within a bifurcation aneurysm with thin-wire anchor legs (B) designed to direct flow downstream. C, Computational flow dynamics study demonstrates decreased peak flow to the aneurysm sac as well as velocity and wall shear stress (D), which is superior in Sphere compared to conventional endoluminal devices in some aneurysms/branch vessel morphologies in animal models. Courtesy of the Weill Cornell School of Medicine, New York, New York.

reasonably expect at least equivalent outcomes, possibly with improved procedural performance. Two devices could be approved in the United States within the next 2 years (the FRED and Surpass). Limited data likely reflect a learning curve for some devices, and outcomes should improve with experience. Further studies are needed to relate technical specifications to device performance and outcomes and hence optimize usage, particularly for the most challenging aneurysm presentations.

Disclosures: Vitor Mendes Pereira—*RELATED: Consulting Fee or Honorarium: Medtronic, Stryker, Balt, Cerenovous, Comments: participating in studies or procuring.* Ajith J. Thomas—RELATED: Fees for Participation in Review Activities Such as Data Monitoring Boards, Statistical Analysis, Endpoint Committees, and the Like: Stryker, Comments: Data Safety Monitoring Board for the SCENT trial*; UNRELATED: Expert Testimony: CRICO, Comments: brain aneurysm treatment. *Money paid to the institution.*

REFERENCES

1. Walcott BP, Stapleton CJ, Choudhri O, et al. **Flow diversion for the treatment of intracranial aneurysms.** *JAMA Neurol* 2016;73:1002–08 CrossRef Medline
2. Al-Mufti F, Amuluru K, Gandhi CD, et al. **Flow diversion for intracranial aneurysm management: a new standard of care.** *Neurotherapeutics* 2016;13:582–89 CrossRef Medline
3. Thompson BG, Brown RD Jr, Amin-Hanjani S, et al; American Heart Association Stroke Council, Council on Cardiovascular and Stroke Nursing, and Council on Epidemiology and Prevention, American Heart Association, American Stroke Association, **Guidelines for the Management of Patients with Unruptured Intracranial Aneurysms: a Guideline for Healthcare Professionals From the American Heart Association/American Stroke Association.** *Stroke* 2015;46:2368–400 CrossRef Medline
4. Briganti F, Leone G, Cirillo L, et al. **Postprocedural, midterm, and long-term results of cerebral aneurysms treated with flow-diverter devices: 7-year experience at a single center.** *Neurosurg Focus* 2017;42:E3 CrossRef Medline
5. Sadasivan C, Cesar L, Seong J, et al. **An original flow diversion device for the treatment of intracranial aneurysms: evaluation in the rabbit elastase-induced model.** *Stroke* 2009;40:952–58 CrossRef Medline
6. Shapiro M, Raz E, Becske T, et al. **Variable porosity of the Pipeline embolization device in straight and curved vessels: a guide for optimal deployment strategy.** *AJNR Am J Neuroradiol* 2014;35:727–33 CrossRef Medline
7. Jou LD, Chintalapani G, Mawad ME. **Metal coverage ratio of Pipeline embolization device for treatment of unruptured aneurysms: reality check.** *Interv Neuroradiol* 2016;22:42–48 CrossRef Medline
8. Chalouhi N, Tjoumakaris S, Phillips JL, et al. **A single Pipeline embolization device is sufficient for treatment of intracranial aneurysms.** *AJNR Am J Neuroradiol* 2014;35:1562–66 CrossRef Medline
9. Moshayedi H, Omofoye OA, Yap E, et al. **Factors affecting the obliteration rate of intracranial aneurysms treated with a single Pipeline embolization device.** *World Neurosurg* 2017;104:205–12 CrossRef Medline
10. Iosif C, Mounayer C, Yavuz K, et al. **Middle cerebral artery bifurcation aneurysms treated by extrasaccular flow diverters: midterm angiographic evolution and clinical outcome.** *AJNR Am J Neuroradiol* 2017;38:3 CrossRef Medline
11. Briganti F, Leone G, Uggla L, et al. **Mid-term and long-term follow-up of intracranial aneurysms treated by the p64 Flow Modulation Device: a multicenter experience.** *J Neurointerv Surg* 2017;9:70–76 CrossRef Medline
12. Pereira VM, Kelly M, Vega P, et al. **New Pipeline Flex device: initial experience and technical nuances.** *J Neurointerv Surg* 2015;7:920–25 CrossRef Medline
13. Martinez-Galdámez M, Gil A, Caniego JL, et al. **Preliminary experience with the Pipeline Flex Embolization Device: technical note.** *J Neurointerv Surg* 2015;7:748–51 CrossRef Medline
14. Martinez-Galdámez M, Lamin SM, Lagios KG, et al. **Periprocedural outcomes and early safety with the use of the Pipeline Flex Embolization Device with Shield Technology for unruptured intracranial aneurysms: preliminary results from a prospective clinical study.** *J Neurointerv Surg* 2017;9:772–76 CrossRef Medline
15. Hanel RA, Aguilar-Salinas P, Brasiliense LB, et al. **First US experience with Pipeline Flex with Shield Technology using aspirin as antiplatelet monotherapy.** *BMJ Case Rep* 2017;2017 CrossRef Medline
16. Nelson PK, Lylyk P, Szikora I, et al. **The Pipeline embolization device for the intracranial treatment of aneurysms trial.** *AJNR Am J Neuroradiol* 2011;32:34–40 CrossRef Medline
17. Becske T, Brinjikji W, Potts MB, et al. **Long-term clinical and angiographic outcomes following Pipeline Embolization Device treatment of complex internal carotid artery aneurysms: five-year results of the Pipeline for uncoilable or failed aneurysms trial.** *Neurosurgery* 2017;80:40–48 CrossRef Medline
18. Becske T, Kallmes DF, Saatci I, et al. **Pipeline for uncoilable or failed aneurysms: results from a multicenter clinical trial.** *Radiology* 2013;267:858–68 CrossRef Medline
19. Becske T, Potts MB, Shapiro M, et al. **Pipeline for uncoilable or failed aneurysms: 3-year follow-up results.** *J Neurosurg* 2017;127:81–88 CrossRef Medline
20. Kallmes DF, Brinjikji W, Boccardi E, et al. **Aneurysm Study of Pipeline in an Observational Registry (ASPIRe).** *Interv Neurol* 2016;5:89–99 CrossRef Medline
21. Kallmes DF, Hanel R, Lopes D, et al. **International retrospective study of the Pipeline Embolization Device: a multicenter aneurysm treatment study.** *AJNR Am J Neuroradiol* 2015;36:108–15 CrossRef Medline
22. Brinjikji W, Lanzino G, Cloft HJ, et al. **Risk factors for ischemic complications following Pipeline Embolization Device treatment of intracranial aneurysms: results from the IntraPED Study.** *AJNR Am J Neuroradiol* 2016;37:1673–78 CrossRef Medline
23. Brinjikji W, Lanzino G, Cloft HJ, et al. **Risk factors for hemorrhagic complications following Pipeline Embolization Device treatment of intracranial aneurysms: results from the international retrospective study of the Pipeline Embolization Device.** *AJNR Am J Neuroradiol* 2015;36:2308–13 CrossRef Medline
24. Brinjikji W, Kallmes DF, Cloft HJ, et al. **Age-related outcomes following intracranial aneurysm treatment with the Pipeline Embolization Device: a subgroup analysis of the IntraPED registry.** *J Neurosurg* 2016;124:1726–30 CrossRef Medline
25. Lopes DK, Jang DK, Cekirge S, et al. **Morbidity and mortality in patients with posterior circulation aneurysms treated with the Pipeline Embolization Device: a subgroup analysis of the international retrospective study of the Pipeline Embolization device.** *Neurosurgery* 2018;83:488–500 CrossRef Medline
26. Liang F, Zhang Y, Guo F, et al. **Use of Pipeline Embolization Device for posterior circulation aneurysms: single-center experiences with comparison with anterior circulation aneurysms.** *World Neurosurg* 2018;112:e683–90 CrossRef Medline
27. Wang CB, Shi WW, Zhang GX, et al. **Flow diverter treatment of posterior circulation aneurysms: a meta-analysis.** *Neuroradiology* 2016;58:391–400 CrossRef Medline
28. Dmytriw AA, Adeeb N, Kumar A, et al. **Flow diversion for the treatment of basilar apex aneurysms.** *Neurosurgery* 2018;83:1298–1305 CrossRef Medline
29. Patel PD, Chalouhi N, Atallah E, et al. **Off-label uses of the Pipeline embolization device: a review of the literature.** *Neurosurg Focus* 2017;42:E4 CrossRef Medline
30. Cagnazzo F, Mantilla D, Lefevre PH, et al. **Treatment of middle cerebral artery aneurysms with flow-diverter stents: a systematic review and meta-analysis.** *AJNR Am J Neuroradiol* 2017;38:2289–94 CrossRef Medline
31. Cagnazzo F, di Carlo DT, Cappucci M, et al. **Acutely ruptured intracranial aneurysms treated with flow-diverter stents: a systematic review and meta-analysis.** *AJNR Am J Neuroradiol* 2018;39:1669–75 CrossRef Medline

32. Yan Y, Zhu D, Tang H, et al. **Safety and efficacy of flow diverter treatment for aneurysm in small cerebral vessels: a systematic review and meta-analysis.** *World Neurosurg* 2018;115:54–64 CrossRef Medline
33. Fang YB, Lin A, Kostynskyy A, et al. **Endovascular treatment of intracranial vertebrobasilar artery dissecting aneurysms: parent artery occlusion versus flow diverter.** *Eur J Radiol* 2018;99:68–75 CrossRef Medline
34. Bouillot P, Brina O, Yilmaz H, et al. **Virtual-versus-real implantation of flow diverters: clinical potential and influence of vascular geometry.** *AJNR Am J Neuroradiol* 2016;37:2079–86 CrossRef Medline
35. Bouillot P, Brina O, Ouared R, et al. **Geometrical deployment for braided stent.** *Med Image Anal* 2016;30:85–94 CrossRef Medline
36. Aguilar-Salinas P, Brasiliense LB, Gonsales D, et al. **Evaluation of Pipeline Flex delivery system for the treatment of unruptured aneurysms.** *Expert Rev Med Device* 2016;13:885–97 CrossRef Medline
37. Colby GP, Lin LM, Caplan JM, et al. **Immediate procedural outcomes in 44 consecutive Pipeline Flex cases: the first North American single-center series.** *J Neurointerv Surg* 2016;8:702–09 CrossRef Medline
38. Martinez-Galdámez M, Pérez S, Vega A, et al. **Endovascular treatment of intracranial aneurysms using the Pipeline Flex embolization device: a case series of 30 consecutive patients.** *J Neurointerv Surg* 2016;8:396–401 CrossRef Medline
39. Le EJ, Miller T, Serulle Y, et al. **Use of Pipeline Flex is associated with reduced fluoroscopy time, procedure time, and technical failure compared with the first-generation Pipeline embolization device.** *J Neurointerv Surg* 2016 Mar 9. [Epub ahead of print] CrossRef Medline
40. Briganti F, Leone G, Ugga L, et al. **Safety and efficacy of flow redirection endoluminal device (FRED) in the treatment of cerebral aneurysms: a single center experience.** *Acta Neurochir (Wien)* 2016; 158:1745–55 CrossRef Medline
41. Murthy SB, Shah S, Shastri A, et al. **The Silk flow diverter in the treatment of intracranial aneurysms.** *J Clin Neurosci* 2014;21: 203–06 CrossRef Medline
42. Alghamdi F, Morais R, Scillia P, et al. **The Silk flow-diverter stent for endovascular treatment of intracranial aneurysms.** *Expert Rev Med Devices* 2015;12:753–62 CrossRef Medline
43. Aurboonyawat T, Blanc R, Schmidt P, et al. **An in vitro study of Silk stent morphology.** *Neuroradiology* 2011;53:659–67 CrossRef Medline
44. Lubicz B, Collignon L, Raphaëli G, et al. **Flow-diverter stent for the endovascular treatment of intracranial aneurysms: a prospective study in 29 patients with 34 aneurysms.** *Stroke* 2010;41:2247–53 CrossRef Medline
45. Byrne JV, Beltechi R, Yarnold JA, et al. **Early experience in the treatment of intra-cranial aneurysms by endovascular flow diversion: a multicentre prospective study.** *PLoS One* 2010;5 CrossRef Medline
46. Pumar JM, Banguero A, Cuellar H, et al. **Treatment of intracranial aneurysms with the Silk Embolization Device in a multicenter study. a retrospective data analysis.** *Neurosurgery* 2017;81:595–601 CrossRef Medline
47. Shankar JJ, Tampieri D, Iancu D, et al. **Silk flow diverter for complex intracranial aneurysms: a Canadian registry.** *J Neurointerv Surg* 2016;8:273–78 CrossRef Medline
48. Berge J, Biondi A, Machi P, et al. **Flow-diverter Silk stent for the treatment of intracranial aneurysms: 1-year follow-up in a multicenter study.** *AJNR Am J Neuroradiol* 2012;33:1150–55 CrossRef Medline
49. Velioglu M, Kizilkilic O, Selcuk H, et al. **Early and midterm results of complex cerebral aneurysms treated with Silk stent.** *Neuroradiology* 2012;54:1355–65 CrossRef Medline
50. Kulcsár Z, Augsburg L, Reymond P, et al. **Flow diversion treatment: intra-aneurysmal blood flow velocity and WSS reduction are parameters to predict aneurysm thrombosis.** *Acta Neurochir (Wien)* 2012;154:1827–34 CrossRef Medline
51. Bouillot P, Brina O, Ouared R, et al. **Computational fluid dynamics with stents: quantitative comparison with particle image velocimetry for three commercial off the shelf intracranial stents.** *J Neurointerv Surg* 2016;8:309–15 CrossRef Medline
52. Bouillot P, Brina O, Ouared R, et al. **Hemodynamic transition driven by stent porosity in sidewall aneurysms.** *J Biomech* 2015;48:1300–09 CrossRef Medline
53. Pereira VM, Bonnefous O, Ouared R, et al. **A DSA-based method using contrast-motion estimation for the assessment of the intracranial flow changes induced by flow-diverter stents.** *AJNR Am J Neuroradiol* 2013;34:808–15 CrossRef Medline
54. Bhogal P, Martinez Moreno R, Ganslandt O, et al. **Use of flow diverters in the treatment of unruptured saccular aneurysms of the anterior cerebral artery.** *J Neurointerv Surg* 2017;9:283–89 CrossRef Medline
55. Luecking H, Engelhorn T, Lang S, et al. **FRED Flow Diverter: a study on safety and efficacy in a consecutive group of 50 patients.** *AJNR Am J Neuroradiol* 2017;38:596–602 CrossRef Medline
56. Gentric JC, Darsaut TE, Makoyeva A, et al. **The success of flow diversion in large and giant sidewall aneurysms may depend on the size of the defect in the parent artery.** *AJNR Am J Neuroradiol* 2014;35: 2119–24 CrossRef Medline
57. Killer-Oberpfalzer M, Kocer N, Griessenauer CJ, et al. **European multicenter study for the evaluation of a dual-layer flow-diverting stent for treatment of wide-neck intracranial aneurysms: the European Flow-Redirection Intraluminal Device Study.** *AJNR Am J Neuroradiol* 2018;39:841–47 CrossRef Medline
58. Drescher F, Weber W, Berlis A, et al. **Treatment of intra- and extracranial aneurysms using the Flow-Redirection Endoluminal Device: multicenter experience and follow-up results.** *AJNR Am J Neuroradiol* 2017;38:105–12 CrossRef Medline
59. Möhlenbruch MA, Herweh C, Jestaedt L, et al. **The FRED flow-diverter stent for intracranial aneurysms: clinical study to assess safety and efficacy.** *AJNR Am J Neuroradiol* 2015;36:1155–61 CrossRef Medline
60. Kocer N, Islak C, Kizilkilic O, et al. **Flow Re-direction Endoluminal Device in treatment of cerebral aneurysms: initial experience with short-term follow-up results.** *J Neurosurg* 2014;120:1158–71 CrossRef Medline
61. Colby GP, Lin LM, Caplan JM, et al. **Flow diversion of large internal carotid artery aneurysms with the Surpass device: impressions and technical nuance from the initial North American experience.** *J Neurointerv Surg* 2016;8:279–86 CrossRef Medline
62. De Vries J, Boogaarts J, Van Norden A, et al. **New generation of flow diverter (Surpass) for unruptured intracranial aneurysms: a prospective single-center study in 37 patients.** *Stroke* 2013;44:1567–77 CrossRef Medline
63. Taschner CA, Vedantham S, de Vries J, et al. **Surpass flow diverter for treatment of posterior circulation aneurysms.** *AJNR Am J Neuroradiol* 2017;38:582–89 CrossRef Medline
64. Zhou Y, Yang PF, Fang YB, et al. **A novel flow-diverting device (Tubridge) for the treatment of 28 large or giant intracranial aneurysms: a single-center experience.** *AJNR Am J Neuroradiol* 2014;35:2326–33 CrossRef Medline
65. Liu JM, Zhou Y, Li Y, et al; PARAT investigators. **Parent artery reconstruction for large or giant cerebral aneurysms using the Tubridge Flow Diverter: a multicenter, randomized, controlled clinical trial (PARAT).** *AJNR Am J Neuroradiol* 2018;39:807–16 CrossRef Medline
66. Fahed R, Raymond J, Ducroux C, et al. **Testing flow diversion in animal models: a systematic review.** *Neuroradiology* 2016;58:375–82 CrossRef Medline
67. Akgul E, Onan HB, Akpınar S, et al. **The DERIVO Embolization Device in the treatment of intracranial aneurysms: short- and mid-term results.** *World Neurosurg* 2016;95:229–40 CrossRef Medline
68. Bouillot P, Brina O, Ouared R, et al. **Particle imaging velocimetry evaluation of intracranial stents in sidewall aneurysm: hemodynamic transition related to the stent design.** *PLoS One* 2014;9: e11376 CrossRef Medline
69. Fischer S, Aguilar-Pérez M, Henkes E, et al. **Initial experience with**

- p64: a novel mechanically detachable flow diverter for the treatment of intracranial saccular sidewall aneurysms.** *AJNR Am J Neuroradiol* 2015;36:2082–89 CrossRef Medline
70. Morais R, Mine B, Bruyère PJ, et al. **Endovascular treatment of intracranial aneurysms with the p64 flow diverter stent: mid-term results in 35 patients with 41 intracranial aneurysms.** *Neuroradiology* 2017;59:263–69 CrossRef Medline
71. Chiu AH, De Vries J, O’Kelly CJ, et al. **The second-generation eCLIPs endovascular clip system: initial experience.** *J Neurosurg* 2018;128:482–89 CrossRef Medline
72. Peach T, Cornhill JF, Nguyen A, et al. **The ‘Sphere’: a dedicated bifurcation aneurysm flow-diverter device.** *Cardiovasc Eng Technol* 2014;5:334–47 CrossRef Medline
73. Griessenauer CJ, Ogilvy CS, Adeeb N, et al. **Pipeline embolization of posterior circulation aneurysms: a multicenter study of 131 aneurysms.** *J Neurosurg* 2018 Apr 1:1–13 CrossRef Medline

Behavioral and Structural Effects of Single and Repeat Closed-Head Injury

Y.-C.J. Kao, Y.W. Lui, C.-F. Lu, H.-L. Chen, B.-Y. Hsieh, and C.-Y. Chen



ABSTRACT

BACKGROUND AND PURPOSE: The effects of multiple head impacts, even without detectable primary injury, on subsequent behavioral impairment and structural abnormality is yet well explored. Our aim was to uncover the dynamic changes and long-term effects of single and repetitive head injury without focal contusion on tissue microstructure and macrostructure.

MATERIALS AND METHODS: We introduced a repetitive closed-head injury rodent model ($n = 70$) without parenchymal lesions. We performed a longitudinal MR imaging study during a 50-day study period (T_2 -weighted imaging, susceptibility-weighted imaging, and diffusion tensor imaging) as well as sequential behavioral assessment. Immunohistochemical staining for astrogliosis was examined in a subgroup of animals. Paired and independent t tests were used to evaluate the outcome change after injury and the cumulative effects of impact load, respectively.

RESULTS: There was no gross morphologic evidence for head injury such as skull fracture, contusion, or hemorrhage on micro-CT and MR imaging. A significant decrease of white matter fractional anisotropy from day 21 on and an increase of gray matter fractional anisotropy from day 35 on were observed. Smaller mean cortical volume in the double-injury group was shown at day 50 compared with sham and single injury ($P < .05$). Behavioral deficits ($P < .05$) in neurologic outcome, balance, and locomotor activity were also aggravated after double injury. Histologic analysis showed astrogliosis 24 hours after injury, which persisted throughout the study period.

CONCLUSIONS: There are measurable and dynamic changes in microstructure, cortical volume, behavior, and histopathology after both single and double injury, with more severe effects seen after double injury. This work bridges cross-sectional evidence from human subject and pathologic studies using animal models with a multi-time point, longitudinal research paradigm.

ABBREVIATIONS: AD = axial diffusivity; CD 68 = Cluster of Differentiation 68; CHI = closed-head injury; FA = fractional anisotropy; GFAP = glial fibrillary acidic protein; MD = mean diffusivity; mNSS = modified Neurological Severity Score; RD = radial diffusivity; TBI = traumatic brain injury

Traumatic brain injury (TBI) is a major public health issue with increasing incidence and enormous cost to society worldwide.^{1,2} Mild TBI is generally imperceptible on conventional diagnostic imaging, yet it can be associated with widespread symptoms. In patients with mild TBI, quantitative MR imaging analysis

assessing macrostructural and microstructural effects of injury has been extremely promising.^{3,4} Specifically, human subject studies suggest regional cortical volume loss^{5,6} and abnormal fractional anisotropy (FA) in white matter regions susceptible to traumatic axonal injury, such as the corpus callosum, internal and external capsules, and anterior and posterior corona radiata.^{4,7} More recently, multishell diffusion with biologic modeling suggests WM pathologic changes.⁸ However, due to the difficulties of performing multiple, rapid, serial imaging studies as well as the

Received December 17, 2018; accepted after revision February 16, 2019.

From the Neuroscience Research Center (Y.-C.J.K., C.-Y.C.) and Translational Imaging Research Center (Y.-C.J.K., C.-Y.C.), Taipei Medical University, Taipei, Taiwan; Department of Radiology (Y.-C.J.K., C.-Y.C.), School of Medicine, College of Medicine, Taipei Medical University, Taipei, Taiwan; Department of Radiology (Y.W.L.), NYU School of Medicine/NYU Langone Health, New York, New York; Department of Biomedical Imaging and Radiological Sciences (C.-F.L.), National Yang-Ming University, Taipei, Taiwan; Departments of Medical Research (H.-L.C.), Medical Imaging (C.-Y.C.), and Radiogenomic Research Center (Y.-C.J.K., C.-Y.C.), Taipei Medical University Hospital, Taipei, Taiwan; and Department of Biomedical Imaging and Radiological Science (B.-Y.H.), China Medical University, Taichung, Taiwan.

This work was supported by the Ministry of Science and Technology, Taiwan (MOST105-2628-B-038-002-MY2, MOST104-2923-B-038-003-MY3, MOST106-2314-B-010-058-MY2, MOST105-2221-E-038-007-MY3 and MOST107-2314-B-038-005), Taipei Medical University (TMU103-AEI-B27), and Taipei Medical University Hospital (105TMUH-SP-01, GH107SP02).

This work originated from Taipei Medical University (Address: 250 Wuxing St., Taipei 110, Taiwan).

Please address correspondence to Cheng-Yu Chen, MD, Department of Radiology, School of Medicine, College of Medicine, Taipei Medical University, 250 Wuxing St., Taipei 110, Taiwan; e-mail: sandy0932@gmail.com; @sandy0932

Indicates open access to non-subscribers at www.ajnr.org

Indicates article with supplemental on-line appendix and tables.

Indicates article with supplemental on-line photos.

<http://dx.doi.org/10.3174/ajnr.A6014>

lack of histopathologic confirmation in human subjects with concussion, we still lack a clear understanding of the evolution of tissue injury across time. Furthermore, there is a specific, growing need to elucidate the effect of multiple head impacts/head injuries on short-term recovery and long-term outcome.

The purpose of this work was to measure dynamic temporal changes of macrostructural and microstructural damage from the acute-to-chronic phase postinjury after both single and repetitive head injury using a well-controlled model of closed-head injury (CHI) without focal contusion/hemorrhage. We describe observed differences among animals after single injury, double injury, and sham surgery and report the behavioral and neuropathologic correlates of injury.

MATERIALS AND METHODS

The study was performed in accordance with the recommendations of National Institutes of Health Guidelines for Animal Research (Guide for the Care and Use of Laboratory Animals) and the Animal Research: Reporting In Vivo Experiments guidelines. The protocol was approved by the Institutional Animal Care and Use Committee at Taipei Medical University. Animals were randomly assigned to 3 groups (single, double CHI, and sham control) for longitudinal and cross-sectional assessment (On-line Fig 1).

Closed-Head Injury Model

Seventy adult male Sprague-Dawley rats weighing 250–400 g (BioLASCO Taiwan Co, Taipei City, Taiwan) were anesthetized using chloral hydrate (400 mg/kg) and placed on a stereotaxic frame for an operation. All surgical procedures were performed under aseptic conditions. This CHI model modifies the protocol from the weight-drop injury model⁹ using the following: 1) fixed head positioning to achieve precise localization and force delivery, 2) addition of a secured impactor, and 3) alteration of the height of a freely dropped brass weight. Briefly, a midline incision was performed on the scalp, and a circular stainless steel helmet (10-mm diameter) was cemented over the skull on top of the left sensorimotor cortex (1.5 mm posterior and 2.5 mm lateral to the bregma). A 600-g weight was dropped from a height of 1 m through a stainless steel tube (1-m height with an inner diameter of 20 mm for clearing a column of stainless brass weights) to the secured impactor with a round tip aimed at the metal helmet. Animals in the double CHI group received 2 impacts with a 1-hour interval.¹⁰ The helmet was immediately removed after the last impact, and the scalp was sutured. Physiologic parameters, including heart rate and blood oxygen saturation level, were continuously monitored using a pulse oximeter (SurgiVet; Smiths Medical, Waukesha, Wisconsin). Rats were given topical antiseptics and lidocaine at the surgical site during the postoperative period.

CT

Micro-CT images were obtained on harvested skulls using a SkyScan 1176 scanner (Bruker BioSpin, Ettlingen, Germany) at an isotropic resolution of 9 μm and were visually assessed for subtle skull fractures by a neuroimaging expert.

MR Imaging

Longitudinal MR imaging was performed in each group before, at 24 hours, 7 days, 21 days, 35 days, and 50 days after CHI or sham surgery using a PharmaScan 7T system (Bruker BioSpin). Animals were anesthetized under $\sim 1.2\%$ isoflurane, and the stereotaxic headpiece and holder, consisting of ear and tooth bars, were used to immobilize the head. Physiologic conditions, including heart rate, arterial pulse extension, oxygen saturation, and rectal temperature, were continually monitored and maintained within normal ranges throughout the experiment.^{11–13} A volume coil was used for radiofrequency excitation, and an array coil was used for signal receiving. Initial localization scans were obtained, and T₂-weighted images using a rapid acquisition with a relaxation enhancement sequence (TR/TE = 3600/40 ms, FOV = 2.0 \times 2.0 cm, matrix size = 256 \times 256, 16 slices, slice thickness = 1 mm) were obtained to acquire anatomic images for rodent models.^{11,13} Diffusion tensor images were acquired with the same geometry using the 4-shot spin-echo EPI with TR/TE = 3000/28 ms, matrix size = 96 \times 96, δ/Δ = 5/15 ms, number of B₀ = 5, number of directions = 30, b-value = 1000 s/mm², number of averages = 4. Susceptibility-weighted images were obtained with the same geometry using the flow-compensated gradient-echo sequence with bandwidth = 30 kHz, TR/TE = 600/18 ms, matrix size = 256 \times 256, flip angle = 40°, and number of averages = 6.

Image Analysis

T₂-weighted imaging and SWI were visually inspected for brain deformation, tissue loss, edema, and the presence of hemorrhage by 1 attending neuroradiologist with >25 years of experience and 1 neuroimaging expert with 5 years of experience in rodent models. Image analysis, including skull stripping and motion correction/coregistration across time points and subjects, was performed using Statistical Parametric Mapping software (<http://www.fil.ion.ucl.ac.uk/spm/software/spm12>) and a custom Matlab (MathWorks, Natick, Massachusetts) script, published previously.^{11,12,14} To measure the cortical volume, we manually drew cortical ROIs and then applied them onto coregistered T₂-weighted images. To better delineate the border between the cortex and WM, we applied a threshold of 2 SDs of the signal intensity of cortical ROIs. All threshold-defined results were visually inspected for gross errors by 2 experienced investigators blinded to the experimental groups.

Parametric diffusion maps were generated for mean diffusivity (MD), axial diffusivity (AD), radial diffusivity (RD), and FA. Rectangular ROIs (5 \times 2.5 mm² per slice) were manually placed on FA maps on 3 consecutive slices subjacent to the impact region in the cortex, WM, and subcortical gray matter (Fig 1A). A threshold of FA > 0.35 was applied to extract WM.¹⁴ Cortical and subcortical tissue was segmented using a pixel-by-pixel classification based on spatial information relative to WM. Rectangular ROIs (1 \times 1.5 mm² per slice) were manually placed on FA maps on 3 consecutive slices (3–5 mm posterior to the bregma) covering the ipsilateral hippocampus. Mean MD, AD, RD, and FA values were calculated in the hippocampal ROIs and WM and cortical and subcortical tissue in the ROIs adjacent to the impact region.

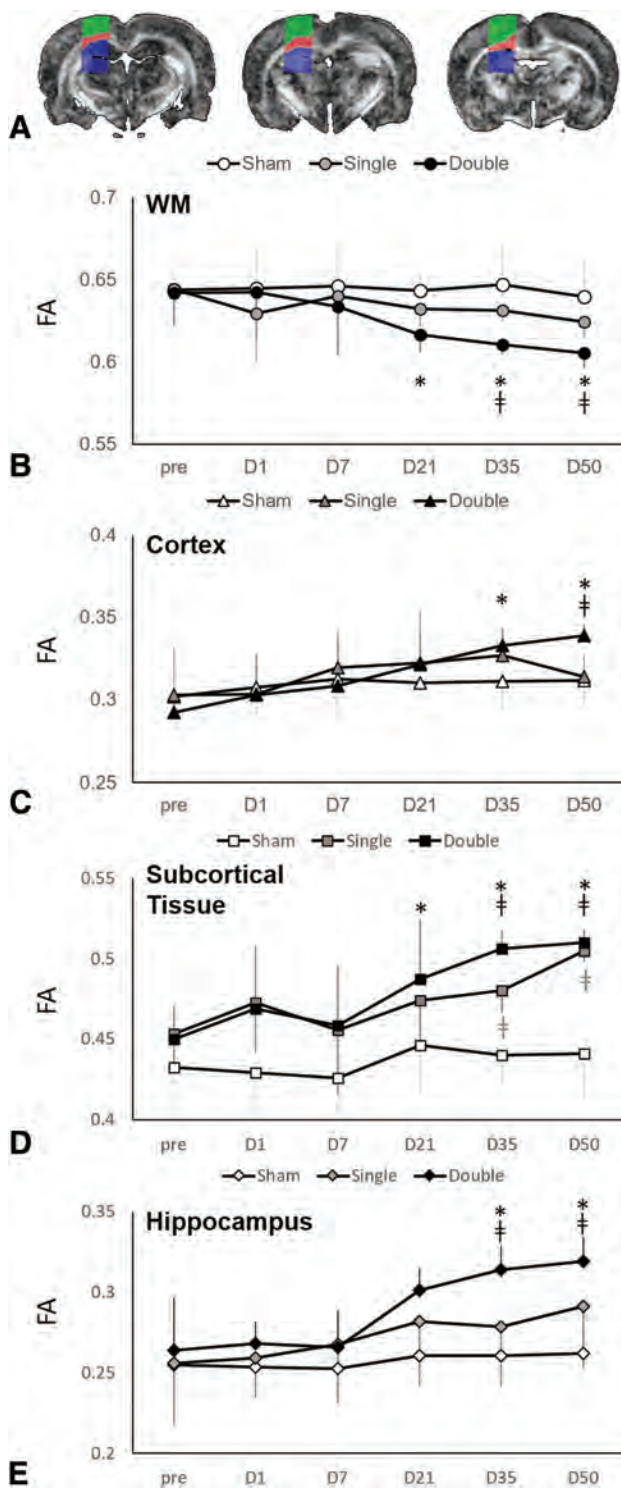


FIG 1. Longitudinal changes in FA after CHI. A, Automatically segmented ROIs deep to the site of impact on 3 consecutive slices show the cortex (green), white matter (red), and subcortical tissue (blue). Longitudinal follow-up during the first 50 days shows the evolution of mean FA values across time, which differ between white matter (B) and gray matter (C–E) structures, as well as important differences between single and double injury. Data are means; † indicates $P < .05$ versus the sham; asterisk, $P < .05$ versus baseline (day 0 [D0]).

Behavioral Assessment

Assessments of the modified Neurological Severity Score (mNSS), the Beam Walk Balance Test, and open-field test were performed

before, at 24 hours, and every 7 days after CHI or sham surgery. The mNSS evaluates motor sensory reflex, muscular status, and balance.^{10,15} Points are awarded for the inability to perform the task, the lack of reflex, or abnormal response with a maximum possible score of 20 (higher score indicates worse outcome.) The Beam Walk Balance Test measures the time required for the animal to cross the beam, assessing balance and coordinated motor function.¹⁶ Animals who fell off the beam or did not finish the task received a score of 180 seconds. The open-field test was used to assess spontaneous activity and anxiety-like behavior.¹⁷ Tracking and calculation of the movement duration, mean travel distance, center entries, and center time of each animal during the trial were analyzed using ActualTract software (Actual Analytics, Edinburgh, United Kingdom) (On-line Appendix).¹⁸

Histology

Immunohistochemical staining of formalin-fixed, paraffin-embedded tissue sections was performed using the Immunoperoxidase Secondary Detection system kit (IHC Select, DAB500; Millipore, Temecula, California). Briefly, the slides were deparaffinized and treated with 3% H₂O₂ to block endogenous peroxidase activity. Citrate buffer was used for antigen retrieval at 90°C. Staining procedures were performed according to manufacturer's recommendation. Specimens were counterstained with hematoxylin and mounted with ProLong Gold Antifade reagent (P36930; ThermoFisher Scientific, Waltham, Massachusetts). To assess neuroinflammation, we used the following antibodies for immunohistochemical staining: anti-glial fibrillary acidic protein (GFAP) (ab68428; Abcam, Cambridge, Massachusetts) and anti-Cluster of Differentiation 68 (CD 68) (GTX41868; GeneTex, Irvine, California).

All images were acquired using a DP 80 light microscope slide scanner (Olympus, Shinjuku, Japan). ROIs of the ipsilateral cortex (2 mm posterior to the bregma) and the CA1 region of the ipsilateral hippocampus (3 mm posterior to the bregma) were traced in 3 consecutive sections from each animal using cellSens Dimension software (Olympus America, Center Valley, Pennsylvania).¹⁰ The number of activated astrocytes and microglia in the ROIs was counted using FIJI/ImageJ software (National Institutes of Health, Bethesda, Maryland).¹⁹

Statistical Analysis

Statistical analyses were performed using SPSS software (IBM, Armonk, New York). Significant differences in DTI metrics, cortical volume, and behavioral outcome between sham, single, and repetitive injuries across the entire study period were assessed using a 2-way mixed ANOVA. Significant differences in GFAP and CD 68 expression were assessed using 2-way ANOVA. Post hoc tests were performed by the Tukey honestly significant difference and the Dunnett T3 post hoc tests for data passing and not passing the homogeneity test, respectively. The significance level was set at $P < .05$.

RESULTS

Inspection of T₂-weighted imaging and SWI revealed no focal brain contusions or hemorrhage at both 24 hours and 50 days

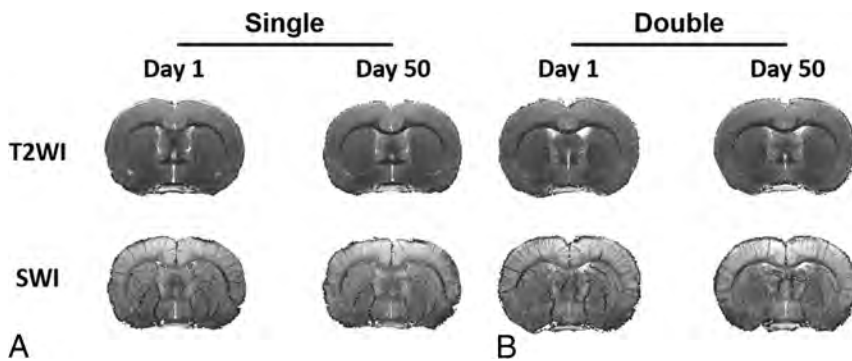


FIG 2. No focal hemorrhage or contusion on conventional MR imaging after experimental CHI. T₂-weighted imaging and susceptibility-weighted imaging with in-plane resolution of 78 μm obtained at 7T on day 1 and day 50 after single (A) and double (B) CHI show no contusion, edema, or microhemorrhage. One representative animal from each group for the longitudinal study is shown here.

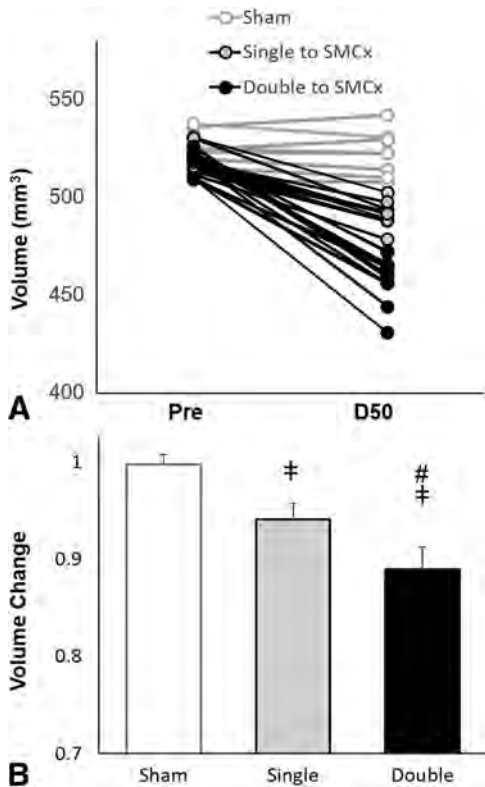


FIG 3. Cortical loss after experimental CHI. There is a clear decrease in cortical volume as measured on T₂-weighted images 50 days postinjury compared with baseline (A), with a greater percentage volume change after double injury ($n = 12$) compared with sham surgery ($n = 9$) and single injury ($n = 12$). Reduction of cortical volume is associated with the number of impacts. Data are means. † indicates $P < .05$ versus the sham; #, $P < .05$ versus the single CHI; SMCx, sensorimotor cortex.

postinjury (Fig 2), and there were no fractures identified using micro-CT.

Cortical Volume Assessment

There were no differences in mean baseline cortical volume among groups (520.169 ± 6.77 , 516.88 ± 6.53 , and $523.68 \pm 10.48 \text{ mm}^3$ for single injury, double injury, and sham groups, respectively). Longitudinal follow-up during 50 days revealed decreased cortical volume in the single- and double-

injury groups ($P < .01$). Furthermore, animals in the double-injury group sustained a significantly larger percentage change in volume ($0.11 \pm 0.02 \text{ mm}^3$) compared the single-injury group at 50 days follow-up ($0.06 \pm 0.02 \text{ mm}^3$) ($P < .01$; Fig 3).

Longitudinal Diffusion MR Imaging Changes

Compared with baseline measurements, while there were no significant changes in MD after sham surgery or injury in all groups (On-line Table 1), significant changes in AD and RD after injury are shown in On-line Fig 2. There were differences in FA compared with baseline

measures in the double-injury group but no change in FA with time in the sham and single-injury group (On-line Table 2). Namely, WM FA showed a significant decrease from the baseline value beginning at 21 days ($P = .04$) after double injury, which was sustained at 50 days. In the cortex, there was a significant increase in FA from baseline beginning at 35 days ($P < .01$) after double injury, sustained at 50 days. Subcortical FA showed a significant increase from baseline at 21 days ($P = .02$) after double injury. Hippocampal FA showed a significant increase from baseline at 35 days ($P = .02$; Fig 1) after double injury.

Cross-Sectional Diffusion MR Imaging Between-Group Comparisons

While there were no differences in MD among groups, significant changes in cortical AD and cortical RD were found between single- and double-injury groups after 35 days (On-line Fig 2). Higher mean subcortical FA ($P < .01$) was observed in the single-injury group compared with the sham group beginning 35 days after injury. Similarly, FA was higher in the double-injury group compared with the sham group in the cortical (at 50 days), subcortical, and hippocampal (beginning at 35 days) regions. FA was lower in the double-injury group compared with the sham group in WM (beginning at 35 days) ($P < .01$; Fig 1). No other differences were seen among groups in terms of diffusion metrics.

Behavioral Assessment

All groups (sham and single- and double-injury) demonstrated significantly increased mNSS 24 hours after ictus (from 1.50 ± 1.09 to 3.00 ± 1.48 for sham, from 2.67 ± 0.58 to 4.42 ± 2.07 for single injury, and from 3.00 ± 1.41 to 6.21 ± 2.75 for double injury; $P < .03$). mNSS in the sham and single-injury groups recovered after days 7 and 28, respectively; however, it continued to be elevated in the double-injury group for the entire study period ($P < .02$). Animals in the double-injury group demonstrated higher mean mNSS compared with the single-injury ($P < .01$) and the sham ($P < .01$) groups from 7 days on (Fig 4A).

Beam-walking duration was significantly increased over baseline (28.50 ± 2.90 seconds) beginning at 24 hours (65.90 ± 23.00 seconds; $P < .01$) following double injury and remained increased during the entire 50-day study period (155.30 ± 28.59 seconds;

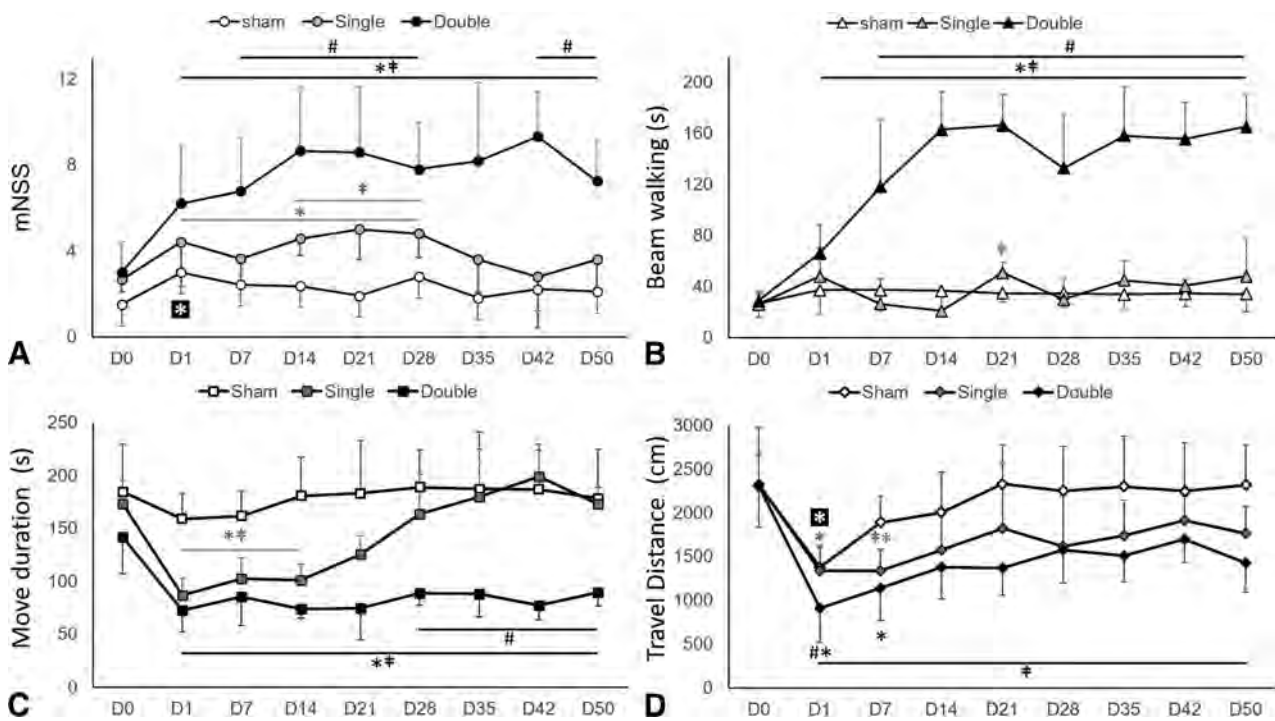


FIG 4. Behavioral deficits after CHI. mNSS (A) and beam-walking duration (B) after single and double CHI compared with sham surgery. In single-injury rodents, the mNSS score and beam-walking duration follow a similar time course compared with animals in the sham group; whereas in double-injury rodents, the mNSS score and beam-walking duration both increase significantly after CHI by day 7 and do not resolve by day 50. Locomotive activity as measured by movement duration (C) and travel distance (D) in the open-field trial after single and double CHI is impaired and persisted at day 50 after double injury. Data are means. † indicates $P < .05$ versus the sham; asterisk, $P < .05$ versus baseline (day 0 [D0]); #, $P < .05$ versus the single CHI.

$P = .02$). Significantly higher average beam-walking duration was observed after double injury (118.00 ± 13.11 seconds) compared with single injury (26.00 ± 19.69 seconds; $P < .01$) after 7 days (Fig 4A, -B). There were no other significant differences in beam-walking duration scores.

With regard to the open-field test, both single- and double-injury groups showed decreased movement duration compared with baseline, beginning at 24 hours after CHI (from 173.30 ± 22.00 to 86.67 ± 15.93 seconds for single injury; and from 141.92 ± 34.63 to 72.36 ± 21.18 seconds for double injury; $P < .01$). While movement duration in animals with single injury recovered after 14 days, movement duration in animals with double injury remained significantly lower compared with baseline for the entire 50-day period (77.27 ± 12.50 seconds; $P < .01$). Between-group differences were seen in movement duration between sham (161.67 ± 23.15 seconds) and single injury (102.34 ± 19.90 seconds; $P < .01$) as well as sham and double injury (85.17 ± 27.13 seconds; $P < .01$) from day 7 through 14. This difference persisted in the double-injury group (178.23 ± 46.69 versus 89.93 ± 12.73 seconds at day 50; $P < .01$), whereas the single-injury animals recovered movement duration scores in a manner more similar to sham animals beyond day 28. From day 28 on, there was also a significant difference between single (163.83 ± 37.31 seconds) and double (88.59 ± 11.45 seconds; $P < .01$) injury groups (Fig 4C).

Travel distance was also measured from the open-field test and was decreased in all groups from baseline measures at 24 hours (from 2314.14 ± 657.09 to 1378.06 ± 224.62 cm for sham, from 2323.30 ± 342.68 to 1340.20 ± 286.26 cm for single injury, and

from 2308.50 ± 479.38 to 906.61 ± 389.05 cm for double injury; $P < .03$). In sham animals, the mean travel distance recovered by day 7 after surgery. In animals with single and double injury, travel distance recovered by day 14 after injury. While differences in travel distance between sham and single-injury groups were seen only on day 7 after CHI, statistical differences between the double-injury and sham groups were consistently present from 24 hours through day 50 ($P < .01$). In addition, a difference in travel distance was also present between single- and double-injury groups initially at 24 hours ($P = .02$) (Fig 4D). To evaluate anxiety-like behavior, we measured center entries and center time from the open-field test (On-line Fig 3).

Immunohistology

Evidence for reactive gliosis was seen using GFAP and CD 68 immunohistologic staining in both the cortex and the CA1 region of the hippocampus after CHI (Fig 5A). GFAP immunoreactivity was observed in the cortex and hippocampus in both single- and double-injury animals compared with the sham animals at 24 hours and was sustained at 50 days ($P < .05$). Involvement of the hippocampus confirms that more diffuse histopathologic changes occurred remote from the direct site of impact. CD 68 expression was also observed in the cortex at 24 hours after double injury ($P = .01$) and increased at day 50 after single and double injury compared with sham injury ($P < .02$). CD 68 expression in the hippocampus was prominent compared with the sham animals at 50 days after double injury ($P < .02$) (Fig 5B-E).

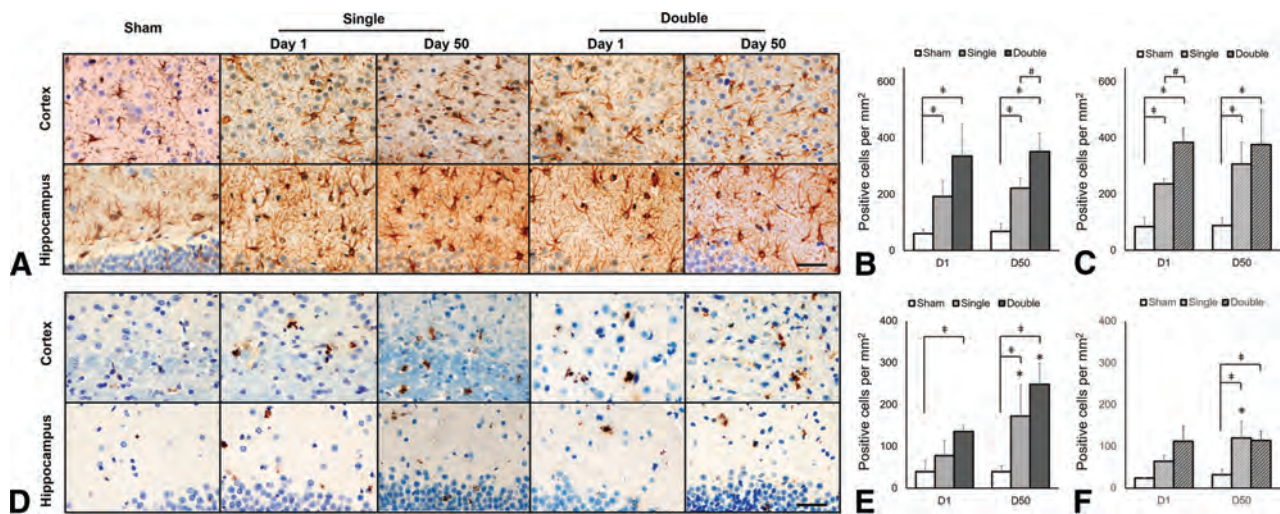


FIG 5. Astroglial and microglial expression in the cortex and hippocampus underlying the impact region after CHI. **A**, GFAP-positive staining and quantification of GFAP expression in the cortex (**B**) and hippocampus (**C**) after CHI. **D**, CD 68-positive staining and quantification of CD 68 expression in the cortex (**E**) and hippocampus (**F**) after CHI. As early as 24 hours after both single and double CHI, elevated GFAP is observed in both the cortex and hippocampus deep to the impact site. CD 68 expression indicating neuroinflammation is also observed at 24 hours postinjury and sustained to day 50 in the cortex after double CHI. Scale bar, 40 μ m.

DISCUSSION

Here we introduce a modified weight-drop model with fixed head positioning to allow a high-degree of control over the strength and location of impact, improving reproducibility of the injury.^{20,21} Our results show this to be a reliable model to deliver experimental CHI without focal traumatic brain lesions, a challenge and limitation of many prior studies of head injury using rodent models.²⁰⁻²² This work provides the most comprehensive longitudinal study to date of single and double head injury using a reliable CHI model and seeks to fill in gaps in our knowledge regarding the temporal evolution of injury and recovery of the brain. We found significant macrostructural, microstructural MR imaging changes, behavioral changes, and histologic differences after injury in both single- and double-injury groups during the first 50 days after injury and describe these temporal changes.

Limited previous studies have reported brain atrophy in experimental TBI; most used a cross-sectional design with potential confounders such as ventricular dilation or tissue loss.^{23,24} Recently, Meconi et al²⁵ studied animals on day 7 after repeat awake CHI and reported no cortical volume loss. We observed a decrease in cortical volume during a longer follow-up period of 50 days, and it might be expected that macrostructural volume loss would be better detected at longer follow-up times as in other neurodegenerative animal models. Moreover, no significant change in the body weight of animals was observed at 50 days after injury compared with the baseline, suggesting that the cortical volume reduction was not associated with dehydration or malnutrition in our animals. Of note, cortical volume was reduced after both single and double injury, and the degree of atrophy was higher after double injury. This finding is in keeping with what we know from clinical experience and human subject research. Cortical atrophy is known to be a major neuropathologic feature of chronic TBI and has been shown in longitudinal studies to occur even after a single mild injury in humans.³ Multiple head injuries, even without focal acute hemorrhage or contusion, are associated with a long-term risk for a number of neurodegenerative disorders asso-

ciated with brain volume loss, including chronic traumatic encephalopathy.²⁶ We found increased cortical GFAP expression as early as 24 hours, which was sustained for 50 days, and we hypothesize that persistent neuroinflammation could predispose to neurodegeneration.²⁷

We found significant changes in cortical volume and FA from baseline after both single and double injury, with differences between the 2 groups suggesting that injury to the brain may be cumulative. Specifically, our results show decreased WM FA after 21 days in the double-injury group. This is in keeping with most human studies of mild TBI that showed decreased FA in WM after injury.²⁸ Previous animal studies of head injury (with contusion) also showed significantly reduced FA in the WM within 1 week of injury, which investigators have related to diffuse axonal injury and loss of myelin.²⁹⁻³² We also found increased GM FA after double CHI in cortical, subcortical, and hippocampal structures. Published evidence of FA changes in gray matter after brain injury is mixed.^{17,31,33} The mechanism behind increased GM FA in TBI models is incompletely understood, though some have suggested this to be reflective of inflammatory changes^{29,30,32} and the orientation of astrocyte processes^{34,35} associated with underlying injury. We did, in fact, observe astrogliosis on immunohistochemical staining in this study. Future work combining atlas-based tissue segmentation and interrogation of a greater number of regions, including those more remote from the injury, will better illustrate the dynamic changes in diffusion anisotropy.

In terms of behavioral changes, worse outcome seen after double injury compared with single injury supports the idea that there is cumulative injury after multiple impacts sustained within a close time period. We found significant deficits in beam walking in animals who sustained double injuries, whereas the performance of animals in the single-injury group approximated the sham group closely at all time points. The clinical correlate may be slower walking speed and multijoint gait abnormalities reported in patients with chronic TBI.³⁶ In addition, in contrast to the recovery of activity in the single-injury paradigm at 28 days,

movement duration after double injury remained short, suggesting prolonged recovery after double injury.¹⁰

Our histopathologic findings confirm that astrogliosis is initiated within 1 day of injury, in keeping with previously published reports.^{10,19} Clinically, there is an association between elevated serum GFAP and the severity of head trauma in patients within 72 hours of injury.³⁷ Taken together, our results support the presence of neuroinflammation occurring shortly after CHI, even with the absence of acute focal macrostructural injury, and this finding is in agreement with studies that point to serum GFAP as a promising noninvasive biomarker in the setting of even mild TBI.^{38,39}

Limitations of the current study include the use of a fixed head position during impact, which, while advantageous to quantify the delivery of impact, lacks the linear translation and rotation common to clinical scenarios of mild TBI. Other animal models are, however, criticized for the inability to quantify and control rebound effects as well as the common occurrence of focal hemorrhage/contusion.^{21,22} We have work currently underway to establish a related setup using unrestrained animals to better model acceleration-deceleration influences on injury. Our results demonstrate that CHI-related alterations are augmented by the number of impacts, though we studied only 1 repetitive paradigm. Additional studies using varying impact regions and repetition schemes would optimally take advantage of a model such as the one proposed here. Last, in addition to neuroinflammation, changes in the neural density, axonal integrity, or abnormal protein accumulation may also contribute to alteration in DTI metrics.^{31,40} We plan to examine this possibility using respective immunohistochemical stains in our future studies.

CONCLUSIONS

Our study describes a repetitive CHI model without acute macroscopic damage that leverages the benefits of controlling impact degree, location, and number. There are measurable neuroimaging abnormalities after CHI that evolve dynamically during the first 50 days postinjury, occurring after the immediate effects on behavior and neuropathology. There is a cumulative effect that the number of injuries has on later cortical atrophy, evolving microstructural changes, and neurobehavioral outcome in the first 50 days following injury. This work bridges predominantly cross-sectional evidence from human subject studies and pathologic studies using animal models with a rich, multi-time point, longitudinal research paradigm.

Disclosures: Yu-Chieh Jill Kao—RELATED: Grant: Ministry of Science and Technology, Republic of China. Cheng-Yu Chen—RELATED: Grant: Ministry of Science and Technology, Republic of China. Comments: 3-year grant for animal model study.* Yvonne W. Lui—UNRELATED: Grants/Grants Pending: National Institutes of Health (R01 NS039135-11, R21 NS090349 and P41 EB017183)*; OTHER RELATIONSHIPS: Siemens-New York University collaboration lead and advisor for Bold Brain Ventures LP. *Money paid to the institution.

REFERENCES

1. Sosin DM, Sniezek JE, Thurman DJ. **Incidence of mild and moderate brain injury in the United States, 1991.** *Brain Inj* 1996;10:47–54 CrossRef Medline
2. Roozenbeek B, Maas AI, Menon DK. **Changing patterns in the epi-**

3. **demology of traumatic brain injury.** *Nat Rev Neurol* 2013;9:231–36 CrossRef Medline
3. Chong CD, Schwedt TJ. **Research imaging of brain structure and function after concussion.** *Headache* 2018;58:827–35 CrossRef Medline
4. Wu X, Kirov II, Gonen O, et al. **MR imaging applications in mild traumatic brain injury: an imaging update.** *Radiology* 2016;279:693–707 CrossRef Medline
5. Cole JH, Leech R, Sharp DJ, et al; Alzheimer's Disease Neuroimaging Initiative. **Prediction of brain age suggests accelerated atrophy after traumatic brain injury.** *Ann Neurol* 2015;77:571–81 CrossRef Medline
6. Coughlin JM, Wang Y, Munro CA, et al. **Neuroinflammation and brain atrophy in former NFL players: an in vivo multimodal imaging pilot study.** *Neurobiol Dis* 2015;74:58–65 CrossRef Medline
7. Castaño Leon AM, Cicuendez M, Navarro B, et al. **What can be learned from diffusion tensor imaging from a large traumatic brain injury cohort? White matter integrity and its relationship with outcome.** *J Neurotrauma* 2018;35:2365–76 CrossRef Medline
8. Chung S, Fieremans E, Wang X, et al. **White matter tract integrity: an indicator of axonal pathology after mild traumatic brain injury.** *J Neurotrauma* 2018;35:1015–20 CrossRef Medline
9. Marmarou A, Foda MA, van den Brink W, et al. **A new model of diffuse brain injury in rats, Part I: pathophysiology and biomechanics.** *J Neurosurg* 1994;80:291–300 Medline
10. Mountney A, Boutte AM, Cartagena CM, et al. **Functional and molecular correlates after single and repeated rat closed-head concussion: indices of vulnerability after brain injury.** *J Neurotrauma* 2017;34:2768–89 CrossRef Medline
11. Kao YC, Li W, Lai HY, et al. **Dynamic perfusion and diffusion MRI of cortical spreading depolarization in photothrombotic ischemia.** *Neurobiol Dis* 2014;71:131–39 CrossRef Medline
12. Kao YJ, Oyarzabal EA, Zhang H, et al. **Role of genetic variation in collateral circulation in the evolution of acute stroke: a multimodal magnetic resonance imaging study.** *Stroke* 2017;48:754–61 CrossRef Medline
13. Lai HY, Albaugh DL, Kao YC, et al. **Robust deep brain stimulation functional MRI procedures in rats and mice using an MR-compatible tungsten microwire electrode.** *Magn Reson Med* 2015;73:1246–51 CrossRef Medline
14. Kuo DP, Lu CF, Liou M, et al. **Differentiation of the infarct core from ischemic penumbra within the first 4.5 hours, using diffusion tensor imaging-derived metrics: a rat model.** *Korean J Radiol* 2017;18:269–78 CrossRef Medline
15. Yarnell AM, Barry ES, Mountney A, et al. **The Revised Neurobehavioral Severity Scale (NSS-R) for rodents.** *Curr Protoc Neurosci* 2016;75:9.52.1–9.52.16 CrossRef Medline
16. Hamm RJ. **Neurobehavioral assessment of outcome following traumatic brain injury in rats: an evaluation of selected measures.** *J Neurotrauma* 2001;18:1207–16 CrossRef Medline
17. Robinson S, Winer JL, Berkner J, et al. **Imaging and serum biomarkers reflecting the functional efficacy of extended erythropoietin treatment in rats following infantile traumatic brain injury.** *J Neurosurg Pediatr* 2016;17:739–55 CrossRef Medline
18. Green EW, O'Callaghan EK, Hansen CN, et al. **Drosophila circadian rhythms in seminatural environments: summer afternoon component is not an artifact and requires TrpA1 channels.** *Proc Natl Acad Sci U S A* 2015;112:8702–07 CrossRef Medline
19. Acabchuk R, Briggs DI, Angoa-Perez M, et al. **Repeated mild traumatic brain injury causes focal response in lateral septum and hippocampus.** *Concussion* 2016;1 CrossRef Medline
20. Namjoshi DR, Good C, Cheng WH, et al. **Towards clinical management of traumatic brain injury: a review of models and mechanisms from a biomechanical perspective.** *Dis Model Mech* 2013;6:1325–38 CrossRef Medline
21. Shultz SR, McDonald SJ, Vonder Haar C, et al. **The potential for animal models to provide insight into mild traumatic brain injury:**

- translational challenges and strategies.** *Neurosci Biobehav Rev* 2017; 76(Pt B):396–414 CrossRef Medline
22. Xiong Y, Mahmood A, Chopp M. **Animal models of traumatic brain injury.** *Nat Rev Neurosci* 2013;14:128–42 CrossRef Medline
 23. Goddoyne C, Nichols J, Wu C, et al. **Repetitive mild traumatic brain injury induces ventriculomegaly and cortical thinning in juvenile rats.** *J Neurophysiol* 2015;113:3268–80 CrossRef Medline
 24. Shultz SR, Bao F, Omana V, et al. **Repeated mild lateral fluid percussion brain injury in the rat causes cumulative long-term behavioral impairments, neuroinflammation, and cortical loss in an animal model of repeated concussion.** *J Neurotrauma* 2012;29:281–94 CrossRef Medline
 25. Meconi A, Wortman RC, Wright DK, et al. **Repeated mild traumatic brain injury can cause acute neurologic impairment without overt structural damage in juvenile rats.** *PLoS One* 2018;13:e0197187 CrossRef Medline
 26. McKee AC, Stein TD, Kiernan PT, et al. **The neuropathology of chronic traumatic encephalopathy.** *Brain Pathol* 2015;25:350–64 CrossRef Medline
 27. Tambalo S, Peruzzotti-Jametti L, Rigolio R, et al. **Functional magnetic resonance imaging of rats with experimental autoimmune encephalomyelitis reveals brain cortex remodeling.** *J Neurosci* 2015; 35:10088–100 CrossRef Medline
 28. Borja MJ, Chung S, Lui YW. **Diffusion MR imaging in mild traumatic brain injury.** *Neuroimaging Clin N Am* 2018;28:117–26 CrossRef Medline
 29. Budde MD, Janes L, Gold E, et al. **The contribution of gliosis to diffusion tensor anisotropy and tractography following traumatic brain injury: validation in the rat using Fourier analysis of stained tissue sections.** *Brain* 2011;134:2248–60 CrossRef Medline
 30. Long JA, Watts LT, Chemello J, et al. **Multiparametric and longitudinal MRI characterization of mild traumatic brain injury in rats.** *J Neurotrauma* 2015;32:598–607 CrossRef Medline
 31. Tu TW, Williams RA, Lescher JD, et al. **Radiological-pathological correlation of diffusion tensor and magnetization transfer imaging in a closed head traumatic brain injury model.** *Ann Neurol* 2016;79: 907–20 CrossRef Medline
 32. Wang ML, Yu MM, Yang DX, et al. **Longitudinal microstructural changes in traumatic brain injury in rats: a diffusional kurtosis imaging, histology, and behavior study.** *AJNR Am J Neuroradiol* 2018; 39:1650–56 CrossRef Medline
 33. Wright DK, Trezise J, Kamnaksh A, et al. **Behavioral, blood, and magnetic resonance imaging biomarkers of experimental mild traumatic brain injury.** *Sci Rep* 2016;6:28713 CrossRef Medline
 34. Salo RA, Miettinen T, Laitinen T, et al. **Diffusion tensor MRI shows progressive changes in the hippocampus and dentate gyrus after status epilepticus in rat: histological validation with Fourier-based analysis.** *Neuroimage* 2017;152:221–36 CrossRef Medline
 35. Sizonenko SV, Camm EJ, Garbow JR, et al. **Developmental changes and injury induced disruption of the radial organization of the cortex in the immature rat brain revealed by in vivo diffusion tensor MRI.** *Cereb Cortex* 2007;17:2609–17 CrossRef Medline
 36. Williams G, Morris ME, Schache A, et al. **Incidence of gait abnormalities after traumatic brain injury.** *Arch Phys Med Rehabil* 2009;90: 587–93 CrossRef Medline
 37. Papa L, Brophy GM, Welch RD, et al. **Time course and diagnostic accuracy of glial and neuronal blood biomarkers GFAP and UCH-L1 in a large cohort of trauma patients with and without mild traumatic brain injury.** *JAMA Neurol* 2016;73:551–60 CrossRef Medline
 38. Kulbe JR, Geddes JW. **Current status of fluid biomarkers in mild traumatic brain injury.** *Exp Neurol* 2016;275(Pt 3):334–52 CrossRef Medline
 39. Shahim P, Tegner Y, Gustafsson B, et al. **Neurochemical aftermath of repetitive mild traumatic brain injury.** *JAMA Neurol* 2016;73: 1308–15 CrossRef Medline
 40. Yu F, Shukla DK, Armstrong RC, et al. **Repetitive model of mild traumatic brain injury produces cortical abnormalities detectable by magnetic resonance diffusion imaging, histopathology, and behavior.** *J Neurotrauma* 2017;34:1364–81 CrossRef Medline

Periventricular White Matter Abnormalities on Diffusion Tensor Imaging of Postural Instability Gait Disorder Parkinsonism

S.Y.Z. Tan, N.C.H. Keong, R.M.P. Selvan, H. Li, L.Q.R. Ooi, E.K. Tan, and L.L. Chan



ABSTRACT

BACKGROUND AND PURPOSE: Postural instability gait disorder is a motor subtype of Parkinson disease associated with predominant gait dysfunction. We investigated the periventricular white matter comprising longitudinal, thalamic, and callosal fibers using diffusion tensor MR imaging and examined clinical correlates in a cohort of patients with Parkinson disease and postural instability gait disorder and healthy controls.

MATERIALS AND METHODS: All subjects underwent the Tinetti Gait and Balance Assessment and brain MR imaging. The DTI indices (fractional anisotropy, mean diffusivity, axial diffusivity, and radial diffusivity) from ROIs dropped over the superior and inferior longitudinal fasciculi, inferior fronto-occipital fasciculus, anterior thalamic radiation, anterior and posterior limbs of the internal capsule, and the genu and body of corpus callosum were evaluated.

RESULTS: Our findings showed that the superior longitudinal fasciculus, inferior longitudinal fasciculus, inferior fronto-occipital fasciculus, anterior thalamic radiation, genu of the corpus callosum, and body of the corpus callosum are more affected in postural instability gait disorder than in those with Parkinson disease or healthy controls, with more group differences among the longitudinal fibers. Only the callosal fibers differentiated the postural instability gait disorder and Parkinson disease groups. DTI measures in the superior longitudinal fasciculus, frontostriatal fibers (anterior thalamic radiation, anterior limb of the internal capsule), and genu of the corpus callosum fibers correlated with clinical gait severity.

CONCLUSIONS: Findings from this case-control cohort lend further evidence to the role of extranigral pathology and, specifically, the periventricular fibers in the pathophysiology of postural instability gait disorder.

ABBREVIATIONS: AD = axial diffusivity; ALIC = anterior limb of the internal capsule; ATR = anterior thalamic radiation; BCC = body of the corpus callosum; FA = fractional anisotropy; GCC = genu of the corpus callosum; HC = healthy controls; IFOF = inferior fronto-occipital fasciculus; ILF = inferior longitudinal fasciculus; MD = mean diffusivity; PIGD = postural instability gait disorder; PD = Parkinson disease; PLIC = posterior limb of the internal capsule; RD = radial diffusivity; SLF = superior longitudinal fasciculus

The 4 hallmark symptoms of Parkinson disease (PD) are shaking tremor, stiffness, bradykinesia, and difficulty with balance and coordination.¹ Postural instability gait disorder (PIGD) is a

motor subtype of PD associated with predominant gait dysfunction. These patients often progress rapidly and are at higher risk for nonmotor deficits such as dementia and cognitive impairment.² Conventional medical interventions for PD are less effective in patients with PIGD, with gait and balance deficits more resistant to levodopa therapy on disease progression,³ thus prompting the need to further explore the pathophysiology underlying the PIGD subtype to evaluate more targeted therapies.

Diffusion tensor imaging is a noninvasive MR imaging tool widely used to evaluate microstructural changes in brain white matter in vivo.⁴ The principle behind DTI is its ability to differentiate the magnitude and directionality of the diffusion of water in neural tissue because water diffuses irregularly and is fastest along the major axis parallel to the neural fibers. An analysis of the DTI indices, namely fractional anisotropy (FA), mean

Received August 24, 2018; accepted after revision January 18, 2019.

From the Department of Diagnostic Radiology, Singapore General Hospital, Singhealth (S.Y.Z.T., N.C.H.K., H.L., E.K.T., L.L.C.), Singapore; Departments of Neurosurgery, Research and Neurology, National Neuroscience Institute, Singhealth (N.C.H.K., R.M.P.S., L.Q.R.O., E.K.T.), Singapore; and Duke-NUS Medical School (N.C.H.K., E.K.T., L.L.C.), Singapore.

This study was funded through a research grant from the National Medical Research Council (Singapore).

Please address correspondence to Ling-Ling Chan, Department of Diagnostic Radiology, Singapore General Hospital, Outram Rd, Singapore 169608; email: chan.ling.ling@sgh.com.sg

Indicates open access to non-subscribers at www.ajnr.org

Indicates article with supplemental on-line tables.

<http://dx.doi.org/10.3174/ajnr.A5993>

(MD), radial (RD), and axial diffusivity (AD), across patient groups may provide insight into the histopathologic process⁵ underlying PIGD.

Traditionally, studies in PD are focused on pathophysiologic changes in the nigrostriatal and extrapyramidal pathways. There is increasing evidence of the role of cortical and subcortical structures in postural control and the freezing of gait.⁶⁻⁹ Recent age-related imaging studies also showed that periventricular white matter lesions play a role in balance impairment, mobility, and cognitive deficits in otherwise healthy elderly individuals, further emphasizing the importance of the integrity of afferent and efferent subcortical-cortical projections.¹⁰

The aim of this study was to investigate whether periventricular white matter longitudinal, thalamic, and callosal fibers are differentially affected in patients with PIGD parkinsonism, compared with patients with typical tremor-dominant PD and healthy, neurologically intact controls (HC) using an ROI approach to brain DTI MR imaging analysis. We hypothesized that microstructural changes in these periventricular white matter fibers on DTI are correlated with motor dysfunction in PD, and especially in PIGD.

MATERIALS AND METHODS

Study Subjects

The study was undertaken with the written informed consent of each subject and the approval of the SingHealth Centralised Institutional Review Board. All protocols were approved by the SingHealth ethics committee.¹¹ Twenty-one patients with PD and 19 with PIGD were recruited at a tertiary referral center, where they were diagnosed by a movement disorders neurologist on the basis of established clinical criteria^{12,13} from the United Kingdom PD Brain Bank (<https://www.parkinsons.org.uk/research/parkinsons-uk-brain-bank>) and Deprenyl and Tocopherol Antioxidative Therapy Of Parkinsonism Trial (DATATOP, <https://jamanetwork.com/journals/jamaneurology/fullarticle/589418>). Exclusion criteria included patients who were wheelchair-bound from severe disability, showed evidence of cognitive dysfunction (based on the Mini-Mental State Examination score), had features of Parkinson-plus syndrome or normal pressure hydrocephalus, or had a history of head injury, encephalitis, stroke, exposure to neuroleptic drugs, and MR imaging contraindications. Patients with evidence of cognitive dysfunction (based on the Mini-Mental State Examination score) were also excluded. Twenty HC who were age- and sex-matched to the patient cohort were also recruited during the same period. All 60 subjects were evaluated with the Tinetti Gait and Balance score (<https://fallpreventiontaskforce.org/wp-content/uploads/2014/10/Tinnetitool.pdf>) as an indicator of his or her mobility and fall risk.¹⁴

MR Imaging

The MR imaging brain scans were acquired on a 3T scanner (Magnetom Trio; Siemens, Erlangen, Germany) using a 12-channel phased array head coil. To minimize head motion during the scan, we secured the subjects' heads with securing straps.

The DTI scan was a spin-echo echo-planar imaging sequence (TR = 8200 ms, TE = 86 ms, diffusion sensitization in 30 non-collinear directions, in-plane resolution = 1.875×1.875 mm,

FOV = 240×240 mm, matrix = 128×128 , 64 contiguous 2-mm-thick slices, b-value = 800 s/mm^2 , integrated parallel acquisition technique factor = 2, B_0 averages = 2). Images from the structural FLAIR and T1- and T2-weighted scans were screened to exclude pathology in the ROIs.

Image Analysis

An ROI approach was adopted for DTI MR imaging analysis, using the commercially available Leonardo workstation, Version VE50A (Siemens, Erlangen, Germany) for image postprocessing. Two independent raters blinded to subject status drew 30-mm³ ROIs over various brain regions on the basis of neuroanatomic knowledge. The DTI indices of FA, MD, AD, and RD were recorded and averaged for paired fibers.

Circular ROIs (Figure) were placed within the periventricular white matter fibers comprising the superior (SLF) and inferior longitudinal fasciculi (ILF), inferior fronto-occipital fasciculus (IFOF), anterior thalamic radiation (ATR), anterior (ALIC) and posterior limbs of internal capsule, and genu (GCC) and body of the corpus callosum on representative sections at -2 mm (IFOF), 0 mm (ILF), +4 mm (ATR, ALIC), +6 mm (posterior limb of the internal capsule), +12 mm (GCC), +26 mm (body of the corpus callosum), and +28 mm (SLF) from the section containing the anterior and posterior commissures. Precaution was taken to avoid focal lesions or infarcts and immediate periventricular margins, so as to reduce spurious partial volume averaging artifacts on the DTI measurements by reviewing the structural images and color FA, diffusion trace, MD map, and B_0 images side by side during ROI placement.

Statistical Analysis

Statistical analysis was performed by using R 3.4.2 (www.r-project.org). Interrater and intrarater reliability for the DTI indices of FA, MD, AD, and RD were assessed using the intraclass correlation coefficient. The Kruskal-Wallis test was used to find group differences in the DTI indices of the periventricular white matter fibers, and a univariable logistic regression was performed to evaluate the ability of the DTI indices of each periventricular ROI to differentiate between PD and PIGD, PD and HC, and PIGD and HC, after adjusting for age and sex. Last, a multivariable linear regression was performed to evaluate the relationship between the DTI indices of each ROI and the Tinetti score (Total, Balance, and Gait) for the patients with PD and PIGD. The 2-sided significance was set at .05.

RESULTS

A total of 60 subjects (19 with PIGD, 21 with PD, 20 HC) were enrolled in this study, and their clinical data are summarized in Table 1. The mean Tinetti scores in PIGD and PD were significantly lower than those for HC ($P < .01$), and PIGD had the lowest score among the 3 subject groups. The interrater and intrarater reliability for the DTI indices (On-line Table 1) had a minimum score of 0.7, with most being >0.8 .

On-line Table 2 details the DTI indices of each periventricular ROI in the 3 subject groups. Results of the Kruskal-Wallis test and logistic regression are addressed in Tables 2 and On-line Table 3, respectively. In general, both PD and PIGD groups had lower median

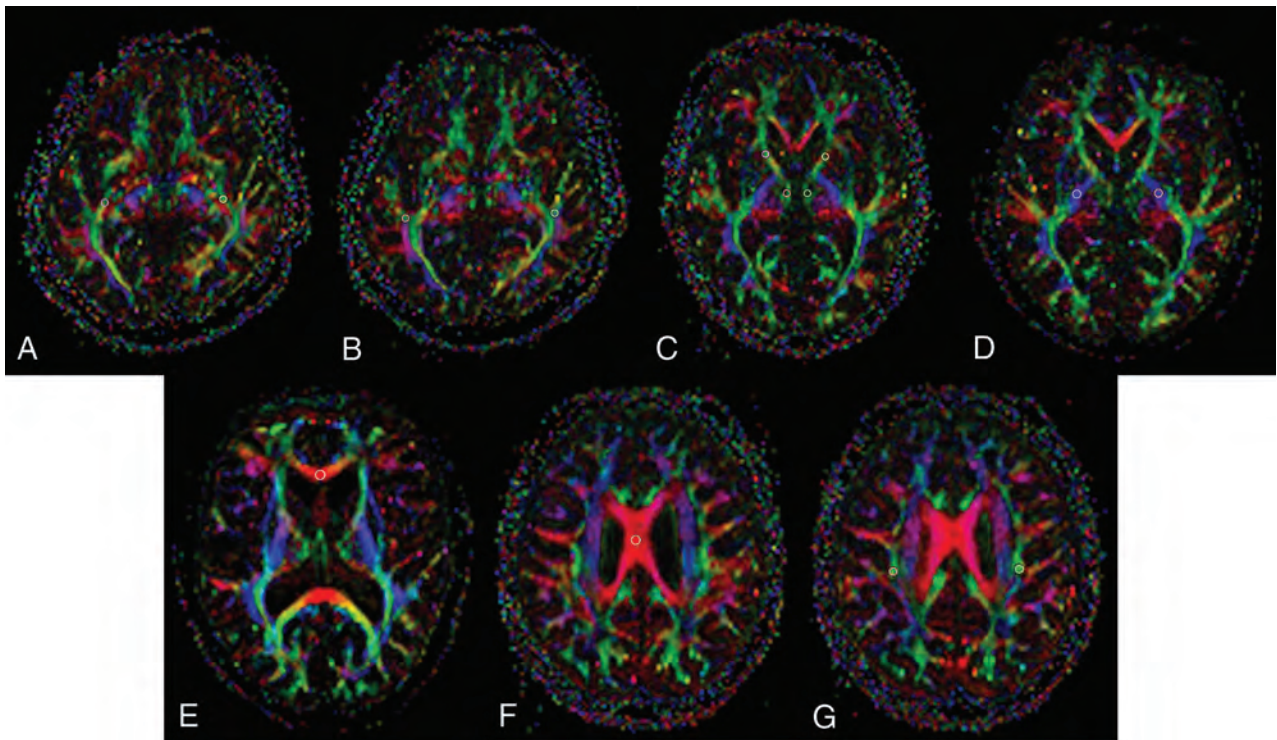


FIGURE. Axial DTI FA color maps depicting placement of *circular ROIs* in the inferior fronto-occipital fasciculus (A), ILF (B), anterior thalamic radiation (paramedian ROIs), and anterior limb of the internal capsule (anterolateral ROIs) (C), posterior limb of the internal capsule (D), genu (E) and body of the corpus callosum (F), and superior longitudinal fasciculus (G).

Table 1: Clinical features of study subjects

Groups	PIGD	PD	HC	P Values		
				PIGD vs HC	PD vs HC	PIGD vs PD
No.	19	21	20			
Sex (male/female)	15:4	17:4	16:4	1.00	1.00	1.00
Mean age (yr)	73.7 ± 6.7	72.0 ± 4.8	71.5 ± 4.9	0.24	0.742	0.36
Tinetti score (median) (IQR)						
Balance	9 (7.5–11)	12 (11–13)	15 (15–16)	<.001	<.001	0.03
Gait	7 (4.5–8.5)	9 (8–10)	12 (11–12)	<.001	<.001	0.01
Total	16 (12–19)	22 (20–23)	27 (26–27.3)	<.001	<.001	0.02

Note:—IQR indicates interquartile range.

Table 2: Results of Kruskal-Wallis test showing group differences in DTI indices among periventricular white matter ROIs^a

Group Comparisons	PIGD vs HC				PD vs HC				PIGD vs PD			
	FA	MD	AD	RD	FA	MD	AD	RD	FA	MD	AD	RD
WM fiber DTI indices												
SLF		+	+									+
P value		0.04 ^b	0.03 ^b									0.04 ^b
Longitudinal												
ILF	–	+		+		+						
P value	0.01 ^b	0.001 ^b		0.004 ^b		0.009 ^b						
IFOF	–	+		+	–	+		+				
P value	0.001 ^b	0.003 ^b		0.008 ^b	0.01 ^b	0.001 ^b		0.04 ^b				
Thalamic												
ATR	–											
P value	0.04 ^b											
Callosal												
BCC			+									+
P value			0.02 ^b									0.003 ^b
GCC										+		+
P value									0.01 ^b	0.03		

Note:—+ indicates higher group value; –, lower group value.

^a Empty cells indicate no significant differences.

^b Significant.

FA and higher median diffusivity (MD, AD, RD) values compared with HC across the periventricular ROIs. The periventricular longitudinal ROIs showed the most DTI differences between disease and HC groups, with all 3 showing differences in at least 2 DTI indices between the PIGD and HC groups. Among the thalamic ROIs, only the ATR differentiated between PIGD and HC groups. Both the ALIC and PLIC did not show any difference for any DTI index between groups. Only callosal ROIs differentiated PIGD and PD disease groups.

Results from the multivariable linear regression are shown in Online Table 4. Some DTI indices from the SLF and ALIC ROIs correlated with both Gait and Balance scores, but those from the GCC fibers correlated only with Gait and Total Tinetti scores. As expected, the Tinetti scores correlated negatively with the diffusivity indices and positively with FA, respectively.

DISCUSSION

Using an ROI approach in our case-control DTI study, we showed that periventricular longitudinal, thalamic, and callosal fibers are differentially affected in PIGD, PD, and HC, with generally reduced FA and increased diffusivity indices, lending further support to their use as biomarkers^{4,5} for identification of gait deficits and quantifying performance. The need for additional biomarkers for gait performance for identification of PIGD is shown by Herman et al,¹⁵ with their findings that gait metrics alone seem to be a poor indicator of the PIGD subtype. Periventricular white matter,¹⁰ in particular, has been shown to play an important role in gait, and additional effort is needed to understand it.

Longitudinal fibers provide the link between orbital, motor, and premotor areas and other areas of the brain,^{16,17} and deficits could affect visuospatial processing in gait.^{8,9} Our study has shown that the IFOF and ILF show statistically significant differences between PD (regardless of subtype) and HC. However, the SLF showed differences between PIGD and HCs, but not PD and HCs. The changes in SLF are more severe in the PIGD subtype, which are supported by other studies showing SLF involvement in gait, and in congruence with SLF having connections to the supplementary motor area (part of cerebral cortex that is involved in the control of movement).^{8,9}

Thalamic fibers have been shown to be implicated in functional studies of the basal ganglia-thalamo-cortical loop, which affects movement and perception.^{6,18} The fibers involved in the loop (ATR) in our study also showed differences between PIGD and HC in DTI indices and a statistically significant correlation with Tinetti scores. Although most studies show disruptions to the basal ganglia functional connectivity,¹⁹ few studies have interrogated the differences in their connecting fibers within PD and PIGD. Additionally, the ATR showed good ability to predict Tinetti Balance, but not Tinetti Gait scores. This suggests that the ATR has a more prominent role in balance, but not gait.

The corpus callosum was the only structure in this study that differentiated the PIGD and PD subtypes. It also showed a significant linear regression to Tinetti Gait and Total scores. This finding concurs with those in other studies showing that damage to the corpus callosum results in freezing of gait,²⁰ supporting the worse Gait scores in patients with PIGD.¹¹ However, because a

relationship between ageing and gait in the corpus callosum has also been reported,²¹ control for age as a potential confounder is important when using it as a biomarker.

Our study supports other findings of compromised functionality in the frontostriatal circuitry reported in gait dysfunction.²²⁻²⁴ Most studies have found that the prefrontal cortex functions are impaired in attention, dual task, set-shifting, and visuospatial activities in freezing of gait,^{6,9,25,26} suggesting underlying changes in various white matter fibers. Our results showed a shift in diffusivity and FA in the periventricular fibers, possibly related to the change in functional performance. DTI indices of white matter fibers may serve as a more direct and clinically accessible measure of white matter integrity rather than functional re-organization. Indeed, our DTI findings of heavier extranigral white matter burden in the PIGD group may aid in understanding the differential gait responsiveness of patients with PIGD to deep brain stimulation compared with patients with PD²⁷ and may potentially play a role in patient selection.

In this study, we were interested in periventricular white matter fibers that could be directly differentiated on the color FA maps on the basis of our knowledge of neuroanatomy and orientation of these fibers. Hence, we used a simple, manual ROI approach with clearly defined brain slices and radiologic landmarks, on readily available, commercial imaging workstations, and yielded good inter- and intrarater reproducibility. An automated approach, such as tract-based spatial statistics would allow faster and more readily reproducible global brain analysis, albeit with attendant image coregistration challenges,²⁸ between a 3D high-resolution T1-weighted structural scan and the DTI scan due to inherent geometric distortions. In addition, this would require computing expertise and was outside the scope of our study.

Although we have shown structural abnormality in these white matter fibers, future studies could integrate whole-brain analyses in diffusion tensor imaging and clinical cognitive testing to further granulate motor and cognitive associations among the fibers. Furthermore, the integration of whole brain analysis and clinical cognitive testing can be elucidated along with advancements in MR imaging techniques such as myelin water imaging.

CONCLUSIONS

Our DTI findings in PIGD implicate reduced white matter integrity in the periventricular fibers of the GCC, ALIC, ATR, and SLF, suggesting that poor gait performance may be the result of impaired structural integration in the subcortical motor neural systems. These findings provide insights into the underlying pathophysiology of PIGD and may have potential impact on future treatment strategies.

ACKNOWLEDGMENTS

We would like to express our appreciation to Dr Ady Thien for his efforts and contributions in this study. We thank Singapore Millennium Foundation, SingHealth Foundation, and Duke National University of Singapore Graduate Medical School for their support.

Disclosures: Nicole C.H. Keong—*RELATED: Grant:* National Medical Research Council Transition Award grant SERENDIPITI, *Comments:* The coauthor is supported by the National Medical Research Council of the Singapore Ministry of Health under the Transition Award, NMRC/TA/0024/2013, SERENDIPITI*; *UNRELATED: Grants/Grants Pending:* The coauthor is supported by the National Medical Research Council of the Singapore Ministry of Health under the Transition Award, MNRC/TA/0024/2013, SERENDIPITI.* Ling-Ling Chan—*RELATED: Grant:* National Medical Research Council Singapore, *Comments:* National Medical Research Council Singapore funded the grant*; *UNRELATED: Grants/Grants Pending:* National Medical Research Council Singapore, *Comments:* work as a clinician scientist funded by the National Medical Research Council, Singapore*; *Payment for Lectures Including Service in Speakers Bureaus:* Organizing Committee of the XXI Symposium Neuroradiologicum 2018, *Comments:* speaker at XXI Symposium Neuroradiologicum 2018 for “Imaging in Gait Disorders: Changes in Clinical Paradigm” in the World Chinese Neuroradiology Forum I session.* Eng King Tan—*UNRELATED: Other:* editorial duties for *European Journal of Neurology* and parkinsonism-related disorders, grant support from National Medical Research Council, provided expert opinion for the Singapore Medical Council inquiry. *Money paid to the institution.

REFERENCES

- Stebbins GT, Goetz CG, Burn DJ, et al. **How to identify tremor dominant and postural instability/gait difficulty groups with the Movement Disorder Society Unified Parkinson's Disease Rating Scale: comparison with the Unified Parkinson's Disease Rating Scale.** *Mov Disord* 2013;28:668–70 CrossRef Medline
- Fereshtehnejad SM, Romenets SR, Anang JB, et al. **New clinical subtypes of Parkinson disease and their longitudinal progression: a prospective cohort comparison with other phenotypes.** *JAMA Neurol* 2015;72:863–73 CrossRef Medline
- Vu TC, Nutt JG, Holford NH. **Progression of motor and nonmotor features of Parkinson's disease and their response to treatment.** *Br J Clin Pharmacol* 2012;74:267–83 CrossRef Medline
- Cochrane CJ, Ebmeier KP. **Diffusion tensor imaging in parkinsonian syndromes: a systematic review and meta-analysis.** *Neurology* 2013;80:857–64 CrossRef Medline
- Chanraud S, Zahr N, Sullivan EV, et al. **MR diffusion tensor imaging: a window into white matter integrity of the working brain.** *Neuropsychol Rev* 2010;20:209–25 CrossRef Medline
- Shine JM, Matar E, Ward PB, et al. **Exploring the cortical and subcortical functional magnetic resonance imaging changes associated with freezing in Parkinson's disease.** *Brain* 2013;136(Pt 4):1204–15 CrossRef Medline
- Snijders AH, Leunissen I, Bakker M, et al. **Gait-related cerebral alterations in patients with Parkinson's disease with freezing of gait.** *Brain* 2011;134(Pt 1):59–72 CrossRef Medline
- Wang M, Jiang S, Yuan Y, et al. **Alterations of functional and structural connectivity of freezing of gait in Parkinson's disease.** *J Neurol* 2016;263:1583–92 CrossRef Medline
- Canu E, Agosta F, Sarasso E, et al. **Brain structural and functional connectivity in Parkinson's disease with freezing of gait.** *Hum Brain Mapp* 2015;36:5064–78 CrossRef Medline
- Bohnen NI, Albin RL. **White matter lesions in Parkinson disease.** *Nat Rev Neurol* 2011;7:229–36 CrossRef Medline
- Chan LL, Ng KM, Rumpel H, et al. **Transcallosal diffusion tensor abnormalities in predominant gait disorder parkinsonism.** *Parkinsonism Relat Disord* 2014;20:53–59 CrossRef Medline
- Hughes AJ, Daniel SE, Kilford L, et al. **Accuracy of clinical diagnosis of idiopathic Parkinson's disease: a clinico-pathological study of 100 cases.** *J Neurol Neurosurg Psychiatry* 1992;55:181–84 CrossRef Medline
- Jankovic J, McDermott M, Carter J, et al. **Variable expression of Parkinson's disease: a base-line analysis of the DATATOP cohort—the Parkinson Study Group.** *Neurology* 1990;40:1529–34 CrossRef Medline
- Kegelmeyer DA, Kloos AD, Thomas KM, et al. **Reliability and validity of the Tinetti Mobility Test for individuals with Parkinson disease.** *Phys Ther* 2007;87:1369–78 Medline
- Herman T, Weiss A, Brozgol M, et al. **Gait and balance in Parkinson's disease subtypes: objective measures and classification considerations.** *J Neurol* 2014;261:2401–10 CrossRef Medline
- Kamali A, Flanders AE, Brody J, et al. **Tracing superior longitudinal fasciculus connectivity in the human brain using high resolution diffusion tensor tractography.** *Brain Struct Funct* 2014;219:269–81 CrossRef Medline
- Wu Y, Sun D, Wang Y, et al. **Subcomponents and connectivity of the inferior fronto-occipital fasciculus revealed by diffusion spectrum imaging fiber tracking.** *Front Neuroanat* 2016;10:88 CrossRef Medline
- Verlinden VJ, de Groot M, Cremers LG, et al. **Tract-specific white matter microstructure and gait in humans.** *Neurobiol Aging* 2016;43:164–73 CrossRef Medline
- Müller-Oehring EM, Sullivan EV, Pfefferbaum A, et al. **Task-rest modulation of basal ganglia connectivity in mild to moderate Parkinson's disease.** *Brain Imaging Behav* 2015;9:619–38 CrossRef Medline
- Dale ML, Mancini M, Curtze C, et al. **Freezing of gait associated with a corpus callosum lesion.** *J Clin Mov Disord* 2016;3:2 CrossRef Medline
- Bhadrelia RA, Price LL, Tedesco KL, et al. **Diffusion tensor imaging, white matter lesions, the corpus callosum, and gait in the elderly.** *Stroke* 2009;40:3816–20 CrossRef Medline
- Owen AM. **Cognitive dysfunction in Parkinson's disease: the role of frontostriatal circuitry.** *Neuroscientist* 2004;10:525–37 CrossRef Medline
- Vercruyssen S, Leunissen I, Vervoort G, et al. **Microstructural changes in white matter associated with freezing of gait in Parkinson's disease.** *Mov Disord* 2015;30:567–76 CrossRef Medline
- Mihara M, Miyai I, Hatakenaka M, et al. **Sustained prefrontal activation during ataxic gait: a compensatory mechanism for ataxic stroke?** *Neuroimage* 2007;37:1338–45 CrossRef Medline
- Peterson DS, Pickett KA, Duncan R, et al. **Gait-related brain activity in people with Parkinson disease with freezing of gait.** *PLoS One* 2014;9:e90634 CrossRef Medline
- Yogev-Seligmann G, Hausdorff JM, Giladi N. **The role of executive function and attention in gait.** *Mov Disord* 2008;23:329–42; quiz 472 Medline
- Katz M, Luciano MS, Carlson K, et al; CSP 468 study group. **Differential effects of deep brain stimulation target on motor subtypes in Parkinson's disease.** *Ann Neurol* 2015;77:710–19 CrossRef Medline
- Cercignani M. **Strategies for patient-control comparison of diffusion MR data.** In: Jones DK, ed. *Diffusion MRI: Theory, Methods, and Applications.* Oxford: Oxford University Press; 2010:485–99

Gadolinium-Enhanced Susceptibility-Weighted Imaging in Multiple Sclerosis: Optimizing the Recognition of Active Plaques for Different MR Imaging Sequences

L.L.F. do Amaral, D.C. Fragoso, R.H. Nunes, I.A. Littig, and A.J. da Rocha



ABSTRACT

BACKGROUND AND PURPOSE: Gadolinium SWI is MR imaging that has recently been reported to be effective in the evaluation of several neurologic disorders, including demyelinating diseases. Our aim was to analyze the accuracy of gadolinium SWI for detecting the imaging evidence of active inflammation on MS plaques when a BBB dysfunction is demonstrated by a focal gadolinium-enhanced lesion and to compare this technique with gadolinium-enhanced T1 spin-echo and T1 spin-echo with magnetization transfer contrast.

MATERIALS AND METHODS: MR imaging studies of 103 patients (170 examinations) were performed using a 1.5T scanner. Two neuroradiologists scrutinized signal abnormalities of the demyelinating plaques on gadolinium SWI and compared them with gadolinium T1 before and after an additional magnetization transfer pulse. Interrater agreement was evaluated among gadolinium T1 magnetization transfer contrast, gadolinium SWI, and gadolinium T1 spin-echo using the κ coefficient. The T1 magnetization transfer contrast sequence was adopted as the criterion standard in this cohort. Thus, the sensitivity, specificity, positive predictive value, and negative predictive value were calculated for gadolinium T1 spin-echo and gadolinium SWI sequences.

RESULTS: Differences in BBB dysfunction were evident among gadolinium SWI, gadolinium T1 spin-echo, and gadolinium T1 magnetization transfer contrast. Gadolinium T1 magnetization transfer contrast demonstrated the highest number of active demyelinating plaques. Gadolinium SWI was highly correlated with gadolinium T1 magnetization transfer contrast in depicting acute demyelinating plaques (κ coefficient = 0.860; sensitivity = 0.837), and these techniques provided better performance compared with gadolinium T1 spin-echo (κ coefficient = 0.78; sensitivity = 0.645).

CONCLUSIONS: Gadolinium SWI was able to better detect BBB dysfunction in MS plaques and had a better performance than gadolinium T1 spin-echo. Increasing SWI sequence applications in clinical practice can improve our knowledge of MS, likely allowing the addition of BBB dysfunction analysis to the striking findings of the previously reported central vein sign.

ABBREVIATIONS: Gd = gadolinium; MTC = magnetization transfer contrast; SE = spin-echo

Multiple sclerosis is a chronic and disabling demyelinating autoimmune disease that mainly affects young adults. MS is a multifactorial condition that probably results from the interaction among immunologic, genetic, and environmental factors,¹

predominantly characterized by the independent processes of inflammation, demyelination, neurodegeneration, remyelination, and axonal repair in different multifocal combinations at different stages of disease progression. MS is one of the most common neurologic disorders in the world and, in many countries, is the leading cause of nontraumatic neurologic disability in young adults.²

MR imaging produces contrasts according to different tissues. Combined with its noninvasiveness, MR imaging has become the technique of choice for in vivo imaging of several disorders. Currently, MR imaging is used in all MS work-up processes³ because it facilitates earlier diagnosis, helps to safely exclude potential differential diagnoses, and contributes to the evaluation of disease activity and potential complications linked to the treatment.^{3,4}

Currently, diagnosis of MS is fundamentally based on demonstrating the dissemination both in time and in space of the demyelinating process, excluding mimicking disorders (no better ex-

Received December 6, 2018; accepted after revision January 24, 2019.

From the Division of Neuroradiology (L.L.F.A., D.C.F., R.H.N., I.A.L., A.J.R.), Faculdade de Ciências Médicas da Santa Casa de São Paulo, São Paulo, Brazil; Neuroradiology Department (L.L.F.A.), BP Medicina Diagnóstica, Hospital BP e BP Mirante da Beneficência Portuguesa de São Paulo, São Paulo, Brazil; Division of Neuroradiology (D.C.F., R.H.N., A.J.R.), Diagnósticos da América S.A. - DASA, São Paulo, Brazil; and Division of Neuroradiology (D.C.F.), Fleury S.A., São Paulo, Brazil.

L.L.F.A. was supported by Coordenação de Aperfeiçoamento de Pessoal de Nível Superior (CAPES), which partially supported this research.

Please address correspondence to Lázaro Luís Faria do Amaral, MD, Rua Dr. Cesario Mota Junior, 112, vila buarque, 01221-020, São Paulo, São Paulo, Brazil; e-mail: neuro.medimagem@gmail.com

Indicates open access to non-subscribers at www.ajnr.org

<http://dx.doi.org/10.3174/ajnr.A5997>

planation).⁵ Although diagnosis of MS mainly consists of the clinical criteria attributable to this process, imaging has become the most important paraclinical tool because it can corroborate or even refute a clinical suspicion,³ especially in cases in which demyelinating plaques involve noneloquent areas with little or no expression (clinical-radiologic paradox).⁶

Magnetic Resonance Imaging in MS (MAGNIMS; <https://www.magnims.eu/>) emphasizes the role of MR imaging in MS evaluations⁷ and indicates a need for an initial examination (first 6 months) and follow-up examinations every 12 months to assess the presence of new T2 lesions and to search for foci of active inflammation using the postgadolinium T1 sequence. Gadolinium (Gd) enhancement of MS plaques is a well-established marker of MS lesion inflammation.⁸ This biomarker has been mainly used in the diagnosis and monitoring of patients with MS because contrast-enhancing lesions reflect BBB dysfunction and the inflammatory response.⁹ Additionally, recent studies have shown the prognostic role and clinical correlation of Gd-enhancing lesions as an independent long-term predictor in clinically isolated syndrome.¹⁰

Susceptibility-weighted imaging is a relatively new MR imaging technique that is currently being implemented in clinical practice in addition to conventional spin density and T1- and T2-weighted imaging methods, which are already used in commercially available MR imaging scanners. A number of studies have investigated a central vein inside white matter lesions, the “central vein sign,” detected by SWI or T2*-weighted magnitude images, as a promising imaging biomarker of inflammatory demyelination, adding MS specificity to the diagnosis.¹¹ To standardize the evaluation of the central vein sign in the diagnosis of MS, the North American Imaging in Multiple Sclerosis group provided statements and recommendations.¹² Although 7T has demonstrated the highest sensitivity for central vein detection,¹³ 1.5T has also shown high rates of central vein sign detection.¹⁴ A finding of nonconfluent lesions 3 mm in length with 1 central vein has been demonstrated as a sensitive and specific discriminator of patients with relapsing-remitting MS from control subjects with benign white matter lesions. A study conducted by Hosseini et al¹³ also demonstrated a hypointense rim around MS lesions as an adjunct imaging biomarker for MS, which may be used with the central vein sign as a radiologic sign to differentiate benign from MS white matter lesions.

Additionally, to provide information about any tissue that has a different susceptibility than its surrounding structures, such as deoxygenated blood, hemosiderin, ferritin, and calcium (which are revealed by the T2* effect),¹⁵ this technique also allows the T2 effect to be analyzed—that is, the effect for brain edema; with an appropriate pulse angle, this approach can also take advantage of tissue longitudinal relaxation time analysis. A recent report also argued that under certain circumstances or for certain disorders, the T1-relaxivity may dominate and a T1 shinerthrough phenomenon may be observed.¹⁶

The applicability of the T1-shinerthrough effect might be pivotal for exploring the characteristics of Gd-based contrast agents on SWI, which primarily have a T1-shortening effect,¹⁷ without compromising the imaging of the normal brain.¹⁸ On the basis of this background, our study was designed to investigate the accuracy of the Gd-SWI sequence to detect BBB dysfunctions in MS

plaques in the brain by comparing it with the performance of sequences that are currently used in clinical practice.

MATERIALS AND METHODS

Standard Protocol Approvals

The study was approved by an institutional review board of Santa Casa de São Paulo, and written informed consent was obtained from all participants.

Study Design and Subjects

This study is an observational retrospective analysis of consecutive brain MR imaging examinations from a series of patients with a defined MS diagnosis. MR images were accessed through the digital archive of the institution and were acquired from December 2013 to December 2016. All patients had imaging findings indicative of MS according to the 2017 revised McDonald Criteria.⁵ Studies that did not fulfill the correct institution protocol, had poor-quality images that limited interpretation, had images with an alternative diagnosis that supported the symptoms, and had discrepancies in parameters that might affect the interpretation and comparison of images were all excluded from the study.

Data Acquisition

All data were acquired on a 1.5T scanner (Achieva; Philips Healthcare, Best, the Netherlands) using a 16-channel sensitivity encoding neurovascular coil. Sagittal volumetric FLAIR images were acquired for brain lesion detection (slice thickness, 0.7 mm; FOV, 220 × 220 × 180 mm³; matrix, 184 × 184; TR/TE/TI, 7,000/263/2,300 ms; and acquisition time, 8 minutes and 31 seconds).

Gd-SWI data were acquired with a flow-compensated 3D gradient-echo method (FOV, 220 × 189 × 150 mm³; matrix, 220 × 189; voxel size, 1.0 × 1.0 × 1.0 mm³; TR/TE, 23/33 ms; flip angle 10°; slice thickness, 1 mm; acquisition time, 3 minutes and 20 seconds).

The 2D-T1 spin-echo (SE) sequence was acquired using the following parameters: 25 slices; slice thickness, 5 mm; FOV, 220 × 189 × 126 mm³; matrix, 244 × 168; TR/TE, 614/15 ms; acquisition time, 1 minute and 45 seconds. A comparative 2D-T1 SE sequence with an additional magnetization transfer contrast (MTC) on-resonance pulse (25 slices; slice thickness, 5 mm; gap, 0.5 mm; FOV, 220 × 200 × 137 mm³; matrix, 212 × 134; TR/TE, 600/12 ms; and acquisition time, 5 minutes and 26 seconds) was also obtained before and after intravenous administration of 0.1 mmol/kg of Gd (Gadovist [gadobutrol]; Bayer Schering Pharma, Berlin, Germany).

The order of acquisition of the postcontrast sequences was uniform in all studies. The SWI sequence was acquired first, followed by the T1 SE, and finally, the T1 MTC.

Imaging Analysis

All images were assessed by 2 experienced neuroradiologists (A.J.d.R. and L.L.F.d.A.) with 18 and 25 years of neuroimaging experience who were blinded to the patient identity and clinical data to avoid any recall bias. The observers separately analyzed Gd-SWI, Gd-T1 SE, and Gd-T1 MTC and always evaluated the results in that order. The precontrast FLAIR sequence was always assessed to the interpretation to confirm the lesion features. Strict criteria were applied to designate a lesion as enhanced on Gd-

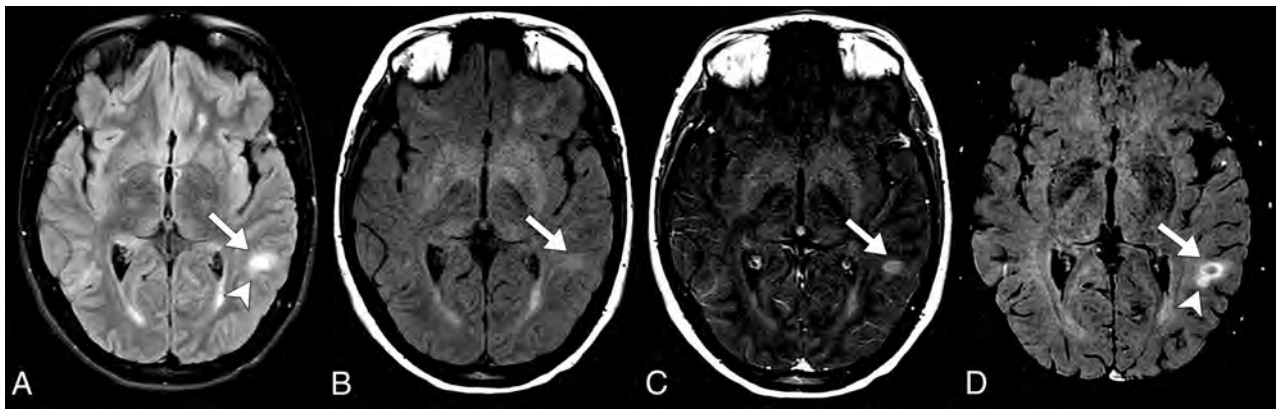


FIG 1. Axial fluid-attenuated inversion recovery sequence (A), axial T1 MTC pre- and postcontrast (B and C), and axial Gd-SWI sequence (D). A definitive acute demyelinating lesion requires the demonstration of a Gd-enhancing lesion along with high signal in the fluid-sensitive sequences, as shown in the left subcortical white matter temporal gyrus lesion (arrows). Note a small ovoid high-signal lesion on a FLAIR sequence adjacent to the aforementioned lesion, which demonstrates BBB dysfunction that is only characterized by the Gd-SWI sequence (arrowheads).

Table 1: Active plaque characteristics^a

Subcortical	Distribution		Morphology			
	Periventricular	Posterior Fossa	Nodular	Annular	Tumefactive	Punctate
50.8	45.3	3.9	68.8	23.1	10.2	21.2

^a Spatial distribution and morphology of the Gd-enhancing lesions.

SWI; all definite enhancing lesions were included (Fig 1), whereas areas of bright signal that were indistinguishable from flow artifacts or Gd-DTPA contrast within vessels or that did not have a comparable high signal on FLAIR were excluded.

The readers were asked to separate Gd-enhancing lesions according to their location in subcortical/juxtacortical, periventricular, or infratentorial (posterior fossa) areas, and the Gd-enhancing pattern was determined to be nodular, annular, punctate, or tumefactive.¹⁹ Similarly, we separately performed a comparative analysis of the interpretation of both Gd-T1 SE and Gd-T1 MTC to search for either a similar Gd enhancement in SWI lesions or a Gd-SWI acquisition that was negative for the presence of lesions enhancing in the other sequences.

The Gd-T1 MTC sequence was considered the criterion standard tool for determining lesions positive for acute plaques because it is considered the preferred method in a 1.5T scanner.²⁰⁻²²

Statistical Analyses

Statistical analysis was performed using the Statistical Package for the Social Sciences, Version 21 (IBM, Armonk, New York).

Interrater agreement for Gd enhancement among postcontrast sequences was assessed with the Cohen κ coefficient. Agreement was graded according to the Altman definition with 0.0–0.20, poor; 0.21–0.40, fair; 0.41–0.60, moderate; 0.61–0.80, good; and 0.81–1.00, very good.

According to the current design, the sensitivity, specificity, positive predictive value, and negative predictive value were calculated for Gd-T1 SE and Gd-SWI sequences to depict active demyelinating lesion–detectability performance.

RESULTS

According to the defined criteria, a total of 170 examinations were included in this cohort. The study population included 103 pa-

Table 2: Frequency characteristics

Sequence	Sensitivity	Specificity	PPV	NPV
Gd-SWI	0.837	0.998	0.891	0.977
Gd-T1 SE	0.645	1	0.995	0.994

Note:—PPV indicates positive predictive value; NPV, negative predictive value.

tients with relapsing-remitting MS (76 women; mean age, 36.4 ± 11.6 years; range, 16–63 years).

A total of 15,756 white matter lesions (range, 2–400 lesions per patient) were detected with a FLAIR sequence. The Gd-T1 MTC sequence showed the highest number of lesions with Gd enhancement with 282 lesions, followed by Gd-SWI with 265 lesions, and finally, Gd-T1 SE with 183 lesions. The spatial distribution and morphology of the Gd-enhancing lesions are shown in Table 1.

Very good interrater agreement was observed for Gd-enhancing lesion detection between the Gd-SWI and Gd-T1 MTC sequences (κ coefficient = 0.86). Although 46 lesions were erroneously interpreted as negative for Gd-enhancement, 29 lesions were only demonstrated in the SWI sequence.

Although moderate interrater agreement was observed between Gd-T1 SE and Gd-T1 MTC (κ coefficient = 0.78), 100 lesions were missed by the SE acquisition.

If one assumes that Gd-T1 MTC was the criterion standard sequence, the Gd-SWI and Gd-T1 SE frequency characteristics in this cohort are demonstrated in Table 2.

When the Gd-T1 SE and Gd-SWI sequence results were compared, we observed that 82 more lesions were detected by the SWI acquisition, which resulted in a sensitivity increase of approximately 29.7%.

Considering the different lesion morphologies, larger lesions (>2.0 cm) had the highest agreement rate (99.3%). Conversely, punctate lesions demonstrated a lower agreement, but there was still a substantial concordance rate (91.0%) among all the post-Gd sequences that were analyzed.

DISCUSSION

A considerable increase in the physiopathogenic mechanisms of MS was achieved with the advent of MR imaging from its debut in the 1970s until today. MS has long been regarded as a chronic inflammatory disease of the white matter that leads to demyelination and, eventually, to progressive neurodegeneration. The pathogenesis of MS is fundamentally characterized by 2 distinct-but-intermingled processes^{23,24}: inflammation, which predominantly occurs in the early stages of the demyelinating process, and neurodegeneration, which is presumably dominant in the later stages of the disease but also begins in the early stages.²⁵

Although activity and progression are very close to one another, in clinical practice, their analysis is approached separately. Disease activity is defined by clinical relapses and/or lesion activity in CNS imaging and is related to episodes of tissue damage associated with inflammation.²⁶ Progression is linked to increasing neurologic dysfunction, which (by current understanding) reflects neurodegenerative processes.²⁷ According to the current criteria,⁵ analysis of the therapeutic evaluation based on the estimation of active disease is performed by MR imaging determining the lesion load (ie, the number of new lesions or increase in the volume of pre-existing lesions) and detecting the BBB dysfunction represented by Gd enhancement.⁷

Gd-based contrast agents used in conjunction with MR imaging have been approved by regulatory agencies around the world. Several studies have shown their efficacy for improving the accuracy of MR imaging studies, and they currently have a positive cumulative safety record.²⁸ Nevertheless, concerns have arisen about the long-term health effects of repeat Gd administration in patients with MS and the incomplete characterization of the MS lesion pathophysiology that results from relying on contrast-enhancement characteristics alone. Investigations have shown evidence of Gd deposition within the human brain after multiple Gd contrast administrations, especially in the dentate nucleus and globus pallidus, particularly when linear compounds are used.²⁹ Thus, the National Institutes of Health recommends that the necessity of Gd administration in specific clinical indications should be carefully re-evaluated given the uncertain long-term public health impact of the deposition of Gd within the brain,²⁸ though the precise causal role, if any, that repeat Gd injections play in MS pathogenesis remains unknown.

Increasing investigations have focused on the search for biomarkers that ideally demonstrate early inflammation and neurodegeneration processes separately, which would allow a more confident analysis of the therapeutic response and prognostic analysis at the individual level.³⁰

Promising alternatives in determining the MS neuroinflammation and excitotoxicity processes in vivo have been demonstrated. It has been documented in the literature and adopted by our institution that the T1 MTC using 1.5T equipment is the most sensitive sequence for the demonstration of a BBB disruption with inflammatory activity in MS.^{20-22,31} Nevertheless, there have been some controversies in the literature on this subject, and the lack of consistency among these methods for different MR imaging scanners is the main debate.

Potential sequences that also require Gd-based contrast that have been recently reported in the literature are the double inver-

sion recovery³² and T1 3D MPRAGE.³³ Nonetheless, some investigations have also evaluated the accuracy of noncontrast MR imaging to confidently detect acute MS plaques.³⁴ Diffusion tensor imaging, particularly through the fractional anisotropy metric,³⁵ and, more recently, analysis of quantitative susceptibility mapping³⁶ have been demonstrated to have high diagnostic accuracy for distinguishing enhancing from nonenhancing MS plaque activity in the absence of Gd administration. It is also worth mentioning sequences that label antibodies targeting surface markers of immune cells in preclinical studies.³⁷ These imaging biomarkers may also have additional benefits for providing insight into the MS pathobiology that is not possible due to the simple dichotomous characterization of the presence or absence of contrast enhancement, and which could increase the accuracy of MS diagnosis, improve disease prognostication, and provide a more robust marker of treatment response.

SWI is a fully velocity-compensated, long-echo, radiofrequency-spoiled, high-resolution, 3D gradient-echo sequence that combines magnitude and filtered-phase information to generate clinical information in addition to anatomic images.³⁸ Since its introduction in the beginning of this century,³⁹ a substantial increase in information has been achieved through magnetic susceptibility sequences.¹⁵ SWI takes advantage of the susceptibility differences among tissues, which leads to phase differences (phase) and causes a signal loss (magnitude).³⁹ In clinical practice, SWI has added to the recognition of small calcifications, parenchymal microbleeds, cavernous malformations, and traumatic shearing injuries.¹⁷ SWI also allows visualization of small vessels and veins within the brain, which is an advantage used for venous thrombosis, arteriovenous malformations, dural arteriovenous fistulas, and stroke,¹⁵ in addition to revealing a vein within a demyelinating lesion (central vein sign), translating the perivenular demyelination, and increasing the specificity and pathologic correlation of the image findings.⁴⁰

SWI is routinely performed without intravenous Gd administration. Nevertheless, no image-quality degradation and no significant signal intensity changes in the gray matter and WM have been recognized after intravenous Gd administration.¹⁸ The magnitude signal intensity depends on T2*, geometry, orientation to the B₀, and differences in magnetic susceptibility, as well as serving as a function of T1. Thus, although T2* and phase effects are dominant, there is still a T1-relaxivity term present when the flip angle is greater than or close to the Ernst angle [$\theta_E = \text{square root}(2TR/T1)$].¹⁶

In certain settings, the T1-relaxivity may dominate and the T1-shinethrough phenomenon may arise, such as the effects that occur in the cerebral venous sinuses after Gd administration, which typically measure a few centimeters in diameter.¹⁸ Through this principle, the evaluation of Gd leakage due to dysfunction of the BBB has been exploited with some benefits and promising results in several situations, especially in the field of neuro-oncologic imaging,⁴¹ as well as in the evaluation of inflammatory disorders, as shown in this study for MS inflammation-activity detection.

Our results support the use of the post-Gd SWI sequence in assessing inflammatory activity in patients with MS (Fig 2) and show that pre- and post-Gd SWI demonstrate a diagnostic

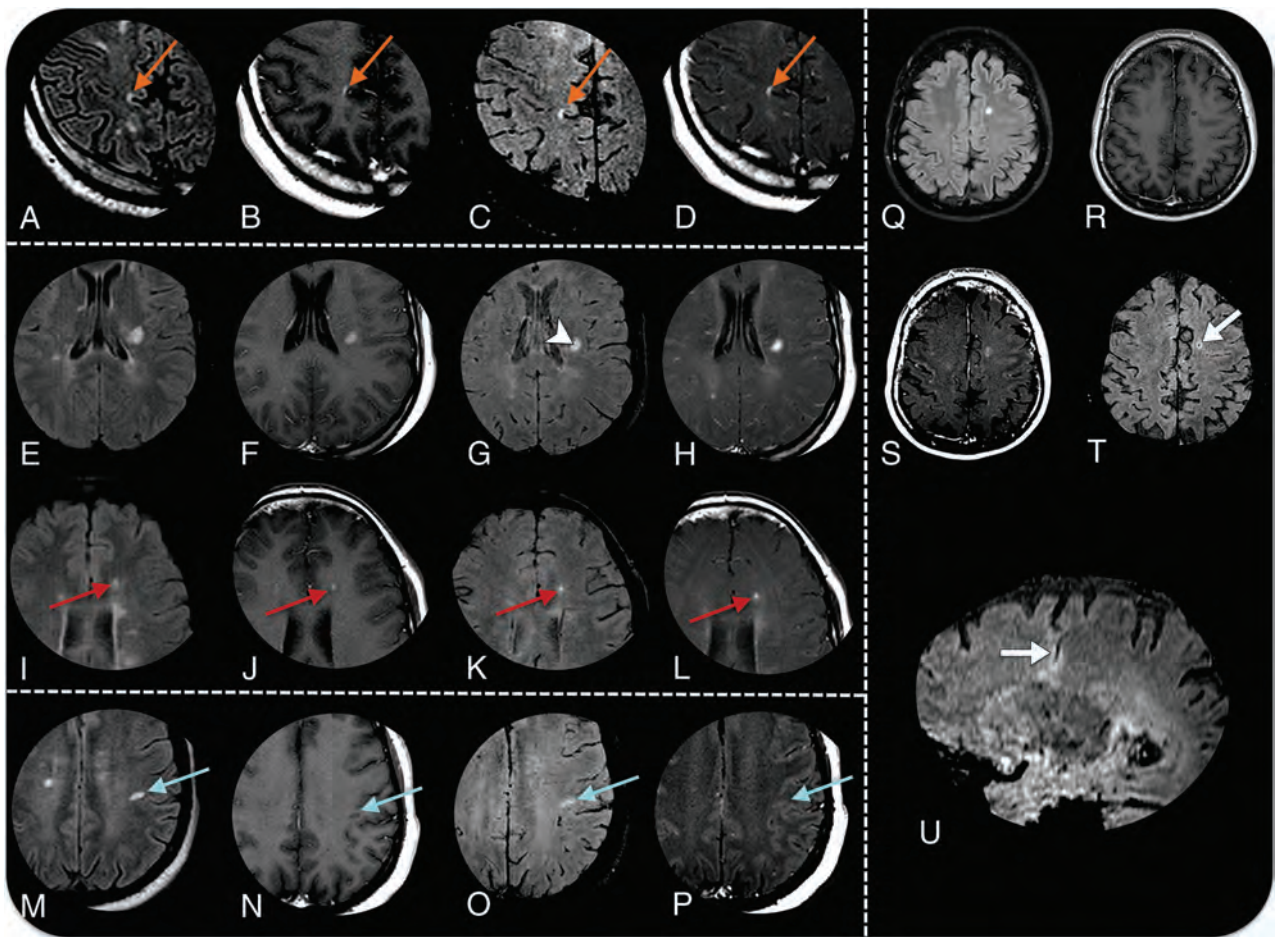


FIG 2. MR imaging detection of active plaques in 4 different patients with MS. Axial fluid-attenuated inversion recovery sequences (A, E, I, M, and Q), axial Gd-T1 SE sequences (B, F, J, N, and R), axial Gd-SWI sequences (C, G, K, O, and T), T1 Gd-T1 MTC sequences (D, H, L, P, and S), and a sagittal reformatting Gd-SWI sequence (U). Patient 1 demonstrates an acute juxtacortical/cortical demyelinating lesion in the right precuneus with Gd enhancement in all sequences (orange arrows in A–D). Patient 2 demonstrates an acute demyelinating plaque on the left corona radiata (E–F). Gd-SWI depicts the central vein within the plaque (arrowhead in G), adding specificity in favor of the demyelinating substrate. Similar to the Gd-T1 SE and Gd-T1 MTC sequences, the Gd-SWI sequence is also able to demonstrate BBB dysfunction in small lesions (red arrows in I–L). Patient 3 shows an acute demyelinating plaque on the subcortical white matter of the left postcentral gyrus that is only characterized by the Gd-SWI sequence (blue arrows in M–P). Patient 4 has a venous developmental anomaly in the left semiovale center, surrounded by a parenchymal hyperintensity on a FLAIR sequence (Q). Both the Gd-T1 MTC and Gd-SWI sequences (S and T) demonstrate a faint enhancement (arrow in T), which is elegantly demonstrated by the sagittal reformatting Gd-SWI sequence (arrow in U).

accuracy similar to that of the adopted criterion standard sequence for this purpose and higher than that of the T1 SE sequence, with excellent agreement among the observers in our cohort.

Despite the large number of lesions analyzed, this report has several limitations because it was a single-center retrospective study with a relatively small number of patients without pathologic correlation. Although the visibility of the deep veins was slightly better with the 3T scanner, El-Koussy et al¹⁸ demonstrated similar sensitivity in comparing 1.5T with 3T scanners. Despite the possibility that the order of the postcontrast sequences could represent a potential limiting bias because the Gd-SWI sequence was acquired first, this reinforces its use as a marker of BBB dysfunction. The use of this new application of the SWI technique requires further study to be incorporated into clinical practice, as well as to implement and standardize the acquisition and interpretation of the results in the context of MS.

CONCLUSIONS

This study confirmed that the Gd-SWI sequence increased the accuracy of detection of MS-typical contrast-enhancing lesions, including all of their locations and morphologies, similar to Gd-T1 MTC and better than Gd-T1 SE. This new application might add to current knowledge, revealing novel findings of the SWI sequence that are not currently envisioned to have a potential use for clinical practice. Because this study was performed on a 1.5T MR imaging scanner, evaluation of the performance of this sequence at 3T would be of interest.

REFERENCES

1. Ebers GC. Environmental factors and multiple sclerosis. *Lancet Neurol* 2008;7:268–77 CrossRef Medline
2. Cristiano E, Rojas JI. Multiple sclerosis epidemiology in Latin America: an updated survey. *Mult Scler J Exp Transl Clin* 2017;3: 2055217317715050 CrossRef Medline
3. Rovira Á, Wattjes MP, Tintoré M, et al; MAGNIMS study group.

- Evidence-based guidelines: MAGNIMS consensus guidelines on the use of MRI in multiple sclerosis—clinical implementation in the diagnostic process. *Nat Rev Neurol* 2015;11:471–82 CrossRef Medline
4. Sicotte NL. Magnetic resonance imaging in multiple sclerosis: the role of conventional imaging. *Neurol Clin* 2011;29:343–56 CrossRef Medline
 5. Thompson AJ, Banwell BL, Barkhof F, et al. Diagnosis of multiple sclerosis: 2017 revisions of the McDonald criteria. *Lancet Neurol* 2018;17:162–73 CrossRef Medline
 6. Barkhof F. The clinico-radiological paradox in multiple sclerosis revisited. *Curr Opin Neurol* 2002;15:239–45 CrossRef Medline
 7. Wattjes MP, Rovira À, Miller D, et al; MAGNIMS study group. Evidence-based guidelines: MAGNIMS consensus guidelines on the use of MRI in multiple sclerosis—establishing disease prognosis and monitoring patients. *Nat Rev Neurol* 2015;11:597–606 CrossRef Medline
 8. Kermode AG, Thompson AJ, Tofts P, et al. Breakdown of the blood-brain barrier precedes symptoms and other MRI signs of new lesions in multiple sclerosis. *Brain* 1990;113:1477–89 CrossRef Medline
 9. Poser CM, Brinar VV. The nature of multiple sclerosis. *Clin Neurol Neurosurg* 2004;106:159–71 CrossRef Medline
 10. Di Filippo M, Anderson VM, Altmann DR, et al. Brain atrophy and lesion load measures over 1 year relate to clinical status after 6 years in patients with clinically isolated syndromes. *J Neurol Neurosurg Psychiatry* 2010;81:204–08 CrossRef Medline
 11. Tallantyre EC, Dixon JE, Donaldson I, et al. Ultra-high-field imaging distinguishes MS lesions from asymptomatic white matter lesions. *Neurology* 2011;76:534–39 CrossRef Medline
 12. Sati P, Oh J, Constable RT, et al; NAIMS Cooperative. The central vein sign and its clinical evaluation for the diagnosis of multiple sclerosis: a consensus statement from the North American Imaging in Multiple Sclerosis Cooperative. *Nat Rev Neurol* 2016;12:714–22 CrossRef Medline
 13. Hosseini Z, Matusinec J, Rudko DA, et al. Morphology-specific discrimination between MS white matter lesions and benign white matter hyperintensities using ultra-high-field MRI. *AJNR Am J Neuroradiol* 2018;39:1473–79 CrossRef Medline
 14. Sparacia G, Agnello F, Gambino A, et al. Multiple sclerosis: high prevalence of the “central vein” sign in white matter lesions on susceptibility-weighted images. *Neuroradiol J* 2018;31:356–61 CrossRef Medline
 15. Mittal S, Wu Z, Neelavalli J, et al. Susceptibility-weighted imaging: technical aspects and clinical applications, Part 2. *AJNR Am J Neuroradiol* 2009;30:232–52 CrossRef Medline
 16. Hsu CC, Haacke EM, Heyn CC, et al. The T1 shine through effect on susceptibility weighted imaging: an under recognized phenomenon. *Neuroradiology* 2018;60:235–37 CrossRef Medline
 17. Sehgal V, Delproposto Z, Haacke EM, et al. Clinical applications of neuroimaging with susceptibility-weighted imaging. *J Magn Reson Imaging* 2005;22:439–50 CrossRef Medline
 18. El-Koussy M, Schenk P, Kiefer C, et al. Susceptibility-weighted imaging of the brain: does gadolinium administration matter? *Eur J Radiol* 2012;81:272–76 CrossRef Medline
 19. He J, Grossman RI, Ge Y, et al. Enhancing patterns in multiple sclerosis: evolution and persistence. *AJNR Am J Neuroradiol* 2001;22:664–69 Medline
 20. Gavra MM, Voumvourakis C, Gouliamos AD, et al. Brain MR post-gadolinium contrast in multiple sclerosis: the role of magnetization transfer and image subtraction in detecting more enhancing lesions. *Neuroradiology* 2004;46:205–10 CrossRef Medline
 21. Silver NC, Good CD, Barker GJ, et al. Sensitivity of contrast enhanced MRI in multiple sclerosis: effects of gadolinium dose, magnetization transfer contrast and delayed imaging. *Brain* 1997;120:1149–61 CrossRef Medline
 22. Bozzao A, Bastianello S, Ferone E, et al. Enhanced and unenhanced MR with magnetization transfer in multiple sclerosis. *AJNR Am J Neuroradiol* 1996;17:1837–42 Medline
 23. Mandolesi G, Gentile A, Musella A, et al. Synaptopathy connects inflammation and neurodegeneration in multiple sclerosis. *Nat Rev Neurol* 2015;11:711–24 CrossRef Medline
 24. Louapre C, Lubetzki C. Neurodegeneration in multiple sclerosis is a process separate from inflammation: yes. *Mult Scler* 2015;21:1626–38 CrossRef Medline
 25. Pérez-Cerdá F, Sánchez-Gómez MV, Matute C. The link of inflammation and neurodegeneration in progressive multiple sclerosis. *Multiple Sclerosis and Demyelinating Disorders* 2016:1–9
 26. Daumer M, Neuhaus A, Morrissey S, et al. MRI as an outcome in multiple sclerosis clinical trials. *Neurology* 2009;72:705–11 CrossRef Medline
 27. Tillema JM, Hulst HE, Rocca MA, et al; MAGNIMS Study Group. Regional cortical thinning in multiple sclerosis and its relation with cognitive impairment: a multicenter study. *Mult Scler* 2016;22:901–09 CrossRef Medline
 28. Malayeri AA, Brooks KM, Bryant LH, et al. National Institutes of Health perspective on reports of gadolinium deposition in the brain. *J Am Coll Radiol* 2016;13:237–41 CrossRef Medline
 29. Stojanov DA, Aracki-Trenkic A, Vojinovic S, et al. Increasing signal intensity within the dentate nucleus and globus pallidus on unenhanced T1W magnetic resonance images in patients with relapsing-remitting multiple sclerosis: correlation with cumulative dose of a macrocyclic gadolinium-based contrast agent, gadobutrol. *Eur Radiol* 2016;26:807–15 CrossRef Medline
 30. Comabella M, Sastre-Garriga J, Montalban X. Precision medicine in multiple sclerosis: biomarkers for diagnosis, prognosis, and treatment response. *Curr Opin Neurol* 2016;29:254–62 CrossRef Medline
 31. Hiehle JF Jr, Grossman RI, Ramer KN, et al. Magnetization transfer effects in MR-detected multiple sclerosis lesions: comparison with gadolinium-enhanced spin-echo images and nonenhanced T1-weighted images. *AJNR Am J Neuroradiol* 1995;16:69–77 Medline
 32. Eichinger P, Kirschke JS, Hoshi MM, et al. Pre- and postcontrast 3D double inversion recovery sequence in multiple sclerosis: a simple and effective MR imaging protocol. *AJNR Am J Neuroradiol* 2017;38:1941–45 CrossRef Medline
 33. Crombé A, Saranathan M, Ruet A, et al. MS lesions are better detected with 3D T1 gradient-echo than with 2D T1 spin-echo gadolinium-enhanced imaging at 3T. *AJNR Am J Neuroradiol* 2015;36:501–07 CrossRef Medline
 34. Gupta A, Al-Dasuqi K, Xia F, et al. The use of noncontrast quantitative MRI to detect gadolinium-enhancing multiple sclerosis brain lesions: a systematic review and meta-analysis. *AJNR Am J Neuroradiol* 2017;38:1317–22 CrossRef Medline
 35. Testaverde L, Caporali L, Venditti E, et al. Diffusion tensor imaging applications in multiple sclerosis patients using 3T magnetic resonance: a preliminary study. *Eur Radiol* 2012;22:990–97 CrossRef Medline
 36. Zhang Y, Gauthier SA, Gupta A, et al. Magnetic susceptibility from quantitative susceptibility mapping can differentiate new enhancing from nonenhancing multiple sclerosis lesions without gadolinium injection. *AJNR Am J Neuroradiol* 2016;37:1794–99 CrossRef Medline
 37. Ciccarelli O, Barkhof F, Bodini B, et al. Pathogenesis of multiple sclerosis: insights from molecular and metabolic imaging. *Lancet Neurol* 2014;13:807–22 CrossRef Medline
 38. Rauscher A, Sedlacik J, Barth M, et al. Magnetic susceptibility-weighted MR phase imaging of the human brain. *AJNR Am J Neuroradiol* 2005;26:736–42 Medline
 39. Haacke EM, Mittal S, Wu Z, et al. Susceptibility-weighted imaging: technical aspects and clinical applications, Part 1. *AJNR Am J Neuroradiol* 2009;30:19–30 CrossRef Medline
 40. Mistry N, Abdel-Fahim R, Samaraweera A, et al. Imaging central veins in brain lesions with 3-T T2*-weighted magnetic resonance imaging differentiates multiple sclerosis from microangiopathic brain lesions. *Mult Scler* 2016;22:1289–96 CrossRef Medline
 41. Fahrendorf D, Schwindt W, Wölfer J, et al. Benefits of contrast-enhanced SWI in patients with glioblastoma multiforme. *Eur Radiol* 2013;23:2868–79 CrossRef Medline

Leptomeningeal Contrast Enhancement Is Related to Focal Cortical Thinning in Relapsing-Remitting Multiple Sclerosis: A Cross-Sectional MRI Study

N. Bergsland, D. Ramasamy, E. Tavazzi, D. Hojnacki, B. Weinstock-Guttman, and R. Zivadinov



ABSTRACT

BACKGROUND AND PURPOSE: Leptomeningeal inflammation is associated with the development of global cortical gray matter atrophy in multiple sclerosis. However, its association with localized loss of tissue remains unclear. The purpose of this study was to evaluate the relationship between leptomeningeal contrast enhancement, a putative marker of leptomeningeal inflammation, and focal cortical thinning in MS.

MATERIALS AND METHODS: Forty-three patients with relapsing-remitting MS and 15 with secondary-progressive MS were imaged on a 3T scanner. Cortical reconstruction was performed with FreeSurfer. Leptomeningeal contrast-enhancement foci were visually identified on 3D-FLAIR postcontrast images and confirmed using subtraction imaging. Leptomeningeal contrast-enhancement foci were mapped onto the cortex, and ROIs were obtained by dilating along the surface multiple times ($n = 5, 10, 15, 20, 25, 30, 35, 40$). Resulting ROIs were then mapped onto the homologous region of the contralateral hemisphere. Paired t tests compared the thickness of the cortex surrounding individual leptomeningeal contrast-enhancement foci and the corresponding contralateral region. Results were corrected for the false discovery rate.

RESULTS: Differences between ipsilateral and contralateral ROIs progressively decreased with larger ROIs, but no significant effects were detected when considering the entire MS sample. In patients with relapsing-remitting MS only, significantly reduced cortical thickness was found for 5 dilations (-8.53% , corrected $P = .04$) and 10 dilations (-5.20% , corrected $P = .044$).

CONCLUSIONS: Focal leptomeningeal contrast enhancement is associated with reduced thickness of the surrounding cortex in patients with relapsing-remitting MS, but not in those with secondary-progressive MS. Our results suggest that pathology associated with the presence of leptomeningeal contrast-enhancement foci has a stronger, localized effect on cortical tissue loss earlier in the disease.

ABBREVIATIONS: LMCE = leptomeningeal contrast enhancement; RRMS = relapsing-remitting MS; SPMS = secondary-progressive MS

Neurodegeneration and inflammation are the 2 main pathogenic processes in multiple sclerosis, leading to irreversible tissue loss and disability accrual with time. However, the reciprocal causal role has not been fully defined.^{1,2} Recently, histopatho-

logic studies have focused on the leptomeninges after the discovery of lymphoid-like structures³ associated with cortical damage in patients with secondary-progressive MS (SPMS). A correlation among leptomeningeal inflammation, subpial cortical lesions, and cortical demyelination/degeneration already in the early stages of the disease has also recently been described.⁴⁻⁸ However, these findings may not be representative of the disease in general. First, postmortem studies tend to involve patients older than the general MS population. Second, biopsied samples of brain tissue likely stem from patients who have experienced nontypical symptoms or a particularly aggressive disease course. Thus, in vivo studies are attractive because they provide the opportunity to investigate cortical pathology across the spectrum of MS.

Because the cell aggregates that form the meningeal follicles are generally very small, the direct in vivo detection of leptomeningeal pathology is outside the reach of clinical MR imaging acquisitions. However, histopathologic evidence suggests that they have an impact on the permeability of the surround-

Received October 9, 2018; accepted after revision February 16, 2019.

From the Buffalo Neuroimaging Analysis Center (N.B., D.R., E.T., R.Z.) and Jacobs Comprehensive MS Treatment and Research Center (D.H., B.W.-G.), Department of Neurology, and Jacobs School of Medicine and Biomedical Sciences, Center for Biomedical Imaging at Clinical Translational Science Institute (R.Z.), University at Buffalo, State University of New York, Buffalo, New York.

Research reported in this publication was supported by the National Center for Advancing Translational Sciences of the National Institutes of Health under award No. UL1TR001412.

The content of this article is solely the responsibility of the authors and does not necessarily represent the official views of the National Institutes of Health.

Please address correspondence to Niels Bergsland, PhD, Buffalo Neuroimaging Analysis Center, Department of Neurology, Jacobs School of Medicine and Biomedical Sciences, State University of New York, Buffalo, New York, 100 High St, Buffalo, NY 14203; e-mail: npbergsland@bnac.net

Indicates open access to non-subscribers at www.ajnr.org

<http://dx.doi.org/10.3174/ajnr.A6011>

ing blood-CSF barrier,⁹ which can be exploited by high-resolution T2WI FLAIR sequences acquired after the administration of gadolinium.¹⁰⁻¹⁴

Foci of leptomeningeal contrast enhancement (LMCE) have been reported in patients with relapsing-remitting MS (RRMS) and SPMS,¹¹⁻¹⁵ which is thought to reflect leptomeningeal inflammation as seen histopathologically.¹¹ Increasing evidence suggests that LMCE is linked to cortical gray matter tissue loss.^{12,14,15} Furthermore, LMCE is apparently independent of white matter tissue volume and white matter lesion load,^{11,12,14,15} supporting the notion that cortical gray matter and white matter pathology are at least partially independent of each other.^{3,16,17}

It has been postulated that the leptomeninges represent a site of chronic inflammation, characterized by the release of soluble inflammatory factors, resulting in progressive damage to the surrounding cortex, ultimately leading to tissue atrophy.⁴ Thus, we hypothesized that cortical areas closer to LMCE foci would be characterized by a greater degree of atrophy and that the relationship would be stronger in patients with SPMS.

MATERIALS AND METHODS

Study Design and Patient Selection

This cross-sectional study combined data that were either acquired as part of an ongoing prospective study investigating the role of cardiovascular, environmental, and genetic factors associated with MS^{14,18} or from patients seen as part of their yearly routine clinical examination. All data were collected between June 2016 to October 2017. Included patients had either an RRMS or SPMS disease course according to the revised 2010 McDonald criteria.¹⁹ The study data collection was approved by the institutional review board of the University at Buffalo. All patients who were part of the prospective study provided written, informed consent. Due to the retrospective nature of the routine clinical data, we were provided an exemption for obtaining informed consent by our institutional review board.

The inclusion criteria were the following: 1) patients with an RRMS or SPMS disease course; 2) 18–75 years of age; 3) images having been acquired on the same 3T MR imaging system with a standardized protocol that included a 3D-T1WI precontrast acquisition as well as pre- and postcontrast 3D-T2WI FLAIR sequences after a single dose of gadolinium injection; 4) 3D-T2WI FLAIR positive for LMCE on pre-/postcontrast subtraction imaging; and 5) physical/neurologic examination within 30 days from MR imaging. Exclusion criteria were the following: 1) the presence of relapse and steroid treatment within the 30 days preceding study entry; 2) pre-existing medical conditions known to be associated with brain pathology (cerebrovascular disease, positive history of substance abuse); or 3) pregnancy.

Of 342 screened subjects, 58 (17%) met the inclusion criteria for LMCE positivity on 3D FLAIR pre-/postcontrast subtraction imaging. Of the included patients in the current study, 43 patients had an RRMS disease course, while the other 15 were diagnosed with SPMS.

MR Imaging Acquisition

All scans were acquired on the same 3T Signa Excite HD 12.0 MR imaging scanner (GE Healthcare, Milwaukee, Wisconsin) with an 8-channel head and neck coil. A magnetization-prepared 3D T1-

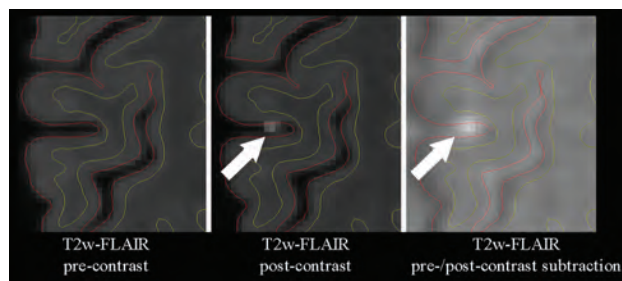


FIG 1. A representative case depicting the T2WI FLAIR precontrast, T2WI FLAIR postcontrast, and T2WI FLAIR pre-/postcontrast subtraction images. The FreeSurfer-derived white and pial surfaces are shown in yellow and red, respectively. The *white arrow* shows a focus of leptomeningeal contrast enhancement.

weighted image (TE/TI/TR = 2.8/900/5.9 ms, flip angle = 10°, 256 × 256 matrix, voxel size = 1 mm³ isotropic, duration = 9 minutes 18 seconds) and pre- and postcontrast 3D-T2WI FLAIR sequences were acquired before and 10 minutes after an intravenous bolus of 0.1 mmol/kg of Gd-DTPA (TR/TI/TE = 9000/2420/600 ms, acquisition matrix = 256 × 192, voxel size = 1.0 × 1.3 × 1.3 mm³, duration = 12 minutes 22 seconds each). The 3D-T2WI FLAIR sequence uses variable flip angles so that the effective TE of 600 ms for the sequence is equal to a TE of 110 ms for a conventional spin-echo sequence. In addition, pre- and postcontrast spin-echo 2D-T1 sequences were acquired before and 5 minutes after Gd-DTPA injection (TE/TR = 16/600 ms, matrix = 256 × 192, voxel size = 1.0 × 1.0 × 3.0 mm³ without a gap, duration = 4 minutes 34 seconds each).

MR Imaging Assessment

All assessments were performed blinded to patient demographic and clinical characteristics.

Lesion Volumetry

T2 and gadolinium lesion volumes were calculated using a reliable semiautomated edge-detection contouring/thresholding technique with JIM software (www.xinapse.com) on T2WI FLAIR and 2D-T1WI postcontrast acquisitions, respectively.

LMCE Assessment

LMCE foci were identified on the 3D-T2WI FLAIR postcontrast image with the aid of a subtraction image (Fig 1).¹³ LMCE foci were defined as signal intensity within the subarachnoid space that was substantially greater than that of brain parenchyma and characterized as being nodular, linear, or plate-like, as previously described.¹¹ All LMCE foci were confirmed in consensus by 2 experienced neuroimagers, each with >15 years of experience.

Cortical Measures

Cortical reconstruction was performed on the 3D-T1 images using the FreeSurfer package, Version 5.3 (<http://www.freesurfer.net/>).^{20,21} Before analysis, the input image was lesion-filled to improve the reliability of cortical thickness measures.²² The 3D-T2 FLAIR precontrast image was then registered to the FreeSurfer-conformed T1 image using the *bbregister* tool (<https://surfer.nmr.mgh.harvard.edu/fswiki/bbregister>).²³ Individual LMCE foci were then automatically mapped onto the nearest vertex of the pial surface

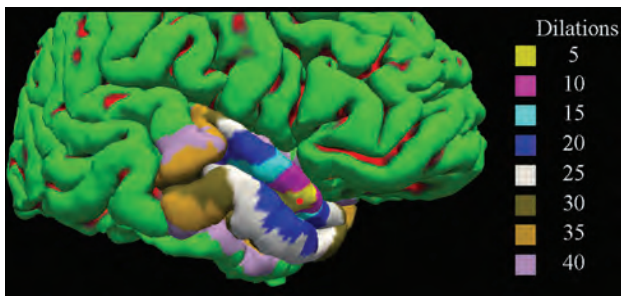


FIG 2. A representative cortical reconstruction from FreeSurfer is shown with dilated ROIs overlaid on the cortical surface. Gyri are shown in green, while sulci are shown in red. The red circle corresponds to the position of the mapped focus of leptomeningeal contrast enhancement. Different-sized ROIs are shown in varying colors.

using the `mri_label2label` tool (https://surfer.nmr.mgh.harvard.edu/fswiki/mri_label2label) in FreeSurfer. Because the putative extent of cortical thinning was not known a priori, the resulting point was morphologically dilated along the surface several times ($n = 5, 10, 15, 20, 25, 30, 35, 40$) to define the ROI surrounding the LMCE foci. A representative LMCE focus and corresponding set of ROIs on the cortical surface are shown in Fig 2. Next, each ROI was mapped onto the homologous region in the contralateral hemisphere via nonlinear registration of the surfaces to one another using the `mris_left_right_register` tool (<https://surfer.nmr.mgh.harvard.edu/fswiki/>) in FreeSurfer. Most important, the registration was performed separately for left to right and right to left rather than using an inverse transformation, to avoid bias in the contralateral mapping procedure. Quality control was performed at each step of the processing (eg, brain extraction, white and pial surface generation, registration), and manual corrections were made as required.

To validate the primary results, we performed 2 additional analyses. First, we randomly selected 4 points on the cortical surface (2 for the left hemisphere and 2 for the right hemisphere) distant from any LMCE foci for each subject. These were then used as seeds for ROI generation. Second, we mapped the LMCE foci for a given subject to another randomly selected subject in the study. For both of these analyses, we then compared ipsilateral and contralateral thickness measures as we did in the primary analysis.

Statistical Analysis

Statistical analyses were performed using SPSS (Version 24; IBM, Armonk, New York). Differences between the RRMS and SPMS groups in terms of demographics, clinical characteristics, and lesion volumetry were analyzed using the Fisher exact, Student *t*, Mann-Whitney *U*, or χ^2 test, as appropriate. Distributions of the data were tested for normality using the Shapiro-Wilk test and examination of histograms.

For each dilation, differences between ipsilateral and contralateral ROIs were examined using paired *t* tests. All tests assessed the entire cohort and patients with RRMS and SPMS separately. Exploratory analyses assessed whether there were any differences when comparing LMCE foci by their appearance (eg, nodular, linear, plate-like).

The Benjamini-Hochberg procedure was used to control the

Table 1: Demographic, clinical, and MR imaging characteristics of the cohort

	RRMS (n = 43)	SPMS (n = 15)	P Value ^a
Women (No.) (%)	38 (88.4)	11 (73.3)	.658
Age (mean) (SD) (yr)	52.8 (12.1)	60.5 (6.7)	.023 ^b
Disease duration (mean) (SD) (yr)	15.2 (8.9)	21.9 (8.3)	.014 ^b
EDSS (median) (IQR)	3.0 (2.0–3.5)	6.0 (3.6–6.5)	.003 ^b
Age at onset (mean) (SD) (yr)	37.6 (12.0)	38.7 (8.5)	.428
Disease-modifying therapy (No.) (%)			
Interferon β -1a I.M.	14 (32.6)	2 (13.3)	.111
Interferon β -1a S.C.	3 (9.3)	0 (0)	
Glatiramer acetate	8 (18.6)	2 (13.3)	
Natalizumab	4 (9.3)	1 (6.7)	
Dimethyl fumarate	2 (4.7)	0 (0)	
Fingolimod	3 (7.0)	0 (0)	
Teriflunomide	1 (2.3)	3 (20.0)	
Rituximab	1 (2.3)	0 (0)	
Ocrelizumab	0 (0)	1 (6.7)	
IVIG	1 (2.3)	1 (6.7)	
No therapy	6 (14.0)	5 (33.3)	
No. of LMCE foci	1 (n = 33) 2 (n = 8) 3 (n = 2)	1 (n = 8) 2 (n = 4) 3 (n = 3)	.292
LMCE shape (No.)			.637
Nodular	36	16	
Linear	7	5	
Plate-like	12	4	
T2 lesion volume (mean) (SD) (mL)	16.0 (16.2)	15.8 (11.4)	.965
Gd lesion volume (median) (IQR) (mL)	0 (0–0)	0 (0–0)	.097

Note:—EDSS indicates Expanded Disability Status Scale; I.M., intramuscular; S.C., subcutaneous; IVIG, intravenous immunoglobulin; Gd, gadolinium.

^a *P* value represents differences between the patients with RRMS and SPMS. The differences between the groups were analyzed using the Fisher exact, Student *t*, Mann-Whitney *U*, or χ^2 test.

^b *P* values < .05.

false discovery rate, with corrected *P* values (ie, *Q* values) < .05 considered significant.

RESULTS

Demographic, Clinical, and MR Imaging Characteristics

Table 1 shows demographic, clinical, and MR imaging characteristics of the 2 subgroups. Patients with SPMS were older ($P = .023$), had a longer disease duration ($P = .014$), and were more disabled ($P = .003$). A total of 80 LMCE foci were identified.

Cortical Thickness Comparison between the Area Surrounding LMCE Foci and the Contralateral Area

Table 2 shows the results comparing cortical thickness measurements in the region surrounding LMCE foci and in the contralateral region. For LMCE in the entire MS sample and in the RRMS cohort, the percentage differences between the 2 regions were greater for more focal ROIs (ie, fewer dilations), but this was not the case for patients with SPMS. When we considered the entire cohort, significant reductions in cortical thickness were detected for 10 and 15 dilations, though these results did not survive multiple-comparison correction. However, when we limited the analysis to only the LMCE foci in the patients with RRMS, significant

Table 2: Cortical thickness measurements in the ipsilateral region surrounding focal areas of leptomeningeal contrast enhancement and in the contralateral region^a

Dilations	Entire Cohort (80 LMCE Foci)				Patients with RRMS (55 LMCE Foci)				Patients with SPMS (25 LMCE Foci)			
	Ipsilateral	Contralateral	Pct. Diff.	P/FDR-P	Ipsilateral	Contralateral	Pct. Diff.	P/FDR-P	Ipsilateral	Contralateral	Pct. Diff.	P/FDR-P
5	2.043 (.515)	2.149 (.556)	-5.06	.07/.187	2.031 (.534)	2.212 (.567)	-8.53	.005/.04 ^b	2.070 (.480)	2.000 (.510)	3.44	.562/.823
10	2.063 (.437)	2.160 (.476)	-4.59	.016/.128	2.099 (.455)	2.211 (.501)	-5.20	.01/.044 ^b	1.979 (.387)	2.039 (.396)	-2.99	.493/.823
15	2.088 (.411)	2.153 (.413)	-3.07	.039/.156	2.141 (.414)	2.208 (.432)	-3.08	.055/.147	1.964 (.383)	2.023 (.339)	-2.96	.384/.823
20	2.114 (.286)	2.136 (.385)	-1.04	.409/.554	2.167 (.394)	2.196 (.395)	-1.33	.365/.417	1.989 (.342)	2.000 (.325)	-.55	.895/.895
25	2.116 (.362)	2.131 (.368)	-.71	.485/.554	2.167 (.376)	2.194 (.377)	-1.24	.306/.408	1.996 (.301)	1.983 (.306)	0.65	.749/.856
30	2.113 (.348)	2.131 (.354)	-.85	.342/.554	2.162 (.363)	2.195 (.361)	-1.51	.137/.274	1.997 (.284)	1.980 (.291)	0.85	.617/.823
35	2.115 (.338)	2.127 (.342)	-.57	.483/.554	2.165 (.353)	2.190 (.347)	-1.15	.191/.306	1.998 (.273)	1.977 (.284)	1.06	.509/.823
40	2.117 (.327)	2.120 (.332)	-.14	.882/.882	2.168 (.341)	2.180 (.336)	-.55	.529/.529	1.998 (.261)	1.979 (.282)	0.95	.485/.823

Note.—Pct. Diff. indicates percentage difference; FDR, false discovery rate.

Ipsilateral and contralateral columns represent mean (standard deviation) cortical thickness measures in millimeters.

^a Paired *t* tests comparing the ipsilateral and contralateral regions were used to calculate *P* values. The Benjamini-Hochberg procedure was used to control the false discovery rate.

^b Corrected *P* values < .05.

differences were found for 5 dilations (-8.53%, corrected *P* = .04) and 10 dilations (-5.20%, corrected *P* = .044). No differences were found in the SPMS cohort. When we compared LMCE type, no significant differences were detected for the entire cohort or when assessing patients with RRMS and SPMS separately (results not shown).

Validation Analyses

No significant results were found for either of the validation analyses, as expected. For the first analysis in which non-LMCE points were used for ROI generation, the minimum corrected *P* values were .878, .912, and .955 for the entire cohort, patients with RRMS, and those with SPMS, respectively. For the second analysis in which LMCE foci were mapped to another randomly selected subject, the minimum corrected *P* values were .782, .825, and .881 for the entire cohort, patients with RRMS, and those with SPMS, respectively.

DISCUSSION

In this cross-sectional study, we demonstrated that LMCE foci are associated with localized cortical atrophy in RRMS, suggesting a direct link between leptomeningeal inflammation and focal thinning of the cortex in these patients. Moreover, we found that the relative decrease of cortical thickness in the area surrounding LMCE foci followed a clear gradient with larger regions progressively reflecting smaller differences. We also performed validation analyses to bolster the overall confidence in our findings. These results suggest that our findings are not driven by age-related atrophy or cortical asymmetries nor are they a consequence of imaging or postprocessing artifacts. However, contrary to our initial hypothesis, we did not find an apparent relationship between focal thinning and LMCE presence in the SPMS cohort.

Histopathologic studies have revealed strong associations between meningeal inflammation and cortical damage in the form of numerous features, including demyelination^{4,24} and loss of neurons, astrocytes, and oligodendrocytes.²⁴ A more focal topographic association between leptomeningeal inflammation and cortical demyelination was reported compared with a relatively wider pattern of neuronal loss in the surrounding cortex.²⁴ These findings support the notion that the meninges play a role in the development and maintenance of an inflammatory milieu.²⁵ In this context, it is likely that cytotoxic cytokines, originating from

ectopic lymphoid-like structures in the meninges,⁹ diffuse through the subarachnoid space and have a direct, causative role in the development of cortical pathology. Although the exact reason for the apparently greater effect on neuronal loss is not yet clear, it might be related to increased sensitivity of neurons to cytotoxic damage.²⁴ Another possibility is that areas farther away from focal meningeal inflammation may have a better chance at successful remyelination due to the reduced frequency of direct contact with diffusing cytokines. Nevertheless, it is perhaps surprising that we were unable to find evidence of increased cortical thinning in the areas surrounding LMCE foci in the SPMS cohort.

The combination of other pathologic processes along with a less localized effect of long-lasting leptomeningeal inflammation might, in part, explain the apparent lack of an association in the advanced stage of MS. Another possibility is that the largest effect of leptomeningeal inflammation on localized neurodegeneration occurs during the early-to-midterm period once an LMCE focus develops. Subsequently, other pathologic features, such as retrograde and anterograde degeneration following axonal transection due to white matter lesions,²⁶ may end up playing a greater role in the development of cortical atrophy. Diffusion tensor imaging studies have revealed a clear link between thinning of the cortex and damage in the so-called normal-appearing white matter of connected fiber tracts.^{27,28} Tract-specific measures of white matter bundles connected to cortical areas surrounding the LMCE foci may be useful to explore this possibility. Finally, it has been reported that even healthy controls may present with nodular LMCE foci; thus, this subtype might not be MS-specific.¹² We did not find, however, any cortical thickness differences when comparing the type of LMCE focus.

An alternative explanation for the lack of significant differences in the SPMS cohort is that the overall degree of leptomeningeal inflammation is greater in these patients compared with those with an RRMS disease course. In such a scenario, one could hypothesize that the contralateral side is affected to a similar degree; thus, no differences in cortical thickness are observed. While the detection of leptomeningeal inflammation, as evidenced by LMCE, may be poorer with 3T MR imaging compared with 7T,^{12,29} such an explanation seems unlikely. A recent study found that global cortical atrophy was numerically greater, but not statistically different, during 5 years of follow-up in patients with

SPMS with LMCE foci compared with those without them.¹⁴ In line with the current findings, that same study found a significantly greater rate of cortical atrophy in patients with RRMS with LMCE foci compared with those without them. One other possibility is that because the overall extent of gray matter loss in patients with SPMS is so extensive throughout the cortex, any focal effects surrounding individual LMCE foci are lost. Finally, LMCE foci might not reflect the exact same underlying pathology throughout the course of the disease, leading to differential effects on cortical atrophy between patients with RRMS and those with SPMS. Currently, this possibility remains purely speculative.

Our study has limitations. First, the data were retrospectively analyzed, and the study was cross-sectional. Although most LMCE foci appear to remain stable with time, at least during the midterm,¹¹ it is unclear how quickly they effect the development of cortical thinning. The study sample was relatively small, especially for the SPMS group, which had only 15 patients. This drawback is somewhat offset, however, because the analysis was performed at the level of individual LMCE foci rather than subject-wise. In this regard, about 31% (25 of 80) of all foci were from patients with SPMS. Moreover, differences between ipsilateral/contralateral ROIs in patients with SPMS did not follow the clear progression that was found in patients with RRMS with respect to ROI size. Nevertheless, future studies are warranted with larger sample sizes. In addition, our study protocol did not include a double inversion recovery sequence to aid in the visualization of cortical lesions. Subpial lesions, which histopathologic data suggest are linked to leptomeningeal inflammation,⁴ are generally not visible even with double inversion recovery at 3T.³⁰ However, a recent 7T study found a limited association between individual LMCE foci and the presence of cortical lesions, suggesting that the role of leptomeningeal inflammation on the development of cortical lesions might actually be weak.³¹

CONCLUSIONS

Our in vivo MR imaging study supports previous histopathologic findings, suggesting that leptomeningeal inflammation, as evidenced by LMCE, is anatomically related to focal cortical thinning in patients with RRMS. These findings, especially the apparent lack of an association in the SPMS phenotype, should be confirmed in prospective studies with larger sample sizes.

Disclosures: Bianca Weinstock-Guttman—UNRELATED: Board Membership: Biogen, TEVA Neuroscience, Novartis, Celgene, EMD Serono, Genentech; Consultancy: Biogen, TEVA Neuroscience, Novartis, Celgene, EMD Serono, Genentech; Grants/Grants Pending: Biogen, TEVA Neuroscience, EMD Serono; Payment for Lectures Including Service on Speakers Bureaus: Biogen, TEVA, Novartis, Genentech. Robert Zivadinov—UNRELATED: Consultancy: Novartis, Sanofi, Celgene, EMD Serono*; Grants/Grants Pending: Novartis, Sanofi, Protombo*; Payment for Lectures Including Service on Speakers Bureaus: Novartis, Sanofi, Celgene, EMD Serono.* David Hojnacki—UNRELATED: Consultancy: Biogen, Genentech, EMD Serono, Novartis; Payment for Lectures Including Service on Speakers Bureaus: Biogen, Genentech, EMD Serono, Novartis. *Money paid to the institution.

REFERENCES

- Mahad DH, Trapp BD, Lassmann H. **Pathological mechanisms in progressive multiple sclerosis.** *Lancet Neurol* 2015;14:183–93 CrossRef Medline
- Herranz E, Gianni C, Louapre C, et al. **Neuroinflammatory compo-**

- ment of gray matter pathology in multiple sclerosis.** *Ann Neurol* 2016;80:776–90 CrossRef Medline
- Magliozzi R, Howell O, Vora A, et al. **Meningeal B-cell follicles in secondary progressive multiple sclerosis associate with early onset of disease and severe cortical pathology.** *Brain* 2007;130:1089–104 Medline
- Lucchinetti CF, Popescu BF, Bunyan RF, et al. **Inflammatory cortical demyelination in early multiple sclerosis.** *N Engl J Med* 2011;365:2188–97 CrossRef Medline
- Haider L, Zrzavy T, Hametner S, et al. **The topography of demyelination and neurodegeneration in the multiple sclerosis brain.** *Brain* 2016;139:807–15 CrossRef Medline
- Choi SR, Howell OW, Carassiti D, et al. **Meningeal inflammation plays a role in the pathology of primary progressive multiple sclerosis.** *Brain* 2012;135:2925–37 CrossRef Medline
- Howell OW, Reeves CA, Nicholas R, et al. **Meningeal inflammation is widespread and linked to cortical pathology in multiple sclerosis.** *Brain* 2011;134:2755–71 CrossRef Medline
- Popescu BF, Lucchinetti CF. **Meningeal and cortical grey matter pathology in multiple sclerosis.** *BMC Neurol* 2012;12:11 CrossRef Medline
- Serafini B, Rosicarelli B, Magliozzi R, et al. **Detection of ectopic B-cell follicles with germinal centers in the meninges of patients with secondary progressive multiple sclerosis.** *Brain Pathol* 2004;14:164–74 CrossRef Medline
- Zurawski J, Lassmann H, Bakshi R. **Use of magnetic resonance imaging to visualize leptomeningeal inflammation in patients with multiple sclerosis: a review.** *JAMA Neurol* 2017;74:100–09 CrossRef Medline
- Absinta M, Vuolo L, Rao A, et al. **Gadolinium-based MRI characterization of leptomeningeal inflammation in multiple sclerosis.** *Neurology* 2015;85:18–28 CrossRef Medline
- Harrison DM, Wang KY, Fiol J, et al. **Leptomeningeal enhancement at 7T in multiple sclerosis: frequency, morphology, and relationship to cortical volume.** *J Neuroimaging* 2017;27:461–68 CrossRef Medline
- Zivadinov R, Ramasamy DP, Hagemeyer J, et al. **Evaluation of leptomeningeal contrast enhancement using pre-and postcontrast subtraction 3D-FLAIR imaging in multiple sclerosis.** *AJNR Am J Neuroradiol* 2018;39:642–47 CrossRef Medline
- Zivadinov R, Ramasamy DP, Vaneckova M, et al. **Leptomeningeal contrast enhancement is associated with progression of cortical atrophy in MS: a retrospective, pilot, observational longitudinal study.** *Mult Scler* 2017;23:1336–45 CrossRef Medline
- Makshakov G, Magonov E, Totolyan N, et al. **Leptomeningeal contrast enhancement is associated with disability progression and grey matter atrophy in multiple sclerosis.** *Neurol Res Int* 2017;2017:8652463 CrossRef Medline
- Bö L, Geurts JG, van der Valk P, et al. **Lack of correlation between cortical demyelination and white matter pathologic changes in multiple sclerosis.** *Arch Neurol* 2007;64:76–80 CrossRef Medline
- Calabrese M, Seppi D, Romualdi C, et al. **Gray matter pathology in MS: a 3-year longitudinal study in a pediatric population.** *AJNR Am J Neuroradiol* 2012;33:1507–11 CrossRef Medline
- Kappus N, Weinstock-Guttman B, Hagemeyer J, et al. **Cardiovascular risk factors are associated with increased lesion burden and brain atrophy in multiple sclerosis.** *J Neurol Neurosurg Psychiatry* 2016;87:181–87 CrossRef Medline
- Polman CH, Reingold SC, Banwell B, et al. **Diagnostic criteria for multiple sclerosis: 2010 revisions to the McDonald criteria.** *Ann Neurol* 2011;69:292–302 CrossRef Medline
- Dale AM, Fischl B, Sereno MI. **Cortical surface-based analysis, I: segmentation and surface reconstruction.** *Neuroimage* 1999;9:179–94 CrossRef Medline
- Fischl B, Salat DH, Busa E, et al. **Whole brain segmentation: automated labeling of neuroanatomical structures in the human brain.** *Neuron* 2002;33:341–55 CrossRef Medline
- Magon S, Gaetano L, Chakravarty MM, et al. **White matter lesion**

- filling improves the accuracy of cortical thickness measurements in multiple sclerosis patients: a longitudinal study. *BMC Neurosci* 2014;15:106 CrossRef Medline
23. Greve DN, Fischl B. Accurate and robust brain image alignment using boundary-based registration. *Neuroimage* 2009;48:63–72 CrossRef Medline
 24. Magliozzi R, Howell OW, Reeves C, et al. A gradient of neuronal loss and meningeal inflammation in multiple sclerosis. *Ann Neurol* 2010;68:477–93 CrossRef Medline
 25. Schläger C, Körner H, Krueger M, et al. Effector T-cell trafficking between the leptomeninges and the cerebrospinal fluid. *Nature* 2016;530:349–53 CrossRef Medline
 26. Sepulcre J, Goñi J, Masdeu JC, et al. Contribution of white matter lesions to gray matter atrophy in multiple sclerosis: evidence from voxel-based analysis of T1 lesions in the visual pathway. *Arch Neurol* 2009;66:173–79 CrossRef Medline
 27. Bergsland N, Laganà MM, Tavazzi E, et al. Corticospinal tract integrity is related to primary motor cortex thinning in relapsing-remitting multiple sclerosis. *Mult Scler* 2015;21:1771–80 CrossRef Medline
 28. Steenwijk MD, Daams M, Pouwels PJ, et al. Unraveling the relationship between regional gray matter atrophy and pathology in connected white matter tracts in long-standing multiple sclerosis. *Hum Brain Mapp* 2015;36:1796–807 CrossRef Medline
 29. Jonas SN, Izbudak I, Frazier AA, et al. Longitudinal persistence of meningeal enhancement on postcontrast 7T 3D-FLAIR MRI in multiple sclerosis. *AJNR Am J Neuroradiol* 2018;39:1799–805 CrossRef Medline
 30. Nielsen AS, Kinkel RP, Tinelli E, et al. Focal cortical lesion detection in multiple sclerosis: 3 Tesla DIR versus 7 Tesla FLASH-T2. *J Magn Reson Imaging* 2012;35:537–42 CrossRef Medline
 31. Harrison D, Jonas S, Izbudak I. Investigating the relationship between meningeal enhancement on 7T MRI and cortical gray matter lesions in multiple sclerosis. In: *Proceedings of the Annual Congress of the European Committee for Treatment and Research in Multiple Sclerosis*, Berlin, Germany. October 10–12, 2018; 489

Moving Toward a Consensus DSC-MRI Protocol: Validation of a Low-Flip Angle Single-Dose Option as a Reference Standard for Brain Tumors

K.M. Schmainda, M.A. Prah, L.S. Hu, C.C. Quarles, N. Semmineh, S.D. Rand, J.M. Connelly, B. Anderies, Y. Zhou, Y. Liu, B. Logan, A. Stokes, G. Baird, and J.L. Boxerman



ABSTRACT

BACKGROUND AND PURPOSE: DSC-MR imaging using preload, intermediate (60°) flip angle and postprocessing leakage correction has gained traction as a standard methodology. Simulations suggest that DSC-MR imaging with flip angle = 30° and no preload yields relative CBV practically equivalent to the reference standard. This study tested this hypothesis in vivo.

MATERIALS AND METHODS: Eighty-four patients with brain lesions were enrolled in this 3-institution study. Forty-three patients satisfied the inclusion criteria. DSC-MR imaging (3T, single-dose gadobutrol, gradient recalled-echo-EPI, TE = 20–35 ms, TR = 1.2–1.63 seconds) was performed twice for each patient, with flip angle = 30°–35° and no preload (P–), which provided preload (P+) for the subsequent intermediate flip angle = 60°. Normalized relative CBV and standardized relative CBV maps were generated, including postprocessing with contrast agent leakage correction (C+) and without (C–) contrast agent leakage correction. Contrast-enhancing lesion volume, mean relative CBV, and contrast-to-noise ratio obtained with 30°/P–/C–, 30°/P–/C+, and 60°/P+/C– were compared with 60°/P+/C+ using the Lin concordance correlation coefficient and Bland-Altman analysis. Equivalence between the 30°/P–/C+ and 60°/P+/C+ protocols and the temporal SNR for the 30°/P– and 60°/P+ DSC-MR imaging data was also determined.

RESULTS: Compared with 60°/P+/C+, 30°/P–/C+ had closest mean standardized relative CBV ($P = .61$), highest Lin concordance correlation coefficient (0.96), and lowest Bland-Altman bias ($\mu = 1.89$), compared with 30°/P–/C– ($P = .02$, Lin concordance correlation coefficient = 0.59, $\mu = 14.6$) and 60°/P+/C– ($P = .03$, Lin concordance correlation coefficient = 0.88, $\mu = -10.1$) with no statistical difference in contrast-to-noise ratios across protocols. The normalized relative CBV and standardized relative CBV were statistically equivalent at the 10% level using either the 30°/P–/C+ or 60°/P+/C+ protocols. Temporal SNR was not significantly different for 30°/P– and 60°/P+ ($P = .06$).

CONCLUSIONS: Tumor relative CBV derived from low-flip angle, no-preload DSC-MR imaging with leakage correction is an attractive single-dose alternative to the higher dose reference standard.

ABBREVIATIONS: C– = postprocessing without contrast agent leakage correction; C+ = postprocessing with contrast agent leakage correction; LCCC = Lin concordance correlation coefficient; nRCBV = normalized relative CBV; P– = a preload of contrast agent was not administered; P+ = a preload of contrast agent was administered; rCBV = relative CBV; sRCBV = standardized relative CBV

DSC-MR imaging measurement of relative cerebral blood volume (rCBV) is the most commonly used approach for brain tumor perfusion imaging, with numerous studies demonstrating its value to predict glioma grade, overall survival, and response to

treatment.^{1–8} Yet, widespread adoption of DSC-MR imaging for clinical trials and daily practice has been impeded by lack of agreement on the best data collection and analysis methodology, including the choice of the preload dose to mitigate the effects of contrast agent extravasation, bolus contrast-agent dose, flip angle, TE, and the use of postprocessing leakage correction. In response,

Received November 13, 2018; accepted after revision January 18, 2019.

From the Departments of Biophysics (K.M.S., M.A.P.), Radiology (K.M.S., S.D.R.), Neurology (J.M.C.), and Division of Biostatistics, Institute for Health and Society (Y.L., B.L.), Medical College of Wisconsin, Milwaukee, Wisconsin; Departments of Radiology (L.S.H., Y.Z.) and Neurosurgery (B.A.), Mayo Clinic, Scottsdale, Arizona; Division of Imaging Research (C.C.Q., N.S., A.S.), Barrow Neurological Institute, Phoenix, Arizona; and Department of Diagnostic Imaging (J.L.B., G.B.), Rhode Island Hospital and Warren Alpert Medical School of Brown University, Providence, Rhode Island.

This work was supported by National Institutes of Health/National Cancer Institute: U01 CA176110 (K.M.S., M.A.P., S.D.R., J.M.C.), R01 CA 082500 (K.M.S., M.A.P., S.D.R., J.M.C.), U01 CA180820 (J.L.B., G.B.), R01 CA158079 (C.C.Q.), R01 CA221938 (K.M.S., C.C.Q., L.S.H., J.L.B.), R01 CA213158 (A.S.), ADHS16-162414 (A.S.), R01 CA213158 (N.S.), and U01 CA220378 (L.S.H.).

Paper previously presented, in part, at: International Society of Magnetic Resonance in Medicine Annual Meeting and Exhibition and 35th Annual Scientific Meeting of the Congress of European Society of Magnetic Resonance in Medicine and Biology, June 16–22, 2018, Paris, France; and Annual Meeting of the American Society of Neuroradiology and the Foundation of the ASNR Symposium, June 2–7, 2018, Vancouver, British Columbia, Canada.

Please address correspondence to Kathleen M. Schmainda, PhD, Medical College of Wisconsin, Department of Biophysics, 8701 W Watertown Plank Rd, Milwaukee, WI 53226; e-mail: kathleen@mcw.edu

Indicates open access to non-subscribers at www.ajnr.org

<http://dx.doi.org/10.3174/ajnr.A6015>

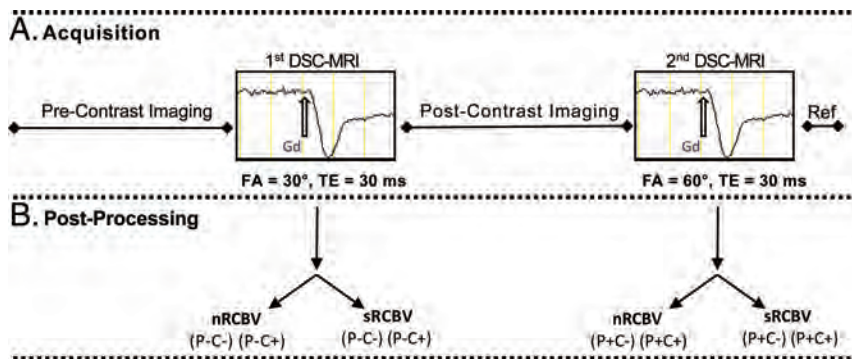


FIG 1. Acquisition protocol with postprocessing options. *A*, After precontrast standard imaging is performed, a standard dose of gadolinium contrast (0.1 mmol/kg) is administered during which DSC-MR imaging data are collected using gradient recalled-echo-EPI with a flip angle (FA) of 30° and TE = 30 ms. This first contrast agent injection serves as the preload (P+) for the second DSC-MR imaging acquisition. Next, postcontrast anatomic images are collected, followed by the second DSC-MR imaging acquisition during which a second dose of gadolinium contrast (0.1 mmol/kg) is administered. Finally, an anatomic reference (Ref) scan is obtained using a slice prescription that exactly matches the DSC-MR imaging slice prescription. *B*, Given the order of the data collection, 8 different rCBV maps can be created for each subject that include both normalized and standardized rCBV for each of these 4 conditions: 1) 30°/P-/C-, 2) 30°/P-/C+, 3) 60°/P+/C-, and 4) 60°/P+/C+.

a study was performed to compare the most commonly published approaches for the determination of brain tumor rCBV⁹; the results were that for single-echo methodologies, the approach using full-dose contrast agent preload and postprocessing leakage correction proved best. This result was confirmed by several subsequent studies,^{1,2,10-12} including a recent multicenter study showing excellent concordance across sites for the analysis of DSC-MR imaging data acquired with a full-dose preload and bolus.¹³

Continued effort toward harmonization includes a recent American Society of Functional Neuroradiology white paper recommending a 60°–70° flip angle, field-strength-dependent TE, and one-fourth-to-full-dose preload with a full-dose bolus.¹⁴ Yet a more recent constraint is that DSC-MR imaging paradigms comply with the standardized brain tumor imaging protocol,¹⁵ requiring postcontrast imaging to be performed after 1 full dose of gadolinium-based contrast agent, either split between the preload and DSC-MR imaging bolus before postcontrast imaging or given fully as a preload with variable-bolus-dose DSC-MR imaging after postcontrast imaging.

To further assist effort toward DSC-MR imaging harmonization, two independent studies using sophisticated computer simulations were recently performed,^{16,17} one of which used a glioblastoma-trained digital reference object permitting an exhaustive search of many possible combinations of acquisition parameters under a range of simulated physiologic conditions.¹⁷ This search revealed that the American Society of Functional Neuroradiology parameters with flip angle = 60° and TE = 30 ms had excellent accuracy and precision at both 1.5T and 3T for single-dose preload and bolus, but substantially degraded performance for fractional dosing schemes, and especially poor performance without preload. However, DSC-MR imaging without preload but with a comparatively lower flip angle (30°) and a midrange TE (30 ms at 3T) performed nearly as well as the double-dosing scheme, but also very well for fractional dosing schemes and even without using any preload dose.

While this theory is promising, data are lacking to support it.

Therefore, this study aimed to confirm these simulation results in vivo and to determine whether single-dose, low-flip angle DSC-MR imaging without preload gives rCBV estimates practically equivalent to double-dose, intermediate-flip angle DSC-MR imaging with full-dose preload and bolus in patients with contrast-enhancing brain lesions, including gliomas. Adoption of this protocol would eliminate preload contrast agent injection and reduce contrast agent usage.

MATERIALS AND METHODS

Patients

All participants provided written, informed consent according to institutional review board policy in this Health Insurance Portability and Accountability Act-compliant study. Patients diagnosed with a brain tumor or vascular malformation who were scheduled for a clinically indicated DSC-MR imaging were considered for inclusion in this 3-institution (Medical College of Wisconsin, Rhode Island Hospital, Mayo Clinic Arizona) prospective study. The lesion was required to be at least 1 mL, and the DSC-MR imaging data had to be of sufficient quality with a discernable signal transient without large motion artifacts to ensure a robust comparison between DSC methods as applied to lesion tissue only.

Imaging

All studies were performed on 3T MR imaging systems (MAGNETOM Skyra (Siemens, Erlangen, Germany), MAGNETOM Verio (Siemens, Erlangen, Germany), PET/MR (GE Healthcare, Milwaukee, Wisconsin) and two Discovery 750W systems (GE Healthcare, Milwaukee, Wisconsin). Figure 1A depicts the image-acquisition protocol. Following standard precontrast FLAIR and T1-weighted spin-echo imaging, we performed low-flip angle (30°) DSC-MR imaging (gradient recalled-echo EPI, TE/TR = 20–35 ms/1200–1630 ms) without contrast agent preload (P-) using a bolus injection of 0.1 mmol/kg of gadobutrol (Gadavist; Bayer Schering Pharma, Berlin, Germany). Additional DSC-MR imaging scan parameters included the following: FOV = 220 mm, matrix = 96 × 96 or 128 × 128, slice thickness = 4–5 mm, skip = 0 mm. Subsequently postcontrast T1-weighted images were obtained according to the clinical protocol of each site, and a second DSC-MR imaging was performed using an intermediate flip angle (60°) and otherwise identical acquisition parameters. The time between the first and second DSC-MR imaging study was 5–8 minutes. By virtue of the acquisition order, the second DSC-MR imaging was performed with a contrast agent preload (P+) provided by the first DSC-MR imaging bolus. For both DSC-MR imaging datasets, 120 time points were collected and gadobutrol was bolus-injected (3–5 mL/s) after 40–60 baseline images. When the DSC-MR slices were not an exact subset of the T1-weighted image slices, an additional T1-weighted “reference” scan was ob-

tained using a slice prescription (orientation and spacing) matching the DSC-MR imaging examination for ease of coregistering the DSC-MR images to the anatomic images.

Image Analysis

All imaging data were anonymized and postprocessed at a central site (Medical College of Wisconsin) using OsiriX Imaging Software (<http://www.osirix-viewer.com>) with IB NeuroTM and IB Delta SuiteTM plugins (Imaging Biometrics, Elm Grove, Wisconsin). Both normalized (nRCBV) to normal-appearing white matter (NAWM) and standardized (sRCBV)¹⁸ maps were created. The NAWM ROI, selected by 1 person (M.A.P.), comprised two 8-mm-diameter circular ROIs placed on 2 separate image slices at the midventricular level within the normal brain near the frontal horns of the lateral ventricles. When this area was abnormal, the ROIs were drawn near the occipital horns. Standardization is a unique machine-learned calibration rule¹⁹ that yields quantitative rCBV maps with consistent values across time and patients.²⁰ Unlike nRCBV, the creation of sRCBV does not require the determination of a reference ROI.

Both nRCBV and sRCBV maps were created for DSC-MR imaging datasets obtained without (C-) and with (C+) application of Boxerman-Schmainda-Weisskoff leakage correction previously described in detail¹⁰ and implemented in a vendor-specific fashion by IB NeuroTM. Therefore, 8 different rCBV maps were created for each subject, including nRCBV and sRCBV for each of 4 conditions: 30°/P-/C-, 30°/P-/C+, 60°/P+/C-, and 60°/P+/C+.

Using the IB Delta SuiteTM, we defined contrast-enhancing lesion volumes from quantitative dT1 (delta T1) maps, computed from the difference between calibrated and registered post- and precontrast T1-weighted images.²¹ The quantitative dT1 maps facilitate visualization of the enhancing lesion, free of intrinsically increased T1 signal from blood products or proteinaceous material. Because dT1 maps are quantitative, a single threshold can be applied to all cases for consistent delineation of contrast-enhancing lesion volume. The DSC-MR imaging volume was likewise coregistered to the contrast-enhanced T1-weighted images via the reference scan. The contrast-enhancing lesion volume ROI was transferred to the rCBV maps from which the rCBV mean and standard error of the mean could be determined using the ROI analysis tools available within OsiriX.

Statistical Analysis

Because subjects were their own control, mean estimates were modeled using generalized mixed modeling with sandwich estimation, assuming normal and log-normal distributions, in which observations were nested within each patient using SAS/GLIMMIX (SAS Institute Inc., Cary, North Carolina). Because residuals were heterogeneous (differences increased with increasing contrast-enhancing lesion volume), a log-normal distribution was also used. As a conservative effort, the Dunnett method was used for multiple comparisons, where P+/C+ was the control to examine whether the alternative approaches deviated significantly. Moreover, a Bonferroni correction was also used, where the *P* value was adjusted for 6 comparisons, 0.05/6 = 0.00833.

The Lin concordance correlation coefficients (LCCCs) and

Bland-Altman plots were calculated across all subjects for nRCBV and sRCBV obtained with 30°/P-/C-, 30°/P-/C+, and 60°/P+/C- protocols relative to the reference standard (60°/P+/C+). Unlike intraclass or Pearson correlation coefficients, the LCCC provides a measure of both accuracy (deviation from the line of equality) and precision (deviation from best-fit line) rather than precision alone.

For methods showing strong agreement with the reference standard, a statistical equivalence test was performed. An equivalence test begins with the null hypothesis that the two tests are not equivalent, but if the 95% CI is contained in the margin, then the null is rejected and equivalence is confirmed for the chosen margins.

The contrast-to-noise ratio was also calculated across all subjects for nRCBV and sRCBV obtained with 30°/P-/C-, 30°/P-/C+, and 60°/P+/C- protocols relative to the reference standard (60°/P+/C+), as follows:

$$CNR = [\mu_x - \mu_y] / [\sigma_x^2 + \sigma_y^2]^{1/2},$$

where μ and σ are the mean and SD of the ROI and *x* and *y* designate tumor and white matter, respectively. As a final comparison of acquisition methods, the temporal signal-to-noise ratio (*tSNR*) was determined as follows:

$$tSNR = [\mu_{BL} - \delta_{BL}] / \sigma_{BL},$$

where μ , σ , and δ are the mean, SD, and minimum of the baseline (BL) signal time points used for the rCBV calculations. The paired Student *t* test was used to compare the mean contrast-to-noise ratio with the reference standard and *tSNR* between the 30° and 60° acquisitions.

RESULTS

Since January 2017, eighty-four subjects from 3 institutions have been enrolled in this study. Of these, 41 were excluded from analysis because of contrast-enhancing lesion volume < 1 mL (*n* = 35) or the DSC-MR imaging image quality being insufficient for analysis (*n* = 6). The diagnoses for the remaining patients (*n* = 43) were grade IV glioblastoma (*n* = 29) and fibrillary and gemistocytic astrocytoma (*n* = 1); grade III anaplastic astrocytoma (*n* = 4) and anaplastic oligodendroglioma (*n* = 1); high-grade glioma with treatment effect (*n* = 1); grade II oligodendroglioma (*n* = 1) and astrocytoma with treatment effect (*n* = 1); grade II atypical meningioma (*n* = 1); cavernous malformation (*n* = 1); and metastases (*n* = 3).

Sample images and parameter maps for a patient with glioblastoma are shown in Fig 2. The sRCBV maps are qualitatively similar for the 30°/P-/C+ (Fig 2D) and 60°/P+/C+ protocols (Fig 2F).

The results from all analyses are listed in Tables 1–3 and plotted in Figs 3–5. Table 1 gives the rCBV statistics for each of the 8 acquisition/postprocessing protocols and the *P* value indicating whether the mean rCBV is significantly different from the 60°/P+/C+ reference. The mean rCBV data are shown in Fig 3 for both nRCBV (Fig 3A) and sRCBV (Fig 3B). The sRCBV using the 30°/P-/C+ protocol was not significantly different from the reference (*P* = .61), while the nRCBV was borderline different (*P* = .06).

There was excellent/substantial agreement^{22,23} between the 30°P-/C+ protocol and the reference standard (60°P+/C+), with LCCC values of 0.952 and 0.960 for nRCBV and sRCBV, respectively (Table 2). The nRCBV and sRCBV LCCC values were

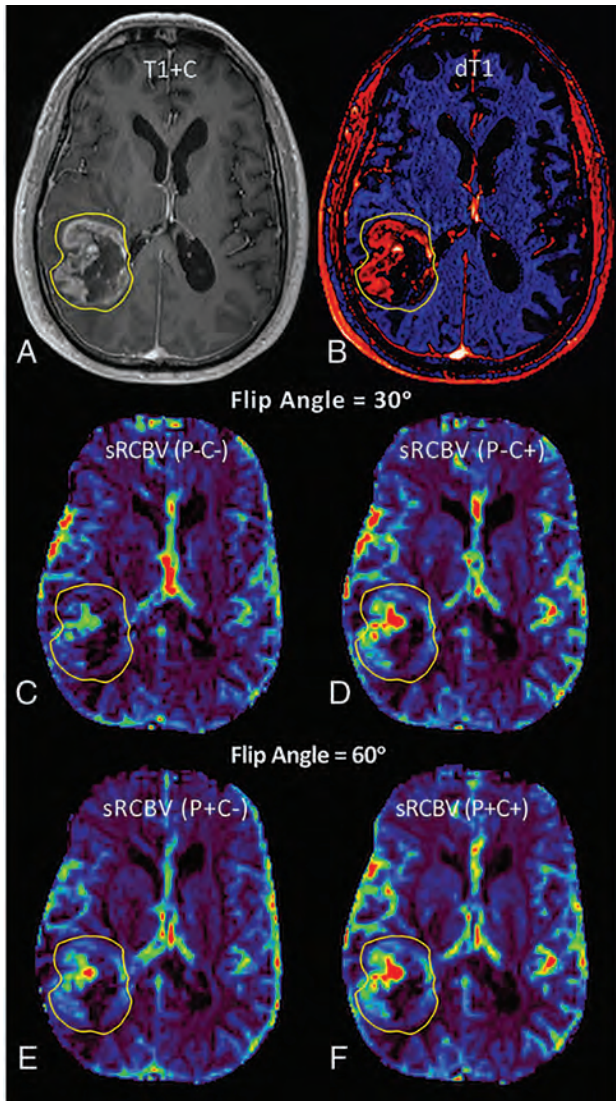


FIG 2. Images and sRCBV parameter maps from a patient with glioblastoma. Shown are the post-contrast T1-weighted (T1+C) (A) and quantitative dT1 (B) images with the corresponding sRCBV maps obtained from the first DSC-MR imaging contrast dose (C and D) without preload (P-) and without leakage correction (C-) and without preload (P-) plus leakage correction (C+). The sRCBVs obtained during the second contrast dose (E and F) and thus after the preload are shown without (P+C-) and with (P+C+) leakage correction.

Table 1: Mean rCBV in reference to flip angle = 60°/P+/C+

Parameter/Metric	30° (P-C-)	30° (P-C+)	60° (P+C-)	60° (P+C+)
nRCBV				
Mean	1.42 ± 0.79	1.67 ± 0.93	2.01 ± 1.06	1.77 ± 1.03
95% CI	1.18–1.66	1.39–1.96	1.68–2.34	1.46–2.09
P value	.003	.06 ^a	.002	NA
sRCBV				
Mean	1.17 ± 0.55	1.34 ± 0.68	1.48 ± 0.64	1.37 ± 0.73
95% CI	1.0–1.34	1.13–1.55	1.28–1.68	1.15–1.60
P value	.05	.61 ^a	.07	NA

Note:—NA indicates not applicable.

^a Significant.

much lower for the 30°P-/C- (0.648, 0.588) and 60°P+/C- (0.884, 0.877) protocols. These results are depicted in Fig 4, with a Deming regression line and the identity line for reference. There was substantial improvement in the concordance provided by postprocessing leakage correction based on the sizable increase in LCCC between 30°P-/C- and 30°P-/C+ for both nRCBV and sRCBV. Likewise, the Bland-Altman plots (Fig 5) and associated bias values (Table 3) demonstrate that 30°P-/C+ yielded substantially improved limits of agreement with minimal bias ($\mu = 1.89$) compared with 30°P-/C- and 60°P+/C- protocols (14.64 and -10.13, respectively) for sRCBV, with similar results for nRCBV.

Equivalence of the 2 measurements (30°P-/C+ versus 60°P+/C+) was determined for a $\pm 10\%$ change at a significance level of .01. For nRCBV and sRCBV, the difference of measurements (30°P-/C+ versus 60°P+/C+) in the log scale was -0.0517 ± 0.132 and -0.0191 ± 0.136 , respectively. The 95% CIs for percentage change for 30°P-/C+ compared with 60°P+/C+ were (-9.12% to, -1.11%) for nRCBV and (-5.92%, -2.31%) for sRCBV. The P values of rejecting the 1-sided null hypothesis (H0: 30°P-/C+ < 90% of 60°P+/C+) were .00531 for nRCBV and .0000782 for sRCBV, indicating equivalence between the methods.

For all protocols, there was no statistically significant difference between the tumor-to-white matter contrast-to-noise ratio with respect to the reference. The temporal SNR of the DSC-MR imaging signal was not significantly different between the 30°P- and 60°P+ acquisitions for white matter ($P = .35$), trended toward significance for tumor ($P = .06$), and was significantly different for gray matter ($P = .008$) with mean temporal SNRs of 2.11 and 2.22 for the 30°P-/C+ and 60°P+/C+ conditions, respectively.

DISCUSSION

This study confirms the theoretic conjecture of recent simulations^{16,17,24} and demonstrates in vivo that low-flip angle, no-preload DSC-MR imaging has excellent/substantial concordance^{22,23} with full-dose preload-based, intermediate-flip angle DSC-MR imaging and should be considered for consensus protocol recommendation. It uses less contrast agent and requires fewer contrast agent injections, eliminating the potential error due to variable preload dosing and timing schemes. However, postprocessing leakage correction is impactful and essential, even for low-flip angle acquisitions with less T1-weighting.

Historically, a higher flip angle (90°) was commonly used for DSC-MR imaging. This was largely motivated by early studies using spin-echo²⁵⁻²⁷ or combined spin-echo plus gradient-echo^{1,2,28} EPI sequences, in which a higher flip angle preserved the SNR. Alternative gradient-echo approaches using a lower flip angle (30°–35°) diminished T1 contamination effects due to contrast agent extravasation; however, longer TEs (ie, 54 ms) were typically chosen to maintain T2* sensitivity to the susceptibility effect induced by the passage of contrast agent

Table 2: Lin concordance correlation coefficient (LCCC) and Deming equations

	nRCBV			sRCBV		
	LCCC	Slope CI	Equation (Deming)	LCCC	Slope CI	Equation (Deming)
P-C-	0.648	(0.48–0.90)	$y = 0.69 \times x + 0.19$	0.588	(0.41–0.90)	$y = 0.65 \times x + 0.27$
P-C+	0.952	(0.82–0.98)	$y = 0.90 \times x + 0.07$	0.960	(0.85–1.01)	$y = 0.93 \times x + 0.07$
P+C-	0.884	(0.88–1.19)	$y = 1.04 \times x + 0.17$	0.877	(0.73–0.99)	$y = 0.86 \times x + 0.30$

Table 3: Bland-Altman results

Metric	nRCBV			sRCBV		
	P-C-	P-C+	P+C-	P-C-	P-C+	P+C-
Bias	21.34	5.14	-12.48	14.64	1.89	-10.13
95% CI	(9.9–32.8)	(1.1–9.2)	(-5.8 to -19.2)	(2.8–26.4)	(-2.3–6.1)	(-3.7 to -16.6)
SD bias	37.29	13.08	21.85	38.35	13.56	20.86
Lower LOA	-51.75	-20.49	-55.31	-60.52	-24.68	-51.01
Upper LOA	94.43	30.78	30.34	89.79	28.46	30.75

Note:—Bias indicates the mean of the percentage difference; LOA, limits of agreement = bias \pm 1.96 \times SD of bias.

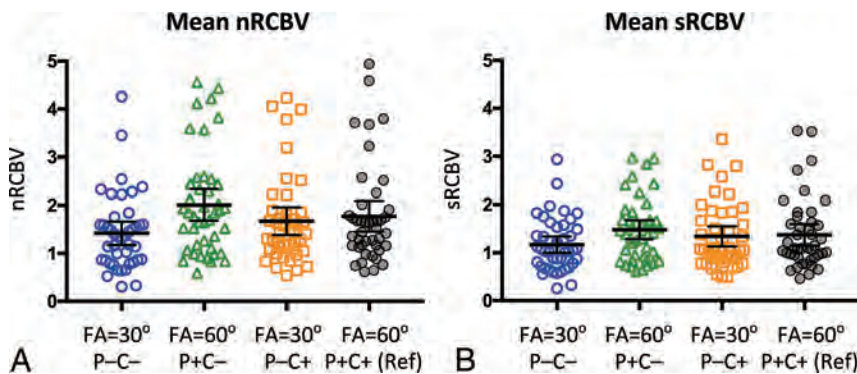


FIG 3. Normalized and standardized mean rCBV results. Mean nRCBV (A) and sRCBV (B) for each of the acquisition/postprocessing conditions without/with preload (P-/P+) and without and with leakage correction (C-/C+).

bolus.^{29,30} Comparative rCBV data from brain tumors indicated that low-flip angle, long-TE approaches were suboptimal for distinguishing high-grade tumor from normal-appearing brain⁹ and often required manual identification of rCBV “hot spots” to obtain clinically relevant results. Instead, preload-based DSC-MR imaging using intermediate-to-high flip angles with a minimum TE and postprocessing leakage correction was found to work best.⁹ Yet a systematic exploration of the image-acquisition-parameter space aimed at maximizing the DSC-MR imaging signal while minimizing contrast agent leakage effects had not been performed until recently. We considered 60°P+/C+ to be the reference standard because its utility,^{1,2} reliability,²⁰ and accuracy^{9,12} have been repeatedly proved in multiple treatment and outcomes studies,^{4-6,31} including those with spatially correlated tissue samples^{8,11,32} and recent simulations as described above.^{16,17,24}

For this study, the $\pm 10\%$ difference chosen for the test of equivalence is clinically justified because clinically relevant rCBV changes of $> 10\%$ have been frequently reported. For example, it was shown that for patients treated with topotecan, the percentage change in rCBV at 1 month for those with progressive disease was +12% versus -29% for those with nonprogressive disease ($P = .02$).³³ Similarly, after treatment with radiation-temozolomide, patients with pseudoprogression had a mean decrease in rCBV of 41% and those with true progression had a mean increase in rCBV of 12%.³⁴ In addition, in a multicenter clinical trial,⁵ all

patients with a statistically significant survival advantage had a mean decrease in rCBV of 53% measured at 2 weeks after starting treatment with bevacizumab. Finally, another indication that the 10% margin is indicative of excellent agreement is the previously reported repeatability of the intermediate-flip angle technique (repeatability coefficient = 1.78),²⁰ measured twice within a few days, which is worse than the estimated agreement in this study between the leakage-corrected low-flip angle and intermediate-flip angle techniques (repeatability coefficient = 0.59).

The ability to obtain comparable rCBV measurements with up to 50% less contrast agent is a step toward addressing concerns regarding the use of suprastandard (> 0.1 mmol/kg) contrast agent dosing. This is important due to recent restrictions imposed by the FDA on the use of gadolinium-based contrast agents due to the small-but-real risk of nephrogenic systemic fibrosis³⁵ and more recent concerns regarding gadolinium deposition in the brain.³⁶ Single-dose, low-flip angle methodology also improves the likelihood of performing DSC-MR imaging more routinely on both adult and pediatric patients because it would require no extra contrast agent beyond standard dosing for conventional T1-weighted postcontrast imaging and could be acquired during the standard bolus injection of contrast agent.

In addition to reducing the contrast agent dose, the low-flip angle, no-preload protocol eliminates the potential for variability in measured rCBV resulting from variations in contrast agent incubation time. Hu et al¹¹ demonstrated that with an incubation time of 5–6 minutes between a single or half-dose preload and bolus injection, rCBV could distinguish posttreatment-related enhancement from recurrent tumor. However, other than simulations showing little dependence of rCBV on incubation time,^{16,17,24} there are no other in vivo data addressing the potential influence of incubation time on rCBV measurements. By not using any preload, the low-flip angle protocol eliminates the chance that measured rCBV fluctuations due

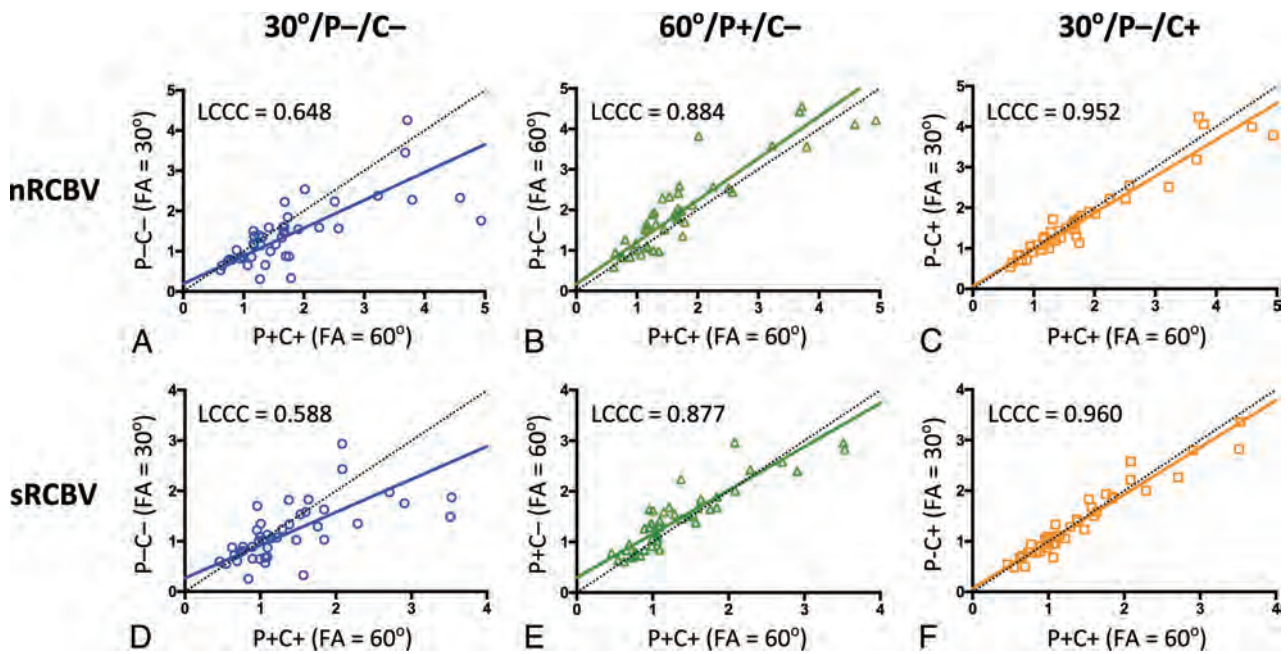


FIG 4. The Lin concordance correlation (LCCC) results, including Deming regression (solid lines), for normalized rCBV (A–C) and standardized rCBV (D–F) for each of the preload (P) and leakage-correction (C) conditions in reference to the 60°/P+/C+ condition. The 30°/P-/C+ condition for both nRCBV (C) and sRCBV (F) has the best concordance. FA indicates flip angle.

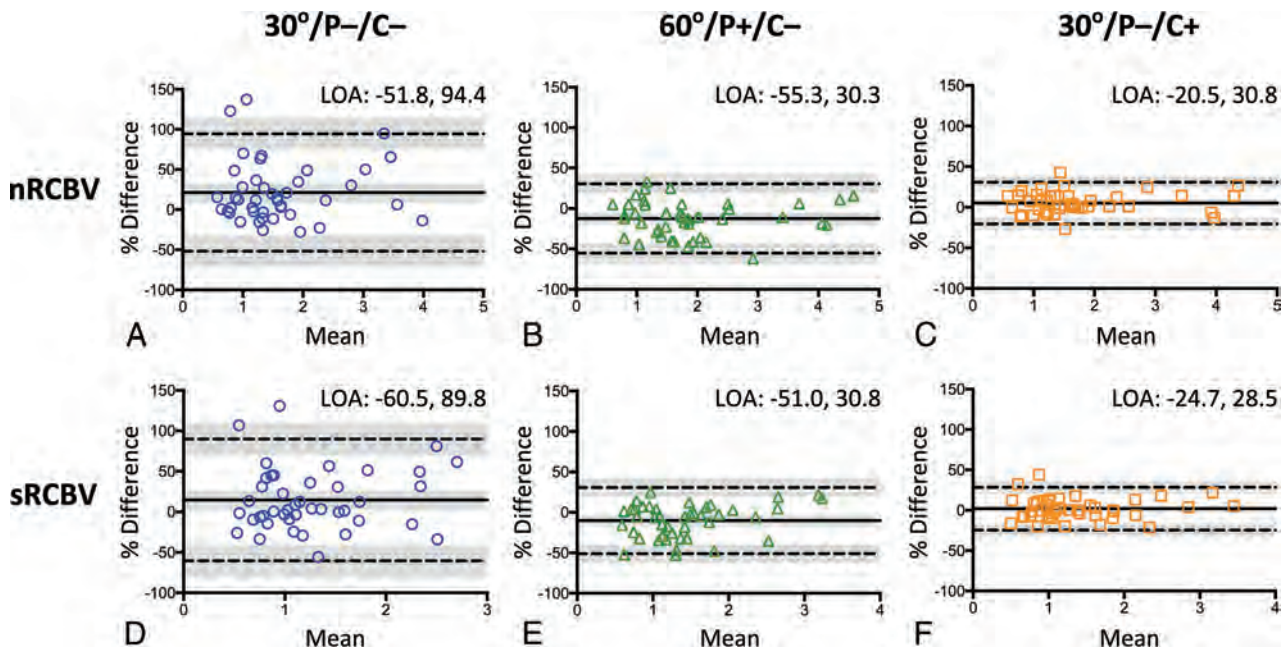


FIG 5. Bland-Altman results for normalized rCBV (A–C) and standardized rCBV (D–F) for each of the preload (P) and leakage-correction (C) conditions in comparison with the 60°/P+/C+ reference standard. The 30°/P-/C+ protocol for both nRCBV (C) and sRCBV (F) shows the best limits of agreement with minimal bias.

to inadvertent differences in incubation time could be mistaken for true differences in tumor rCBV.

The complete elimination of the preload dose would be an important advancement for efforts to harmonize DSC-MR imaging acquisitions. Balancing the experimentally proven benefit of preload with the goal of maintaining total contrast dose near single-dose levels (0.1 mmol/kg) has resulted in several disparate dosing protocols. While many studies have reported clinically relevant results using a single-dose preload,^{9,11} others have used

fractional preload doses consistent with the American Society of Functional Neuroradiology recommendation¹⁴ but unproven experimentally. Additionally, in an effort to comply with the contrast agent dosing and timing required for the consensus brain tumor imaging protocol,¹⁵ some have chosen to split the single dose between the preload and bolus dose, again without experimental evidence to justify this choice. Given the recent simulation results,^{16,17,24} there is concern that split-dose protocols will yield suboptimal rCBV estimations, potentially impacting decisions re-

garding the efficacy of clinical trials and the utility of rCBV as a treatment-response biomarker. Therefore, this study motivates adoption of a single-dose, no-preload protocol that would overcome current limitations regarding harmonization of DSC-MR imaging acquisition and dosing protocols.

Although several previous studies collected DSC-MR imaging data using a lower flip angle,^{29,30,37-39} these studies also used a longer TE of approximately 50 ms in an effort to accentuate T2*-weighting. This combination of a low flip angle with intermediate-long TEs may explain why earlier low-flip angle approaches proved less reliable compared with other higher flip angle techniques,⁹ which provided clinically relevant results only when tumor hot spots were sampled.³⁹ Simulations have also demonstrated that the combination of a lower flip angle with a longer TE at 3T is less accurate and reliable.¹⁷

The temporal SNR was reduced in gray matter for the lower flip angle method, with a statistically significant difference in comparison with the 60°P+/C+ method. Although no differences were found for white matter and tumor, a reduced SNR must be considered when balancing the benefits of using less contrast agent with a reduced SNR when using lower flip angle methods.

Additional limitations of this study include a small number of patients and therefore necessitate performing a larger multicenter trial in which a greater range of tumor types and grades are studied. Also, as the simulations predict, low-flip angle methods may be less reliable compared with the preload/higher flip angle methods at 1.5T. Therefore, repeating this study at 1.5T is necessary to confirm the 30°P-/C+ method as a general replacement for the reference standard 60°P+/C+. Although statistical tests indicate excellent agreement, further evaluation of the repeatability of these methods and their ability to predict clinical outcomes are required. Finally, the results of this study were obtained using a single postprocessing platform. Thus, equivalent results obtained with other platforms cannot be guaranteed solely on the basis of the results reported here.

CONCLUSIONS

This study provides experimental evidence showing that rCBV can be reliably determined using a single dose of contrast agent and a low-flip angle, no-preload acquisition at 3T.

ACKNOWLEDGMENTS

We thank Cathy Marszalkowski, Radiology Research Coordinator, who has played a key role in the recruitment of patients with brain tumor at the Medical College of Wisconsin, and the Robert C. Olson MD Endowment for providing support for Dr Kathleen Schmainda.

Disclosures: Kathleen M. Schmainda—RELATED: Grant: National Institutes of Health/National Cancer Institute, Comments: U01 and R01 grants*; UNRELATED: Grants/Grants Pending: National Institutes of Health, Comments: several grants pending*; Stock/Stock Options: IQ-AI, Comments: ownership interest; Other: IQ-AI, Comments: spouse's salary. Leland S. Hu—RELATED: Grant: National Institutes of Health, Comments: U01 CA220378, R01 CA221938.* Christopher C. Quarles—RELATED: Grant: National Institutes of Health. **Money paid to the institution.

REFERENCES

1. Donahue KM, Krouwer HGJ, Rand SD, et al. Utility of simultaneously acquired gradient-echo and spin-echo cerebral blood volume and morphology maps in brain tumor patients. *Magn Reson Med* 2000;43:845–53 CrossRef Medline
2. Schmainda KM, Rand SD, Joseph AM, et al. Characterization of a first-pass gradient-echo spin-echo method to predict brain tumor grade and angiogenesis. *AJNR Am J Neuroradiol* 2004;25:1524–32 Medline
3. Kong DS, Kim ST, Kim EH, et al. Diagnostic dilemma of pseudoprogression in the treatment of newly diagnosed glioblastomas: the role of assessing relative cerebral blood flow volume and oxygen-6-methylguanine-DNA methyltransferase promoter methylation status. *AJNR Am J Neuroradiol* 2011;32:382–87 CrossRef Medline
4. Schmainda KM, Prah M, Connelly J, et al. Dynamic-susceptibility contrast agent MRI measures of relative cerebral blood volume predict response to bevacizumab in recurrent high-grade glioma. *Neuro Oncol* 2014;16:880–88 CrossRef Medline
5. Schmainda KM, Zhang Z, Prah M, et al. Dynamic susceptibility contrast MRI measures of relative cerebral blood volume as a prognostic marker for overall survival in recurrent glioblastoma: results from the ACRIN 6677/RTOG 0625 multicenter trial. *Neuro Oncol* 2015;17:1148–56 CrossRef Medline
6. Kickingereder P, Wiestler B, Burth S, et al. Relative cerebral blood volume is a potential predictive imaging biomarker of bevacizumab efficacy in recurrent glioblastoma. *Neuro Oncol* 2015;17:1139–47 CrossRef Medline
7. Hu LS, Eschbacher JM, Heiserman JE, et al. Reevaluating the imaging definition of tumor progression: perfusion MRI quantifies recurrent glioblastoma tumor fraction, pseudoprogression, and radiation necrosis to predict survival. *Neuro Oncol* 2012;14:919–30 CrossRef Medline
8. Prah MA, Al-Gizawiy MM, Mueller WM, et al. Spatial discrimination of glioblastoma and treatment effect with histologically-validated perfusion and diffusion magnetic resonance imaging metrics. *J Neurooncol* 2018;136:13–21 CrossRef Medline
9. Paulson ES, Schmainda KM. Comparison of dynamic susceptibility-weighted contrast-enhanced MR methods: recommendations for measuring relative cerebral blood volume in brain tumors. *Radiology* 2008;249:601–13 CrossRef Medline
10. Boxerman JL, Schmainda KM, Weisskoff RM. Relative cerebral blood volume maps corrected for contrast agent extravasation significantly correlate with glioma tumor grade, whereas uncorrected maps do not. *AJNR Am J Neuroradiol* 2006;27:859–67 Medline
11. Hu LS, Baxter LC, Pinnaduwege DS, et al. Optimized preload leakage-correction methods to improve the diagnostic accuracy of dynamic susceptibility-weighted contrast-enhanced perfusion MR imaging in posttreatment gliomas. *AJNR Am J Neuroradiol* 2010;31:40–48 CrossRef Medline
12. Boxerman JL, Prah DE, Paulson ES, et al. The role of preload and leakage correction in gadolinium-based cerebral blood volume estimation determined by comparison with MION as a criterion standard. *AJNR Am J Neuroradiol* 2012;33:1081–87 CrossRef Medline
13. Schmainda KM, Prah MA, Rand SD, et al. Multisite concordance of DSC-MRI analysis for brain tumors: results of a National Cancer Institute Quantitative Imaging Network Collaborative Project. *AJNR Am J Neuroradiol* 2018;39:1008–16 CrossRef Medline
14. Boxerman JL, Shiroishi MS, Ellingson BM, et al. Dynamic susceptibility contrast MR imaging in glioma: review of current clinical practice. *Magn Reson Imaging Clin N Am* 2016;24:649–70 CrossRef Medline
15. Ellingson BM, Bendszus M, Boxerman J, et al; Jumpstarting Brain Tumor Drug Development Coalition Imaging Standardization Steering Committee. Consensus recommendations for a standardized brain tumor imaging protocol in clinical trials. *Neuro Oncol* 2015;17:1188–98 CrossRef Medline
16. Leu K, Boxerman JL, Ellingson BM. Effects of MRI protocol parameters, preload injection dose, fractionation strategies, and leakage

- correction algorithms on the fidelity of dynamic-susceptibility contrast MRI estimates of relative cerebral blood volume in gliomas. *AJNR Am J Neuroradiol* 2017;38:478–84 CrossRef Medline
17. Semmineh NB, Bell LC, Stokes AM, et al. **Optimization of acquisition and analysis methods for clinical dynamic susceptibility contrast MRI using a population-based digital reference object.** *AJNR Am J Neuroradiol* 2018;39:1981–88 CrossRef Medline
 18. Bedekar D, Jensen TR, Schmainda KM. **Standardization of relative cerebral blood volume (rCBV) image maps for ease of both inter- and inpatient comparisons.** *Magn Reson Med* 2010;64:907–13 CrossRef Medline
 19. Nyúl LG, Udupa JK. **On standardizing the MR image intensity scale.** *Magn Reson Med* 1999;42:1072–81 CrossRef Medline
 20. Prah MA, Stufflebeam SM, Paulson ES, et al. **Repeatability of standardized and normalized relative CBV in patients with newly diagnosed glioblastoma.** *AJNR Am J Neuroradiol* 2015;36:1654–61 CrossRef Medline
 21. Bedekar D, Jensen T, Rand S, et al. **Delta T1 Method: an automatic post-contrast ROI selection technique for brain tumors.** In: *Proceedings of the International Society for Magnetic Resonance in Medicine*, Stockholm, Sweden. May 1–7, 2010
 22. Altman DG. *Practical Statistics for Medical Research*. London: Chapman and Hall/CRC Texts in Statistical Science Series, Taylor & Francis; 1990
 23. McBride GB. **A proposal for strength-of-agreement criteria for Lin's concordance correlation coefficient.** *NIWA Client Report: HAM2005–062* 2005:62
 24. Semmineh NB, Stokes AM, Bell LC, et al. **A population-based digital reference object (DRO) for optimizing dynamic susceptibility contrast (DSC)-MRI methods for clinical trials.** *Tomography* 2017;3: 41–49 CrossRef Medline
 25. Oh J, Henry RG, Pirzkall A, et al. **Survival analysis in patients with glioblastoma multiforme: predictive value of choline-to-N-acetylaspartate index, apparent diffusion coefficient, and relative cerebral blood volume.** *J Magn Reson Imaging* 2004;19:546–54 CrossRef Medline
 26. Lev MH, Ozsunar Y, Henson JW, et al. **Glial tumor grading and outcome prediction using dynamic spin-echo MR susceptibility mapping compared with conventional contrast-enhanced MR: confounding effect of elevated rCBV of oligodendrogliomas [corrected].** *AJNR Am J Neuroradiol* 2004;25:214–21 Medline
 27. Aronen HJ, Gazit IE, Louis DN, et al. **Cerebral blood volume maps of gliomas: comparison with tumor grade and histologic findings.** *Radiology* 1994;191:41–51 CrossRef Medline
 28. Schmiedeskamp H, Straka M, Newbould RD, et al. **Combined spin- and gradient-echo perfusion-weighted imaging.** *Magn Reson Med* 2012;68:30–40 CrossRef Medline
 29. Law M, Young RJ, Babb JS, et al. **Gliomas: predicting time to progression or survival with cerebral blood volume measurements at dynamic susceptibility-weighted contrast-enhanced perfusion MR imaging.** *Radiology* 2008;247:490–98 CrossRef Medline
 30. Cha S, Lu S, Johnson G, et al. **Dynamic susceptibility contrast MR imaging: correlation of signal intensity changes with cerebral blood volume measurements.** *J Magn Reson Imaging* 2000;11:114–19 CrossRef Medline
 31. Harris RJ, Cloughesy TF, Hardy AJ, et al. **MRI perfusion measurements calculated using advanced deconvolution techniques predict survival in recurrent glioblastoma treated with bevacizumab.** *J Neurooncol* 2015;122:497–505 CrossRef Medline
 32. Hu LS, Eschbacher JM, Dueck AC, et al. **Correlations between perfusion MR imaging cerebral blood volume, microvessel quantification, and clinical outcome using stereotactic analysis in recurrent high-grade glioma.** *AJNR Am J Neuroradiol* 2012;33:69–76 CrossRef Medline
 33. Surapaneni K, Kennedy BC, Yanagihara TK, et al. **Early cerebral blood volume changes predict progression after convection-enhanced delivery of topotecan for recurrent malignant glioma.** *World Neurosurg* 2015;84:163–72 CrossRef Medline
 34. Mangla R, Singh G, Ziegelitz D, et al. **Changes in relative cerebral blood volume 1 month after radiation-temozolomide therapy can help predict overall survival in patients with glioblastoma.** *Radiology* 2010;256:575–84 CrossRef Medline
 35. Prince MR, Zhang HL, Roditi GH, et al. **Risk factors for NSF: a literature review.** *J Magn Reson Imaging* 2009;30:1298–308 CrossRef Medline
 36. McDonald RJ, McDonald JS, Kallmes DF, et al. **Intracranial gadolinium deposition after contrast-enhanced MR imaging.** *Radiology* 2015;275:772–82 CrossRef Medline
 37. Cha S. **Perfusion MR imaging: basic principles and clinical applications.** *Magn Reson Imaging Clin N Am* 2003;11:403–13 CrossRef Medline
 38. Law M, Cha S, Knopp EA, et al. **High-grade gliomas and solitary metastases: differentiation by using perfusion and proton spectroscopic MR imaging.** *Radiology* 2002;222:715–21 CrossRef Medline
 39. Law M, Oh S, Babb J, et al. **Cerebral blood volume predicts patient outcome better than histopathology in low-grade gliomas using dynamic susceptibility contrast-perfusion MR imaging.** In: *Proceedings of the Annual Meeting of the American Society of Neuroradiology*, Toronto, Ontario, Canada. May 23–27, 2005:488

Morphologic Features on MR Imaging Classify Multifocal Glioblastomas in Different Prognostic Groups

J. Pérez-Beteta, D. Molina-García, M. Villena, M.J. Rodríguez, C. Velásquez, J. Martino, B. Meléndez-Asensio, Á. Rodríguez de Lope, R. Morcillo, J.M. Sepúlveda, A. Hernández-Laín, A. Ramos, J.A. Barcia, P.C. Lara, D. Albillo, A. Revert, E. Arana, and V.M. Pérez-García



ABSTRACT

BACKGROUND AND PURPOSE: Multifocal glioblastomas (ie, glioblastomas with multiple foci, unconnected in postcontrast pretreatment T1-weighted images) represent a challenge in clinical practice due to their poor prognosis. We wished to obtain imaging biomarkers with prognostic value that have not been found previously.

MATERIALS AND METHODS: A retrospective review of 1155 patients with glioblastomas from 10 local institutions during 2006–2017 provided 97 patients satisfying the inclusion criteria of the study and classified as having multifocal glioblastomas. Tumors were segmented and morphologic features were computed using different methodologies: 1) measured on the largest focus, 2) aggregating the different foci as a whole, and 3) recording the extreme value obtained for each focus. Kaplan-Meier, Cox proportional hazards, correlations, and Harrell concordance indices (c-indices) were used for the statistical analysis.

RESULTS: Age ($P < .001$, hazard ratio = 2.11, c-index = 0.705), surgery ($P < .001$, hazard ratio = 2.04, c-index = 0.712), contrast-enhancing rim width ($P < .001$, hazard ratio = 2.15, c-index = 0.704), and surface regularity ($P = .021$, hazard ratio = 1.66, c-index = 0.639) measured on the largest focus were significant independent predictors of survival. Maximum contrast-enhancing rim width ($P = .002$, hazard ratio = 2.05, c-index = 0.668) and minimal surface regularity ($P = .036$, hazard ratio = 1.64, c-index = 0.600) were also significant. A multivariate model using age, surgery, and contrast-enhancing rim width measured on the largest foci classified multifocal glioblastomas into groups with different outcomes ($P < .001$, hazard ratio = 3.00, c-index = 0.853, median survival difference = 10.55 months). Moreover, quartiles with the highest and lowest individual prognostic scores based on the focus with the largest volume and surgery were identified as extreme groups in terms of survival ($P < .001$, hazard ratio = 18.67, c-index = 0.967).

CONCLUSIONS: A prognostic model incorporating imaging findings on pretreatment postcontrast T1-weighted MRI classified patients with glioblastoma into different prognostic groups.

ABBREVIATIONS: CE = contrast-enhancing; c-index = concordance index; GBM = glioblastoma; HR = hazard ratio; IPSLV = individual prognosis score based on the focus with the largest volume; IPSLVS = individual prognosis score based on the focus with the largest volume and surgery; IPSLW = individual prognosis score based on the focus with the largest width; IPSLWS = individual prognosis score based on the focus with the largest width and surgery; MGBM = multifocal glioblastoma

The computation of quantitative, radiomic features from MR imaging to construct imaging biomarkers has gained attention in recent years, due to its potential practical applications. The

main premise of radiomics is that clinical end points could be more often associated with quantitative voxel-based features than with the more qualitative radiologic and clinical data used today.¹

Received September 25, 2018; accepted after revision February 25, 2019.

From the Department of Mathematics (J.P.-B., D.M.-G., V.M.P.-G.), Mathematical Oncology Laboratory, Universidad de Castilla-La Mancha, Ciudad Real, Spain; Departments of Neurosurgery (M.V.) and Radiology (M.J.R.), Hospital General de Ciudad Real, Ciudad Real, Spain; Department of Neurosurgery (J.M., C.V.), Hospital Universitario Marqués de Valdecilla and Fundación, Instituto de Investigación Marqués de Valdecilla, Santander, Spain; Departments of Molecular Biology (B.M.-A.), Neurosurgery (Á.R.d.L.), and Radiology (R.M.), Hospital Virgen de la Salud, Toledo, Spain; Departments of Neuro-Oncology (J.M.S.), Pathology (A.H.-L.), and Radiology (A. Ramos), Hospital Universitario 12 de Octubre, Madrid, Spain; Department of Neurosurgery (J.A.B.), Hospital Clínico San Carlos, Madrid, Spain; Department of Radiation Oncology (P.C.L.), San Roque University Hospital/Universidad Fernando Pessoa Canarias, Gran Canaria, Spain; Department of Radiology (D.A.), Hospital Universitario de Salamanca, Salamanca, Spain; Department of Radiology (A. Revert),

Hospital de Manises, Valencia, Spain; and Department of Radiology (E.A.), Fundación Instituto Valenciano de Oncología, Valencia, Spain.

Drs Pérez-Beteta and Molina-García contributed equally to this work.

This work was supported by the Ministerio de Economía y Competitividad/Fondo Europeo de Desarrollo Regional (FEDER), Spain (grant No. MTM2015-71200-R) and the James S. McDonnell Foundation 21st Century Science Initiative in Mathematical and Complex Systems Approaches for Brain Cancer (Collaborative Award 220020450).

Please address correspondence to David Molina-García, PhD, Mathematical Oncology Laboratory, Edificio Politécnico, Avenida de Camilo José Cela, 3, Universidad de Castilla-La Mancha, 13071 Ciudad Real, Spain; e-mail: david.molina@uclm.es

Indicates open access to non-subscribers at www.ajnr.org

Indicates article with supplemental on-line table.

<http://dx.doi.org/10.3174/ajnr.A6019>

Glioblastomas (GBMs) are the most common and deadliest type of primary brain tumor. Even with the best current standard of care, the median survival of patients with GBM is only 14 months.² Contrast-enhanced (CE) T1-weighted and T2/FLAIR MR imaging sequences are the mainstay for GBM diagnosis, treatment planning, and follow-up,³ and many authors have investigated the use of image-based quantifiers as predictors of survival.^{2,4-13}

GBMs frequently appear as solitary lesions at diagnosis on CE-T1-weighted MRI, but multiple enhancing lesions can occur. In these cases, tumors are termed “multifocal” if there is a connection between enhancing lesions (typically visible on FLAIR sequences)² or, less commonly, “multicentric” when no communication is demonstrated.¹⁴ However, no pathologic or prognostic differences have been found between multifocal and multicentric GBMs,¹⁵⁻¹⁸ so the convention of denoting both as multifocal GBM (MGBM) is followed here.

MGBMs account for 10%–20% of all GBMs.^{17,19} Their prognosis is generally poor, with a median survival of 6–8 months from diagnosis,^{14,20} which may be due to a more aggressive phenotype and the difficulties in performing therapy safely.

In this study, we constructed 3D morphologic image-based measures for MGBMs obtained from pretreatment volumetric CE-T1-weighted MRI. Those features were used to build prognostic models for patients with MGBM.

MATERIALS AND METHODS

Patients

The study was approved by the institutional review boards of the participating institutions.

We retrospectively reviewed 1155 patients with GBMs from 10 local medical institutions diagnosed during 2006–2017 with pathologically proved GBMs according to the 2007 World Health Organization Classification of Tumors of the Central Nervous System. Inclusion criteria for this study were the following: multiple foci of enhancing tumor and availability of the relevant clinical variables: age, treatment followed (surgery type, radiation therapy, and/or chemotherapy), survival information at last follow-up, and availability of a pretreatment volumetric contrast-enhanced T1-weighted MR imaging sequences (slice thickness, ≤2.00 mm; no gap; pixel spacing, ≤1.20 mm). Only 97 patients with MGBM (8.40%, 62 ± 13 years of age, 48% women and 52% men) with 239 tumors fulfilled these criteria.

Overall survival was computed from the date of the preoperative MR imaging until death or last follow-up examination (censored events). Patients lost to follow-up were considered censored. Treatment followed after resection or biopsy consisted of radiation therapy and chemotherapy, following the Stupp scheme whenever possible. The Table shows the main patient characteristics.

Image Acquisition

The pretreatment volumetric CE-T1-weighted MR imaging sequence was gradient-echo using 3D spoiled gradient recalled-echo or 3D fast-field echo after intravenous administration of a single dose of gadobenate dimeglumine (0.10 mmol/kg) with a 6- to 8-minute delay.

MR images were acquired with a 1.5T ($n = 87$) or 3T ($n = 10$) scanner with TR/TE, 6–22/1.5–10 ms. GE Healthcare (Milwaukee,

Summary of patient characteristics and MR imaging and volumetric parameters for the cohort of patients with MGBM considered in the study

MGBM Cohort	
Patient characteristics	
No. of patients (censored)	97 (7)
Age (median) (range) (yr)	64 (23–83)
Sex (percentage) (age range)	49 F, 50.52% (25–82 yr)
	46 M, 49.48% (23–83 yr)
Survival (median) (range) (mo)	7.39 (0.13–56.08)
Type of resection (percentage)	55 MSR (56.70%)
	42 B (43.30%)
Type of treatment (percentage)	63 CT + RT (64.95%)
	6 RT alone (6.19%)
	5 CT alone (5.15%)
	23 No treatment (23.71%)
MRI characteristics	
Pixel spacing (mean) (range) (mm)	0.78 (0.39–1.17)
Slice thickness (mean) (range) (mm)	1.55 (1.00–2.00)
No. of slices (mean) (range)	171 (84–248)
Volumetric parameters ^a	
Tumor volume (mean) (range) (cm ³)	24.04 (0.20–115.79)
	28.55 (0.39–125.59)
CE volume (mean) (range) (cm ³)	14.60 (0.20–64.35)
	17.92 (0.39–73.18)
Necrotic volume (mean) (range) (cm ³)	9.43 (0.00–63.43)
	10.63 (0.00–63.44)
CE rim width (mean) (range) (cm)	0.53 (0.15–1.17)
	0.59 (0.19–1.24)
Maximum diameter (mean) (range) (cm)	4.59 (1.07–9.15)
	6.95 (2.42–14.75)
Total surface (mean) (range) (cm ²)	54.31 (2.32–183.63)
	69.53 (5.01–212.20)
Surface regularity (mean) (range)	0.62 (0.15–0.93)
	NA

Note:—MSR indicates maximal safe resection; NA, not applicable; CT, chemotherapy; RT, radiation therapy; B, biopsy.

^a There are 2 volumetric parameters: those measured for the lesion with the largest volume (first row) and those computed for the aggregated tumor (second row).

Wisconsin) ($n = 51$), Philips Healthcare (Best, the Netherlands) ($n = 30$), and Siemens (Erlangen, Germany) ($n = 16$) scanners were used.

Other image and patient characteristics are summarized in the Table.

Image Analysis

MRIs were retrospectively analyzed by the same image expert (J.P.-B. with 5 years of experience). The DICOM files were imported into the scientific software Matlab (R2017b; MathWorks, Natick, Massachusetts). Each MGBM lesion was automatically delineated using a gray-level threshold chosen to identify the CE tumor volume. Then, segmentations were corrected manually slice by slice using in-house software. Necrotic tissue was defined as hypointense tumor regions inside CE tissue. Figure 1 shows an example of the segmentation and 3D reconstruction of tumors for a patient with MGBM.

Geometric Measures

The contrast-enhancing (V_{CE}), necrotic (or inner) (V_I), and total volumes ($V = V_{CE} + V_I$) were computed for each focus. Contrast-enhancing spheric rim width (CE rim width) obtained for each focus from the CE and necrotic volumes is represented as

$$CE\ Rim\ Width = \sqrt[3]{\left(\frac{3(V_{CE} + V_I)}{4\pi}\right)} - \sqrt[3]{\left(\frac{3V_I}{4\pi}\right)}.$$

It measures the averaged width of the CE areas by assuming the sphericity of necrotic and total tumor regions. More details, with

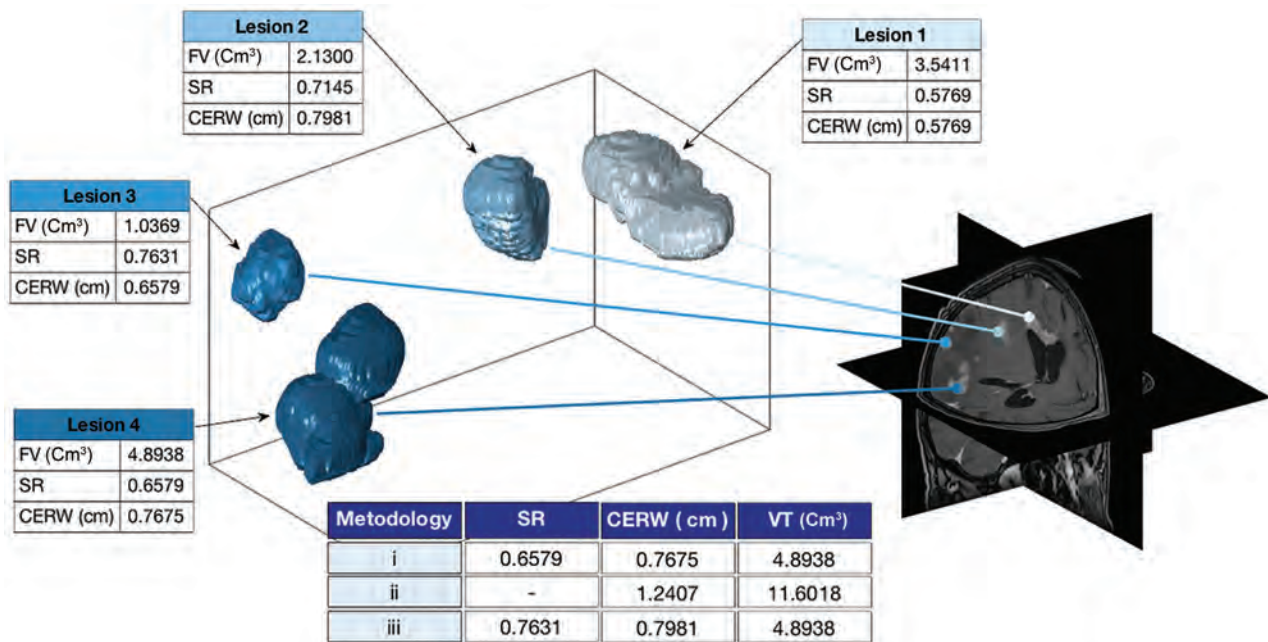


FIG 1. 3D reconstruction of the different foci in a patient with multifocal glioblastoma. Morphologic measures are computed for each focus following the different methodologies discussed in the Materials and Methods section, including focus volume (FV), contrast-enhanced rim width (CERW), surface regularity (SR), and volume in total (VT).

examples of tumors with high and low CE rim widths, can be found in Pérez-García et al.²¹

Surface was obtained from the discrete sets of voxels defining the tumor by reconstructing the tumor surface using the Matlab “isosurface” command.

Surface regularity (S_R) is a dimensionless ratio between the segmented tumor volume and the volume that a spheric tumor with the same surface would have. It was computed for each focus as

$$S_R = 6 \sqrt{\pi} \frac{\text{Total Volume}}{\sqrt{(\text{Total Surface})^3}}$$

This parameter is bounded between 0 (“complex” tumors with very irregular surfaces) and 1 (spheric tumors). More details, with examples of tumors with high and low CE rim widths, can be found in Pérez-Beteta et al.⁷

Maximum diameter was computed for each focus as the maximal distance between 2 points located on the surface of the CE tumor and provides the largest longitudinal measure of the tumor.

Due to the multiple nature of tumors, morphologic measures for each patient were calculated using 3 different methodologies: 1) computed on the focus with the largest volume, 2) considering the different tumor foci as an aggregated tumor, and 3) considering the highest value for each measure computed for the different foci. Methodology 2 did not apply to CE rim width, surface regularity, and maximum diameter. For surface regularity, methodology 3 was computed using the highest irregularity (lowest value). Figure 1 shows an example of the different methodologies.

Statistical Methods

We used Kaplan-Meier analysis to identify individual parameters associated with prognosis, using the log-rank test to assess the

significance of the results. A 2-tailed significance level of $<.05$ was applied. For each parameter, we analyzed all possible thresholds splitting patients population in two groups satisfying that patient populations sizes have ratios $<5:1$. Then, the lowest log-rank P value in an interval of contiguous significant threshold values was selected.²¹ Univariate Cox proportional hazards regression analysis was used to obtain the hazard ratio (HR) and its adjusted 95% confidence interval.

The Spearman correlation coefficient was used to assess the dependence among variables.

Multivariate Cox proportional hazards analysis with the stepwise Wald method was used to construct prognostic models. SPSS software (Version 22.0.00; IBM, Armonk, New York) was used for the statistical analysis.

The concordance index (c-index) between the predicted hazard using a multivariate Cox proportional hazards overall survival model and final outcome was also computed to evaluate the performance of the models constructed.²²

RESULTS

Ninety-seven patients with MGBMs (62 ± 13 years of age, 48% women and 52% men) composed the population of the study. Seven patients were censored, and the median survival of our population was 7.39 months.

Independent Predictors of Survival

Kaplan-Meier analysis provided age ($P < .001$, HR = 2.11, c-index = 0.71), surgery (ie, patients undergoing surgical resection compared with those undergoing biopsy; $P < .001$, HR = 2.04, c-index = 0.71), and CE rim width as the most significant parameters. CE rim width yielded statistically significant results when computed for the tumor focus showing the largest volume ($P < .001$, HR = 2.15, c-index = 0.70) and considering the largest CE rim

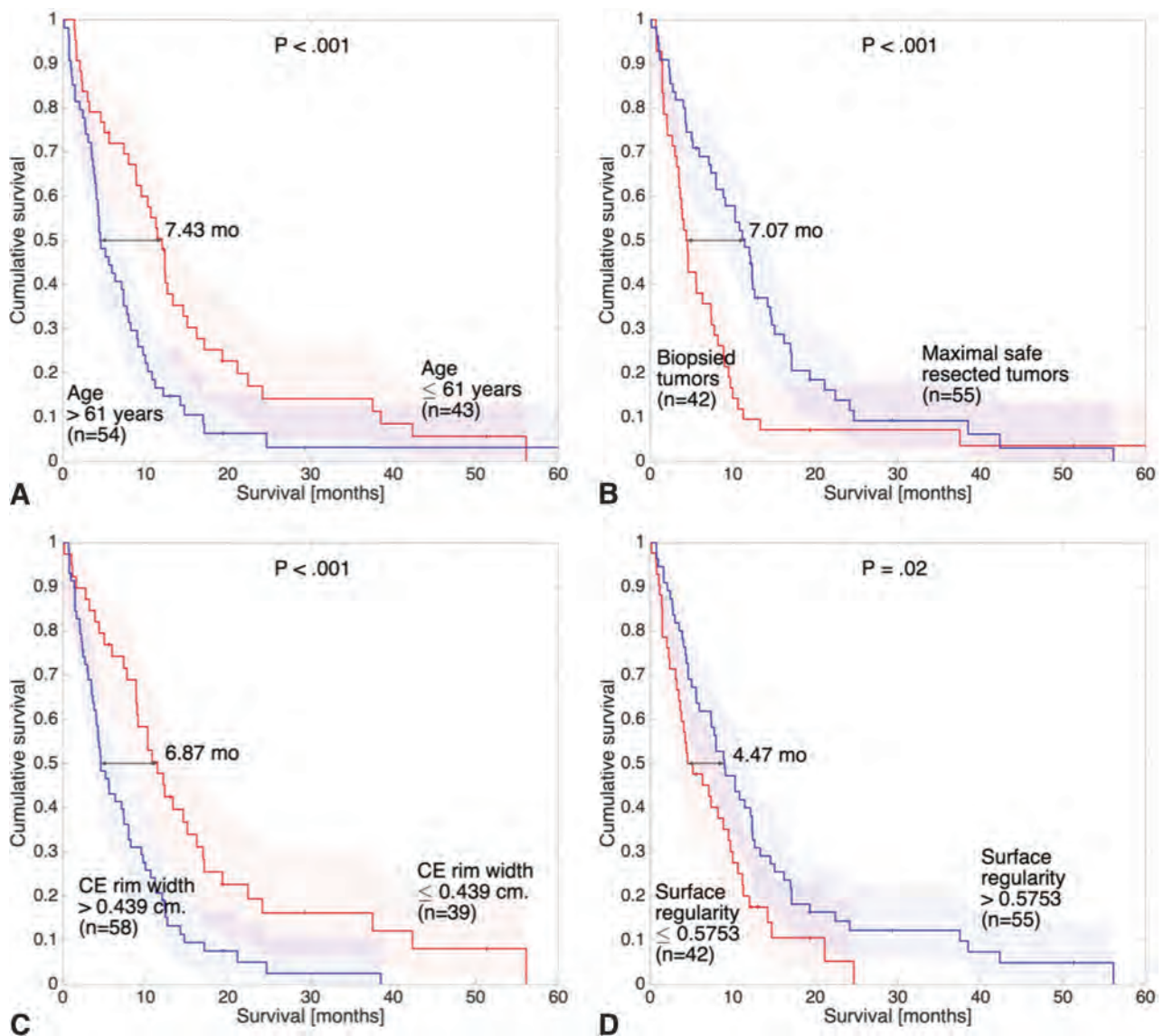


FIG 2. Kaplan-Meier plots of some of the significant prognostic parameters of the study. Curves correspond to age (A), surgery (B), CE rim width (C), and surface regularity (D) measured on the foci with the largest volume (similar results were found for the latter 2 parameters measured on foci with the highest values).

width value obtained for all foci of a given patient ($P = .002$, HR = 2.05, c-index = 0.67).

Surface regularity was also statistically significant, both when computed for the focus with the largest volume ($P = .02$, HR = 1.66, c-index = 0.64) and when considering the smallest value on all foci ($P = .04$, HR = 1.64, c-index = 0.600).

No other volume- or surface-based parameter reached significant results. Figure 2 shows the Kaplan-Meier graphs of age (Fig 2A), surgery (Fig 2B), CE rim width (Fig 2C), and surface regularity (Fig 2D) measured on the foci with the largest volume.

Age, CE rim width, and surface regularity were correlated with neither each other nor other volumetric or surface-based parameters. Volumes (total, CE, and necrotic), maximum diameter, and total surface (ie, all of the “size”-related measures) showed high and significant correlations. Figure 3 shows the correlations among all the parameters computed using the different methodologies.

Prognostic Value of Multivariate Linear Models

Multivariate Cox regression was used to construct prognostic models joining the significant noncorrelated parameters of the study. The model retained only age and both CE rim widths as relevant parameters for building prognostic models. Because different CE rim widths were correlated, 2 different models were constructed.

When combining age and the CE rim width measured on the focus with the largest volume, we obtained a first Cox-based prognostic model (individual prognosis score based on the focus with the largest volume [IPSLV]). The best Kaplan-Meier threshold for this model (2.18) obtained an excellent differentiation among groups ($P < .001$, HR = 2.56, c-index = 0.78, median survival difference = 7.98 months).

The second model was constructed by considering the largest CE rim width of each patient computed on the different foci (individual prognosis score based on the focus with the largest width

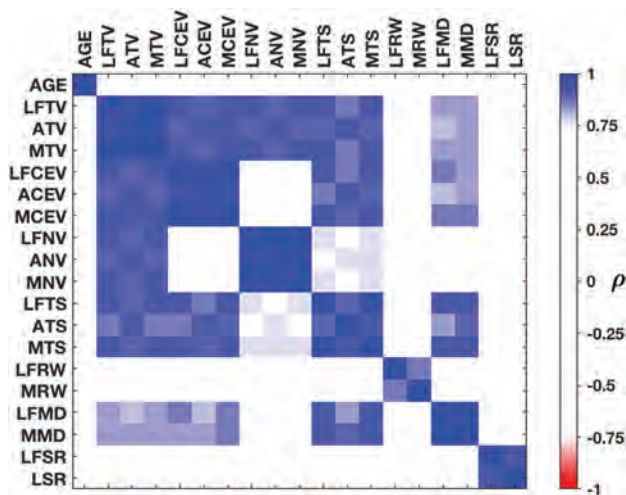


FIG 3. Spearman correlations between the measures. Correlation values between variables of >0.75 are regarded as strong. AGE indicates age. The prefixes LF, A, and M indicate the largest focus, aggregated, and maximum, respectively, regarding the 3 methodologies used. Regarding the suffixes, TV indicates tumor volume; CEV, CE volume; NV, necrotic volume; TS, total surface; RW, CE rim width; MD, maximum diameter; SR, surface regularity; LSR, lowest surface regularity.

[IPSLW]). The best result was obtained for $IPSLW = 2.14$ ($P < .001$, $HR = 3.04$, $c\text{-index} = 0.80$, median survival difference = 10.00 months).

The addition of surface regularity to these models worsened the results. The On-line Table shows the prognostic value of all the individual parameters and multivariate models considered.

New instances of the 2 models described in the previous section were constructed including the surgical treatment (maximal safe resection or biopsy). When combining the IPSLV with surgical information (individual prognosis score based on the focus with the largest volume and surgery [IPSLVS]), results were substantially improved ($P < .001$, $HR = 3.00$, $c\text{-index} = 0.85$, median survival difference = 10.55 months). There were many thresholds giving significant results in the Kaplan-Meier analysis. The best threshold was 1.45, and the equation of the model was

$$IPSLVS = 0.025 \cdot \text{Age} + 1.496 \cdot \text{CE Rim Width} - 0.677 \cdot \text{Surgery},$$

where in this equation “Surgery” takes value 1 for maximal safe resection and 0 for biopsy. Figure 4A shows the Kaplan-Meier curve of the IPSLVS.

The IPSLW combined with surgery (individual prognosis score based on the focus with the largest width and surgery [IPSLWS]) obtained a better differentiation among groups than its presurgical instance ($P < .001$, $HR = 2.72$, $c\text{-index} = 0.81$, median survival difference = 7.98 months), with 1.525 as the best threshold. The On-line Table shows the results of these multivariate models.

Extreme Groups of IPSLVS Model

Using the IPSLVS model, we split the patient population into 4 groups of equal size (24 patients): the first quartile (Q1) contained patients with an IPSLVS below 1.43, the second quartile (Q2) joined patients with an IPSLVS between 1.43 and 1.91, the third quartile (Q3) contained patients with an IPSLVS between 1.91

and 2.619, and the fourth quartile (Q4) joined patients with an IPSLVS above 2.619. A Kaplan-Meier analysis showed that there were no statistical differences between Q2 and Q3 ($P = .827$, $HR = 1.07$, $c\text{-index} = 0.513$), while significant differences were observed between these 2 quartiles and Q1 ($P < .001$, $HR = 3.10$, $c\text{-index} = 0.806$ and $P = .005$, $HR = 2.41$, $c\text{-index} = 0.802$, respectively) and Q4 ($P = .001$, $HR = 2.94$, $c\text{-index} = 0.670$ and $P = .036$, $HR = 1.95$, $c\text{-index} = 0.606$, respectively).

Then, quartiles of patients with the highest (>2.619) and lowest (<1.43) IPSLVS values, that is, Q4 and Q1 respectively, were compared using a Kaplan-Meier analysis, and highly significant differences ($P < .001$, $HR = 18.67$, $c\text{-index} = 0.97$, median survival difference = 11.93 months) were found. Figure 4B shows the Kaplan-Meier plot of the 4 quartiles but focuses on the differences between the extreme quartiles Q4 and Q1.

DISCUSSION

In this study, we used different methodologies to find prognostic morphologic imaging biomarkers for MGBM. Pretreatment post-contrast T1-weighted CE rim width computed for the focus with the largest volume or the extreme CE rim width for each patient was highly prognostic and was added to patient’s age to develop pretreatment multivariate models. The addition of the type of surgery improved the results of the model.

Finding groups of patients with MGBMs with potentially better survival is of relevance for clinical practice. Moreover, there are still no clear clinical guidelines for these patients.^{16–20,23} Some clinical variables (age, Karnofsky Performance Status (KPS), type of treatment, extent of surgery, and radiation dose) have been previously found to have prognostic information in limited studies of MGBMs.^{14,16–18,23} However, no morphology-based imaging biomarkers have been developed.

In this article, we used different methodologies to characterize tumor morphologies and investigate their relationships to patient outcome. The best ones were measuring features in the focus with the largest volume and considering the highest value computed for the different foci. The first methodology was grounded in the hypothesis that the largest focus could be the one determining patient outcome. The latter was chosen under the hypothesis that the most aggressive lesion, independent of their size, could be the ones determining patient outcome. Correlations between these 2 methodologies were high and significant for all measures having prognostic value.

CE rim width and surface regularity were identified as independent predictors of survival. The former measure was hypothesized²⁴ and found²¹ to correlate with tumor growth speed on unifocal GBMs. Also, tumor boundary regularity on MR imaging had prognostic value on unifocal GBMs.^{7,8} Age showed significant results in our study, in line with other studies.^{14,17,18} In addition, patients significantly benefited from an operation in our analysis, while the literature has shown contradictory results.^{16,19,23} Most interesting, CE rim width showed a prognostic value as high as age and surgery in our study. On the other hand, volume- and surface-based morphologic parameters (including total, necrotic, and CE tumor volume) were not predictors of survival, while contradictory results have been found in the literature.^{12,13,25,26} Recently, it has been hypothesized that these con-

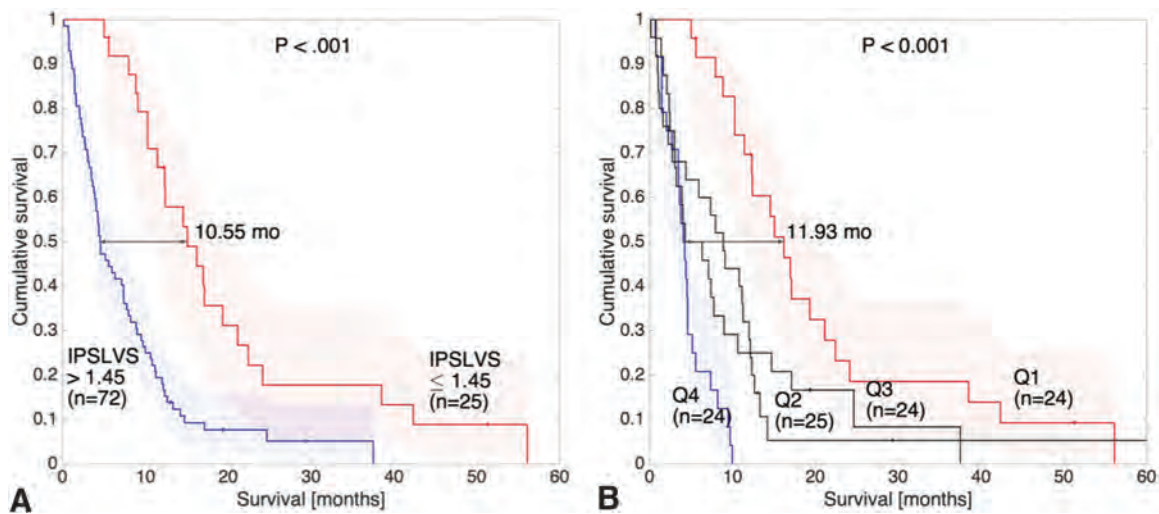


FIG 4. Kaplan-Meier plots of the IPSLVS model considering the whole cohort of patients (A) and considering its 4 quartiles (Q1, Q2, Q3, and Q4) (B). Differences between quartiles of the highest (>2.619, Q4) and lowest (<1.43, Q1) IPSLVS values are emphasized.

traditions could be due to different proportions of patients undergoing different types of surgical resections.²⁷

Multivariate Cox-based models were developed by combining age, CE rim width, and surface regularity. The latter added no information to the models, possibly due to the addition of complexity on models constructed over a dataset of limited statistical power, so it was finally removed. Both significant measures of MGBM CE rim width were used to construct accurate prognostic models (c-indices of 0.779 and 0.801 for IPSLV and IPSLW, respectively). Adding surgical information to the models improved the results (c-indices of 0.853 and 0.810 for IPSLVS and IPSLWS, respectively).

Quartiles of patients with the highest (worst prognosis) and lowest (best prognosis) IPSLVS had a median survival difference of 11.93 months and obtained an outstanding c-index of 0.967. All patients in the quartile of highest IPSLVS survived <10 months.

The multivariate models constructed in this article for MGBMs had prognostic values higher than the best models reported in studies for unifocal tumors.⁶⁻¹³

This study has several strengths: First, it is novel in finding MR imaging-derived measures with prognostic value for MGBM.^{14,16-19,23} Second, it was performed on a large dataset by MGBM standards.^{14,17,23} Third, this new form of analysis compares different methodologies and establishes an initial pathway to analyze the aggressiveness of MGBMs using pretreatment data. Fourth, the study provides real clinical practice data, while limitations of clinical trials are commonly encountered. Fifth, it only uses simple morphologic features that can be obtained straightforwardly from segmented tumors.

Regarding the limitations, public MGBM data is sparse. Specifically, The Cancer Imaging Archive²⁸ only contained 13 patients with MGBM satisfying the inclusion criteria, and many of them were censored. As a result, we could not validate our findings on external public databases. Also, the overall size of our population (97 patients) was relatively small, and 7% of patients were censored. The second limitation was the lack of genetic and molecular information for the cohorts, which pre-

cluded the identification of a possible correlation between the groups found on the basis of imaging data and biologic features. The third limitation is that although there was great effort to homogenize data, given the multicenter nature of the study, there were differences in the imaging protocols or clinical follow-up. The fourth limitation is that due to these differences, the manual segmentation process has a degree of subjectivity, though all segmentations were performed by the same image expert.

CONCLUSIONS

This study addressed the prognostic value of meaningful morphologic imaging parameters obtained from pretreatment volumetric CE-T1-weighted MRI of patients with MGBM. Age, surgery, CE rim width, and surface regularity were significant independent parameters in terms of survival, and a combined model linking age, surgery, and CE rim width improved the results. The index obtained allowed patients to be classified into 2 groups with substantially different prognoses.

ACKNOWLEDGMENTS

We thank J.A. Ortiz Alhambra (Mathematical Oncology Laboratory) and A. Fernández-Romero (Mathematical Oncology Laboratory) for their help in the tumor segmentation tasks. We also thank C. López (Radiology Department, Hospital General de Ciudad Real), M. Claramonte (Neurosurgery Department, Hospital General de Ciudad Real), L. Iglesias (Neurosurgery Department, Hospital Clínico San Carlos), J. Avelillas (Radiology Department, Hospital Clínico San Carlos), J. M. Villanueva (Radiology Department, Hospital Universitario de Salamanca), and J.C. Paniagua (Radiology Department, Hospital Universitario de Salamanca) for their help in the data collection.

Disclosures: Juan M. Sepúlveda—UNRELATED: Consultancy: Pfizer, Bayer AG; Payment for Development of Educational Presentations: Astellas Pharma, Pfizer; Travel/Accommodations/Meeting Expenses Unrelated to Activities Listed: Ipsen. Estanislao Arana—UNRELATED: Employment: Ivo Foundation, Comments: consultant radiologist.

REFERENCES

1. Gillies RJ, Kinahan PE, Hricak H. **Radiomics: images are more than pictures, they are data.** *Radiology* 2016;278:563–77 CrossRef Medline
2. Ellingson BM. **Radiogenomics and imaging phenotypes in glioblastoma: novel observations and correlation with molecular characteristics.** *Curr Neurol Neurosci Rep* 2015;15:506 CrossRef Medline
3. Wen PY, Macdonald DR, Reardon DA, et al. **Updated response assessment criteria for high-grade gliomas: Response Assessment in Neuro-Oncology Working Group.** *J Clin Oncol* 2010;28:1963–72 CrossRef Medline
4. Narang S, Lehrer M, Yang D, et al. **Radiomics in glioblastoma: current status, challenges and opportunities.** *Translational Cancer Research* 2016;5:383–97 CrossRef
5. Abrol S, Kotrotsou A, Salem A. **Radiomic phenotyping in brain cancer to unravel hidden information in medical images.** *Top Magn Reson Imaging* 2017;26:43–53 CrossRef Medline
6. Cui Y, Tha KK, Teresaka S, et al. **Prognostic imaging biomarkers in glioblastoma: development and independent validation on the basis of multiregion and quantitative analysis of MR images.** *Radiology* 2016;278:546–53 CrossRef Medline
7. Pérez-Beteta J, Molina-García D, Ortiz-Alhambra JA, et al. **Tumor surface regularity at MR imaging predicts survival and response to surgery in patients with glioblastoma.** *Radiology* 2018; 288:218–55 CrossRef Medline
8. Rathore S, Akbari H, Rozycki M, et al. **Radiomic MRI signature reveals three distinct subtypes of glioblastoma with different clinical and molecular characteristics, offering prognostic value beyond IDH1.** *Sci Rep* 2018;8:5087 CrossRef Medline
9. Cui Y, Ren S, Tha KK, et al. **Volume of high-risk intratumoral subregions at multi-parametric MR imaging predicts overall survival and complements molecular analysis of glioblastoma.** *Eur Radiol* 2017;27:3583–92 CrossRef Medline
10. Kickingereder P, Burth S, Wick A, et al. **Radiomic profiling of glioblastoma: identifying an imaging predictor of patient survival with improved performance over established clinical and radiologic risk models.** *Radiology* 2016;280:880–89 CrossRef Medline
11. Lao J, Chen Y, Li ZC, et al. **A deep learning-based radiomics model for prediction of survival in glioblastoma multiforme.** *Sci Rep* 2017; 7:10353 CrossRef Medline
12. Wangaryattawanich P, Hatami M, Wang J, et al. **Multicenter imaging outcomes study of The Cancer Genome Atlas glioblastoma patient cohort: imaging predictors of overall and progression-free survival.** *Neuro Oncol* 2015;17:1525–37 CrossRef Medline
13. Ingrisich M, Schneider MJ, Nörenberg D, et al. **Radiomic analysis reveals prognostic information in T1-weighted baseline magnetic resonance imaging in patients with glioblastoma.** *Invest Radiol* 2017;52:360–66 CrossRef Medline
14. Lasocki A, Gaillard F, Tacey M, et al. **Multifocal and multicentric glioblastoma: improved characterisation with FLAIR imaging and prognostic implications.** *J Clin Neurosci* 2016;31:92–98 CrossRef Medline
15. Singh G, Mehrotra A, Sardhara J, et al. **Multiple glioblastomas: are they different from their solitary counterparts?** *Asian J Neurosurg* 2015;10:266–71 CrossRef Medline
16. Showalter TN, Andrej J, Andrews DW, et al. **Multifocal glioblastoma multiforme: prognostic factors and patterns of progression.** *Int J Radiat Oncol Biol Phys* 2007;69:820–24 CrossRef Medline
17. Di Carlo DT, Cagnazzo F, Benedetto N, et al. **Multiple high-grade gliomas: epidemiology, management, and outcome: a systematic review and meta-analysis.** *Neurosurg Rev* 2017 Nov 14. [Epub ahead of print] CrossRef Medline
18. Patil CG, Yi A, Elramsisy A, et al. **Prognosis of patients with multifocal glioblastoma: a case-control study.** *J Neurosurg* 2012;117: 705–11 CrossRef Medline
19. Giannopoulos S, Kyritsis AP. **Diagnosis and management of multifocal gliomas.** *Oncology* 2010;79:306–12 CrossRef Medline
20. Paulsson AK, Holmes JA, Peiffer AM, et al. **Comparison of clinical outcomes and genomic characteristics of single focus and multifocal glioblastoma.** *J Neurooncol* 2014;119:429–35 CrossRef Medline
21. Pérez-Beteta J, Martínez-González A, Molina D, et al. **Glioblastoma: does the pretreatment geometry matter? A postcontrast T1 MRI-based study.** *Eur Radiol* 2017;27:1096–104 CrossRef Medline
22. Harrell FE Jr, Califf R, Pryor D, et al. **Evaluating the yield of medical tests.** *JAMA* 1982;247:2543–46 CrossRef Medline
23. Hassaneen W, Levine NB, Suki D, et al. **Multiple craniotomies in the management of multifocal and multicentric glioblastoma.** *J Neurosurg* 2011;114:576–84 CrossRef Medline
24. Pérez-García VM, Calvo GF, Belmonte-Beitia J, et al. **Bright solitary waves in malignant gliomas.** *Phys Rev E Stat Nonlin Soft Matter Phys* 2011;84:021921 CrossRef Medline
25. Grabowsky MM, Recinos PF, Nowacki AS, et al. **Residual tumor volume versus extent of resection: predictors of survival after surgery for glioblastoma.** *J Neurosurg* 2014;121:1115–23 CrossRef Medline
26. Henker C, Kriesen T, Glass Á, et al. **Volumetric quantification of glioblastoma: experiences with different measurement techniques and impact on survival.** *J Neurooncol* 2017;135:391–402 CrossRef Medline
27. Pérez-Beteta J, Molina-García D, Martínez-González A, et al. **Morphological MRI-based features provide pretreatment survival prediction in glioblastoma.** *Eur Radiol* 2018 Oct 15. [Epub ahead of print] CrossRef Medline
28. Prior FW, Clark K, Commeyan P, et al. **TCIA: an information resource to enable open science.** *Conf Proc IEEE Eng Med Biol Soc* 2013; 2013:1282–85 CrossRef Medline

Effects of Acute Alcohol Consumption on the Human Brain: Diffusional Kurtosis Imaging and Arterial Spin-Labeling Study

L.M. Kong, J.Y. Zeng, W.B. Zheng, Z.W. Shen, and R.H. Wu



ABSTRACT

BACKGROUND AND PURPOSE: Brain function and microstructure are affected by alcohol consumption. Until recently, the effect of alcohol on neural mechanisms has not been fully elucidated. Our aim was to explore the acute effects of alcohol on healthy human brains by diffusional kurtosis imaging and 3D arterial spin-labeling and elucidate structural and functional changes in the brain on acute alcohol intake.

MATERIALS AND METHODS: Conventional MR imaging, diffusional kurtosis imaging, and 3D arterial spin-labeling were performed on 24 healthy volunteers before and 0.5 and 1 hour after drinking alcohol. Participants were divided into 2 groups according to the response to alcohol: blushing ($n = 12$) and unblushing ($n = 12$) groups. Twenty brain regions were analyzed.

RESULTS: Diffusional kurtosis imaging revealed an increase in mean kurtosis and fractional anisotropy at 0.5 hour post-alcohol intake in most brain regions, whereas mean diffusion was decreased in several brain regions at 1 hour after drinking. 3D arterial spin-labeling showed increased cerebral blood flow in most brain regions, particularly in the frontal regions. However, perfusion in the anterior commissure decreased. Regional changes in the brain correlated with various behavioral performances with respect to blush response and sex. In general, blushing individuals and men are more sensitive to alcohol with acute effects.

CONCLUSIONS: Physiologic and microstructural alterations in the brain on alcohol consumption were examined. Brain areas with blood flow alteration detected by 3D arterial spin-labeling were highly consistent with susceptible areas detected by diffusional kurtosis imaging. The current study provides new insight into the effects of alcohol on the brain and behavioral performance in different blush response and sex populations.

ABBREVIATIONS: ALDH = aldehyde dehydrogenase; ASL = arterial spin-labeling; BAES = Biphasic Alcohol Effects Scale; DKI = diffusional kurtosis imaging; FA = fractional anisotropy; MD = mean diffusion; MK = mean kurtosis; pre = controls

Studies of acute alcohol challenge have revealed the neural and behavioral impairments that accompany intoxication. Alcohol affects multiple neurotransmitter systems in the brain and brain functions.^{1,2} Acute alcohol consumption has marked effects on brain metabolism and produces functional and morphologic

changes. Until recently, the effect of alcohol on neural mechanisms has not been fully elucidated. Alcohol abuse and dependence are a huge societal and economic burden that results in lost productivity, increased health care costs, and traffic accidents and contributes to domestic violence. The economic, social, and health consequences related to the consumption of drugs and alcohol are a global concern with 0.8% of the overall causes in global disability-adjusted life years attributable to illicit drugs and alcohol.³

There are several types of treatment for alcohol use disorders; however, the mechanistic physiologic substrates of treatment remain to be elucidated.⁴ Alcohol dehydrogenase catalyzes the conversion of ethanol to acetaldehyde, which is further converted to acetic acid by aldehyde dehydrogenase (ALDH).⁵ Individuals carrying the *ALDH2*2* allele of the *ALDH2* gene produce an inactive ALDH2 enzyme resulting in excessive acetaldehyde production.^{6,7} Subsequent to alcohol consumption, the accumulation of acetaldehyde relaxes the capillaries resulting in facial blushing. Individuals carrying the *ALDH2*2* allele may also have rapid heartbeat, headache, dizziness, sweating, nausea, or vomiting. Al-

Received September 16, 2018; accepted after revision January 22, 2019.

From the Department of Radiology (L.M.K., J.Y.Z., W.B.Z., Z.W.S., R.H.W.), the Second Affiliated Hospital, Medical College of Shantou University, Shantou, China; and China Provincial Key Laboratory of Medical Molecular Imaging (R.H.W.), Guangdong, Shantou, China.

This study was supported by the National Natural Science Foundation of China (grant No. 81471730, 31870981, 81571627); Medical Scientific Research Foundation of Guangdong Province, China (grant No. B2014284); Shantou University "Innovation Powerhouse" Project, Training Program of Guangdong Province, China (No. 923-38040239), and Shantou University Student, Innovation and Entrepreneurship Training Program of Guangdong Province, China (No. 201610560111).

Please address correspondence to Renhua Wu, MD, PhD, Department of Radiology, the Second Affiliated Hospital, Medical College of Shantou University, Shantou 515041 China; e-mail: rhwu@stu.edu.cn

Indicates open access to non-subscribers at www.ajnr.org

Indicates article with supplemental on-line tables.

<http://dx.doi.org/10.3174/ajnr.A5992>

cohol-related facial blushing is an indicator of an inherited variant enzyme, aldehyde dehydrogenase, that impairs alcohol metabolism and increases the drinker's lifetime risk of certain aerodigestive cancers. Thus, it is suggested that people who blush should stop drinking permanently.⁸

Brain function and microstructure are affected by alcohol consumption. Our previous diffusion tensor imaging study showed alterations in brain tissue diffusion after acute alcohol intake, which underscores the susceptibility of neural systems to acute alcohol ingestion.⁹ Diffusional kurtosis imaging (DKI) quantifies non-Gaussian diffusion and has been suggested to be advantageous over DTI and better characterizes both normal and pathologic brain tissue, particularly for the assessment of gray matter.¹⁰ One of the primary indices of DKI, mean kurtosis (MK), measures the degree of diffusion restriction and indicates microstructural complexity.¹¹ DKI has proved useful in diagnosing numerous cerebral pathologies such as congenital sensorineural hearing loss,¹² gliomas,¹³ and acute cerebral infarction.¹⁴ Arterial spin-labeling (ASL), on the other hand, uses magnetically labeled arterial blood as an endogenous tracer to measure regional cerebral blood flow. While brain perfusion abnormalities might exist before morphologic changes, we hypothesized that the effects of acute alcohol on the physiology and structure of the brain are better determined by DKI and ASL.

The purpose of this study was to evaluate the feasibility of DKI and ASL to evaluate effect of acute alcohol intake on brain and to investigate both sex and blush effects.

MATERIALS AND METHODS

Subjects

Twenty-four healthy right-handed volunteers (12 men, 12 women; 23–27 years of age) with no history of alcohol or drug abuse were recruited for this study. They were light-moderate drinkers who reported drinking occasionally (mean, 3 ± 0.8 times per year). All procedures were performed in accordance with the ethical standards of the Second Affiliated Shantou Medical University Hospital and institutional review board. Written informed consent was obtained from all subjects before participation. Participants were familiarized with the setup and the scanner before the first experimental session. To ensure that the participants were not under the influence of alcohol, we requested that they abstain from alcohol for 24 hours and refrain from food for 6 hours before each experimental session.

Study Protocols

A dose of 0.65 g of alcohol per kilogram of body weight was given orally in the form of spirit (53° Maotai spirit, 2016; Maotai, Renhuai, Guizhou, China). Alcohol consumption was calculated on the basis of weight with the following equation: Alcohol Consumption (Milliliters) = Amount of Alcohol Intake (Grams) / Alcohol Concentration (Percentage) \times 0.8 (Ethanol Attenuation). Subjects were allowed to drink along with eating some snacks, such as peanuts. The alcohol was consumed in 6–10 minutes. Because no electronic devices could be used inside the scanner room, we measured breath alcohol concentrations, an index to estimate blood alcohol concentration, using a hand-held breathalyzer before the subjects entered the scanner (about 29

minutes, 59 minutes) and after taking them out of the scanner (about 40 minutes, 70 minutes). Heart rate and blood pressure were also measured. Participants were divided into 2 groups according to the response to alcohol: blushing ($n = 12$, 6 men, 6 women) and unblushing ($n = 12$, 6 men, 6 women). Subjective responses to alcohol were measured using the Biphasic Alcohol Effects Scale (BAES)¹⁵ at approximately 30 minutes before drinking and again at 25 and 55 minutes after the initiation of alcohol consumption.

MR Imaging Protocols

T2-weighted imaging, DKI, and 3D-arterial spin-labeling were acquired using a 3T MR imaging system (Signa; GE Healthcare, Milwaukee, Wisconsin) with an 8-channel head coil (HD 8Ch HiRes BRAIN ARRAY, GE Healthcare). Echo-planar imaging was used for DKI acquisition with the following parameters: TR/TE = 4500/98.6 ms; slice thickness = 4 mm with a 1-mm gap; FOV = 240×240 mm; matrix = 256×256 ; average = 1; and b-values = 0, 1000, 2000 s/mm² in 15 diffusion-encoding directions; imaging time = 3 minutes, 5 seconds. ASL was performed with the following parameters: TR/TE = 4580/9.8 ms; 4-mm slice thickness with no gap; FOV = 240×240 mm; postlabeling delay time = 1.5 seconds; average imaging time = 4 minutes, 26 seconds. Foam pads were used to reduce head movement. Subjects were asked to lie still with their eyes closed during data acquisition.

Data Analysis

All data were transferred to the workstation (Advantage Workstation 4.6; GE Healthcare) and FuncTool software package (GE Healthcare) for data processing. DKI metrics, including fractional anisotropy (FA), mean diffusivity (MD), and MK, were derived by a research tool in the FuncTool environment developed by the GE Applied Science Lab (see <http://www.nitrc.org/projects/dke/>).

Twenty brain regions (superior frontal gyrus, middle frontal gyrus, inferior frontal gyrus, precentral gyrus, postcentral gyrus, frontal white matter, anterior cingulate cortex, posterior cingulate cortex, cuneus cortex, occipital gyrus, superior temporal gyrus, hippocampal gyrus, parahippocampal gyrus, lenticular nucleus, dorsal thalamus, hypothalamus, amygdaloid body, anterior commissure, posterior commissure, and cerebellar hemisphere) were manually delineated by 2 experienced radiologists (5–6 years' experience) for ROI analysis (sample images in Fig 1), in which each ROI was approximately 12 mm². Both hemispheres were analyzed, which resulted in 40 ROIs. The DKI and ASL values for the ROIs were acquired and averaged over 3 replicates by every radiologist and were averaged by 2 surveyors to correct for inter- and intraobserver error.

Statistical Analysis

All statistical analyses were performed with SPSS 20.0 for Windows (IBM, Armonk, New York). Data were analyzed using univariate repeated-measures analysis of variance for the elimination of individual differences. To compare the difference in MK, FA, and MD, we used BAES ratings in the control (pre), 0.5 hour, and 1-hour time points and used a repeat 1-way analysis of variance test. If the overall test of the 2 means for the MK, FA, MD, and

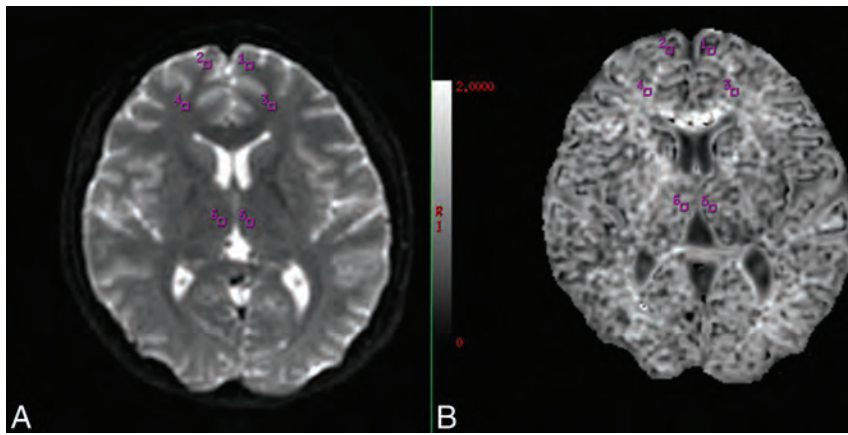


FIG 1. Example of the selection of ROIs from 3/20 brain regions under study. A, The raw DKI map. B, The gray level of the MK map. Two radiologists manually drew the ROIs on the raw DKI map and then obtained the MK values automatically. For ASL, the ROIs were also drawn on the raw ASL map manually and then the CBF values were obtained automatically.

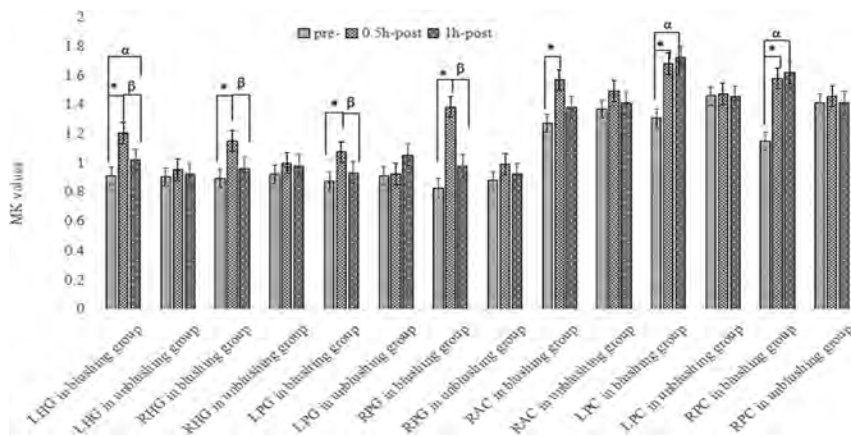


FIG 2. Blushing effect in MK at different time points. LHG indicates left hippocampal gyrus; RHG, right hippocampal gyrus; LPG, left parahippocampal gyrus; RPG, right parahippocampal gyrus; RAC, right anterior commissure; LAC, left anterior commissure; LPC, left posterior commissure; RPC, right posterior commissure; asterisk, a statistically significant difference between 0.5 hour and pretreatment ($P < .05$); α , a statistically significant difference between 1 hour and pretreatment ($P < .05$); β , a statistically significant difference between 1 hour and 0.5 hour ($P < .05$); pre, before; post, after.

BAES ratings values showed statistically significant differences, then multiple comparisons of the means of any 2 groups were performed using the Bonferroni post hoc test. A Wilcoxon rank sum test for continuous variables was used to determine the intra- and interobserver variability in MK, FA, and MD. All measurements were expressed as means \pm SDs. A P value $< .05$ was considered statistically significant.

RESULTS

Clinical Manifestations

Symptoms at 0.5 hour after alcohol consumption included headache ($n = 16$), nausea and vomiting ($n = 16$), dizziness ($n = 15$), walking unsteadily ($n = 12$), blushing ($n = 12$), increased speech ($n = 11$), excitement ($n = 10$), dysphoria ($n = 9$), depressed mood ($n = 9$), feeling tired ($n = 6$), and sleepiness ($n = 5$). Symptoms were generally improved at 1 hour. Some symptoms (dizziness, increased speech, excitement, and dysphoria) were more long-lasting and stronger in blushing than nonblushing individuals. Nausea and vomiting were more severe and greater excitement and

increased speech were seen in women more than in men at 0.5 hour. However, these more severe symptoms in women had apparently improved at 1 hour. On-line Table 1 shows the mean (SD) of baseline ratings for the BAES items at different time points.

Breath alcohol concentration and heart rate increased and peaked at 0.5 hour after alcohol consumption, then decreased to baseline. There were no significant changes in blood pressure. No correlation was found among changes in breath alcohol concentration, heart rate, or blood pressure index or blushing (On-line Table 2).

MR Imaging

Conventional T2WI showed no observable differences in signal intensities between pre- and post-alcohol consumption. MK increased and peaked at 0.5 hour in 38/40 ROIs and remained elevated in 31/40 ROIs at 1 hour compared with baseline. A delayed decrease in MD was observed, in which decreased MD was found in 3/40 ROIs at 0.5 hour, and 18/40 ROIs at 1 hour following alcohol consumption compared with baseline. An increase in FA was found in 23/40 ROIs at 0.5 hour. FA in 36/40 ROIs returned to baseline, whereas 4/40 ROIs remained elevated at 1 hour. ASL indicated increased CBF in 36/40 ROIs at 0.5 hour after alcohol consumption. This effect declined dramatically, with CBF returning to baseline at 1 hour. Most interesting, bilateral anterior commissure CBF decreased at 0.5 hour compared with baseline. CBF in the left precentral and right inferior frontal gyri increased, whereas CBF in the left anterior commissure was decreased at 1 hour compared with baseline. MK, MD, FA, and CBF values for 20 different brain regions are summarized in On-line Table 3. Moreover, MK and CBF alterations were found in both white and gray matter.

Blush Effect

At 0.5 hour, MK in the bilateral hippocampal gyrus, parahippocampal gyrus and posterior commissure, and right anterior commissure was increased for blushing individuals but not for nonblushing individuals (Fig 2). At 0.5 hour, MD was increased in the left anterior commissure for blushing individuals but not for nonblushing individuals. At 1 hour, MK in the right superior frontal gyrus, left parahippocampal gyrus, and posterior commissure was increased in the blushing group. At 1 hour, MD in the right middle frontal gyrus decreased in the blushing group, whereas decreased MD in the superior temporal gyrus was found in the nonblushing group.

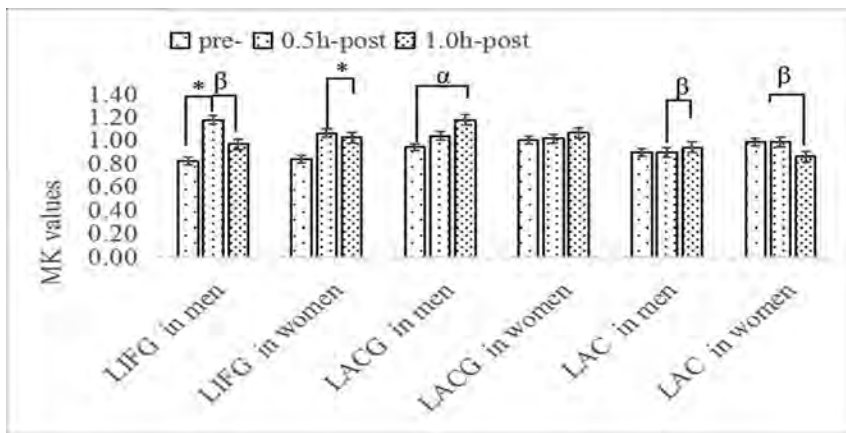


FIG 3. Sex effects in MK at different time points. LIFG indicates left inferior frontal gyrus; LACG, left anterior central gyrus; LAC, left anterior cingulate; *asterisk*, a statistically significant difference between 0.5 hour and pretreatment ($P < .05$); α , a statistically significant difference between 1 hour and pretreatment ($P < .05$); β , a statistically significant difference between 1 hour and 0.5 hour ($P < .05$); pre, before; post, after.

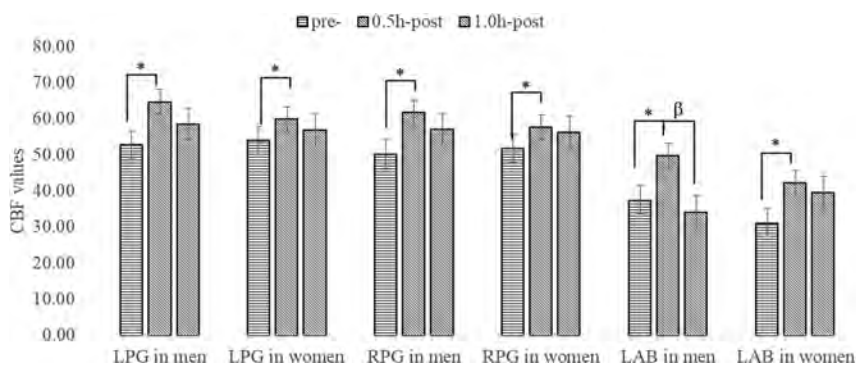


FIG 4. Sex effect in CBF at different time points. LPG indicates left parahippocampal gyrus; RPG, right parahippocampal gyrus; LAB, left amygdaloid body; *asterisk*, a statistically significant difference between 0.5 hour and pretreatment ($P < .05$); β , a statistically significant difference between 1 hour and 0.5 hour ($P < .05$); pre, before; post, after.

At 1 hour compared with 0.5 hour, MK was significantly decreased in the left frontal white matter, hippocampal gyrus, right dorsal thalamus, and parahippocampal gyrus in the blushing group, whereas MK was increased in the nonblushing group. We observed increased MK in the right parahippocampal gyrus in the blushing group but not in the nonblushing group. CBF appeared higher in the superior temporal gyrus in blushing individuals at 0.5 hour.

Sex Effect

MK in the left inferior frontal gyrus showed a larger increase in men than in women at 0.5 hour, and a larger increase in the left anterior central gyrus was found in men at 1 hour. At 1 hour compared with 0.5 hour, MK in left inferior frontal gyrus decreased more in men. MK in the left anterior cingulate in women decreased, whereas it increased in men (Fig 3). At 1 hour, MD in the left dorsal thalamus decreased more in men than in women. Figure 4 shows a larger increase in CBF in men than in women in the bilateral parahippocampal gyrus and left amygdaloid body at 0.5 hour. Moreover, CBF returned to baseline values in the left amygdaloid body in men yet remained elevated in women at 1 hour.

DISCUSSION

The current study investigated the physiologic and microstructural alterations in the brain on alcohol consumption. MD was decreased in several brain regions at 1 hour after drinking. Some studies suggest that reduction in MD could be related to cytotoxic edema, whereas an elevation in MD indicates vasogenic edema.¹⁶ Cytotoxic edema may occur after alcohol consumption, which is in line with prior studies in both humans and animals.^{9,17,18} Yet, another study reported no changes in diffusion parameters measured using diffusion MR imaging in acute alcohol intake.¹⁹ On the other hand, DKI revealed an increase in MK and FA at 0.5 hour post-alcohol intake in most brain regions. This increase in MK could be related to cell swelling during cytotoxic edema, during which the space between myelin fiber bundles is reduced and the volume fraction of restricted water diffusion is increased.²⁰ Thus, the extracellular tortuosity and microstructural complexity of the organization is likely increased and reflected by an increase in MK and FA. The alteration of microstructural complexity is related to brain edema, suggestive of direct toxicity. Increased diffusional kurtosis in the brain could be associated with decreased membrane permeability²¹ and cell swelling during cytotoxic edema in specific brain regions. The results suggested that edema

may be more severe in the blushing groups, translating into potential neurologic injury and impaired function of these brain regions. MK is altered at 0.5 hour after alcohol consumption, whereas MD changes occurred at 1 hour. Moreover, alterations in MK were detected in numerous brain regions compared with MD. These may indicate that MK has a higher sensitivity to detect microstructural changes in both white matter and gray matter after acute alcohol intake.

The increased CBF detected in most brain regions, particularly in the frontal regions, was consistent with that in previous studies using ASL.^{22,23} This finding could be because alcohol increases the generation of reactive oxygen species (such as nitric oxide and lipid peroxidation products)²⁴ and augments endothelium-dependent vasodilation.²⁵ In particular, the effect of alcohol on perfusion might be related to its metabolic effect and might be dominated by the direct vasodilatory effects of alcohol.²³ The coupling between neuronal activity and CBF could also be disrupted by biphasic vasoactive properties of alcohol.²⁶ Although acetaldehyde, a metabolite of alcohol, acts as a vasodilator, high concentrations of alcohol constrict blood vessels depending on calcium ions. Global changes in CBF are an important marker of cerebral

autoregulation, and increased CBF in the sensory and motor areas may be related to the disinhibitory effects of alcohol on related functions.²⁷ The return of CBF to baseline at 1 hour may reflect compensation. However, perfusion in the anterior commissure decreased. One explanation for such a decrease might be the impairment in autoregulation of brain blood flow.²⁸ The anterior commissure is an attenuated white matter structure with little vasculature. The blood flow of this deep white matter structure may decrease relative to the increase of cortical perfusion. Acute alcohol intake exerts differential effects in various brain regions.^{29,30}

Our findings of both DKI and ASL imply that the thalamus, limbic system, cerebellum, and especially the frontal lobes are more subject to alcohol-related brain damage than other cerebral regions. We hypothesize that alcohol-induced microstructural changes in these sensitive brain regions, which are associated with the function of these regions, likely result in both physiologic and psychological consequences on behavior. The limbic system primarily includes the nucleus accumbens, amygdala, and hypothalamus and predominantly controls appropriate responses to stimuli with social, emotional, or motivational salience,³¹ it is involved in the regulation of sensorial and visceral activity and closely related to psychological activities such as learning, memory, the generation of emotional responses, and behavior. Alcohol-induced parameter changes in the thalamus were associated with changes in mood. These alcohol-induced changes in mood have also been predicted by changes in thalamic connectivity, whereas changes in motor performance have been associated with the cerebellothalamic network.³² The prefrontal cortex is thought to be one of the most complex anatomic and functional structures of the human brain. Acute ethanol administration in humans has been shown to cause deficits in executive activities and language performance associated with the prefrontal cortex. The deleterious effects of acute ethanol administration on prefrontal cortex-dependent behaviors may result from the breakdown of functional specificity in different brain regions.³³

The blush effect of the brain was investigated by DKI and ASL. To our knowledge, blush effects have not been previously examined by these techniques. Blushing and nonblushing individuals showed differential changes in brain regions, which could be related to emotional, neuropsychological, and language-expression changes in the 2 groups. Alcohol-use disorders may induce alterations in gene expression, including *ALDH*, in brain regions such as the prefrontal cortex,³⁴ and the superior frontal gyrus is involved in a variety of functions, such as execution³⁵ and language functions.³⁶ The parahippocampal gyrus plays a key role in the information flow between cortical association areas and the hippocampal formation,³⁷ and this region may reflect particular sensitivity to the subjective emotional state during emotional regulation.³⁸ Increased MK at 1 hour in the right superior frontal gyrus of blushing individuals might mean that these individuals were easily affected in language expression and execution, whereas increased MK in the left parahippocampal gyrus in the nonblushing group may be associated with the lag of emotional and neuropsychological function. In combination with our data on CBF, these findings further suggest that alcohol exerts regional effects on the brain and that the regional distribution of CBF might reflect alcohol effects on functional brain activity.³⁹

Cognitive-behavioral abilities are affected differently by ethanol. Not all regions of the brain had significant differences in DKI parameters and CBF values at 0.5- and 1.0-hour time points in the blushing-versus-nonblushing group. Regional MK and CBF changes could be associated with clinical symptoms. MR imaging studies of sex differences in brain function of alcoholics have yielded contradictory results, with some studies showing women to be more susceptible than men to brain impairment and vice versa.^{32,40} In general, we found more microstructural changes in the left inferior frontal gyrus, amygdaloid body, precentral gyrus, anterior cingulate, and bilateral parahippocampal gyrus in men. One plausible explanation is that a few brain regions of men are more susceptible to alcohol, which manifests in changes in language expression, executive function, memory, and emotion of men after alcohol consumption. Moreover, the primary somatic motor center and limbic system of men are more likely to be affected across time with a longer duration, which may impact limb movement.

Apart from microstructural changes, sex effects in brain perfusion changes remain controversial. Increased frontal perfusion in men was reported by Rickenbacher et al,⁴¹ whereas Marxen et al²³ detected a significantly higher brain perfusion in women. The discrepancies between these studies and ours might be related to the difference in alcohol dosage and the time course of imaging. Additional imaging studies with larger samples, together with age, blushing, sex, population, breath alcohol concentration, alcohol history, and different time points after drinking are needed to sort out the effects of alcohol intoxication. A multivariate analysis might be beneficial to account for demographic and physiologic covariates.

This study has several limitations. More subjects are needed to further investigate the potential effects of blushing, sex, and the time course of diffusion and perfusion responses. In particular, the current study only investigated the effect of acute alcohol (within 1 hour) consumption with a few time points. More time points and longer time spans are required to better investigate the changes of brain function with time. Last, subjects recruited in this study were young adults. More age groups, including adolescents, middle-aged adults, and the elderly, will be included in future studies.

CONCLUSIONS

The extent of alteration in DKI and ASL parameters in various brain areas may be useful in quantifying the extent of damage to brain tissue. People who consume alcohol on a regular basis with imperceptible changes in cognitive abilities, DKI, ASL, and cognitive test findings will be measured regularly (for example, yearly) in a future study. The correlation of DKI and ASL parameters to cognitive function will be examined to determine the most relevant indicators of decrements in cognitive function. Because blushing individuals are more sensitive to alcohol with acute effects, people who blush should stop drinking on the basis of current findings. The current study demonstrated that brain areas with blood flow alterations detected by 3D-ASL were highly consistent with susceptible areas detected by DKI after acute alcohol intake. Regional changes in the brain vary with respect to

blush response and sex. Blushing individuals and men are more sensitive to alcohol with acute effects.

ACKNOWLEDGMENTS

The authors thank Yuelin Guo, MD, PhD, in the Department of Radiology, the Second Affiliated Hospital, Medical College of Shantou University, Guangdong, China, for technologic assistance.

Disclosures: Wenbin B. Zheng—RELATED: Grant: National Natural Science Foundation of China.* Renhua H. Wu—RELATED: Grant: National Natural Science Foundation of China.* *Money paid to the institution.

REFERENCES

1. Mukherjee S, Das SK, Vaidyanathan K, et al. **Consequences of alcohol consumption on neurotransmitters: an overview.** *Curr Neurovasc Res* 2008;5:266–72 CrossRef Medline
2. White AM. **What happened? Alcohol, memory blackouts, and the brain.** *Alcohol Res Health* 2003;27:186–96 Medline
3. Hoang VP, Shanahan M, Shukla N, et al. **A systematic review of modelling approaches in economic evaluations of health interventions for drug and alcohol problems.** *BMC Health Serv Res* 2016;16:127 CrossRef Medline
4. Nielsen AS, Nielsen B. **Implementation of a clinical pathway may improve alcohol treatment outcome.** *Addict Sci Clin Pract* 2015;10:7 CrossRef Medline
5. de la Monte SM, Kril JJ. **Human alcohol-related neuropathology.** *Acta Neuropathol* 2014;127:71–90 CrossRef Medline
6. Helminen A, Väkeväinen S, Salaspuro M. **ALDH2 genotype has no effect on salivary acetaldehyde without the presence of ethanol in the systemic circulation.** *PLoS One* 2013;8:e74418 CrossRef Medline
7. Pavlova SI, Jin L, Gasparovich SR, et al. **Multiple alcohol dehydrogenases but no functional acetaldehyde dehydrogenase causing excessive acetaldehyde production from ethanol by oral streptococci.** *Microbiology* 2013;159(Pt 7):1437–46 CrossRef Medline
8. Ding LY, Yuen LW, Newman IM, et al. **University students' willingness to assist fellow students who experience alcohol-related facial flushing to reduce their drinking.** *Int J Environ Res Public Health* 2018;15 CrossRef Medline
9. Kong LM, Zheng WB, Lian GP, et al. **Acute effects of alcohol on the human brain: diffusion tensor imaging study.** *AJNR Am J Neuroradiol* 2012;33:928–34 CrossRef Medline
10. Jensen JH, Helpert JA. **MRI quantification of non-Gaussian water diffusion by kurtosis analysis.** *NMR Biomed* 2010;23:698–710 CrossRef Medline
11. Van Cauter S, Veraart J, Sijbers J, et al. **Gliomas: diffusion kurtosis MR imaging in grading.** *Radiology* 2012;263:492–501 CrossRef Medline
12. Zheng WB, Wu CX, Huang LX, et al. **Diffusion kurtosis imaging of microstructural alterations in the brains of paediatric patients with congenital sensorineural hearing loss.** *Sci Rep* 2017;7:1543 CrossRef Medline
13. Bai Y, Lin Y, Tian J, et al. **Grading of gliomas by using monoexponential, biexponential, and stretched exponential diffusion-weighted MR imaging and diffusion kurtosis MR imaging.** *Radiology* 2016;278:496–504 CrossRef Medline
14. Guo YL, Zhang ZP, Zhang GS, et al. **Evaluation of mean diffusion and kurtosis MRI mismatch in subacute ischemic stroke: comparison with NIHSS score.** *Brain Research* 2016;1644:231–39 CrossRef Medline
15. Rueger SY, McNamara PJ, King AC. **Expanding the utility of the Biphasic Alcohol Effects Scale (BAES) and initial psychometric support for the Brief-BAES (B-BAES).** *Alcohol Clin Exp Res* 2009;33:916–24 CrossRef Medline
16. Cernak I, Vink R, Zapple DN, et al. **The pathologies of moderate diffuse traumatic brain injury as identified using a new experimental model of injury in rats.** *Neurobiol Dis* 2004;17:29–43 CrossRef Medline
17. Liu HM, Zheng WB, Yan G, et al. **Acute ethanol-induced changes in edema and metabolite concentrations in rat brain.** *Biomed Res Int* 2014;2014:351903 CrossRef Medline
18. Chen XR, Zeng JY, Shen ZW, et al. **Diffusion kurtosis imaging detects microstructural changes in the brain after acute alcohol intoxication in rats.** *Biomed Res Int* 2017;2017:4757025 CrossRef Medline
19. Duning T, Kugelc H, Menke R, et al. **Diffusion-weighted magnetic resonance imaging at 3.0 Tesla in alcohol intoxication.** *Psychiatry Res* 2008;163:52–60 CrossRef Medline
20. Sotak CH. **The role of diffusion tensor imaging in the evaluation of ischemic brain injury: a review.** *NMR Biomed* 2002;15:561–69 CrossRef Medline
21. Jensen JH, Helpert JA, Ramani A, et al. **Diffusional kurtosis imaging: the quantification of non-gaussian water diffusion by means of magnetic resonance imaging.** *Magn Reson Med* 2005;53:1432–40 CrossRef Medline
22. Tolentino NJ, Wierenga CE, Hall S, et al. **Alcohol effects on cerebral blood flow in subjects with low and high responses to alcohol.** *Alcohol Clin Exp Res* 2011;35:1034–40 CrossRef Medline
23. Marxen M, Gan G, Schwarz D, et al. **Acute effects of alcohol on brain perfusion monitored with arterial spin-labeling magnetic resonance imaging in young adults.** *J Cereb Blood Flow Metab* 2014;34:472–79 CrossRef Medline
24. Zahr NM, Kaufman KL, Harper CG. **Clinical and pathological features of alcohol-related brain damage.** *Nat Rev Neurol* 2011;7:284–94 CrossRef Medline
25. Puddey IB, Zilkens RR, Croft KD, et al. **Alcohol and endothelial function: a brief review.** *Clin Exp Pharmacol Physiol* 2001;28:1020–24 CrossRef Medline
26. Kawano Y. **Physio-pathological effects of alcohol on the cardiovascular system: its role in hypertension and cardiovascular disease.** *Hypertens Res* 2010;33:181–91 CrossRef Medline
27. Rose AK, Duka T. **The influence of alcohol on basic motoric and cognitive disinhibition.** *Alcohol Alcohol* 2007;42:544–51 CrossRef Medline
28. Jochum T, Reinhard M, Boettger MK, et al. **Impaired cerebral autoregulation during acute alcohol withdrawal.** *Drug Alcohol Depend* 2010;110:240–46 CrossRef Medline
29. Grundersen H, van Wageningen H, Grüner R. **Alcohol-induced changes in cerebral blood flow and cerebral blood volume in social drinkers.** *Alcohol Alcohol* 2013;48:160–65 CrossRef Medline
30. Bjorka JM, Gilman JM. **The effects of acute alcohol administration on the human brain: insights from neuroimaging.** *Neuropharmacology* 2014;84:101–10 CrossRef Medline
31. Sokolowski K, Corbin JG. **Wired for behaviors: from development to function of innate limbic system circuitry.** *Front Mol Neurosci* 2012;5:55 CrossRef Medline
32. Shokri-Kojori E, Tomasi D, Wiers CE, et al. **Alcohol affects brain functional connectivity and its coupling with behavior: greater effects in male heavy drinkers.** *Mol Psychiatry* 2017;22:1185–95 CrossRef Medline
33. Abernathy K, Chandler LJ, Woodward JJ. **Alcohol and the prefrontal cortex.** *Int Rev Neurobiol* 2010;91:289–320 CrossRef Medline
34. Zhang HP, Wang F, Xu HQ, et al. **Differentially co-expressed genes in postmortem prefrontal cortex of individuals with alcohol use disorders: influence on alcohol metabolism-related pathways.** *Hum Genet* 2014;133:1383–94 CrossRef Medline
35. Li W1, Qin W, Liu H, et al. **Subregions of the human superior frontal gyrus and their connections.** *Neuroimage* 2013;78:46–58 CrossRef Medline
36. Fujii M, Maesawa S, Motomura K, et al. **Intraoperative subcortical mapping of a language-associated deep frontal tract connecting the superior frontal gyrus to Broca's area in the dominant hemisphere of patients with glioma.** *J Neurosurg* 2015;122:1390–96 CrossRef Medline
37. Echávarri C, Aalten P, Uylings HB, et al. **Atrophy in the parahippocampal gyrus as an early biomarker of Alzheimer's disease.** *Brain Struct Funct* 2011;215:265–71 CrossRef Medline

38. Frank DW, Dewitt M, Hudgens-Haney M, et al. **Emotion regulation: quantitative meta-analysis of functional activation and deactivation.** *Neurosci Biobehav Rev* 2014;45:202–11 CrossRef Medline
39. Khalili-Mahani N, van Osch MJ, Baerends E, et al. **Pseudocontinuous arterial spin-labeling reveals dissociable effects of morphine and alcohol on regional cerebral blood flow.** *J Cereb Blood Flow Metab* 2011;31:1321–33 CrossRef Medline
40. Ide JS, Zhornitsky S, Hu S, et al. **Sex differences in the interacting roles of impulsivity and positive alcohol expectancy in problem drinking: a structural brain imaging study.** *Neuroimage Clin* 2017;14:750–59 CrossRef Medline
41. Rickenbacher E, Greve DN, Azma S, et al. **Effects of alcohol intoxication and gender on cerebral perfusion: an arterial spin-labeling study.** *Alcohol* 2011;45:725–37 CrossRef Medline

Measuring Glymphatic Flow in Man Using Quantitative Contrast-Enhanced MRI

R. Watts, J.M. Steinklein, L. Waldman, X. Zhou, and C.G. Filippi



ABSTRACT

SUMMARY: On the basis of animal models, glymphatic flow disruption is hypothesized to be a factor in the development of Alzheimer's disease. We report the first quantitative study of glymphatic flow in man, combining intrathecal administration of gadobutrol with serial T1 mapping to produce contrast concentration maps up to 3 days postinjection, demonstrating performing a quantitative study using the techniques described feasibility and providing data on pharmacokinetics.

ABBREVIATION: AD = Alzheimer's disease

Protein aggregation is the pathologic signature of many neurodegenerative diseases, including Alzheimer's disease (AD).¹ The recently discovered glial lymphatic ("glymphatic") system² may play a critical role in protein removal, including soluble amyloid- β ³ and HPF- τ (Hyperphosphorylated- τ).⁴ This perivascular glymphatic pathway drives exchange between CSF and interstitial fluid, and dysfunction may be a causal factor in the development of Alzheimer's disease.⁵ In rodent models, glymphatic flow decreases with age,⁶ increases during sleep,⁷ and can be pharmacologically manipulated,⁷ suggesting similar approaches for patients with AD.

Qualitative MR imaging using percentage signal enhancement on T1-weighted images has been reported in animal models⁸ and humans.⁹⁻¹² However, the percentage signal change on a T1-weighted image with contrast concentration depends on the intrinsic T1 of each tissue, the corresponding change in T2*, and the imaging parameters selected. To be able to apply pharmacokinetic models requires consistent determination of contrast concentrations across tissue types and concentrations. Here we use the combination of an intrathecal administration of a gadolinium-based

contrast agent (gadobutrol) with quantitative MR imaging to provide maps of contrast concentration versus time, measuring glymphatic flow throughout the brain in a human volunteer at 3T.

MATERIALS AND METHODS

Patient History

A 55-year-old man referred for MR myelography was recruited for this Health Insurance Portability and Accountability Act-compliant, institutional review board (The Feinstein Institute for Medical Research)-approved study using an intrathecal injection of 0.5 mL of 1.0 mmol of gadobutrol. The patient gave written, informed consent.

Data Acquisition and Analysis

Quantitative T1-mapping data were acquired on a 3T Achieva TX MR imaging scanner (Philips Healthcare, Best, the Netherlands) with an 8-channel head coil using a multiple flip angle 3D spoiled gradient-echo sequence with TE/TR = 2.8/20 ms; flip angles = 2°, 5°, 10°, 20°, 40°; FOV = 240 × 228 × 120 mm³; acquired resolution = 1.2 × 1.2 × 1.2 mm³. Acquisition time was 3 minutes 47 seconds for each flip angle using a sensitivity encoding factor of 2, to give a total time of 24 minutes. Scans were acquired at baseline and at 9 further acquisitions during the first 10 hours (60, 210, 240, 270, 370, 450, 500, 560, and 620 minutes), followed by acquisitions at 26, 50, and 79 hours. The subject was not restricted but was asked to remain supine for as much as possible during the first 10 hours but then was allowed to move normally for the remaining time. He had a normal night's sleep before being scanned the final 3 times.

Data Analysis: Theory

The method is based on the nuclear MR steady-state signal equation,

Received August 22, 2018; accepted after revision November 13.

From the Department of Radiology (R.W.), University of Vermont, Burlington, Vermont; and Department of Radiology (J.M.S., L.W., X.Z., C.G.F.), Lenox Hill Hospital and Donald and Barbara Zucker School of Medicine at Hofstra/Northwell, East Garden City, New York.

This study was funded by the Foundation of the American Society of Neuroradiology Boerger Research Fund for Alzheimer's Disease and Neurocognitive Disorders.

Paper previously presented, in part, at: Annual Meeting of the American Society of Functional Neuroradiology, October 15-17, 2018; Coronado, California.

Please address correspondence to Christopher G. Filippi, MD, Lenox Hill Hospital and Donald and Barbara Zucker School of Medicine at Hofstra/Northwell, Department of Radiology, 100 E 77th Street, NY, NY 10075; e-mail: cfilippi@northwell.edu and sairaallapeikko@gmail.com

<http://dx.doi.org/10.3174/ajnr.A5931>

$$S_i = M_0 \sin \alpha_i \frac{1 - E_1}{1 - \cos \alpha_i E_1},$$

where $E_1 = \exp\left(\frac{-TR}{T_1}\right)$, S_i is the signal intensity for each flip angle α_i , and M_0 is a constant representing the equilibrium magnetization. This equation can be transformed to a linear form, from which the gradient E_1 and hence the tissue T_1 can be determined.¹³

The T_1 value is related to the contrast agent concentration by

$$\frac{1}{T_1} = \frac{1}{T_{10}} + r_1 C,$$

Where T_{10} is the native T_1 value of the tissue (s), and r_1 is the relaxivity of the contrast agent, assumed to be 5.1 l/mmol/s for gadobutrol.

Data Processing

Each volume was coregistered to the 20° flip angle acquisition from the first scan acquired before contrast injection using SPM12 (<http://www.fil.ion.ucl.ac.uk/spm/software/spm12>). T1 maps were generated using least squares fitting to the signal equation using custom Matlab (MathWorks, Natick, Massachusetts) scripts. The precontrast map provided the baseline T_1 values (T_{10}), enabling contrast concentration to be calculated at each subsequent time.

Brain segmentation was performed using SPM12 on the 20° flip angle acquisition from the first scan acquired before contrast injection, resulting in native space gray matter, white matter, and CSF components. Cortical gray matter masks were defined by the intersection of the gray matter mask and the corresponding regions of the Montreal Neurological Institute structural atlas transformed to native space. Juxtacortical white matter and CSF masks were defined by the intersection of their native tissue components with the cortical gray matter mask expanded by 3 mm using only voxels with >95% probability of being the target tissue.

RESULTS

The time course of contrast concentration during 79 hours postinjection is shown in Fig 1. Contrast arrived in the cisterna magna between 1 and 3 hours postinjection and covered the entire subarachnoid space at 8 hours. The subarachnoid CSF concentration peaked between 10 and 15 hours at approximately 0.5 mmol/L. Cortical enhancement measurable from 4 hours peaked between 10 and 26 hours, with a maximum concentration of approximately 0.1 mmol/L. The largest concentration was noted in the temporal lobes and insula in the first 10 hours. Cortical contrast remained at 50 hours with near-complete clearance at 79 hours. Depending on location, white matter concentration peaked between 26 and 50 hours.

Concentration-time curves were calculated for cortical gray matter and juxtacortical white matter (Fig 2). Biologic half-life of gadobutrol in the subarachnoid CSF, based on the washout curve, was approximately 12 hours. A 2-compartment model provided a good fit to the cortical contrast concentration curve.

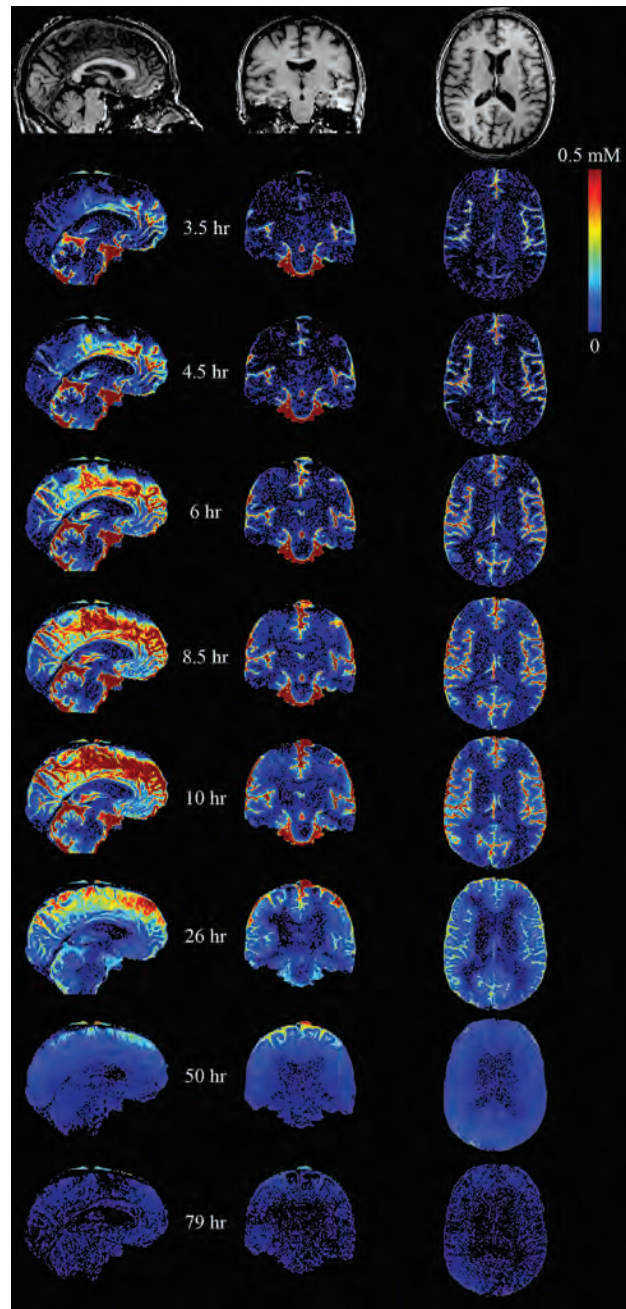


FIG 1. Quantitative maps of gadolinium tracer across time. The tracer arrived in the cisterna magna between 1 and 3.5 hours after intrathecal injection. Superior parts of the subarachnoid space enhance late, with clearance also delayed.

DISCUSSION

Most current literature on glymphatic flow is based on rodent models using highly invasive techniques. A few studies used MR imaging qualitatively to investigate glymphatic flow in rodents⁸ and humans.⁹⁻¹² Our report improves on those studies by quantifying contrast concentration. We are only aware of a single study that has used similar quantification in rats at 9.4T.¹⁴ Compared with rodents, contrast uptake and clearance are much slower in our subject but are still faster than would be expected due to only passive diffusion, which provides further evidence that intrathecal administration of drugs may provide access to the entire brain parenchyma.

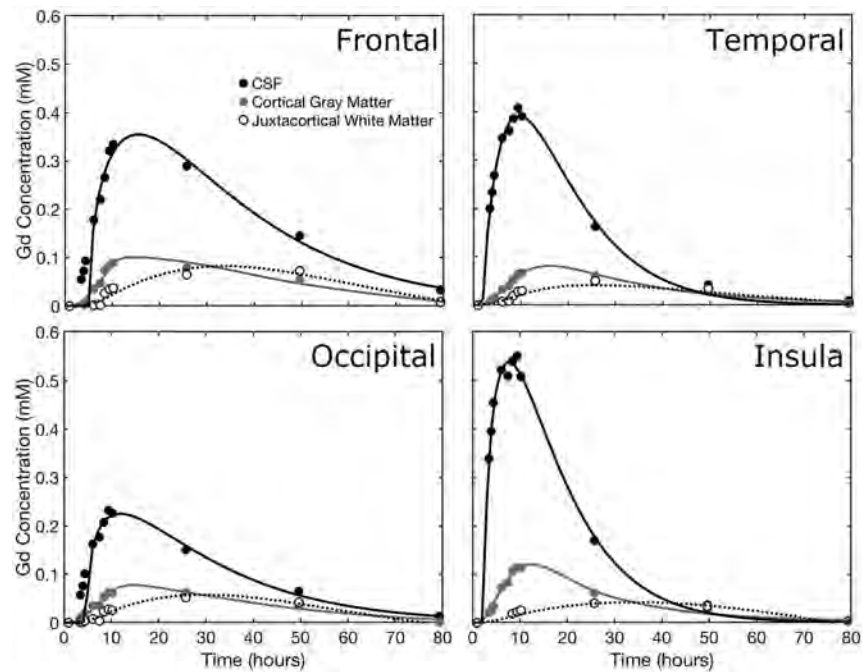


FIG 2. The time course of gadolinium concentration for the frontal, temporal, occipital, and parietal lobes. CSF concentration, cortical gray matter, and juxtacortical white matter curves are shown. Juxtacortical white matter is within 3 mm of the cortex. In each case, the CSF tracer concentration is fitted to a γ -variate distribution, while the tissue concentrations are fitted by 2-compartment pharmacokinetic models.

We observed minimal enhancement of the lateral ventricles at any time, suggesting that contrast entering the ventricular system is rapidly diluted.

Although only a single individual was imaged, the acquisition of serial quantitative data at many time points during 3 days represents a unique dataset. While cost and inconvenience to patients of an identical approach are prohibitive for routine use, our results suggest that an abbreviated protocol may suffice.

Regarding retention of gadolinium-based contrast agents, recent studies including long-term follow-up after intrathecal contrast injection have not identified adverse effects.^{15,16} Gadolinium retention after intrathecal administration was not observed for gadobutrol at the same dose used in the current study.¹¹

CONCLUSIONS

We have demonstrated the feasibility of using T1 mapping to quantify contrast concentration to analyze glymphatic flow in man, for which there is increasing interest in its use as a biomarker and potential therapeutic target in AD.

Disclosures: Richard Watts—RELATED: Grant: Foundation of the American Society of Neuroradiology Boerger Research Fund for Alzheimer's Disease and Neurocognitive Disorders.* Christopher G. Filippi—RELATED: Grant: Foundation of the American Society of Neuroradiology, Comments: Grant money was given by the Foundation of the American Society of Neuroradiology Boerger Fund to support this research study*; UNRELATED: Consultancy: Syntactx Inc, Comments: I read MR imaging examinations as part of clinical trials work. *Money paid to the institution.

REFERENCES

1. Ross CA, Poirier MA. Protein aggregation and neurodegenerative disease. *Nat Med* 2004;10(Suppl):S10–17 Medline
2. Iliff JJ, Wang M, Liao Y, et al. A paravascular pathway facilitates CSF flow through the brain parenchyma and the clearance of interstitial solutes, including amyloid β . *Sci Transl Med* 2012;4:147ra111 CrossRef Medline

3. Hawkes CA, Sullivan PM, Hands S, et al. Disruption of arterial perivascular drainage of amyloid- β from the brains of mice expressing the human APOE $\epsilon 4$ allele. *PLoS One* 2012;7:e41636 CrossRef Medline
4. Iliff JJ, Chen MJ, Plog BA, et al. Impairment of glymphatic pathway function promotes tau pathology after traumatic brain injury. *J Neurosci* 2014;34:16180–93 CrossRef Medline
5. Bakker EN, Bacskai BJ, Arbel-Ornath M, et al. Lymphatic clearance of the brain: perivascular, paravascular and significance for neurodegenerative diseases. *Cell Mol Neurobiol* 2016;36:181–94 CrossRef Medline
6. Hawkes CA, Hartig W, Kacza J, et al. Perivascular drainage of solutes is impaired in the ageing mouse brain and in the presence of cerebral amyloid angiopathy. *Acta Neuropathol* 2011;121:431–43 CrossRef Medline
7. Xie L, Kang H, Xu Q, et al. Sleep drives metabolite clearance from the adult brain. *Science* 2013;342:373–77 CrossRef Medline
8. Iliff JJ, Lee H, Yu M, et al. Brain-wide pathway for waste clearance captured by contrast-enhanced MRI. *J Clin Invest* 2013;123:1299–309 CrossRef Medline
9. Eide PK, Ringstad G. MRI with intrathecal MRI gadolinium contrast medium administration: a possible method to assess glymphatic function in human brain. *Acta Radiol Open* 2015;4:2058460115609635 CrossRef Medline
10. Eide PK, Ringstad G. Delayed clearance of cerebrospinal fluid tracer from entorhinal cortex in idiopathic normal pressure hydrocephalus: a glymphatic magnetic resonance imaging study. *J Cereb Blood Flow Metab* 2018;Feb 27:271678X18760974. [Epub ahead of print] CrossRef Medline
11. Ringstad G, Valnes LM, Dale AM, et al. Brain-wide glymphatic enhancement and clearance in humans assessed with MRI. *JCI Insight* 2018 Jul 12;3(13). [Epub ahead of print] CrossRef Medline
12. Ringstad G, Vatnehol SAS, Eide PK. Glymphatic MRI in idiopathic normal pressure hydrocephalus. *Brain* 2017;140:2691–705 CrossRef Medline
13. Cheng HL, Wright GA. Rapid high-resolution T(1) mapping by variable flip angles: accurate and precise measurements in the pres-

- ence of radiofrequency field inhomogeneity. *Magnetic Reson Med* 2006;55:566–74 CrossRef Medline
14. Lee H, Mortensen K, Sanggaard S, et al. **Quantitative Gd-DOTA uptake from cerebrospinal fluid into rat brain using 3D VFA-SPGR at 9.4T.** *Magnetic Reson Med* 2018;79:1568–78 CrossRef Medline
15. Safriel Y, Ang R, Ali M. **Gadolinium use in spine pain management procedures for patients with contrast allergies: results in 527 procedures.** *Cardiovasc Intervent Radiol* 2008;31:325–31 CrossRef Medline
16. Nacar Dogan S, Kizilkilic O, Kocak B, et al. **Intrathecal gadolinium-enhanced MR cisternography in patients with otorhinorrhea: 10-year experience of a tertiary referral center.** *Neuroradiology* 2018;60:471–77 CrossRef Medline

Risk of Acute Kidney Injury with Consecutive, Multidose Use of Iodinated Contrast in Patients with Acute Ischemic Stroke

Z.Y. Jia, S.X. Wang, L.B. Zhao, Y.Z. Cao, H.B. Shi, and S. Liu



ABSTRACT

SUMMARY: Currently, CTA is the imaging technique most frequently used to evaluate acute ischemic stroke, and patients with intracranial large-vessel occlusion usually undergo endovascular treatment. This single-center, prospective, cohort study showed that consecutive, multidose use of contrast during CTA and DSA does not increase the incidence of acute kidney injury in patients with acute ischemic stroke, though acute kidney injury tended to have a higher incidence in the contrast multiexposure group ($P = .172$).

ABBREVIATIONS: AKI = acute kidney injury; AIS = acute ischemic stroke

CTA and CTP are the most frequently used noninvasive vascular imaging techniques to evaluate acute ischemic stroke (AIS).^{1,2} Analyses from a number of observational studies suggest that the risk of contrast-induced acute kidney injury (AKI) secondary to CTA/CTP imaging is relatively low in patients with AIS, particularly those with no history of renal impairment.¹⁻³

Apart from CTA/CTP, most patients with AIS, within the time window of recanalization, undergo intra-arterial thrombectomy, which is associated with exposure to additional iodinated contrast medium during DSA.⁴⁻⁸ Because the potential risk from iodinated contrast exposure is proportional to the dose of contrast medium administered, multiple, consecutive doses of contrast medium could imply a greater risk for AKI.^{9,10} Although several studies have cited data regarding the safety of the consecutive use of contrast medium in patients with AIS for CTA/CTP and DSA, the sample sizes have been small, most of the studies were retrospective, and the definition of AKI differed among the studies.¹¹⁻¹⁴ Hence, AKI induced by consecutive multidosing of contrast medium is still a perceived risk. We therefore performed this prospective study to determine whether consecutive, multidose use

of contrast increases the incidence of AKI compared with its single use in patients with AIS.

MATERIALS AND METHODS

Study Design and Patient Enrollment

This study is a prospective, registered, cohort study performed from September 2016 to September 2017 at a single medical center with the approval of the institutional review board of the center. Informed consent was obtained from all patients or their legal representatives.

Patient inclusion criteria were the following: 1) 18 years of age or older; 2) suspicion of AIS; 3) seen within 6 hours of developing anterior circulation symptoms or within 24 hours of posterior circulation symptoms; 4) no intracranial hemorrhage; and 5) underwent CTA. Exclusion criteria were lack of a baseline creatinine level or lack of a follow-up creatinine level 48 hours after CTA.

Imaging

All imaging was performed on a 64-section CT scanner (Optima CT660, GE Healthcare, Milwaukee, Wisconsin). For CTA, isotonic contrast material (1.5 mL/kg) (iodixanol, 320 mg I/mL, Visipaque 320; GE Healthcare, Piscataway, New Jersey) was injected at a rate of 4 mL/s, followed by a 20-mL saline bolus chaser using a dual-head injector. The upper limit volume of the contrast material was 100 mL.

Endovascular Treatment

Intra-arterial treatment consisted of thrombolysis, mechanical thrombectomy with a stent retriever or aspiration catheter, balloon angioplasty and stent insertion, or carotid artery stent placement. The volume of the contrast (iodixanol, 320 mg I/mL, Visipaque 320) used during the procedure was recorded.

Received September 17, 2018; accepted after revision November 18.

From the Department of Radiology, The First Affiliated Hospital with Nanjing Medical University, Nanjing, Jiangsu Province, China.

Zhen Yu Jia and Shao Xian Wang contributed equally to this work.

This work was supported by the Construction Program of Jiangsu Provincial Clinical Research Center Support System (BL 2014084). Clinical Trial Registration: <http://www.clinicaltrials.gov>; NCT03132558.

Please address correspondence to Sheng Liu, MD, PhD, Department of Radiology, The First Affiliated Hospital with Nanjing Medical University, 300 Guangzhou Rd, Gulou District, Nanjing, Jiangsu Province 210029, China; e-mail: liusheng@njmu.edu.cn

Indicates open access to non-subscribers at www.ajnr.org

<http://dx.doi.org/10.3174/ajnr.A5959>

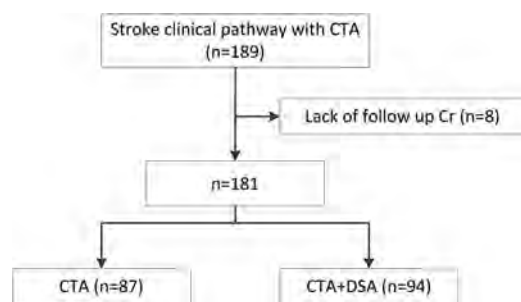


FIGURE. Flow chart of the study.

Table 1: Baseline demographics and characteristics^a

	CTA Group (n = 87)	DSA Group (n = 94)	P Value
Age (yr) (mean)	66.5 ± 11.4	67.2 ± 13.0	.708
Female sex	28 (32.2)	37 (39.4)	.315
Hypertension	50 (57.5)	55 (58.5)	.887
Diabetes	27 (31.0)	18 (19.1)	.065
Hyperlipidemia	4 (4.6)	2 (2.1)	.430
Smoking	18 (20.7)	19 (20.2)	.937
Prior stroke	23 (26.4)	15 (16.0)	.084
Atrial fibrillation	10 (11.5)	47 (50.0)	.000
Heart failure	1 (1.1)	10 (10.6)	.010
CKD	0 (0.0)	0 (0.0)	1.000
Previous use of contrast	4 (4.6)	3 (3.2)	.712
NSAID	11 (12.6)	9 (9.6)	.511
Baseline NIHSS (median) (IQR)	3 (2–4)	14 (10–19)	.000
Hemoglobin (mean) (g/L)	137.9 ± 16.0	133.5 ± 16.4	.707
WBC count (mean) (× 10 ⁹ /L)	7.4 ± 2.6	8.0 ± 2.7	.121
rtPA	38 (43.7)	28 (29.8)	.052
mRS score at 3 mo of <3	85 (97.7)	86 (91.5)	.102

Note:—CKD indicates chronic kidney dysfunction; NSAID, nonsteroidal anti-inflammatory drugs; IQR, interquartile range; WBC, white blood cells; BUN, blood urea nitrogen.

^a Data are number and percentage unless otherwise indicated.

Definition of AKI

AKI was defined as a >25% increase in the serum creatinine value over the baseline value 48 hours after CTA. The incidence of AKI was compared between patients given iodinated contrast medium for CTA (single exposure, CTA group) versus those given contrast medium for CTA and DSA (consecutive multiexposure, DSA group).

Statistical Analysis

The Student *t* test or the Mann-Whitney *U* test (for unevenly distributed categorical variables) was used to identify the difference in continuous variables. The difference in each of the categorical variables between the 2 groups was tested using a χ^2 or Fisher exact test. Two-tailed *P* < .05 was considered statistically significant.

RESULTS

Altogether, 181 patients with AIS were included in this study (Figure and Table 1), of whom 87 underwent CTA examinations and 94 underwent both CTA and DSA examinations. All patients were given intravenous normal saline for hydration.

The mean serum creatinine levels are shown in Table 2. Nine patients (5.0%) met the diagnostic criteria for AKI: 2 in the CTA group (2.3%) and 7 in the DSA group (7.4%) (*P* = .172). On

Table 2: Incidence of acute kidney injury in 2 study cohorts

	CTA (n = 87)	CTA + DSA (n = 94)	P Value
Baseline Cr (mg/dL)	0.84 ± 0.21	0.90 ± 0.36	.137
48-Hour Cr (mg/dL)	0.82 ± 0.19	0.98 ± 0.91	.064
ΔCr (mg/dL)	−0.02 ± 0.13	0.10 ± 0.79	.169
AKI (No.) (%)	2 (2.3)	7 (7.4)	.172
Contrast for CTA (mL) (mean)	95.0 ± 6.9	94.0 ± 7.5	.369
Contrast for DSA (ml) (mean)	/	93.4 ± 15.7	/
Total contrast (mL) (mean)	95.02 ± 6.85	187.04 ± 15.68	.000

Note:—/ indicates non-applicable.

average, patients with AKI had creatinine level increases: 0.24 ± 0.06 mg/dL (31.0% ± 6.9%) in the CTA group and 1.71 ± 2.42 mg/dL (131.6% ± 160.2%) in the DSA group.

DISCUSSION

This prospective study showed that the additional use of contrast for endovascular treatment after CTA did not increase the incidence of AKI, consistent with the results of previous studies.^{10–15}

Although the study was designed prospectively, we did not expect that the postimaging laboratory studies would be unavailable for patients with mild symptoms who left the hospital early. Loss of patients presents a potential risk of biasing the results. In addition, the prevalence of underlying medical comorbidities, such as atrial fibrillation and heart failure, was higher in the DSA group, which may predispose the patients to develop AKI.

There was no statistically significant difference in AKI incidence between the CTA and DSA groups, though a trend toward a higher incidence of AKI was observed with consecutive, multi-dose use of contrast (7.4% versus 2.3%). We agree that the benefits of the endovascular treatment most likely outweigh the potential risks of AKI because these benefits were confirmed in 5 prior trials.^{4–8} We do think that controlling the total volume of contrast medium during the endovascular treatment is still necessary.

The definition of AKI varied in previous studies, ranging from an increase in the serum creatinine level of 25%–50% from the baseline level to an absolute increase of 0.3 or 0.5 mg/dL.^{10–15} In the current study, we chose a >25% increase in the serum creatinine level as the threshold for an AKI diagnosis, which was more sensitive than the criterion of a >50% increase or a >0.5-mg/dL increase, and it may have led to a higher incidence of AKI (7.4% in the DSA group) compared with the rate of AKI reported in previous studies (0%–9%) with varying standards.^{10–15}

CONCLUSIONS

This prospective study showed that consecutive, multidose use of contrast for CTA and DSA did not significantly increase the rate of AKI in patients with AIS compared with the 1-time use of contrast for CTA. The trend toward an increased AKI incidence after using more contrast should be further investigated.

REFERENCES

1. Brinjikji W, Demchuk AM, Murad MH, et al. **Neurons over nephrons: systematic review and meta-analysis of contrast-induced nephropathy in patients with acute stroke.** *Stroke* 2017;48:1862–68 CrossRef Medline
2. Ehrlich ME, Turner HL, Currie LJ, et al. **Safety of computed tomographic angiography in the evaluation of patients with acute stroke: a single-center experience.** *Stroke* 2016;47:2045–50 CrossRef Medline

3. Demel SL, Grossman AW, Khoury JC, et al. **Association between acute kidney disease and intravenous dye administration in patients with acute stroke: a population-based study.** *Stroke* 2017;48:835–39 CrossRef Medline
4. Berkhemer OA, Fransen PS, Beumer D, et al. **A randomized trial of intraarterial treatment for acute ischemic stroke.** *N Engl J Med* 2015;372:11–20 CrossRef Medline
5. Campbell BC, Mitchell PJ, Kleinig TJ, et al; EXTEND-IA Investigators. **Endovascular therapy for ischemic stroke with perfusion-imaging selection.** *N Engl J Med* 2015;372:1009–18 CrossRef Medline
6. Goyal M, Demchuk AM, Menon BK, et al; ESCAPE Trial Investigators. **Randomized assessment of rapid endovascular treatment of ischemic stroke.** *N Engl J Med* 2015;372:1019–30 CrossRef Medline
7. Jovin TG, Chamorro A, Cobo E, et al; REVASCAT Trial Investigators. **Thrombectomy within 8 hours after symptom onset in ischemic stroke.** *N Engl J Med* 2015;372:2296–306 CrossRef Medline
8. Saver JL, Goyal M, Bonafe A, et al; SWIFT PRIME Investigators. **Stent-retriever thrombectomy after intravenous t-PA vs. t-PA alone in stroke.** *N Engl J Med* 2015;372:2285–95 CrossRef Medline
9. Rao QA, Newhouse JH. **Risk of nephropathy after intravenous administration of contrast material: a critical literature analysis.** *Radiology* 2006;239:392–97 CrossRef Medline
10. Krol AL, Dzialowski I, Roy J, et al. **Incidence of radiocontrast nephropathy in patients undergoing acute stroke computed tomography angiography.** *Stroke* 2007;38:2364–66 CrossRef Medline
11. Hall SL, Munich SA, Cress MC, et al. **Risk of acute kidney injury associated with neuroimaging obtained during triage and treatment of patients with acute ischemic stroke symptoms.** *J Neurointerv Surg* 2016;8:1231–34 CrossRef Medline
12. Sharma J, Nanda A, Jung RS, et al. **Risk of contrast-induced nephropathy in patients undergoing endovascular treatment of acute ischemic stroke.** *J Neurointerv Surg* 2013;5:543–45 CrossRef Medline
13. Loh Y, McArthur DL, Vespa P, et al. **The risk of acute radiocontrast-mediated kidney injury following endovascular therapy for acute ischemic stroke is low.** *AJNR Am J Neuroradiol* 2010;31:1584–87 CrossRef Medline
14. Lima FO, Lev MH, Levy RA, et al. **Functional contrast-enhanced CT for evaluation of acute ischemic stroke does not increase the risk of contrast-induced nephropathy.** *AJNR Am J Neuroradiol* 2010;31:817–21 CrossRef Medline
15. Ahmad N, Nayak S, Jadun C, et al. **Mechanical thrombectomy for ischaemic stroke: the first UK case series.** *PLoS One* 2013; 8:e82218 CrossRef Medline

Clot Burden Score and Early Ischemia Predict Intracranial Hemorrhage following Endovascular Therapy

V. Yogendrakumar, F. Al-Ajlan, M. Najm, J. Puig, A. Calleja, S.-I. Sohn, S.H. Ahn, R. Mikulik, N. Asdaghi, T.S. Field, A. Jin, T. Asil, J.-M. Boulanger, M.D. Hill, A.M. Demchuk, B.K. Menon, and D. Dowlatshahi, on behalf of the INTERRSeCT Investigators



ABSTRACT

BACKGROUND AND PURPOSE: Intracranial hemorrhage is a known complication following endovascular thrombectomy. The radiologic characteristics of a CT scan may assist with hemorrhage risk stratification. We assessed the radiologic predictors of intracranial hemorrhage following endovascular therapy using data from the INTERRSeCT (Identifying New Approaches to Optimize Thrombus Characterization for Predicting Early Recanalization and Reperfusion With IV Alteplase and Other Treatments Using Serial CT Angiography) study.

MATERIALS AND METHODS: Patients undergoing endovascular therapy underwent baseline imaging, postprocedural angiography, and 24-hour follow-up imaging. The primary outcome was any intracranial hemorrhage observed on follow-up imaging. The secondary outcome was symptomatic hemorrhage. We assessed the relationship between hemorrhage occurrence and baseline patient characteristics, clinical course, and imaging factors: baseline ASPECTS, thrombus location, residual flow grade, collateralization, and clot burden score. Multivariable logistic regression with backward selection was used to adjust for relevant covariates.

RESULTS: Of the 199 enrolled patients who met the inclusion criteria, 46 (23%) had an intracranial hemorrhage at 24 hours. On multivariable analysis, postprocedural hemorrhage was associated with pretreatment ASPECTS (OR, 1.56 per point lost; 95% CI, 1.12–2.15), clot burden score (OR, 1.19 per point lost; 95% CI, 1.03–1.38), and ICA thrombus location (OR, 3.10; 95% CI, 1.07–8.91). In post hoc analysis, clot burden scores of ≤ 3 (sensitivity, 41%; specificity, 82%; OR, 3.12; 95% CI, 1.36–7.15) and pretreatment ASPECTS ≤ 7 (sensitivity, 48%; specificity, 82%; OR, 3.17; 95% CI, 1.35–7.45) robustly predicted hemorrhage. Residual flow grade and collateralization were not associated with hemorrhage occurrence. Symptomatic hemorrhage was observed in 4 patients.

CONCLUSIONS: Radiologic factors, early ischemia on CT, and increased CTA clot burden are associated with an increased risk of intracranial hemorrhage in patients undergoing endovascular therapy.

ABBREVIATIONS: aOR = adjusted OR; CBS = clot burden score; EVT = endovascular therapy; ICH = intracranial hemorrhage

With the results of the Clinical Mismatch in the Triage of Wake-up and Late Presenting Strokes Undergoing Neurointervention with Trevo (DAWN) and Endovascular Therapy

Following Imaging Evaluation for Ischemic Stroke 3 (DEFUSE-3) trials, the use of endovascular therapy (EVT) for large-vessel occlusion stroke will continue to increase as we transition from time-to tissue-based decision-making.^{1,2} While there is great potential to prevent disability and mortality, procedural risks still remain. Of note, post-EVT intracranial hemorrhage (ICH) con-

Received November 23, 2018; accepted after revision February 11, 2019.

From the Department of Medicine (Neurology) (V.Y., D.D.), University of Ottawa and Ottawa Hospital Research Institute, Ottawa, Canada; Department of Neurosciences (F.A.-A.), King Faisal Specialist Hospital and Research Center, Riyadh, Saudi Arabia; Calgary Stroke Program (M.N., M.D.H., A.M.D., B.K.M.), Department of Clinical Neurosciences, University of Calgary, Calgary, Canada; Institut de Diagnostic per la Imatge (J.P.), Girona Biomedical Research Institute, University Hospital Dr Josep Trueta, Girona, Spain; Department of Neurology (A.C.), Stroke Unit, Hospital Clínico Universitario de Valladolid, Universidad de Valladolid, Valladolid, Spain; Department of Neurology (S.-I.S.), Keimyung University, Daegu, Republic of Korea; Department of Neurology (S.H.A.), Chosun University School of Medicine and Hospital, Gwangju, Republic of Korea; International Clinical Research Center (R.M.), St. Anne's University Hospital, Brno, Czech Republic; Department of Neurology (N.A.), Miller School of Medicine, University of Miami, Miami, Florida; Division of Neurology (T.S.F.), Vancouver Stroke Program, University of British Columbia, Vancouver, Canada; Division of Neurology (A.J.), Queen's University, Kingston, Canada; Bezmi-alem Vakif Üniversitesi Nöroloji (T.A., J.-M.B.), Istanbul, Turkey; and Department of Medicine (J.-M.B.), Charles LeMoine Hospital, Greenfield Park, Canada.

INTERRSeCT was originally funded by an operating grant from the Canadian Institutes of Health Research. Dr Dowlatshahi was funded by a University of Ottawa Department of Medicine Clinician-Scientist Research Chair award and a Heart and Stroke Foundation of Canada New Investigator Award. Dr Yogendrakumar is supported by the Queen Elizabeth II Graduate Scholarship for Science and Technology and the Canadian Institutes of Health Research Banting and Best Graduate Scholarship. Dr Mikulik was supported by No. LQ1605 from the National Program of Sustainability II (MEYS CR) and by The International Clinical Research Center of St. Anne's University Hospital in Brno No. CZ.1.05/1.1.00/02.0123 (Operační program Výzkum a vývoj pro inovace).

Please address correspondence to Vignan Yogendrakumar, MD, Division of Neurology, University of Ottawa, Rome C2182, The Ottawa Hospital: Civic Campus, 1053 Carling Ave, Ottawa, ON, Canada. K1Y4E9; e-mail: vyogendrakumar@toh.on.ca

Indicates open access to non-subscribers at www.ajnr.org

<http://dx.doi.org/10.3174/ajnr.A6009>

tinues to be observed consistently across studies.³ The incidence of intracranial hemorrhage varies from 9% to 25%.⁴ In recent randomized controlled trials, symptomatic hemorrhage was observed in 4%–8% of patients^{1,2,5}; in nonrandomized studies, it was as high as 16%.^{4,6,7}

Baseline imaging can help predict ICH following EVT.^{6,7} Low ASPECTS on presentation, low cerebral blood volume on perfusion, and thrombus length are associated with an increased risk of ICH following EVT.⁷⁻¹⁰ It remains to be seen whether emerging scores such as the clot burden score (CBS), residual flow grade, and collateral grade similarly predict post-EVT ICH because these scores may be more practical for clinicians in the acute setting.¹¹ This knowledge may assist with pre-EVT prognostication and in the selection of borderline or “off-protocol”/higher risk individuals. The objective of our study was to investigate the predictors of ICH after EVT, with a focus on identifying imaging factors that may assist with risk stratification.

MATERIALS AND METHODS

Local research ethics board approval was obtained at all enrolling sites as part of the Identifying New Approaches to Optimize Thrombus Characterization for Predicting Early Recanalization and Reperfusion with IV Alteplase and Other Treatments Using Serial CT Angiography (INTERRSeCT) study.¹² Participants provided written consent. Data can be obtained from the senior author on reasonable request.

Patients

Patients were participants enrolled in the INTERRSeCT study.¹² Briefly, INTERRSeCT was a prospective multicenter observational cohort study assessing recanalization rates with or without intravenous alteplase in patients with acute ischemic stroke. Patients enrolled in the study received treatment with intravenous tPA, EVT, both, or neither. Any patient presenting to the emergency department with symptoms consistent with ischemic stroke 12 hours from last known well and older than 40 years of age with a baseline CTA (before alteplase bolus if that drug was given) with evidence of a symptomatic intracranial thrombus was eligible. Patients with primary vertebrobasilar artery occlusions or a presenting ASPECTS of <6 were excluded from the study. Patients were also excluded if they had mRS > 2 at baseline, renal impairment (creatinine clearance level, <60 mL/min), contrast allergy, or hypoglycemia (serum glucose level, <2 mmol/L), or if they were unlikely to participate in follow-up. For this substudy, patients treated with IV tPA alone were excluded.

Imaging Evaluation and Treatment

Each patient was examined with noncontrast CT to exclude intracranial hemorrhage and to estimate signs of early ischemia via ASPECTS. Baseline CTA was used to identify acute occlusions in the anterior circulation and the following clot characteristics: thrombus location, CBS, residual flow grade, and collateralization grade. The CBS is a quantified assessment of the intracranial thrombus burden within the anterior circulation.¹³ Starting at 10, points are deducted on the basis of the loss of contrast opacification on CTA. Two points are deducted for contrast opacification within the supraclinoid ICA, proximal M1 MCA, or distal M1

MCA. One point is subtracted for opacification within the infraclinoid ICA, M2 branches of the MCA, or A1 segment of the anterior cerebral artery. A score of zero indicates occlusion of all major anterior circulation arteries. Residual flow was defined as the presence of attenuated contrast signal through the clot and was categorized as the following: Grade 0 is complete absence of contrast attenuation (no residual flow); grade 1, contrast attenuation denser than the surrounding brain parenchyma; and grade 2, a tiny lumen or streak of well-defined contrast is observed.¹⁴ Collaterals were graded as “good,” “intermediate,” or “poor” as per the Endovascular Treatment for Small Core and Proximal Occlusion Ischemic Stroke (ESCAPE) protocol.¹⁵ Clinical stroke severity was measured via the NIHSS at initial presentation, post-procedure, and at 24 hours. Follow-up at 24 hours was performed with MR imaging or CT. To maintain a pragmatic study design, participating sites were not required to use dual-energy CT. All imaging was sent to a core laboratory at the University of Calgary and reviewed by blinded study investigators.

Primary and Secondary Outcomes

The primary outcome of this study was any new intracranial hemorrhage diagnosed at 24-hour follow-up imaging. ICH was classified per the Heidelberg Bleeding system.¹⁶ Briefly, the Heidelberg system is based on the original European Cooperative Acute Stroke Study III definitions.¹⁷ To better reflect ICH in the context of intra-arterial therapy, hemorrhages are categorized into 5 major groups: 1a (hemorrhagic infarction [HI] 1), 1b (HI2), 1c (parenchymal hemorrhage [PH] 1), 2 (PH2), and 3 (other: remote ICH, intraventricular hemorrhage, subarachnoid, or subdural hemorrhage).¹⁸ Secondary outcome was symptomatic hemorrhage, defined as intracranial hemorrhage associated with an NIHSS \geq 4 between the postprocedural assessment and 24-hour follow-up.

Statistical Analysis

Associations among patient characteristics (demographics, medical history, stroke severity, serum biomarkers), clinical course, imaging characteristics, and the occurrence of any intracranial hemorrhage were explored with the Fisher exact test, ANOVA, and Mann-Whitney *U* test, as appropriate. Factors with marginal significance ($P < .1$) were considered for inclusion in multivariable modeling. Continuous variables that did not meet the linearity assumption were categorized into quantiles, dichotomous variables or categorical variables. Collinearity was assessed using pair-wise correlations. Variables with a Spearman correlation of >0.25 were further assessed using 2-variable logistic regression models. Variables with confidence interval widening were assessed in separate multivariable models. Multivariable logistic regression with backward selection was performed to assess independent predictors of postprocedural intracranial hemorrhage. In post hoc analysis, radiologic score variables that were found to be statistically significant underwent further assessment via a receiver operating characteristic curve, and Youden’s index was used to determine a clinically relevant threshold that predicts postprocedural hemorrhage. Statistical analysis was performed using SPSS, Version 25.0 (IBM, Armonk, New York) and SAS, Version 9.4 (SAS Institute, Cary, North Carolina).

Table 1: Exploratory analysis of patients stratified by hemorrhage occurrence at 24-hour follow-up^a

	Hemorrhage on 24-Hour Follow-Up (n = 46)	No Hemorrhage (n = 153)	P Value
Age (yr)	71 (63–77)	69 (59–78)	.875
Female (No.) (%)	27 (56.5%)	62 (40.5%)	.055
Medical history (No.) (%)			
Hypertension	31 (67.4%)	86 (56.2%)	.177
Previous stroke/TIA	4 (8.7%)	29 (18.9%)	.101
Antiplatelet use	13 (28.3%)	53 (34.6%)	.420
Anticoagulant use	6 (13.0%)	26 (16.9%)	.523
Clinical information			
Serum glucose level (mmol/L)	7.2 (6.1–8.3)	6.2 (5.5–7.2)	<.001
Low density lipoprotein level ^b	2.1 (1.5–2.9)	2.3 (1.9–2.9)	.348
International normalized ratio	1.0 (0.9–1.1)	1.0 (1.0–1.1)	.756
Partial thromboplastin time (sec) ^c	27 (24–31)	28 (25–30)	.985
Platelet count	205 (159–248)	200 (166–247)	.788
Clinical course			
Baseline NIHSS	19 (15–21)	17 (12–20)	.084
Systolic blood pressure (mm Hg) ^d	148 (128–167)	140 (125–160)	.306
Administration of IV tPA (No.) (%)	35 (76.1%)	125 (81.7%)	.400
General anesthesia (No.) (%)	4 (9.3%)	12 (8.4%)	.852
Recanalization (No.) (%)	41 (89.1%)	144 (94.1%)	.246
Onset to recanalization (min)	203 (141–314)	150 (111–216)	.001
Imaging			
Baseline ASPECTS ^c	8 (7–9)	9 (8–10)	<.001
CBS ^c	4 (1–6)	6 (4–8)	.014
Location of occlusion (No.) (%)			
Internal carotid artery	21 (45.7%)	40 (26.1%)	.012
Proximal M1 segment	14 (30.4%)	51 (33.3%)	.713
Distal M1 segment	5 (10.9%)	29 (19.0%)	.201
M2 horizontal segment	3 (6.5%)	24 (15.7%)	.111
M2 Sylvian segment	3 (6.5%)	9 (5.9%)	.873
Residual flow grade (No.) (%)			
Grade 0	41 (89.1%)	123 (80.4%)	.355
Grade 1	3 (6.5%)	14 (9.2%)	
Grade 2	2 (4.4%)	16 (10.5%)	
Collateral grade (No.) (%)			
Good	9/14 (64.3%)	44/61 (72.1%)	.664
Intermediate	4/14 (28.6%)	11/61 (18.0%)	
Poor	1/14 (7.1%)	6/61 (9.8%)	

^a Values are median (interquartile range) unless otherwise stated.

^b Missing 12 values.

^c Missing 3 values.

^d Missing 2 values.

RESULTS

Of the 655 patients initially enrolled in the INTERRSeCT study, 199 were included in the primary analysis. Three hundred ninety-seven patients were not treated with mechanical thrombectomy. Forty-nine patients with vertebrobasilar occlusions, baseline modified Rankin Scale scores of > 2 , and serum creatinine clearance levels of < 60 mL/min were also excluded. Ten patients were excluded from analysis due to a presenting ASPECTS of 1–5, scores that would normally have excluded these patients from mechanical thrombectomy on the basis of selection criteria of the major treatment trials.^{2,15,19} The median age of the primary analysis population was 70 years (interquartile range, 59–78 years), and the median NIHSS score at initial presentation was 17 (interquartile range, 13–21). One hundred sixty of 199 (80%) patients received IV tPA along with mechanical thrombectomy. Forty-six patients (23%) had an ICH on 24-hour follow-up imaging. The breakdown of ICH subtypes is as follows: 1a (52.2%), 1b (17.4%),

1c (8.7%), 2 (19.6%), and 3 (2.2%). Only 4 of the 46 hemorrhage events were symptomatic (9%). Thirty patients with hemorrhage had a poor clinical outcome at 3 months (mRS 3–6). Patients with a postprocedural hemorrhage were associated with poor outcome (43% versus 12%, $P < .001$). The mean time to follow-up imaging was 24.4 ± 9.5 hours. There was no significant difference in mean follow-up time between patients positive for and negative for ICH ($P = .86$). MR imaging was used for follow-up imaging in 69 (35%) patients.

The associations between baseline patient characteristics and ICH occurrence are highlighted in Table 1. On univariate analysis, serum glucose and time to recanalization were higher in patients with ICH than in those without. Both ASPECTS and clot burden score were lower (indicating more early ischemia and increased clot burden, respectively) in patients with ICH. Occlusions located more proximally (eg, in the ICA) were associated with increased odds of post-EVT ICH. No significant relationship was observed among residual flow grade, collateralization, and hemorrhage incidence.

Collinearity between CBS and clot location was suspected on the basis of significant pair-wise correlation (Spearman rank correlation, 0.87; $P < .001$) and confidence interval widening in 2-variable logistic models. The median CBSs for the ICA and proximal M1 locations were 1 and 6, respectively. The CBS for the remaining locations (distal M1, M2 horizontal, M2 Sylvian) ranged from 6 to 9. Clot location was included

in an alternate multivariable regression model in which the clot burden score was not included (Table 2). No collinearity between CBS and time to recanalization was observed, and there was no relationship between CBS and a successful final recanalization state.

If we adjusted for the relevant covariates, pretreatment ASPECTS (adjusted OR [aOR], 1.56 per point lost; 95% CI, 1.12–2.15) and clot burden score (aOR, 1.19 per point lost; 95% CI, 1.03–1.38) were associated with postprocedural hemorrhage. ICA occlusions were associated with a 3.10 times increased odds of postprocedure hemorrhage (95% CI, 1.07–8.91). Clinically, female sex (aOR, 2.34; 95% CI, 1.04–5.29), an elevated serum glucose level (aOR, 1.28 per 1 mmol/L increase; 95% CI, 1.09–1.51 mmol/L), and a prolonged time to recanalization (aOR, 1.33 per 60 minutes; 95% CI, 1.02–1.74 minutes) increased the risk of hemorrhage.

Table 2:—Multivariable analysis—predictors of intracranial hemorrhage after endovascular therapy

	Model 1 ^a			Model 2 ^b		
	aOR	95% CI	P Value	aOR	95% CI	P Value
Clinical information						
Female sex	2.34	1.04–5.29	.040	2.43	1.07–5.52	.033
Serum glucose level (per 1 mmol/L increase)	1.28	1.09–1.51	.003	1.27	1.07–1.50	.007
Onset to recanalization (per 60 min)	1.31	0.99–1.71	.052	1.33	1.02–1.74	.037
Imaging						
Baseline ASPECTS (per point lost)	1.56	1.12–2.15	.008	1.57	1.13–2.18	.007
CBS (per point lost)	1.19	1.03–1.38	.017	—	—	—
ICA clot location	—	—	—	3.10	1.07–8.91	.035
Proximal M1 MCA location	—	—	—	2.04	0.69–6.05	.197

Note: — indicates that this variable is not included in that particular model.

^a Adjusted also for baseline NIHSS.

^b Additional adjustment of distal M1 MCA location, M2 MCA horizontal clot location, and M2 MCA Sylvian clot location.

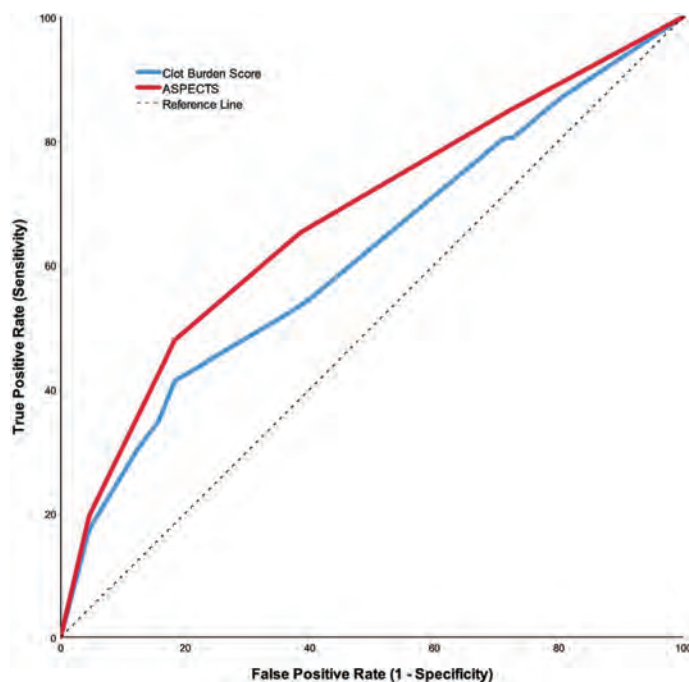


FIGURE. Receiver operating characteristic curves. Curves for baseline ASPECTS (area under the curve, 0.68; 95% confidence interval: 0.58–0.77) and CBS (area under the curve, 0.62; 95% confidence interval: 0.52–0.72).

Baseline ASPECTS and CBS were selected for post hoc analysis. The receiver operating characteristic curves comparing these 2 radiologic scores with hemorrhage occurrence are shown in the Figure. According to Youden’s index, the mathematically optimal cut-point for ASPECTS was ≤ 7 (sensitivity, 48%; specificity, 82%). Adjusted for relevant covariates, ASPECTS ≤ 7 was associated with a 3.17 times increased odds of ICH (95% CI, 1.35–7.45). Likewise, the ideal optimal cut-point for CBS was ≤ 3 (sensitivity, 41%; specificity, 82%; OR, 3.12; 95% CI, 1.36–7.15), indicative of extensive clot burden.

DISCUSSION

Our study assessed whether imaging features of large-vessel occlusion could help identify patients who are at high risk of post-EVT ICH. In a prospective cohort representative of the real-world application of EVT, we found that lower pretreatment ASPECTS, ICA clot location, and increased clot burden independently predicted ICH. Our study suggests that imaging features may be helpful for prognostication and risk stratification for EVT.

The findings of pretreatment ASPECTS affecting the risk of hemorrhage are in keeping with previous studies and provide further evidence that patients presenting with increasing amounts of early ischemia are at risk of developing postprocedural hemorrhage.^{7,20,21} States of relative hyperglycemia have been previously associated with postprocedural hemorrhage, and our findings are in line with previous work in this area.^{22,23} Prolonged symptom-to-recanalization times have also been previously associated with postprocedural hemorrhage and may aid in bedside prognostication.⁷ We hypothesize that a prolonged time to recanalization allows more time for the development of ischemia, ultimately increasing the risk of hemorrhage formation. Technical factors that could be associated with an increased time to recanalization, such as an increased number of stent-retriever passes, may play a contributing role as well.^{7,24}

The CBS is a surrogate representation of both thrombus length and location.¹¹ Accordingly, CBS was colinear with thrombus location. This idea is supported by the low clot burden scores observed in the ICA and proximal M1 locations and the increased

risk of ICH associated with the ICA thrombus location in our alternate multivariable model. Our findings suggest that proximal occlusions in the ICA will often exhibit a high clot burden, thereby increasing the risk of hemorrhage in this particular patient subgroup. This finding, however, does not mean that clot burden equates to a difficult recanalization because we found no relationship among clot burden, time to recanalization, or successful recanalization.

Our findings complement safety data recently published from the Highly Effective Reperfusion evaluated in Multiple Endovascular Stroke Trials (HERMES) collaboration, a pooled patient-level analysis of the 7 major randomized controlled EVT trials.²¹ In this analysis, clot burden score, pooled into 3 groups (8–10, 5–7, 0–4), was not associated with symptomatic ICH. The symptomatic ICH event rate in INTERRSeCT was relatively low, and we therefore cannot comment on the associations between CBS and symptomatic ICH. However, asymptomatic hemorrhages are associated with poor outcome,²⁵ and postprocedural ICH occurrence is still an important contributor to clinical outcome, symptomatic or not. While the risk of hemorrhage increases with certain locations and extensive clot burden ($CBS \leq 3$), it is exactly these same patients who stand to benefit the most from EVT. Thus, our findings are important prognostic elements that can be discussed with patients and their families, even if they do not specifically influence the decision to offer EVT.

We expected to see an increased risk of hemorrhage in patients undergoing combined therapy; this was not observed. If IV tPA does not increase the risk of ICH, the size of the brain injury may ultimately have the largest influence on hemorrhagic transformation risk^{7,8,10}; this notion is further supported by our results. Furthermore, our study supports the safety of combined therapy and provides additional context for the ongoing debate around whether EVT alone should be offered instead of combined therapy.²⁶

Our study has several limitations. It can be difficult to differentiate contrast staining from reperfusion hemorrhage. Contrast staining is seen in approximately one-third of patients, and unlike reperfusion hemorrhage, it does not have a negative prognosis.²⁷ For those 69 (35%) patients who underwent follow-up MR imaging, this concern is less because MR imaging can effectively differentiate blood from contrast staining.²⁸ However, for the remaining scans, CT was the primary imaging technique of choice. Ideally, dual-energy CT would be used to effectively distinguish contrast from blood,²⁹ but study sites were not required to do this. While the reported washout period of IV contrast is estimated to take place within 24–48 hours,^{29,30} studies seeking to differentiate contrast from hemorrhage have, in fact, used imaging at the 24-hour mark as a comparative end point.³⁰ In addition, a recent study by Dekeyser et al³¹ reported that follow-up CT scans performed at least 19 hours after the initial CT can differentiate contrast and hemorrhage with high specificity. The mean time to follow-up in our study was 24.4 ± 9.5 hours. Thus, while the risk of mistaking hemorrhage for contrast remains, we believe that we have reduced the risk of potential bias by strictly following our protocol timeline for follow-up imaging. Additional limitations include the use of an observational design, which may have introduced selection bias toward those patients offered EVT. Finally,

given that EVT was not yet considered standard of care, technical data on the endovascular therapy procedure (number of passes, device used, aspiration used) were not collected.

CONCLUSIONS

Imaging characteristics, namely pretreatment ASPECTS, clot burden score, and clot location, are predictive of post-EVT ICH. These radiologic factors can be acquired with relative ease during an acute stroke and therefore can be practical tools to assist with EVT prognostication and can complement risk/benefit conversations with patients and their caregivers.

Disclosures: Robert Mikulik—RELATED: Grant: Project No. LQ1605 from the National Program of Sustainability II and the project of the International Clinical Research Center of St. Anne's University Hospital in Brno No. CZ.1.05/1.1.00/02.0123 (Operační program Výzkum a vývoj pro inovace).* Thalia S. Field—RELATED: Grant: Canadian Institutes of Health Research operating funds, Comments: The research program of the Vancouver Stroke Program received a per-patient payment to offset the cost of research nurse time and non-standard-of-care neuroimaging for the INTERRSeCT study*; UNRELATED: Consultancy: Bayer Canada, Pfizer-Bristol-Myers Squibb, Servier Laboratories, Comments: Advisory Board Honoraria; Grants/Grants Pending: Canadian Institutes of Health Research, Heart and Stroke Foundation of Canada, Canadian Stroke Consortium, Bayer Canada, Boehringer-Ingelheim, Comments: Canadian Institutes of Health Research, Heart and Stroke Foundation of Canada, Canadian Stroke Consortium operating funds, Boehringer Canada operating funds, and Bayer Canada in-kind study medication*; Payment for Lectures Including Service on Speakers Bureaus: Bayer Canada, Pfizer-Bristol-Myers Squibb, Servier Laboratories, Boehringer-Ingelheim, Comments: Speakers Bureau honoraria from Bayer Canada, Pfizer-Bristol-Myers Squibb, Servier Laboratories, and Boehringer-Ingelheim Canada. Jean-Martin Boulanger—UNRELATED: Consultancy: Novartis, Bayer, Pfizer, Comments: conferences and Advisory Boards. Michael D. Hill—RELATED: Grant: Canadian Institutes of Health Research, Comments: grant to the University of Calgary. The principal Investigator was Dr A.M. Demchuk. I was a coinvestigator on the grant*; UNRELATED: Board Membership: Canadian Neuroscience Federation, Comments: not-for-profit entity; Consultancy: Boehringer-Ingelheim; Grants/Grants Pending: Medtronic, Stryker, Bayer Canada, Boehringer-Ingelheim, NoNO Inc, Canadian Institutes of Health Research, Alberta Innovates, British Heart Foundation, Comments: grants for ongoing studies; Stock/Stock Options: Calgary Scientific Inc, Comments: stock ownership. Andrew M. Demchuk—RELATED: Consulting Fee or Honorarium: Medtronic. Bijoy K. Menon—RELATED: Grant: Canadian Institutes of Health Research, Comments: operating grant.* Dar Dowlatshahi—UNRELATED: Consultancy: ApoPharma, Bayer; Payment for Lectures Including Service on Speakers Bureaus: Bristol-Myers Squibb. *Money paid to the institution.

REFERENCES

1. Albers GW, Marks MP, Kemp S, et al; DEFUSE 3 Investigators. **Thrombectomy for stroke at 6 to 16 hours with selection by perfusion imaging.** *N Engl J Med* 2018;378:708–18 CrossRef Medline
2. Nogueira RG, Jadhav AP, Haussen DC, et al; DAWN Trial Investigators. **Thrombectomy 6 to 24 hours after stroke with a mismatch between deficit and infarct.** *N Engl J Med* 2018;378:11–21 CrossRef Medline
3. Yaghi S, Willey JZ, Cucchiara B, et al; American Heart Association Stroke Council; Council on Cardiovascular and Stroke Nursing; Council on Clinical Cardiology; and Council on Quality of Care and Outcomes Research. **Treatment and Outcome of Hemorrhagic Transformation After Intravenous Alteplase in Acute Ischemic Stroke: A Scientific Statement for Healthcare Professionals from the American Heart Association/American Stroke Association.** *Stroke* 2017;48:e343–61 CrossRef Medline
4. Balami JS, White PM, McMeekin PJ, et al. **Complications of endovascular treatment for acute ischemic stroke: prevention and management.** *Int J Stroke* 2018;13:348–61 CrossRef Medline
5. Goyal M, Menon BK, van Zwam WH, et al; HERMES collaborators. **Endovascular thrombectomy after large-vessel ischaemic stroke: a meta-analysis of individual patient data from five randomised trials.** *Lancet* 2016;387:1723–31 CrossRef Medline
6. Enomoto Y, Yoshimura S, Egashira Y, et al; Committee of Endovas-

- cular Salvage for Cerebral Ultra-acute Embolism (RESCUE)-Japan Study Group. **The risk of intracranial hemorrhage in Japanese patients with acute large vessel occlusion; subanalysis of the RESCUE-Japan registry.** *J Stroke Cerebrovasc Dis* 2016;25:1076–80 CrossRef Medline
7. Hao Y, Yang D, Wang H, et al. **Predictors for symptomatic intracranial hemorrhage after endovascular treatment of acute ischemic stroke.** *Stroke* 2017;48:1203–09 CrossRef Medline
 8. Soize S, Barbe C, Kadziolka K, et al. **Predictive factors of outcome and hemorrhage after acute ischemic stroke treated by mechanical thrombectomy with a stent-retriever.** *Neuroradiology* 2013;55:977–87 CrossRef Medline
 9. Yoo AJ, Khatri P, Mocco J, et al; THERAPY Trial Investigators. **Impact of thrombus length on outcomes after intra-arterial aspiration thrombectomy in the THERAPY Trial.** *Stroke* 2017;48:1895–900 CrossRef Medline
 10. Mishra NK, Christensen S, Wouters A, et al; DEFUSE 2 Investigators. **Reperfusion of very low cerebral blood volume lesion predicts parenchymal hematoma after endovascular therapy.** *Stroke* 2015;46:1245–49 CrossRef Medline
 11. Tan IY, Demchuk AM, Hopyan J, et al. **CT angiography clot burden score and collateral score: correlation with clinical and radiologic outcomes in acute middle cerebral artery infarct.** *AJNR Am J Neuroradiol* 2009;30:525–31 CrossRef Medline
 12. Menon BK, Al-Ajlan FS, Najm M, et al. **Association of clinical, imaging, and thrombus characteristics with recanalization of visible intracranial occlusion in patients with acute ischemic stroke.** *JAMA* 2018;320:1017–26 CrossRef Medline
 13. Puetz V, Dzialowski I, Hill MD, et al; Calgary CTA Study Group. **Intracranial thrombus extent predicts clinical outcome, final infarct size and hemorrhagic transformation in ischemic stroke: the clot burden score.** *Int J Stroke* 2008;3:230–36 CrossRef Medline
 14. Mishra SM, Dykeman J, Sajobi TT, et al. **Early reperfusion rates with IV tPA are determined by CTA clot characteristics.** *AJNR Am J Neuroradiol* 2014;35:2265–72 CrossRef Medline
 15. Goyal M, Demchuk AM, Menon BK, et al; ESCAPE Trial Investigators. **Randomized assessment of rapid endovascular treatment of ischemic stroke.** *N Engl J Med* 2015;372:1019–30 CrossRef Medline
 16. von Kummer R, Broderick JP, Campbell BC, et al. **The Heidelberg Bleeding Classification: classification of bleeding events after ischemic stroke and reperfusion therapy.** *Stroke* 2015;46:2981–86 CrossRef Medline
 17. Trouillas P, von Kummer R. **Classification and pathogenesis of cerebral hemorrhages after thrombolysis in ischemic stroke.** *Stroke* 2006;37:556–61 CrossRef Medline
 18. Neuberger U, Möhlenbruch MA, Herweh C, et al. **Classification of Bleeding Events: comparison of ECASS III (European Cooperative Acute Stroke Study) and the New Heidelberg Bleeding Classification.** *Stroke* 2017;48:1983–85 CrossRef Medline
 19. Berkhemer OA, Fransen PS, Beumer D, et al. **A randomized trial of intraarterial treatment for acute ischemic stroke.** *N Engl J Med* 2015;372:11–20 CrossRef Medline
 20. Lin K, Zink WE, Tsiouris AJ, et al. **Risk assessment of hemorrhagic transformation of acute middle cerebral artery stroke using multimodal CT.** *J Neuroimaging* 2012;22:160–66 CrossRef Medline
 21. Román LS, Menon BK, Blasco J, et al. **Imaging features and safety and efficacy of endovascular stroke treatment: a meta-analysis of individual patient-level data.** *Lancet Neurol* 2018;17:895–904 CrossRef Medline
 22. Osei E, den Hertog HM, Berkhemer OA, et al; MR CLEAN Investigators. **Admission glucose and effect of intra-arterial treatment in patients with acute ischemic stroke.** *Stroke* 2017;48:1299–305 CrossRef Medline
 23. Poppe AY, Majumdar SR, Jeerakathil T, et al; Canadian Alteplase for Stroke Effectiveness Study Investigators. **Admission hyperglycemia predicts a worse outcome in stroke patients treated with intravenous thrombolysis.** *Diabetes Care* 2009;32:617–22 CrossRef Medline
 24. Bourcier R, Saleme S, Labreuche J, et al; ASTER Trial Investigators. **More than three passes of stent retriever is an independent predictor of parenchymal hematoma in acute ischemic stroke.** *J Neurointerv Surg* 2018 Nov 2. [Epub ahead of print] CrossRef Medline
 25. Dzialowski I, Pexman JH, Barber PA, et al; CASES Investigators. **Asymptomatic hemorrhage after thrombolysis may not be benign: prognosis by hemorrhage type in the Canadian alteplase for stroke effectiveness study registry.** *Stroke* 2007;38:75–79 CrossRef Medline
 26. Fischer U, Kaesmacher J, Mendes Pereira V, et al. **Direct mechanical thrombectomy versus combined intravenous and mechanical thrombectomy in large-artery anterior circulation stroke: a topical review.** *Stroke* 2017;48:2912–18 CrossRef Medline
 27. Parrilla G, García-Villalba B, Espinosa de Rueda M, et al. **Hemorrhage/contrast staining areas after mechanical intra-arterial thrombectomy in acute ischemic stroke: imaging findings and clinical significance.** *AJNR Am J Neuroradiol* 2012;33:1791–96 CrossRef Medline
 28. Greer DM, Koroshetz WJ, Cullen S, et al. **Magnetic resonance imaging improves detection of intracerebral hemorrhage over computed tomography after intra-arterial thrombolysis.** *Stroke* 2004;35:491–95 CrossRef Medline
 29. Phan CM, Yoo AJ, Hirsch JA, et al. **Differentiation of hemorrhage from iodinated contrast in different intracranial compartments using dual-energy head CT.** *AJNR Am J Neuroradiol* 2012;33:1088–94 CrossRef Medline
 30. Payabvash S, Qureshi MH, Khan SM, et al. **Differentiating intraparenchymal hemorrhage from contrast extravasation on post-procedural noncontrast CT scan in acute ischemic stroke patients undergoing endovascular treatment.** *Neuroradiology* 2014;56:737–44 CrossRef Medline
 31. Dekeyser S, Nikoubashman O, Lutin B, et al. **Distinction between contrast staining and hemorrhage after endovascular stroke treatment: one CT is not enough.** *J Neurointerv Surg* 2017;9:394–98 CrossRef Medline

Metallic Hyperdensity Sign on Noncontrast CT Immediately after Mechanical Thrombectomy Predicts Parenchymal Hemorrhage in Patients with Acute Large-Artery Occlusion

C. Xu, Y. Zhou, R. Zhang, Z. Chen, W. Zhong, X. Gong, X. Ding, and M. Lou



ABSTRACT

BACKGROUND AND PURPOSE: Parenchymal hemorrhage is a severe complication following mechanical recanalization in patients with acute ischemic stroke with large-vessel occlusion. This study aimed to assess whether the metallic hyperdensity sign on noncontrast CT performed immediately after mechanical thrombectomy can predict parenchymal hemorrhage at 24 hours.

MATERIALS AND METHODS: We included consecutive patients with acute ischemic stroke with large-vessel occlusion who underwent noncontrast CT immediately after mechanical thrombectomy between January 2014 and September 2018. The metallic hyperdensity sign was defined as a nonpetechial intracerebral hyperdense lesion (diameter, ≥ 1 cm) in the basal ganglia and a maximum CT density of >90 HU. The sensitivity, specificity, and positive and negative predictive values of the metallic hyperdensity sign in predicting parenchymal hemorrhage were calculated.

RESULTS: A total of 198 patients were included. The metallic hyperdensity sign was found in 59 (29.7%) patients, and 51 (25.7%) patients had parenchymal hemorrhage at 24 hours. Patients with the metallic hyperdensity sign are more likely to have parenchymal hemorrhage than those without it (76.3% versus 4.3%, $P < .001$). The sensitivity, specificity, positive predictive value, and negative predictive value of the metallic hyperdensity sign in predicting parenchymal hemorrhage were 88.2%, 90.5%, 76.3%, and 95.7%, respectively.

CONCLUSIONS: The presence of the metallic hyperdensity sign on noncontrast CT performed immediately after mechanical thrombectomy in patients with large-vessel occlusion could predict the occurrence of parenchymal hemorrhage at 24 hours, which might be helpful in postinterventional management within 24 hours after mechanical thrombectomy.

ABBREVIATIONS: HT = hemorrhagic transformation; MT = mechanical thrombectomy; PH = parenchymal hemorrhage

Reperfusion therapy with mechanical thrombectomy (MT) improves functional outcome in patients with acute ischemic stroke with large-vessel occlusion.¹⁻⁵ However, $>50\%$ of patients still experience unfavorable outcome.^{6,7} One of the most common reasons is hemorrhagic transformation (HT), especially parenchymal hemorrhage (PH), which is closely related to deterioration of neurologic symptoms.^{8,9} Early prediction of

HT, therefore, is important for postinterventional therapy adjustment—that is, whether to start treatment with the glycoprotein IIb/IIIa inhibitor tirofiban to prevent early re-occlusion due to endothelial damage.¹⁰

In some hospitals, immediate postinterventional non-contrast-enhanced CT has been introduced to estimate bleeding complications. Hyperdense areas may frequently be detected on NCCT after intervention.¹¹⁻¹⁴ However, such hyperdense areas on NCCT have not been well understood, and different interpretations have been reported in various publications.

For instance, Yoon et al¹³ demonstrated that intracerebral hyperdense lesions with a maximum Hounsfield unit measurement of >90 were highly associated with symptomatic hemorrhage after intra-arterial thrombolysis. On the other hand, Jang et al¹⁴ reported that the possibility of HT depended on different morphologic features of intracerebral hyperdense lesions after intra-arterial thrombolysis, and they proposed the concept of metallic hyperdensity lesions, which were closely related to a high proportion of HT after intra-arterial throm-

Received October 16, 2018; accepted after revision February 7, 2019.

From the Departments of Neurology (C.X., Y.Z., R.Z., Z.C., W.Z., X.G., M.L.) and Radiology (X.D.), the Second Affiliated Hospital of Zhejiang University, School of Medicine, Hangzhou, China.

This study was supported by the National Natural Science Foundation of China (81622017, 81471170), the National Key Research and Development Program of China (2016YFC1301503), the Science Technology Department of Zhejiang Province (2018C04011), and Fundamental Research Funds for the Central Universities (2017XZZX002-09).

Please address correspondence to Min Lou, MD, PhD, Department of Neurology, the Second Affiliated Hospital of Zhejiang University, School of Medicine, 88 Jiefang Rd, Hangzhou, 310009, China; e-mail: lm99@zju.edu.cn

Indicates open access to non-subscribers at www.ajnr.org

<http://dx.doi.org/10.3174/ajnr.A6008>

Table 1: Predictive value of characteristics of metallic hyperdensity for parenchymal hemorrhage

	AUC	95% CI	P Value	Sensitivity	Specificity	Positive Predictive Value	Negative Predictive Value
Presence of metallic hyperdensity sign	0.894	0.835–0.952	<.001	0.882	0.905	0.763	0.957

Note:—AUC indicates area under the curve.

Table 2: Comparison of characteristics between patients with and without the metallic hyperdensity sign

Characteristics	Presence of Metallic Hyperdensity Sign (n = 59)	Absence of Metallic Hyperdensity Sign (n = 139)	P Value
Age (mean) (yr)	70.5 ± 10.5	69.4 ± 12.2	.568
Female (No.) (%)	26 (44.1)	56 (40.3)	.639
Comorbid conditions			
Hypertension (No.) (%)	37 (62.7)	84 (60.4)	.874
Diabetes mellitus (No.) (%)	14 (23.7)	24 (17.3)	.326
Atrial fibrillation (No.) (%)	35 (59.3)	50 (35.9)	.003
Clinical variables			
Baseline NIHSS (median) (IQR)	15 (12–18)	14 (10–17)	.116
Onset-to-puncture time (median) (IQR) (min)	334 (237–425)	306 (213–415)	.289
Retrieval attempts (median) (IQR)	2 (1–3)	1 (1–3)	.039
Radiologic data			
Baseline infarct volume (median) (IQR) (mL)	59.9 (34.7–80.9)	46.3 (27.5–80.0)	.096
Baseline hypoperfusion volume (median) (IQR) (mL)	108.9 (79.2–153.6)	107.1 (68.0–160.0)	.639
Recanalization (No.) (%)	48 (81.4)	123 (88.4)	.181
24-Hour hemorrhagic transformation (No.) (%)	58 (98.3)	54 (38.8)	<.001
24-Hour parenchymal hemorrhage (No.) (%)	45 (76.3)	6 (4.3)	<.001

Note:—IQR indicates interquartile range.

bolysis. At present, thrombectomy has been demonstrated as an effective therapy for patients with acute ischemic stroke with large-vessel occlusion.¹⁵ However, the relationship between the occurrence of parenchymal hemorrhage at 24 hours and hyperdense lesions on NCCT immediately after thrombectomy is still unclear.

Here, we propose a new kind of metallic hyperdensity sign combining maximum Hounsfield units and morphologic features to predict PH at 24 hours. The aim of our study was to evaluate the value of the newly defined metallic hyperdensity sign following MT for predicting PH at 24 hours in patients with acute ischemic stroke with large-vessel occlusion.

MATERIALS AND METHODS

Ethics Statement

Written informed consent was obtained from each patient or an appropriate family member. The human ethics committee of the Second Affiliated Hospital of Zhejiang University approved the protocol of this study. All clinical investigations were conducted according to the principles expressed in the Declaration of Helsinki.

Patient Selection

We analyzed our prospectively collected data base for consecutive patients with acute ischemic stroke who received mechanical thrombectomy between January 2014 and September 2018, as NCCT examination immediately after mechanical thrombectomy was performed since January 2014. We enrolled patients with the following qualifications: 1) They underwent MT due to large-vessel occlusion of the anterior circulation within 24 hours post-symptom onset based on multimodal imaging, 2) they underwent postinterventional

NCCT immediately after MT, and 3) they had a follow-up CT or MR imaging at 24 hours.

Definition of the Metallic Hyperdensity Sign

All CT examinations were performed on a multidetector CT scanner with axial 5-mm section thickness. “Hyperdense lesion” was defined as the presence of high density within the brain parenchymal area. First, the hyperdense lesions on each layer were manually segmented, respectively, by 2 experienced neurologists (C.X. and Y.Z.), with the open-source software RadiAnt DICOM Viewer (<https://www.radiantviewer.com>). Second, we measured the density value (Hounsfield unit) of the segmented area on each layer and recorded the maximum value. The metallic hyperdensity sign was defined when a maximum CT density of >90 HU was identified within the non-petechial intracerebral hyperdense lesion (diameter, ≥1 cm) in the basal ganglia.

Two experienced neurologists (X.C. and Z.Y.) blinded to clinical data reviewed images for assessing the presence or absence of the metallic hyperdensity sign on NCCT independently, and the inconsistent data were reviewed by another experienced neurologist and settled by consensus discussion afterward.

Evaluation of HT and PH

HT (including hemorrhagic infarction and PH) was assessed on the basis of imaging characteristics at 24 hours after MT, referring to the European Cooperative Acute Stroke Study II (ECASS II) criteria.¹⁶ According to previous studies, intracerebral hyperdense lesions that were no longer discernible on the 24-hour follow-up CT were defined as contrast enhancement, while lesions persisting on follow-up CT were considered hemorrhagic lesions.¹⁷

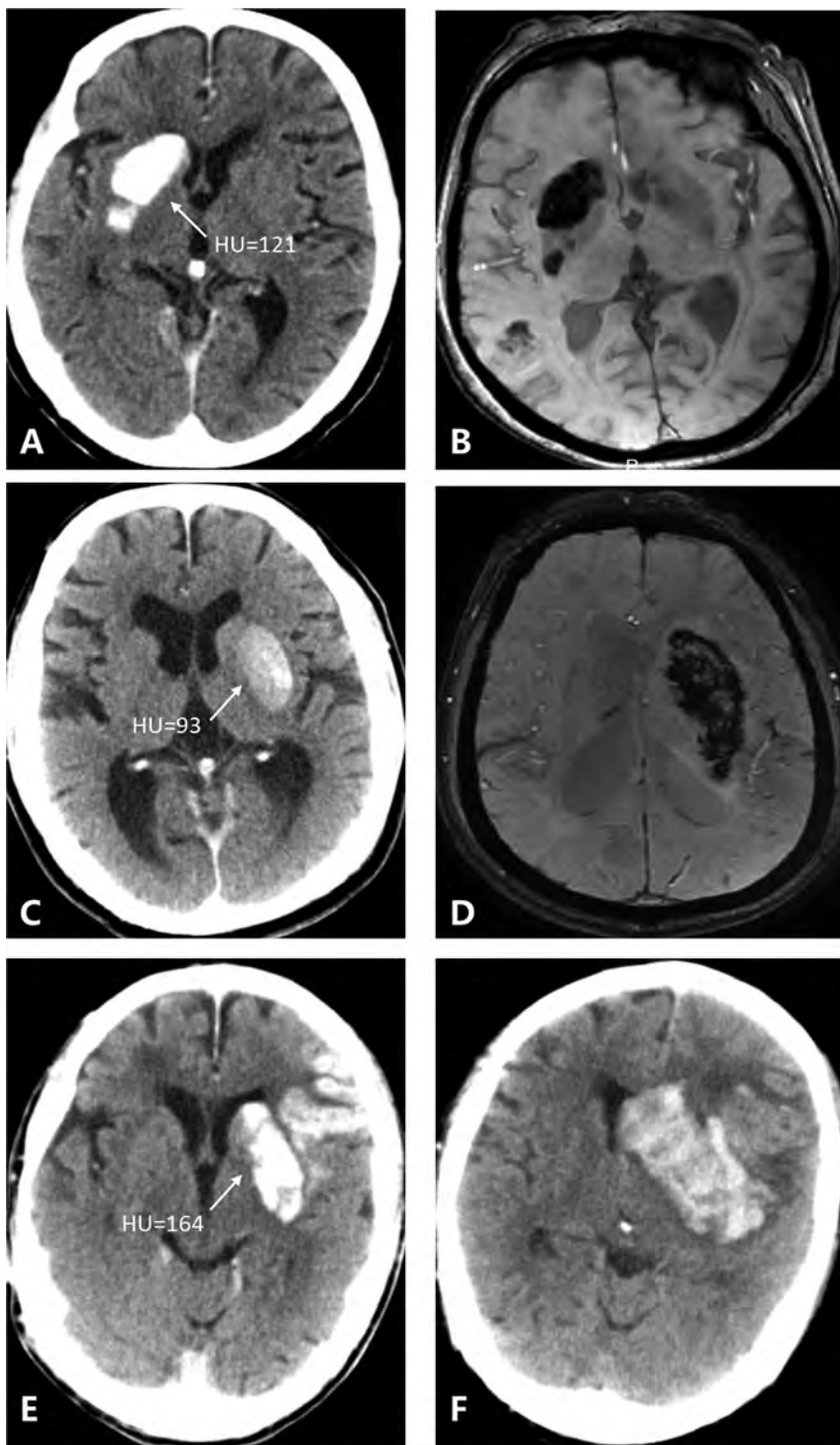


FIG 1. Three patients with 3 kinds of metallic hyperdensity signs. A, C, and E, NCCT images obtained immediately after mechanical thrombectomy. B and D, SWI at 24 hours after mechanical thrombectomy. F, NCCT image at 24 hours after mechanical thrombectomy. A 77-year-old woman with a hyperdense lesion and a maximum CT density of 121 HU in the right caudate nucleus on NCCT images immediately after mechanical thrombectomy (A) has parenchymal hemorrhage on SWI at 24 hours (B). A 71-year-old man with a hyperdense lesion and a maximum CT density of 93 HU in the left lenticular nucleus on NCCT images immediately after mechanical thrombectomy (C) has parenchymal hemorrhage on SWI at 24 hours (D). An 81-year-old man with a hyperdense lesion and a maximum CT density of 164 HU in the left lenticular nucleus on NCCT images immediately after mechanical thrombectomy (E) has parenchymal hemorrhage on the NCCT image at 24 hours (F).

Statistical Analysis

All statistical analyses were performed with the SPSS package (Version 19.0; IBM, Armonk, New York). Metric and normally

distributed variables were reported as mean \pm SD; non-normally distributed variables were reported as median and interquartile range. Categorical variables were presented as frequency (percentage). The Fisher exact test was used to compare the dichotomous variables, and the Mann-Whitney *U* test was used for the non-normally distributed continuous variables. Normally distributed continuous variables were assessed with the Student *t* test. Statistical significance was set at $P < .05$. κ statistics were used to test inter- and intrarater reliability for detecting the presence of the metallic hyperdensity sign. Receiver operating characteristic curve analysis was used to determine the predictive value.

RESULTS

A total of 198 patients were included. The mean age was 69.8 ± 11.7 years, and 82 (41.4%) were women. The median baseline NIHSS was 14 (interquartile range = 11–18). One hundred twelve (56.5%) patients had HT, and 51 (25.7%) patients had PH at 24 hours.

Intracerebral hyperdense lesions were found in 155 (78.3%) patients, among whom 59 (38.1%) patients had the metallic hyperdensity sign and the remaining 96 (61.9%) patients had a nonmetallic hyperdensity sign. Moreover, 14 (14.6%) patients had hyperdense lesions in the cortical area; 10 (10.4%), in the subcortical area; 64 (66.7%), in the basal ganglia; and 8 (8.3%), in both cortical and subcortical areas and basal ganglia. The inter- and intrarater observer agreement for assessing the presence of intracerebral hyperdense lesions ($\kappa = 0.924$, $\kappa = 0.947$) and the presence of the metallic hyperdensity sign ($\kappa = 0.874$, $\kappa = 0.912$) was good. Patients with the metallic hyperdensity sign were more likely to have PH than those without the sign (76.3% versus 4.3%; odds ratio, 71.250; odds ratio, 75.553 after adjusting for atrial fibrillation, onset to puncture time, and recanalization; $P < .001$). The sensitivity, specificity, positive predictive value, and negative predictive value of the metallic hyperdensity sign in predicting PH were 88.2% (95% CI, 79.1%–97.4%), 90.5% (95% CI, 85.7%–95.3%), 76.3% (95% CI, 65.1%–87.4%), and 95.7% (95% CI, 92.3%–99.1%), respectively (Table 1).

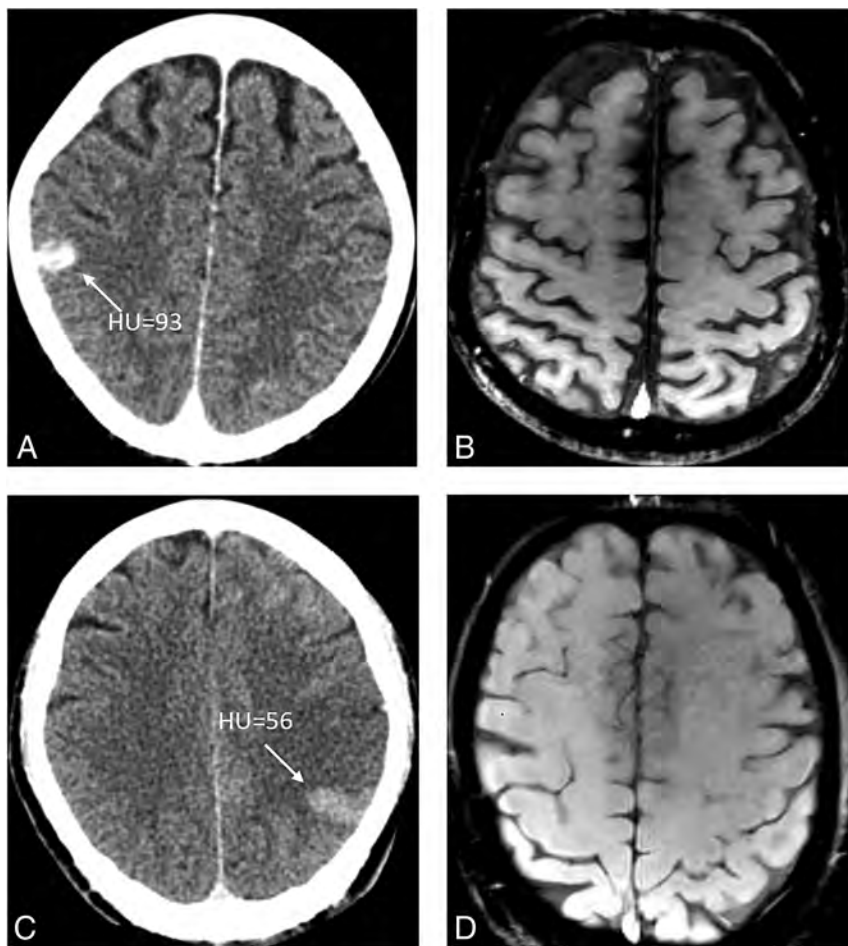


FIG 2. Two patients who show the typical cortical hyperdense lesion on NCCT immediately after MT (A and C) have no HT on follow-up SWI (B and D).

Patients with the metallic hyperdensity sign were more likely to have atrial fibrillation ($P = .003$) and underwent more retrieval attempts ($P = .039$) than those without the sign. Other demographic and clinical variables including age, sex, hypertension, diabetes mellitus, baseline NIHSS, baseline hypoperfusion volume, onset-to-puncture time, and recanalization did not significantly differ between patients with and without the metallic hyperdensity sign (Table 2).

Figure 1 shows 3 patients with 3 kinds of metallic hyperdensity signs.

DISCUSSION

Our study demonstrates that the metallic hyperdensity sign on NCCT performed immediately after MT can predict PH at 24 hours with high specificity and negative predictive value.

Intracerebral hyperdense lesions were first reported on NCCT immediately after intra-arterial thrombolysis in patients with acute ischemic stroke early in the 1990s.^{18,19} The rates of intracerebral hyperdense lesions shown on NCCT after intra-arterial reperfusion therapy varied greatly, from 32.9% to 84.2%.^{13,14,17,20} The reason for such a wide variation may be due to the differences in the definition of hyperdense lesions, number of patients, recanalization rate, and the quality of the imaging equipment.²¹ Compared with previous studies, the incidence of intracerebral hyper-

dense lesions in our center was relatively high (our center versus other centers, 83.3% versus 32.9%–84.2%); this finding may result from the relatively high recanalization rate (our center versus other centers, 86.3% versus 77.2%–80%).^{21,22} In addition, MT would increase the direct damage to the endothelium of cerebral arteries when pulling thrombus,²³ compared with intra-arterial thrombolysis, which might increase the incidence of intracerebral hyperdense lesions.

Currently, the most widely accepted hypothesis is that intracerebral hyperdense lesions are caused by leakage of contrast medium into the extracellular spaces via vessels, as a result of microvascular damage and increased permeability of the BBB.^{17,21,22} Yoon et al¹³ documented that high-density areas (>90 HU) found on NCCT after intra-arterial thrombolysis are closely associated with PH, possibly due to pathologic changes of ischemic injury to the degradation of the basal lamina, a structural barrier. Moreover, PH is the result of severe microvascular damage extended to the basal lamina. In our study, 51 (25.7%) patients had PH at 24 hours, which is higher than that in published trials such as the Multicenter Randomized Clinical trial of Endovascular treatment for

Acute ischemic stroke in the Netherlands (MR CLEAN), Endovascular Treatment for Small Core and Proximal Occlusion Ischemic Stroke (ESCAPE), Extending the Time for Thrombolysis in Emergency Neurological Deficits–Intra-Arterial (EXTEND-IA), Solitaire with the Intention for Thrombectomy as Primary Endovascular Treatment (SWIFT PRIME), and Endovascular Revascularization With Solitaire Device Versus Best Medical Therapy in Anterior Circulation Stroke Within 8 Hours (REVASCAT) at 6%, 3.6%, 11%, 5%, and 5.8%, respectively.^{1–5} However, our rate is actually based on the real-world data for mechanical thrombectomy. The median time from stroke onset to groin puncture in these above studies was not >270 minutes (4.5 hours), which, to some extent, is difficult to achieve in the real world. Indeed, in previous retrospective studies, the occurrence of PH varied greatly, from 5.9% to 23.5%.^{17,24} Another reason for the relatively higher rate of PH is the use of SWI to detect hemorrhage because SWI accounted for 48% of the 24-hour follow-up examinations, which may result in a visual overestimation in hematoma size due to susceptibility effects.²⁵

In addition, we found that the metallic hyperdensity sign was more likely in patients with atrial fibrillation and a higher number of retrieval attempts. Actually, the extent of BBB disruption was more severe in cardiogenic embolism stroke than in other stroke

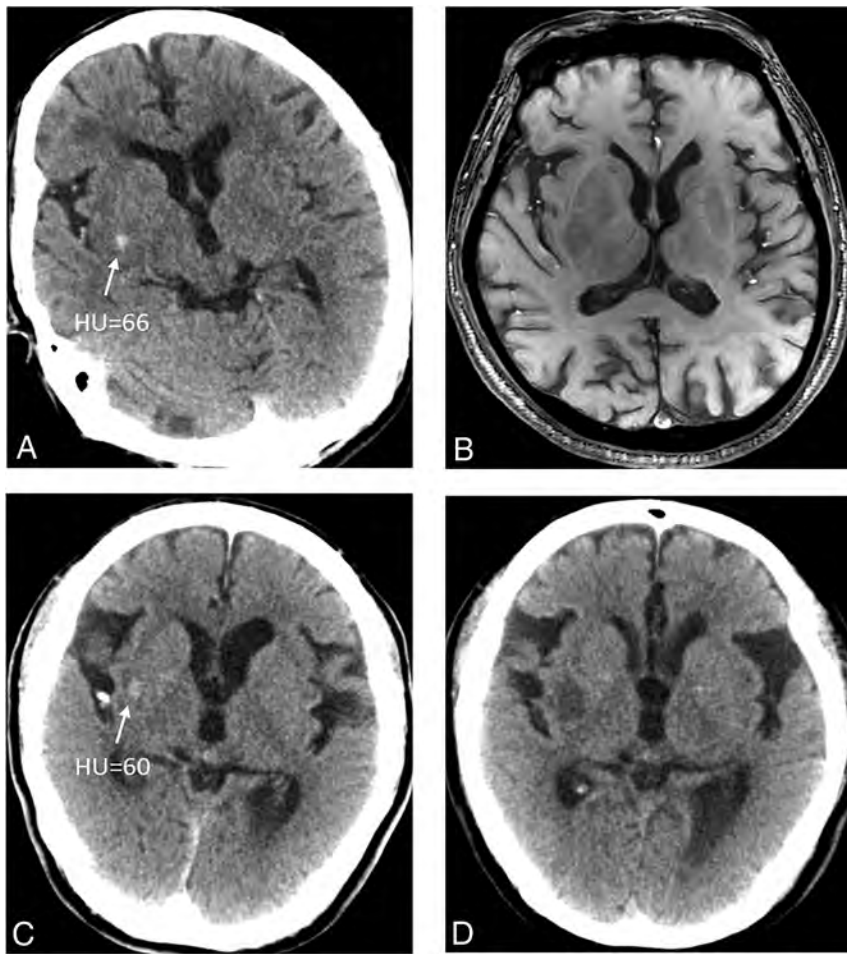


FIG 3. Two patients who show a petechial hyperdense lesion in the basal ganglia on NCCT immediately after MT (A and C) have no HT on follow-up SWI (B) and the remaining low densities on follow-up NCCT (D).

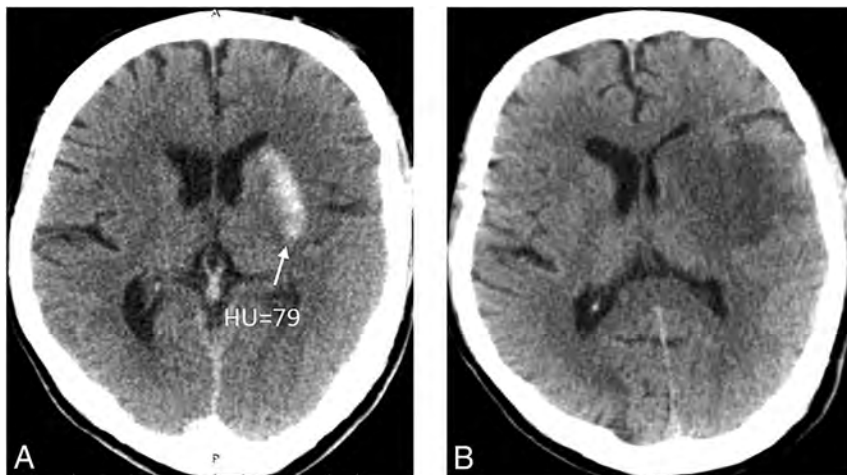


FIG 4. A patient who shows a nonpetechial hyperdense lesion on NCCT immediately after MT (A) has no HT on follow-up NCCT and the remaining low densities (B).

subtypes during the hyperacute stage²⁶; with the increased number of retrieval attempts, the damage to the endothelium of cerebral arteries would be more severe.²³ Besides, previous experimental research has shown that massive HT, with the distinguishing features of a rapid extravasation of blood leading to

the compression of contiguous tissues, occurs when the BBB integrity is lost.²⁷ Therefore, we propose that the presence of our defined metallic hyperdense sign in the current study might reflect severe microvascular damage and extensive BBB disruption because the study focused on those subjects with relatively high contrast leakage, which leads to massive HT, especially PH.

To our knowledge, this is the first study focusing on both the density and extent of intracerebral hyperdense lesions on NCCT performed immediately after MT and its predictive value for PH at 24 hours. The metallic hyperdense sign, a readily available and reliable NCCT-based imaging marker, might be helpful in identifying those patients with a higher risk of PH after MT and is easily applied in clinical practice. It may not only provide prognostic information for clinicians and patients but also be helpful in clinical management after MT. For instance, patients with the metallic hyperdense sign should receive all possible care, including relatively strict blood pressure control and delayed or no antiplatelet and anticoagulation treatments.

Limitations included the retrospective nature in our single stroke center and the moderate number of cases, resulting in a potential risk of selection bias, though data were prospectively established using a stroke registry. Second, there was heterogeneity in the evaluation of PH, which was due to 2 methods of follow-up imaging (NCCT versus SWI, 52% versus 48%). Third, despite our effort to find the optimal Hounsfield unit threshold for the metallic hyperdense sign, the selection of 90 HU was still based on previous literature. In addition, 6 patients in our study without the metallic hyperdense sign on NCCT obtained immediately after MT still developed PH on follow-up images. Although the number of these patients is very small, the causes and mechanisms of this situation and the optimal HU threshold are worthy of further study.

Although a CT scan obtained at least 19–24 hours after endovascular therapy was reported as a reliable method to differentiate contrast from hemorrhage,²⁸ contrast enhancement could still be relatively dense 24 hours after thrombectomy, and the differentiation would be better with the extended time after an intervention. Finally, we did not measure BBB per-

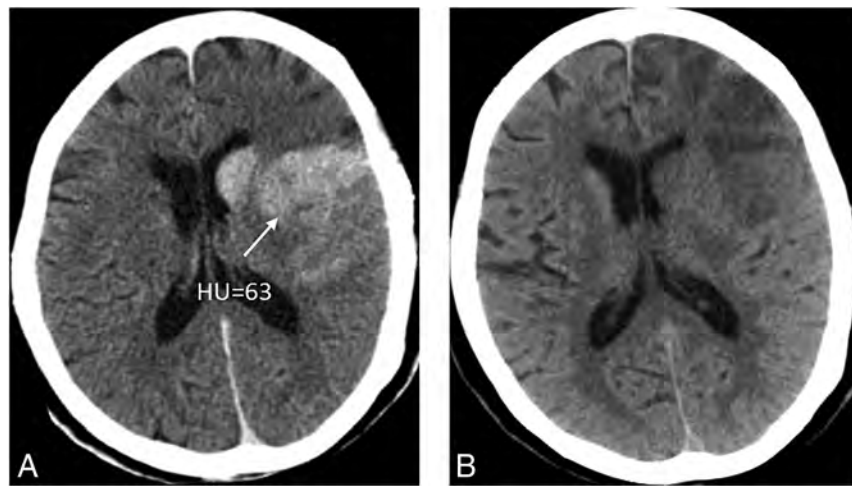


FIG 5. A patient who shows the subcortical hyperdense lesion involving both the basal ganglia and subcortical white matter on NCCT immediately after MT (A) has no HT on NCCT immediately after MT and the remaining low densities on follow-up NCCT (B).

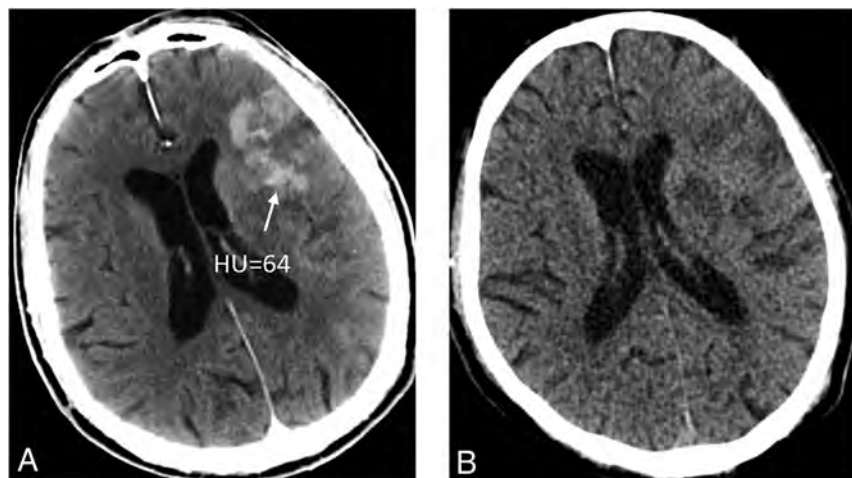


FIG 6. A patient who shows the subcortical hyperdense lesion on NCCT immediately after MT (A) but has no HT on follow-up NCCT and the remaining low densities (B).

meability on multimodal imaging, and the underlying mechanisms of hyperdense intracerebral lesions need to be clarified with further experimental and pathologic studies.

CONCLUSIONS

The NCCT-based metallic hyperdensity sign immediately after MT in patients with large-vessel occlusion may indicate a high risk of PH at 24 hours with a high specificity of 90.5% (odds ratio, 90.576; 95% CI, 85.7%–95.3%) and negative predictive value of 95.7% (odds ratio, 95.683; 95% CI, 92.3%–99.1%), which may be helpful in postinterventional management 24 hours after mechanical thrombectomy.

Disclosures: Min Lou—RELATED: Grant: National Natural Science Foundation of China (81471170 and 81622017), Fundamental Research Funds for the Central Universities (2017XZZX002-09), and the National Key Research and Development Program of China (2016YFC1301503). *Money paid to the institution.

REFERENCES

1. Berkhemer OA, Fransen PS, Beumer D, et al. **A randomized trial of intraarterial treatment for acute ischemic stroke.** *N Engl J Med* 2015; 372:11–20 CrossRef Medline
2. Campbell BC, Mitchell PJ, Kleinig TJ, et al; EXTEND-IA Investigators. **Endovascular therapy for ischemic stroke with perfusion-imaging selection.** *N Engl J Med* 2015;372:1009–18 CrossRef Medline
3. Goyal M, Demchuk AM, Menon BK, et al; ESCAPE Trial Investigators. **Randomized assessment of rapid endovascular treatment of ischemic stroke.** *N Engl J Med* 2015;372:1019–30 CrossRef Medline
4. Jovin TG, Chamorro A, Cobo E, et al; REVASCAT Trial Investigators. **Thrombectomy within 8 hours after symptom onset in ischemic stroke.** *N Engl J Med* 2015;372:2296–306 CrossRef Medline
5. Saver JL, Goyal M, Bonafe A, et al; SWIFT PRIME Investigators. **Stent-retriever thrombectomy after intravenous T-PA vs. t-PA alone in stroke.** *N Engl J Med* 2015;372:2285–95 CrossRef Medline
6. Volny O, Krajina A, Belaskova S, et al. **Mechanical thrombectomy performs similarly in real world practice: a 2016 nationwide study from the Czech Republic.** *J Neurointerv Surg* 2018;10:741–45 CrossRef Medline
7. Serles W, Gattlinger T, Mutzenbach S, et al; Austrian Stroke Unit Registry Collaborators. **Endovascular stroke therapy in Austria: a nationwide 1-year experience.** *Eur J Neurol* 2016;23:906–11 CrossRef Medline
8. Jiang S, Fei A, Peng Y, et al. **Predictors of outcome and hemorrhage in patients undergoing endovascular therapy with Solitaire stent for acute ischemic stroke.** *PLoS One* 2015;10:e0144452 CrossRef Medline

9. van Kranendonk KR, Treurniet KM, Boers AMM, et al; MR CLEAN investigators. **Hemorrhagic transformation is associated with poor functional outcome in patients with acute ischemic stroke due to a large vessel occlusion.** *J Neurointerv Surg* 2018 Oct 8. [Epub ahead of print] CrossRef Medline
10. Kellert L, Hametner C, Rohde S, et al. **Endovascular stroke therapy: tirofiban is associated with risk of fatal intracerebral hemorrhage and poor outcome.** *Stroke* 2013;44:1453–55 CrossRef Medline
11. Payabvash S, Khan AA, Qureshi MH, et al. **Detection of intraparenchymal hemorrhage after endovascular therapy in patients with acute ischemic stroke using immediate postprocedural flat-panel computed tomography scan.** *J Neuroimaging* 2016;26:213–18 CrossRef Medline
12. Payabvash S, Qureshi MH, Khan SM, et al. **Differentiating intraparenchymal hemorrhage from contrast extravasation on postprocedural noncontrast CT scan in acute ischemic stroke patients undergoing endovascular treatment.** *Neuroradiology* 2014; 56:737–44 CrossRef Medline
13. Yoon W, Seo JJ, Kim JK, et al. **Contrast enhancement and contrast extravasation on computed tomography after intra-arterial thrombolysis in patients with acute ischemic stroke.** *Stroke* 2004;35: 876–81 CrossRef Medline
14. Jang YM, Lee DH, Kim HS, et al. **The fate of high-density lesions on the non-contrast CT obtained immediately after intra-arterial thrombolysis in ischemic stroke patients.** *Korean J Radiol* 2006;7: 221–28 CrossRef Medline
15. Powers WJ, Rabinstein AA, Ackerson T, et al; American Heart Association Stroke Council. **2018 Guidelines for the Early Management of Patients with Acute Ischemic Stroke: A Guideline for Healthcare Professionals From the American Heart Association/ American Stroke Association.** *Stroke* 2018;49:e46–110 CrossRef Medline
16. Larrue V, von Kummer RR, Müller A, et al. **Risk factors for severe hemorrhagic transformation in ischemic stroke patients treated with recombinant tissue plasminogen activator: a secondary analysis of the European-Australasian Acute Stroke Study (ECASS II).** *Stroke* 2001;32:438–41 CrossRef Medline
17. Lummel N, Schulte-Altendorneburg G, Bernau C, et al. **Hyperattenuated intracerebral lesions after mechanical recanalization in acute stroke.** *AJNR Am J Neuroradiol* 2014;35:345–51 CrossRef Medline
18. Komiyama M, Nishijima Y, Nishio A, et al. **Extravasation of contrast medium from the lenticulostriate artery following local intracarotid fibrinolysis.** *Surg Neurol* 1993;39:315–19 CrossRef Medline
19. Wildenhain SL, Jungreis CA, Barr J, et al. **CT after intracranial intraarterial thrombolysis for acute stroke.** *AJNR Am J Neuroradiol* 1994;15:487–92 Medline
20. Nakano S, Iseda T, Kawano H, et al. **Parenchymal hyperdensity on computed tomography after intra-arterial reperfusion therapy for acute middle cerebral artery occlusion: incidence and clinical significance.** *Stroke* 2001;32:2042–48 CrossRef Medline
21. Parrilla G, Garcia-Villalba B, Espinosa de Rueda M, et al. **Hemorrhage/contrast staining areas after mechanical intra-arterial thrombectomy in acute ischemic stroke: imaging findings and clinical significance.** *AJNR Am J Neuroradiol* 2012;33:1791–96 CrossRef Medline
22. Tomsick T. **Hyperattenuated intracerebral lesions after mechanical recanalization in acute stroke: contrast and compare.** *AJNR Am J Neuroradiol* 2014;35:352–53 CrossRef Medline
23. Teng D, Pannell JS, Rennert RC, et al. **Endothelial trauma from mechanical thrombectomy in acute stroke: in vitro live-cell platform with animal validation.** *Stroke* 2015;46:1099–106 CrossRef Medline
24. Kim JT, Heo SH, Cho BH, et al. **Hyperdensity on non-contrast CT immediately after intra-arterial revascularization.** *J Neurol* 2012; 259:936–43 CrossRef Medline
25. Burgess RE, Warach S, Schaewe TJ, et al. **Development and validation of a simple conversion model for comparison of intracerebral hemorrhage volumes measured on CT and gradient recalled echo MRI.** *Stroke* 2008;39:2017–20 CrossRef Medline
26. Liu C, Shi F, Chen Z, et al. **Severe blood-brain barrier disruption in cardioembolic stroke.** *Front Neurol* 2018;9:55 CrossRef Medline
27. Jickling GC, Liu D, Stamova B, et al. **Hemorrhagic transformation after ischemic stroke in animals and humans.** *J Cereb Blood Flow Metab* 2014;34:185–99 CrossRef Medline
28. Dekeyser S, Nikoubashman O, Lutin B, et al. **Distinction between contrast staining and hemorrhage after endovascular stroke treatment: one CT is not enough.** *J Neurointerv Surg* 2017;9:394–98 CrossRef Medline

Endovascular Treatment for Low-Grade (Spetzler-Martin I–II) Brain Arteriovenous Malformations

 H. Baharvahdat,  R. Blanc,  R. Fahed,  S. Smajda,  G. Ciccio,  J.-P. Desilles,  H. Redjem,  S. Escalard,  M. Mazighi,  D. Chauvet,  T. Robert,  P. Sasannejad, and  M. Piotin

ABSTRACT

BACKGROUND AND PURPOSE: Surgical resection is usually considered as the first-line curative strategy for low-grade (Spetzler-Martin grade I–II) brain arteriovenous malformations because it has a high cure rate and low complications. The role of endovascular treatment remains to be clarified in this indication, especially after A Randomized Trial of Unruptured Brain Arteriovenous Malformations. Our objective was to assess the safety and efficacy of first-line endovascular treatment in low-grade brain arteriovenous malformation management at our institution.

MATERIALS AND METHODS: Patients with low-grade brain arteriovenous malformations treated primarily with embolization in our department between January 2005 and December 2015 were retrieved from our prospectively collected registry. The primary outcome was the brain arteriovenous malformation obliteration rate, and secondary outcomes were disability or death secondary to brain arteriovenous malformation embolization assessed through modification of the modified Rankin Scale.

RESULTS: Two hundred twenty-four patients completed endovascular treatment during the study period and represent our study population. Complete exclusion of brain arteriovenous malformations was achieved in 205 patients (92%), including 62.1% of brain arteriovenous malformation exclusions after a single endovascular treatment session. One patient died of a hemorrhagic complication after endovascular treatment, leading to a mortality rate of 0.4%. Twelve patients (5%) kept a permanent neurologic deficit secondary to a complication of the endovascular treatment. An overall good outcome (mRS 0–2) was reported in 179 patients (80%).

CONCLUSIONS: Endovascular treatment might be a suitable alternative to surgical resection for complete exclusion of selected low-grade brain arteriovenous malformations.

ABBREVIATIONS: BAVM = brain arteriovenous malformation; EVT = endovascular treatment

Surgery is considered the first-line treatment for low-grade (Spetzler-Martin grades I and II) brain arteriovenous malformations (BAVMs), with high cure rates (94%–100%) and low complications (0%–6%).¹ After the publication of A Randomized Trial of Unruptured Brain Arteriovenous Malformations (ARUBA) results in favor of medical conservative management,² multiple criticisms emerged.³ Notably, some authors suggested that the 3-fold increase in death or stroke in the interventional group was

at least partially due to the low rate of patients treated surgically and the preferable use of endovascular treatment (EVT). In ARUBA, low-grade BAVMs⁴ were also poorly represented (13%). To assess the safety and efficacy of EVT of low-grade BAVMs, we reviewed our experience with low-grade cerebral BAVM management at Rothschild Foundation, Paris, where embolization is the first-line therapy.

MATERIALS AND METHODS

Baseline Characteristics of Patients and BAVMs

From our prospectively collected data base, we retrieved low-grade BAVMs treated by an endovascular approach in our Interventional Neuroradiology Department between January 2005 and December 2015. Patients with low-grade BAVMs who completed all treatment procedures were enrolled in the study. We excluded the patients who had ongoing treatment or were lost during follow-up. Baseline clinical characteristics of patients were reviewed. Clinical status was assessed according to the modified Rankin Scale at the initial and follow-up visits. Cross-sectional imaging

Received September 25, 2018; accepted after revision January 8, 2019.

From the Department of Interventional Neuroradiology (H.B., R.B., R.F., S.S., G.C., J.-P.D., H.R., S.E., M.M., P.S., M.P.) and Neurosurgical Department (D.C.), Rothschild Foundation, Paris, France; and Neurosurgical Department (T.R.), Ente-Ospedaliero-Cantonale Ospedale Civico di Lugano, Lugano, Switzerland.

Clinical Study: Long Term Follow-up after Embolization of Brain Arteriovenous Malformations (MAV-endovasc), <https://clinicaltrials.gov/ct2/show/NCT02879071>.

Please address correspondence to Raphaël Blanc, MD, Department of Interventional Neuroradiology, Rothschild Foundation, 25 rue Manin, Paris, France; e-mail: rblanc@for.paris

<http://dx.doi.org/10.3174/ajnr.A5988>

and angiograms were reviewed for precise BAVM location, size, and angioarchitecture and classification according to the Spetzler-Martin grade. BAVMs were classified as cortical, deep, or infratentorial. The anatomic grading was established by 2 senior operators independent of the endovascular treatments.

The study protocol was approved by the local ethics committee. According to the French regulations, the board waived the need for signed consent for patients included in the study.

Endovascular Procedures

Patients were allocated to treatment after multidisciplinary discussions involving interventional neuroradiologists (with a neurosurgical or a radiologic background) and at least 1 vascular neurosurgeon. During the investigation, EVT was the first choice for low-grade BAVMs with a curative goal (ie, complete obliteration of the nidus by an endovascular approach in 1 single session whenever possible).

EVTs were performed with the patient under general anesthesia. In the study period, Onyx (Covidien, Irvine, California) was the most commonly used agent for embolization of AVMs. Occasionally, *n*-butyl-2-cyanoacrylate (Histoacryl; Braun, Melsungen, Germany) or Glubran 2 (GEM, Viareggio, Italy) was injected during the procedure for high-flow fistulas. Only a transarterial approach was used. The procedure was stopped when complete occlusion was achieved or when there was a 2-cm reflux of Onyx in the nondetachable microcatheter or Onyx reflux to the proximal end of the detachable part in the detachable microcatheter. If necessary, multiple pedicles were embolized in 1 session to achieve the desired occlusion of the AVM. A head CT scan was performed in the operating room after each procedure or immediately if any perforation occurred. After the procedure, all patients were admitted to the intensive care unit with control of systolic blood pressure for 24–48 hours and were discharged within 4–5 days if there was no complication. Cerebral MR imaging was performed before and after the procedure for all patients. In case of multiple sessions, the interval between the 2 procedures was 1–4 months. Pre- and postprocedural complications were prospectively collected.

Angiographic and Clinical Outcome

All patients treated in our center systematically underwent a 6-month follow-up DSA after the last treatment session: BAVM occlusion, defined by a complete nidus occlusion with no residual arteriovenous shunt and no early venous filling, was assessed by an interventional neuroradiologist who was independent of the operators who performed the treatment.

Clinical assessment of the patient was performed by neurologists from the same center who were independent of the operators performing the endovascular treatments. Imaging evaluation was also performed by independent interventional neuroradiologists. Any new neurologic deficit was collected and considered as transient if it resolved within 1 month after endovascular treatment or as permanent if it remained for >1 month. The outcomes were classified as poor for mRS 3–6 and as good for mRS 0–2.

Statistical Analysis

Continuous data are presented as means \pm SDs, and categorical data, as count and percentage. Statistical comparisons were per-

formed by a Student *t* test for normally distributed data, the Mann-Whitney *U* test for data with a skewed distribution, and the χ^2 and Fisher exact tests for the categorical data. To assess the risk factors of poor outcome (mRS > 2), we performed univariate analysis using baseline characteristics of the patients, AVM angioarchitecture, and endovascular procedure variables. Multivariate analysis was performed to define independent predictive variables of poor outcome using binary logistic regression. A *P* value < .05 was statistically significant. The data were analyzed using the Statistical Package for the Social Sciences (Version 16.0; IBM, Armonk, New York).

By increasing the time of the study and the number of patients, we attempted to reduce the bias effects related to the structural design of the study. Data, analytic methods, and study materials will be made available to any researcher for reproducing the results or replicating the procedure. Requests to receive these materials should be sent to the corresponding author, who will maintain their availability.

RESULTS

Basic Characteristics of Patients

From 2005 to 2015, a total of 330 patients with low-grade AVMs were managed in our hospital. Two hundred eighty-eight patients received EVT. Fifty-six patients who were still undergoing treatment during this period and 8 patients who were lost during follow-up were excluded from the study. These 8 patients did not experience any immediate complications after embolization. Two hundred twenty-four patients who completed EVT (ie, patients with AVM exclusion after EVT confirmed on 6-month follow-up angiography or patients with a remnant AVM but no residual access that would allow pursuing EVT) were included in the present study (baseline characteristics available in Table 1).

Treatment Outcome

The mean duration of angiographic follow-up after treatment was 9.7 ± 11.9 months. Complete exclusion of BAVMs was achieved in 205 patients (92%). From 224 patients, 139 patients (62.1%) were cured with a single endovascular procedure; 51 (22.8%), with 2 procedures; 26 (11.6%), with 3 procedures; and 8 (3.6%), with >3 procedures. In 19 patients with incomplete AVM exclusion after EVT, treatment was completed with an operation in 8 patients (3.6%) and radiosurgery in 9 patients (4%). The 2 remaining patients underwent no further treatment. The complete exclusion rate did not differ among the cortical and subcortical BAVMs, deeply located BAVMs, or infratentorially located BAVMs (Table 2). Delayed hemorrhagic complications after EVT were encountered in 11 patients (5%), and severe ischemic complication occurred in 5 patients (2%). Thirty-two patients (14%) developed a new neurologic deficit: Twenty patients (9%) improved completely within 30 days of the operation, and 12 patients (5%) kept a permanent deficit (7 patients [3%] from hemorrhagic complications and 5 patients [2%] from ischemic complications). An overall good outcome (mRS 0–2) was reported in 179 patients (80%). Thirteen patients (6%) had a worse mRS score compared with their preoperative status, including 9 patients (69%) with a hemorrhagic presentation. The mortality rate was 0.4%.

Table 1: Baseline characteristics and results of endovascular treatment^a

	Total (n = 224)	Ruptured BAVMs (n = 136)	Unruptured BAVMs (n = 88)	P Value
Age (yr)	37.8 ± 16	37.9 ± 17.7	37.6 ± 13.3	.087
Male	127 (57%)	81 (60%)	46 (52%)	.282
Presentation				NA
Hemorrhage	136 (60%)	136 (100%)	0 (0%)	
Seizure	42 (19%)	0 (0%)	42 (48%)	
Incidental	37 (17%)	0 (0%)	37 (42%)	
Other	9 (4%)	0 (0%)	9 (10%)	
Initial mRS score				.0001
Good (0–2)	178 (79%)	91 (67%)	87 (99%)	
Poor (3–5)	46 (21%)	45 (33%)	1 (1%)	
BAVM location				.001
Cortical and subcortical	176 (79%)	96 (71%)	80 (90%)	
Deep	19 (8%)	15 (11%)	4 (5%)	
Infratentorial	29 (13%)	25 (18%)	4 (5%)	
Eloquent area	77 (34%)	55 (40%)	22 (25%)	.017
Spetzler-Martin grade				.361
I	71 (32%)	40 (29%)	31 (35%)	
II	153 (68%)	96 (71%)	57 (65%)	
Mean nidus diameter (cm)	2.1 ± 1.1	1.9 ± 1.1	2.4 ± 1.1	.0001
Deep venous drainage	45 (20%)	32 (24%)	13 (15%)	.126
Venous ectasia	54 (24%)	27 (20%)	27 (31%)	.061
Arterial aneurysm	20 (9%)	14 (10%)	6 (7%)	.475
Intranidal aneurysm	42 (19%)	33 (24%)	9 (10%)	.020
Mean No. of procedures	1.6 ± 0.9	1.4 ± 0.8	1.8 ± 1.1	.003
Duration of follow-up angiography (mo)	9.7 ± 11.9	8.7 ± 10.4	11.3 ± 13.8	.117
Angiographic result				.091
Complete exclusion	205 (92%)	128 (94%)	77 (88%)	
Remnant	19 (8%)	8 (6%)	11 (12%)	1.000
Post-EVT AVM surgery	7 (3%)	4 (3%)	3 (4%)	NA
Post-EVT radiosurgery	8 (4%)	2 (2%)	6 (8%)	NA
Severe post-EVT hematoma	11 (5%)	7 (5%)	4 (5%)	1.000
Significant post-EVT ischemia	5 (2%)	4 (3%)	1 (1%)	.651
Postop outcome (mRS)				.001
Good (0–2)	179 (80%)	96 (71%)	83 (94%)	
Poor (3–5)	44 (19%)	40 (29%)	4 (5%)	
Mortality (6)	1 (0.4%)	0 (0%)	1 (1%)	
Improved/unchanged mRS score	211 (94%)	127 (93%)	85 (96%)	1.000

Note:—NA indicates not applicable; postop, postoperative.

^a Data are presented as No. (%) or means.

Table 2: Cure rate according to location of AVM^a

Location	Total	Complete Exclusion	Remnant	P Value ^b
Cortical and subcortical	176 (100%)	159 (90.3%)	17 (9.7%)	.338
Deep	19 (100%)	19 (100%)	0 (0%)	
Infratentorial	29 (100%)	27 (93.1%)	2 (6.9%)	
Eloquent	77 (100%)	76 (98.7%)	1 (1.3%)	.004
Noneloquent	147 (100%)	129 (87.8%)	18 (12.2%)	

^a Data are presented as No. (%).

^b Fisher exact test.

Predictive Variables of Clinical Outcome

Univariate analysis showed that factors associated with poor outcome were hemorrhagic history ($P = .000$), preoperative condition (mRS 0–1 versus mRS 2–5) ($P = .000$), eloquent location of the AVM ($P = .008$), and infratentorial location of the AVM ($P = .010$). In contrast, no association was found with age, sex, Spetzler-Martin grade, lateralization of the AVM, presence of deep drainage, presence

of an intranidal aneurysm, number of procedures, volume of Onyx, use of *n*-butyl-2-cyanoacrylate, and the number of embolized pedicles.

A multivariate analysis was performed, including the 4 factors associated with poor outcome in univariate analysis, which were entered into the model. In this analysis, only the preoperative condition (poor preoperative mRS score) was associated with poor outcome (OR = 0.029, $P = .000$). The hemorrhagic history of the AVM, eloquent location of the AVM, infratentorial location of the AVM, and supplementary grade ≤ 3 were not found to be predictive factors of poor outcome.

DISCUSSION

This study represents the results of endovascular management as the first-line treatment approach for low-grade BAVMs in a single high-volume center: Ninety-two percent of BAVMs were completely obliterated by an endovascular approach alone (62.1% of those in 1 single EVT session), with a permanent neurologic deficit of 5% and a 0.4% mortality rate. According to their size, low-grade BAVMs were reported to be suitable for complete exclusion by only a single session.^{5–8} The development of new tools allows supraselective catheterization of the nidus with prolonged embolization resulting in better exclusion of the nidus and draining veins.^{9,10}

The deeply located, the infratentorial, and eloquently located BAVMs were reported to be associated with higher rates of treatment failure and complications.⁷ Nevertheless, in our experience, the cure rate in those locations is as high as that in the cortical location with a similar complication rate.

The treatment of unruptured BAVMs remains controversial, even more so since the publication of the ARUBA trial² and the Scottish Intracranial Vascular Malformation Study.¹¹ Nevertheless, our study shows encouraging results of EVT for low-grade unruptured BAVMs, with 88% complete exclusion and 6% poor outcome, which need to be confirmed in randomized trials with a comparative group undergoing conservative management.

In the literature search we performed, overall cure rates of AVM EVT ranged from 23.5% to 94%.^{1,7,12–20} When low-grade AVMs were extracted from the studies, the cure rate was about 93%. In a review of 439 low-grade AVMs treated solely by EVT, the complication rate was about 4.1% and the mortality was about 0.5% (Table 3).

Surgery is considered the standard and first-choice treatment for low-grade AVMs, with a mean cure rate of 98% (94%–100%), mean complications of 2.2% (0%–6%), and mortality rate of 0%–

Table 3: Summary of endovascular treatment for low-grade brain arteriovenous malformations^a

Author, Year	No. of Patients	Morbidity	Mortality	Cure Rate
Maimon et al, 2010 ¹⁰	8	0 (0%)	0 (0%)	5 (63%)
van Rooij WJ et al, 2012 ⁷	20	0 (0%)	0 (0%)	19 (96%)
Xu et al, 2011 ¹⁹	16	1 (6.3%)	0 (0%)	9 (56%)
Saatci et al, 2011 ¹⁸	158	4 (2.5%)	1 (0.6%)	155 (98%)
Abud et al, 2011 ¹²	8	1 (12.5%)	0 (0%)	8 (100%)
Durst et al, 2015 ²⁰	5	NA	0 (0%)	5 (100%)
Our study, 2018	224	12 (5.4%)	1 (0.4%)	206 (92%)
Total	439	18 (4.1%)	2 (0.5%)	407 (93%)

Note:—NA indicates not applicable.

^a Data are presented as No. (%).

2%.^{1,4,21-28} However, the deep and eloquently located AVMs can be inaccessible or at high risk for surgery.^{2,24,29,30} Although 8%–45% of low-grade AVMs benefit from preoperative embolization that results in easier AVM surgery with fewer complications,^{2,23,24,31} only 7.5% of our patients required surgery or radiosurgery for completing exclusion of the AVM. Cosmetic problems are another issue for brain surgery, which is not the case in endovascular treatments.

The eloquently located AVMs are associated with a higher risk of neurologic complications (4%–10%).^{1,23,24,32} Use of functional MR imaging before an operation does not seem to reduce the neurologic complication rate following the operation.³² The complete resection of deeply located AVMs is less frequent with higher morbidity of 0%–13% and higher mortality of 0%–6%.^{27,30,31,33-36} The deeply located AVMs also benefit from preoperative embolization in up to 54% of cases, more than the superficial ones.^{31,35} The diffuse architecture of AVMs is also an important limitation for surgery.¹ Supplementary grading, patient age, architecture of AVMs, and location of AVMs are shown to be important preoperative factors for correct stratification of patients for an operation to increase the rate of complete resection and reduce the risk of complications.¹

Radiosurgery is considered an effective alternative approach to surgery for small AVMs, especially those located in deep or eloquent areas. Yet, the 2- to 3-year delayed response puts patients at risk of hemorrhage, particularly in ruptured cases, and it even seems not to be limited to 3 years but could be up to 8 years after AVM obliteration.^{37,38} The cure rate of radiosurgery is about 70%–93% for low-grade AVMs, with permanent symptomatic complications of 3%–12%, rebleeding of 1.7%–10%, and mortality of 0%–3%.^{1,39-46} In a recent multicentric study of 2236 patients treated by gamma knife,⁴⁶ complications, including symptomatic and permanent radiation-induced changes, were reported in 9% and 3%, respectively, and the risk of postradiation hemorrhage was 1.1% annually and 9% in total for patients with a history of hemorrhage and 6% for those without a history of hemorrhage. The risk of hemorrhage increases with increasing age, deeply located AVMs, and increasing prescription isodose volume.³⁸ The radiation-induced complications occurred at intervals of 6–18 months, and the most important risk factors were radiation dose and location of the AVM.^{46,47} Brain stem and deep location such as the thalamus were reported to have about 4 and 2 times more irreversible symptomatic adverse radiation reaction (11% and 7%) than other locations, respectively.⁴⁷

Limitations

Our study presents several limitations. There are inherent selection biases due to the observational design of this work. Notably, about 20% of patients were not included in the study because their treatment was still ongoing, and the outcomes of these patients might modify our results. The monocentric nature of the study could also affect the results. No treatment from this series was performed through a venous approach (an alternative endovascular approach that has recently gained wider acceptance); our study thus does not have insight into this technique. Other interesting anatomic features (such as number of feeders) were not prospectively collected.

Further multicenter studies, with different treatment modalities such as an operation, EVT, and radiosurgery, may better clarify the different aspects in the management of low-grade AVMs. More randomized trials are also necessary to confirm the benefits of curative treatment for unruptured BAVMs because current evidence is in favor of conservative management.

CONCLUSIONS

The results of our study show a high rate of complete exclusion by EVT for low-grade AVMs with a low complication rate (5%). Accordingly, EVT may be effective and safe for treatment of low-grade BAVMs, especially in deep and eloquent locations where an operation has many limitations.

REFERENCES

- Potts MB, Lau D, Abula AA, et al. **Current surgical results with low-grade brain arteriovenous malformations.** *J Neurosurg* 2015;122:912–20 CrossRef Medline
- Mohr JP, Parides MK, Stapf C, et al; international ARUBA investigators. **Medical management with or without interventional therapy for unruptured brain arteriovenous malformations (ARUBA): a multicentre, non-blinded, randomised trial.** *Lancet* 2014;383:614–21 CrossRef Medline
- Magro E, Gentric JC, Darsaut TE, et al. **Responses to ARUBA: a systematic review and critical analysis for the design of future arteriovenous malformation trials.** *J Neurosurg* 2017;126:486–94 CrossRef Medline
- Spetzler RF, Martin NA. **A proposed grading system for arteriovenous malformations.** *J Neurosurg* 1986;65:476–83 CrossRef Medline
- Crowley RW, Ducruet AF, McDougall CG, et al. **Endovascular advances for brain arteriovenous malformations.** *Neurosurgery* 2014;74(Suppl 1):S74–82 CrossRef Medline
- Möhlenbruch M, Bendzus M, Rohde S. **Comment on: curative embolization of brain arteriovenous malformations with Onyx—patient selection, embolization technique, and results.** *Clin Neuroradiol* 2012;22:181–82 CrossRef Medline
- van Rooij WJ, Jacobs S, Sluzewski M, et al. **Curative embolization of brain arteriovenous malformations with Onyx: patient selection, embolization technique, and results.** *AJNR Am J Neuroradiol* 2012;33:1299–304 CrossRef Medline
- van Rooij WJ, Sluzewski M, Beute GN. **Brain AVM embolization with Onyx.** *AJNR Am J Neuroradiol* 2007;28:172–77; discussion 178 Medline
- Herial NA, Khan AA, Sherr GT, et al. **Detachable-tip microcatheters for liquid embolization of brain arteriovenous malformations and fistulas: a United States single-center experience.** *Neurosurgery* 2015;11(Suppl 3):404–11; discussion 411 CrossRef Medline
- Maimon S, Strauss I, Frolov V, et al. **Brain arteriovenous malformation treatment using a combination of Onyx and a new detachable tip microcatheter, SONIC: short-term results.** *AJNR Am J Neuroradiol* 2010;31:947–54 CrossRef Medline

11. Al-Shahi Salman R, White PM, Counsell CE, et al; Scottish Audit of Intracranial Vascular Malformations Collaborators. **Outcome after conservative management or intervention for unruptured brain arteriovenous malformations.** *JAMA* 2014;311:1661–69 CrossRef Medline
12. Abud DG, Riva R, Nakiri GS, et al. **Treatment of brain arteriovenous malformations by double arterial catheterization with simultaneous injection of Onyx: retrospective series of 17 patients.** *AJNR Am J Neuroradiol* 2011;32:152–58 CrossRef Medline
13. Baharvahdat H, Blanc R, Termechi R, et al. **Hemorrhagic complications after endovascular treatment of cerebral arteriovenous malformations.** *AJNR Am J Neuroradiol* 2014;35:978–83 CrossRef Medline
14. Elsenousi A, Aletich VA, Alaraj A. **Neurological outcomes and cure rates of embolization of brain arteriovenous malformations with n-butyl cyanoacrylate or Onyx: a meta-analysis.** *J Neurointerv Surg* 2016;8:265–72 CrossRef Medline
15. Katsaridis V, Papagiannaki C, Aimar E. **Curative embolization of cerebral arteriovenous malformations (AVMs) with Onyx in 101 patients.** *Neuroradiology* 2008;50:589–97 CrossRef Medline
16. Mounayer C, Hammami N, Piotin M, et al. **Nidal embolization of brain arteriovenous malformations using Onyx in 94 patients.** *AJNR Am J Neuroradiol* 2007;28:518–23 Medline
17. Pierot L, Cognard C, Herbretau D, et al. **Endovascular treatment of brain arteriovenous malformations using a liquid embolic agent: results of a prospective, multicentre study (BRAVO).** *Eur Radiol* 2013;23:2838–45 CrossRef Medline
18. Saatci I, Geyik S, Yavuz K, et al. **Endovascular treatment of brain arteriovenous malformations with prolonged intranidal Onyx injection technique: long-term results in 350 consecutive patients with completed endovascular treatment course.** *J Neurosurg* 2011; 115:78–88 CrossRef Medline
19. Xu F, Ni W, Liao Y, et al. **Onyx embolization for the treatment of brain arteriovenous malformations.** *Acta Neurochir (Wien)* 2011; 153:869–78 CrossRef Medline
20. Durst CR, Starke RM, Gaughen J, et al. **A method for complete angiographic obliteration of a brain arteriovenous malformation in a single session through a single pedicle.** *J Clin Neurosci* 2015;22: 391–95 CrossRef Medline
21. Hamilton MG, Spetzler RF. **The prospective application of a grading system for arteriovenous malformations.** *Neurosurgery* 1994;34: 2–6; discussion 6–7 Medline
22. Heros RC, Korosue K, Diebold PM. **Surgical excision of cerebral arteriovenous malformations: late results.** *Neurosurgery* 1990;26: 570–77; discussion 577–78 CrossRef Medline
23. Javadpour M, Al-Mahfoudh R, Mitchell PS, et al. **Outcome of microsurgical excision of unruptured brain arteriovenous malformations in ARUBA-eligible patients.** *Br J Neurosurg* 2016;30:619–22 CrossRef Medline
24. Morgan MK, Rochford AM, Tsahtsarlis A, et al. **Surgical risks associated with the management of grade I and II brain arteriovenous malformations.** *Neurosurgery* 2007;61(1 Suppl):417–22; discussion 422–24 CrossRef Medline
25. Pikus HJ, Beach ML, Harbaugh RE. **Microsurgical treatment of arteriovenous malformations: analysis and comparison with stereotactic radiosurgery.** *J Neurosurg* 1998;88:641–46 CrossRef Medline
26. Schaller C, Schramm J. **Microsurgical results for small arteriovenous malformations accessible for radiosurgical or embolization treatment.** *Neurosurgery* 1997;40:664–72; discussion 672–74 CrossRef Medline
27. Sisti MB, Kader A, Stein BM. **Microsurgery for 67 intracranial arteriovenous malformations less than 3 cm in diameter.** *J Neurosurg* 1993;79:653–60 CrossRef Medline
28. Sundt TM Jr, Piepgras DG, Stevens LN. **Surgery for supratentorial arteriovenous malformations.** *Clin Neurosurg* 1991;37:49–115 Medline
29. Davidson AS, Morgan MK. **How safe is arteriovenous malformation surgery? A prospective, observational study of surgery as first-line treatment for brain arteriovenous malformations.** *Neurosurgery* 2010;66:498–504; discussion 504–05 CrossRef Medline
30. Gross BA, Duckworth EA, Getch CC, et al. **Challenging traditional beliefs: microsurgery for arteriovenous malformations of the basal ganglia and thalamus.** *Neurosurgery* 2008;63:393–410; discussion 410–11 CrossRef Medline
31. Lawton MT, Hamilton MG, Spetzler RF. **Multimodality treatment of deep arteriovenous malformations: thalamus, basal ganglia, and brain stem.** *Neurosurgery* 1995;37:29–35; discussion 35–36 CrossRef Medline
32. Lin F, Jiao Y, Wu J, et al. **Effect of functional MRI-guided navigation on surgical outcomes: a prospective controlled trial in patients with arteriovenous malformations.** *J Neurosurg* 2017;126:1863–72 CrossRef Medline
33. Johnston JL, Johnston IH. **The surgical treatment of small deep intracranial arteriovenous malformations: a report of 85 cases.** *J Clin Neurosci* 1996;3:338–45 CrossRef Medline
34. Liu KD, Lee LS. **Microsurgical treatment of deep arteriovenous malformations—basal ganglia and thalamus.** *Zhonghua Yi Xue Za Zhi (Taipei)* 2001;64:23–30 Medline
35. Potts MB, Jahangiri A, Jen M, et al; UCSF Brain AVM Study Project. **Deep arteriovenous malformations in the basal ganglia, thalamus, and insula: multimodality management, patient selection, and results.** *World Neurosurg* 2014;82:386–94 CrossRef Medline
36. U HS, Kerber CW, Todd MM. **Multimodality treatment of deep periventricular cerebral arteriovenous malformations.** *Surg Neurol* 1992;38:192–203 CrossRef Medline
37. Arslan I, Tezcanli E, Yilmaz M, et al. **Gamma knife radiosurgery for arteriovenous malformations: clinical series of 199 patients.** *Turk Neurosurg* 2017;27:301–08 CrossRef Medline
38. Pollock BE, Link MJ, Stafford SL, et al. **Stereotactic radiosurgery for arteriovenous malformations: the effect of treatment period on patient outcomes.** *Neurosurgery* 2016;78:499–509 CrossRef Medline
39. Bin Rosli FJ, Mohammed Haspani MS, Izaini Ab Ghani AR. **Comparing monomodality treatments of low-grade intracranial arteriovenous malformation at Hospital Kuala Lumpur between 2008 and 2011: a retrospective study.** *Asian J Neurosurg* 2016;11:22–28 CrossRef Medline
40. Boström JP, Bruckermann R, Pintea B, et al. **Treatment of cerebral arteriovenous malformations with radiosurgery or hypofractionated stereotactic radiotherapy in a consecutive pooled linear accelerator series.** *World Neurosurg* 2016;94:328–38 CrossRef Medline
41. Ding D, Yen CP, Xu Z, et al. **Radiosurgery for low-grade intracranial arteriovenous malformations.** *J Neurosurg* 2014;121:457–67 CrossRef Medline
42. Friedman WA, Bova FJ, Bollampally S, et al. **Analysis of factors predictive of success or complications in arteriovenous malformation radiosurgery.** *Neurosurgery* 2003;52:296–307; discussion 307–08 CrossRef Medline
43. Kano H, Kondziolka D, Flickinger JC, et al. **Stereotactic radiosurgery for arteriovenous malformations after embolization: a case-control study.** *J Neurosurg* 2012;117:265–75 CrossRef Medline
44. Koltz MT, Polifka AJ, Saltos A, et al. **Long-term outcome of gamma knife stereotactic radiosurgery for arteriovenous malformations graded by the Spetzler-Martin classification.** *J Neurosurg* 2013;118: 74–83 CrossRef Medline
45. Pollock BE, Lunsford LD, Kondziolka D, et al. **Patient outcomes after stereotactic radiosurgery for “operable” arteriovenous malformations.** *Neurosurgery* 1994;35:1–7; discussion 7–8 CrossRef Medline
46. Starke RM, Kano H, Ding D, et al. **Stereotactic radiosurgery for cerebral arteriovenous malformations: evaluation of long-term outcomes in a multicenter cohort.** *J Neurosurg* 2017;126:36–44 CrossRef Medline
47. Kano H, Flickinger JC, Tonetti D, et al. **Estimating the risks of adverse radiation effects after gamma knife radiosurgery for arteriovenous malformations.** *Stroke* 2017;48:84–90 CrossRef Medline

Curing Low-Grade Brain AVMs with Embolization?

In the article by Baharvahdat et al¹ in this issue entitled, “Endovascular Treatment for Low-Grade (Spetzler-Martin I–II) Brain Arteriovenous Malformations,” the authors retrospectively reviewed a prospectively maintained data base of low-grade brain arteriovenous malformations (bAVMs) using endovascular therapy (EVT) as first-line therapy with attempts to cure during an 11-year period (2005–2015). The primary outcome studied was AVM obliteration, and secondary outcomes included disability or death secondary to embolization using the modified Rankin Scale. The authors included in their analysis only those patients in whom EVT was completed. Patients who were lost to follow-up or for whom additional EVT was planned were excluded. The grading of the AVMs was performed by 2 senior operators not involved in the treatment. Onyx (Covidien, Irvine, California) was the embolic most commonly used, but other agents were also used. The embolization was always transarterial, and a CT scan was obtained after all procedures or immediately if there was a perforation. The procedure was stopped if the AVM was obliterated or if there was unacceptable reflux onto the microcatheter. Clinical assessment using the modified Rankin Scale was performed at “the initial and follow-up visits,” whose timing was not defined. Obliteration of the bAVM was defined as negative findings on an angiogram at 6 months. Clinical assessments were performed by a “neurologist independent from the operators . . .” His or her experience level, board certification, or even the number of different doctors involved was not defined. Neurologic deficits were considered transient if they resolved by 1 month. A modified Rankin Scale score of 0–2 was considered a good outcome.

In total, the authors’ interventional team, also not defined in terms of number of operators or experience level, evaluated 330 patients. Only 288 were treated by EVT. The fate of the remaining 42 and the reason they did not receive EVT were not explained. Of the 288 patients, 8 were lost to follow-up and 56 had not yet completed their EVT, leaving a total of 224 patients with completed EVTs who formed the basis of this studied cohort. Of these, 60% presented with hemorrhage, with 21% of the total cohort having a poor initial mRS score (almost all of whom presented with bleeds). Complete obliteration was achieved in 92%; more

than two-thirds of the obliterations were accomplished with 1 session. Eleven patients had a delayed hemorrhage (timing not specified), of whom 7 had a permanent deficit. Severe ischemic permanent deficits occurred in 5 patients. In total, 32 patients (14%) developed a new deficit, but 20 patients resolved their deficit by 30 days, yielding a total permanent neurologic complication rate of 5%. Eighty percent of patients had a good mRS score at follow-up, with 6% having a worse postprocedural mRS score on follow-up. There was 1 procedure-related death. The authors found no difference between the success of obliteration and the bAVM location. The only risk factor for a poor mRS score in both the univariate and multivariate analyses was a poor presenting mRS score. The authors concluded that EVT is a good alternative for achieving a complete cure of low-grade bAVMs, with a low complication rate.

The authors quote and compare their series with the A Randomized Trial of Unruptured Brain Arteriovenous Malformations (ARUBA) study.² The comparison and referencing of the ARUBA study is, however, not relevant. The ARUBA study was limited to unruptured lesions, whereas most patients in the current study (60%) presented with hemorrhage. Another inaccuracy of the current article is that the authors stated that the ARUBA study did not include many low-grade lesions. In fact, approximately 56% of the lesions in ARUBA were grade I or II. Another reason for the poor comparison is that the ARUBA study was a prospective, randomized trial with protocols for enrollment and management and strict inclusion and exclusion criteria with clinical and radiographic outcomes adjudicated by an international committee and an intention-to-treat analysis. This study has none of that and, in fact, has most of the downsides of a retrospective analysis. There is no explanation as to why 42 patients evaluated did not get EVT. Were they somehow deemed different in any way? Potential bias may have been introduced.

The current article does not seem to have any protocol for clinical follow-up and simply states that it was performed. Multiple different interventionalists with different experience using different agents seem to have been used. A heterogeneous group of both hemorrhagic and nonhemorrhagic lesions was included, which makes it impossible to tease out whether the mRS score was

related to the initial bleed or some complication from EVT. Onyx embolic was only released in the United States for clinical use in 2005, and the detachable catheters followed after that. Therefore, some experience across time may have been gained by this interventional team, suggesting that a lesion treated by them in 2015 may have benefitted from a different experience and understanding of the embolic agents and catheter technology than one treated in 2005.

Last, by not including the fate of those who failed EVT, the current study excludes any morbidity accrued from further therapy, which downplays the risk of embarking on EVT as a first-line therapy, something that an intention-to-treat analysis would capture. I would also question whether all of these lesions were, in fact, grade I or II. The lesions included 77 (34%) in an eloquent area of the brain. According to the Spetzler-Martin Grading Scale, if any of these had deep drainage, they would automatically be graded at least a III.³ Furthermore, they had 19 (8%) lesions that were considered “deep.” Many of these were in the eloquent brain and drained to the deep venous system. If any of these were, in fact, eloquent and had deep drainage, they too would be at least a grade III. Again, without independent adjudication, we are left to assume that the lesions were graded correctly, but with such high numbers characterized as “deep” and “eloquent,” how confident should we be?

Despite these shortcomings, this publication represents one of the largest series in the modern era of bAVMs treated with an EVT intent-to-cure approach. Restricting their treatment to good grade (Spetzler/Martin I–II) makes it unique. Their obliteration rate (92%) is quite impressive and certainly competitive with the other treatment modalities, namely radiosurgery and surgical excision. Their complication rate, while acceptable, needs to be scrutinized a bit and may not be as sanguine as the authors suggest. The modified Rankin Scale is a coarse scale, which measures function, and does not necessarily take into account subtle or even more overt cognitive dysfunction. Twenty patients in this study had new neurologic deficits after treatment, which resolved within 30 days. It is likely that had MR imaging been performed on these patients, some would have shown strokes with possible accompanying neuropsychological deficits that might not be elicited on a routine neurologic examination.

One of the less discussed results of the ARUBA study was that the natural history risk of unruptured bAVMs was significantly less than previously thought.⁴ This result had been previously demonstrated, and evidence suggests that some lesions, particularly certain subsets of bAVMs such as small noneloquent-placed lesions without deep venous drainage, may bleed at a yearly rate of <1%.^{5,6} Furthermore, when unruptured AVMs bleed, the resultant morbidity has recently been shown to be less than initially thought.⁶ As a result, any offered treatment for unruptured bAVMs must carry quite a low risk to beat the natural history risk. Whether the 5% permanent morbidity (or possibly even higher as outlined above) and 0.4% mortality of EVT for low-grade lesions presented here beats the natural history risk and, more important, whether a given patient would elect to take such a risk is not completely clear. A randomized trial would be needed to help shed light on this important issue.

REFERENCES

1. Baharvahdat H, Blanc R, Fahed R, et al. **Endovascular treatment for low-grade (Spetzler-Martin I-II) brain arteriovenous malformations.** *AJNR Am J Neuroradiol* 2019;40:668–72 CrossRef Medline
2. Mohr JP, Parides MK, Stapf C, et al; International ARUBA Investigators. **Medical management with or without interventional therapy for unruptured brain arteriovenous malformations (ARUBA): a multicentre, non-blinded, randomized trial.** *Lancet* 2014;383:614–21 CrossRef Medline
3. Spetzler RF, Martin NA. **A proposed grading system for arteriovenous malformations.** *J Neurosurg* 1986;65:476–83 Medline
4. Stapf C, Mast H, Sciacca RR, et al; New York Islands AVM Study Collaborators. **The New York Islands AVM study: design study progress and initial results.** *Stroke* 2003;34:e29–33 Medline
5. Mohr JP, Overbey JR, von Kummer R, et al; International ARUBA Investigators. **Functional impairments for outcomes in a randomized trial of unruptured brain AVMs.** *Neurology* 2017;89:1499–506 CrossRef Medline
6. Choi JH, Mast H, Sciacca RR, et al. **Clinical outcome after first and recurrent hemorrhage in patients with untreated brain arteriovenous malformation.** *Stroke* 2006;37:1243–47 CrossRef Medline

©J.L. Brisman
Lake Success, NY

Note: The authors were given the opportunity to respond and declined.

<http://dx.doi.org/10.3174/ajnr.A6017>

Morphologic Change of Flow-Related Aneurysms in Brain Arteriovenous Malformations after Stereotactic Radiosurgery

Y.-S. Tsuei, C.-B. Luo, L.-Y. Fay, H.-C. Yang, W.-Y. Guo, H.-M. Wu, W.-Y. Chung, and M.M.H. Teng

ABSTRACT

BACKGROUND AND PURPOSE: The natural history of flow-related aneurysms after obliteration of brain arteriovenous malformations is poorly understood. The purpose of this study was to evaluate the angioarchitecture and morphologic change in flow-related aneurysms after gamma knife surgery of brain arteriovenous malformations.

MATERIALS AND METHODS: During a 12-year period, 823 patients with brain arteriovenous malformations underwent gamma knife surgery at our institution with complete peritherapeutic angiographic evaluation. From this population, a series of 72 patients (8.8%) with 111 flow-related aneurysms were enrolled (1.5 aneurysms per patient). There were 43 men and 29 women; ages ranged from 18 to 72 years (mean, 43 years). The morphologic change of flow-related aneurysms was longitudinally evaluated before and after obliteration of brain arteriovenous malformations. After gamma knife surgery, angiographic follow-up varied from 26 to 130 months (mean, 58 months).

RESULTS: All flow-related aneurysms were small (mean, 4.1 mm; range, 2–9 mm). There were 72 proximal flow-related aneurysms (mean size, 4.3 mm) and 39 distal flow-related aneurysms (mean size, 3.7 mm). Spontaneous thrombosis occurred more frequently in distal flow-related aneurysms than in proximal flow-related aneurysms ($P < .001$). Smaller flow-related aneurysms (<5 mm) tended to spontaneously occlude after obliteration of brain arteriovenous malformations ($P = .036$). Two patients had ruptures of proximal flow-related aneurysms at 27- and 54-month follow-ups, respectively.

CONCLUSIONS: Spontaneous thrombosis occurred more frequently in distal flow-related aneurysms due to occlusion or normalization of distal feeders. Smaller flow-related aneurysms also tended to spontaneously thrombose after obliteration of brain arteriovenous malformations. The rate of flow-related aneurysm rupture in our series was similar to that of natural intradural aneurysms.

ABBREVIATIONS: ACA = anterior cerebral artery; BAVM = brain arteriovenous malformation; FA = flow-related aneurysm; GKS = gamma knife surgery

The association between brain arteriovenous malformations (BAVMs) and flow-related aneurysms (FAs) is well-documented in the literature. The risk of hemorrhage is reported to be 7%–10% annually in patients with concomitant BAVMs and intradural aneurysms, and it is higher in patients with concomitant BAVMs than in patients with only BAVMs.^{1,2} Current management of FAs of BAVMs is controversial because of the inherent risk associated with aggressive interventional management and

the unclear natural course of FAs. Some authors propose that symptomatic BAVMs should be the primary treatment target, with FAs left to observation because of the possibility that they can spontaneously occlude after an alteration in hemodynamics following BAVM obliteration.³ On the other hand, some authors claim that FAs should be actively treated at the time of BAVM management because FAs are a critical risk factor for intracranial hemorrhage.^{4–8} The natural history of FAs after BAVM obliteration by stereotactic gamma knife surgery (GKS) remains unclear. Understanding the morphologic change of FAs during the latency period after stereotactic GKS would greatly impact the FA management strategy. The purpose of this study was to longitudinally evaluate changes in FA morphology after hemodynamic alterations produced by BAVM obliteration.

MATERIALS AND METHODS

Patient Demographics

From September 1994 to August 2015, a total of 936 patients with BAVMs were referred to Taipei Veterans General Hospital to de-

Received May 26, 2018; accepted after revision January 25, 2019.

From the Department of Neurosurgery (Y.-S.T.), Taichung Veterans General Hospital, Taichung, Taiwan; Departments of Neurosurgery (Y.-S.T.) and Radiology (C.-B.L.), Tri-Service General Hospital, National Defense Medical Center, Taipei, Taiwan; Departments of Radiology (C.-B.L., W.-Y.G., H.-M.W., M.M.H.T.) and Neurosurgery (L.-Y.F., H.-C.Y., W.-Y.C.), Taipei Veterans General Hospital and National Yang-Ming University, School of Medicine, Taipei, Taiwan; and Department of Radiology (M.M.H.T.), Cheng-Hsin General Hospital, Taipei, Taiwan.

Please address correspondence to Chao-Bao Luo, MD, Department of Radiology, Taipei Veterans General Hospital, 201, Section 2, Shih-Pai Rd, Taipei 112, Taiwan, ROC; e-mail: cbluo@vghtpe.gov.tw

<http://dx.doi.org/10.3174/ajnr.A6018>

Table 1: Demographics of patients with BAVMs enrolled and characteristics of FAs

	Value
No. of eligible patients	936
No. of excluded patients	113
No. of patients with <50% obliteration of BAVM	39
No. of patients without DSA follow-up	57
No. of interventions of FAs	17
No. of patients enrolled	823
No. of patients with FAs enrolled	72 (8.8%)
Mean age (yr)	43 (range, 18–72)
Sex (No.)	
Female	29 (40%)
Male	43 (60%)
No., location, and size of FAs (mm)	
Total No. of FAs (mean size)	111 (4.1)
Mean size of proximal FAs	4.3
Mean size of distal FA	3.7
No. of FAs per patient	1.5
No. of FAs in supratentorium	98
No. of FAs in ICA	42
No. of FAs in proximal/distal MCA	16/14
No. of FAs in proximal/distal ACA	9/17
No. of FAs in infratentorium	13
No. of proximal FAs	5
No. of distal FAs	8

termine the feasibility of GKS. One hundred thirteen patients were excluded because of incomplete follow-up by DSA ($n = 57$), insufficient hemodynamic alteration by obliteration of <50% of the BAVM ($n = 39$), and interventional management of the FA ($n = 17$). A series of 823 patients with >24 months of DSA follow-up after GKS were enrolled (Table 1). Before GKS, the patients underwent 4-vessel cerebral DSA to evaluate the BAVM angioarchitecture (including location/size of the BAVM), the association of intranidal aneurysms with flow-related aneurysms, and the coexistence of a high-flow arteriovenous fistula and venous outflow. 3D reconstruction of rotational DSA, which has been part of the standard protocol for angioarchitectural analysis of BAVM since 2002, was performed to evaluate the angioarchitecture of BAVMs and to search for FAs. Therefore, a total of 346 patients (42%) did not have 3D reconstruction of rotational DSA. The absence of this modern protocol may lead to underestimation of the real incidence of FAs in our series.

GKS was performed once in 689 patients; it was repeated a second ($n = 106$) or third ($n = 28$) time in 134 patients because of residual BAVMs. After GKS, patients were followed up for progression and obliteration of BAVMs by MR imaging and MRA every 3–6 months. DSA was performed when the MRA showed partial regression or total occlusion of BAVMs 3 years after GKS to check the angioarchitecture. This study was approved by the ethics committee of the institution in 2014.

Angiographic Analyses

FA was defined as an arterial pouch in the feeders of BAVMs; the size of the aneurysms in this study was at least 2 mm. FAs were grouped by the size of their maximal dimension into small (<5 mm) and large (at least 5 mm); by distribution of FAs into ICA, anterior cerebral artery (ACA), and MCA as well as infratentorium; and by location into proximal and distal FAs based on Re-

dekok et al.² FAs in the supraclinoid ICA, M1 segment of the MCA, A1 segment of the ACA, anterior communicating artery, basilar artery, and P1 of posterior cerebral artery were considered proximal, while those located beyond this territory were considered distal. FAs were also classified by morphologic change into enlargement, stable, and partial or complete regression. These angiographic decisions were made by 2 experienced interventional neuroradiologists (C.-B.L. and Y.-S.T.) independently, using the same workstation. Any discrepancy in the angiographic findings of these 2 interventional neuroradiologists was resolved through reassessment and discussion of the DSA.

Statistical Analyses

The differences in continuous variables (ie, mean age of patients, mean volume of BAVM, and mean size of FA) between stable and regressive FAs were compared by means of an independent-samples *t* test. The differences in categorical variables (ie, sex, ruptured/unruptured BAVMs, and complete/incomplete obliteration of the BAVM as well as location/size of the FAs) between stable and regressive FAs were compared using the Fisher exact test. Data analyses were performed using SPSS 22 (IBM, Armonk, New York). A 2-sided *P* value < .05 was considered statistically significant. No adjustment of multiple testing (multiplicity) was made in this study.

RESULTS

Overall Findings

A total of 72 patients (8.8%; 43 men and 29 women; mean age, 43 years; range, 18–72 years) with 111 FAs (1.5 FAs per patient) were enrolled in this study and had complete DSA follow-up after partial ($n = 11$, 50%–80%), subtotal ($n = 9$, >80%), or total obliteration ($n = 52$) of BAVMs by GKS. The major clinical manifestations were headache ($n = 39$), seizure ($n = 23$), and neurologic deficits ($n = 29$). Ruptured BAVMs with intracranial hemorrhage were found in 31 patients, while unruptured BAVMs were found in 41. Post-GK DSA follow-up varied from 26 to 130 months (mean, 58 months).

Angioarchitecture of FAs

The location and size of 111 FAs are summarized in Table 1. The number of patients with 1, 2, 3, and >3 FAs was 46 (Fig 1), 16 (Figs 2 and 3), 7, and 3. Multiple FAs were found in 26 of 72 patients (36%). The size of the FAs varied from 2 to 9 mm (mean, 4.1 mm). The locations of the FAs were the ICA in 42 patients, MCA in 30, ACA in 26, and infratentorium in 13. Seventy-two were proximal FAs with a mean size of 4.3 mm, and 39 were distal FAs with a mean size 3.7 mm. Ninety-nine (89%) FAs were small (<5 mm); the other 12 (11%) were at least 5 mm.

Morphologic Change and Natural Course of FAs after GKS

Of the 111 FAs, 60 (54%) showed stable size, 25 (23%) showed partial size regression, and 26 (23%) showed total obliteration. In 51 FAs with size regression, 11 demonstrated total occlusion of distal feeders, while 40 trended toward normalization of features of the parent arteries. No instance of enlargement of FAs was found in a mean 58-month period of DSA follow-up. In terms of regressive FAs during follow-up, there was no statistical signifi-

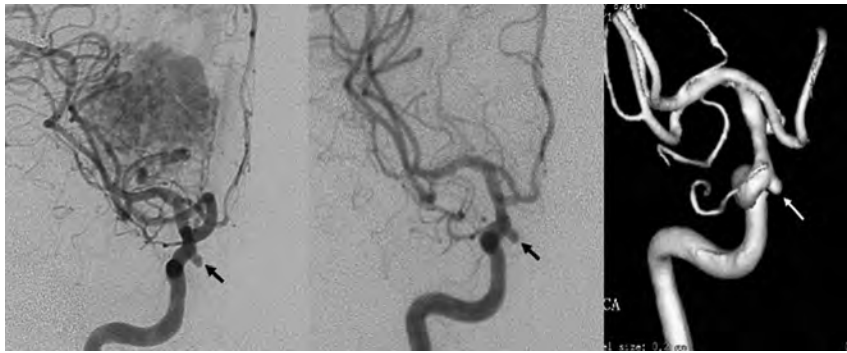


FIG 1. *Left*, The patient had a right parieto-occipital brain arteriovenous malformation with a small flow-related aneurysm (*arrow*) at the right medial paraclinoid internal carotid artery. *Right*, Conventional angiography at 54 months after stereotactic gamma knife surgery demonstrates almost total obliteration of the BAVM but no obvious morphologic change in the proximal FA.

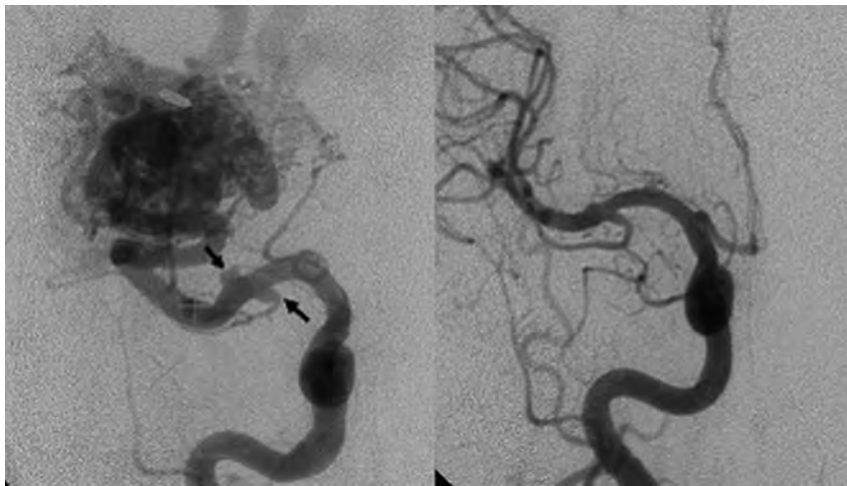


FIG 2. *Left*, The patient had a right frontotemporal BAVM and small proximal FAs at the M1 segment of the right middle cerebral artery (*arrows*). *Right*, Conventional angiography at 38 months after GKS demonstrates almost total regression of the proximal FAs.

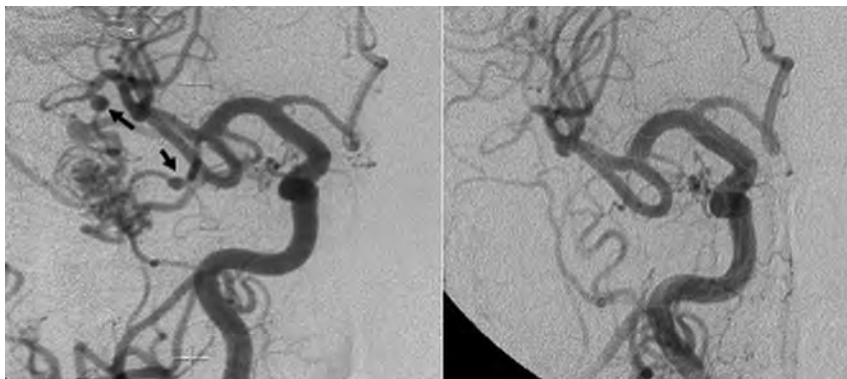


FIG 3. *Left*, The patient had a right inferior temporal BAVM and 2 distal FAs at the M2 segment of the right middle cerebral artery (*arrows*). *Right*, Conventional angiography at 37 months after GKS demonstrates total obliteration of the distal FAs with normalization of blood flow through the feeders to the BAVM and FAs.

cance in sex ($P = .70$), patient age ($P = .21$), ruptured/unruptured BAVMs ($P = .85$), or complete/incomplete obliteration of BAVMs ($P = .286$), but FA regression demonstrated statistical significance in the volume of BAVMs ($P = .048$) and size of FAs ($P = .0001$) (Table 2). The rate of partial or complete obliteration was statistically significantly lower in proximal-versus-distal FAs

($P < .001$, Table 3); proximal-versus-distal FAs of the MCA showed statistical significance (38% versus 86%; $P = .01$). However, proximal-versus-distal FA regression was not significant in the ACA territory (44% versus 76%, $P = .19$) and in those proximal-versus-distal FAs of the infratentorium (25% versus 89%; $P = .052$). Partial or complete obliteration was found in 49 of 99 FAs of <5 mm (49%). FAs of <5 mm (in contrast to larger FAs) had a slightly greater tendency to regress in size (49% versus 17%, $P = .04$, Table 4), but the difference in regression between the 2 groups in individual territories of the MCA (64% versus 40%, $P = .364$), ICA (19% versus 0%, $P = .57$), and infratentorium (75% versus 0%, $P = .31$) was not statistically significant (Table 4). Two patients had ruptured proximal FAs (basilar tip and ICA) in the 27th and 54th months of clinical follow-up, respectively, and 1 rupture was associated with a fatal SAH.

DISCUSSION

The exact mechanism of FA formation in BAVMs is not fully understood. Increased blood flow stress of the BAVM is presumed to be a major factor undoing the balance between hemodynamic stress and the integrity of the internal elastic lamina and intima of the arterial wall. Rapid or turbulent blood flow in the feeders of BAVMs is also reported to be a more important hemodynamic factor in FA formation than intravascular pressure.² Previous studies had shown that older patients with larger BAVMs and posterior circulation supply to the BAVM are prone to FAs.^{9,10} The reported incidence of FAs ranges from 6% to 27%.^{4,9,10-16} This variation of the incidence of FAs may be attributed to different criteria of FA and DSA protocols, overlooked small FAs, and a lack of superselective microcatheterization of cerebral arteries.¹⁷ In the past, conventional 2D-DSA was the criterion standard method of evaluating BAVM angioarchitecture.

Nevertheless, because of the overlap of FAs by the parent artery or arterial branch on conventional DSA and the lack of rotational and 3D-reconstruction DSA, 2D-DSA may overlook 6.8%–21% of intracranial aneurysms, particularly, aneurysms of <3 mm.¹⁸⁻²¹

In our series, the incidence of FAs was 8.8%; this was within

Table 2. Demographics of 111 FAs in 72 patients with BAVMs after radiosurgery^a

Parameters	Stable FAs (n = 60)	Regressive FAs (n = 51)	P Value
Sex			.70
Male (n = 43)	35 (57)	27 (44)	
Female (n = 29)	25 (51)	24 (49)	
Mean age of patients (yr)	41 ± 10	44 ± 15	.21
Mean volume of BAVM (mL)	36 ± 9	40 ± 12	.048 ^b
Mean size of FAs (mm)	4.5 ± 0.9	3.6 ± 0.5	.0001 ^b
No. of ruptured/unruptured BAVMs			.85
Ruptured (n = 31)	26 (55)	21 (45)	
Unruptured (n = 41)	34 (53)	30 (47)	
No. of complete/incomplete obliteration of BAVMs			.29
Complete (n = 52)	41 (51)	40 (49)	
Incomplete (n = 20)	19 (63)	11 (37)	

^a Data are means. Numbers in parentheses do not add up to 100% due to rounding. Data in parentheses are percentages.

^b $P < .05$, indicates statistical significance.

Table 3: Location and morphologic change of FAs of BAVMs^a

Location of FA	No. of FAs	No. of Stable FAs	No. of Regressive FAs/Total Regression	P Value of Regression in Proximal and Distal FAs
Supratentorium	98	56 (57)	42 (43)/20 (20)	
ACA	26			
Proximal (%)	9	5 (56)	4 (44)/1 (11)	.19
Distal (%)	17	4 (24)	13 (76)/8 (47)	
MCA	30			
Proximal (%)	16	10 (63)	6 (38)/2 (13)	.01
Distal (%)	14	2 (14)	12 (86)/9 (62)	
ICA (proximal)	42	35 (83)	7 (17)/0 (0)	NA
Infratentorium	13			
Proximal	4	3 (75)	1 (25)/1 (25)	.052
Distal	9	1 (11)	8 (89)/5 (56)	
Overall	111	60 (54)	51 (46)/26 (23)	
Proximal (%)	71	53 (75)	18 (25)/4 (6)	<.001 ^b
Distal (%)	40	7 (18)	33 (83)/22 (55)	

Note:—NA indicates not available.

^a Data in parentheses are percentages. Numbers in parentheses do not add up to 100% due to rounding.

^b $P < .05$, indicates statistical significance.

the range of previously reported rates but slightly lower than the average detection rate. The lower detection rate was likely due to the lack of superselective microcatheter DSA in all patients and the absence of rotational/reconstruction DSA in 42% of patients in our series. Multiple FAs were found in 26 of 72 patients (36%); the number of FAs per patient was 1.5. The frequency of multiple FAs in our series was compatible with that in the series of Redekop et al,² in which 123 FAs occurred in 71 patients, but it was much higher than that in the series of Morgan et al⁹ with 4 of 67 patients (6%) with multiple FAs. Most FAs are small and <8 mm.^{4,8,9,22} In our series, all FAs were small (mean size, 4.1 mm), with proximal FAs (mean size, 4.3 mm) being a little larger than distal FAs (mean size, 3.7 mm). However, in recently published data of 172 hemodynamic saccular aneurysms of BAVMs,⁸ 62% of aneurysms were <6 mm, but 38% of aneurysms were >7 mm, with 17% of aneurysms >16 mm. This result may be attributed to the coincidence of natural intracranial aneurysms with BAVMs.

The annual growth rate of most natural unruptured intracra-

Table 4: Size and morphologic change of FAs of BAVMs^a

Location of FA	No. of FAs	No. of Stable FAs	No. of Regressive FAs/Total Regression	P Value of Regression in Small FAs (<5 mm)
Supratentorium	98	56 (57)	42 (43)/20 (20)	
ACA	26			
<5 mm (%)	26	9 (35)	17 (65)/13 (50)	NA
≥5 mm (%)	0	0 (0)	0 (0)	
MCA	30			
<5 mm (%)	25	9 (36)	16 (64)/9 (36)	.36
≥5 mm (%)	5	3 (60)	2 (40)/0 (0)	
ICA	42			
<5 mm (%)	36	29 (80)	7 (19)/0 (0)	.57
≥5 mm (%)	6	6 (100)	0 (0)	
Infratentorium	13	3 (25)	9 (75)/2 (17)	.31
<5 mm (%)	12			
≥5 mm (%)	1	1 (100)	0 (0)	
Overall	111	60 (54)	51 (46)/26 (23)	.036 ^b
<5 mm (%)	99	50 (51)	49 (49)/26 (26)	
≥5 mm (%)	12	10 (83)	2 (17)/0 (0)	

^a Data in parentheses are percentages. Numbers in parentheses do not add up to 100% due to rounding.

^b $P < .05$, indicates statistical significance.

nial aneurysms is highly variable and unpredictable.¹⁵ Spontaneous partial or complete thrombosis is uncommon in intracranial aneurysms.²³ FAs can be differentiated from natural unruptured intracranial aneurysms because they are impacted by the hemodynamic stress of BAVMs, and the latter are not. In our series, FAs tended to be regressive in larger BAVMs ($P = .048$) and smaller FAs ($P = .0001$) during follow-up and showed statistical significance, but there was no statistical significance in sex ($P = .70$), patient age ($P = .21$), ruptured/unruptured BAVMs ($P = .85$), or complete/incomplete obliteration of BAVMs ($P = .29$). Larger BAVM obliteration was usually associated with greater alteration of hemodynamics, leading to size regression of FAs. Smaller FAs were more commonly found in distal FAs than proximal FAs. Redekop et al² reported the tendency of distal FAs to spontaneously disappear after complete BAVM occlusion, which occurred in 4 of 5 FAs (80%) in their series, whereas only 21.7% (23 of 106 proximal FAs) decreased in size after BAVM treatment. This result was similar to our results with statistical significance ($P < .001$): Thirty-three of 40 (83%) distal FAs partially or totally disappeared, but only 18 of 71 (25%) proximal FAs regressed in size or totally disappeared. In terms of the individual territory of size regression of distal-versus-proximal FAs, the MCA territory showed statistical significance ($P = .01$), but the territories of the ACA and infratentorium were not statistically significant ($P = .19$, $P = .052$).

Spontaneous thrombosis of a distal FA tends to occur largely because most distal feeders provide blood to the BAVM, where total BAVM obliteration usually leads to total occlusion and significant reduction of the caliber of the distal feeder and thereby to total or partial regression of the FA. By contrast, the parent artery of proximal FAs supplies both normal brain tissue and the BAVM, where total or subtotal occlusion of the BAVM normalizes the blood flow of the parent artery, reducing the hemodynamic stress on feeders; however, the hemodynamic flow from the normal parent artery to the proximal FA persists, reducing the frequency of spontaneous thrombosis of proximal FAs to less than that of

distal FAs. Although small-sized FAs tended to disappear after integration of the data of all territories ($P = .04$), the frequency of FA regression was not statistically significantly related to FA size in individual territories of the MCA ($P = .36$), ICA ($P = .57$), and infratentorium ($P = .31$). In our study, there was no significant enlargement of FA size at a mean 58-month DSA follow-up.

Stereotactic radiosurgery has been widely used to manage patients with BAVMs with promising results. The reported cure rate for BAVMs at 3 years after stereotactic radiosurgery may be as high as 56%–85% in some selected patients.^{6,24} In terms of peritherapeutic hemodynamic change, GKS differs from endovascular embolization and surgical removal by obliterating BAVMs gradually and slowly so that the hemodynamic impact on brain tissue and FAs is progressively decreased with less risk of an acute sudden increase in the transmural pressure across the dome of the FA, leading to rupture. Previous studies had shown that the presence of an associated aneurysm significantly increases the risk of rehemorrhaging after stereotactic radiosurgery.⁶ FAs are an independent determinant for increased risk of incident BAVM hemorrhage²¹, and FAs may change the natural course of BAVM with increasing hemorrhage.⁹ These findings suggest the need for additional interventional management of the aneurysm to reduce the risk of bleeding during the latency interval after stereotactic radiosurgery for BAVMs.^{6,7} However, in our 72 patients with 111 FAs and an average of 58 months of angiographic and clinical follow-up, only 2 patients developed a ruptured FA; 1 rupture had fatal consequences. The rupture rate per aneurysm/year was calculated to be 0.37%, and the incidence of FA rupture was similar to that reported for natural unruptured intradural aneurysms.^{25,26}

Aggressive management of FAs has been reported with promising results.⁸ For distal FAs that usually have a wide neck or fusiform dilation, it is feasible in some selected patients to perform embolization with liquid embolic materials to obliterate the BAVMs and distal FAs in the same session.⁴ For small smooth-contoured proximal FAs with a relatively low risk of rupture, conservative management is an acceptable option. Nevertheless, with ruptured or symptomatic FAs, proximal FAs larger than 5 mm, irregularly shaped FAs, and those patients with a family history of a ruptured aneurysm, aggressive management by interventional procedures is indicated. Because most proximal FAs are wide-necked, stent-assisted coiling may be necessary to prevent coil migration to the parent artery; however, this technique should be used with caution because of the need for peritherapeutic antiplatelet medication to prevent stent-related thromboembolic complications. Antiplatelet treatment will worsen bleeding from ruptured or reruptured BAVMs or residual BAVMs. The technique of balloon-assisted FA coiling is an alternative. It is better to perform stent-assisted coil embolization and endovascular management of BAVMs during the same session to totally eliminate the risk of bleeding or rebleeding (eg, bleeding from an intranidal aneurysm) rather than wait for total obliteration of the BAVM. In our series, most FAs were small (mean size, 4.1 mm). Considering the natural course of small, unruptured FAs, most of our FAs were conservatively managed by neuroimaging follow-up.

There were some limitations to our study: First, this is a retrospective study of long duration. A prospective study is warranted to confirm our observations, and the mean angiographic fol-

low-up time is not long enough to justify the real morphologic change of FAs after GKS. Second, some patients did not undergo rotational DSA, and all patients lacked microcatheter angiography. These factors may lead to underestimating the true incidence of FAs, particularly distal FAs, because of superimposition on BAVMs.

CONCLUSIONS

Distal FAs tend to shrink more frequently due to occlusion or normalization of angiographic features of distal feeders after BAVM obliteration by GKS. By contrast, proximal FAs shrink less frequently after BAVM obliteration. Spontaneous thrombosis of smaller FAs is more frequent than in larger FAs. The natural history and bleeding risk of unruptured FAs in those peritherapeutically managed by GKS were similar to those of asymptomatic intradural aneurysms in our study.

Disclosures: All authors declare that there are no conflict of interest related to the subject matter or material discussed in this article.

REFERENCES

1. Brown RD Jr, Wiebers DO, Forbes GS. **Unruptured intracranial aneurysms and arteriovenous malformations: frequency of intracranial hemorrhage and relationship of lesions.** *J Neurosurg* 1990;73:859–63 Medline
2. Redekop G, TerBrugge K, Montanera W, et al. **Arterial aneurysms associated with cerebral arteriovenous malformations: classification, incidence, and risk of hemorrhage.** *J Neurosurg* 1998;89:539–46 Medline
3. Berenstein A, Lasjaunias P. **Classification of brain arteriovenous malformation.** In: Berenstein A, Lasjaunias P, eds. *Surgical Neuroangiography: Endovascular Treatment of Cerebral Lesion*. Vol 4. Berlin: Springer-Verlag; 1992:48–55
4. Lv X, Wu Z, He H, et al. **Proposal of classification of aneurysms coexisting with AVM and possible treatment strategies.** *Turk Neurosurg* 2016;26:229–33 CrossRef Medline
5. Flores BC, Klingler DR, Rickert KL, et al. **Management of intracranial aneurysms associated with arteriovenous malformations.** *Neurosurg Focus* 2014;37:E11 CrossRef Medline
6. Kano H, Kondziolka D, Flickinger JC, et al. **Aneurysms increase the risk of rebleeding after stereotactic radiosurgery for hemorrhagic arteriovenous malformations.** *Stroke* 2012;43:2586–91 CrossRef Medline
7. Nataf F, Ghossoub M, Schlienger M, et al. **Bleeding after radiosurgery for cerebral arteriovenous malformations.** *Neurosurgery* 2004;55:298–306; discussion 305–06 CrossRef Medline
8. Eliava S, Dmitriev A, Shekhtman O, et al. **Treatment of brain arteriovenous malformations with hemodynamic aneurysms: a series of 131 consecutive cases.** *World Neurosurg* 2018;110:e917–27 CrossRef Medline
9. Morgan MK, Alsahli K, Wiedmann M, et al. **Factors associated with proximal intracranial aneurysms to brain arteriovenous malformations: a prospective cohort study.** *Neurosurgery* 2016;78:787–92 CrossRef Medline
10. Yang WY, Luo CB, Tsuei YS, et al. **A single-institution study of predisposing factors of patients with BAVMs to flow-related aneurysm.** *J Formos Med Assoc* 2019;118:707–12 CrossRef Medline
11. Lv X, Li Y, Yang X, et al. **Characteristics of arteriovenous malformations associated with cerebral aneurysms.** *World Neurosurg* 2011;76:288–91 CrossRef Medline
12. Halim AX, Singh V, Johnstone C, et al; UCSF BAVM Study Project. **Brain Arteriovenous Malformation. Characteristics of brain arteriovenous malformations with coexisting aneurysm: a comparison of two referral centers.** *Stroke* 2002;33:675–79 CrossRef Medline

13. Batjer H, Suss R, Samson D. **Intracranial arteriovenous malformations associated with aneurysms.** *Neurosurgery* 1986;18:29–35 CrossRef Medline
14. Meisel HJ, Mansmann U, Alvarez H, et al. **Cerebral arteriovenous malformations and associated aneurysms: analysis of 305 cases from a series of 662 patients.** *Neurosurgery* 2000;46:793–800; discussion 800–02 Medline
15. Chmayssani M, Rebeiz JG, Rebeiz TJ, et al. **Relationship of growth to aneurysm rupture in asymptomatic aneurysms \leq 7 mm: a systematic analysis of the literature.** *Neurosurgery* 2011;68:1146–71; discussion 1171 CrossRef Medline
16. Cagnazzo F, Brinjikji W, Lanzino G. **Arterial aneurysms associated with arteriovenous malformations of the brain: classification, incidence, risk of hemorrhage, and treatment—a systematic review.** *Acta Neurochir (Wien)* 2016;158:2059–104 CrossRef Medline
17. Turjman F, Massoud TF, Viñuela F, et al. **Aneurysm related to cerebral arteriovenous malformations: superselective angiographic assessment in 58 patients.** *AJNR Am J Neuroradiol* 1994;15:1601–05 Medline
18. Rammos SK, Gardenghi B, Bortolotti C, et al. **Aneurysms associated with brain arteriovenous malformations.** *AJNR Am J Neuroradiol* 2016;37:1966–71 CrossRef Medline
19. Wong SC, Nawawi O, Ramli N, et al. **Benefits of 3D rotational DSA compared with 2D DSA in the evaluation of intracranial aneurysm.** *Acad Radiol* 2012;19:701–07 CrossRef Medline
20. van Rooij WJ, Sprengers ME, de Gast AN, et al. **3D rotational angiography: the new gold standard in the detection of additional intracranial aneurysms.** *AJNR Am J Neuroradiol* 2008;29:976–79 CrossRef Medline
21. Shi WY, Li YD, Li MH, et al. **3D rotational angiography with volume rendering: the utility in the detection of intracranial aneurysms.** *Neurol India* 2010;58:908–13 CrossRef Medline
22. Stapf C, Mohr JP, Pile-Spellman J, et al. **Concurrent arterial aneurysms in brain arteriovenous malformations with haemorrhagic presentation.** *J Neurol Neurosurg Psychiatry* 2002;73:294–98 CrossRef Medline
23. Luo CB, Chen YL, Hsu SW, et al. **Spontaneous healing and complete disappearance of a giant basilar tip aneurysm in a child.** *Interv Neuroradiol* 2001;7:141–45 CrossRef Medline
24. Chung WY, Shiau CY, Wu HM, et al. **Staged radiosurgery for extra-large cerebral arteriovenous malformations: method, implementation, and results.** *J Neurosurg* 2008;109:65–72 Medline
25. International Study of Unruptured Intracranial Aneurysms Investigators. **Unruptured intracranial aneurysms: risk of rupture and risks of surgical intervention.** *N Engl J Med* 1998;339:1725–33 CrossRef Medline
26. Elhamandy MS, Aziz-Sultan MA, Heros RC. **The management of cerebral arteriovenous malformations associated with aneurysms.** *World Neurosurg* 2013;80:e123–29 CrossRef Medline

Comparison of Prasugrel and Clopidogrel Used as Antiplatelet Medication for Endovascular Treatment of Unruptured Intracranial Aneurysms: A Meta-Analysis

F. Cagnazzo, P. Perrini, P.-H. Lefevre, G. Gascou, C. Dargazanli, C. Riquelme, I. Derraz, D. di Carlo, A. Bonafe, and V. Costalat



ABSTRACT

BACKGROUND: Clopidogrel is routinely used to decrease ischemic complications during neurointerventional procedures. However, the efficacy may be limited by antiplatelet resistance.

PURPOSE: Our aim was to analyze the efficacy of prasugrel compared with clopidogrel in the cerebrovascular field.

DATA SOURCES: A systematic search of 2 large databases was performed for studies published from 2000 to 2018.

STUDY SELECTION: According to the Preferred Reporting Items for Systematic Reviews and Meta-Analyses guidelines, we included studies reporting treatment-related outcomes of patients undergoing neurointerventional procedures under prasugrel, and studies comparing prasugrel and clopidogrel.

DATA ANALYSIS: Random-effects meta-analysis was used to pool the overall rate of complications, ischemic and hemorrhagic events, and influence of the dose of prasugrel.

DATA SYNTHESIS: In the 7 included studies, 682 and 672 unruptured intracranial aneurysms were treated under prasugrel (cases) and clopidogrel (controls), respectively. Low-dose (20 mg/5 mg; loading and maintenance doses) prasugrel compared with the standard dose of clopidogrel (300 mg/75 mg) showed a significant reduction in the complication rate (OR = 0.36; 95% CI, 0.17–74, $P = .006$; $I^2 = 0\%$). Overall, the ischemic complication rate was significantly higher in the clopidogrel group (40/672 = 6%; 95% CI, 3%–13%; $I^2 = 83\%$ versus 16/682 = 2%; 95% CI, 1%–5%; $I^2 = 73\%$; $P = .03$). Low and high loading doses of prasugrel were associated with 0.6% (5/535; 95% CI, 0.1%–1.6%; $I^2 = 0\%$) and 9.3% (13/147; 95% CI, 0.2%–18%; $I^2 = 60\%$) intraperiprocedural hemorrhages, respectively ($P = .001$), whereas low and high maintenance doses of prasugrel were associated with 0% (0/433) and 0.9% (2/249; 95% CI, 0.3%–2%; $I^2 = 0\%$) delayed hemorrhagic events, respectively ($P = .001$).

LIMITATIONS: Retrospective series and heterogeneous endovascular treatments were limitations.

CONCLUSIONS: In our study, low-dose prasugrel compared with clopidogrel premedication was associated with an effective reduction of the ischemic events with an acceptable rate of hemorrhagic complications.

ABBREVIATIONS: ASA = acetylsalicylic acid; AT = antiplatelet therapy; CP = clopidogrel; PRU = P2Y12 reaction unit; PS = prasugrel

Prophylactic antiplatelet therapy (AT) is widely used to prevent thromboembolic complications in patients undergoing endovascular treatment of intracranial aneurysms, especially when stent-assisted techniques are adopted.¹ Clopidogrel (an inhibitor of the P2Y12 adenosine diphosphate receptors) is one of the most

common ATs adopted to minimize the risk of thromboembolic events.² However, one of the limitations of this drug is the individual patient variability of its efficacy, with approximately 30% of patients showing clopidogrel (CP) resistance.³ Given that patients who are resistant to CP have a higher risk of ischemic events, different types of AT have been proposed. Prasugrel (PS) (Effient) is a new antiplatelet agent that has been used extensively among patients undergoing cardiovascular treatment.⁴ Like CP, this drug works through the inhibition of the P2Y12 adenosine diphos-

Received November 14, 2018; accepted after revision January 28, 2019.

From the Neuroradiology Department (F.C., P.-H.L., G.G., C.D., C.R., I.D., A.B., V.C.), University Hospital G  i de Chaumi  re, Centre Hospitalier Universitaire de Montpellier, Montpellier, France; and Department of Neurosurgery (P.P., D.D.C.), University of Pisa, Pisa, Italy.

Please address correspondence to Federico Cagnazzo, MD, Neuroradiology Department, CHU G  i de Chaumi  re, 80 Ave Augustin Fliche, 34000 Montpellier, France; e-mail: f.cagnazzo86@gmail.com

Indicates article with supplemental on-line tables.

Indicates article with supplemental on-line photos.

<http://dx.doi.org/10.3174/ajnr.A6004>

phate receptors. However, different from CP, PS requires a 1-step activation, allowing more effective platelet inhibition and a lower degree of resistance.⁴ The experience with PS in the field of cerebrovascular diseases is still limited, and its safety and efficacy remain unclear. The aim of our meta-analysis was to investigate whether PS can be a conceivable alternative to CP during the endovascular treatment of unruptured intracranial aneurysms.

MATERIALS AND METHODS

Literature Search

A comprehensive literature search of PubMed and Ovid EMBASE was conducted for studies published from January 2000 to October 2018. The Preferred Reporting Items for Systematic Reviews and Meta-Analyses⁵ guidelines were followed. The key words and the detailed search strategy are reported in On-line Table 1, and the studies included in our review are reported in On-line Table 2. The inclusion criteria were the following: 1) studies reporting series of patients with unruptured intracranial aneurysms endovascularly treated in whom PS was administered as an AT; 2) studies reporting outcome comparisons between PS (cases) and CP (control) used as an AT for the endovascular treatment of unruptured intracranial aneurysms. Exclusion criteria were the following: 1) case reports, 2) review articles, 3) studies published in languages other than English, and 4) in vitro/animal studies. In cases of overlapping patient populations, only the series with the largest number of patients or the most detailed data were included. Two independent readers screened articles in their entirety to determine eligibility for inclusion. A third author solved discrepancies.

Data Collection

We extracted the following: 1) treatment-related complications, 2) type of complications, 3) clinical outcome, 4) mean P2Y12 reaction unit (PRU) value, 5) mean percentage of platelet inhibition, and 6) angiographic outcome. The reported results were compared between the PS and CP groups of patients.

Treatment-related complications were divided into the following: 1) periprocedural/early events (within 30 days) and delayed events (after 30 days); 2) transient (asymptomatic events or complete neurologic recovery) and permanent complications (symptomatic events with permanent deficits); and 3) ischemic and hemorrhagic complications. Finally, good outcome was defined as a modified Rankin Scale score of 0–2 or a Glasgow Outcome Score of 4–5, or it was assumed if the study used terms such as “no morbidity,” “good recovery,” and “no symptoms.”

Outcomes

The primary objectives of this study were to compare treatment-related complication rates between the PS and CP groups. The secondary objectives were to define the type of complications and the influence of the loading and maintenance doses of PS on the periprocedural and delayed hemorrhagic events, respectively.

Quality Scoring

The Newcastle-Ottawa Scale⁶ was used for the quality assessment of the included studies (details in On-line Tables 3 and 4). The

quality assessment was performed by 2 authors independently, and a third author solved discrepancies.

Statistical Analysis

We estimated, from each cohort, the cumulative prevalence (percentage) and 95% confidence interval for each outcome. Heterogeneity of the data were assessed by the Higgins index (I^2), and subsequently, the DerSimonian and Laird random-effects model was applied. The graphic representation is shown by a forest plot. To evaluate the heterogeneity and bias, we analyzed the metaregression and the funnel plot that was followed by the Egger linear regression test, respectively. To verify the consistency of outcome meta-analysis results, we assessed the influence of each individual study on the summary effect estimate by the sensitivity analysis (leave-one-out approach) and the subgroups analysis. To compare the percentages of each group and to calculate the P values, we used the 1-way analysis of variance and the Z -test when appropriate. Differences were considered significant at $P < .05$. Meta-analysis was performed with ProMeta-2 (Internovi, Cesena, Italy) and OpenMeta[Analyst] (<http://www.ccbm.brown.edu/openmeta/download.html>).

RESULTS

Literature Review

Studies included in our meta-analysis are summarized in On-line Table 2. The search flow diagram is shown in On-line Fig 1.

Seven studies and 1354 aneurysms/procedures (1232 patients) were included in our review. Overall, 682 unruptured aneurysms were treated endovascularly using PS (cases), whereas 672 unruptured aneurysms were treated endovascularly using CP (controls). Five studies compared treatment-related outcomes between the PS and the CP groups,^{7–10,14} whereas 2 studies reported series of patients exclusively treated with PS.^{12,13}

Quality of Studies

Six studies were retrospective series,^{7,8,10,12,13} whereas 1 study presented a prospective design.⁹ Overall, 5 articles were rated as “high-quality” studies. Details of the ratings of the included studies are reported in the On-line Tables 3 and 4.

Patient Population and Aneurysm Characteristics

Detailed characteristics of the patient population are reported in On-line Table 5. The mean age of patients was comparable between the 2 groups. The proportion of male patients was higher among the PS group (56%; 95% CI, 51%–59% versus 45.6%; 95% CI, 41%–49%; $P = .001$), as well as the proportion of aneurysms in the anterior circulation (87%; 95% CI, 84%–89% versus 82%; 95% CI, 78%–85%) ($P = .01$). Posterior circulation aneurysms were more common among the CP group (18%; 95% CI, 14%–21% versus 13%; 95% CI, 10%–15%) ($P = .01$). Mean aneurysm size was comparable between the 2 groups. The proportion of aneurysms treated with stent-assisted coiling or flow diversion was higher among the PS group (63.6%; 95% CI, 58%–67% versus 54.7%; 95% CI, 50%–58%) ($P = .001$).

In 4 studies,^{8,13,14} the loading dose of PS was 20 mg 1 day before treatment; in one study⁹ it was 30 mg 1 day before treatment; in 2 studies,^{10,12} the loading dose was between 40 and 60 mg

1 day before treatment; and in 1 study,⁷ 60 mg of PS was associated with 325 mg of acetylsalicylic acid (ASA). In 3 studies, CP, 75 mg, was combined with ASA, 100 mg^{7,9} or ASA, 325 mg¹⁰, 5 days before treatment, whereas CP, 300 mg, was used alone in 2 studies^{8,14} 5 days before the procedure. The maintenance dose of PS was 5 mg/day in 3 studies,^{8,13,14} 5–10 mg/day in 2 studies,^{9,12} and 10 mg/day in 2 studies.^{7,10} The maintenance dose of AT in the CP group was CP, 75 mg/day, + ASA, 75–100 mg/day, in 4

studies,^{8–10,14} whereas in 1 study CP, 75 mg/day, was associated with ASA, 325 mg/day.⁷

The VerifyNow P2Y12 assay (Accumetrics, San Diego, California) was used to test the platelet activity in all the reported studies (in 1 series, there were no data about the platelet function testing¹⁰).

The mean radiologic follow-up was 14 months (range, 12–24 months; median, 12 months; interquartile range = 12–24 months) and 13 months (range, 12–22 months; median, 12 months; interquartile range = 12–22 months) among the PS and CP groups, respectively. The mean clinical follow-up was 15 months for both groups.

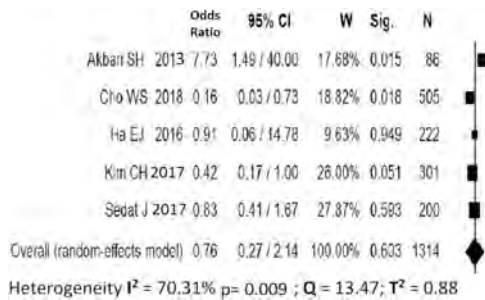
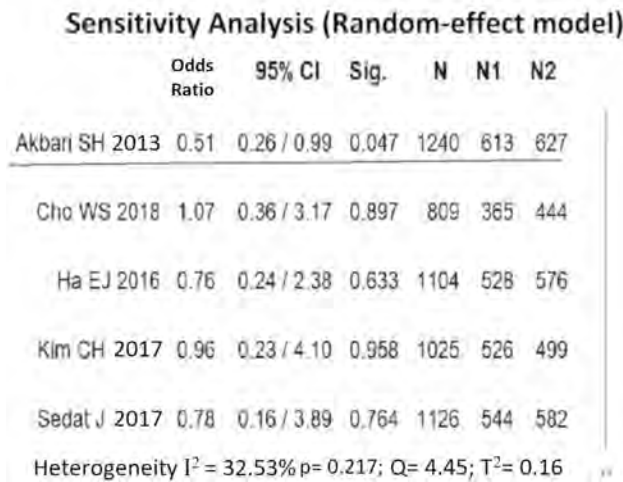


FIG 1. Forest plot with the random-effects model demonstrating the overall effect (odds ratio) of prasugrel versus clopidogrel on the treatment-related complication rate.



Treatment-Related Outcomes among PS and CP Groups

Treatment-related complications were analyzed with random-effect meta-analysis because this model incorporates heterogeneity among studies. When we included all series comparing PS and CP (5 studies^{7–10,14}), AT with PS was not significantly associated with a reduction of the overall rate of treatment-related complications (OR = 0.76; 95% CI, 0.27–2.14; *P* = .603; I² = 70.31%) (Fig 1). The funnel plot followed by the Egger linear regression test excluded publication bias (*P* = .798). Meta-regression showed a significant variation of the effect size (*P* = .001) during the investigated period (from 2013 to 2018) (On-line Fig 2).

The sensitivity analysis (Fig 2 and On-line Fig 3), removing 1 study at a time, showed that the removal of the study of Akbari et al,⁷ was associated with a significant reduction of the overall complication rates with the use of PS (OR = 0.51; 95% CI, 0.26–0.99; *P* = .047; I² = 32.5%). This study reported the highest dose of AT: loading-dose of 60 mg of PS + 325 mg of ASA and maintenance dose of 10 mg of PS + 325 mg of ASA.

The aneurysm occlusion rate was comparable between the 2 groups (OR = 1.21; 95% CI, 0.43–3.39; *P* = .723; I² = 60.2%) (Table).

FIG 2. Sensitivity analysis (leave-one-out meta-analysis) with the random-effects model showing a significant reduction (odds ratio) of the treatment-related complications with the use of PS compared with CP after the removal of the study of Akbari et al.⁷

Treatment-related complication rates and mean values of PRU and platelet inhibition among PS and CP groups of patients

Type of Complications ^a	PS Group (95% CI)	No. of Articles	CP Group (95% CI)	No. of Articles	<i>P</i> Value
Permanent complications	6/651 = 1% (1–4) (I ² = 19%)	6	11/617 = 2% (1–4) (I ² = 81%)	12	.6
Ischemic/thromboembolic	16/682 = 2% (1–5) (I ² = 73%)	7	40/672 = 6% (3–13) (I ² = 83%)	5	.003 ^b
Hemorrhagic	17/682 = 3% (1–9) (I ² = 73%)	7	16/672 = 3% (1–5) (I ² = 19%)	5	.7
Periprocedural complications	23/682 = 4% (1–11) (I ² = 80%)	7	35/672 = 5% (2–11) (I ² = 82%)	5	.7
Delayed complications	12/682 = 3% (1–6) (I ² = 41%)	7	23/672 = 3% (1–8) (I ² = 71%)	5	.8
Treatment-related mortality	0/682	7	1/617 = 0.4% (0.1–2) (I ² = 0%)	4	.09
Good neurologic outcome	631/635 = 98% (96–99) (I ² = 5%)	6	606/617 = 97% (97–99) (I ² = 20%)	4	.2
Platelet inhibition values ^c					
Mean resistance rate	9/433 = 1.8% (0.5–3) (I ² = 0%)	4	99/344 = 30% (23–33) (I ² = 0%)	2	.001 ^b
Mean PRU	125.2 (118–132) (I ² = 0%)	3	247.8 (239–256) (I ² = 18%)	2	.00 ^b
Aneurysm occlusion rate (PS vs CP)	Odds Ratio = 1.21 (95% CI, 0.43–3.39, I ² = 60.2%)			3	.723

^a Complications rates were pooled using proportional meta-analysis.

^b Significant.

^c Platelet inhibition values were pooled using proportional meta-analysis.

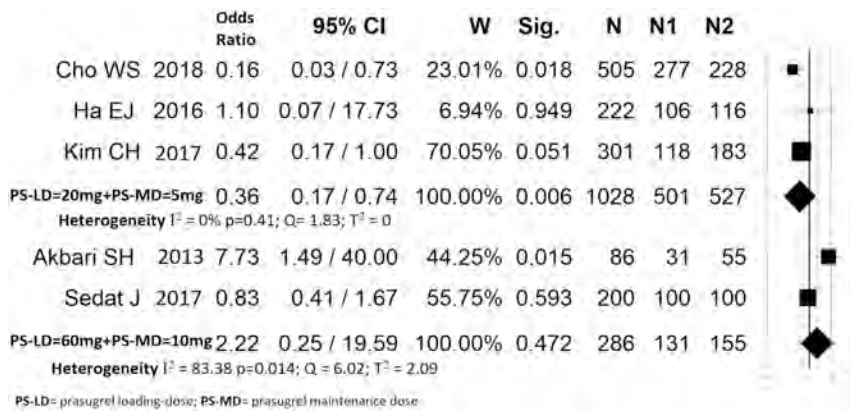


FIG 3. Subgroup analysis of the low and high doses of PS versus a standard dose of CP. Low-dose PS was associated with a significant reduction (odds ratio) of the treatment-related complication rate compared with CP.

Subgroup Analysis: Relationship between the Dose of PS and Treatment-Related Complications

Studies comparing PS and CP were dichotomized into 2 groups (low-dose versus high-dose) based on the PS loading (20 versus 60 mg) and maintenance doses (5 versus 10 mg) (Fig 3). Subgroup analysis of studies reporting a low dose (20 mg/5 mg) of PS^{8,9,14} (the series of Kim et al⁹ was the only study reporting 30 mg of PS as loading dose) showed a significant reduction in the complication rate (OR = 0.36; 95% CI, 0.17–74; $P = .006$; $I^2 = 0\%$). On the contrary, meta-analysis of studies reporting a high dose (60 mg/10 mg) of PS^{7,10} showed higher odds of complications among the PS group, though this result was not statistically significant (OR = 2.22; 95% CI, 0.25–19.59; $P = .472$; $I^2 = 83.38\%$).

Low and high loading doses of PS were associated with 0.6% (5/535; 95% CI, 0.1%–1.6%; $I^2 = 0\%$) and 9.3% (13/147; 95% CI, 0.2%–18%; $I^2 = 60\%$) intraprocedural/very early (within 24 hours) hemorrhagic events, respectively ($P = .001$). Low and high maintenance doses of PS were associated with 0% (0/433) and 0.9% (2/249; 95% CI, 0.3%–2%; $I^2 = 0\%$) hemorrhagic events during follow-up, respectively ($P = .001$) (On-line Table 6).

Subgroups of Treatment-Related Complications

When we investigating data about the type of complications retrieved from all the included series (7 studies), the rates of periprocedural complications, delayed complications, hemorrhagic events, treatment-related morbidity/mortality, and good neurologic outcome were comparable between the 2 groups ($P > .05$) (Table). On the contrary, the ischemic complication rate was significantly higher among the CP group (40/672 = 6%; 95% CI, 3%–13%; $I^2 = 83\%$ versus 16/682 = 2%; 95% CI, 1%–5%; $I^2 = 73\%$; $P = .003$). When we compared the PS and CP groups, the PRU values were 125.2 (95% CI, 118–132; $I^2 = 0\%$) and 247.8 (95% CI, 239–256; $I^2 = 18\%$; $P = .001$) and the mean platelet resistance rates were 1.8% (9/433; 95% CI, 0.5%–3%; $I^2 = 0\%$) and 30% (99/344; 95% CI, 23%–33%; $I^2 = 0\%$) ($P = .001$), respectively. Meta-regression (On-line Fig 4) showed a trend toward a significant association between the ischemic complication rate and the PRU value ($P = .06$).

In both the prasugrel and clopidogrel groups, treatment-related complications were higher among patients treated with flow diverters or stent-assisted coiling, compared with those treated with coiling or balloon-assisted coiling. Among the prasugrel group, the overall

complication rates were 7% (22/254; 95% CI, 2%–13%; $I^2 = 70\%$) and 1.1% (3/281; 95% CI, 0.5%–13%; $I^2 = 0\%$) after treatment with stents/flow diverters and coiling, respectively. Among the clopidogrel group, the overall complication rates were 10% (28/265; 95% CI, 3%–20%; $I^2 = 90\%$) and 2% (5/247; 95% CI, 0.1%–4%; $I^2 = 0\%$) after treatment with stents/flow diverters and coiling, respectively (On-line Table 7).

Study Heterogeneity

Substantial heterogeneity ($>50\%$) was noted for the overall effect size of treatment-related complications (Fig 1) and the complication rate among the subgroup of high-dose PS (Fig 3). Among the subtypes of complications, substantial heterogeneity was reported for ischemic and periprocedural complications, permanent and delayed complications (CP group), and hemorrhagic complications (PS group) (Table). Heterogeneity was also reported for the analysis of the aneurysm occlusion rate.

DISCUSSION

Our meta-analysis of 1354 unruptured intracranial aneurysms highlighted several important findings comparing PS with CP used as an AT for endovascular treatment. Both sensitivity and subgroup analysis demonstrated that low-dose PS (loading and maintenance doses with 20 and 5 mg, respectively) was associated with a reduction of the overall rate of treatment-related complications. In addition, intra-, periprocedural, and delayed hemorrhagic events were significantly lower when the low-dose PS was used instead of the high-dose. Overall, the ischemic complication rate was significantly lower among the PS group (2% versus 6%, $P = .003$), and it is likely related to the lower PRU value after treatment with PS. Because clinical data of PS are limited in the field of cerebrovascular pathology, these findings are important, suggesting that low-dose PS can be safe and effective compared with CP premedication in patients undergoing endovascular treatment of intracranial aneurysms.

Previous series have demonstrated that premedication with CP (irreversible P2Y12 inhibitor) was associated with a reduction of the treatment-related ischemic events during cerebrovascular intervention.² While approximately 85% of CP is hydrolyzed to an inactive metabolite, about 15% of the drug is converted in the liver into the active form through the activity of the cytochrome P450 enzymes.³ One of the main shortcomings of this drug is the variable responsiveness of individuals, related to a genetic polymorphism of cytochrome P450 2C19, one of the hepatic cytochrome P450 enzymes.¹⁵ Accordingly, almost 30% of patients are biochemically CP-resistant, partially due to enzyme or P2Y12 receptor polymorphisms.³ Higher PRU values have been associated with increased thromboembolic complications both after percutaneous coronary intervention¹⁶ and in the neurointerventional field.¹⁷

PS is a third-generation thienopyridine (P2Y12 receptor an-

tagonist) largely used for coronary heart disease because it is associated with high efficacy and a notable decrease of ischemic events.⁴ Indeed, PS is rapidly converted into the active metabolite in 1 step, without dead-end inactive pathways, with a faster onset of action and less variability in response.⁴ However, data about the use of PS for the treatment of cerebrovascular disease are scanty and heterogeneous. One of the first series was described in 2013 by Akbari et al.⁷ The author reported 22% and 4% of treatment-related complications in the PS and CP groups, respectively. Most complications (85%) in the PS group were hemorrhagic events. In this study, PS, 60 mg, + ASA, 325 mg, were used 1 day before the treatment, whereas PS, 20 mg, was used as a maintenance dose. However, more recent series reporting lower doses of PS showed different results. Comparing low-dose PS and a standard dose of CP in a large series of 277 (PS group) and 228 (CP group) intracranial aneurysms treated endovascularly, Cho et al⁸ reported approximately 1% and 4% treatment-related complications, respectively. Similar results were achieved by other authors reporting low-dose PS with 20 and 5 mg used as loading and maintenance doses, respectively.^{9,13,14}

To our knowledge, our meta-analysis is the largest study comparing the outcomes of low-dose and high-dose PS versus standard-dose CP. First, the leave-one-out sensitivity meta-analysis (it was performed by iteratively removing 1 study at a time) showed that the exclusion of the series of Akbari et al⁷ resulted in a significant reduction in the overall complication rate with the use of PS (OR = 0.51; 95% CI, 0.26–0.99; $P = .047$) with low heterogeneity among studies ($I^2 = 32.5\%$). As described above, this study on the series of Akbari et al⁷ reported the highest dose of AT with a not negligible rate of hemorrhagic events. These findings are in accordance with the concern that larger doses of PS can be associated with higher cerebrovascular hemorrhagic risk. Accordingly, because this was one of the main concerns with the use of PS in the cerebrovascular field, we performed a subgroups analysis investigating the influence of the drug doses on the hemorrhagic intra-, periprocedural, and delayed events, based on the loading and maintenance doses of PS, respectively. Most interesting, we found that 20 mg/5 mg (low dose) of PS was associated with <1% hemorrhagic events, compared with 40–60 mg/10 mg (high dose), which was related to higher rates of bleeding events, especially in the perioperative period (9%) (On-line Table 6).

In addition, the subgroup analysis confirmed a significant reduction of the overall rate of complications exclusively in the group of patients treated with low-dose PS (OR = 0.36; 95% CI, 0.17–74; $P = .006$, $I^2 = 0\%$) (Fig 3).

Finally, in our meta-analysis, both the PRU value (125 versus 247) and the mean platelet resistance rates (1.8% versus 30%) were significantly lower in the PS group. In recent studies, low-dose PS with 20 mg/5 mg (loading and maintenance doses) achieved stronger inhibition of platelet activity and a lower rate of resistance than the standard dose of CP (300 mg/75 mg).^{8,18} In accordance with studies reporting a direct correlation between PRU values and ischemic complications,^{2,16,17} meta-regression of all the included studies (On-line Fig 4) found a trend toward a significant association between the ischemic complication rate

and the PRU value ($P = .06$): The lower the PRU value, the better were outcomes in terms of ischemic complications. Accordingly, one of the main results highlighted by our meta-analysis was the effective reduction of the thromboembolic events with the use of PS: The overall rate of ischemic events was 2% and 6% in the PS and CP groups, respectively ($P = .003$).

Strengths and Limitations

Our study has limitations. Most series had a retrospective design. Although the heterogeneity among studies has been, in part, explained with the sensitivity and subgroup analyses, there was heterogeneity within studies related to different endovascular techniques adopted. The influence of the intraprocedural heparin administration was not evaluated. In addition, the duration and dose of ASA in conjunction with prasugrel or clopidogrel and the length of the antiplatelet therapy were not evaluated, and they can have a significant impact on the bleeding risk. The overall effect size (reduction of the treatment-related complication rate among the prasugrel group) could be overestimated due to the search strategy and terminology. However, publication bias was reasonably excluded, and our study is the largest to date comparing PS and CP for the endovascular treatment of intracranial aneurysms.

CONCLUSIONS

Compared with clopidogrel premedication, low-dose prasugrel is associated with an effective reduction of ischemic events with an acceptable rate of hemorrhagic complications. Our results support prasugrel as an alternative to clopidogrel in patients undergoing endovascular treatment of unruptured intracranial aneurysms.

Disclosures: Paolo Perrini—UNRELATED: Employment: Azienda Ospedaliero Universitaria Pisana, Comments: Associate Professor of Neurosurgery, University of Pisa. Pierre-Henri Lefevre—UNRELATED: Payment for Lectures Including Service on Speakers Bureaus: Medtronic; Travel/Accommodations/Meeting Expenses Unrelated to Activities Listed: MicroVention. Vincent Costalat—UNRELATED: Consultancy: Balt, Stryker, Medtronic; Grants/Grants Pending: Medtronic, Stryker*; Payment for Development of Educational Presentations: Medtronic, Stryker, MicroVention. *Money paid to the institution.

REFERENCES

1. Yamada NK, Cross DT 3rd, Pilgram TK, et al. **Effect of antiplatelet therapy on thromboembolic complications of elective coil embolization of cerebral aneurysms.** *AJNR Am J Neuroradiol* 2007;28:1778–82 CrossRef Medline
2. Kang HS, Han MH, Kwon BJ, et al. **Is clopidogrel premedication useful to reduce thromboembolic events during coil embolization for unruptured intracranial aneurysms?** *Neurosurgery* 2010;67:1371–76; discussion 1376 CrossRef Medline
3. Hall R, Mazer CD. **Antiplatelet drugs: a review of their pharmacology and management in the perioperative period.** *Anesth Analg* 2011;112:292–318 CrossRef Medline
4. Wiviott SD. **Intensity of antiplatelet therapy in patients with acute coronary syndromes and percutaneous coronary intervention: the promise of prasugrel?** *Cardiol Clin* 2008;26:629–37 CrossRef Medline
5. Moher D, Liberati A, Tetzlaff J, et al; PRISMA Group. **Preferred reporting items for systematic reviews and meta-analyses: the PRISMA statement.** *Int J Surg* 2010;8:336–41 CrossRef Medline
6. Wells G, Shea B, O'Connell D. **The Newcastle-Ottawa Scale (NOS) for Assessing the Quality of Nonrandomized Studies in Meta-Analyses.** Ottawa: Ottawa Hospital Research Institute; 2011
7. Akbari SH, Reynolds MR, Kadkhodayan Y, et al. **Hemorrhagic complications after prasugrel (Effient) therapy for vascular neurointer-**

- ventional procedures. *J Neurointerv Surg* 2013;5:337–43 CrossRef Medline
8. Cho WS, Lee J, Ha EJ, et al. **Low-dose prasugrel vs clopidogrel-based tailored premedication for endovascular treatment of cerebral aneurysms.** *Neurosurgery* 2018 Aug 20. [Epub ahead of print] CrossRef Medline
 9. Kim CH, Hwang G, Kwon OK, et al. **P2Y12 reaction units threshold for implementing modified antiplatelet preparation in coil embolization of unruptured aneurysms: a prospective validation study.** *Radiology* 2017;282:542–51 CrossRef Medline
 10. Sedat J, Chau Y, Gaudart J, et al. **Prasugrel versus clopidogrel in stent-assisted coil embolization of unruptured intracranial aneurysms.** *Interv Neuroradiol* 2017;23:52–59 CrossRef Medline
 11. Lee K, Park H, Park I, et al. **Y-configuration stent-assisted coil embolization for wide-necked intracranial bifurcation aneurysms.** *J Cerebrovasc Endovasc Neurosurg* 2016;18:355–62 CrossRef Medline
 12. Stetler WR, Chaudhary N, Thompson BG, et al. **Prasugrel is effective and safe for neurointerventional procedures.** *J Neurointerv Surg* 2013;5:332–36 CrossRef Medline
 13. Lee D, Song Y, Han M, et al. **Low-dose prasugrel in patients with resistance to clopidogrel for the treatment of cerebral aneurysms.** *Neurointervention* 2018;13:124–27 CrossRef Medline
 14. Ha EJ, Cho WS, Kim JE, et al. **Prophylactic antiplatelet medication in endovascular treatment of intracranial aneurysms: low-dose prasugrel versus clopidogrel.** *AJNR Am J Neuroradiol* 2016;37:2060–65 CrossRef Medline
 15. Caplain H, Donat F, Gaud C, et al. **Pharmacokinetics of clopidogrel.** *Semin Thromb Hemost* 1999;25(Suppl) 2:25–28 Medline
 16. Gurbel PA, Bliden KP, Samara W, et al. **Clopidogrel effect on platelet reactivity in patients with stent thrombosis: results of the CREST study.** *J Am Coll Cardiol* 2005;46:1827–32 CrossRef Medline
 17. Kim B, Kim K, Jeon P, et al. **Thromboembolic complications in patients with clopidogrel resistance after coil embolization for unruptured intracranial aneurysms.** *AJNR Am J Neuroradiol* 2014;35:1786–92 CrossRef Medline
 18. Choi HH, Lee JJ, Cho YD, et al. **Antiplatelet premedication for stent-assisted coil embolization of intracranial aneurysms: low-dose prasugrel vs clopidogrel.** *Neurosurgery* 2018;83:981–88 CrossRef Medline

Treatment of Unruptured Distal Anterior Circulation Aneurysms with Flow-Diverter Stents: A Meta-Analysis

F. Cagnazzo, P. Perrini, C. Dargazanli, P.-H. Lefevre, G. Gascou, R. Morganti, D. di Carlo, I. Derraz, C. Riquelme, A. Bonafe, and V. Costalat



ABSTRACT

BACKGROUND: The safety and efficacy of flow diversion among distal anterior circulation aneurysms must be proved.

PURPOSE: Our aim was to analyze the outcomes after flow diversion among MCA, anterior communicating artery, and distal anterior cerebral artery aneurysms.

DATA SOURCES: A systematic search of 3 databases was performed for studies published from 2005 to 2018.

STUDY SELECTION: According to Preferred Reporting Items for Systematic Reviews and Meta-Analyses guidelines, we included studies reporting flow diversion of distal anterior circulation aneurysms.

DATA ANALYSIS: Random-effects meta-analysis was used to pool aneurysm occlusion and complication rates. From the individual patient data, univariate and multivariate analyses were used to test predictors of occlusion and complications.

DATA SYNTHESIS: We included 27 studies (484 aneurysms). The long-term adequate occlusion rate (O'Kelly-Marotta scale, C–D) was 82.7% (295/364; 95% CI, 77.4%–87.9%; $I^2 = 52\%$). Treatment-related complications were 12.5% (63/410; 95% CI, 9%–16%; $I^2 = 18.8\%$), with 5.4% (29/418; 95% CI, 3.2%–7.5%; $I^2 = 0\%$) morbidity. MCA location was an independent factor associated with lower occlusion (OR = 0.5, $P = .03$) and higher complication rates (OR = 1.8, $P = .02$), compared with anterior communicating artery and distal anterior cerebral artery aneurysms. The Pipeline Embolization Device (versus other stents) gave better occlusion rates (OR = 2.6, $P = .002$), whereas large/giant aneurysms were associated with higher odds of complications (OR = 2.2, $P = .03$). The rates of occlusion and narrowing of arteries covered by flow-diverter stents were 6.3% (29/283; 95% CI, 3.5%–9.1%; $I^2 = 4.2\%$) and 23.8% (69/283; 95% CI, 15.7%–32%; $I^2 = 80\%$), respectively. Symptoms related to occlusion and narrowing of the jailed arteries were 3.5% (6/269; 95% CI, 1.1%–5%; $I^2 = 0\%$) and 3% (6/245; 95% CI, 1%–4%; $I^2 = 0\%$), respectively.

LIMITATIONS: We reviewed small and retrospective series.

CONCLUSIONS: Flow diversion among distal anterior circulation aneurysms is effective, leading to adequate aneurysm occlusion in 83% of cases. However, this strategy has some limitations among MCA and larger lesions, especially related to the higher rate of complications. Compared with the other devices, the Pipeline Embolization Device seems to be associated with a higher occlusion rate.

ABBREVIATIONS: AC = anterior circulation; AcomA = anterior communicating artery; AT = antiplatelet therapy; DACA = distal anterior cerebral artery; FD = flow diversion

The off-label uses of flow diversion (FD) for the treatment of intracranial aneurysms have increased, including distal locations and bifurcation aneurysms.¹ The smaller diameters of the

arteries, the technical challenges of the distal navigation, and the coverage of bifurcation branches and perforators may increase the risk of treatment-related complications.^{1–4} Few series have investigated the safety and efficacy of these devices among distal anterior circulation (AC) aneurysms. The aim of our meta-analysis was to report the outcome after FD treatment among the 3 most common AC distal locations: the MCA, anterior communicating

Received December 5, 2018; accepted after revision January 28, 2019.

From the Neuroradiology Department (F.C., C.D., P.-H.L., G.G., I.D., C.R., A.B., V.C.), University Hospital Gui-de-Chauliac, Centre Hospitalier Universitaire de Montpellier, Montpellier, France; and Department of Neurosurgery (P.P., D.d.C.) and Section of Statistics (R.M.), University of Pisa, Pisa, Italy.

Please address correspondence to Federico Cagnazzo, MD, Neuroradiology Department, CHU Gui De Chauliac, 80 Ave Augustin Fliche, 34000 Montpellier, France; e-mail: f.cagnazzo86@gmail.com

Indicates article with supplemental on-line tables.

indicates article with supplemental on-line photos.

<http://dx.doi.org/10.3174/ajnr.A6002>

artery (AcomA), and distal anterior cerebral artery (DACA) (pericallosal) segments.

MATERIALS AND METHODS

Literature Search

A comprehensive literature search of PubMed, Ovid EMBASE, and Scopus was conducted for studies published from January 2005 to November 2018. Preferred Reporting Items for Systematic Reviews and Meta-Analyses guidelines⁵ were followed. The detailed search strategy is reported in On-line Table 1, and the included studies are reported in On-line Table 2. The inclusion criteria were the following: studies reporting series with distally located AC unruptured aneurysms treated with FD. We considered the following distal locations: MCA (early cortical branches and MCA main bifurcation⁶), AcomA, and DACA arising at or beyond the A2 segment. Previously ruptured aneurysms showing recanalization after embolization in the acute phase were included if flow diversion was used as a retreatment strategy. Exclusion criteria were the following: 1) case reports, 2) review articles, 3) studies published in languages other than English, 4) in vitro/animal studies, and 5) series reporting an A1 location. In cases of overlapping patient populations, only the series with the largest number of patients or the most detailed data were included. Two independent readers screened articles in their entirety to determine eligibility for inclusion. A third author solved discrepancies.

Data Collection

We extracted the following: 1) occlusion rate, 2) treatment-related complications, and 3) clinical outcome.

Complete/near-complete aneurysm occlusion was defined on the basis of the following: O' Kelly Marotta grades C–D,⁷ Raymond-Roy classification⁸ (classes I–II), or when “complete occlusion” and “neck remnant” were used in the study. Treatment-related complications were divided into the following: 1) periprocedural (within 30 days) and delayed events (after 30 days); 2) transient (asymptomatic events or complete neurologic recovery) and permanent complications (symptomatic events with permanent deficits); and 3) ischemic and hemorrhagic complications. Small and large aneurysms were considered <10 mm and ≥10 mm, respectively. Flow diversion and coiling, compared with the group of flow diversion alone, was considered if coiling was performed in the same treatment session as the flow diverter procedure; patients with a previously coiled aneurysm were not counted in this subgroup. The angiographic outcome of covered arteries was evaluated as follows: 1) normal, 2) arterial narrowing, and 3) arterial occlusion. Finally, good outcome was defined as a modified Rankin Scale score of 0–2 or when the study reported “no morbidity,” “good recovery,” or “no symptoms.”

Outcomes

The primary objectives of this study were to define the safety (treatment-related complications, morbidity rates) and the efficacy (technical success rate, long-term occlusion) of FD for distal AC aneurysms. The secondary objectives were to define the influence of aneurysm, patient, and treatment characteristics on the analyzed outcomes.

Quality Scoring

A modified version of the Newcastle-Ottawa Scale⁹ was used for the quality assessment of the included studies (details in On-line Table 3). The quality assessment was performed by 2 authors independently, and a third author solved discrepancies.

Statistical Analysis

Meta-Analysis. We estimated, from each cohort, the cumulative prevalence and 95% confidence interval for each outcome. Heterogeneity of the data was assessed by the Higgins Index (I^2), and subsequently, the DerSimonian and Laird random-effects model were applied. The graphic representation was performed by forest plots. To evaluate the heterogeneity and bias, we analyzed the meta-regression and the funnel plots followed by the Egger linear regression test, respectively. To verify the consistency of the meta-analysis results outcome, we assessed the influence of each individual study by the sensitivity analysis (leave-one-out approach). Differences among subgroups of analyses were considered significant at $P < .05$. Meta-analysis was performed with ProMeta-2 (Internovi, Cesena, Italy) and OpenMeta[Analyst] (<https://idostatistics.com/prometa3/>).

Univariate and Multivariate Analyses. From the individual patient data,¹⁰ we extracted the following dependent variables: aneurysm occlusion (complete-versus-incomplete occlusion) and treatment-related complications (complications versus no complications). Individual patient data of dissecting and fusiform aneurysms were reasonably excluded, and the analysis was mostly performed on the saccular type. The χ^2 test was used to evaluate qualitative factors associated with occlusion and complications (type of FD, aneurysm location, number of stents, FD alone versus FD and coiling). The independent variables significantly associated (in the univariate analysis) with aneurysm complete occlusion or complications were analyzed together in a binary logistic regression (multivariate analysis) to assess the independent contribution of each factor. The results of the regression model were calculated by the Wald test and expressed using P values and related odds ratio. All statistical analyses were performed with SPSS, Version 24 (IBM, Armonk, New York).

RESULTS

Literature Review

Studies included in our meta-analysis are summarized in On-line Table 2. The search flow diagram is shown in On-line Fig 1.

A total of 27 studies and 484 distal AC aneurysms treated with FD were included. Overall, we extracted 286 MCA aneurysms from 16 studies, 145 AcomA aneurysms from 12 studies, and 53 DACA aneurysms from 6 studies.

Quality of Studies

Overall, 22 included studies were retrospective series,^{1,2,4,11–28} whereas 5 articles were prospective series (details in On-line Table 3).^{29–33}

Patient Population and Aneurysm Characteristics

The mean age of patients was 54.5 years (range, 18–82 years), and the proportion of male patients was 36% (95% CI, 31%–41%)

Table 1: Outcomes after flow diversion treatment of distal anterior circulation intracranial aneurysms

Variables	Results of Systematic		
	Review and Meta-Analysis	No. of Articles	Statistic (95% CI) (I ²)
Angiographic outcomes			
Rate of successful stent deployment	422/429 = 97.5%	29	(96–98.9) (I ² = 0%)
Immediate aneurysm occlusion rate (OKM C–D)	44/333 = 11.1%	18	(6.5–16) (I ² = 55%)
Overall long-term aneurysm occlusion rate (OKM C–D)	295/364 = 82.7%	28	(77.4–87.9) (I ² = 52%)
Long-term occlusion rate (MCA location)	163/206 = 78%	13	(69–88) (I ² = 73.7%)
Long-term occlusion rate (AcomA location)	91/105 = 88%	13	(82–94) (I ² = 0%)
Long-term occlusion rate (DACA location)	41/53 = 82%	6	(70.7–90.7) (I ² = 0%)
Long-term occlusion rate (FRED device)	37/53 = 73.8%	7	(60.1–87.5) (I ² = 31.7)
Long-term occlusion rate (p64 device)	18/22 = 82%	2	(64–98) (I ² = 41.7%)
Long-term occlusion rate (PED device)	143/165 = 87.3%	13	(82.4–92.3) (I ² = 0%)
Long-term occlusion rate (Surpass device)	11/14 = 80.9%	2	(55.5–98) (I ² = 29.3%)
Treatment-related complications and clinical outcomes			
Overall treatment-related complications	63/410 = 12.5%	28	(9–16) (I ² = 18.8%)
Treatment-related complications (MCA location)	44/231 = 18%	12	(12–25) (I ² = 42%)
Treatment-related complications (AcomA location)	14/126 = 8%	10	(3–13) (I ² = 0%)
Treatment-related complications (DACA location)	5/53 = 9%	6	(5–17) (I ² = 0%)
Periprocedural/early complications (within 30 days)	30/418 = 5.9%	28	(3.7–8) (I ² = 0%)
Delayed complications (after 30 days)	35/418 = 6.5%	28	(3.4–8.4) (I ² = 20%)
Transient complications	37/418 = 6.7%	28	(4.4–9) (I ² = 0%)
Permanent complications	29/418 = 5.4%	28	(3.3–7.5) (I ² = 0%)
Treatment-related complications (FRED device)	9/66 = 11.7%	28	(3.2–20.3) (I ² = 29%)
Treatment-related complications (p64 device)	3/23 = 12.5%	2	(1–26) (I ² = 0%)
Treatment-related complications (PED device)	20/159 = 9.2%	12	(4.9–13.5) (I ² = 0%)
Treatment-related complications (Silk device)	2/20 = 8.2%	3	(3.2–19.5) (I ² = 0%)
Treatment-related mortality	5/374 = 2.2%	23	(0.8–3.7) (I ² = 0%)
Overall rate of good neurologic outcome	290/304 = 97%	23	(96–99) (I ² = 0%)
Type of complications and location			
Thromboembolic complications	54/418 = 9.9%	29	(7–12.7) (I ² = 6.6%)
Thromboembolic complications (MCA location)	40/239 = 14.6%	12	(9–20) (I ² = 33%)
Thromboembolic complications (AcomA location)	10/126 = 6%	10	(2–10) (I ² = 0%)
Thromboembolic complications (DACA location)	4/53 = 7%	6	(1.5–16) (I ² = 0%)
Hemorrhagic complications	7/418 = 2.6%	29	(1.1–4) (I ² = 0%)
Premature discontinuation of AT and related ischemic events	6/418 = 2.8%	29	(1.3–4.3) (I ² = 0%)

Note:—OKM indicates O’Kelly-Marotta scale.

(On-line Table 4). Aneurysms included in our study were unruptured lesions with a mean size of 6 mm (median, 5.7 mm; range, 2–21 mm). The most common device was the Pipeline Embolization Device (PED; Covidien, Irvine, California) (62%; 95% CI, 57%–66%), followed by the Flow-Redirection Endoluminal Device (FRED; MicroVention, Tustin, California) (15.5%; 95% CI, 12%–19%), the Silk flow diverter (Balt Extrusion, Montmorency, France) (10.5%; 95% CI, 8%–13%), the p64 (phenox, Bochum, Germany) (7%; 95% CI, 4%–9%), and the Surpass stent (Stryker Neurovascular, Kalamazoo, Michigan) (5%; 95% CI, 3%–7%).

The mean radiologic (digital subtraction angiography) follow-up was 12 months (range, 4–28 months; median, 12.5 months; interquartile range = 10–12.5 months), and the mean clinical follow-up was 13 months (range, 6–30 months; median, 12 months; interquartile range = 10–14 months).

Angiographic Outcomes

Given the interstudy differences in terms of patient population, aneurysm features, aneurysm locations, and type of device used, random-effects meta-analysis was adopted to report the studied outcomes because this model incorporates heterogeneity among studies. The technical success rate was 97.5% (422/429; 95% CI, 96%–98.9%; I² = 0%) (Table 1). Immediate angiographic occlusion (O’Kelly-Marotta scale, C–D) after treatment was obtained

in 11.1% (44/333; 95% CI, 6.5%–16%; I² = 55%) of aneurysms. The rate of long-term complete/near-complete occlusion was 82.7% (295/364; 95% CI, 77.4%–87.9%; I² = 52%). Meta-regression showed a nonsignificant variation of the effect size ($P = .91$) during the analyzed period, and the funnel plot (Egger linear regression test) excludes publication bias ($P = .09$). The sensitivity analysis showed that no individual study significantly influenced the combined aneurysm occlusion rate, indicating the robust results of this meta-analysis (On-line Fig 2).

Treatment-Related Complications

The overall complication rate was 12.5% (63/410; 95% CI, 9%–16%; I² = 18.8%) (Table 1). Meta-regression showed a trend toward lower rates of complications during the analyzed period ($P = .058$). The funnel plot excludes publication bias ($P = .33$). In addition, no individual study significantly influenced the treatment-related complication rate (On-line Fig 3). Periprocedural/early complications were 5.9% (30/418; 95% CI, 3.7%–8%; I² = 0%). Delayed complications were 6.5% (35/418; 95% CI, 3.4%–8.4%; I² = 0%). Transient and permanent complications were 6.7% (33/418; 95% CI, 4.4%–9%; I² = 0%) and 5.4% (29/418; 95% CI, 3.3%–7.5%; I² = 0%), respectively.

Overall, ischemic/thromboembolic and hemorrhagic events were 9.9% (54/418; 95% CI, 7%–12.7%; I² = 6.6%) and 2.6%

Table 2: Univariate and multivariate analysis of predicting factors for aneurysm occlusion and treatment-related complications

	Univariate, P Value	Univariate OR	Multivariate		
			Odds Ratio	95% CI	P Value
Independent variables for occlusion					
Type of FD (PED vs other)	.002	1.4	2.6	1.6–5.3	.02 ^a
No. of FDs (multiple vs single)	.07	1.3	2.3	0.8–7.2	.08
Aneurysm size (large vs small) ^b	.3	1.1			
FD + coils vs FD alone	.006	1.9	1.8	0.8–3.4	.11
Aneurysm location (MCA vs AcomA/DACA)	.01	0.9	0.5	0.2–0.7	.03 ^a
Independent variables for complications					
Type of FD (PED vs other)	.5	1.3			
No. of FDs (multiple vs single)	.4	1.5			
Aneurysm size (large vs small) ^b	.06	2.4	2.2	1–8.3	.03 ^a
FD + coils vs FD alone	.5	0.9			
Aneurysm location (MCA vs AcomA/DACA)	.01	2.9	1.8	1.1–7.6	.02 ^a

^a Significant.

^b Small aneurysms, ≤ 10 mm; Large aneurysms, ≥ 10 mm.

(7/418; 95% CI, 1.1%–4%; $I^2 = 0\%$), respectively. Ischemic events were higher in the MCA location (40/239 = 14.6%; 95% CI, 9%–20%; $I^2 = 33\%$) compared with the AcomA (10/126 = 6%; 95% CI, 2%–10%; $I^2 = 0\%$) and DACA locations (4/53 = 7%; 95% CI, 1.5%–16%; $I^2 = 0\%$). The rate of ischemic complications related to the premature discontinuation of the antiplatelet therapy (AT) (which means that the patient discontinued the AT before the required period) was 2.8% (6/418; 95% CI, 1.3%–4.3%; $I^2 = 0\%$). There was only 1 case of rupture after treatment during 2 years of follow-up: it was a previously ruptured MCA aneurysm treated with coils and multiple FDs.²⁶

Treatment-related mortality was 2.2% (5/374; 95% CI, 0.8%–3.7%; $I^2 = 0\%$), and the rate of good neurologic outcome was 97% (290/304; 95% CI, 96%–99%; $I^2 = 0\%$).

Subgroups Analysis: Factors Related to Aneurysm Occlusion

The long-term complete/near-complete occlusion rate was higher among AcomA (91/105 = 88%; 95% CI, 82%–94%; $I^2 = 0\%$) and DACA (41/53 = 82%; 95% CI, 70.7%–90.7%; $I^2 = 0\%$) compared with the MCA location (163/206 = 78%; 95% CI, 69%–88%; $I^2 = 73.7\%$). Treatment with the PED was associated with a higher occlusion rate (143/165 = 87.3%; 95% CI, 82.4%–92.3%; $I^2 = 0\%$) compared with the other devices (FRED, Surpass, p64) (Table 1). Overall, occlusion rates were comparable among aneurysms treated with FD alone versus FD and coils, single FD versus multiple FDs, and small (< 10 mm) versus large (≥ 10 mm) aneurysms ($P > .05$). In addition, the occlusion rate was comparable among fusiform/dissecting and saccular aneurysms (On-line Table 5). The mean aneurysm size of lesions completely and incompletely occluded was 6 ± 4.6 and 6.5 ± 6.3 mm ($P = .3$). There was a trend toward a lower mean age in patients with complete aneurysm occlusion (54 versus 60 years, $P = .06$).

Overall, individual patient data were available for 80% of patients (Table 2). The multivariate analysis showed that PED devices (versus other stents) were associated with higher occlusion (OR = 2.6, $P = .02$), whereas the MCA location (versus AcomA/DACA) was associated with lower occlusion (OR = 0.5, $P = .03$).

Subgroup Analysis: Factors Related to Complications

The complication rate was higher for MCA aneurysms (44/231 = 18%; 95% CI, 12%–25%; $I^2 = 42\%$) compared with AcomA (14/126 = 8%; 95% CI, 3%–13%; $I^2 = 0\%$) and DACA aneurysms (5/53 = 9%; 95% CI, 5%–17%; $I^2 = 0\%$). Complication rates after the PED (20/159 = 9.2%; 95% CI, 4.9%–13.5%; $I^2 = 0\%$) and Silk devices (2/20 = 8.2%; 95% CI, 3.2%–19.5%; $I^2 = 0\%$) were slightly lower compared with the FRED (9/66 = 11.7%; 95% CI, 3.2%–20.3%; $I^2 = 29\%$) and p64 devices (3/23 = 12.5%; 95% CI, 1%–26%; $I^2 = 0\%$). Overall, treatment-related complication rates were not significantly associated with the number of stents, treatment with or without coils, age, and type of aneurysm (fusiform/dissecting versus saccular) ($P > .05$). There was a trend toward higher mean aneurysm size in patients presenting with complications (7 ± 4.3 versus 4.4 ± 4.5 mm) ($P = .06$). The adverse event rate was lower among small aneurysms (< 10 mm) versus large lesions (≥ 10 mm) (OR = 0.4, $P = .04$) (On-line Table 5).

The multivariate analysis confirmed larger size aneurysms (≥ 10 mm) (OR = 2.2, $P = .03$) and MCA location (OR = 1.8, $P = .02$) as factors independently associated with higher rates of complications (Table 2).

Outcome of Covered Arteries

Overall, the rates of occlusion and narrowing of arterial branches covered by FD were 6.3% (29/283; 95% CI, 3.5%–9.1%; $I^2 = 4.2\%$) and 23.8% (69/283; 95% CI, 15.7%–32%; $I^2 = 80\%$), respectively (On-line Table 6 and On-line Fig 4). Symptoms related to occlusion and narrowing/slow flow of covered branches were 3.5% (6/269; 95% CI, 1.1%–5%; $I^2 = 0\%$) and 3% (6/245; 95% CI, 1%–4%; $I^2 = 0\%$), respectively. The rate of occlusion of covered vessels in the MCA location (M2 or early cortical branches) was 7.3% (22/207; 95% CI, 3.5%–11%; $I^2 = 15\%$), whereas in the anterior cerebral artery location (A2, callosomarginal artery, artery of Heubner), it was 5.5% (7/76; 95% CI, 1%–11%; $I^2 = 0\%$), respectively. The rates of occlusion of jailed arteries were 7.7% (11/124; 95% CI, 3.2%–12%; $I^2 = 0\%$) and 7% (9/61; 95% CI, 3.5%–10%; $I^2 = 0\%$) among the PED group and other devices, respectively.

Study Heterogeneity

Heterogeneity was low ($< 50\%$) for all the reported outcomes except for the following: immediate aneurysm occlusion, long-

term occlusion among MCA aneurysms, and rate of narrowing of covered vessels.

DISCUSSION

Our meta-analysis of approximately 500 AC distal aneurysms showed that FD treatment was effective, with a rate of technical success and long-term adequate aneurysm occlusion (O'Kelly-Marotta scale, C–D) close to 97% and 83%, respectively. Most interesting, the subgroup analysis showed better angiographic occlusion among AcomA and DACA aneurysms (88% and 82%; O'Kelly-Marotta scale, C–D) compared with MCA location (78%). The binary logistic regression revealed MCA location and treatment with the PED as independent factors associated with lower (OR = 0.5, $P = .03$) and higher occlusion rates (OR = 2.6, $P = .02$), respectively. Although FD treatment was relatively safe with overall rates of complications and morbidity of 12% and 5%, respectively, the MCA location was associated with higher adverse events (18%). Accordingly, in the multivariate analysis, MCA aneurysms (OR = 1.8, $P = .02$) and the aneurysm size (large aneurysms [≥ 10 mm] versus small aneurysms [< 10 mm]) (OR = 2.2, $P = .03$) were independent factors associated with adverse events. These results can guide the practitioners during the off-label use of FD stents for the treatment of distal AC aneurysms.

Angiographic Outcome

Overall, large prospective studies and meta-analyses reported a complete occlusion rate after FD close to 75%.^{34,35} Our study demonstrated comparable results among distal AC aneurysms, with an 82% complete/near-complete occlusion rate. The MCA location was an independent factor of incomplete occlusion (OR = 0.5, $P = .03$). A previous meta-analysis focusing on the endovascular treatment of MCA aneurysms before the era of FD revealed approximately 83% adequate occlusion.³⁶ On the contrary, a very recent review comparing coiling versus clipping of unruptured MCA aneurysms reported 53% and 95% long-term complete occlusion, respectively.³⁷ These data highlighted heterogeneous rates of adequate occlusion among endovascular series of MCA aneurysms. These outcomes are likely related to different factors: 1) the anatomic variations (sometime with an unfavorable configuration); 2) the presence of wide-neck and branching vessels arising from the aneurysm; and 3) the more difficult angiographic visualization of the aneurysm neck and sac. In addition, most of the MCA aneurysms arose from the main bifurcation point, whereas approximately 20% of lesions originated from an early cortical branch (temporal or frontal).⁶ Very few studies reported a distinction between early cortical branch aneurysms (that have a close relation with perforators) and bifurcation aneurysms (that are close to or incorporate M2 branches); this can influence the outcomes after the endovascular treatments.³ All of the above reported features can partially explain the higher rate of heterogeneity of the occlusion rate of MCA aneurysms found in our meta-analysis.

Since the FDA approval of the PED in 2011, its off-label uses have expanded, including at distal locations. In our series, nearly 60% of distal aneurysms were treated with the PED. This device was associated with higher occlusion rates compared with the other flow diverters, and the multivariate analysis confirmed that

the PED was an independent factor associated with better angiographic results (OR = 2.6, $P = .02$). Möhlenbruch et al,³¹ in a recent prospective series, reported a 65% complete/near-complete occlusion among 12 AcomA aneurysms treated with the FRED Jr, whereas Colby et al¹⁴ showed approximately 85% adequate occlusion after treatment with the PED of 34 AcomA aneurysms. Similarly, occlusion among pericallosal aneurysms ranged from 50% to 70%^{15,31} and from 75% to 100%^{1,2,16,22} after treatment with the FRED Jr and PED, respectively.

Finally, consistent with the recent literature,^{38,39} the angiographic outcomes were not significantly influenced by using adjunctive coils and multiple stents.

Treatment-Related Complications

The Aneurysm Study of Pipeline in an Observational Registry³⁵ and the International Retrospective Study of Pipeline Embolization Device (IntrePED)⁴⁰ studies reported treatment-related complication rates close to 11%, with 6% morbidity. Our meta-analysis, focusing on the distal AC aneurysms, showed comparable rates of complications. Most interesting, 10% of them were ischemic events largely related to perforator injury, acute in-stent thrombosis, or covered side branches. Accordingly, the MCA had the highest rate of complications (18%), and this location was an independent factor related to adverse events (OR = 1.8, $P = .02$). This finding is consistent with a recent meta-analysis of FD for MCA aneurysms reporting an overall rate of complications of 21%, with 10% morbidity.³ Overall, almost 3% of complications were related to the premature discontinuation of the AT. Caroff et al,¹³ in a series of 15 MCA aneurysms treated with FD, reported a transient ischemic attack in the MCA territory after the termination of the dual AT. In a recent series of 17 pericallosal aneurysms, the authors reported 1 complete PED occlusion leading to an irreversible ischemic infarct due to the inadvertent discontinuation of the AT.² These data emphasize the close relationship between antiplatelet function and FD in small and distal vessels.

Binary logistic regression of the individual patient data, consistent with the subgroup analysis, underlined aneurysm size (large aneurysms [≥ 10 mm] versus small aneurysms [< 10 mm]) as a factor associated with a higher risk of complications (OR = 2.2, $P = .03$). Due to their size, intrasaccular thrombosis, neck dimension, and the relationship with neural structures, large/very large aneurysms are often difficult to treat and are associated with high rates of treatment-related morbidity.⁴¹ Gawlitza et al,¹⁸ in a series of AcomA and MCA aneurysms treated with FD, reported complications in 5 of the 6 patients with large/giant lesions, while adverse events among small aneurysms were significantly lower (3 of 11 patients). This finding is in accordance with the results of a recent meta-analysis of very large/giant aneurysms showing 29% complications after FD, without significant differences between FD alone and FD plus coiling.⁴¹

Outcome of Covered Vessels

FD stents at the bifurcation points have a potential risk of occlusion of the covered arteries. We found 6% and 24% occlusion and narrowing of covered vessels, respectively. There were not significant differences among the studied locations and the devices. Most important, symptoms related to occlusion and arterial nar-

rowing were both 3%. In the series by Caroff et al,¹³ immediately after treatment, slow flow of the covered M2 caused 6% and 13% of transient and permanent deficits, respectively. Pistocchi et al²³ reported 5 cases of occlusion and 4 cases of slow flow of the covered A2, among 14 patients with AcomA aneurysm treated with the Silk device, with only 1 patient experiencing a transitory hemiparesis. Saleme et al,⁴ in a series of 9 AcomA aneurysms treated with the PED, described 2 cases of asymptomatic A2 occlusion during follow-up. Finally, among DACA aneurysms, the rate of flow modification of the covered callosomarginal artery was between 0% and 30%,^{1,2,15,16,22} with only 1 case of transient ischemic symptoms.³¹

Strengths and Limitations

Our study has limitations. Most of the series are small retrospective studies. Although the AT was quite comparable among the studies (On-line Table 2), the influence of the platelet inhibition levels was not evaluated. Fusiform/dissecting aneurysms reported in a few included series can impact the results of our meta-analysis, though we performed a subgroup analysis (dissecting/fusiform versus saccular) and we reasonably excluded this kind of aneurysm from the binary logistic regression. However, publication bias was reasonably excluded, and our review is the largest today on this topic.

CONCLUSIONS

In general, flow diversion among distal AC aneurysms is effective, leading to adequate aneurysm occlusion in 83% of cases. Nevertheless, this strategy presents some limitations among MCA and larger lesions, especially related to the higher rate of complications. Compared with the other devices, the PED seems to be associated with a higher occlusion rate.

Disclosures: Paolo Perrini—UNRELATED: Employment: University of Pisa, Comments: Associate Professor at University of Pisa. Davide di Carlo—UNRELATED: Employment: University of Pisa. Alain Bonafe—UNRELATED: Consultancy: Medtronic, Stryker, MicroVention. Vincent Costalat—UNRELATED: Consultancy: Medtronic, Balt, Stryker, Cerenovus; Grants/Grants Pending: Medtronic, Stryker, Cerenovus, Balt, Penumbra*; Payment for Development of Educational Presentations: Stryker, Medtronic, Balt, MicroVention. Pierre-Henri Lefevre—UNRELATED: Payment for Development of Educational Presentations: Medtronic. *Money paid to the institution.

REFERENCES

- Lin N, Lanzino G, Lopes DK, et al. **Treatment of distal anterior circulation aneurysms with the Pipeline Embolization Device: a US multi-center experience.** *Neurosurgery* 2016;79:14–22 CrossRef Medline
- Cagnazzo F, Cappucci M, Dargazanli C, et al. **Treatment of distal anterior cerebral artery aneurysms with flow-diverter stents: a single-center experience.** *AJNR Am J Neuroradiol* 2018;39:1100–06 CrossRef Medline
- Cagnazzo F, Mantilla D, Lefevre PH, et al. **Treatment of middle cerebral artery aneurysms with flow-diverter stents: a systematic review and meta-analysis.** *AJNR Am J Neuroradiol* 2017;38:2289–94 CrossRef Medline
- Saleme S, Iosif C, Ponomarjova S, et al. **Flow-diverting stents for intracranial bifurcation aneurysm treatment.** *Neurosurgery* 2014; 75:623–31; quiz 631 CrossRef Medline
- Moher D, Liberati A, Tetzlaff J, et al; PRISMA Group. **Preferred Reporting Items for Systematic Reviews and Meta-Analyses: the PRISMA statement.** *Int J Surg* 2010;8:336–41 CrossRef Medline
- Elsharkawy A, Lehečka M, Niemelä M, et al. **A new, more accurate**

classification of middle cerebral artery aneurysms: computed tomography angiographic study of 1,009 consecutive cases with 1,309 middle cerebral artery aneurysms. *Neurosurgery* 2013;73:94–102; discussion 102 CrossRef Medline

- O’Kelly CJ, Krings T, Fiorella D, et al. **A novel grading scale for the angiographic assessment of intracranial aneurysms treated using flow diverting stents.** *Interv Neuroradiol* 2010;16:133–37 CrossRef Medline
- Roy D, Milot G, Raymond J. **Endovascular treatment of unruptured aneurysms.** *Stroke* 2001;32:1998–2004 CrossRef Medline
- Wells G SB, O’Connell D. **The Newcastle-Ottawa Scale (NOS) for Assessing the Quality of Nonrandomized Studies in Meta-Analyses.** Ottawa: Ottawa Hospital Research Institute; 2011. http://www.ohri.ca/programs/clinical_epidemiology/oxford.asp. Accessed November 5, 2018
- Riley RD, Lambert PC, Abo-Zaid G. **Meta-analysis of individual participant data: rationale, conduct, and reporting.** *BMJ* 2010;340:c221 CrossRef Medline
- Bhogal P, Martinez R, Ganslath O, et al. **Management of unruptured saccular aneurysms of the M1 segment with flow diversion: a single centre experience.** *Clin Neuroradiol* 2018;28:209–16 CrossRef Medline
- Briganti F, Delehay L, Leone G, et al. **Flow diverter device for the treatment of small middle cerebral artery aneurysms.** *J Neurointerv Surg* 2016;8:287–94 CrossRef Medline
- Caroff J, Neki H, Mihalea C, et al. **Flow-diverter stents for the treatment of saccular middle cerebral artery bifurcation aneurysms.** *AJNR Am J Neuroradiol* 2016;37:279–84 CrossRef Medline
- Colby GP, Bender MT, Lin LM, et al. **Endovascular flow diversion for treatment of anterior communicating artery region cerebral aneurysms: a single-center cohort of 50 cases.** *J Neurointerv Surg* 2017;9:679–85 CrossRef Medline
- Dabus G, Grossberg JA, Cawley CM, et al. **Treatment of complex anterior cerebral artery aneurysms with Pipeline flow diversion: mid-term results.** *J Neurointerv Surg* 2017;9:147–51 CrossRef Medline
- De Macedo Rodrigues K, Kühn AL, Tamura T, et al. **Pipeline Embolization Device for pericallosal artery aneurysms: a retrospective single center safety and efficacy study.** *Oper Neurosurg (Hagerstown)* 2018;14:351–58 CrossRef
- De Vries J, Boogaarts J, Van Norden A, et al. **New generation of flow diverter (Surpass) for unruptured intracranial aneurysms: a prospective single-center study in 37 patients.** *Stroke* 2013;44:1567–77 CrossRef Medline
- Gawlitza M, Januel AC, Tall P, et al. **Flow diversion treatment of complex bifurcation aneurysms beyond the circle of Willis: a single-center series with special emphasis on covered cortical branches and perforating arteries.** *J Neurointerv Surg* 2016;8:481–87 CrossRef Medline
- Lin LM, Bender MT, Colby GP, et al. **Use of a next-generation multi-durometer long guide sheath for triaxial access in flow diversion: experience in 95 consecutive cases.** *J Neurointerv Surg* 2018;10: 137–42 CrossRef Medline
- Lin LM, Iyer RR, Bender MT, et al. **Rescue treatment with Pipeline embolization for postsurgical clipping recurrences of anterior communicating artery region aneurysms.** *Interv Neurol* 2017;6: 135–46 CrossRef Medline
- Lubicz B, Collignon L, Raphaeli G, et al. **Pipeline flow-diverter stent for endovascular treatment of intracranial aneurysms: preliminary experience in 20 patients with 27 aneurysms.** *World Neurosurg* 2011; 76:114–19 CrossRef Medline
- Nossek E, Zumofen DW, Setton A, et al. **Treatment of distal anterior cerebral artery aneurysms with the Pipeline Embolization Device.** *J Clin Neurosci* 2017;35:133–38 CrossRef Medline
- Pistocchi S, Blanc R, Bartolini B, et al. **Flow diverters at and beyond the level of the circle of Willis for the treatment of intracranial aneurysms.** *Stroke* 2012;43:1032–38 CrossRef Medline
- Rautio R, Rahi M, Katila A, et al. **Single-center experience with six-month follow-up of FRED Jr flow diverters for intracranial aneu-**

- rysms in small arteries. *Acta Radiol* 2018 Oct 25. [Epub ahead of print] CrossRef Medline
25. Toma AK, Robertson F, Wong K, et al. **Early single centre experience of flow diverting stents for the treatment of cerebral aneurysms.** *Br J Neurosurg* 2013;27:622–28 CrossRef Medline
 26. Topcuoglu OM, Akgul E, Daglioglu E, et al. **Flow diversion in middle cerebral artery aneurysms: is it really an all-purpose treatment?** *World Neurosurg* 2016;87:317–27 CrossRef Medline
 27. Yavuz K, Geyik S, Saatci I, et al. **Endovascular treatment of middle cerebral artery aneurysms with flow modification with the use of the Pipeline embolization device.** *AJNR Am J Neuroradiol* 2014;35:529–35 CrossRef Medline
 28. Zanaty M, Chalouhi N, Tjoumakaris SI, et al. **Flow diversion for complex middle cerebral artery aneurysms.** *Neuroradiology* 2014;56:381–87 CrossRef Medline
 29. Bhogal P, AlMatter M, Bätzner H, et al. **Flow diversion for the treatment of MCA bifurcation aneurysms: a single centre experience.** *Front Neurol* 2017;8:20 CrossRef Medline
 30. Iosif C, Mounayer C, Yavuz K, et al. **Middle cerebral artery bifurcation aneurysms treated by extrasaccular flow diverters: midterm angiographic evolution and clinical outcome.** *AJNR Am J Neuroradiol* 2017;38:310–16 CrossRef Medline
 31. Möhlenbruch MA, Kizilkilic O, Killer-Oberpfalzer M, et al. **Multi-center experience with FRED Jr Flow Re-Direction Endoluminal Device for intracranial aneurysms in small arteries.** *AJNR Am J Neuroradiol* 2017;38:1959–65 CrossRef Medline
 32. Pierot L, Spelle L, Berge J, et al. **Feasibility, complications, morbidity, and mortality results at 6 months for aneurysm treatment with the Flow Re-Direction Endoluminal Device: report of SAFE study.** *J Neurointerv Surg* 2018;10:765–70 CrossRef Medline
 33. Wakhloo AK, Lylyk P, de Vries J, et al; Surpass Study Group. **Surpass flow diverter in the treatment of intracranial aneurysms: a prospective multicenter study.** *AJNR Am J Neuroradiol* 2015;36:98–107 CrossRef Medline
 34. Brinjikji W, Murad MH, Lanzino G, et al. **Endovascular treatment of intracranial aneurysms with flow diverters: a meta-analysis.** *Stroke* 2013;44:442–47 CrossRef Medline
 35. Kallmes DF, Brinjikji W, Boccardi E, et al. **Aneurysm Study of Pipeline in an Observational Registry (ASPIRE).** *Interv Neurol* 2016;5:89–99 CrossRef Medline
 36. Brinjikji W, Lanzino G, Cloft HJ, et al. **Endovascular treatment of middle cerebral artery aneurysms: a systematic review and single-center series.** *Neurosurgery* 2011;68:397–402; discussion 402 CrossRef Medline
 37. Alreshidi M, Cote DJ, Dasenbrock HH, et al. **Coiling versus microsurgical clipping in the treatment of unruptured middle cerebral artery aneurysms: a meta-analysis.** *Neurosurgery* 2018;83:879–89 CrossRef Medline
 38. Sweid A, Atallah E, Herial N, et al. **Pipeline-assisted coiling versus Pipeline in flow diversion treatment of intracranial aneurysms.** *J Clin Neurosci* 2018;58:20–24 CrossRef Medline
 39. Cagnazzo F, di Carlo DT, Cappucci M, et al. **Acutely ruptured intracranial aneurysms treated with flow-diverter stents: a systematic review and meta-analysis.** *AJNR Am J Neuroradiol* 2018;39:1669–75 CrossRef Medline
 40. Kallmes DF, Hanel R, Lopes D, et al. **International retrospective study of the Pipeline embolization device: a multicenter aneurysm treatment study.** *AJNR Am J Neuroradiol* 2015;36:108–15 CrossRef Medline
 41. Cagnazzo F, Mantilla D, Rouchaud A, et al. **Endovascular treatment of very large and giant intracranial aneurysms: comparison between reconstructive and deconstructive techniques—a meta-analysis.** *AJNR Am J Neuroradiol* 2018;39:852–58 CrossRef Medline
 42. Morais R, Mine B, Bruyère PJ, et al. **Endovascular treatment of intracranial aneurysms with the p64 flow diverter stent: mid-term results in 35 patients with 41 intracranial aneurysms.** *Neuroradiology* 2017;59:263–69 CrossRef Medline

Aneurysm Remnants after Flow Diversion: Clinical and Angiographic Outcomes

T.P. Madaelil, J.A. Grossberg, B.M. Howard, C.M. Cawley, J. Dion, R.G. Nogueira, D.C. Haussen, and F.C. Tong

ABSTRACT

BACKGROUND AND PURPOSE: Flow diversion is an established method to treat complex intracranial aneurysms. The natural history of flow-diversion treatment failure resulting in aneurysm remnants is not well-defined. We aimed to delineate the clinical and angiographic features of this entity.

MATERIALS AND METHODS: Review of a prospectively maintained Pipeline Embolization Device data base from inception to October 2017 was performed for aneurysms that demonstrated residual filling on follow-up imaging. Procedural and follow-up clinical details were recorded. Independent, blinded, angiographic assessment of occlusion was performed on the basis of the O'Kelly-Marotta scale. Aggregated outcomes were analyzed using the Fisher exact and Mann-Whitney *U* tests for categorical and continuous variables, respectively (statistical significance, $\alpha = .05$).

RESULTS: During the study period, 283 sequential patients were treated; 87% (246/283) were women. The median patient age was 55 years (interquartile range, 47–65 years). Six-month follow-up imaging was available in 83.7% (237/283) of patients, which showed 62.4% (148/237) complete occlusion (class D, O'Kelly-Marotta grading scale). Adjunctive coiling ($P = .06$), on-label Pipeline Embolization Device use ($P = .04$), and multiple device constructs ($P = .02$) had higher rates of complete occlusion at 6 months. Aneurysm remnants were identified in 25 cases on long-term follow-up imaging (median, 16 months; interquartile range, 12–24 months). No patient with an aneurysm remnant after flow diversion presented with delayed rupture or other clinical sequelae, with a median clinical follow-up of 31 months (interquartile range, 23–33 months).

CONCLUSIONS: Aneurysm remnants after flow diversion are infrequent with minimal clinical impact. When appropriate, the presence of overlapping devices and possibly adjunctive coiling may result in higher rates of complete occlusion.

ABBREVIATIONS: IQR = interquartile range; OKM = O'Kelly-Marotta grading scale

Flow diversion with the Pipeline Embolization Device (PED; Covidien, Irvine, California) was first reported in 2008.¹ Since that time, multiple trials^{2,3} and retrospective case series^{4,5} have supported the role of the PED in the treatment of complex intracranial aneurysms. Current follow-up data show high rates of angiographic occlusion at 5 years with only a 4.8% rate of aneurysm persistence and no evidence of recanalization of previously

occluded aneurysms.⁶ In contrast, coil embolization of intracranial aneurysms results in higher rates of aneurysm persistence.⁷ Increasingly, natural history data describing the angiographic⁸ and clinical outcomes⁹ of aneurysm remnants after endovascular therapy are now available. Preliminary evidence suggests that the type of aneurysm remnant (neck versus body filling) dictates the rate of recanalization after coil embolization (with neck filling having lower rates of recanalization compared with body filling)⁸ and remnants of previously ruptured aneurysms are at a higher risk of rerupture.⁹ However, long-term imaging and clinical data with respect to aneurysm remnants after flow diversion remain sparse. Our goal was to evaluate the longitudinal angiographic and clinical outcomes of aneurysm remnants after flow diversion with the PED.

MATERIALS AND METHODS

A prospectively maintained institutional (Emory University) data base of patients treated with the PED from 2011 through October 2017 was searched for patients who demonstrated resid-

Received September 3, 2018; accepted after revision February 4, 2019.

From the Departments of Neurointerventional Radiology and Neurosurgery (T.P.M., J.A.G., B.M.H., C.M.C., F.C.T.), Emory University School of Medicine, Atlanta, Georgia; Marcus Stroke and Neuroscience Center (R.G.N., D.C.H.), Departments of Neurology and Neurosurgery, Grady Memorial Hospital, Atlanta, Georgia; and MicroVention (J.D.), Aliso Viejo, California.

Drs Thomas P. Madaelil and Jonathan A. Grossberg are co-first authors.

Paper previously presented at: Annual Meeting of the American Society of Neuroradiology and the Foundation of the ASNR Symposium, June 2–7, 2018; Vancouver, British Columbia, Canada.

Please address correspondence to Jonathan Grossberg, MD, Department of Neurosurgery, 1364 Clifton Road, Atlanta, GA 30322; e-mail: jonathan.a.grossberg@emory.edu

<http://dx.doi.org/10.3174/ajnr.A6010>

ual filling on follow-up imaging. Patient-level information regarding aneurysm characteristics, procedural details, and clinical follow-up was collected into an electronic data base. The main exclusion criterion was ruptured aneurysms treated in the acute or subacute period (0–14 days). Collected data points included patient characteristics of age, sex, family history of aneurysms, tobacco use; aneurysm characteristics, including type, size, and location; and procedural details such as the number of devices used, adjunctive coiling, and clinical outcome along with the duration of both clinical and radiographic follow-up. If data were available at 6 months, changes to dual antiplatelet therapy after aneurysm occlusion status were noted. Incomplete occlusion status was defined as classes A–C based on the O’Kelly-Marotta (OKM) grading scale¹⁰ for assessment of aneurysms treated by flow diversion. Independent, retrospective review of follow-up imaging was completed by a fellowship-trained neuroradiologist (3 years of dedicated cerebrovascular experience) who did not participate in the initial procedure. Complete occlusion was defined as class D based on the OKM grading scale.

The association between demographic and clinical risk factors with incomplete occlusion and long-term clinical outcome for patients with incomplete occlusion versus patients with complete occlusion was evaluated using the Fisher exact and Mann-Whitney *U* test for categorical and continuous variables, respectively. The threshold of statistical significance was $\alpha = .05$. All statistical analyses were performed using SPSS, Version 22 (IBM, Armonk, New York) and Excel 2007 (Microsoft, Redmond, Washington).

RESULTS

During the study period, 296 interventions were performed in 283 patients to treat 294 aneurysms. Overwhelmingly, the patients treated were women (87%). The median patient age was 55 years (interquartile range [IQR], 47–65 years). Minimum 6-month follow-up imaging was available in 83.7% (237/283) of patients, which included either DSA (50.2%; 119/237), MRA and DSA

(36.3%; 86/237), or MRA (13.5%; 32/237). Table 1 provides summary demographic data.

At 6 months, 62.4% (148/237) of aneurysms demonstrated complete occlusion (class D, OKM scale), 24.1% (57/237) of aneurysms had an entry remnant (class C, OKM scale), and 13.5% (32/237) of aneurysms had subtotal filling (class B, OKM scale). In patients with available late surveillance imaging at a median duration of 16 months (IQR, 12–24 months), progressive complete occlusion was observed in 40.5% (17/42) of aneurysms (class D, OKM scale). The most common dual antiplatelet regimen (73.4%; 174/237) at midterm follow-up imaging was 75 mg of clopidogrel and 325 mg of aspirin. Tapering of antiplatelet therapy was initiated by the treating physician only if progressive aneurysm occlusion was noted on midterm imaging and in the absence of in-stent intimal hyperplasia. The precise regimen was both patient- and operator-specific. Higher rates of progressive complete occlusion were observed in aneurysms with remnant necks (44.4%, 12/27; class C, OKM scale) as opposed to aneurysms with subtotal filling (33.3%, 5/15; class B, OKM scale), though this trend was not statistically significant ($P = .53$). Figure 1 demonstrates progressive occlusion rates of aneurysms with residual filling on late surveillance imaging in a pictorial format.

Procedural characteristics and aneurysm morphology played an important role in aneurysm occlusion on midterm (6 month) imaging follow-up. Adjunctive coiling during the initial PED placement resulted in higher rates of complete occlusion at 6 months (73.9%, 34/46 versus 58.6%, 99/169); this result almost reached statistical significance ($P = .06$). On-label use of the PED was associated with a higher rate of occlusion (73.0%, 54/74) than off-label use (58.5%, 93/159) ($P = .04$). In addition, deployment of >1 device resulted in higher rates of complete occlusion at 6 months (79.5%, 31/39) versus a single device (58.9%, 116/197) ($P = .02$). No correlation between wide-neck aneurysms (>4 mm; $P = .29$) or diameter (>10 mm; $P = .52$) and the rate of occlusion was found.

A total of 25 aneurysm remnants were available for clinical analysis based on last known follow-up imaging. No patient with an aneurysm remnant after flow diversion presented with delayed rupture or other clinical sequelae (median clinical follow-up, 31 months; IQR, 23–33 months). Details related to aneurysm remnants are noted in Table 2. In addition, angiographic follow-up demonstrated no progression of neck remnants. Figure 2 is one such representative case.

Table 1: Basic clinical and imaging demographics

Demographics	Count (% or IQR as Appropriate)
Interventions	296
Aneurysms	294
Patients	283
Median age (yr)	55 (IQR, 47–65)
Female sex	246 (86.9%)
Follow-up imaging at 6 mo	237 (83.7%)
MRA + DSA at 6 mo	86 (36.3%)
MRA at 6 mo	32 (13.5%)
DSA at 6 mo	119 (50.2%)

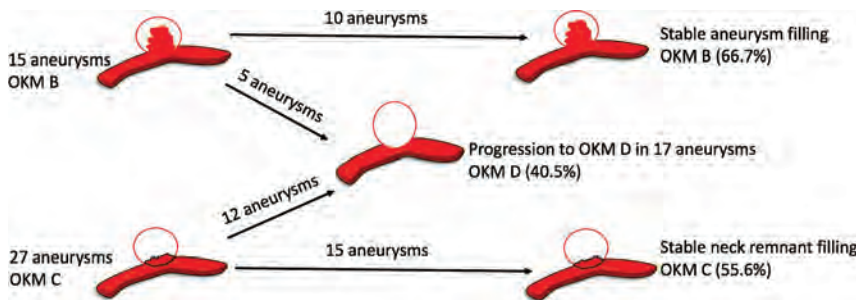


FIG 1. Occlusion status on late-surveillance follow-up imaging.

DISCUSSION

Flow diversion has emerged as a paradigm shift in the treatment of intracranial aneurysms. As more data define characteristics associated with aneurysm persistence after flow diversion,^{11–13} improved patient selection and procedural technique may increase long-term occlusion rates. Parent vessel remodeling resulting in aneurysm occlusion after flow diversion is a remarkably different mechanism compared with coil emboli-

Table 2: Characteristics of aneurysm remnants after flow diversion

Characteristics	Count (% or IQR)
Anterior circulation	21 (84%)
Posterior circulation	4 (16%)
Neck remnant	15 (60%)
Sac remnant	10 (40%)
Branch vessel arising from aneurysm neck	19 (76%)
Median size of remnant (mm)	3 (2–4)
Overlapping devices	1 (4%)

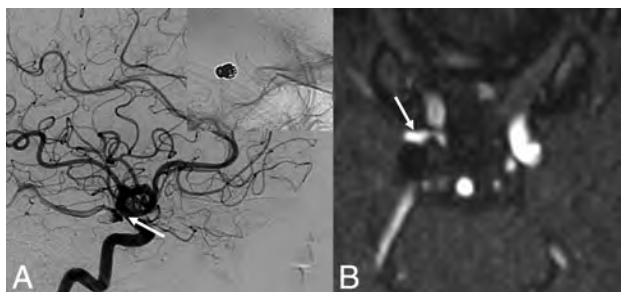


FIG 2. Aneurysm persistence after flow diversion. A 67-year-old woman who had a previously ruptured right posterior communicating artery aneurysm with evidence of recanalization on the 6-month follow-up angiogram. She was treated with flow diversion for the neck recurrence. A 6-month follow-up DSA (lateral x-ray) after flow diversion demonstrates class C OKM grade (continued filling at the neck of the aneurysm) (*white arrow*). At last clinical and angiographic follow-ups at 3 years, there is no evidence of aneurysm rerupture or progression of the neck remnant on MRA (*white arrow*).

zed aneurysms. In addition, high rates of aneurysm occlusion and durability of treatment⁶ make studying aneurysm remnants after flow diversion difficult. Therefore, the natural history of this entity is ill-defined. Our study emphasizes the importance of adjunctive coiling and overlapping devices when appropriate to achieve higher rates of occlusion on midterm imaging follow-up. Moreover, we find that the clinical impact of aneurysm remnants after flow diversion is benign, with no evidence of rerupture in our cohort.

Predictors of Occlusion after Flow Diversion

Adjunctive coil embolization during flow diversion has been previously described by many reports.^{14,15} The placement of loosely packed coils inside the aneurysm at the time of flow diversion provides an additional element of flow disruption to aid aneurysm thrombosis. This observation is confirmed in our study and falls in line with the literature: The presence of adjunctive coiling leads to greater rates of aneurysm occlusion on midterm follow-up imaging. Although our result is slightly underpowered to reach statistical significance ($P = .06$), Lin et al¹⁴ noted a higher proportion of complete occlusion with adjunctive coiling at the time of flow diversion in 29 patients compared with flow diversion alone in 75 patients (93.1% versus 74.7%; $P = .03$). High rates of occlusion on follow-up imaging were similarly replicated by Nossek et al¹⁵ because all aneurysms that underwent flow diversion and adjunctive coiling were occluded. Enthusiasm for adjunctive coiling has been tempered by a few studies¹⁶ reporting that robust coil packing during flow diversion can cause device occlusion due to mass effect and increased thrombogenicity from the large coil mass. However, we did not experience device occlusion

or an increased rate of ischemic complications with adjunctive coiling. This outcome has been confirmed by multiple case series that show the equivalent risk profile of flow diversion with or without adjunctive coiling.^{14,15,17}

Aneurysm occlusion after flow diversion is dependent on metal surface coverage.¹⁸ Constructs with multiple overlapping flow diverters placed across the aneurysm neck favorably increase surface coverage both in ex vivo¹⁹ and computational fluid dynamics models.²⁰ Multiple studies corroborate these basic science observations, with both the Pipeline embolization device for the Intracranial Treatment of Aneurysms trial (PITA)³ and Pipeline for Uncoilable or Failed Aneurysms (PUFS)² trials supporting the efficacy of using overlapping flow diverters to treat aneurysms. Similarly, we show that the use of multiple devices resulted in higher rates of occlusion compared with 1 device ($P = .02$). Understandably, increased metal surface coverage and number of devices may increase thrombogenicity and, as a result, thromboembolic complications.²¹ Chalouhi et al²² proposed a single-device rationale for treatment of aneurysms on the basis of decreased complication rates and equivalent rates of occlusion between single- and multiple-device constructs. On the contrary, a larger study by Brinjikji et al²³ showed that in 906 treated aneurysms, only fusiform aneurysm morphology was independently associated with ischemic complications after multivariate analysis ($P < .001$). Given the conflicting data, larger trials will be required to determine the safety profile of overlapping devices.

Aneurysm Remnants after Flow Diversion

The natural history of remnants after coil embolization of a ruptured aneurysm is well-defined: The more complete occlusion on postprocedural DSA, the lower is the risk of rerupture.²⁴ Increasingly, studies show that unruptured neck remnants after endovascular treatment (stent-assisted coiling/coiling) are both angiographically⁸ and clinically⁹ benign on long-term follow-up. Mascitelli et al⁸ showed that in 99 completely occluded aneurysms and 110 neck remnants after coil embolization, angiographic outcome was similar with very few recanalizations. Munich et al⁹ analyzed the rerupture rate in 626 aneurysms with residual filling on immediate posttreatment angiography. Ruptured aneurysms with neck remnants pose a high risk of rerupture (3.4%), while unruptured aneurysms with residual necks confer a very low risk of rerupture (0.6%). Although these results may not directly correlate with aneurysm remnants after flow diversion, the benign nature of unruptured flow-diverted aneurysm neck remnants should be considered. In addition, the progressive occlusion, parent vessel remodeling, and stasis of flow within the aneurysm sac after flow diversion may be protective against progression of aneurysm neck remnants to definite recurrence. In 25 aneurysm remnants with a median clinical follow-up of 31 months, we did not observe any evidence of rerupture or neck progression. Moreover, in a recent report by Kan et al,²⁵ none of 16 cerebral aneurysms that failed to occlude after flow diversion ruptured during the follow-up period (mean follow-up duration, 24 months). Like the results of Mascitelli et al and Munich et al, the results of Kan et al suggest that remnants of unruptured aneurysms, despite being treated by different devices, are benign.

Although these results are preliminary, the clinical implications of our findings can be considered. Treatment failures after

flow diversion resulting in neck remnants or persistent aneurysm filling did not progress in our series. Therefore, these cases could be monitored with noninvasive temporal MRA imaging.²⁶ If progression of an aneurysm is confirmed on DSA, then a treatment decision about a second device can be considered. In addition, antiplatelet therapy can be de-escalated in cases in which remnants have persisted past 12 months because endothelialization of the stent construct has likely already occurred.

Limitations

The retrospective nature of this study and analysis from a single academic center introduces sampling bias and possibly limits external validity. In addition, other angiographic findings that may be associated with aneurysm persistence that were not measured include inflow angle to aneurysm ostium, vessel size arising from aneurysm neck, and degree of malapposition as measured by VasoCT (Philips Healthcare, Best, the Netherlands).²⁷ Angiographic follow-up at the 6-month time point was relatively consistent for the entire cohort; however, long-term imaging follow-up (MRA/DSA) was variable and at the discretion of the treating neurointerventionalist. The variable regiment of long-term imaging follow-up of the treating physician introduces heterogeneity with respect to our results of occlusion rates on long-term follow-up. In addition, long-term imaging follow-up was not available for all patients (52.8%; 47/89) with aneurysm persistence at 6 months. Some patients were lost to follow-up (72.3%; 34/47), or no follow-up was available for miniscule aneurysm remnants (27.7%; 13/47) that were initially interpreted as complete thrombosis or a tiny remnant that would eventually thrombose.

CONCLUSIONS

Preliminary results suggest that aneurysm remnants after flow diversion are infrequent with minimal clinical impact. When appropriate, the presence of overlapping devices and possibly adjunctive coiling may result in higher rates of complete occlusion. Larger studies with long-term clinical follow-up will be needed to confirm these findings.

ACKNOWLEDGMENTS

We thank Duk Soo Han, MPH, for statistical review.

Disclosures: Jonathan A. Grossberg—UNRELATED: Consultancy: Cognition Medical, Comments: no fees, only stock options; Grants/Grants Pending: Georgia Research Alliance; Stock/Stock Options: equity in Neurotechnology Investors (NTI); Jacques Dion—UNRELATED: Employment: MicroVention/Terumo, Comments: employee, Vice President of Scientific Affairs; Travel/Accommodations/Meeting Expenses Unrelated to Activities Listed: MicroVention/Terumo, Comments: as part of my employment duties. Raul G. Nogueira—OTHER RELATIONSHIPS: Stryker Neurovascular (DAWN Trial Principal Investigator, no compensation; TREVO Registry Steering Committee, no compensation; TREVO 2 trial Principal Investigator, modest; consultant, modest), Medtronic (SWIFT Trial Steering Committee, modest; SWIFT PRIME Trial Steering Committee, no compensation; STAR Trial Angiographic Core Lab, modest compensation), Penumbra (3D Separator Trial Executive Committee, no compensation), Cerenovus/Neuravi (ENDOLOW Trial Principal Investigator; EXCELLENT Registry Principal Investigator; ARISE 2 trial Steering Committee, no compensation; Physician Advisory Board, modest compensation), phenox (Physician Advisory Board, modest compensation), Anaconda (Physician Advisory Board, modest compensation), Genentech (Physician Advisory Board, modest compensation), Biogen (Physician Advisory Board, modest compensation), Prolong Pharmaceuticals (Physician Advisory Board, modest compensation), Allm Inc (Physician Advisory Board, no compensation), iSchemaView (speaker, modest compensation), Brainomix (research

software use, no compensation), Sensome (research device use, no compensation), Viz.ai (Physician Advisory Board, stock options), Philips Healthcare (research software use, no compensation; speaker, modest), Corindus Vascular Robotics (Physician Advisory Board, stock options).

REFERENCES

1. Fiorella D, Woo HH, Albuquerque FC, et al. **Definitive reconstruction of circumferential, fusiform intracranial aneurysms with the Pipeline embolization device.** *Neurosurgery* 2008;62:1115–20; discussion 1120–21 CrossRef Medline
2. Besske T, Kallmes DF, Saatci I, et al. **Pipeline for Uncoilable or Failed Aneurysms: results from a multicenter clinical trial.** *Radiology* 2013; 267:858–68 CrossRef Medline
3. Nelson PK, Lylyk P, Szikora I, et al. **The Pipeline embolization device for the intracranial treatment of aneurysms trial.** *AJNR Am J Neuroradiology* 2011;32:34–40 CrossRef Medline
4. Lylyk P, Miranda C, Ceratto R, et al. **Curative endovascular reconstruction of cerebral aneurysms with the Pipeline Embolization Device: the Buenos Aires experience.** *Neurosurgery* 2009;64:632–42; discussion 642–43; quiz N6 CrossRef Medline
5. Kallmes DF, Brinjikji W, Cekirge S, et al. **Safety and efficacy of the Pipeline Embolization Device for treatment of intracranial aneurysms: a pooled analysis of 3 large studies.** *J Neurosurg* 2017; 127:775–80 CrossRef Medline
6. Besske T, Brinjikji W, Potts MB, et al. **Long-term clinical and angiographic outcomes following Pipeline Embolization Device treatment of complex internal carotid artery aneurysms: five-year results of the Pipeline for Uncoilable or Failed Aneurysms trial.** *Neurosurgery* 2017;80:40–48 CrossRef Medline
7. Lecler A, Raymond J, Rodriguez-Régent C, et al. **Intracranial aneurysms: recurrences more than 10 years after endovascular treatment—a prospective cohort study, systematic review, and meta-analysis.** *Radiology* 2015;277:173–80 CrossRef Medline
8. Mascitelli JR, Oermann EK, De Leacy RA, et al. **Angiographic outcome of intracranial aneurysms with neck remnant following coil embolization.** *J Neurointerv Surg* 2015;7:484–89 CrossRef Medline
9. Munich SA, Cress MC, Rangel-Castilla L, et al. **Neck remnants and the risk of aneurysm rupture after endovascular treatment with coiling or stent-assisted coiling: much ado about nothing?** *Neurosurgery* 2019;84:421–27 CrossRef Medline
10. O’Kelly C, Krings T, Fiorella D, et al. **A novel grading scale for the angiographic assessment of intracranial aneurysms treated using flow diverting stents.** *Interv Neuroradiol* 2010;16:133–37 CrossRef Medline
11. Adeeb N, Moore J, Wirtz M, et al. **Predictors of incomplete occlusion following Pipeline embolization of intracranial aneurysms: is it less effective in older patients?** *AJNR Am J Neuroradiol* 2017;38:2295–300 CrossRef Medline
12. Trivelato FP, Salles Rezende MT, Ulhôa AC, et al. **Occlusion rates of intracranial aneurysms treated with the Pipeline Embolization Device: the role of branches arising from the sac.** *J Neurosurg* 18 Apr 1:1–7. [Epub ahead of print] CrossRef Medline
13. Bender MT, Colby GP, Lin LM, et al. **Predictors of cerebral aneurysm persistence and occlusion after flow diversion: a single-institution series of 445 cases with angiographic follow-up.** *J Neurosurg* 2018 Mar 1:1–9. [Epub ahead of print] CrossRef Medline
14. Lin N, Brouillard AM, Krishna C, et al. **Use of coils in conjunction with the Pipeline embolization device for treatment of intracranial aneurysms.** *Neurosurgery* 2015;76:142–49 CrossRef Medline
15. Nossek E, Chalif DJ, Chakraborty S, et al. **Concurrent use of the Pipeline Embolization Device and coils for intracranial aneurysms: technique, safety, and efficacy.** *J Neurosurg* 2015;122:904–11 CrossRef Medline
16. Siddiqui AH, Kan P, Abula AA, et al. **Complications after treatment with Pipeline embolization for giant distal intracranial aneurysms with or without coil embolization.** *Neurosurgery* 2012;71:E509–13 CrossRef Medline
17. Park M, Kilburg C, Taussky P, et al. **Pipeline embolization device with or without adjunctive coil embolization: analysis of complica-**

- tions from the IntrePED Registry. *AJNR Am J Neuroradiol* 2016;37:1127–31 CrossRef Medline
18. Wang K, Huang Q, Hong B, et al. **Correlation of aneurysm occlusion with actual metal coverage at neck after implantation of flow-diverting stent in rabbit models.** *Neuroradiology* 2012;54:607–13 CrossRef Medline
 19. Shapiro M, Raz E, Becks T, et al. **Building multidevice Pipeline constructs of favorable metal coverage: a practical guide.** *AJNR Am J Neuroradiol* 2014;35:1556–61 CrossRef Medline
 20. Kim M1, Levy EI, Meng H, et al. **Quantification of hemodynamic changes induced by virtual placement of multiple stents across a wide-necked basilar trunk aneurysm.** *Neurosurgery* 2007;61:1305–12; discussion 1312–13 CrossRef Medline
 21. Tan LA, Keigher KM, Munich SA, et al. **Thromboembolic complications with Pipeline Embolization Device placement: impact of procedure time, number of stents and pre-procedure P2Y12 reaction unit (PRU) value.** *J Neurointerv Surg* 2015;7:217–21 CrossRef Medline
 22. Chalouhi N, Tjoumakaris S, Phillips J, et al. **A single Pipeline embolization device is sufficient for treatment of intracranial aneurysms.** *AJNR Am J Neuroradiol* 2014;35:1562–66 CrossRef Medline
 23. Brinjikji W, Lanzino G, Cloft H, et al. **Risk factors for ischemic complications following Pipeline Embolization Device treatment of intracranial aneurysms: results from the IntrePED study.** *AJNR Am J Neuroradiol* 2016;37:1673–78 CrossRef Medline
 24. Johnston SC, Dowd CF, Higashida RT, et al; CARAT Investigators. **Predictors of rehemorrhage after treatment of ruptured intracranial aneurysms: the Cerebral Aneurysm Rerupture After Treatment (CARAT) study.** *Stroke* 2008;39:120–25 CrossRef Medline
 25. Kan P, Srinivasan VM, Mbabuik N, et al. **Aneurysms with persistent patency after treatment with the Pipeline Embolization Device.** *J Neurosurg* 2017;126:1894–98 CrossRef Medline
 26. Boddu S, Tong F, Dehkharghani S, et al. **Contrast-enhanced time-resolved MRA for follow-up of intracranial aneurysms treated with the Pipeline Embolization Device.** *AJNR Am J Neuroradiol* 2014;35:2112–18 CrossRef Medline
 27. van der Marel K, Gounis MJ, Weaver JP, et al. **Grading of Regional Apposition after Flow-Diverter Treatment (GRAFT): a comparative evaluation of VasoCT and intravascular OCT.** *J Neurointerv Surg* 2016;8:847–52 CrossRef Medline

Imaging-Guided Superior Ophthalmic Vein Access for Embolization of Dural Carotid Cavernous Fistulas: Report of 20 Cases and Review of the Literature

M.K.S. Heran, D. Volders, C. Haw, and J.R. Shewchuk



ABSTRACT

SUMMARY: Dural carotid cavernous fistulas are usually treated via a transvenous approach through the inferior petrosal sinus. Surgical exposure and direct access to the superior ophthalmic vein have been previously described in situations in which conventional transvenous access, including the inferior petrosal sinus, is not possible. In this retrospective study of 20 patients, we report our results of imaging-guided percutaneous superior ophthalmic vein access in dural carotid cavernous fistula treatment. The superior ophthalmic vein was accessed after direct percutaneous puncture under sonographic guidance in 16 patients and biplane roadmap guidance in 4 patients. In all 20 patients, it was possible to access the superior ophthalmic vein and cure the dural carotid cavernous fistula. Two patients developed a retrobulbar hematoma after postseptal puncture, which required emergency lateral canthotomy. In our experience, direct imaging-guided percutaneous superior ophthalmic vein access is a safe alternative approach for treatment in situations in which conventional transvenous approaches are not possible.

ABBREVIATIONS: dCCF = dural carotid cavernous fistula; IPS = inferior petrosal sinus; SOV = superior ophthalmic vein

Dural arteriovenous fistulas represent 10%–15% of intracranial high-flow lesions.^{1–3} Dural arteriovenous fistulas consist of a nidus of multiple fistulas in the wall of the dural sinus. The arterial feeders are mostly meningeal branches arising from the external carotid artery or internal carotid artery. Dural arteriovenous fistulas are usually acquired conditions occurring in postmenopausal women.^{1,4,5} Occasionally, they occur in younger patients in association with pregnancy or are related to prior trauma or surgery.⁶ A dural carotid cavernous fistula (dCCF) is a specific type of dural arteriovenous fistula characterized by abnormal arteriovenous shunting within the cavernous sinus. Barrow et al⁵ classified dCCFs into 4 groups according to arterial feeders. Types B, C, and D are dural fistulas, with supply respectively arising from the ICA only, the external carotid artery only, or both the ICA and external carotid artery. The arterIALIZED blood usually drains into the dural sinus itself, either directly or indirectly

through venous anastomoses. Symptoms are typically related to the route of venous drainage and the degree of shunting.^{7–9} When venous drainage is diverted to the ophthalmic veins, ocular symptoms such as conjunctival injection, diplopia, glaucoma, and proptosis may occur.^{1,4} The natural evolution of dCCF is variable, and some may spontaneously resolve by thrombosis of the fistula.^{1,7}

Treatment is considered in those cases in which symptoms persist or worsen. dCCF can be treated by transvenous and/or transarterial endovascular techniques. The transvenous route is usually preferred and is performed by accessing the cavernous sinus via the inferior petrosal sinus (IPS) through the internal jugular vein, with embolization of the cavernous sinus then performed. In the case of a thrombosed IPS, access through the obstructed sinus is not always possible and access to the cavernous sinus can be achieved through other venous approaches such as the contralateral IPS and across intercavernous sinus communications or via the superior ophthalmic vein (SOV). Previous case studies have described an operative exposure of the SOV, with placement of a vascular sheath into the SOV under direct visualization.^{10,11} Given the limited number of case studies describing imaging-guided access rather than operative exposure, we present our experience in obtaining minimally invasive imaging-guided access to the SOV in situations in which conventional transvenous access to the cavernous sinus is not possible for management of patients with dCCF.

Received October 26, 2018; accepted after revision January 23, 2019.

From the Department of Radiology (M.K.S.H., D.V., J.R.S.), University of British Columbia, Vancouver, British Columbia, Canada; Division of Neuroradiology (M.K.S.H., J.R.S.) and Department of Neurosurgery (C.H.), Vancouver General Hospital, University of British Columbia, Vancouver, British Columbia, Canada; and Department of Radiology (M.K.S.H.), British Columbia's Children's Hospital, University of British Columbia, Vancouver, British Columbia, Canada.

Manraj K.S. Heran and David Volders contributed equally to this work.

Please address correspondence to Manraj K.S. Heran, MD, FRCPC, Division of Neuroradiology, Vancouver General Hospital, University of British Columbia, 899 West 12th Ave, Vancouver, BC Canada V5Z 1M9; e-mail: manraj.heran@vch.ca

<http://dx.doi.org/10.3174/ajnr.A5994>

Twenty patients who underwent endovascular treatment for dCCF with transvenous embolization after direct imaging-guided percutaneous SOV puncture^a

Age (yr)/Sex	Side	IPS Outflow	Imaging	Puncture	Hematoma
67/F	Left	None	US	Preseptal	None
66/M	Right	None	US	Preseptal	None
59/M	Left	None	Biplane roadmap	Postseptal	Preseptal
18/F	Right	None	US	Preseptal	Preseptal
59/F	Left	None	US	Postseptal	None
47/F	Bilateral	None	US	Preseptal	Preseptal
98/F	Right	None	US	Preseptal	None
77/F	Left	None	US	Preseptal	None
71/F	Left	None	US	Preseptal	None
70/M	Right	None	US	Preseptal	None
84/F	Left	Minimal	US	Preseptal	None
69/F	Right	None	Biplane roadmap	Preseptal	Preseptal
66/M	Right	None	US	Postseptal	Retrobulbar
66/F	Bilateral	Minimal	US	Preseptal	None
75/M	Right	None	US	Preseptal	None
27/F	Right	None	Biplane roadmap	Postseptal	Retrobulbar
67/F	Bilateral	Minimal	Biplane roadmap	Preseptal	None
76/F	Right	None	US	Preseptal	None
56/F	Right	None	US	Preseptal	None
73/F	Left	None	US	Preseptal	None

Note:—US indicates ultrasound.

^a All patients achieved an angiographic cure.

Case Series

Between July 2012 and November 2017, twenty patients underwent endovascular treatment for dCCF with transvenous embolization after percutaneous imaging-guided SOV puncture (Table). All procedures were performed with the patient under general anesthesia without administration of heparin. The patient group consisted of 5 male and 15 female patients (age range, 18–98 years; mean, 67 years). In all patients, the SOV was evaluated with a high-frequency 15- to 7-MHz hockey stick sonography probe (Philips, Markham, Ontario, Canada) using a broadband acoustic lens for imaging at the transducer surface. Endovascular procedures were performed with an Allura Xper FD 20/20 biplane system (Philips Healthcare, Best, the Netherlands) with high-quality roadmap technology. The SOV could be accessed by sonography in 16 patients (Fig 1). In the remaining 4 patients, SOV access was obtained using biplane roadmap (Philips Healthcare) with a biplane road-mapping technique (Fig 2). The SOV was accessed preseptally in 16 patients. In 4 patients, the SOV had to be accessed in a postseptal location due to SOV thrombosis (2 patients) or high-grade stenosis at the ophthalmic-trochlear vein junction (2 patients). The vascular approach was through the trochlear vein in 2 cases and the SOV in 18 cases. Clinical findings included proptosis and chemosis (20 patients), diplopia and increased ocular pressure (13 patients), decreased visual acuity (13 patients), and sixth nerve palsy (1 patient). The dCCF was on the right side in 10, on the left side in 7, and bilateral in 3 cases. Nineteen dCCF cases were spontaneous, and 1 case was post-traumatic. In most lesions (18/20), the arterial supply was from both the internal and external carotid arteries (type D, Barrow classification). Two cases were of Barrow types B and C, in which arterial supply was from the internal or external carotid artery, respectively.

Treatment indications with an SOV approach included IPS thrombosis and/or cavernous sinus compartmentalization pre-

cluding access to the anterior part of the cavernous sinus from the IPS, favorable anatomic configuration with predominant venous drainage toward the SOV, and type D dCCF.

In 17 of 20 patients, dCCF venous drainage did not flow toward the IPS due to IPS occlusion/thrombosis. In 3 patients, the IPS was visualized during the late venous phase of carotid angiography, indicating patency without communication between the IPS and cavernous sinus compartment with its dCCF shunts. All 20 patients were treated during 1 embolization session, with elimination of the fistula in all cases.

Our standard vascular imaging-guided orbital approach was a preseptal SOV puncture with a 22-ga angiocatheter cannula with initial placement of a 0.014-inch Transend guidewire (Stryker, Kalamazoo, Michigan) in the cavernous sinus. Subsequently, the 2F inner cannula of a micropuncture access set (Cook, Bloomington, Indiana) was advanced over the guidewire and the Transend guidewire was exchanged for a stiffer V-18 guidewire (Boston Scientific, Natick, Massachusetts) to upsize the entire access to the 4F or 5F outer micropuncture cannula in the SOV. This cannula was connected to a system of two 30-cm connection tubes (Cook) and a Tuohy Borst hemostatic valve (Merit Medical, South Jordan, Utah). In 2 cases, we used a Synchro 0.014-inch (Stryker) guidewire instead of the Transend guidewire. In 3 cases, we used a 24-ga angiocatheter cannula instead of the 22-ga angiocatheter cannula due to the smaller SOV size. Hydrophilic microcatheters used were PX SLIM (Penumbra, Alameda, California) in 8 cases, Excelsior SL-10 (Stryker) in 6 cases, and Renegade (Boston Scientific) in 4 cases (in the earlier cases in the series).

Coiling was performed starting from the posterior part of the cavernous sinus moving anteriorly to the level of the SOV using PC400 and Smart coils (Penumbra, Alameda, California) and Target detachable coils (Stryker Neurovascular). We finished the embolization by Gelfoam (Pfizer, New York, New York) of the SOV through the 4F or 5F micropuncture cannula before sheath removal. Control angiography was performed during the procedure from a 4F or 5F catheter, which was selectively positioned into the feeding arteries. Clinical charts and radiologic studies were retrospectively reviewed after ethics committee approval.

In all 20 cases, it was possible to catheterize the SOV under imaging guidance, to reach the cavernous sinus, and to treat the dCCF with an angiographic cure. In most cases (14/20), the procedure was uneventful. In 4 cases, a procedural preseptal hematoma developed, which did not require further management. In 2 cases of postseptal SOV puncture, 1 sonography and 1 biplane roadmap, increased chemosis and proptosis of the ipsilateral globe was seen due to a developing retrobulbar hematoma, with increased intraocular pressure of >50 mm Hg (normal pressure is 12–22 mm Hg). After we successfully embolized the dCCF, our colleagues from ophthalmology performed a lateral canthotomy in the angiography suite. The intraocular pressure immediately normalized in both cases after decompressive canthotomy (<20 mm Hg). Angiographic cure was seen in all 20 patients. Clinical cure was achieved in 15 patients, and improvement was achieved in 5. The 2 patients who developed a postseptal hematoma had normalization of their vision with no residual visual symptoms from their dCCF.

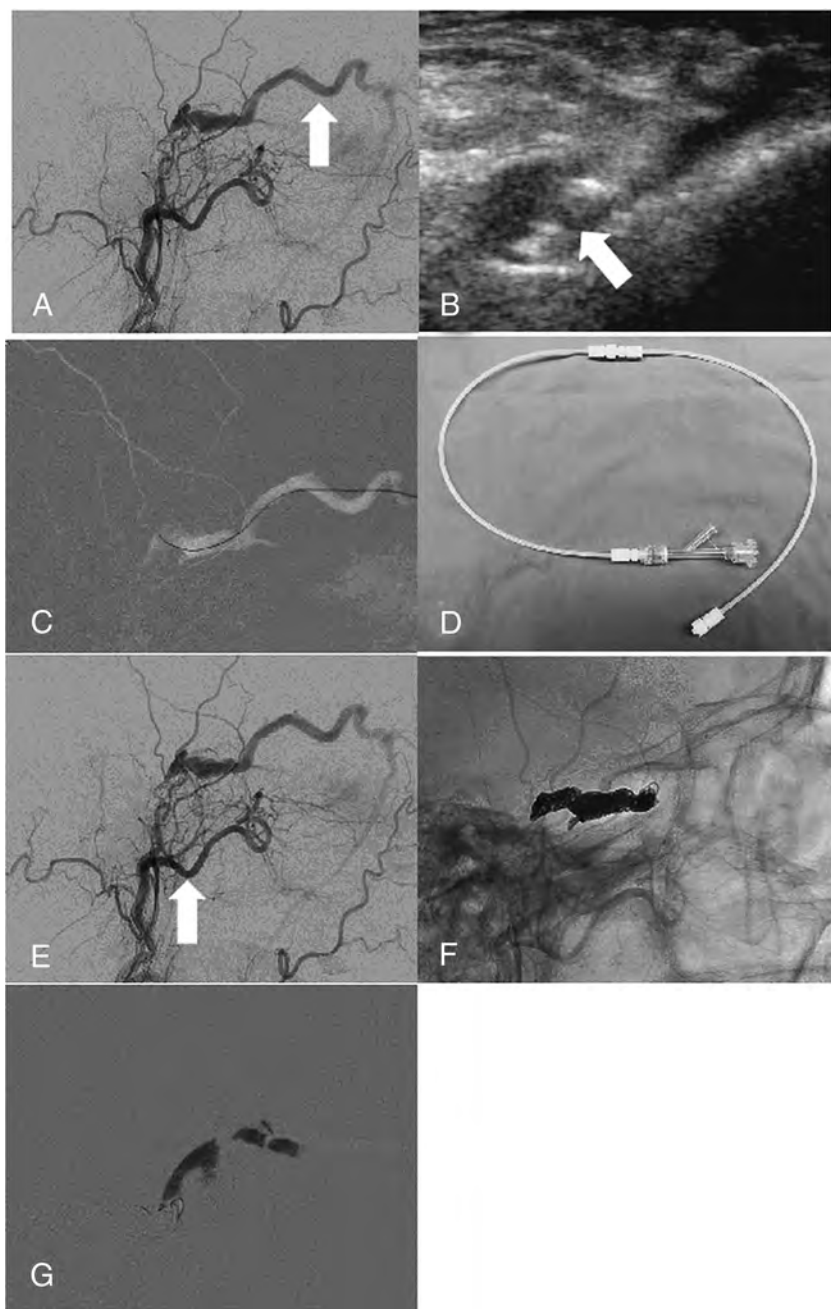


FIG 1. dCCF of the right cavernous sinus in a 56-year-old woman. *A*, Lateral-view angiogram from the right external carotid artery, obtained before embolization, shows a dCCF. The inferior petrosal sinus is thrombosed at the level of its inferior portion. There is predominant venous drainage toward the SOV (arrow). *B*, Direct percutaneous sonographically guided SOV puncture with a 22- or 24-ga angiocatheter cannula (arrow) using a high-frequency 15- to 7-MHz hockey stick sonography probe. *C*, Lateral-view roadmap, obtained after injecting the right external carotid artery, shows how a Transend 0.014-inch guidewire is advanced to the posterior aspect of the cavernous sinus. This allows subsequent exchange of a 2F inner for a 4F outer piece of a micropuncture set over a V-18 guidewire. *D*, Connecting system of two 30-cm connecting tubes and a Tuohy Borst hemostatic valve, which is connected to the micropuncture cannula. *E*, Lateral-view angiogram from the right external carotid artery shows the location in the posterior part of the cavernous sinus where a PX Slim microcatheter is placed (arrow). *F*, Lateral subtracted-view angiogram from the right external carotid artery shows how the coils are placed from posterior to anterior. *G*, Lateral blank subtraction roadmap demonstrating Gelfoam embolization of SOV from downstream to upstream while withdrawing the micropuncture cannula.

DISCUSSION

dCCFs are, in most cases, treated by endovascular cavernous sinus embolization using a transvenous approach, typically via the IPS.

In 4 patients (4/16), a preseptal hematoma developed during the procedure. However, these resolved without issue in all

However, in some patients, this access is absent due to IPS thrombosis or anatomic variation with an absent connection between the IPS and internal jugular vein. In these scenarios, endovascular access to the cavernous sinus through direct surgical access of the dilated SOV can be a useful alternative route, a technique that has been described by several authors in the literature previously.^{10,11}

There are, however, only a few reports that specifically focus on imaging-guided percutaneous SOV access for treatment of a dCCF. In our large case series, we were able to demonstrate that imaging-guided SOV access can be a very valuable alternative to surgical SOV access, with angiographic cure in all of our patients (20/20) and an acceptable risk of associated complications.

The 2 imaging modalities to access the SOV are sonography and fluoroscopic roadmap-assisted techniques, such as biplane roadmap. Of these 2 techniques, real-time sonography-guided access is our preferred first-line approach. We start our procedure by evaluating the size of the SOV, as well as potential problems we may encounter during direct puncture, such as vascular stenosis and loops, as well as the ability to access the SOV in a preseptal location.

The major advantage of imaging-guided SOV access over surgical SOV exposure is that imaging-guided access is less traumatic and avoids (sometimes difficult) coordination of services. The patient does not need to transfer from the operating theater to the angiography suite (if the surgeon chooses to perform the cutdown and exposure in the surgical suite), and the procedure can be performed in a 1-step process. There are also disadvantages to surgical exposure of the SOV because this, too, has an associated learning curve. Specific disadvantages include cut-down and cutaneous scars, which can be cosmetically important.^{12,13} Oishi et al¹⁴ reported blepharoptosis and bilateral forehead dysesthesia in patients undergoing surgical SOV exposure.

Choosing a pre- or postseptal access to the SOV can have important implications. None of the patients (0/16) with a preseptal SOV access had a major complication.



FIG 2. dCCF of the right cavernous sinus in a 66-year-old man. Anteroposterior (A) and lateral (B) view roadmap, obtained after injecting the right external carotid artery, shows how the needle is directed toward the SOV.

cases. This minor complication does not require active management, and it will settle spontaneously within a week.

In situations in which preseptal SOV access is not possible, postseptal SOV puncture can be performed. In our case series, we had 4 patients in whom we performed a postseptal SOV puncture (4/20). Despite our being able to access the SOV in all 4 cases, 2 patients (2/4) developed a retrobulbar hematoma shortly after SOV access. Contrary to a preseptal hematoma, which is a relatively benign condition, a postseptal hematoma is a potentially dangerous condition that can result in increased intraorbital pressure with permanent vision compromise. In the situation of worrisome increased intraorbital pressure, emergency lateral canthotomy is a low-morbidity procedure to relieve the intraorbital pressure, which can easily be performed in the angiography suite. The 2 patients in our case series who developed a retrobulbar hematoma requiring lateral canthotomy had immediate relief of their elevated intraocular pressure and rapid normalization of their vision after the procedure.

In our experience, an initial attempt at SOV access should always be performed preseptally because of the low associated morbidity. Only if this approach is unsuccessful or not possible may postseptal puncture be considered in experienced hands. In this scenario, it is crucial to observe clinical signs of increased intraocular pressure such as proptosis and to have close communication with the ophthalmology service in case lateral canthotomy may be required.

Potential limitations of this study are its retrospective nature and not being a randomized controlled trial in which we compare our technique with surgical SOV exposure. Complications of SOV exposure include bleeding and difficulty in identifying the vein. Some authors have also reported injury of the levator muscle and supraorbital nerve, infection, granuloma, and damage to the trochlea.¹⁵

CONCLUSIONS

Minimally invasive percutaneous imaging-guided access to the SOV can be obtained in situations in which conventional trans-

venous access to the cavernous sinus is not possible for management of patients with dCCF. In our experience, direct imaging-guided percutaneous SOV access is a valuable and time-saving alternative route compared with direct surgical SOV access.

Disclosures: Jason R. Shewchuk—UNRELATED: Travel/Accommodations/Meeting Expenses Unrelated to Activities Listed: European Society of Neuroradiology, Comments: Travel and accommodations reimbursed as invited speaker to European Course in Neuroradiology in May 2018.

REFERENCES

1. Newton T, Hoyt W. **Dural arteriovenous shunts in the region of the cavernous sinus.** *Neuroradiology* 1970;1:71–81 CrossRef
2. Halbach V, Hieshima G, Higashida R, et al. **Carotid cavernous fistulae: indications for urgent treatment.** *AJR Am J Roentgenol* 1987;8:627–33 Medline
3. Toya S, Shiobara R, Izumi J, et al. **Spontaneous carotid-cavernous fistula during pregnancy or in the postpartum stage: report of two cases.** *J Neurosurg* 1981;54:252–56 Medline
4. Phelps C, Thompson H, Ossoinig K. **The diagnosis and prognosis of atypical carotid-cavernous fistula (red-eye shunt syndrome).** *Am J Ophthalmol* 1982;93:423–36 CrossRef Medline
5. Barrow D, Spector R, Braun J, et al. **Classification and treatment of spontaneous carotid cavernous fistulas.** *J Neurosurg* 1985;62:248–56 Medline
6. Watanabe A, Takahara Y, Ibuchi Y, et al. **Two cases of dural arteriovenous malformation occurring after intracranial surgery.** *Neuroradiology* 1984;26:375–80 CrossRef Medline
7. Viñuela F, Fox A, Debrun G, et al. **Spontaneous carotid-cavernous fistulas: clinical, radiological and therapeutic considerations—experience with 20 cases.** *J Neurosurg* 1984;60:976–84 Medline
8. Lasjaunias P, Chiu M, ter Brugge K, et al. **Neurological manifestations in intracranial dural arteriovenous malformations.** *J Neurosurg* 1986;64:724–30 Medline
9. Awad I, Little J, Akrawi W, et al. **Intracranial dural arteriovenous malformations: factors predisposing to an aggressive neurological course.** *J Neurosurg* 1990;72:839–50 Medline
10. Miller NR, Monsein LH, Debrun GM, et al. **Treatment of carotid-cavernous sinus fistulas using a superior ophthalmic vein approach.** *J Neurosurg* 1995;83:838–42 Medline
11. Biondi A, Milea D, Cognard C, et al. **Cavernous sinus dural fistulae treated by transvenous approach through the facial vein: report of seven cases and review of the literature.** *AJNR Am J Neuroradiol* 2003;24:1240–46 Medline
12. Goldberg RA, Goldey SH, Duckwiler G, et al. **Management of cavernous sinus-dural fistulas: indications and techniques for primary embolization via the superior ophthalmic vein.** *Arch Ophthalmol* 1996;114:707–14 Medline
13. Naito I, Magarisawa S, Wada H. **Facial vein approach by direct puncture at the base of the mandible for dural carotid-cavernous fistula: an alternative to the superior ophthalmic vein approach—a case report.** *Interv Neuroradiol* 2002;8:67–70 CrossRef Medline
14. Oishi H, Arai H, Sato K, et al. **Complications associated with transvenous embolisation of cavernous dural arteriovenous fistula.** *Acta Neurochir (Wien)* 1999;141:1265–71 CrossRef Medline
15. Quiñones D, Duckwiler G, Gobin PY, et al. **Embolization of dural cavernous fistulas via superior ophthalmic vein approach.** *AJNR Am J Neuroradiol* 1997;18:921–28 Medline

Flow Patterns in Carotid Webs: A Patient-Based Computational Fluid Dynamics Study

K.C.J. Compagne, K. Dilba, E.J. Postema, A.C.G.M. van Es, B.J. Emmer, C.B.L.M. Majoie, W.H. van Zwam, D.W.J. Dippel, J.J. Wentzel, A. van der Lugt, and F.J.H. Gijssen, for the MR CLEAN investigators



ABSTRACT

BACKGROUND AND PURPOSE: Carotid webs are increasingly recognized as an important cause of (recurrent) ischemic stroke in patients without other cardiovascular risk factors. Hemodynamic flow patterns induced by these lesions might be associated with thrombus formation. The aim of our study was to evaluate flow patterns of carotid webs using computational fluid dynamics.

MATERIALS AND METHODS: Patients with a carotid web in the Multicenter Randomized Clinical Trial of Endovascular Treatment of Acute Ischemic Stroke in the Netherlands (MR CLEAN) were selected for hemodynamic evaluation with computational fluid dynamics models based on lumen segmentations obtained from CT angiography scans. Hemodynamic parameters, including the area of recirculation zone, time-averaged wall shear stress, transverse wall shear stress, and the oscillatory shear index, were assessed and compared with the contralateral carotid bifurcation.

RESULTS: In our study, 9 patients were evaluated. Distal to the carotid webs, recirculation zones were significantly larger compared with the contralateral bifurcation (63 versus 43 mm², $P = .02$). In the recirculation zones of the carotid webs and the contralateral carotid bifurcation, time-averaged wall shear stress values were comparable (both: median, 0.27 Pa; $P = .30$), while transverse wall shear stress and oscillatory shear index values were significantly higher in the recirculation zone of carotid webs (median, 0.25 versus 0.21 Pa; $P = .02$ and 0.39 versus 0.30 Pa; $P = .04$). At the minimal lumen area, simulations showed a significantly higher time-averaged wall shear stress in the web compared with the contralateral bifurcation (median, 0.58 versus 0.45 Pa; $P = .01$).

CONCLUSIONS: Carotid webs are associated with increased recirculation zones and regional increased wall shear stress metrics that are associated with disturbed flow. These findings suggest that a carotid web might stimulate thrombus formation, which increases the risk of acute ischemic stroke.

ABBREVIATIONS: CFD = computational fluid dynamics; IQR = interquartile range; OSI = oscillatory shear index; TAWSS = time-averaged wall shear stress; TransWSS = transverse wall shear stress; WSS = wall shear stress

Carotid webs are fibrous shelf-like lesions causing narrowing in the proximal internal carotid bulb. Although these lesions are rare, carotid webs are an important cause of (recurrent) ischemic stroke in patients without cardiovascular risk factors.^{1,2} Previous studies reported that carotid webs are more frequently observed in younger women and are associated with a high risk of

recurrent ischemic stroke.^{1,3} The underlying mechanism for the association between carotid webs and stroke is unknown, but it was speculated that the impact of the web morphology on flow patterns might lead to thrombus formation¹; nonetheless, this speculation has never been studied.

Hemodynamic flow patterns have been extensively studied in atherosclerotic carotid arteries by computational fluid dynamics (CFD).⁴⁻⁷ This computer-based technique simulates fluid flow patterns based on the Navier-Stokes equations. By means of the image-based geometry of vessels, boundary conditions, and fluid properties, it is possible to simulate hemo-

Received October 15, 2018; accepted after revision February 7, 2019.

From the Departments of Radiology and Nuclear Medicine (K.C.J.C., K.D., A.C.G.M.v.E., A.v.d.L.), Neurology (K.C.J.C., D.W.J.D.), and Biomedical Engineering (K.D., E.J.P., J.J.W., F.J.H.G.), Erasmus MC, University Medical Center, Rotterdam, the Netherlands; Department of Radiology (B.J.E., C.B.L.M.M.), Amsterdam University Medical Center, University of Amsterdam, Amsterdam, the Netherlands; Department of Radiology (W.H.v.Z.), Maastricht University Medical Center, Maastricht, the Netherlands; and Cardiovascular Research Institute Maastricht (W.H.v.Z.), Maastricht, the Netherlands.

The MR CLEAN trial was partly funded by the Dutch Heart Foundation and by unrestricted grants from Angiocare BV, Medtronic/Covidien/ev3, Medac GmbH/Lampero, Penumbra, Stryker, and Top Medical/Concentric.

MR CLEAN investigators are listed in the On-line Appendix.

Please address correspondence to F. Gijssen, PhD, Department of Bioengineering, Erasmus MC, University Medical Center, PO Box 2040 3000 CA Rotterdam, the Netherlands; e-mail f.gijssen@erasmusmc.nl

Indicates article with supplemental on-line appendix and table.

Indicates article with supplemental on-line photos.

<http://dx.doi.org/10.3174/ajnr.A6012>

dynamic patterns. For example, areas of recirculation of blood flow can be investigated and quantified. These recirculation zones are observed in healthy carotid bifurcations but increase in size distal to a stenosis.⁸⁻¹³ In addition, frictional force induced by the blood flow (ie, wall shear stress [WSS]) can be investigated by CFD models. WSS affects many pathophysiologic processes related to atherosclerosis and is associated with ischemic stroke.^{4,14} Several WSS-derived parameters may be of interest in patients with webs. Time-averaged WSS (TAWSS) describes the wall shear stress magnitude over a cardiac cycle. Lower TAWSS values might stimulate atherosclerosis, while high values can cause endothelial trauma.⁴ Evaluating transverse WSS (TransWSS) can quantify multidirectional flows.¹⁵ TransWSS is the average of all WSS components perpendicular to the mean flow direction, consequently taking multidirectionality into account. This recently defined metric corresponds with the location of atherosclerotic lesions.¹⁶ Finally, the oscillatory shear index (OSI) can be assessed to characterize the temporal variability of WSS during a cardiac cycle.¹⁷ Larger changes in the direction of WSS during a cardiac cycle result in a higher OSI and are associated with atherogenesis.¹⁸

Both carotid webs and atherosclerotic stenosis are narrowing of the lumen at the level of the carotid bifurcation. However, the hemodynamic profiles may not be comparable due to differences in 3D morphology. In general, at the proximal part of both lesions, the lumen becomes gradually smaller. However, the lumen distal to the carotid webs differs from an atherosclerotic stenosis due to the shelf-like fibrous lesion, which may greatly influence the distal flow patterns. Gaining insight into the flow patterns of carotid webs might improve the understanding of the risk of (recurrent) ischemic stroke in patients with carotid webs.

In this study, we evaluated simulated flow patterns of carotid webs in patients with acute ischemic stroke with the use of patient-based CFD and compared these with the flow patterns in the contralateral carotid bifurcation.

MATERIALS AND METHODS

Patients and Imaging Data

Patients were selected from the Multicenter Randomized Clinical Trial of Endovascular Treatment of Acute Ischemic Stroke in the Netherlands (MR CLEAN trial).¹⁹ Briefly, patients were included in the MR CLEAN trial ($n = 500$) if a proximal intracranial arterial occlusion was radiographically confirmed and had a minimum score of 2 on the NIHSS at baseline. The study protocol was approved by a central medical ethics committee and the research board of each participating center. Written informed consent before randomization was provided by all patients or their legal representatives. The MR CLEAN trial is registered under No. NTR1804 in the Dutch trial register and under ISRCTN10888758 in the International Standard Randomised Controlled Trial Number (ISRCTN) register.

Patients with a carotid web ($n = 9$) had a CTA scan with a slice increment of 0.5 mm and an average in-plane resolution of 0.46×0.46 mm². Stenosis measurements on CTA were semiautomatically performed by a cross-sectional area measurement at the level of the narrowest lumen divided by the disease-free area distal to the lesion.

Segmentation and Meshing

Semiautomated segmentations of both carotid arteries using a region-growing algorithm were performed with the open-source DICOM viewer Horos (Version 2.0.1).²⁰ Due to different rates of contrast load in each CTA scan, the threshold intensity value was chosen for each patient on the basis of the best representation of morphology by 1 observer (K.C.J.C.). Vascular side branches and remaining calcifications were removed from the 3D volume-rendered lumen. The final segmentation included the common carotid artery, external carotid artery, and internal carotid artery. Flow extensions were added with a length of 3 diameters at the inlet and both outlets. Volumetric meshes of tetrahedral elements and prism layers were generated using ICEM CFD software, Version 17.1 (ANSYS, Canonsburg, Pennsylvania). The number of elements ranged between 2.45×10^6 and 7.80×10^6 , with a minimal and maximal element size of 0.05 and 0.15 mm, respectively.

Computational Fluid Dynamics and Analysis

A plug-like inflow profile was chosen. The average inlet velocity was calculated as a function of the diameter to obtain a wall shear stress of 1.2 Pa at the inlet flow extension.²¹ Due to the absence of patient-specific boundary conditions and because no (>50%) stenosis was present, the outflow ratios for the internal carotid artery/common carotid artery and external carotid artery/common carotid artery were assumed to be, respectively, 0.65 and 0.35.²² Blood was modeled as an incompressible fluid with a density of 1.06 g/cm³, and the Carreau model was applied to account for the non-Newtonian shear thinning behavior.²³ Time-dependent simulations were performed using generic flow waveform shapes as proposed by Lee et al.²⁴ Two cardiac cycles were included, with a time-step of 0.01 seconds. Because the first cycle potentially contains numeric artifacts, only the results of the second cycle were used for the analyses.

From the time-dependent simulations, we extracted various hemodynamic parameters: TAWSS, TransWSS, and OSI. 2D-TAWSS maps were created and used to determine the region of reversed flow (recirculation zone). Subsequently, the total surface area (square millimeters) and length (millimeters) of the recirculation zone were computed.²⁵ Furthermore, TAWSS was assessed at the minimal lumen area of the carotid web or stenosis and in the recirculation zone. Transverse WSS and OSI were both assessed in the recirculation zone (On-line Fig 1). Transverse WSS was introduced by Peiffer et al¹⁵ as follows:

$$TransWSS = \frac{1}{T} \int_0^T \left| \vec{\tau}_w \left(\frac{\int_0^T \vec{\tau}_w dt}{\left| \int_0^T \vec{\tau}_w dt \right|} \right) \right| dt,$$

where \vec{n} represents the normal-to-arterial surface.

For illustration, streamlines were created on the basis of the time-average velocity field. All CFD simulations were performed within Fluent 17.1 (ANSYS) using standard numeric techniques.

Statistical Analysis

Descriptive statistics of the characteristics of flow patterns are presented as medians and interquartile ranges (IQR) due to a non-normal distribution. Hemodynamic parameters of flow patterns in carotid bifurcations with a web were compared with the

Table 1: Baseline characteristics of included patients

Pt.	Sex, Age (yr)	Carotid Web in Symptomatic Bifurcation	Location Intracranial Occlusion	Previous Stroke	Smoking	Diabetes	Atrial Fibrillation	Myocardial Infarction
1	F, 45	Yes	M1 right	Yes	No	No	No	No
2	M, 77	Yes	M1 right	No	No	No	Yes	No
3	F, 67	Yes	M1 right	No	No	No	No	No
4	F, 44	Yes	ICA-T right	No	No	No	No	No
5	F, 66	Yes	M2 right	No	No	No	No	No
6	F, 45	Yes	ICA-T right	No	No	No	No	No
7	F, 59	Yes	M1 right	No	No	No	No	No
8	F, 46	Yes	M1 right	No	No	No	No	No
9	F, 73	No	M1 left	No	No	No	No	No

Note:—Pt. indicates patient; ICA-T, ICA terminus.

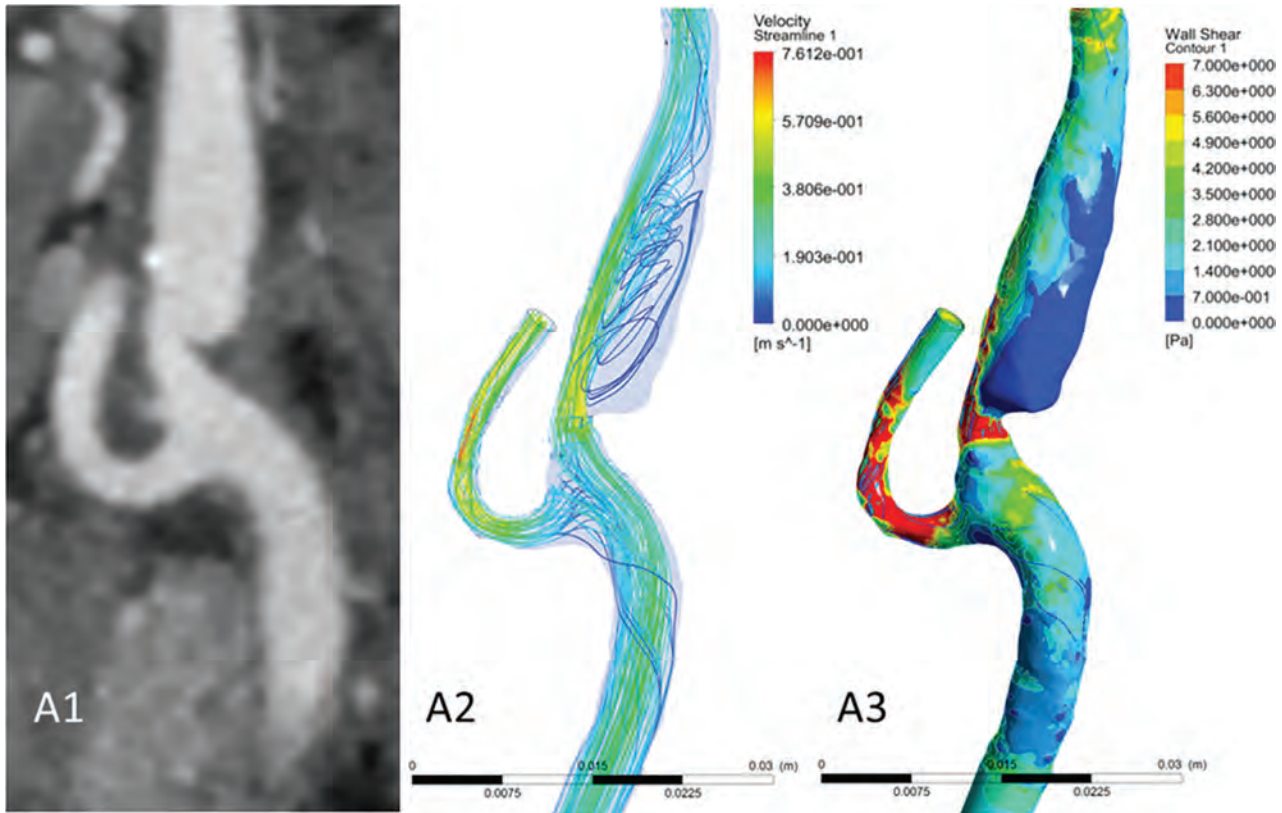


FIG 1. A case with a carotid web in the ipsilateral carotid bifurcation of a patient with ischemic stroke. Images of CTA (A1) and CFD simulations (A2, streamlines; A3, wall shear stress). Focused on the region distal from the carotid web, a large recirculation zone is observed with low time-averaged WSS values. At the minimal lumen area at the location of the web, a high TAWSS is observed. Streamlines were based on the time-averaged velocity field.

contralateral carotid bifurcation (control group) in patients and evaluated with a paired Wilcoxon signed rank test. The degree of stenosis was correlated with the length of the recirculation zone using a Spearman rank correlation test. Statistical analyses were performed using R Studio (Version 3.4.2; <http://rstudio.org/download/desktop>) and R packages haven, Hmisc, foreign, ggpaired, and ggpubr.

RESULTS

Included patients were mostly women ($n = 8$ [89%]) with a median age of 59 years (IQR, 45–70 years). All patients had a carotid web in the symptomatic carotid bifurcation of acute ischemic stroke, except for 1 patient in whom the carotid web was located

in the asymptomatic carotid bifurcation. One patient had a history of atrial fibrillation (Table 1).

A representative case of a carotid artery web is shown in Fig 1. The streamlines show that in the region distal from the carotid web, a large recirculation zone is observed. Furthermore, at the minimal lumen area at the location of the web, a high TAWSS is observed.

The results of the CFD simulation of the carotid bifurcations are summarized in Table 2 and On-line Fig 2. The severity of the stenosis caused by the web varied from 13% to 70%. At the contralateral carotid bifurcation, stenoses were observed in 3 patients (range, 14%–56%). In both carotid arteries with webs as well as in the contralateral carotid arteries, recirculation zones were ob-

Table 2: Results of hemodynamic parameters between the carotid web and the contralateral carotid bifurcation

	Carotid Web	Contralateral Carotid Bifurcation	P Value ^a
Recirculation zone			
Area (median) (IQR) (mm ²)	63.61 (50.60–99.38)	43.0 (36.46–50.34)	.02
Length (median) (IQR) (mm)	6.90 (5.60–8.60)	1.80 (1.40–2.10)	.01
Mean TAWSS (median) (IQR) (Pa)	0.27 (0.23–0.34)	0.27 (0.22–0.28)	.30
Maximum TransWSS (median) (IQR) (Pa)	0.25 (0.20–0.31)	0.21 (0.10–0.23)	.02
Maximum OSI (median) (IQR)	0.39 (0.36–0.43)	0.30 (0.19–0.33)	.04
At level of minimum lumen area			
Maximum TAWSS (median) (IQR) (Pa)	0.58 (0.51–0.61)	0.45 (0.34–0.47)	.01

^a P values were obtained from a paired Wilcoxon signed rank test.

served. However, total surface and length of the recirculation zone were significantly larger in a carotid bifurcation with a web compared with the contralateral carotid bifurcation (mean within-patient differences, 38 mm² and 6 mm, respectively) (Table 2 and Fig 2A). This difference was present in all patients except the patient who had a web in the asymptomatic carotid bifurcation (Online Table). TAWSS in the recirculation zones of carotid bifurcations with webs and in the contralateral carotid bifurcation did not significantly differ. Maximum TransWSS values were significantly higher in the recirculation zones distal to the carotid web (mean within-patient difference, 0.09 Pa; 87%) (Fig 2B). Likewise, OSI values were significantly higher in the recirculation zones in the carotid bifurcations with webs (mean within-patient difference, 0.12; 55%) (Fig 2C). At the minimal lumen area at the location of the carotid web, simulations showed a significantly higher maximum TAWSS compared with the contralateral bifurcation (mean within-patient difference, 0.20 Pa; 44%) (Fig 2D).

In the carotid bifurcations with a web, no correlation between the degree of stenosis and the surface or length of the recirculation zone was observed ($\rho = 0.23$, $P = .55$ and $\rho = 0.27$, $P = .49$, respectively).

DISCUSSION

This study provided insight into the flow patterns associated with carotid webs in the carotid bifurcation. We observed that carotid webs show increased recirculation zones with corresponding higher OSI and TransWSS values compared with the contralateral carotid bifurcation in patients with acute ischemic stroke. Furthermore, at the minimal lumen area, higher maximum TAWSS values were observed in the carotid bifurcations with a web.

Recirculation of blood is associated with an increase in platelet deposition and aggregation, which could lead to thrombogenesis with time.²⁶ All patients in our study had a larger total surface of recirculation in the bifurcation with a carotid web compared with the contralateral side, except in 1 patient who had a web in the asymptomatic carotid bifurcation. In our study, we did not find a significant association between the length or total surface of the recirculation zone and the degree of stenosis caused by a carotid web. It is possible that the degree of stenosis does not reflect the complex geometry distal from the stenosis, which is the main driver of the hemodynamic patterns.

We observed a high maximum TAWSS at the site of minimal lumen area caused by the carotid web. This finding has also been observed proximal to the minimal lumen area in patients with a stenosed artery due to atherosclerosis.^{4,21,27} In perspective, healthy individuals have an averaged WSS in the carotid arteries of approximately 1.2 Pa.²¹ However, in recirculation zones, low

WSS is characteristically common.²⁸ Vascular walls exposed to low WSS are prone to atherosclerosis and platelet aggregation, while high WSS induces platelet activation.^{4,29} Despite similar TAWSS values in the recirculation zones of carotid bifurcations with webs and their contralateral carotid bifurcations, higher TransWSS and OSI values in carotid bifurcations with a carotid web were observed. These observations represent a multidirectional disturbed blood flow, which might be prone to vascular wall dysfunction.³⁰ Along with larger recirculation zones promoting platelet aggregation to the endothelium, shear-induced activated platelets might be more likely to adhere and cohere with each other, eventually leading to thrombus formation distal to the carotid web.

A limitation of our study is the small number of evaluated patients. This is partly due to the low prevalence of carotid webs. However, we also excluded 3 patients from CFD analysis due to poor 3D segmentation caused by insufficient imaging quality of the CTA scan. Thus, the statistical power of our analysis is limited, and results must be interpreted with care. Second, due to the retrospective study design, only data from CTA scans were available, resulting in missing patient-specific boundary conditions. Thus, in- and outlet properties were estimated and generalized for all our patients.²² None of our patients had a significant (>50%) stenosis in both carotid arteries, suggesting that the assumed flow ratio between ICA/common carotid artery and external carotid artery/common carotid artery would be more reliable compared with estimations based on the Murray law.³¹ Further studies on flow patterns of carotid webs could overcome this problem by measuring blood flow with phase-contrast MR imaging scans.³² In addition, patient-specific waveforms can be determined instead of generic waveforms as in the current study. Furthermore, turbulence models were not considered in our study despite the presence of a stenosis caused by the carotid web. However, previous research has shown that flow instabilities might occur under these conditions, but turbulence is not expected to occur.³³

Recent studies have shown that carotid webs might be associated with acute ischemic stroke in younger patients without cardiovascular risk factors.^{34–36} The results of the simulated flow patterns in the current study might be helpful in defining a therapeutic strategy for evaluation. Despite the use of antithrombotic agents, patients with a carotid web have a high risk of recurrent stroke.^{2,3} However, thrombus formation in a carotid web might be comparable with thrombus formation in the atrial appendage, which is currently treated with oral anticoagulants.³⁷ Other potential treatment strategies of carotid webs are endovascular

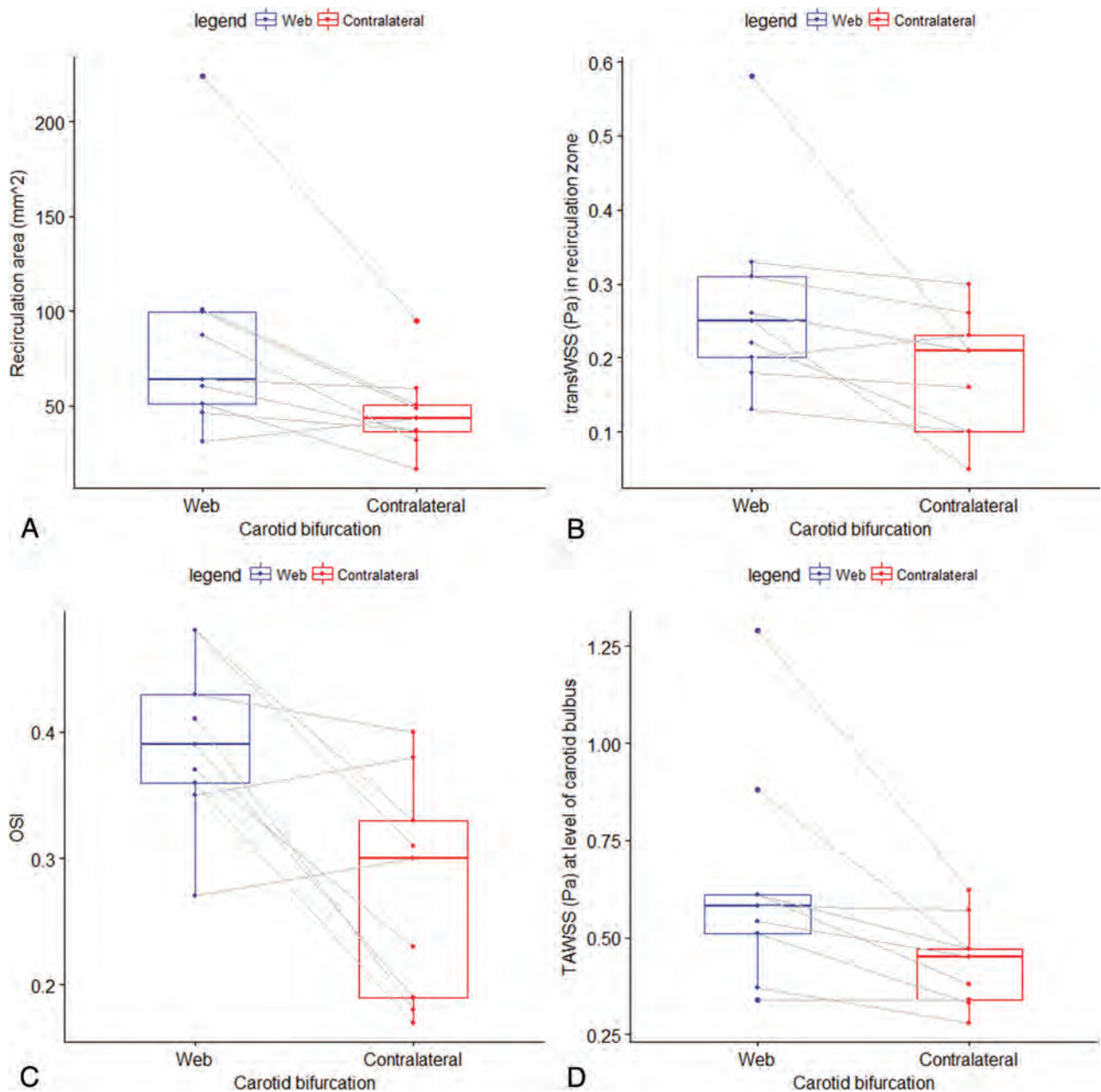


FIG 2. Boxplots showing the distribution of the total surface of the recirculation zone, TransWSS, OSI, and TAWSS for the carotid bifurcation with a web and the contralateral bifurcation. *P* values were obtained from a paired Wilcoxon signed rank test. *A*, Distribution of the total surface of the recirculation area, which was statistically significant ($P = .02$) larger in carotid bifurcations with a web compared with the contralateral carotid bifurcation (control group) within patients. *B*, Distribution of TransWSS in the recirculation zone, which was statistically significant ($P = .02$) larger in carotid bifurcations with a web compared with the contralateral carotid bifurcation (control group) within patients. *C*, Distribution of maximum OSI in the recirculation zone, which was statistically significant ($P = .04$) larger in carotid bifurcations with a web compared with the contralateral carotid bifurcation (control group) within patients. *D*, Distribution of maximum time-averaged wall shear stress (Pascal) at the level of the carotid bulb, which was statistically significant ($P = .01$) larger in carotid bifurcations with a web compared with the contralateral carotid bifurcation (control group) within patients.

treatment (eg, carotid angioplasty or stent placement) or carotid endarterectomy.^{1,38,39}

CONCLUSIONS

Carotid webs are associated with considerable recirculation zones and regional increased WSS. These findings suggest that a carotid web might stimulate thrombus formation, which increases the risk of acute ischemic stroke.

Disclosures: Diederik W.J. Dippel—UNRELATED: Grants/Grants Pending: Dutch Heart Foundation, Brain Foundation Netherlands, the Netherlands Organisation for Health Research and Development, Health Holland Top Sector Life Sciences and Health, Angiocare BV, Covidien/ev3, Penumbra, Medac Gmbh/Lampero, Top Medical/Concentric, Stryker, Stryker European Operations BV, Medtronic, Thrombolytic Science International.* Charles B.L.M. Majoie—RELATED: Grant: Twin Foundation*; UNRELATED: Grant: CVON/Dutch Heart Foundation, European Commission, Stryker*; OTHER RELATIONSHIPS: Shareholder Nico.lab (modest compensation), a company that focuses on the use of artificial intelligence for medical image analysis. Aad van der Lugt—RELATED: Grant: Dutch Heart Foundation, Angiocare BV, Medtronic/Covidien/ev3, Medac Gmbh/Lampero, Penumbra, Stryker, Top Medi-

cal/Concentric. *Comments*: Erasmus University Medical Center received unrestricted grants for the MR CLEAN studies*; *UNRELATED: Consultancy*: Stryker, *Comments*: Erasmus University Medical Center Rotterdam received support for consultations*; *Grants/Grants Pending*: Stryker, *Comments*: Erasmus University Medical Center Rotterdam received a grant for conducting EVT studies.* Wim H. van Zwam—*RELATED: Grant*: Codman Neuro, Stryker*; *UNRELATED: Grants/Grants Pending*: the Netherlands Organisation for Health Research and Development.* *Money paid to the institution.

REFERENCES

- Choi PM, Singh D, Trivedi A, et al. **Carotid webs and recurrent ischemic strokes in the era of CT angiography.** *AJNR Am J Neuro-radiol* 2015;36:2134–39 CrossRef Medline
- Joux J, Chausson N, Jeannin S, et al. **Carotid-bulb atypical fibromuscular dysplasia in young Afro-Caribbean patients with stroke.** *Stroke* 2014;45:3711–13 CrossRef Medline
- Haussen DC, Grossberg JA, Bousslama M, et al. **Carotid web (intimal fibromuscular dysplasia) has high stroke recurrence risk and is amenable to stenting.** *Stroke* 2017;48:3134–37 CrossRef Medline
- Malek AM, Alper SL, Izumo S. **Hemodynamic shear stress and its role in atherosclerosis.** *JAMA* 1999;282:2035–42 CrossRef Medline
- Sui B, Gao P, Lin Y, et al. **Blood flow pattern and wall shear stress in the internal carotid arteries of healthy subjects.** *Acta Radiol* 2008;49:806–14 CrossRef Medline
- Perktold K, Resch M, Florian H. **Pulsatile non-Newtonian flow characteristics in a three-dimensional human carotid bifurcation model.** *J Biomech Eng* 1991;113:464–75 CrossRef Medline
- Kamenskiy AV, Dzenis YA, Mactaggart JN, et al. **In vivo three-dimensional blood velocity profile shapes in the human common, internal, and external carotid arteries.** *J Vasc Surg* 2011;54:1011–20 CrossRef Medline
- Cebral JR, Yim PJ, Löhner R, et al. **Blood flow modeling in carotid arteries with computational fluid dynamics and MR imaging.** *Acad Radiol* 2002;9:1286–99 CrossRef Medline
- Lee SE, Lee SW, Fischer PF, et al. **Direct numerical simulation of transitional flow in a stenosed carotid bifurcation.** *J Biomech* 2008;41:2551–61 CrossRef Medline
- Stroud JS, Berger SA, Saloner D. **Numerical analysis of flow through a severely stenotic carotid artery bifurcation.** *J Biomech Eng* 2002;124:9–20 CrossRef Medline
- Steinman DA, Thomas JB, Ladak HM, et al. **Reconstruction of carotid bifurcation hemodynamics and wall thickness using computational fluid dynamics and MRI.** *Magn Reson Med* 2002;47:149–59 CrossRef Medline
- Marshall I, Zhao S, Papatanasopoulou P, et al. **MRI and CFD studies of pulsatile flow in healthy and stenosed carotid bifurcation models.** *J Biomech* 2004;37:679–87 CrossRef Medline
- Lancellotti RM, Vergara C, Valdetaro L, et al. **Large eddy simulations for blood dynamics in realistic stenotic carotids.** *Int J Numer Method Biomed Eng* 2017;33 CrossRef Medline
- Carallo C, Lucca LF, Ciamei M, et al. **Wall shear stress is lower in the carotid artery responsible for a unilateral ischemic stroke.** *Atherosclerosis* 2006;185:108–13 CrossRef Medline
- Peiffer V, Sherwin SJ, Weinberg PD. **Computation in the rabbit aorta of a new metric, the transverse wall shear stress, to quantify the multidirectional character of disturbed blood flow.** *J Biomech* 2013;46:2651–58 CrossRef Medline
- Mohamied Y, Sherwin SJ, Weinberg PD. **Understanding the fluid mechanics behind transverse wall shear stress.** *J Biomech* 2017;50:102–09 CrossRef Medline
- He X, Ku DN. **Pulsatile flow in the human left coronary artery bifurcation: average conditions.** *J Biomech Eng* 1996;118:74–82 CrossRef Medline
- Cheng C, Tempel D, van Haperen R, et al. **Atherosclerotic lesion size and vulnerability are determined by patterns of fluid shear stress.** *Circulation* 2006;113:2744–53 CrossRef Medline
- Berkhemer OA, Fransen PS, Beumer D, et al. **A randomized trial of intraarterial treatment for acute ischemic stroke.** *N Engl J Med* 2015;372:11–20 CrossRef Medline
- Horos Project. DICOM image viewing and measuring. Horos. <https://horosproject.org/about/>. Accessed March 5, 2019
- Cheng C, Helderma F, Tempel D, et al. **Large variations in absolute wall shear stress levels within one species and between species.** *Atherosclerosis* 2007;195:225–35 CrossRef Medline
- Groen HC, Simons L, van den Bouwhuisen QJ, et al. **MRI-based quantification of outflow boundary conditions for computational fluid dynamics of stenosed human carotid arteries.** *J Biomech* 2010;43:2332–38 CrossRef Medline
- Seo T, Schachter LG, Barakat AI. **Computational study of fluid mechanical disturbance induced by endovascular stents.** *Ann Biomed Eng* 2005;33:444–56 CrossRef Medline
- Lee SW, Antiga L, Spence JD, et al. **Geometry of the carotid bifurcation predicts its exposure to disturbed flow.** *Stroke* 2008;39:2341–47 CrossRef Medline
- Schrauwen JT, Karanasos A, van Ditzhuijzen NS, et al. **Influence of the accuracy of angiography-based reconstructions on velocity and wall shear stress computations in coronary bifurcations: a phantom study.** *PLoS One* 2015;10:e0145114 CrossRef Medline
- Schoepfoerster RT, Oynes F, Nunez G, et al. **Effects of local geometry and fluid dynamics on regional platelet deposition on artificial surfaces.** *Arterioscler Thromb* 1993;13:1806–13 CrossRef Medline
- Slager CJ, Wentzel JJ, Gijzen FJ, et al. **The role of shear stress in the destabilization of vulnerable plaques and related therapeutic implications.** *Nat Clin Pract Cardiovasc Med* 2005;2:456–64 CrossRef Medline
- Botnar R, Rappitsch G, Scheidegger MB, et al. **Hemodynamics in the carotid artery bifurcation: a comparison between numerical simulations and in vitro MRI measurements.** *J Biomech* 2000;33:137–44 CrossRef Medline
- Chatzizisis YS, Coskun AU, Jonas M, et al. **Role of endothelial shear stress in the natural history of coronary atherosclerosis and vascular remodeling: molecular, cellular, and vascular behavior.** *J Am Coll Cardiol* 2007;49:2379–93 CrossRef Medline
- Zhang Q, Gao B, Gu K, et al. **The study on hemodynamic effect of varied support models of BJUT-II VAD on coronary artery: a primary CFD study.** *ASAIO J* 2014;60:643–51 CrossRef Medline
- Sherman TF. **On connecting large vessels to small: the meaning of Murray's law.** *J Gen Physiol* 1981;78:431–53 CrossRef Medline
- von Schulthess GK, Higgins CB. **Blood flow imaging with MR: spin-phase phenomena.** *Radiology* 1985;157:687–95 CrossRef Medline
- Gijzen FJ, Palmen DE, van der Beek MH, et al. **Analysis of the axial flow field in stenosed carotid artery bifurcation models: LDA experiments.** *J Biomech* 1996;29:1483–89 CrossRef Medline
- Compagne KC, van Es AC, Berkhemer OA, et al; MR CLEAN Trial Investigators. **Prevalence of carotid web in patients with acute intracranial stroke due to intracranial large vessel occlusion.** *Radiology* 2018;286:1000–07 CrossRef Medline
- Pereira BJ, Batista UC, Tosello RT, et al. **Web vessels: literature review and neurointerventional management.** *World Neurosurg* 2018;110:e907–16 CrossRef Medline
- Coutinho JM, Derkatch S, Potvin AR, et al. **Carotid artery web and ischemic stroke: a case-control study.** *Neurology* 2017;88:65–69 CrossRef Medline
- Kirchhof P, Benussi S, Kotecha D, et al. **2016 ESC guidelines for the management of atrial fibrillation developed in collaboration with EACTS.** *Rev Esp Cardiol (Engl Ed)* 2017;70:50 CrossRef Medline
- Elmokadem AH, Ansari SA, Sangha R, et al. **Neurointerventional management of carotid webs associated with recurrent and acute cerebral ischemic syndromes.** *Interv Neuroradiol* 2016;22:432–37 CrossRef Medline
- Brinjikji W, Agid R, Pereira VM. **Carotid stenting for treatment of symptomatic carotid webs: a single-center case series.** *Interv Neurol* 2018;7:233–40 CrossRef Medline

Prevalence of Superior Semicircular Canal Dehiscence on High-Resolution CT Imaging in Patients without Vestibular or Auditory Abnormalities

A.W. Berning, K. Arani, and B.F. Branstetter, IV

ABSTRACT

BACKGROUND AND PURPOSE: Prior studies of radiologic superior semicircular canal dehiscence have suggested that CT may overcall dehiscence. However, many of those studies were performed before the advent of multichannel helical CT. Furthermore, there are limited data investigating the prevalence of radiologic superior semicircular canal dehiscence in asymptomatic individuals. The purpose of this study was to determine the rate of radiologic superior semicircular canal dehiscence in an asymptomatic population using 64-channel helical CT.

MATERIALS AND METHODS: We retrospectively enrolled 500 consecutive adult patients without symptoms of superior semicircular canal dehiscence who had undergone CT of the temporal bones in the emergency department of a tertiary academic center between February 2012 and June 2017. The superior semicircular canals were evaluated bilaterally by 2 dedicated head and neck radiologists and subjectively classified as either dehiscent or nondehiscent. A secondary group of 110 scans of patients with symptoms consistent with superior semicircular canal dehiscence was similarly interpreted, and the rate of radiologic superior semicircular canal dehiscence was calculated for each group.

RESULTS: Ten of the 500 asymptomatic patients (2.0%; 95% CI, 1.1%–3.6%) had CT evidence of superior semicircular canal dehiscence, compared with 15 of 110 symptomatic patients (13.6%; 95% CI, 7.8%–21.5%). There was excellent interobserver agreement ($\kappa = 0.91$).

CONCLUSIONS: Only 2% of asymptomatic patients had radiologic evidence of superior semicircular canal dehiscence on 64-detector row helical CT. This is markedly lower than previous reports and approaches the postmortem rate of asymptomatic superior semicircular canal dehiscence. We therefore recommend that asymptomatic patients with CT evidence of superior semicircular canal dehiscence undergo audiologic evaluation because the rate of false-positive scans is extremely low.

ABBREVIATION: SSCD = superior semicircular canal dehiscence

Following its initial description in 1998, superior semicircular canal dehiscence (SSCD) syndrome has become recognized as a frequent cause of auditory and vestibular abnormalities.¹ The syndrome is associated with variable patient presentations including vertigo, conductive hearing loss, autophony, tinnitus, sound-induced vertigo (Tullio phenomenon), and other related symptoms.² In SSCD, these symptoms appear in the setting of dehiscence of the bony roof of the superior semicircular canal, which is thought to cause symptoms by creating an abnormal pathway (a so-called “third window”) for sound and pressure conduction.³ The suspected diag-

nosis of SSCD is aided by audiometry and vestibular testing and confirmed by high-resolution CT demonstrating dehiscence on coronally reformatted images.⁴ Symptoms may be treated with vestibular sedation or surgical repair.⁵

Cadaveric studies have demonstrated dehiscence of the superior semicircular canal in 0.5% of specimens, and near-dehiscence (defined as a bone thickness of ≤ 0.1 mm) in an additional 1.4%.⁶ In contrast, imaging studies of temporal bone CT have reported rates of radiologic dehiscence between 3.0% and 9.0%, suggesting that CT may overcall dehiscence.^{7–11} However, many of these studies are limited by small sample sizes, and many were conducted before the advent of multislice helical CT. Furthermore, there are limited data directly describing the prevalence of dehiscence in individuals without symptoms of SSCD (so-called “incidental radiologic dehiscence”). These data would be useful to guide management of patients in whom SSCD is incidentally detected on CT.

Received September 15, 2018; accepted after revision January 28, 2019.

From the University of Pittsburgh School of Medicine (A.W.B.) and Departments of Radiology (K.A., B.F.B.) and Otolaryngology (B.F.B.), University of Pittsburgh Medical Center, Pittsburgh, Pennsylvania.

Please address correspondence to Aric W. Berning, MD, S530 Scaife Hall, 3550 Terrace St, Pittsburgh, PA 15213; e-mail: aric.berning@pitt.edu

<http://dx.doi.org/10.3174/ajnr.A5999>

The present study, therefore, attempts to address this gap in the literature by assessing the prevalence of radiologic SSCD in patients without auditory or vestibular symptoms, using current high-resolution CT protocols. The primary aim of this study was to report the prevalence of SSCD in this asymptomatic population to guide clinical management of these patients. A secondary analysis was to compare the rate of incidental radiologic SSCD with the rate of radiologic SSCD in patients presenting with symptoms associated with the diagnosis.

MATERIALS AND METHODS

This study received ethics approval from our institutional review board.

Subjects

We retrospectively reviewed the records of patients presenting to the emergency department of a large, tertiary care, university hospital between February 2012 and August 2017. Patients were included if they were 18 years of age or older and had undergone CT of the temporal bone. Patients were excluded if the CT was not conducted using the appropriate high-resolution temporal bone protocol or if the semicircular canal could not be visualized due to pathology or artifacts. To prevent interpretation bias, we initially included CT scans regardless of patient clinical history. After interpretation of the scans, subjects were sorted into 2 groups based on provided indications for imaging: those without symptoms consistent with SSCD (asymptomatic patients) and those with symptoms consistent with SSCD (symptomatic patients). Vertigo, hearing loss, dizziness, and tinnitus were considered symptoms consistent with SSCD in this study. On the basis of an *a priori* power analysis assuming a prevalence of 3.0% and confidence interval half-widths of 1.5%, we consecutively enrolled patients until we reached 500 asymptomatic patients.

Imaging Protocol and Techniques

CT was acquired using LightSpeed 64-channel CT scanners (GE Healthcare, Milwaukee, Wisconsin) with a slice thickness of 0.63 mm, spacing of 0.375 mm, 120 kV(peak), 195 mA, pitch of 0.53, bone kernel, and matrix of 512×512 . Images were obtained in the axial plane with coronal reformats (1-mm-thick, 1-mm spacing) because prior studies have demonstrated that these views are sufficient to accurately identify dehiscence compared with reformats in the planes of Stenver and Poschl.⁴

Data Collection

Patient age, sex, and indication for imaging were recorded. Patients' CT scans were independently reviewed by 2 fellowship-trained, dedicated head and neck radiologists who were blinded to the clinical history of the patient. For each scan, the superior semicircular canals were evaluated bilaterally, and the bone overlying the canal was subjectively classified as either intact (Figs 1 and 2) or dehiscent (Fig 3). Very thin bone overlying the superior semicircular canal was not considered dehiscent (Fig 4). After we assessed interobserver reliability, discrepancies between observers were resolved by consensus to establish descriptive statistics.

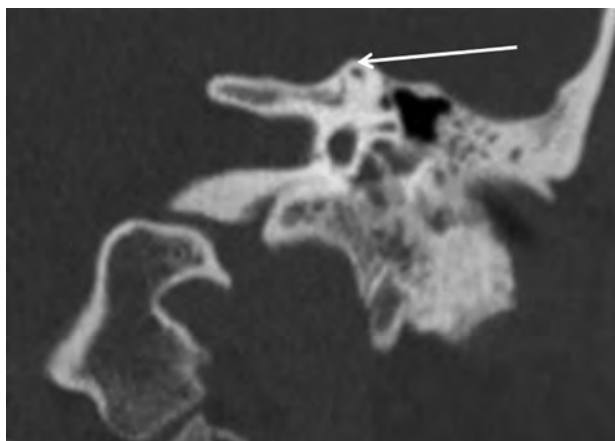


FIG 1. Intact superior semicircular canal. Coronally reformatted CT of the temporal bone demonstrates an intact roof of the superior semicircular canal (arrow).

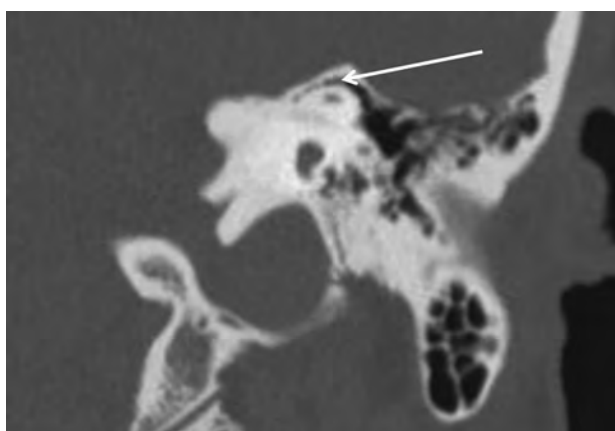


FIG 2. Air cells overlying the superior semicircular canal. Coronally reformatted CT of the temporal bone demonstrates an intact superior semicircular canal (arrow) with overlying air cells. When air cells are present, the canal should be classified as nondehiscent, regardless of the thickness of bone covering the canal or underlying the dura.

Statistical Analysis

The prevalence of radiologic SSCD in both asymptomatic and symptomatic patient groups was calculated, along with 95% confidence intervals using the Newcombe method for extreme percentages.¹² Comparisons between patient groups were conducted using the Fisher exact test for categorical variables and the Student *t* test for continuous variables. Interrater reliability was calculated using the Cohen κ statistic. A *P* value of .05 was the threshold for all tests of significance. Statistical calculations were performed using the SPSS software package, Version 23 (IBM, Armonk, New York).

RESULTS

A total of 681 patient records were evaluated for possible inclusion. Of these, 24 were excluded due to incomplete data, and 33 were excluded for protocol errors. An additional 14 were excluded for inability to evaluate the semicircular canals due to motion artifacts or overlying pathology. One hundred ten patients were excluded from the primary analysis due to symptoms consistent with SSCD, leaving 500 asymptomatic patients for prevalence cal-

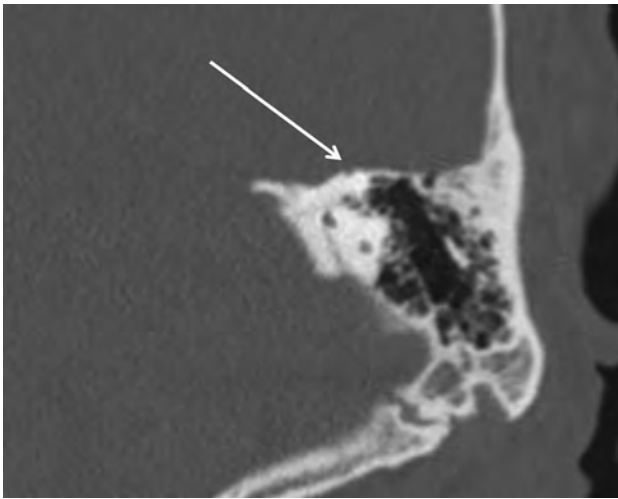


FIG 3. A thin-but-intact superior semicircular canal. Coronally reformatted CT of the temporal bone demonstrates very thin bone overlying the superior semicircular canal (*arrow*). This quantity of bone should be classified as intact in patients with and without suggestive symptoms.

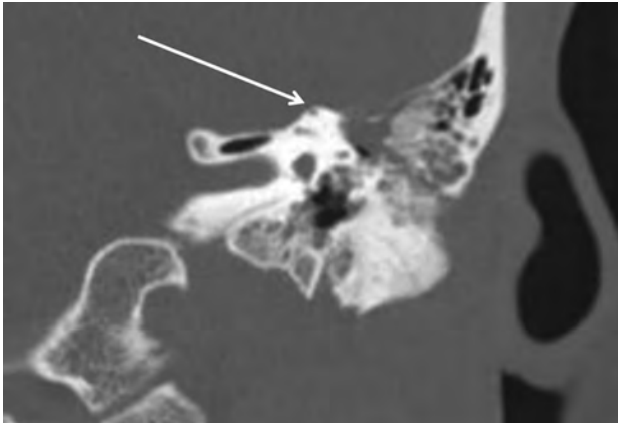


FIG 4. Dehiscent superior semicircular canal. Coronally reformatted CT of the temporal bone demonstrates dehiscence of the roof of the superior semicircular canal (*arrow*).

Table 1: Asymptomatic (n = 500) patient characteristics and indications for CT

Characteristics/Indications	
Mean age (range) (yr)	50.7 ± 15.8 (19–87)
No. male (%)	336 (67.2%)
Imaging indication (No.) (%)	
Trauma	368 (77.6%)
Mass	45 (9.0%)
Infection	33 (6.6%)
Pain	26 (5.2%)
CSF leak/cephalocele	14 (2.8%)
Cranial nerve palsy	5 (1.0%)
Otosclerosis	4 (0.8%)
Surgical planning	3 (0.6%)
Radionecrosis	2 (0.4%)

ulation. Patient demographics and indications for imaging are summarized in Tables 1 and 2.

Ten of the 500 asymptomatic patients had CT evidence of SSCD (2.0%; 95% CI, 1.0%–3.8%). Of these 10 patients, 7 were imaged for trauma; 2, for evaluation of a mass; and 1, for evalua-

Table 2: Symptomatic (n = 110) patient characteristics and indications for CT

Characteristics/Indications	
Mean age (range) (yr)	47.6 ± 18.9 (18–100)
No. male (%)	41 (37.3%)
Imaging indication (No.) (%)	
Dizziness	62 (56.4%)
Suspected SSCD	31 (28.1%)
Hearing loss	23 (20.1%)
Vertigo	6 (5.5%)
Tinnitus	6 (5.5%)

tion of infection. Three patients, all imaged for trauma, demonstrated bilateral SSCD. The most common indication for imaging in the asymptomatic group was trauma; 7 of the 368 patients with this indication were found to have radiologic dehiscence (1.9%; 95% CI, 0.8%–4.0%).

In contrast, radiologic SSCD was detected in 15 of the 110 symptomatic patients (13.6%; 95% CI, 8.1%–21.8%). Two of the symptomatic patients demonstrated bilateral dehiscence. The rate of bilateral dehiscence did not differ significantly between groups ($P = .22$). The difference in prevalence of radiologic SSCD between the 2 groups was statistically significant ($P < .001$).

For 31 of the 110 symptomatic patients, the provided indication for CT was evaluation of suspected SSCD. Ten patients in this subgroup demonstrated radiologic SSCD (32.3%; 95% CI, 17.3%–51.5%). Five of the remaining 79 symptomatic patients demonstrated radiologic SSCD (6.3%; 95% CI, 2.4%–14.8%). The difference in the rate of radiologic SSCD was statistically significant both among these subgroups of symptomatic patients ($P < .001$) and between each subgroup and the group of asymptomatic patients ($P < .05$).

There was excellent interrater agreement between the 2 observers ($\kappa = 0.91$), with disagreement on only 5 of the 1220 temporal bones that were evaluated (0.4%).

DISCUSSION

In a retrospective study of 500 patients without symptoms of SSCD, radiologic evidence of dehiscence was detected in 2.0% of cases, with excellent agreement between expert observers. This was significantly lower than the 13.6% prevalence of dehiscence in a similar group of 110 patients with symptoms that might be seen in SSCD.

This prevalence of 2% is notably lower than the prevalence of 9.0% reported by Williamson et al,¹¹ which has been cited in 2 recent comprehensive review articles on SSCD.^{2,13} Most important, this previous work was conducted before the advent of 64-detector row helical CT, which may explain the higher prevalence reported in earlier studies. More recent studies with contemporary CT protocols have reported a lower prevalence of SSCD; however, these studies are limited by relatively small sample sizes or include patients with symptoms consistent with SSCD and thus do not provide reliable estimates of the prevalence of SSCD in asymptomatic individuals. For example, Nadgir et al⁹ reported dehiscence of 7.8% in a study of 306 CT scans, but the focus of the study was to categorize the prevalence of SSCD by age and included patients with a variety of vestibular and auditory symptoms. Similarly, Crovetto et al¹⁴ reported radiologic SSCD in 3.6% of studied ears but did not exclude symptomatic patients.

Our results are most consistent with a recent study by Klopp-Dutote et al,¹⁵ in which radiologic SSCD was detected in 1.7% of a population of 180 patients, but it is unclear whether this population included patients with otologic symptoms and may be limited by a small sample size.

In an anatomic study of 1000 temporal bones from 596 individuals, Carey et al⁶ identified complete dehiscence in 0.5% of specimens. An additional 1.4% of specimens was noted to have markedly thin (≤ 0.1 mm) bone overlying the superior semicircular canal. Individuals with such thin coverings may appear dehiscent even on high-resolution CT scans; thus, our results correlate well with the reported postmortem rate of dehiscence.

The results of our study suggest that incidental radiologic SSCD is rare in individuals without clinical symptoms of auditory or vestibular dysfunction. Given that the rate of false-positive scans is low, we recommend that patients in whom radiologic dehiscence is discovered incidentally on CT undergo audiologic evaluation to screen for SSCD.

The present study is limited by its retrospective design and incomplete access to patient data. The clinical syndrome of SSCD is highly variable, and it is possible that patients categorized as asymptomatic in our study may have otologic symptoms that were not reported at their emergency department presentation and thus have been erroneously classified as asymptomatic. Also due to the retrospective study design, we are unable to determine whether patients subsequently developed otologic symptoms following their initial emergency department presentation. Furthermore, a multitude of entities besides SSCD can present with symptoms of hearing loss, vertigo, tinnitus, and dizziness.

Our population of asymptomatic patients had a male predominance, likely due to the high number of trauma cases in our emergency department population. This male predominance was not mirrored in our concurrent sample of symptomatic patients. However, SSCD is not known to have a sex predilection. Our results may not be generalizable to examinations performed on scanners with fewer than 64 channels.

Furthermore, our inclusion of patients evaluated for suspected SSCD biases the reported prevalence of SSCD in the larger group of symptomatic patients. Of the 15 cases of radiologic SSCD in our symptomatic population, 10 belonged to this subgroup, which demonstrated a prevalence of radiologic SSCD of 32.3%. Excluding patients who underwent CT for evaluation of suspected SSCD lowers the prevalence of radiologic SSCD in the symptomatic group to 6.3%, which remains significantly higher than the rate of 2% detected in the asymptomatic group. Our reported prevalence of SSCD in symptomatic patients should be cautiously interpreted due to its small sample size; however, our reported prevalence of SSCD in asymptomatic patients does not have this limitation.

CONCLUSIONS

There is radiologic evidence of SSCD in 2% of patients without clinical symptoms of auditory or vestibular dysfunction. Given this low rate of false-positives, we recommend audiologic evaluation for patients in whom SSCD is incidentally discovered on CT imaging.

REFERENCES

1. Minor LB, Solomon D, Zinreich JS, et al. **Sound- and/or pressure-induced vertigo due to bone dehiscence of the superior semicircular canal.** *Arch Otolaryngol Head Neck Surg* 1998;124:249–58 CrossRef Medline
2. Mau C, Kamal N, Badeti S, et al. **Superior semicircular canal dehiscence: diagnosis and management.** *J Clin Neurosci* 2018;48:58–65 CrossRef Medline
3. Rosowski JJ, Songer JE, Nakajima HH, et al. **Clinical, experimental, and theoretical investigations of the effect of superior semicircular canal dehiscence on hearing mechanisms.** *Otol Neurotol* 2004;25:323–32 CrossRef Medline
4. Branstetter BF 4th, Harrigal C, Escott EJ, et al. **Superior semicircular canal dehiscence: oblique reformatted CT images for diagnosis.** *Radiology* 2006;238:938–42 CrossRef Medline
5. Minor LB. **Clinical manifestations of superior semicircular canal dehiscence.** *Laryngoscope* 2005;115:1717–27 CrossRef Medline
6. Carey JP, Minor LB, Nager GT. **Dehiscence or thinning of bone overlying the superior semicircular canal in a temporal bone survey.** *Arch Otolaryngol Head Neck Surg* 2000;126:137–47 CrossRef Medline
7. Gartrell BC, Gentry LR, Kennedy TA, et al. **Radiographic features of superior semicircular canal dehiscence in the setting of chronic ear disease.** *Otol Neurotol* 2014;35:91–96 CrossRef Medline
8. Masaki Y. **The prevalence of superior canal dehiscence syndrome as assessed by temporal bone computed tomography imaging.** *Acta Otolaryngol* 2011;131:258–62 CrossRef Medline
9. Nadgir RN, Ozonoff A, Devaiah AK, et al. **Superior semicircular canal dehiscence: congenital or acquired condition?** *AJNR Am J Neuroradiol* 2011;32:947–49 CrossRef Medline
10. Stimmer H, Hamann KF, Zeiter S, et al. **Semicircular canal dehiscence in HR multislice computed tomography: distribution, frequency, and clinical relevance.** *Eur Arch Otorhinolaryngol* 2012;269:475–80 CrossRef Medline
11. Williamson RA, Vrabec JT, Coker NJ, et al. **Coronal computed tomography prevalence of superior semicircular canal dehiscence.** *Otolaryngol Head Neck Surg* 2003;129:481–89 CrossRef Medline
12. Newcombe RG. **Statistical applications in orthodontics, Part II: confidence intervals for proportions and their differences.** *J Orthod* 2000;27:339–40 CrossRef Medline
13. Ward BK, Carey JP, Minor LB. **Superior canal dehiscence syndrome: lessons from the first 20 years.** *Front Neurol* 2017;8:177 CrossRef Medline
14. Crovetto M, Whyte J, Rodriguez OM, et al. **Anatomo-radiological study of the superior semicircular canal dehiscence: radiological considerations of superior and posterior semicircular canals.** *Eur J Radiol* 2010;76:167–72 CrossRef Medline
15. Klopp-Dutote N, Kolski C, Biet A, et al. **A radiologic and anatomic study of the superior semicircular canal.** *Eur Ann Otorhinolaryngol Head Neck Dis* 2016;133:91–94 CrossRef Medline

Determinants of Radiation Dose in Selective Ophthalmic Artery Chemosurgery for Retinoblastoma

A.M. Qureshi, L.K. Davies, P.A. Patel, A. Rennie, and F. Robertson



ABSTRACT

BACKGROUND AND PURPOSE: Retinoblastoma is the most common pediatric ocular neoplasm. Multimodality treatment approaches are commonplace, and selective ophthalmic artery chemosurgery has emerged as a safe and effective treatment in selected patients. Minimizing radiation dose in this highly radiosensitive patient cohort is critical. We explore which procedural factors affect the radiation dose in a single-center cohort of children managed in the UK National Retinoblastoma Service.

MATERIALS AND METHODS: A retrospective review was performed of 177 selective ophthalmic artery chemosurgery procedures in 48 patients with retinoblastoma (2013–2017). Medical records, angiographic imaging, and radiation dosimetry data (including total fluoroscopic screening time, skin dose, and dose-area product) were reviewed.

RESULTS: The mean fluoroscopic time was 13.5 ± 13 minutes, the mean dose-area product was 11.7 ± 9.7 Gy.cm², and the mean total skin dose was 260.9 ± 211.6 mGy. One hundred sixty-three of 177 procedures (92.1%) were technically successful. In 14 (7.9%), the initial attempt was unsuccessful (successful in 13/14 re-attempts). Screening time and radiation dose were associated with drug-delivery microcatheter location and patient age; screening time was associated with treatment cycle.

CONCLUSIONS: In selective ophthalmic artery chemosurgery, a microcatheter tip position in the proximal or ostial ophthalmic artery and patient age 2 years or younger were associated with reduced fluoroscopic screening time and radiation dose; treatment beyond the first cycle was associated with reduced fluoroscopic screening time.

ABBREVIATIONS: DAP = dose-area product; OA = ophthalmic artery; SOAC = selective ophthalmic artery chemosurgery

Retinoblastoma is the most common pediatric ocular neoplasm, occurring in approximately 1 in 20,000 live births. In the United Kingdom, approximately 40–50 new cases are diagnosed annually.¹ Retinoblastoma develops from a retinal cone precursor cell in response to bi-allelic inactivation of the *RB1* gene on chromosome 13.^{1,2} The *RB1* gene product is the retinoblastoma protein, a tumor suppressor. Gene mutations may be hereditary (40%) or sporadic (60%). Hereditary disease is more likely to present earlier with bilateral disease and be associated with other cancers.

Overall patient survival in retinoblastoma is high (exceeding 95%) in resource-rich settings, where detection and treatment of

disease are prompt.³ Several options exist for treatment, guided by the extent of tumor spread, as determined by the International Classification of Retinoblastoma (Table 1).⁴ Selective ophthalmic artery chemosurgery (SOAC) has emerged as a valid treatment technique for group A–D tumors, with substantial ocular salvage rates, particularly in lower tumor grades.^{5,6} Potential SOAC benefits include ocular preservation and less systemic toxicity associated with standard intravenous chemotherapy regimens. Exposure to ionizing radiation during angiography and fluoroscopic positioning of the delivery microcatheter are potential detriments. Adverse effects of external beam radiation therapy treatment used historically in retinoblastoma treatment are well established. These include cataract formation, ocular dryness, facial dysmorphism, and secondary neoplasms.⁷ Although radiation doses used in SOAC are substantially lower than in external beam radiation therapy, this patient group is exquisitely radiosensitive (familial retinoblastoma has a predilection for second tumor formation) and strategies to minimize radiation dose are imperative (according to the As Low As Reasonably Achievable principles).^{8,9} This can be achieved in SOAC by judicious adjustment of fluoro-

Received October 30, 2018; accepted after revision January 25, 2019.

From the Department of Radiology, Great Ormond Street Hospital for Children, National Health Service Foundation Trust, London, UK.

Please address correspondence to Fergus Robertson, MD, Department of Radiology, Great Ormond Street Hospital for Children NHS Foundation Trust, Great Ormond Street, London WC1N 3JH, UK; e-mail: fergusrobertson@nhs.net

Indicates article with supplemental on-line photo.

<http://dx.doi.org/10.3174/ajnr.A6000>

Table 1: The International Classification of Retinoblastoma⁴

Group	Features
A	Tumor ≤ 3 mm
B	Tumor > 3 mm or macular location (≤ 3 mm to foveola), juxtapapillary location (≤ 1.5 mm to disc), clear subretinal fluid (≤ 3 mm from margin)
C	Tumor with subretinal and/or vitreous seeds ≤ 3 mm from tumor
D	Tumor with subretinal and/or vitreous seeds > 3 mm from tumor
E	Extensive retinoblastoma occupying $> 50\%$ of globe or neovascular glaucoma; opaque media from hemorrhage in anterior chamber, vitreous, or subretinal space; invasion of postlaminar optic nerve, choroid (> 2 mm), sclera, orbit, anterior chamber

scopic exposure settings, limiting screening times, and minimizing angiography.¹⁰ This study assessed SOAC radiation dose in a single center with the aim of informing further dose-reduction strategies. The study group was selected from the latter half of a 10-year institutional experience of over 320 SOAC procedures in > 100 patients, reflecting an experienced service with established protocols.

MATERIALS AND METHODS

We conducted a retrospective review of 177 consecutive SOAC procedures, performed between January 2013 and December 2017 in 48 patients with a diagnosis of retinoblastoma. This study was registered as a Service Evaluation with the hospital Clinical Audit Department and was exempt from approval from a local research ethics committee. All patients undergoing SOAC had group C or D tumors, and all had relapsed after first-line systemic chemotherapy. No patients underwent SOAC as a first-line treatment. Data collection encompassed review of medical records, angiographic imaging, and radiation dosimetry data, which were obtained from our system dose reports. These included total fluoroscopic time, skin dose, and dose-area product (DAP) (currently DAP is designated Kerma area product by the International Commission on Radiologic Protection¹¹). Twenty procedures in 14 patients were excluded due to incomplete dose reports. “Technical procedural failure” was defined as failure to deliver a complete planned dose of intra-arterial chemotherapy in the given treatment episode. There were no clinically apparent angiographic complications during this period.

SOAC Technique

Patients were selected for SOAC by a multidisciplinary team including oncology, ophthalmology, and neurointerventional radiology. Pediatric neurointerventional subspecialists with > 5 years’ postfellowship experience performed SOAC with the patient under general anesthesia. A 4F catheter was positioned in the ipsilateral internal carotid artery via a transfemoral approach following full intravenous heparinization (75 U/kg). A preliminary control biplane angiogram was obtained. In conventional anatomy, the ophthalmic artery was catheterized using a variety of over-the-wire and flow-directed microcatheters (typically Magic microcatheter 1.2F or 1.8F; Balt, Montmorency, France) using 0.007- or 0.008-inch wires such as Hybrid 0.007 (Balt), ASAHI CHIKAI 0.008 (Asahi-Intecc, Aichi, Japan), and Mirage 0.008 (Covidien,

Irvine, California). In variant anatomy, accessory ophthalmic supply from the external carotid artery was used (typically through the anterior division of the middle meningeal artery). A single patient had bilateral SOAC in a single session (2 episodes total). This was due to synchronous bilateral disease relapse, and these 2 treatment episodes were excluded from analysis because the doses could not be separated. In all other cases with bilateral disease, a single eye was treated at each session.

Before delivering chemotherapy, we confirmed stable tip position and antegrade ophthalmic artery contrast flow with evidence of choroidal blush by superselective biplane microcatheter angiography (On-line Figure). When a stable ostial position could not be achieved in the ophthalmic artery (OA) origin, the vessel was catheterized more distally. Microcatheter tip delivery position was recorded as “origin” when located at the ostium, “proximal” when in the OA proximal to the midpoint between the ostium and the angiographic angle, and “distal” when beyond this midpoint.¹² Chemotherapy was typically delivered during 30 minutes, with occasional short single-plane fluoroscopic pulses to confirm stable catheter tip position when there were stability concerns. No further angiography was performed.

Fluoroscopic Protocol

All procedures were performed on an Artis zee (Siemens, Erlangen, Germany) biplane flat panel angiography suite used exclusively for pediatric work. Digital subtraction angiography used both frontal and lateral intensifiers with automatic exposure control parameters set to maximal values of 3 μ Gy per frame at 4 frames per second. Fluoroscopic screening was performed with automatic adjustment of kilovolt and milliampere-second, at 7.5 or 10 pulses per second. Detector dose was set to 29 or 36 nGy/p. Magnification during initial angiography was set at 32 cm on the frontal detector and 42 cm on the lateral detector and magnified to 22 or 16 cm on the lateral detector during superselective ophthalmic artery angiography/fluoroscopy.

The radiation dose was minimized by optimizing collimation, filtration, and reducing patient-to-detector distance and magnification when possible.

Statistical Analysis

Data are summarized by descriptive statistics. Mean and SD are reported for radiation dose parameters. By means of SPSS software, Version 25 (IBM, Armonk, New York), a 2-tailed independent-samples *t* test was used to compare the radiation dose parameters for patient age category, treatment cycle, and successful-versus-abandoned procedures. A Kruskal-Wallis test was used to compare radiation doses among years, injected vessels, and operators. Bland-Altman statistics were used to compare the association between screening times and abandoned procedures. $P \leq .05$ was considered statistically significant for all tests.

RESULTS

Forty-eight patients underwent selective ophthalmic artery chemosurgery (male/female ratio = 22:26). Thirty-three patients had bilateral retinoblastoma, and 15 had unilateral disease. In 177 procedures, 163 (92.1%) were technically successful. Fourteen (7.9%) procedures were unsuccessful, usually due to induced OA

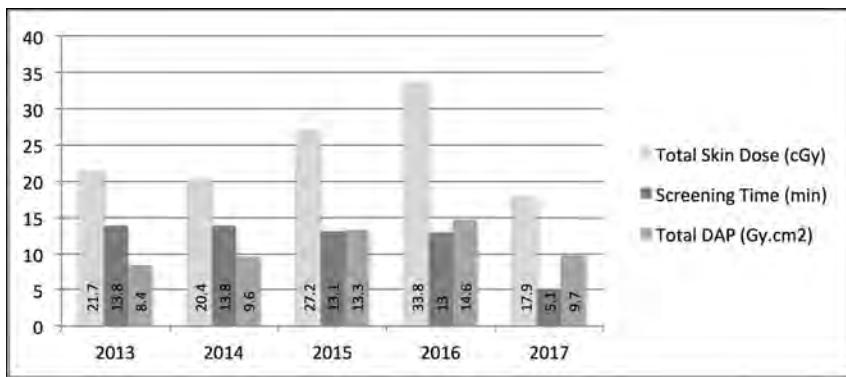


FIG 1. Mean screening times, total skin dose, and total DAP by year.

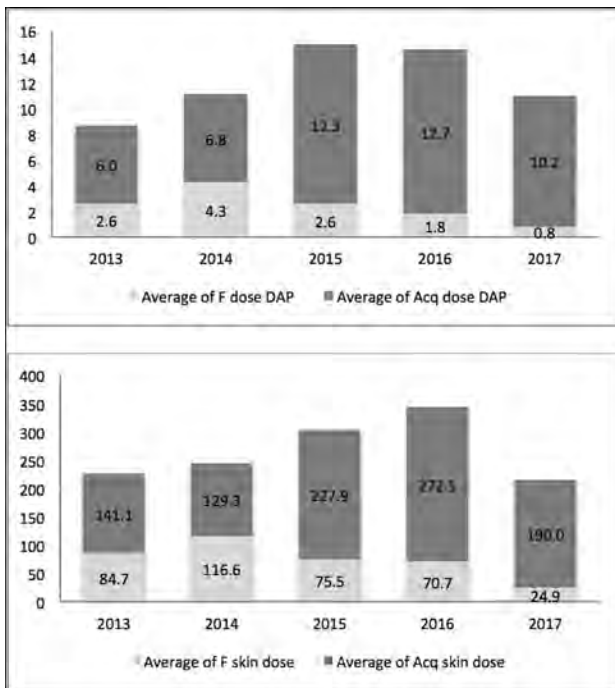


FIG 2. Angiographic acquisitions (Acq) were responsible for most of the radiation dose, and its proportion of the contribution to the overall dose gradually increased between 2014 and 2017. F indicates fluoroscopic.

ostial spasm. Repeat procedures were successful on subsequent attempts in all except 1 patient, in whom anomalous anatomy prevented stable microcatheter positioning.

The mean fluoroscopic time was 13.5 ± 13 minutes, (range, 1.5–67.2 minutes).

The mean dose-area product was 11.7 ± 9.7 Gy.cm² (range, 1.7–55.4 Gy × cm²).

The mean total skin dose was 260.9 ± 211.6 mGy (range, 43–1243 mGy).

All parameters were higher in abandoned procedures: screening time (35.7 ± 16 versus 11.5 ± 10.8 minutes) ($P < .01$), dose-area product (22 ± 13 versus 10.8 ± 8.8 Gy.cm²) ($P < .01$), and skin dose (543.7 ± 255.4 versus 236.6 ± 189.5 mGy) ($P < .01$). When screening time exceeded 25 minutes, the procedure was successful in only 11% of patients, with a mean DAP of 18.5 Gy.cm² and a skin dose of 470.7 mGy in this group.

There was a progressive reduction in screening time during the

study period, with increasing experience and latterly reflecting a move toward a more proximal/ostial OA catheter position, which was almost exclusive in 2017 (Fig 1). The total DAP and skin dose also fell in 2017. A greater proportion of the radiation dose came from angiographic acquisitions versus fluoroscopic screening (Fig 2).

In the 163 technically successful procedures, infusion was performed via the OA in 128 (78.5%) and via the external carotid artery collateral supply to the OA in 35 (21.5%). Of the 128 OA infusions, 67 (52%) were made at the origin/ostium, 17 (13%) at the proximal vessel, and 44 (35%) at the distal vessel. The screening times, total DAP, and total skin doses were lower with ostial or proximal OA microcatheter tip positions compared with more distal OA or external carotid artery positions (Table 2).

Among operators, there were no significant differences in screening time (12.3 ± 11 versus 10.5 ± 10.2 versus 14.4 ± 15 minutes) or total DAP (10.6 ± 7.9 versus 11.3 ± 9.9 versus 8.8 ± 7.1 Gy.cm²), though a significant difference was noted in total skin dose (258.1 ± 200.6 versus 207.4 ± 165.9 versus 295.6 ± 259.4 mGy).

There were significantly higher total DAP (12.8 ± 9.5 versus 10.8 ± 11.3 Gy.cm²) and total skin doses (281.9 ± 218.3 versus 194 ± 146.6 mGy) in procedures performed on children older than 2 years of age. Although the screening time was also greater in this age group (12.4 ± 10.4 versus 10.8 ± 11.3 minutes), this difference was not significant.

Mean screening time was significantly longer in the first cycle of treatment compared with follow-up cycles (12.7 ± 11.5 versus 8 ± 7.4 minutes). This screening time did not translate into a significant difference in radiation dose (total DAP, 10.8 ± 8.9 versus 11 ± 8.7 Gy.cm²; and total skin dose, 238.5 ± 200 versus 230.9 ± 154.6 mGy) between cycles, however.

DISCUSSION

We report the radiation dose for SOAC procedures during the second 5-year period of our 10-year experience.

The mean screening time in this cohort was 13.5 minutes and mainly reflects the duration of fluoroscopic radiation exposure. This has multiple determinants, including anatomic considerations, microcatheterization strategy, fluoroscopic protocol, and operator experience.¹³ Lower mean screening times were reported by Cooke et al¹⁰ and Boddu et al¹⁴ at 8.5 and 10.2 minutes, respectively. However in this cohort, there was a wide range of screening times (maximal time of 67.2 minutes), and a median screening time of 7.3 minutes is more reflective of local practice.

Dose-area product/Kerma area product and patient entrance dose/skin dose are considered more accurate surrogate measures of patient radiation exposure. The DAP is a product of the radiation dose within the field and the area of tissue irradiated. This influences but is not synonymous with patient dose (which incorporates additional factors, such as patient body habitus, x-ray

Table 2: Comparison among fluoroscopic screening time, total DAP, and total skin dose between ophthalmic artery and ECA branch injections

	Mean (\pm SD)	P Value
Screening time (min)		
OA origin	9.2 (\pm 9.65)	.0001
OA proximal	11.9 (\pm 7.1)	
OA distal	14.3 (\pm 11)	
ECA	12.5 (\pm 13.5)	
Total DAP (Gy.cm ²)		
OA origin	10.2 (\pm 9.5)	.016
OA proximal	6.9 (\pm 2.9)	
OA distal	11.3 (\pm 6.6)	
ECA	13.3 (\pm 11)	
Total skin dose (mGy)		
OA origin	205.7 (\pm 170.7)	.001
OA proximal	146.8 (\pm 71.1)	
OA distal	271.4 (\pm 168.9)	
ECA	295.7 (\pm 254.7)	

Note:—ECA indicates external carotid artery.

beam quality, and radiation sensitivity of the irradiated tissue).¹⁵ The skin dose in our study measures the total skin dose (or cumulative radiation dose absorbed at the skin). Total skin dose differs from but correlates with¹⁶ peak skin dose. Peak skin dose correlates more closely with skin injury, but its calculation requires a priori analysis and is not the primary output parameter of the Siemens system. The DAP values in our series were higher than those reported by Boddu et al,¹⁴ reflecting a difference in procedural techniques. Ipsilateral internal carotid artery digital subtraction angiography was performed initially in all procedures to delineate vessel anatomy in our cohort, while others relied solely on lower dose fluoroscopic road-mapping techniques.

Figure 2 demonstrates a reduction in the component of radiation dose from fluoroscopy across the years (commensurate with reducing screening times), leading to a greater contribution to dose from angiographic acquisitions. Other dose-reducing methods such as lowering the fluoroscopic pulse rate and DSA frame rates and more active collimation and reduction of patient-intensifier distance are reflected in falling doses across time.¹⁷ Manufacturer innovations such as CAREposition (Siemens) have further helped reduce screening time. This technology allows patient repositioning in the imaging field without radiographic exposure using a moving outline box and crosshair on a last-image hold display. The procedural radiation exposure in this series remains below that described for cerebral angiography in children, but there is clearly room for further improvement.¹⁸

Extended procedures have a significant impact on radiation dose with diminishing returns. Our practice has evolved to abandon the procedure if protracted attempts at vessel catheterization are unsuccessful, particularly when faced with spasm in target vessels. In all except 1 patient, the first re-attempt was successful.

Our superselective approach (distal catheterization of the ophthalmic artery) provides a viable alternative in challenging anatomy but can be time-consuming and almost certainly contributes to increased screening times and radiation dose. Alternative strategies such temporary balloon occlusion of the ICA distal to the ophthalmic artery to redirect the microcatheter or chemotherapy into the target artery have been described by other groups.¹⁹ We have not resorted to this technique out of concern

for ICA damage and distal embolism. With our approach, there have been no vessel dissections or cerebral embolic complications in >350 procedures. The lowest radiation doses occurred with proximal and ostial microcatheter positions, and now superselective catheterization is only used when a stable ostial position cannot be achieved.

Patients younger than 2 years of age had significantly lower radiation exposure, explained by smaller patient size, active lowering of fluoroscopic dose, and aggressive collimation.

Screening times were higher in the first cycle of treatment, compared with subsequent cycles, a finding consistent with other groups.¹⁴ Once a successful catheterization strategy is identified, this generally proves reproducible. The reduction in screening time on subsequent treatment cycle was not reflected in reduced DAP or skin dose, however, because angiographic runs contributed to the bulk of that dose.

There are limitations of a retrospective single-center study. A number of patients were excluded from the study due to incomplete dose-data recording. In our practice, SOAC was only used as salvage therapy in C and D eyes relapsed after systemic chemotherapy, whereas most published cohorts tended toward broader indications (eg, B eyes) and with SOAC as first-line treatment.

CONCLUSIONS

SOAC is established as a safe and effective treatment for retinoblastoma in selected cases in which disease is limited to the orbit. Minimizing radiation dose must be a priority in this exquisitely radiosensitive patient cohort. Our data support a strategy of proximal or ostial OA microcatheter positioning and minimizing the use of angiographic runs in favor of fluoroscopic techniques. Procedures in children younger than 2 years of age were associated with reduced screening time and radiation dose. Screening times fall in subsequent treatment cycles as a patient-specific catheterization strategy is established.

Careful procedural planning, operator experience, judicious use of dose-reducing techniques, advances in angiographic imaging technology, and the use of specific imaging equipment parameters for pediatric populations all contribute to reducing radiation dose.

Disclosures: Ayman M. Qureshi—UNRELATED: Travel/Accommodations/Meeting Expenses Unrelated to Activities Listed: MicroVention, ev3, Medtronic, Balt Extrusion, Cerenovus, Johnson & Johnson, Penumbra, Comments: The mentioned neurovascular medical device companies have sponsored my travel and accommodation for various training courses/workshops hosted by the respective company. Adam Rennie—UNRELATED: Payment for Lectures Including Service on Speakers Bureaus: European Course in Minimally Invasive Neurological Therapy lecture.

REFERENCES

1. Yun J, Li Y, Xu CT, et al. **Epidemiology and Rb1 gene of retinoblastoma.** *Int J Ophthalmol* 2011;4:103–09 CrossRef Medline
2. Xu XL, Singh HP, Wang L, et al. **Rb suppresses human cone-precursor-derived retinoblastoma tumours.** *Nature* 2014;514:385–88 CrossRef Medline
3. Broadus E, Topham A, Singh AD. **Survival with retinoblastoma in the USA: 1975–2004.** *Br J Ophthalmol* 2009;93:24–27 CrossRef Medline
4. Shields CL, Mashayekhi A, Au AK, et al. **The International Classification of Retinoblastoma predicts chemoreduction success.** *Ophthalmology* 2006;113:2276–80 CrossRef Medline

5. Wyse E, Handa JT, Friedman AD, et al. **A review of the literature for intra-arterial chemotherapy used to treat retinoblastoma.** *Pediatr Radiol* 2016;46:1223–33 CrossRef Medline
6. Yousef YA, Soliman SE, Astudillo PP, et al. **Intra-arterial chemotherapy for retinoblastoma: a systematic review.** *JAMA Ophthalmol* 2016 Mar 17. [Epub ahead of print] CrossRef Medline
7. Jabbour P, Chalouhi N, Tjoumakaris S, et al. **Pearls and pitfalls of intraarterial chemotherapy for retinoblastoma: a review.** *J Neurosurg Pediatr* 2012;10:175–81 CrossRef Medline
8. Strauss KJ, Kaste SC. **ALARA in pediatric interventional and fluoroscopic imaging: striving to keep radiation doses as low as possible during fluoroscopy of pediatric patients—a white paper executive summary.** *J Am Coll Radiol* 2006;3:686–88 Medline
9. Khong PL, Ringertz H, Donoghue V, et al; ICRP. **ICRP Publication 121: radiological protection in paediatric diagnostic and interventional radiology.** *Ann ICRP* 2013;42:1–63 CrossRef Medline
10. Cooke DL, Stout CE, Kim WT, et al. **Radiation dose reduction in intra-arterial chemotherapy infusion for intraocular retinoblastoma.** *J Neurointerv Surg* 2014;6:785–89 CrossRef Medline
11. **3 quantities and units for measurement and calculation in medical x-ray imaging.** *J ICRU* 2005;5:25–34 Medline
12. Hayreh SS, Dass R. **The ophthalmic artery, II: intra-orbital course.** *Br J Ophthalmol* 1962;46:165–85 CrossRef Medline
13. Pron G, Bennett J, Common A, et al; Ontario UFE Collaborative Group. **Technical results and effects of operator experience on uterine artery embolization for fibroids: the Ontario Uterine Fibroid Embolization Trial.** *J Vasc Interv Radiol* 2003;14:545–54 CrossRef Medline
14. Boddu SR, Abramson DH, Marr BP, et al. **Selective ophthalmic artery chemosurgery (SOAC) for retinoblastoma: fluoroscopic time and radiation dose parameters—a baseline study.** *J Neurointerv Surg* 2017;9:1107–12 CrossRef Medline
15. Huda W. **Kerma-area product in diagnostic radiology.** *AJR Am J Roentgenol* 2014;203:W565–69 CrossRef Medline
16. Chida K, Kagaya Y, Saito H, et al. **Total entrance skin dose: an effective indicator of maximum radiation dose to the skin during percutaneous coronary intervention.** *AJR Am J Roentgenol* 2007;189:W224–27 CrossRef Medline
17. Pearl MS, Torok C, Wang J, et al. **Practical techniques for reducing radiation exposure during cerebral angiography procedures.** *J Neurointerv Surg* 2015;7:141–15 CrossRef Medline
18. Schneider T, Wyse E, Pearl MS. **Analysis of radiation doses incurred during diagnostic cerebral angiography after the implementation of dose reduction strategies.** *J Neurointerv Surg* 2017;9:384–88 CrossRef Medline
19. Klufas MA, Gobin YP, Marr B, et al. **Intra-arterial chemotherapy as a treatment for intraocular retinoblastoma: alternatives to direct ophthalmic artery catheterization.** *AJNR Am J Neuroradiol* 2012;33:1608–14 CrossRef Medline

Morphologic Evolution and Coordinated Development of the Fetal Lateral Ventricles in the Second and Third Trimesters

Z. Li, F. Xu, Z. Zhang, X. Lin, G. Teng, F. Zang, and S. Liu



ABSTRACT

BACKGROUND AND PURPOSE: Few investigators have studied the lateral ventricle formation related to the development of the calcarine sulcus. Our purpose was to establish the relationship between the lateral ventricles and the calcarine sulcus in the second and third trimesters.

MATERIALS AND METHODS: Fetal brain MR imaging (3T and 7T) was performed in 84 fetuses at 14–35 gestational weeks. The lateral ventricles and calcarine sulcus were 3D-reconstructed, and quantitative measurements were obtained.

RESULTS: The lateral ventricle volume decreases slowly at 14–23 gestational weeks and then increases rapidly at 24–35 gestational weeks. The depth and length of the calcarine sulcus develop with the increase in gestational weeks, leading to be squeezed in the lateral ventricle posterior horn. A linear correlation occurs between the calcarine sulcus length and posterior horn length: Right-length = $2.4204 (L_{PH}) - 27.5706$, Left-length = $2.0939 (L_{PH}) - 23.4099$.

CONCLUSIONS: The variation of lateral ventricle volume evolved from a slow to rapid increase at 14–35 gestational weeks. The shrinkage in the lateral ventricle posterior horn is accompanied by the development of the calcarine sulcus, resulting in a better linear correlation between the calcarine sulcus length and the posterior horn length. The present results are valuable in elucidating the evolution of lateral ventricle development and provide clues for the diagnosis of lateral ventricle abnormalities in the prenatal examination.

ABBREVIATIONS: L_{APP} = width between the anterior and posterior parts; L_{BIH} = width between the bilateral inferior horns; L_{CI} = length between the central part and inferior horn; L_{HCP} = intraventricular height at the central part; L_{PH} = length of the posterior horn; L_{TAP} = total anteroposterior length

Fetal brain development is a highly complex and delicate process, during which the size and the shape of the brain change rapidly. The lateral ventricles occupy most of the fetal brain, and their changes are closely related to the changes in brain structures. At present, studies on the development of the lateral ventricles are focused on the second trimester, and the data on the third trimester

are still lacking. It would be valuable to study the changes in the lateral ventricles within a wide range of gestational ages.

Many ultrasonographic and in utero MR imaging studies on the size of the lateral ventricles are limited to subjective descriptions and 2D measurements, which cannot reflect the size and the shape of lateral ventricles correctly.¹ A number of recent studies have started using postmortem specimens to study the development in the lateral ventricles and have found that the changes in the lateral ventricles are related to the development of the surrounding structures during fetal development.² The volumes of the basal ganglia and the ganglionic eminences increase with gestational weeks, whereas the volume of the lateral ventricles decrease later in the second trimester.³ Fetal total lateral ventricle and thalamus volumes were correlated at 22–38 gestational weeks.⁴ A recent study found that the inward folding and development of the neonatal cerebral surface were considered the main cause of the decrease in the volume of the lateral ventricles.⁵ It was observed that the changes in the lateral ventricles are consistent with not only the growth of internal surrounding structures but also the external cortical folding. The calcarine sulcus is an important and consistent sulcus in the occipital lobe, which is consid-

Received October 27, 2018; accepted after revision February 13, 2019.

From the Research Center for Sectional and Imaging Anatomy (Z.L., F.X., Z.Z., X.L., S.L.), Institute of Brain and Brain-Inspired Science, Shandong University Cheeloo Medical College, Shandong, China; Department of Medical Imaging (Z.Z., X.L.), Provincial Hospital Affiliated with Shandong University, Shandong, China; Department of MR Imaging (X.L.), Shandong Medical Imaging Research Institute, Shandong, China; and Department of Radiology (G.T., F.Z.), Zhong Da Hospital, Southeast University School of Clinical Medicine, Jiangsu, China.

This work was supported by the National Natural Science Foundation of China (No. 31771328, 31571237).

Please address correspondence to Shuwei Liu, MD, Research Center for Sectional and Imaging Anatomy, Institute of Brain and Brain-Inspired Science, Shandong University Cheeloo Medical College, 44 Wen-hua Xi Rd, 250012 Jinan, Shandong, China; e-mail: liusw@sdu.edu.cn

Indicates open access to non-subscribers at www.ajnr.org

<http://dx.doi.org/10.3174/ajnr.A6013>

ered the most valuable landmark for the recognition of the medial surface of the occipital lobe.⁶ On the basis of the location correlation of the calcarine sulcus and the lateral ventricles, some scholars have pointed out that there is a certain relationship between them during their development.

Animal-based research confirmed that the decrease in ventricular volume was accompanied by an increase in the depth of the calcarine sulcus in cynomolgus monkey fetuses.⁷ The study concluded that the degree of infolding of the calcarine sulcus can be used as the anatomic landmark for evaluating the cerebral maturation. Then, the correlation investigation was conducted between the morphologic maturation of the calcarine sulcus and the width of lateral ventricles in human fetuses with isolated mild ventriculomegaly at 20–36 gestational weeks.⁸ The study indicated that there was a negative correlation between the fetal calcarine sulcus depth and the width of the lateral ventricles in fetuses with isolated mild ventriculomegaly. It was also found that the lateral ventricle volume began to decrease after the appearance of the calcarine sulcus in the gyral development of the human brain.⁹ Studies have depicted the relationship between the lateral ventricles and calcarine sulcus in animals and fetuses with isolated mild ventriculomegaly.^{7,8} This relationship is also fascinating and interesting in healthy fetuses and needs to be studied to further elucidate the evolution of the fetal brain. Thus, the present study planned to first investigate the development of the lateral ventricles and then explore the developmental correlation during the normal human fetal development across 14–35 gestational weeks using high-field-strength MR imaging.

MATERIALS AND METHODS

Subjects

A total of 161 fetuses at 14–35 gestational weeks were selected from medically indicated or spontaneous abortions within 24 hours, fetal deaths attributed to maternal diseases, stillbirths caused by abnormal delivery, and premature deaths caused by diseases outside the brain such as respiratory diseases, from hospitals in the Shandong Province of China. According to the strict inclusion criteria that were established on the basis of the size of the cerebrum and the developmental status of the sulci, lateral ventricles, and corpus callosum in previous studies,^{10,11} 84 specimens were included in this study to minimize the influence of brain deformation on experimental results. Previous studies have confirmed the clinical application of the volume and the sulcal width in fetuses with formalin fixation.^{12,13} Therefore, all the specimens were immersed in 10% formalin and scanned by MR imaging within 2 months after the fetal death.

The gestational age of fetuses at 14–35 gestational weeks was estimated according to their crown–rump length and/or pregnancy records and was expressed as weeks from the last menstrual period.¹⁴ The Table presents the number of subjects in each gestational week, including the numbers of males and females. The specific protocol of this study was approved by the Human Research Ethics Committees of the School of Medicine of Shandong University. The parents' consent to donate the fetal cadaver was obtained.

Distribution of gestational age and number of specimens in each age selected (n = 84)

GA	Total No.	Sex (Male/Female)	GA	Total No.	Sex (Male/Female)
14	2	1:1	25	4	4:0
15	4	2:2	26	5	5:0
16	6	3:3	27	1	1:0
17	5	1:4	28	3	1:2
18	3	2:1	29	4	1:3
19	3	2:1	30	3	0:3
20	8	2:6	31	3	0:3
21	5	1:4	32	1	0:1
22	7	2:5	33	3	0:3
23	6	4:2	34	1	0:1
24	6	4:2	35	1	0:1

Note:—GA indicates gestational age in weeks.

Image Acquisition

The specimens were scanned by keeping the brain in situ without destroying the ventricular system and subarachnoid space to ensure that the extrauterine environment was consistent with the intrauterine environment of the lateral ventricles. We performed 3T and 7T MR imaging at 2 stages for clear images and accurate 3D reconstruction. We used 7T MR imaging to scan the fetus at 14–22 gestational weeks because the structure of the fetus was immature during this period. The 3T MR images of the fetal brain at 23–35 gestational weeks were sufficient to show the structural boundaries. Postmortem MR imaging ensures the consistency of measurement and the accuracy of results, avoiding the effects of motion artifacts, field strength limitations, and so forth.¹⁵ Finally, 41 specimens at 14–22 gestational weeks were scanned by 7T micro-MR imaging (70/16 PharmaScan; Bruker Biospin, Ettlingen, Germany). The inner diameter of the rat body coil used was 60 mm. The acquisition parameters of T1-weighted images were the following: TR/TE, 384.4/15.8 ms; matrix size, 512 × 512; slice thickness, 0.8 mm; number of excitations, 1; FOV, 6 × 6 cm; voxel size, 0.8 × 0.12 × 0.12 mm³. The acquisition parameters of T2-weighted slice images were the following: TR/TE, 17,000/50 ms; matrix size, 256 × 256; slice thickness, 0.5 mm; number of excitations, 4; FOV, 6 × 6 cm; voxel size, 0.5 × 0.23 × 0.23 mm³.¹⁴

Due to the coil limitations, 43 specimens at 23–35 gestational weeks were scanned with a Signa 3T MR imaging scanner (GE Healthcare, Milwaukee, Wisconsin). The acquisition parameters of T1-weighted slice images were the following: TR/TE, 2580.0/23.4 ms; matrix size, 512 × 512; slice thickness, 2 mm; number of excitations, 1; voxel size, 2 × 1.9 × 1.9 mm³. The acquisition parameters of T2-weighted slice images were the following: TR/TE, 4600.0/111.6 ms; matrix size, 512 × 512; slice thickness, 2 mm; number of excitations, 1; voxel size, 2 × 1.9 × 1.9 mm³.

Image Processing

This work was performed using manual segmentation. The selected structures were segmented on horizontal, sagittal, and coronal planes using the inner interface in Amira 5.2.2 software (www.amira.com) (Fig 1). Segmenting these structures was performed manually by 2 experienced anatomists based on a histology atlas of second-trimester fetal brains.¹⁶ Then, the 3D reconstruction models were obtained as shown in Fig 2.

Data Measurement

The lateral ventricle volume was obtained by Amira software, and we measured the following lengths of the 3D ventricle model: total anteroposterior length (L_{TAP}), width between the anterior and posterior parts (L_{APP}), length of the posterior horn (L_{PH}), intraventricular height at the central part (L_{HCP}), length between the central part and the inferior horn (L_{CI}), and width between the bilateral inferior horns (L_{BIH}) (Fig 2). These measures reflect the elongation and narrowing of the ventricles and also reflect the changes of surrounding structures around the lateral ventricles.²

Sulcal depth is defined as the distance between the superficial and deep ridges (Fig 3A, -B). When the sulcus is curved, the sum of the paths is the sulcal depth (Fig 3E). The length of the calcarine sulcus was measured on the sagittal plane (Fig 3C). It is the sum of the anterior and the posterior parts of the calcarine sulcus (Fig 3D). For the sulcal depth and length, the maximum value on the multiple layers was obtained by 2 anatomists, and the mean value was used as the last measurement.

Statistical Analysis

We used 3T and 7T MR imaging data to obtain high-precision segmentation and measurement data. Thus, all data were analyzed with SPSS software, Version 17.0 (IBM, Armonk, New York) in 1 group. Simple correlation analysis was used to analyze the correlation between the lateral ventricle posterior horn length and the measurement of the calcarine sulcus. A 2-sample *t* test for

dependent samples was used to test sex differences. The differences in the hemispheres were compared using the paired-sample *t* test for dependent samples. $P < .05$ was considered statistically significant.

RESULTS

Morphologic Evolution of the Lateral Ventricles

Figure 4 delineates the morphologic evolution of the lateral ventricles at 14–31 gestational weeks. The lateral ventricles were immature at 14 gestational weeks, and they gradually developed into 4 parts at 21 gestational weeks: the anterior horn, inferior horn, posterior horn, and central part. The anterior horn, inferior horn, and central part became thin at 27 gestational weeks. The posterior horn became flat at 31 gestational weeks.

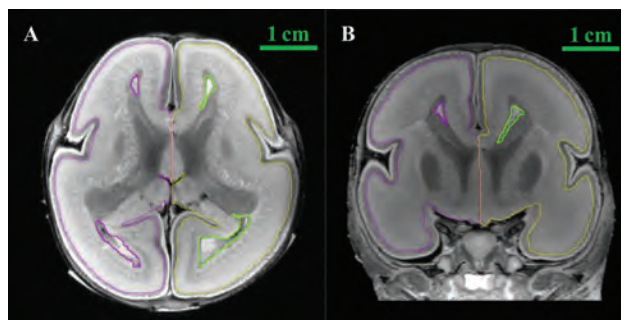


FIG 1. Segmentation of the brain structures with Amira 5.2.2. A, Segmentation on the axial plane. B, Segmentation on the coronal plane.

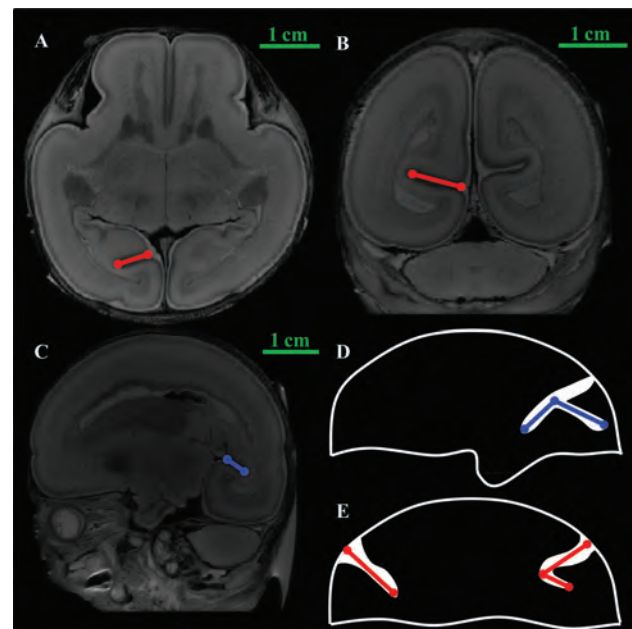


FIG 3. Measurement of the calcarine sulcus. A, The depth of the calcarine sulcus (axial plane). B, The depth of the calcarine sulcus (coronal plane). C, The length of the calcarine sulcus (sagittal plane). D and E, The measurements of the depth and the length in the calcarine sulcus. The blue line shows the length of the sulcus. The red line shows the depth of the sulcus.

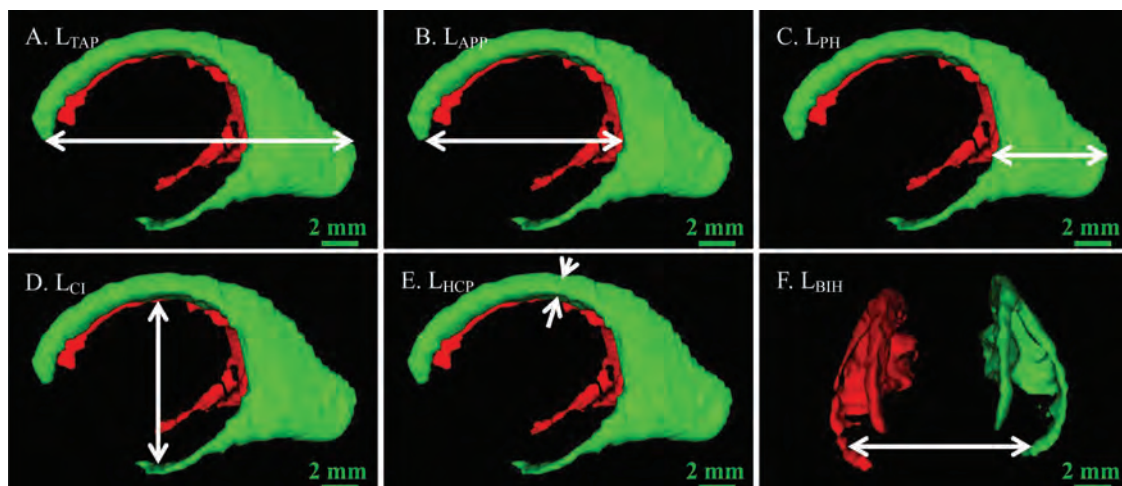


FIG 2. Length measurements of the lateral ventricle. Arrows indicate the length. A, L_{TAP} . B, L_{APP} . C, L_{PH} . D, L_{CI} . E, L_{HCP} . F, L_{BIH} .

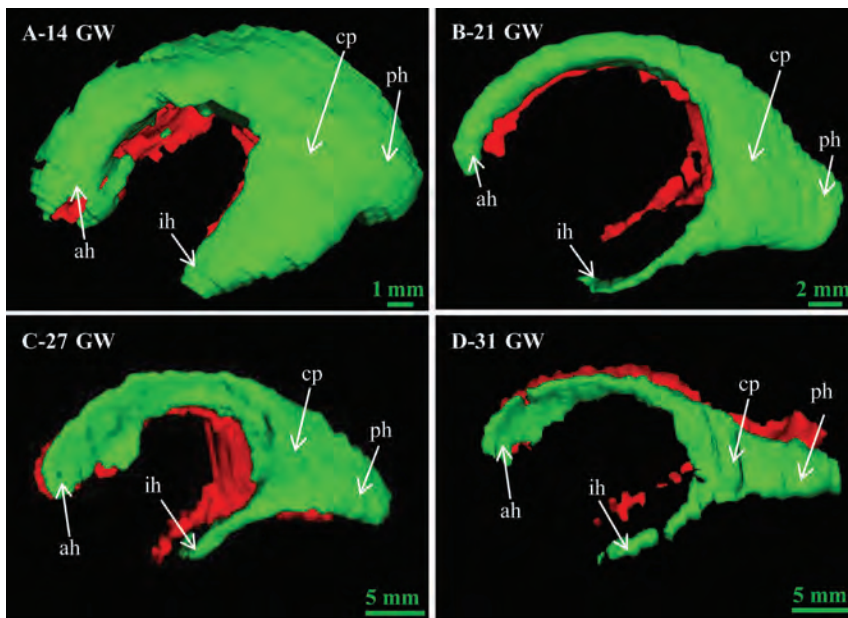


FIG 4. The morphologic evolution of fetal lateral ventricles at 14–31 weeks. ah indicates anterior horn; ph, posterior horn; ih, inferior horn; cp, central part; GW, gestational weeks.

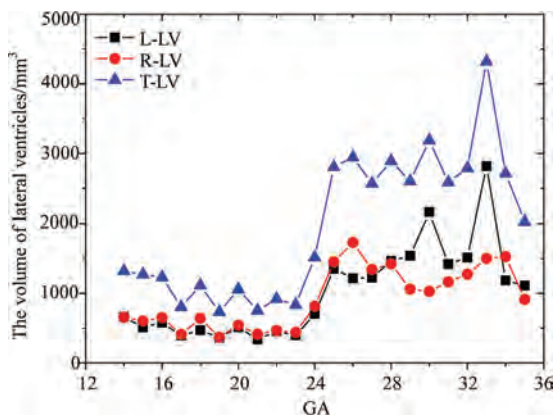


FIG 5. Volume measurements of the lateral ventricles. L-LV indicates the left lateral ventricle volume; R-LV, right lateral ventricle volume; T-LV, total lateral ventricle volume; GA, gestational age.

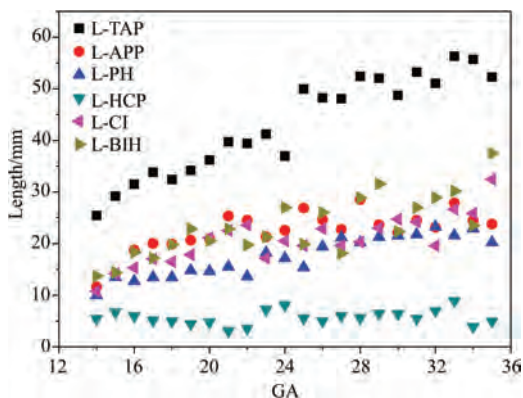


FIG 6. Quantitative measurements of the lateral ventricles.

Lateral Ventricular Volume

The left, right, and total ventricular volume were obtained after 3D reconstruction (Fig 5). The variation of ventricular volume

can be divided into 2 stages: a stable stage at 14–23 gestational weeks and a fluctuant stage at 24–35 gestational weeks. The total volume of the lateral ventricles declined slowly at the stable stage and then increased to the first peak of 2945.68 mm³ at 26 gestational weeks. Then the lateral ventricle volume fluctuated from 26 to 35 gestational weeks, reaching the maximum value of 4321 mm³ at 33 gestational weeks and a low value of 2023.288 mm³ at 35 gestational weeks. After a slow descent, the left volume increased to the first peak of 1215.7 mm³ at 26 gestational weeks and then fluctuated twice until 33 gestational weeks, reaching the maximum value of 2820.015 mm³. The right volume was smaller than the volume of the left lateral ventricles at the fluctuant stage. The right volume decreased slowly at the stable stage and rose to 1729.98 mm³ at 26 gestational weeks. After a relatively stable plateau, the right volume reached 1527.73 mm³ at 33 gestational weeks and then dropped to 912.968 mm³ at 35 gestational weeks.

Length Parameters

Figure 6 represents the variation of 6 length parameters with the gestational weeks, where the L_{TAP} obviously increased from 25.46 to 52.28 mm, reflecting the development of the whole brain. There was no obvious change in the L_{HCP} , which may correspond to the relatively stable development of the body of the corpus callosum.^{17,18} For the other 4 curves, the L_{BIH} increased from 13.74 to 37.53 mm. A smaller magnitude of increase occurred in the L_{CI} and L_{APP} , 10.785–32.45 and 11.61–23.81 mm, respectively.

Depth and Length of the Calcarine Sulcus

Figure 7 reflects the changes in the depth and length of the calcarine sulcus at 14–35 gestational weeks with an increasing trend. The distribution of the sulcus length was more concentrated than that of the depth, showing a smaller individual difference. The depth had a linear increase compared with the smooth variation in the length at 14–23 gestational weeks (Fig 7A). At 14 gestational weeks, the average depth reached 2.82 mm and then increased to 5.67 mm at 15 gestational weeks and 8.61 mm at 23 gestational weeks. At 24–35 gestational weeks, the average depth increased from 10.11 to 12.71 mm with a linear growth law (Fig 7C). The length development was nonlinear growth with the increase in gestational weeks, which was not consistent with the depth of the calcarine sulcus. After a platform period from 14–23 gestational weeks, the length of the calcarine sulcus increased rapidly (Fig 7D).

Location Correlation

The calcarine sulcus and lateral ventricles were reconstructed in 1 space to show the spatial position relationship (Fig 8). The calca-

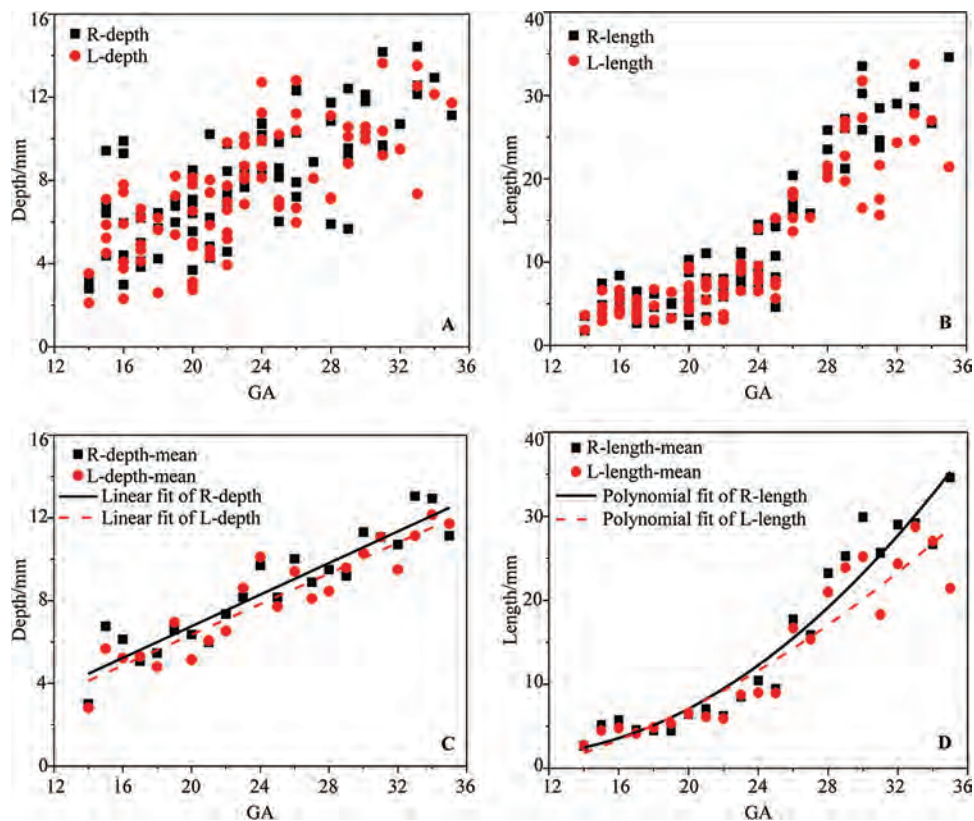


FIG 7. The depth and length of the calcarine sulcus. *A*, The depth of the calcarine sulcus. *B*, The length of the calcarine sulcus. *C*, The mean depth of the calcarine sulcus. *D*, The mean length of the calcarine sulcus.

rine sulcus was close to the posterior part of the lateral ventricles (Fig 8*A1*, *B1*, and *C1*). The inner side of the calcarine sulcus was parallel to the cerebral median fissure. The lateral ventricles became thin with the increase of gestational weeks, and the calcarine sulcus became wider and longer. The posterior view showed that part of the 2 structures overlapped and the morphologic characteristics were not obvious. On the lateral view, the calcarine sulcus and lateral ventricles overlapped before 21 gestational weeks. With the development of the calcarine sulcus, the posterior part gradually extended longer backward. The occipital part of the lateral ventricles narrowed with the lengthening of the calcarine sulcus.

Measurements Correlation

According to the results of location correlation, the length and depth of the left and right calcarine sulcus and the posterior horn length in the lateral ventricles were selected for analysis in this study. The depth and length of the calcarine sulcus were linearly related to the posterior horn length (Fig 9). The length and depth of the calcarine sulcus can be expressed by the following equation: Right-length = $2.4204 (L_{PH}) - 27.5706$, Right-depth = $0.5145 (L_{PH}) - 2.3072$, Left-length = $2.0939 (L_{PH}) - 23.4099$, Left-depth = $0.5902(L_{PH}) - 2.3403$.

Sex and Side Difference

There was almost no difference between the left and right lateral ventricle volume before 24 gestational weeks and a large difference after 24 gestational weeks (Fig 5). However, statistics showed that there was no hemispheric difference in the lateral ventricle

volume during the entire period ($P > .05$). The depth and length of the calcarine sulcus in the right hemisphere were greater than those in the left, which was statistically significant (all $P < .05$). There were no sexual dimorphisms in those measurements (all $P > .05$).

DISCUSSION

Formation of the Fetal Lateral Ventricle

The morphologic evolution of the lateral ventricles is affected by many aspects such as the cortical folding and the development of subcortical structures.³ At 10–13 gestational weeks, the lateral ventricles account for most of the brain because of the vesicular period of the ventricular system.¹⁹ In this study, it was found that the lateral ventricle morphology still had the characteristics of the vesicular period at 14 gestational weeks (Fig 4*A*). The shape of the lateral ventricles evolves from an embryonic crescent into the immature lateral ventricles with 4 horns.²⁰ With the development of the fetal brain, the lateral ventricles begin to lose the features of the vesicular period and gradually separates into 4 distinct parts at 16 gestational weeks.² The increase in L_{APP} , L_{CI} , and L_{BIH} indicates the development of the basal nuclei and thalamus at this stage, resulting in the narrowing of the anterior horn of the lateral ventricles (Fig 4*B*, *-C*). It is evident that the slope of the L_{PH} is less than that of the L_{TAP} , findings in agreement with the shrinkage of the lateral ventricular occipital region (Fig 6, Fig 4*D*). Eventually, the lateral ventricle morphology development approaches that of adults.

The volume of the lateral ventricles decreased at 14–23 gesta-

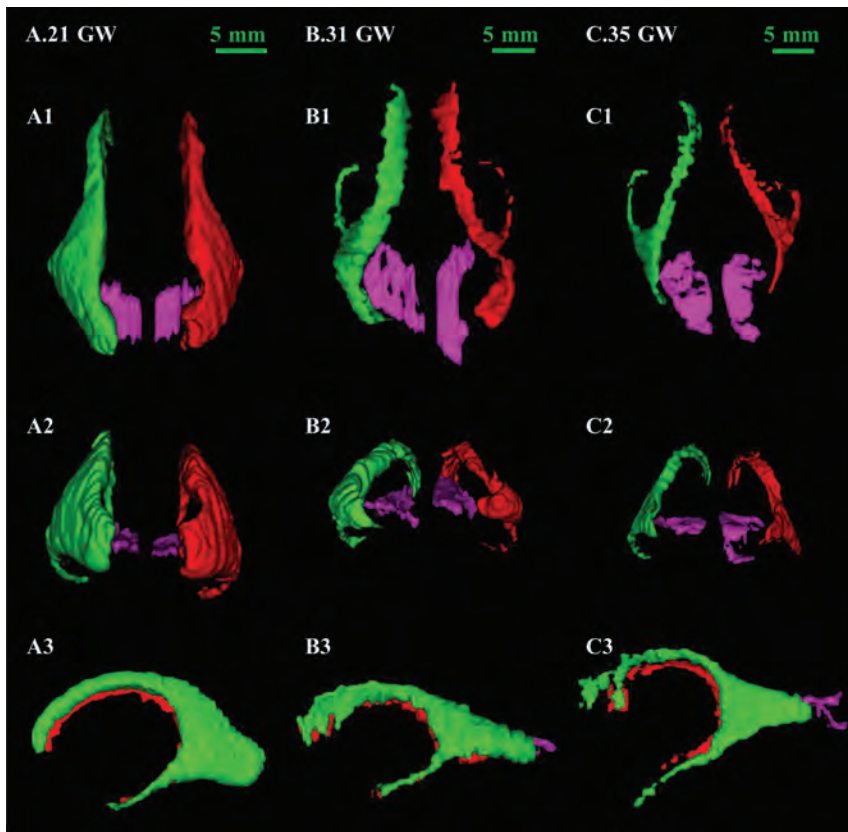


FIG 8. The location of the calcarine sulcus in 3D space: superior view (A1, B1, C1), posterior view (A2, B2, C2), lateral view (A3, B3, C3). A, Twenty-one GW (A1, A2, A3). B, Thirty-one GW (B1, B2, B3). C, Thirty-five GW (C1, C2, C3). The left lateral ventricle is green, the right lateral ventricle is red, and the calcarine sulcus is pink. GW indicates gestational weeks.

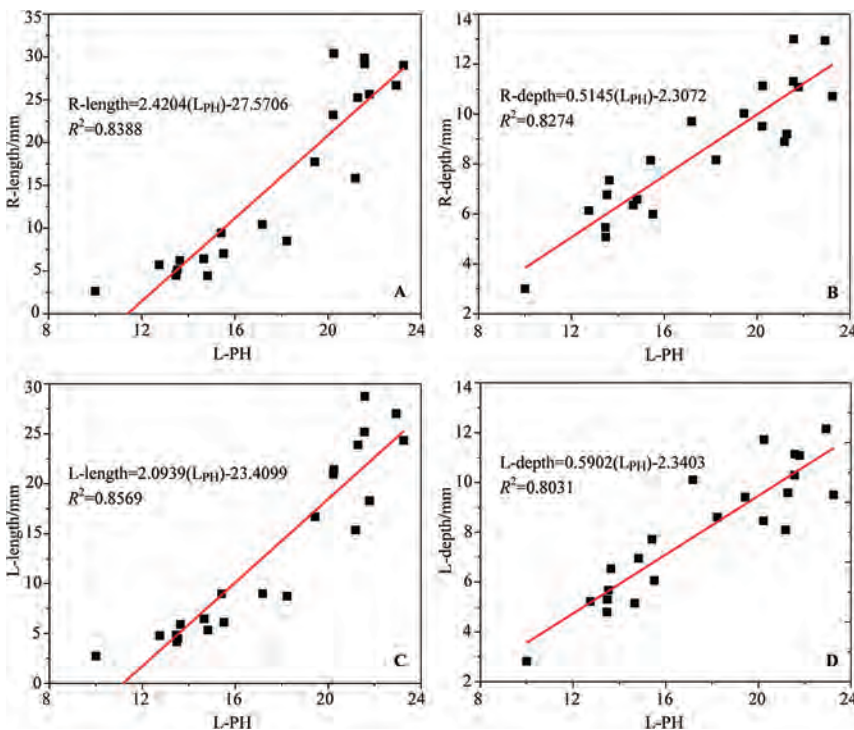


FIG 9. The correlation between the L_{PH} and the depth and length of the calcarine sulcus.

tional weeks (Fig 5), which is in agreement with the study by Clouchoux et al.²¹ However, Huang et al³ found that the volume of the lateral ventricles first increased and then decreased at 13–21 gestational weeks. Kinoshita et al¹⁹ observed that the volume of the lateral ventricles increased at 7–23 gestational weeks. The results of the lateral ventricle volume are different in these studies. One reason is the differences in the sample sizes and individual fetuses. Another reason could be the differences in the structural anatomic definition and inclusion of the third ventricle or the cavum septum pellucidum. It is conceivable that the decrease in volume is associated with the change of the ventricular morphology. At 14 gestational weeks, the vesicular effect of the ventricles gradually disappears and the volume of the lateral ventricles is reduced correspondingly. Meanwhile, the volume of the germinal matrix and subcortical structures such as the basal nuclei also increases with the gestational week.²² It is inferred that the shrinkage in the lateral ventricles is accompanied by the expansion of the germinal matrix and basal nuclei. The lateral ventricles and these subcortical structures develop together and affect each other in the morphologic evolution of the lateral ventricles.

At 23–35 gestational weeks, the volume of the lateral ventricles increases with the fluctuating trend. The L_{TAP} grows faster than the L_{APP} , L_{HCP} , and L_{CI} , reflecting the growth in the brain volume being faster than that of the basal ganglia, thalamus, and other structures around the ventricles (Fig 6). Thus, the lateral ventricle volume increases rapidly at 23–26 gestational weeks. This finding is in agreement with a previous study that found that fetal brain volume increases linearly and subcortical structures such as germinal matrix volume decrease at this stage.²² After 26 gestational weeks, the fetal brain volume increases quickly and the germinal matrix decreases. The germinal matrix gradually develops into the caudate, putamen, globus pallidus, and basal ganglia.³ The increase in L_{APP} , L_{BIH} , and L_{CI} represents these subcortical structures beginning to expand. Then the increased velocity of the lateral ventricle volume

becomes slower. It is inferred that the individual differences in development are more obvious at this stage, resulting in the increase in the volume of the lateral ventricles with the fluctuating trend.

A difference occurred in the development of left and right lateral ventricle volume after 24 gestational weeks, which may be related to the lateralization of cerebral hemisphere development. Lateral differences in the cerebral hemispheres already exist at birth. The growth of the cerebral hemisphere structures may affect the lateral ventricles, resulting in this large difference in lateral ventricle volume. Meanwhile, this difference may also be related to other features such as the number of specimens and the method of measurement and so forth. However, the cerebral lateralization is a very complex problem that requires more data to reach a conclusion. The change in the lateral ventricle volume is stable at 14–23 gestational weeks and fluctuates after 23 gestational weeks. The lateral ventricle volume can reflect the development of the lateral ventricles comprehensively compared with the lateral ventricle width on a 2D level.⁴ It is suggested that the lateral ventricle volume measured by 3D sonography techniques needs to be used to improve prenatal diagnostic accuracy after 23 gestational weeks.

Correlation Analysis Between the Lateral Ventricles and the Calcarine Sulcus

The growth of the calcarine sulcus length accelerated noticeably after a slow developmental period. It is consistent with the variation of the lateral ventricle volume (Fig 7D). This finding indicates that there is a certain relationship between the calcarine sulcus and lateral ventricles. Thus, we elucidated the relationship between the lateral ventricles and the calcarine sulcus, including the location and measurement correlations.

The calcarine sulcus is located at the inner side of the lateral ventricle occipital part. The inner sides of the calcarine sulcus on both sides are parallel (Fig 8A1). The calcarine sulcus gradually increases backward and exceeds the occipital part of the lateral ventricles (Fig 8B1, -C1). The curvature of the posterior calcarine sulcus is related to the acceleration of cortical folding in the later developmental period (Fig 8A3–C3).⁵ The calcarine sulcus depth increases and extends outward. The lateral ventricle occipital part becomes flattened, and the size relatively decreases (Fig 8A3–C3).

Combined with the development of the fetal brain, the variation of calcarine sulcus length and the volume of lateral ventricles is associated with the whole-brain development.²³ At 14–23 gestational weeks, the whole calcarine sulcus does not exceed the boundary of the lateral ventricle occipital part. The lateral ventricles and the calcarine sulcus gradually develop with fetal brain development. At 24–35 gestational weeks, the calcarine sulcus posterior part size exceeds the lateral ventricle occipital part and becomes a wave type. Both of them are in a relatively slow growth period; then, the growth becomes faster. The variation of the calcarine sulcus length and lateral ventricle volume is roughly consistent with the trend of fetal brain volume.

On the basis of the above analysis, the lateral ventricle occipital part is affected by the calcarine sulcus in its development. As the increase in the calcarine sulcus depth, the posterior horn length becomes smaller. There is a better linear correlation between the

left calcarine sulcus length and the posterior horn length represented by the value of the L_{PH} (Fig 9). The fitting effect between the L_{PH} and calcarine sulcus length is better than that between the L_{PH} and the calcarine sulcus depth, which is consistent with the phenomenon that the point dispersion degree of the calcarine sulcus depth is greater than that of calcarine sulcus length (Fig 9 and Fig 7A, -B). This feature indicates that the stability of the calcarine sulcus length is better than that of the calcarine sulcus depth. The linear correlation between the lateral ventricle and the calcarine sulcus is helpful to elucidate the development of the lateral ventricles and improve the prenatal diagnosis of fetal ventriculomegaly.

CONCLUSIONS

The lateral ventricle volume increases, with a slow-to-rapid growth period at 14–35 gestational weeks. The shrinkage in the lateral ventricle posterior horn is accompanied by the development of the calcarine sulcus, resulting in a better linear correlation between the calcarine sulcus length and the posterior horn length. The relevant results are helpful in understanding the evolution of the lateral ventricles and providing a basis for the diagnosis of lateral ventricle abnormality. Our future work is to study the relationship between the fetal lateral ventricles and the calcarine sulcus in patients with ventriculomegaly, to provide more valuable data for a differential diagnosis and prenatal examination of ventriculomegaly.

ACKNOWLEDGMENTS

We thank Derong Duan, Qing Xia, Wenjia Liang, and Wenjun Wang for language help during the revision.

REFERENCES

1. Perlman S, Shashar D, Hoffmann C, et al. **Prenatal diagnosis of fetal ventriculomegaly: agreement between fetal brain ultrasonography and MR imaging.** *AJNR Am J Neuroradiol* 2014;35:1214–18 CrossRef Medline
2. Taketani K, Yamada S, Uwabe C, et al. **Morphological features and length measurements of fetal lateral ventricles at 16–25 weeks of gestation by magnetic resonance imaging.** *Congenit Anom (Kyoto)* 2015;55:99–102 CrossRef Medline
3. Huang H, Xue R, Zhang J, et al. **Anatomical characterization of human fetal brain development with diffusion tensor magnetic resonance imaging.** *J Neurosci* 2009;29:4263–73 CrossRef Medline
4. Kyriakopoulou V, Vatansever D, Elkommos S, et al. **Cortical overgrowth in fetuses with isolated ventriculomegaly.** *Cereb Cortex* 2014;24:2141–50 CrossRef Medline
5. Dubois J, Benders M, Cachia A, et al. **Mapping the early cortical folding process in the preterm newborn brain.** *Cereb Cortex* 2008; 18:1444–54 Medline
6. Baffero GM, Crovetto F, Fabietti I, et al. **Prenatal ultrasound predictors of postnatal major cerebral abnormalities in fetuses with apparently isolated mild ventriculomegaly.** *Prenat Diagn* 2015;35: 783–88 CrossRef Medline
7. Fukunishi K, Sawada K, Kashima M, et al. **Correlation between formation of the calcarine sulcus and morphological maturation of the lateral ventricle in cynomolgus monkey fetuses.** *Acta Neurobiol Exp (Wars)* 2011;71:381–86 Medline
8. Li H, Liang H, Wu H. **Magnetic resonance imaging-based correlation analysis between calcarine sulcus development and isolated fetal ventriculomegaly.** *Congenit Anom (Kyoto)* 2017;57:52–56 CrossRef Medline

9. Chi JG, Dooling EC, Gilles FH. **Gyral development of the human brain.** *Ann Neurol* 1977;1:86–93 CrossRef Medline
10. Zhang Z, Hou Z, Lin X, et al. **Development of the fetal cerebral cortex in the second trimester: assessment with 7T postmortem MR imaging.** *AJNR Am J Neuroradiol* 2013;34:1462–67 CrossRef Medline
11. Zhang Z, Liu S, Lin X, et al. **Development of fetal cerebral cortex: assessment of the folding conditions with post-mortem magnetic resonance imaging.** *Int J Dev Neurosci* 2010;28:537–43 CrossRef Medline
12. Tubbs RS, Shoja MM, Aggarwal A, et al. **Choroid plexus of the fourth ventricle: review and anatomic study highlighting anatomical variations.** *J Clin Neurosci* 2016;26:79–83 CrossRef Medline
13. Ballesteros MC, Hansen PE, Soila K, et al. **MR imaging of the developing human brain, Part 1: prenatal development.** *Radiographics* 1993;13:611–22 CrossRef Medline
14. Zhang H, Zhang Z, Yin X, et al. **Early development of the fetal central sulcus on 7.0T magnetic resonance imaging.** *Int J Dev Neurosci* 2016;48:18–23 CrossRef Medline
15. Habas PA, Scott JA, Roosta A, et al. **Early folding patterns and asymmetries of the normal human brain detected from in utero MRI.** *Cereb Cortex* 2012;22:13–25 CrossRef Medline
16. Bayer SA, Altman J. The human brain during the second trimester. In: *Atlas of Human Central Nervous System Development*, Indianapolis: CRC Press; 2005
17. Rakic P, Yakovlev PI. **Development of the corpus callosum and cavum septi in man.** *J Comp Neurol* 1968;132:45–72 CrossRef Medline
18. Achiron R, Achiron A. **Development of the human fetal corpus callosum: a high-resolution, cross-sectional sonographic study.** *Ultrasound Obstet Gynecol* 2001;18:343–47 CrossRef Medline
19. Kinoshita Y, Okudera T, Tsuru E, et al. **Volumetric analysis of the germinal matrix and lateral ventricles performed using MR images of postmortem fetuses.** *AJNR Am J Neuroradiol* 2001;22:382–88 Medline
20. Shiraishi N, Katayama A, Nakashima T, et al. **Morphology and morphometry of the human embryonic brain: a three-dimensional analysis.** *Neuroimage* 2015;115:96–103 CrossRef Medline
21. Clouchoux C, Guizard N, Evans AC, et al. **Normative fetal brain growth by quantitative in vivo magnetic resonance imaging.** *Am J Obstet Gynecol* 2012;206:173.e1–08 CrossRef Medline
22. Meng H, Zhang Z, Geng H, et al. **Development of the subcortical brain structures in the second trimester: assessment with 7.0-T MRI.** *Neuroradiology* 2012;54:1153–59 CrossRef Medline
23. Scott JA, Habas PA, Rajagopalan V, et al. **Volumetric and surface-based 3D MRI analyses of fetal isolated mild ventriculomegaly: brain morphometry in ventriculomegaly.** *Brain Struct Funct* 2013;218:645–55 CrossRef Medline

Brain MRI Findings in Pediatric-Onset Neuromyelitis Optica Spectrum Disorder: Challenges in Differentiation from Acute Disseminated Encephalomyelitis

E. Bulut, J. Karakaya, S. Salama, M. Levy, T.A.G.M. Huisman, and I. Izbudak

ABSTRACT

BACKGROUND AND PURPOSE: Differentiating pediatric-onset neuromyelitis optica spectrum disorder from acute disseminated encephalomyelitis could be challenging, especially in cases presenting with only brain manifestations. Our purpose was to investigate brain MR imaging features that may help distinguish these 2 entities.

MATERIALS AND METHODS: We retrospectively examined initial brain MR imaging studies of 10 patients with pediatric-onset neuromyelitis optica spectrum disorder (female/male ratio, 7:3) and 10 patients with acute disseminated encephalomyelitis (female/male ratio, 2:8). The mean age of the patients was 10.3 ± 5.6 and 8.7 ± 5.3 years, respectively. Brain lesions were evaluated with respect to location, extent, expansion, T1 hypointensity, contrast enhancement/pattern, and diffusion characteristics. The χ^2 test (Yates or Fisher exact χ^2 tests) was used to compare differences between groups.

RESULTS: Cerebral subcortical \pm juxtacortical and pons \pm middle cerebellar peduncle were the most frequent locations involved in both neuromyelitis optica spectrum disorder ($n = 5$ and 4 , respectively) and acute disseminated encephalomyelitis ($n = 9$ and 7 , respectively). Thalamic lesions were more frequent in acute disseminated encephalomyelitis ($P = .020$) and were detected only in 1 patient with neuromyelitis optica spectrum disorder. None of the patients with neuromyelitis optica spectrum disorder had hypothalamic, internal capsule, or cortical lesions. The internal capsule involvement was found to be significantly different between groups ($P = .033$). There was no significant difference in terms of extent, expansion, T1 hypointensity, contrast enhancement/pattern, and diffusion characteristics.

CONCLUSIONS: Although there is a considerable overlap in brain MR imaging findings, thalamic and internal capsule involvement could be used to differentiate pediatric-onset neuromyelitis optica spectrum disorder from acute disseminated encephalomyelitis.

ABBREVIATIONS: ADEM = acute disseminated encephalomyelitis; anti-AQP4 = anti-aquaporin-4; AQP4 = aquaporin-4; NMOSD = neuromyelitis optica spectrum disorder

Neuromyelitis optica spectrum disorder (NMOSD) is a distinct inflammatory CNS disease characterized primarily by recurrent attacks of optic neuritis and/or longitudinally extensive transverse myelitis. The discovery of a highly specific serum

marker for neuromyelitis optica, the anti-aquaporin-4 (anti-AQP4) antibody, provided increased recognition of previously precluded brain involvement^{1,2} and further expanded the clinical spectrum by identification of seropositive patients with atypical presentations.^{3,4}

Previous studies in NMOSD defined the brain MR imaging lesions mostly as “nonspecific,” located in areas of high or low aquaporin-4 (AQP4) expression.^{5,6} More recent characterizations of brain MR imaging abnormalities reported in seropositive patients include periependymal lesions surrounding the ventricles and cerebral aqueduct, dorsal medullary lesions often continuous with cervical cord lesions, extensive hemispheric white matter lesions, and lesions in the corticospinal tracts (posterior limb of the internal capsule and cerebral peduncle).⁷⁻¹⁰

Relative to adult-onset, NMOSD is infrequent in children (3%–5% of all cases). In series of pediatric-onset NMOSD, brain lesions are reported more frequently¹¹⁻¹⁴; this feature makes the task of distinguishing the clinical picture of pediatric-onset

Received December 11, 2018; accepted after revision February 2, 2019.

From the Departments of Radiology (E.B.) and Statistics (J.K.), Hacettepe University Faculty of Medicine, Ankara, Turkey; Department of Neurology and Psychiatry (S.S.), University of Alexandria, Alexandria, Egypt; Department of Neurology (M.L.), Johns Hopkins School of Medicine, Baltimore, Maryland; Section of Pediatric Neuroradiology (I.I.), Division of Neuroradiology, The Russell H. Morgan Department of Radiology and Radiological Science, Johns Hopkins School of Medicine, Baltimore, Maryland; and Edward B. Singleton Chair of Radiology (T.A.G.M.H.), Texas Children's Hospital, Houston, Texas.

Paper previously presented, in part, as an oral presentation at: Annual Meeting of the American Society of Neuroradiology and the Foundation of the ASNR Symposium, June 2–7, 2018; Vancouver, British Columbia, Canada. The presentation was No. O-246.

Please address correspondence to Elif Bulut, MD, Department of Radiology, Hacettepe University Faculty of Medicine, Sıhhiye, 06230 Ankara, Turkey; e-mail: drelibbulut@yahoo.com

<http://dx.doi.org/10.3174/ajnr.A6003>

NMOSD from other acquired demyelinating syndromes, such as acute disseminated encephalomyelitis (ADEM), very challenging. This is especially difficult in cases presenting with brain manifestations without optic neuritis or myelitis at onset.^{15,16} A timely and accurate diagnosis is important for effective management of NMOSD, which has a very different treatment approach compared with ADEM and other demyelinating diseases.^{17,18}

The aim of our study was to identify brain MR imaging findings at disease onset that could help distinguish pediatric-onset NMOSD from ADEM.

MATERIALS AND METHODS

Patient Selection

We obtained approval from the Johns Hopkins institutional review board to conduct a retrospective search of pediatric patients diagnosed with neuromyelitis optica or NMOSD between 2002 and 2017 at the Johns Hopkins Hospital. Inclusion criteria were as follows: pediatric onset (18 years or younger); fulfillment of the 2006 and 2015 criteria for neuromyelitis optica and NMOSD, respectively^{2,3}; and cerebral manifestations at disease onset with technically available brain MRIs for review. The results of anti-AQP4 antibody tests were also recorded.

For the ADEM group, the Johns Hopkins Hospital radiologic data base was queried for pediatric-onset ADEM. Inclusion criteria were as follows: patients fulfilling the 2007 consensus definition for ADEM,¹⁹ brain MR imaging studies obtained within 2 months of the first clinical event, and a follow-up time of at least 2 years. We excluded patients with further attacks that could suggest an alternative diagnosis.

Image Acquisition

All MR images were obtained using either 1.5T or 3T scanners (Achieva, Philips Healthcare, Best, the Netherlands; Signa Excite, GE Healthcare, Milwaukee, Wisconsin; and Area, Avanto, Skyra, Siemens, Erlangen, Germany). Brain MR imaging sequences were T1WI, fast spin-echo T2WI, fast spin-echo FLAIR, and postgadolinium T1-weighted imaging. DWI was also included except for 2 children with NMOSD. The T1WI was performed with the following parameters: TR range, 520–696 ms; TE range, 4.6–14 ms; matrix size range, 192 × 192 to 512 × 196; FOV range, 190 × 190 to 240 × 240 mm; section thickness/spacing range, 1/1 to 5/7 mm. The T2WI was performed with the following parameters: TR range, 2500–7000 ms; TE range, 83–112 ms; matrix size range, 256 × 184 to 448 × 335; FOV range, 159 × 200 to 240 × 240 mm; section thickness/spacing range, 2/2 to 5/5 mm. The axial FLAIR sequence was performed with the following parameters: TR range, 6000–9000 ms; TE range, 81–120 ms; TI range, 2000–2600 ms; matrix size range, 256 × 256 to 416 × 512; FOV range, 159 × 200 to 240 × 240 mm; section thickness range, 4–5 mm. The axial EPI DWI was performed with the following parameters: TR range, 5400–9000 ms; TE range, 70–100 ms; matrix size range, 128 × 128 to 192 × 192; FOV range, 300 × 230 to 350 × 260 mm; section thickness range, 4–5 mm.

Image Evaluation

All brain MRIs were reviewed in consensus by 2 neuroradiologists (I.I. and E.B.). Brain lesions were evaluated with respect to loca-

Table 1: The clinical features of patients with pediatric-onset NMOSD vs ADEM

Characteristics	NMOSD	ADEM
F/M ratio	7:3	2:8
Mean age at initial manifestation (yr)	10.3 ± 5.6	8.7 ± 5.3
Involvement at initial manifestation		
n (%)		
Brain	4 (40%)	5 (50%)
Brain + spinal cord	2 (20%)	5 (50%)
Brain + optic nerve	2 (20%)	0
Brain + spinal cord + optic nerve	2 (20%)	0
Mean follow-up time (yr)	5.1	3.4

tion, extent, expansion, T1 hypointensity, contrast enhancement/pattern, and diffusion characteristics.

Statistical Analysis

Data analysis was performed with SPSS Statistics 23.0 (IBM, Armonk, New York). Descriptive statistics were expressed as mean ± SD for age. The independent-samples *t* test was performed to compare the means of the 2 groups for age. Categorical variables are presented as count and percentage. The χ^2 test (Yates or Fisher exact χ^2 tests) was used to compare differences between groups for all categorical variables. Results with *P* values < .05 were considered statistically significant. Post hoc power analysis was performed to justify the sample size.

RESULTS

Ten patients with the diagnosis of NMOSD (female/male ratio, 7:3; mean age, 10.3 ± 5.6 years) and 10 patients with the diagnosis of ADEM (female/male ratio, 2:8; mean age, 8.7 ± 5.3 years) were included in the study. The clinical variables of the 2 cohorts are compared in Table 1. There was no significant difference in terms of sex (*P* = .07) or mean age (*P* = .5) of the patients in the 2 groups. The patients with NMOSD presented either with cerebral manifestations alone (40%) or in conjunction with optic neuritis and/or transverse myelitis (60%). Two (20%) of them were seropositive for AQP4, and 1 patient was found to be seropositive for the anti-myelin oligodendrocyte glycoprotein antibody a few months after onset.

A summary of the imaging findings of patients with NMOSD and ADEM is provided in Table 2. The most frequent locations of involvement were the cerebral hemispheric white matter and pons ± middle cerebellar peduncle in both NMOSD (*n* = 5 and 4, respectively) and ADEM (*n* = 9 and 7, respectively). The periventricular area of the fourth ventricle was involved in 5 patients with NMOSD (50%). The periependymal area appeared to be affected via extension of large lesions at the brain stem or cerebellum rather than being the center of involvement (Fig 1A–C). Periventricular extension of brain stem lesions (*n* = 6, 60%) was also common in patients with ADEM.

The periaqueductal area (*n* = 1), thalamus (*n* = 1), basal ganglia (*n* = 1), and corpus callosum (*n* = 1) were rare lesion locations in patients with NMOSD. There were no lesions in the periependymal area around the third ventricle, in the posterior limb of the internal capsule, or in the cerebral cortex. The single thalamic lesion in the NMOSD cohort was small and nonspecific and distant from the ependymal lining of the third ventricle. In contrast to patients with NMOSD, unilateral/bilateral (*n* = 4/3)

Table 2: Brain MRI findings of patients with pediatric-onset NMOSD vs ADEM

Characteristics	NMOSD (n = 10)	ADEM (n = 10)	P Value
Lesion localization/infratentorial			
Medulla	4 (40%)	2 (20%)	1
Area postrema	2 (20%)	1 (10%)	1
Cerebellum	2 (20%)	2 (20%)	1
Pons	4 (40%)	7 (70%)	.37
Middle cerebellar peduncle	4 (40%)	6 (60%)	.65
Periventricular	5 (50%)	6 (60%)	1
Mesencephalon	2 (20%)	4 (40%)	.63
Periaqueductal	1 (10%)	1 (10%)	1
Lesion localization/supratentorial			
Diencephalon			
Thalamus	1 (10%)	7 (70%)	.02 ^a
Hypothalamus	0	3 (30%)	.21
Periventricular	0	5 (50%)	.37
Internal capsule	0	5 (50%)	.03 ^a
Basal ganglia	1 (10%)	3 (30%)	.58
Corpus callosum	1 (10%)	2 (20%)	1
Cerebral white matter			
Periventricular	3 (30%)	6 (60%)	.37
Juxtacortical-subcortical	5 (50%)	9 (90%)	.57
Cerebral cortex	0	3 (30%)	.21
Size (≥2 cm)	6 (60%)	8 (80%)	.63
T1 hypointensity	7 (70%)	6 (60%)	1
Expansion	7 (70%)	8 (80%)	1
Contrast enhancement	8 (80%)	5 (50%)	.35
Enhancement pattern			
Patchy, nodular	5	2	
Diffuse	0	3	
Leptomeningeal	3	0	
Ring-incomplete ring	1	1	
Perivenular	1	0	
Restricted diffusion	2 ^b	3 (30%)	1

^a Significant.^b DWI was not performed in 2 children with NMOSD.

thalamic and internal capsule involvement were common in patients with ADEM (Fig 2) and demonstrated a significant difference between these 2 groups ($P = .020$ and $P = .033$, respectively). The post hoc power values of 82% and 80% were calculated for the thalamic and internal capsule variables, respectively.

There was no significant difference in terms of extent, expansion, T1 hypointensity, contrast enhancement/pattern, and diffusion characteristics. Contrast enhancement was frequent in patients with NMOSD ($n = 8$), with the most common pattern described as cloudlike parenchymal enhancement ($n = 5$). We also detected regional cerebral or cerebellar leptomeningeal enhancement (Fig 1D–F) in patients with NMOSD ($n = 3$) contrary to the ADEM group ($P = .23$). There was no specific type of enhancement in patients with ADEM; most of the contrast-enhanced lesions showed mild diffuse enhancement ($n = 3$). Restricted diffusion was a rare finding in patients with both NMOSD ($n = 2$) and ADEM ($n = 3$).

DISCUSSION

The most recent consensus criteria for the diagnosis of NMOSD make special mention of the difficulty in distinguishing pediatric-onset NMOSD from ADEM.⁴ Pediatric ADEM may also present with longitudinally extensive transverse myelitis similar to NMOSD; therefore, myelitis is not a reliable predictor of NMOSD in chil-

dren.^{4,20} Further complicating the issue, brain lesions are more frequent in children compared with adult-onset NMOSD.^{12–14,21,22} Imaging findings that can help distinguish these rare neuroimmunologic diseases may help to confirm a diagnosis in children. Accordingly, in this study, we aimed to find differences in brain MR imaging features that could distinguish pediatric-onset NMOSD from its primary mimicker, ADEM.

Pediatric-onset NMOSD–related brain involvement, similar to adult-onset disease, has been characterized by large (>2 cm) subcortical white matter lesions and lesions within the areas of high AQP4 expression such as periependymal areas of the fourth and third ventricles.^{12,14} Our results were similar to those of previous studies in regard to the high frequency of confluent lesions in the cerebral subcortical white matter and brain stem, though periventricular involvement was not distinctive. The periventricular areas of the fourth ventricle rather seemed to be secondarily involved by extension of confluent brain stem lesions. The bandlike circumventricular lesions with or without pencil-thin ependymal enhancement, which are highly suggestive of an immune-mediated reaction against ependymal linings, were not detected. Therefore, periventricular involvement around the fourth ventricle was not specific enough to be distinguished from periventricular extension of large, confluent brain stem lesions frequently observed in the ADEM cohort. This finding along with the lack of previously described periependymal diencephalic lesions could be partially explained by a low anti-AQP4 seropositivity ratio in the NMOSD cohort. Also, this pattern of diencephalic involvement was not a common MR imaging finding, even in the largest study conducted on children with anti-AQP4 antibodies,¹² and its absence may be due to the small number of cases in our study.

We have found that thalamic and internal capsule involvement could differentiate pediatric-onset NMOSD from ADEM. Thalamic involvement was infrequent and limited to a nonspecific lesion in 1 patient with NMOSD. This result was similar to those in the previous cohorts of pediatric-onset NMOSD, which noted frequencies of thalamic lesions ranging from none to 13%.^{12,13,18,20} On the other hand, thalamic involvement in the ADEM cohort was frequent and characteristic, with mostly asymmetric, large, and poorly marginated lesions as previously reported.²³ The consistency of our findings with previous reports allowed us to postulate that thalamic lesion location could favor a diagnosis of ADEM over pediatric-onset NMOSD.

Another lesion location that resulted in a significant difference between these disease entities was the posterior limb of the internal capsule. We did not detect any posterior limb of the internal capsule lesion in the NMOSD cohort, contrary to ADEM. Prior pediatric-onset NMOSD cohorts did not specify involvement of the internal capsule; therefore, a correlation with the current study is not possible. However, previous reports of adult-onset NMOSD showed varying frequencies of corticospinal tract involvement from 3% to 44%.^{5,7,10} The inconsistency of our findings with adult-onset NMOSD cohorts may reflect differences in disease mechanisms between children and adults. The statistical effects of small cohort size may also be responsible for this result. Re-evaluation with larger comparative cohorts is needed for validation.

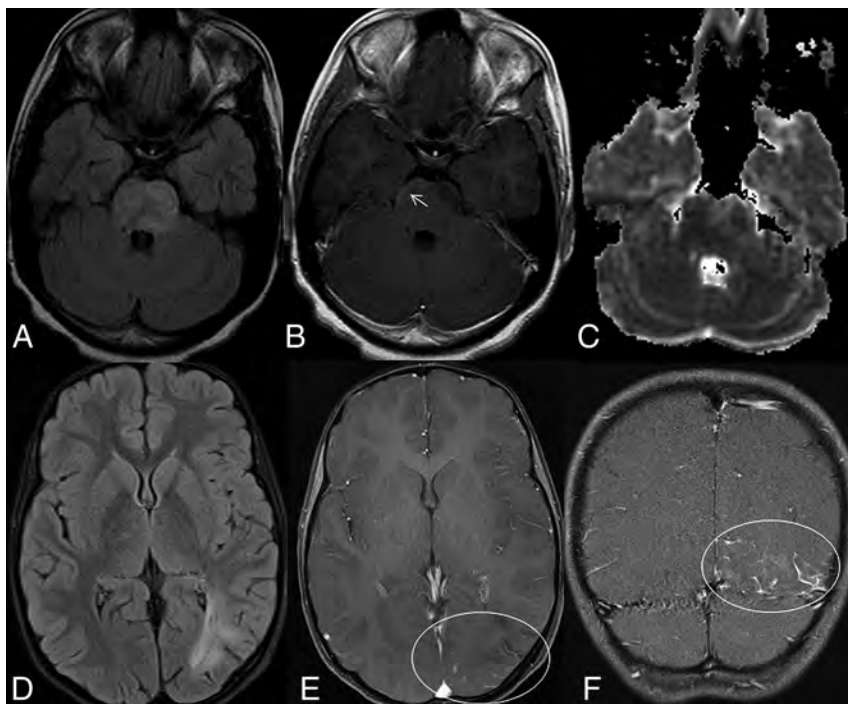


FIG 1. MR images of 2 patients in the NMOSD group. The axial FLAIR image (A) of an 11-year-old female patient shows a minimally expansile, large, hyperintense lesion involving the pons. The postcontrast T1-weighted image (B) reveals inconspicuous subpial enhancement in the lesion (arrow). The patchy areas of restricted diffusion can be seen on the DWI (C). The axial FLAIR image (D) of another patient shows extensive white matter lesions in the left occipital lobe. The axial (E) and the coronal (F) post-contrast T1-weighted images reveal accompanying leptomeningeal enhancement (circles).

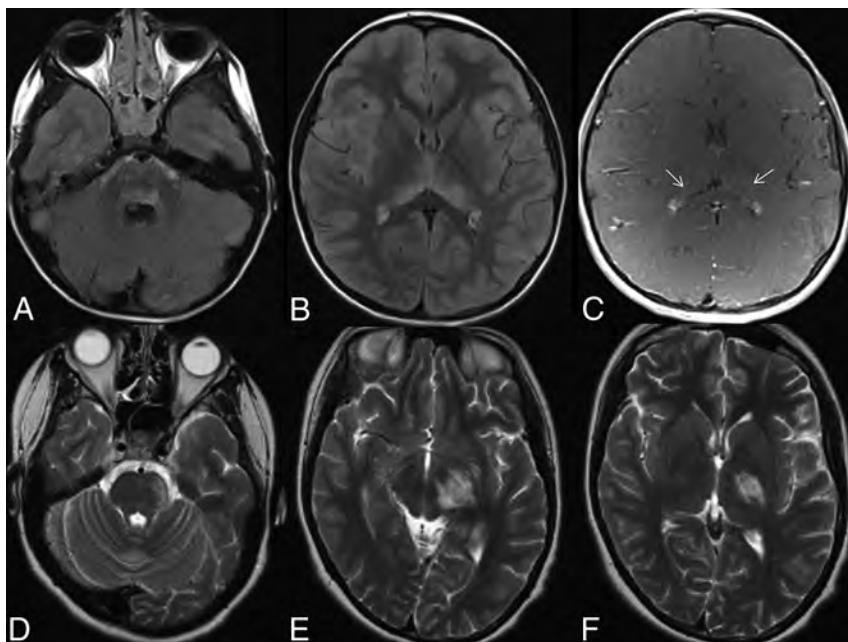


FIG 2. MR images of 2 patients in the ADEM group. The axial FLAIR images (A and B) of a 5-year-old male patient show confluent pontine and symmetric thalamic lesions, respectively. The postcontrast T1-weighted image (C) reveals inconspicuous enhancement in the thalamic lesions (arrows). The axial T2-weighted images (D–F) of a 16-year-old female patient show extensive lesions involving the pons, cerebral peduncle, and posterior limb of the internal capsule along the course of left corticospinal tract.

Remarkably, no other MR imaging findings including lesion expansion, T1 hypointensity, contrast enhancement/pattern, and diffusion characteristics could be identified to differentiate

pediatric-onset NMOSD from ADEM. Expansion and T1 hypointensity are common features in the acute attack of demyelinating/inflammatory entities as contrast enhancement.^{23,24} Different patterns of contrast enhancement have been identified in NMOSD, such as cloudlike parenchymal, pencil-thin ependymal, leptomeningeal, or perivascular enhancement.^{24–28} Among these, ependymal and leptomeningeal enhancement was found significantly more frequently in patients with NMOSD than in those with MS and was suggested as a characteristic feature in NMOSD.²⁷ In our study, we found similar results regarding leptomeningeal enhancement; it was seen in 3 patients (37.5%) with NMOSD and was not detected in patients with ADEM ($P = .23$). Although differences between the 2 entities were not statistically significant, considering the previous remarks on leptomeningeal enhancement in NMOSD and the possible statistical effects of our small-sized cohorts together, we hypothesized that this enhancement pattern could favor the diagnosis of NMOSD over ADEM. Future investigations with larger comparative cohorts are required to confirm this hypothesis.

Two patients with leptomeningeal enhancement tested negative for anti-AQP4 antibodies. This finding is difficult to explain by the anti-AQP4 antibody-mediated immune response alone, which was the previously proposed mechanism for leptomeningeal enhancement. Fluctuating anti-AQP4 antibody titers, relatively lower antibody titers that are undetectable by serum assays, or varied AQP4 expression could be responsible for leptomeningeal enhancement in these seronegative patients, or perhaps some other underlying pathophysiologic mechanisms could exist. Although the patchy or so-called cloudlike enhancement was frequent in the NMOSD group, it was not discriminative and was also seen in patients with ADEM.

There are only a few case series in the literature defining diffusion characteristics of brain lesions in NMOSD.^{16,19,29} Brain lesions in those series were characterized by facilitated diffusion, which was attributed to vasogenic edema associated with acute inflammation. We present 2 NMOSD cases having brain lesions with patchy areas of restricted diffusion,

different from previous data. Restricted diffusion in the affected regions may be due to swelling of myelin sheaths, reversible vascular compromise, or intense cell infiltration due to acute inflammatory reaction. Similar to findings in a previous report,³⁰ restricted diffusion in the brain lesions was not frequent in our ADEM cohort, either. All these findings suggest that restricted diffusion could infrequently associate brain lesions in both pediatric-onset NMOSD and patients with ADEM and could not help in differentiating these 2 entities.

As the main limitation, our comparative cohort comprised a relatively small number of patients in each group. Therefore, future studies with larger sizes are needed to test the validity of the identified MR imaging discriminators and to further investigate the role of leptomeningeal enhancement in the differentiation of pediatric-onset NMOSD from ADEM.

Another limitation is that not all patients were tested for the anti-myelin oligodendrocyte glycoprotein antibody because testing for this antibody was not widely available at the time of the study design. Anti-myelin oligodendrocyte glycoprotein antibody has been found in a subgroup of anti AQP4 antibody negative NMOSD patients including children. Although anti-myelin oligodendrocyte glycoprotein antibody disease emerged as a distinct entity with more favorable clinical outcomes recently,³¹ it is not specified in the NMOSD diagnostic criteria yet. Larger cohorts with anti-myelin oligodendrocyte glycoprotein antibody testing are needed to characterize brain MR imaging findings distinctive of this group of patients in future studies.

Other limitations were due to retrospective design of the study. MR images were obtained from scanners with different magnet strengths, there were differences in imaging parameters including slice thickness, and DWI was not performed in 2 children with NMOSD. All of these could affect the sensitivity of image evaluation and comparisons.

CONCLUSIONS

Although there is a considerable overlap in brain MR imaging findings, the present study suggests that thalamic or internal capsule involvement could be used to differentiate pediatric-onset NMOSD from ADEM. Prospective studies with larger numbers of patients are required for validation of these findings.

Disclosures: Thierry A.G.M. Huisman—UNRELATED: Board Membership: *American Journal of Neuroradiology* Senior Editor. Izlem Izbudak—UNRELATED: Consultancy: Alexion Pharmaceuticals, Comments: reviewing MRI spine examinations of patients with neuromyelitis optica for adjudication about recurrence findings on MRI as part of an NMO trial; Grants/Grants Pending: Biogen, Comments: MS PATHS study site.* Sara Salama—RELATED: Grant: Ministry of Higher Education, Egypt, Comments: The Joint Supervision Scholarship number is JS-3725. Michael Levy—UNRELATED: Consultancy: Alexion Pharmaceuticals, Quest Diagnostics; Expert Testimony: various law firms; Grants/Grants Pending: National Institutes of Health, National MS Society.* *Money paid to the institution.

REFERENCES

- Wingerchuk DM, Hogancamp WF, O'Brien PC, et al. **The clinical course of neuromyelitis optica (Devic's syndrome).** *Neurology* 1999; 53:1107–14 CrossRef Medline
- Wingerchuk DM, Lennon VA, Pittock SJ, et al. **Revised diagnostic criteria for neuromyelitis optica.** *Neurology* 2006;66:1485–89 CrossRef Medline
- Wingerchuk DM, Lennon VA, Lucchinetti CF, et al. **The spectrum of neuromyelitis optica.** *Lancet Neurol* 2007;6:805–15 CrossRef Medline
- Wingerchuk DM, Banwell B, Bennett JL, et al; International Panel for NMO Diagnosis. **International consensus diagnostic criteria for neuromyelitis optica spectrum disorders.** *Neurology* 2015;85:177–89 CrossRef Medline
- Pittock SJ, Lennon VA, Krecke K, et al. **Brain abnormalities in neuromyelitis optica.** *Arch Neurol* 2006;63:390–96 CrossRef Medline
- Pittock SJ, Weinshenker BG, Lucchinetti CF, et al. **Neuromyelitis optica brain lesions localized at sites of high aquaporin 4 expression.** *Arch Neurol* 2006;63:964–68 CrossRef Medline
- Kim W, Park MS, Lee SH, et al. **Characteristic brain magnetic resonance imaging abnormalities in central nervous system aquaporin-4 autoimmunity.** *Mult Scler* 2010;16:1229–36 CrossRef Medline
- Kim HJ, Paul F, Lana-Peixoto MA, et al; Guthy-Jackson Charitable Foundation NMO International Clinical Consortium & Biorepository. **MRI characteristics of neuromyelitis optica spectrum disorder: an international update.** *Neurology* 2015;84:1165–73 CrossRef Medline
- Katz Sand I. **Neuromyelitis optica spectrum disorders.** *Continuum (Minneapolis)* 2016;22:864–96 CrossRef Medline
- Kim JE, Kim SM, Ahn SW, et al. **Brain abnormalities in neuromyelitis optica.** *J Neurol Sci* 2011;302:43–48 CrossRef Medline
- Tenembaum S, Chitnis T, Nakashima I, et al. **Neuromyelitis optica spectrum disorders in children and adolescents.** *Neurology* 2016;87: S59–66 CrossRef Medline
- McKeon A, Lennon VA, Lotze T, et al. **CNS aquaporin-4 autoimmunity in children.** *Neurology* 2008;71:93–100 CrossRef Medline
- Absoud M, Lim MJ, Appleton R, et al. **Paediatric neuromyelitis optica: clinical, MRI of the brain and prognostic features.** *J Neurol Neurosurg Psychiatry* 2015;86:470–72 CrossRef Medline
- Collongues N, Marignier R, Zéphir H, et al. **Long-term follow-up of neuromyelitis optica with a pediatric onset.** *Neurology* 2010;75: 1084–88 CrossRef Medline
- Rostasy K, Bajer-Kornek B, Venkateswaran S, et al. **Differential diagnosis and evaluation in pediatric inflammatory demyelinating disorders.** *Neurology* 2016;87:S28–37 CrossRef Medline
- Kim W, Kim SH, Lee SH, et al. **Brain abnormalities as an initial manifestation of neuromyelitis optica spectrum disorder.** *Mult Scler* 2011;17:1107–12 CrossRef Medline
- Wingerchuk DM, Weinshenker BG. **Neuromyelitis optica.** *Curr Treat Options Neurol* 2008;10:55–66 CrossRef Medline
- Lotze TE, Northrop JL, Hutton GJ, et al. **Spectrum of pediatric neuromyelitis optica.** *Pediatrics* 2008;122:e1039–47 CrossRef Medline
- Matsushita T, Isobe N, Matsuoka T, et al. **Extensive vasogenic edema of anti-aquaporin-4 antibody-related brain lesions.** *Mult Scler* 2009; 15:1113–17 CrossRef Medline
- Banwell B, Tenembaum S, Lennon VA, et al. **Neuromyelitis optica-IgG in childhood inflammatory demyelinating CNS disorders.** *Neurology* 2008;70:344–52 CrossRef Medline
- Kremer L, Mealy M, Jacob A, et al. **Brainstem manifestations in neuromyelitis optica: a multicenter study of 258 patients.** *Mult Scler* 2014;20:843–47 CrossRef Medline
- Peña JA, Ravelo ME, Mora-La Cruz E, et al. **NMO in pediatric patients: brain involvement and clinical expression.** *Arq Neuropsiquiatr* 2011;69:34–38 CrossRef Medline
- Marin SE, Callen DJ. **The magnetic resonance imaging appearance of monophasic acute disseminated encephalomyelitis: an update post application of the 2007 consensus criteria.** *Neuroimaging Clin N Am* 2013;23:245–66 CrossRef Medline
- Orman G, Wang KY, Pekcevik Y, et al. **Enhancing brain lesions during acute optic neuritis and/or longitudinally extensive transverse myelitis may portend a higher relapse rate in neuromyelitis optica spectrum disorders.** *AJNR Am J Neuroradiol* 2017; 38:949–53 CrossRef Medline
- Ito S, Mori M, Makino T, et al. **“Cloud-like enhancement” is a magnetic resonance imaging abnormality specific to neuromyelitis optica.** *Ann Neurol* 2009;66:425–28 CrossRef Medline
- Banker P, Sonni S, Kister I, et al. **Pencil-thin ependymal enhance-**

- ment in neuromyelitis optica spectrum disorders. *Mult Scler* 2012; 18:1050–53 CrossRef Medline
27. Long Y, Chen M, Zhang B, et al. **Brain gadolinium enhancement along the ventricular and leptomeningeal regions in patients with aquaporin-4 antibodies in cerebral spinal fluid.** *J Neuroimmunol* 2014;269:62–67 CrossRef Medline
28. Pekcevik Y, Izbudak I. **Perivascular enhancement in a patient with neuromyelitis optica spectrum disease during an optic neuritis attack.** *J Neuroimaging* 2015;25:686–87 CrossRef Medline
29. Saiki S, Ueno Y, Moritani T, et al. **Extensive hemispheric lesions with radiological evidence of blood-brain barrier integrity in a patient with neuromyelitis optica.** *J Neurol Sci* 2009;284:217–19 CrossRef Medline
30. Zuccoli G, Panigrahy A, Sreedher G, et al. **Vasogenic edema characterizes pediatric acute disseminated encephalomyelitis.** *Neuroradiology* 2014;56:679–84 CrossRef Medline
31. Narayan R, Simpson A, Fritsche K, et al. **MOG antibody disease: a review of MOG antibody seropositive neuromyelitis optica spectrum disorder.** *Mult Scler Relat Disord* 2018;25:66–72 CrossRef Medline

CT and Multimodal MR Imaging Features of Embryonal Tumors with Multilayered Rosettes in Children

V. Dangouloff-Ros, A. Tauziède-Espariat, C.-J. Roux, R. Levy, D. Grévent, F. Brunelle, A. Gareton, S. Puget, K. Beccaria, T. Blauwblomme, J. Grill, C. Dufour, P. Varlet, and N. Boddarta



ABSTRACT

BACKGROUND AND PURPOSE: Embryonal tumors with multilayered rosettes, C19MC-altered, are brain tumors occurring in young children, which were clearly defined in the 2016 World Health Organization classification of central nervous system neoplasms. Our objective was to describe the multimodal imaging characteristics of this new entity.

MATERIALS AND METHODS: We performed a retrospective monocentric review of embryonal brain tumors and looked for embryonal tumors with multilayered rosettes with confirmed C19MC alteration. We gathered morphologic imaging data, as well as DWI and PWI data (using arterial spin-labeling and DSC).

RESULTS: We included 16 patients with a median age of 2 years 8 months. Tumors were both supratentorial (56%, 9/16) and infratentorial (44%, 7/16). Tumors were large (median diameter, 59 mm; interquartile range, 48–71 mm), with absent (75%, 12/16) or minimal (25%, 4/16) peritumoral edema. Enhancement was absent (20%, 3/15) or weak (73%, 11/15), whereas intratumoral macrovessels were frequently seen (94%, 15/16) and calcifications were present in 67% (10/15). Diffusion was always restricted, with a minimal ADC of 520 mm²/s (interquartile range, 495–540 mm²/s). Cerebral blood flow using arterial spin-labeling was low, with a maximal CBF of 43 mL/min/100 g (interquartile range, 33–55 mL/min/100 g 5). When available (3 patients), relative cerebral blood volume using DSC was high (range, 3.5–5.8).

CONCLUSIONS: Embryonal tumors with multilayered rosettes, C19MC-altered, have characteristic imaging features that could help in the diagnosis of this rare tumor in young children.

ABBREVIATIONS: ASL = arterial spin-labeling; ETANTR = embryonal tumors with abundant neuropil and true rosettes; ETMR = embryonal tumors with multilayered rosettes; IQR = interquartile range

The classification of embryonal brain tumors has been redefined in the 2016 World Health Organization classification of central nervous system neoplasms,¹ with the disappearance of the term “primitive neuroectodermal tumors.” Among the newly de-

scribed entities, embryonal tumors with multilayered rosettes, C19MC-altered, were defined by amplification or gain of the C19MC region on chromosome 19 (19q13.42).^{2–4} These tumors include the previously known embryonal tumors with abundant neuropil and true rosettes (ETANTR, also referred to as embryonal tumors with multilayered rosettes [ETMR]), ependymoblastoma, and, in some cases, medulloepithelioma.^{2,4} They can be histopathologically suspected by *LIN28A*-positive immunostaining, but full confirmation warrants molecular confirmation of the C19MC alteration.

Because this type of tumor is rare and was only recently clearly isolated, reports of confirmed C19MC-altered tumors are scarce and most studies did not report detailed imaging data,^{2–14} except for the recent cohort of 7 patients reported by Wang et al.¹⁵ Nowak et al^{16–18} reported imaging data from 22 patients with ependymoblastoma and *LIN28A* immunostaining, but molecular confirmation was absent because these articles were published before the 2016 World Health Organization classification. These reports described ETMRs as large tumors with absent-to-moderate enhancement after contrast media injection and, when DWI

Received October 24, 2018; accepted after revision January 28, 2019.

From the Departments of Pediatric Radiology (V.D.-R., C.-J.R., R.L., D.G., F.B., N.B.) and Pediatric Neurosurgery (S.P., K.B., T.B.), Hôpital Necker Enfants Malades, Paris, France; University René Descartes (V.D.-R., A.T.-E., C.-J.R., R.L., D.G., F.B., S.P., K.B., T.B. P.V., N.B.), Pôle de Recherche et d'Enseignement Supérieur Sorbonne Paris Cité, Paris, France; French National Institute of Health and Medical Research U1000 (V.D.-R., C.-J.R., R.L., D.G., F.B., N.B.), Paris, France; Institut Imagine 1163 (V.D.-R., C.-J.R., R.L., D.G., F.B., N.B.), Paris, France; Department of Neuropathology (A.T.-E., A.G., P.V.), Centre Hospitalier Sainte Anne, Paris, France; and Department of Pediatric and Adolescent Oncology (J.G., C.D.), Gustave Roussy Institute, Villejuif, France.

Paper previously presented at: Journées Francophones de Radiologie, October 12–15, 2018, Paris, France.

Please address correspondence to Volodia Dangouloff-Ros, MD, MSc, Assistance-Publique Hôpitaux de Paris, Hôpital Necker-Enfants Malades, Department of Pediatric Radiology, 149 rue de Sèvres, 75015 Paris, France; e-mail: volodia.dangouloff-ros@aphp.fr; @Volodia_DR



Indicates article with supplemental on-line tables.



Indicates article with supplemental on-line photos.

<http://dx.doi.org/10.3174/ajnr.A6001>

images were available, a hypersignal on DWI. Nevertheless, because these tumors were rare and gathered during a long time, PWI data and detailed DWI data (such as ADC) were missing.

Our aim was to assess multimodal imaging characteristics of ETMR, C19MC-altered, through a retrospective review of molecularly confirmed cases, including DWI and PWI data.

MATERIALS AND METHODS

Patients

We performed a retrospective review from 2005 to 2018 of the prospective data base of pediatric brain tumors from the Necker Enfants Malades Hospital, Paris, France, as well as a review of the pathology data base. We gathered all tumors previously considered as ependyoblastoma, medulloepithelioma, embryonal tumors with abundant neuropils and true rosettes, and ETMR. They were histopathologically confirmed by an experienced neuropathologist (A.T.-E.) and molecularly confirmed by the presence of a gain or an amplification of C19MC by the CC19MC/TPM4 FISH Probe kit, ref CT-PAC033 (CytoTest; <https://www.cytotest.com/enn/index.asp>). When MR images were available, patients were included in the study.

Ethics committee approval was obtained to study multimodal imaging of children's brain tumors. Agreement of patients was prospectively obtained to perform molecular testing of tumor samples and to use medical images for research purposes.

Imaging

MR imaging was performed at our institution using a Signa HDxt 1.5 T system (GE Healthcare, Milwaukee, Wisconsin) and a 12-channel head-neck-spine coil. Acquired sequences were the following: 3D-T1-weighted, 3D-T2-weighted, FLAIR, DTI, pseudo-continuous 3D-arterial spin-labeling (ASL), DSC if available, and 3D-T1-weighted imaging after contrast media injection. If available, postgadolinium T1-weighted spine imaging was also reviewed. Assessment of calcifications was performed using precontrast CT when available and T2*-weighted sequences (gradient-echo T2 or B₀ of the DWI sequence) otherwise.

Acquisition parameters for the ASL sequence were as follows: TR/TE, 4428/10.5 ms; postlabeling delay, 1025 ms; 80 axial partitions; FOV, 240 × 240 mm; slice thickness, 4 mm; acquisition matrix, 8 spiral arms in each 3D partition with 512 points per arm; flip angle, 155°; acquisition time, 4 minutes 17 seconds. Acquisition parameters for the DTI sequence were the following: 24 directions, b-value = 1000 s/mm², TR = 8000 ms, TE = minimum according to the specific absorption rate, slice thickness = 3 mm, FOV = 240 × 240 mm, matrix size = 512 × 512.

Two senior neuroradiologists (V.D.-R. and R.L.) analyzed MRIs in consensus. Images were qualitatively analyzed using a PACS.

DTI data were analyzed using an Advantage Workstation (Version 4.7; GE Healthcare) to obtain isotropic diffusion maps and average diffusion coefficient maps. ADC, CBF, relative CBF using ASL, and relative CBV using DSC were measured within the whole tumor and within the most diffusion-restricted area or the most perfused area (ROI size, 50 mm²). To obtain relative perfusion values, we used an ROI within the temporal cortex for ASL and a ROI in normal-appearing white matter for DSC.

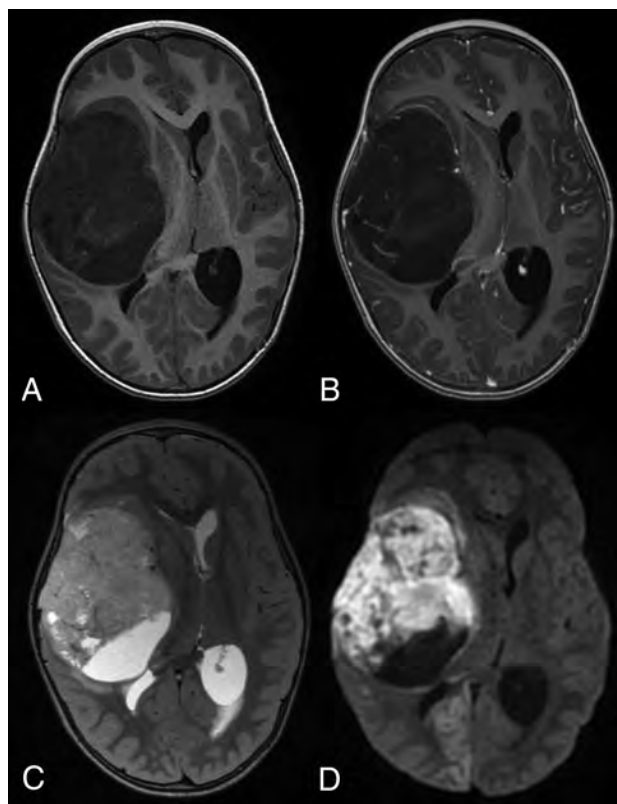


FIG 1. Brain imaging of patient 6. Axial plane MR images show a large heterogeneous right temporal tumor, with mass effect and midline shift. The tumor displays hypointensity on the T1-weighted image (A), hyperintensity on the T2-weighted image (C), and weak enhancement after contrast media injection (B). An intratumoral vessel is seen (B). Diffusion signal is high (D) with low ADC. Diffusion is also restricted in the right occipital lobe (D) because of an ischemic injury caused by compression of the posterior cerebral artery.

Statistical Analysis

Data description was performed using proportions for categorical data and median and interquartile range (IQR) for quantitative data (ADC, CBF, and relative CBF using ASL, relative CBV and relative CBF using DSC).

RESULTS

Patients

Among 2568 patients in the data base, 22 patients with suspected ETMR were histopathologically reviewed. Sixteen patients (12 girls, 4 boys) with ETMR, C19MC-altered, were included, with a median age of 2 years 8 months (range, 1 year 2 months to 11 years 10 months).

Imaging

Findings are reported in On-line Table 1 and On-line Table 2.

Both MR imaging and CT scans were available for 9/16 patients; 6/16 had only MR images, whereas 1/16 had only CT images (patient 14, who died within 1 day of her admission in the hospital). DWI with ADC was available for 13/16 patients; ASL, for 8/16 patients; and DSC, for 3/16 patients. Spinal imaging was available for 7/16 patients.

Tumors were always intra-axial, supratentorial in 9 cases (within hemispheres with variable involvement of the basal gan-

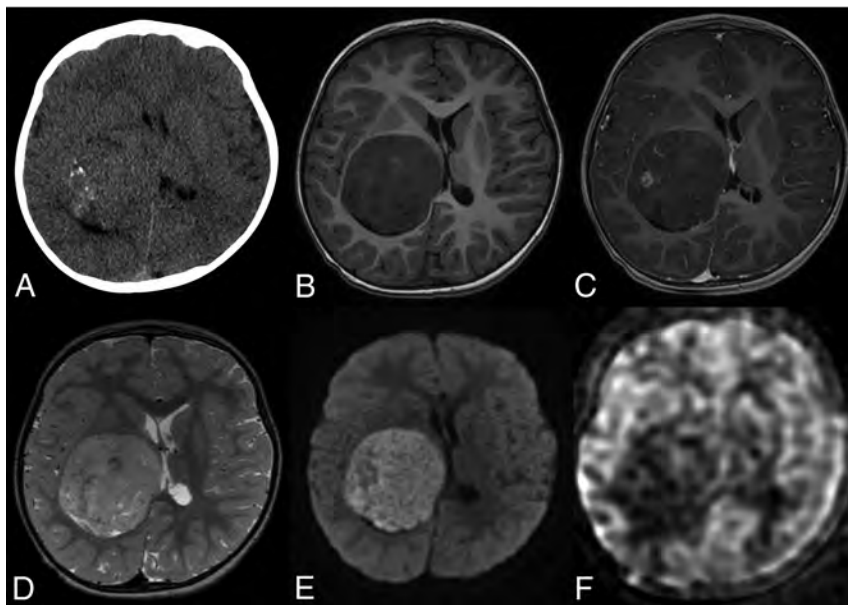


FIG 2. Brain imaging of patient 11. Axial plane image on CT (A) shows a right thalamic mass with microcalcifications. The tumor displays hypointensity on the T1-weighted image (B), hyperintensity on the T2-weighted image (D), and weak nodular enhancement after contrast media injection (C). An intratumoral vessel is seen (C). Diffusion signal is high (E) with low ADC. Cerebral blood flow (F) is low (maximum, 46 mL/min/100 g) within the tumor.

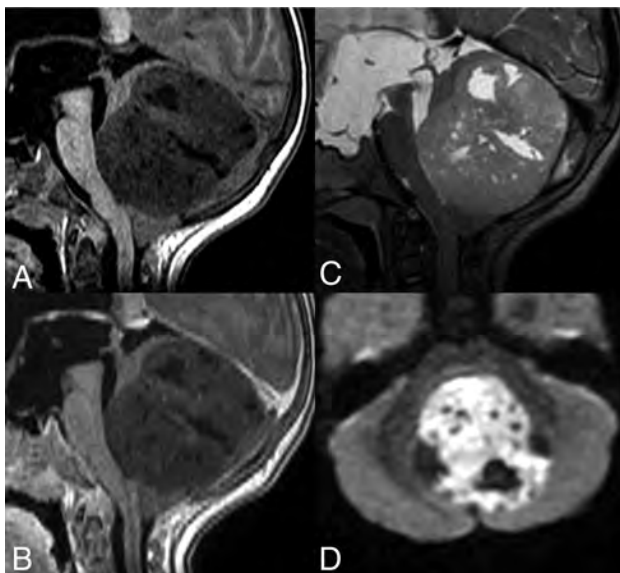


FIG 3. Brain imaging of patient 3. Sagittal plane (A–C) MR images show a large midline vermian tumor, with mass effect on the fourth ventricle causing hydrocephalus. The tumor displays hypointensity on the T1-weighted image (A), hyperintensity on the T2-weighted image (C), and no enhancement after contrast media injection (B). Diffusion signal is high (D) with low ADC.

glia) (Figs 1 and 2) and infratentorial in 7 cases (2 lateralized within the tentorial incisura, equally supra- and infratentorial, posterior and lateral to the cerebral peduncle, with mass effect on the cerebral peduncle [On-line Fig 1]; 2 in the cerebellar vermis [Fig 3]; 1 in the fourth ventricle; and 2 within the brain stem [Fig 4 and On-line Fig 2]). Their median largest diameter was 59 mm (IQ, 48–71 mm), causing mass effect and frequent brain herniation. Peritumoral edema was rare (4/16) and not very extended when present.

No intracranial dissemination was seen at diagnosis, nor spinal metastasis when spine MR imaging was available.

Calcifications were present in 67% (10/15, Fig 2), and tumor density on CT was variable, though more frequently hyperdense (5/10). Tumors were always hypointense on T1-weighted images and hyperintense on T2-weighted and FLAIR images. Enhancement was weak and heterogeneous, sometimes nodular, except for the older patient (patient 16, 11 years of age) in whom the tumor had high and homogeneous enhancement. All patients except 1 (patient 15, On-line Fig 2) had curvilinear homogeneous enhancement connected to cortical veins, consistent with large intratumoral macroscopic veins (diameter, 1–2.5 mm).

Diffusion was always restricted, with a median minimal ADC measured at 520 mm^2/s (IQR 495–540 mm^2/s) and a median ADC within the whole tumor of 728 mm^2/s (IQR, 611–802 mm^2/s).

CBF using ASL was low, with a median value within the most perfused area of 43 mL/min/100 g (IQR, 33–55 mL/min/100 g) and a median value within the whole tumor of 30 mL/min/100 g (IQR, 24–40 mL/min/100 g). DSC-PWI was performed for only 3 patients (between 2 and 3 years of age) and showed high maximal and mean relative CBV (range, 3.5–5.8, and 1.7–2.7, respectively; On-line Table 2). DSC-derived relative CBF was also high (maximal range and mean range, 2.6–4.4 and 1.1–1.9, respectively).

DISCUSSION

In this cohort, we report the characteristic imaging features of confirmed ETMR, C19MC-altered: large tumors with frequent calcifications, little-to-no edema, absent or weak contrast enhancement, intratumoral veins, restricted diffusion, and low CBF values using ASL.

Fifty-six percent of the tumors were hemispheric with variable basal ganglia involvement. This is slightly lower than previous larger clinical or pathologic cohorts, which reported 70%–76% supratentorial tumors.^{2–4,13,16} The distribution of posterior fossa tumors between the fourth ventricle/cerebellum and brain stem was also reported.^{3,15,16} Most interesting, we found 2 tumors lateralized within the tentorial incisura, equally supra- and infratentorial, posterior and lateral to the cerebral peduncle, with mass effect on the cerebral peduncle, which has rarely been reported.^{19–21} Nevertheless, because previous articles reported few imaging details, these tumors may have been classified as posterior fossa tumors or superior cerebellum vermis tumors. Their anatomic localization was difficult to define because of their large size.

Weak contrast enhancement is quite an original feature for this high-grade neoplasm and supports contrast enhancement not being a criterion for high-grade tumors in children.²² This absent or min-

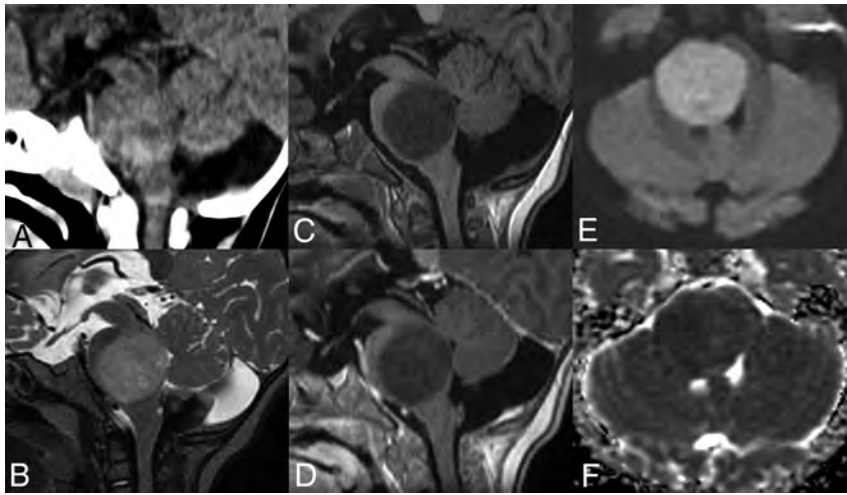


FIG 4. Brain imaging of patient 4. Sagittal plane image on CT (A) shows a pontine isodense mass. The tumor displays hypointensity on the T1-weighted image (C), hyperintensity on the T2-weighted image (B), and no enhancement after contrast media injection (D). Diffusion signal is high (E) with low ADC (F).

imal enhancement was also reported in several cases of confirmed ETMR^{6,9,12,14,15} and in the *LIN28A*-stained ependyoblastoma cohort published by Nowak et al.¹⁶ The only outlier (patient 16) who had high contrast enhancement was clearly atypical because this patient was by far the oldest (11 years of age) and had high CBF. On the other hand, intratumoral large vessels were seen in all patients except 1 (patient 15, who had a mostly cystic tumor with peripheral tissular content). This feature was not detailed in previous reports, except in a few cases reports of histopathologically diagnosed ETANTR.²³⁻²⁶

Diffusion was restricted in all tumors, with a median ADC of 728 mm²/s for the whole tumor and 520 mm²/s for the area of maximum diffusion restriction. Hypersignal on DWI in confirmed ETMR was also previously reported,^{12,15} as well as in the ependyoblastoma cohort of Nowak et al,¹⁶ but no ADC values have been reported yet. This result is in line with the classic diffusion restriction in embryonal tumors in children, formerly known as primitive neuroectodermal tumors.²⁷

CBF using ASL was low (ie, <50 mL/min/100 g) for most patients, with a median maximal CBF of 43 mL/min/100 g. To our knowledge, no previous PWI data were reported. This feature may be surprising for these high-grade neoplasms because high-grade pediatric tumors usually have high CBF using ASL.^{22,28-31} However, this is consistent with the study of Dangouloff-Ros et al²² on the posterior fossa, which reported that tumors with a moderate CBF (25–50 mL/min/100 g) but a weak contrast enhancement were high-grade neoplasms, including embryonal tumors. This CBF/enhancement ratio was not reported in hemispheric tumors, but supratentorial embryonal tumors (former primitive neuroectodermal tumors) were absent in this cohort.

Relative CBV using DSC was available for only 3 patients; it has become less frequently used in our institution after the introduction of the ASL sequence because it requires contrast media injection with high flow, which is difficult to obtain in young children. Relative CBV was high in all 3 cases (range, 3.5–5.8), even if CBF using ASL was as low as in other patients. This finding underlines the different pathophysiologic mechanisms involved in ASL and DSC PWI.³² The presence of calcifications in 2 of these

patients (CT not available for the third patient) may have caused artifacts while using DSC and consequently less consistent results.

These homogeneous imaging characteristics may help to distinguish ETMR from other brain tumors in children between 1 and 4 years of age. Pilocytic astrocytoma is quite easily differentiated because it has no diffusion restriction and strong contrast enhancement.³³ Ependyoma differs by its morphology, T2-weighted high signal, and variable DWI pattern.^{18,33} Most of all, some characteristics may be useful to distinguish ETMR from other embryonal brain tumors (ie, medulloblastoma and atypical teratoid/rhabdoid tumor, which may look like ETMR because they

are aggressive tumors with high cellularity causing diffusion restriction).^{33,34} ETMR localization was different from that of classic medulloblastomas because it was not localized in the fourth ventricle (except in the one 11-year-old outlier patient). When localized in the cerebellar hemispheres (Sonic HedgeHog subgroup), medulloblastomas are different again because this subgroup has high contrast enhancement.³⁴ Contrast uptake of ETMR was low, contrary to reported data concerning atypical teratoid/rhabdoid tumors.³⁵ Furthermore, atypical teratoid/rhabdoid tumors usually have a much more necrotic pattern, with central cysts,³⁵ than that in our ETMR cohort. Finally, medulloblastomas and atypical teratoid/rhabdoid tumors usually have high cerebral blood flow using ASL.²²

Our study has several limitations. DSC was performed in only 3/16 patients, and one should use caution generalizing our relative CBV values. Also, we did not have spectroscopy data within the tumor because spectroscopy was not routinely performed in our institution.

CONCLUSIONS

We report the imaging data of 16 patients with confirmed ETMR, C19MC-altered. Imaging features were characteristic and should help to diagnose these rare tumors in young children between 1 and 4 years of age.

Disclosures: Jacques Grill—UNRELATED: Expert Testimony: Hoffmann-La Roche*; Grants/Grants Pending: Bristol-Myers Squibb, Novartis, Roche.* Pascale Varlet—UNRELATED: Consultancy: Hoffmann-La Roche Novartis*; Grants/ Grants Pending: Boehringer Ingelheim. *Money paid to the institution.

REFERENCES

1. Louis DN, Perry A, Reifenberger G, et al. **The 2016 World Health Organization Classification of Tumors of the Central Nervous System: a summary.** *Acta Neuropathol (Berl)* 2016;131:803–20 CrossRef Medline
2. Korshunov A, Sturm D, Ryzhova M, et al. **Embryonal tumor with abundant neuropil and true rosettes (ETANTR), ependyoblastoma, and medulloepithelioma share molecular similarity and comprise a single clinicopathological entity.** *Acta Neuropathol (Berl)* 2014;128:279–89 CrossRef Medline
3. Korshunov A, Remke M, Gessi M, et al. **Focal genomic amplification at 19q13.42 comprises a powerful diagnostic marker for embryonal**

- tumors with ependymoblastic rosettes. *Acta Neuropathol (Berl)* 2010;120:253–60 CrossRef Medline
4. Spence T, Sin-Chan P, Picard D, et al. **CNS-PNETs with C19MC amplification and/or LIN28 expression comprise a distinct histogenetic diagnostic and therapeutic entity.** *Acta Neuropathol (Berl)* 2014;128:291–303 CrossRef Medline
 5. Ryzhova MV, Zheludkova OG, Ozerov SS, et al. **A new entity in WHO classification of tumors of the central nervous system—embryonic tumor with abundant neuropil and true rosettes: case report and review of literature.** *Zh Vopr Neirokhir Im N N Burdenko* 2011;75:25–33
 6. Woehrer A, Slavc I, Peyrl A, et al. **Embryonal tumor with abundant neuropil and true rosettes (ETANTR) with loss of morphological but retained genetic key features during progression.** *Acta Neuropathol (Berl)* 2011;122:787–90 CrossRef Medline
 7. Kleinschmidt-DeMasters BK, Boylan A, Capocelli K, et al. **Multinodular leptomeningeal metastases from ETANTR contain both small blue cell and maturing neuropil elements.** *Acta Neuropathol (Berl)* 2011;122:783–85 CrossRef Medline
 8. Nobusawa S, Orimo K, Horiguchi K, et al. **Embryonal tumor with abundant neuropil and true rosettes with only one structure suggestive of an ependymoblastic rosette.** *Pathol Int* 2014;64:472–77 CrossRef Medline
 9. Hervey-Jumper SL, Altshuler DB, Wang AC, et al. **The role of CD133+ cells in a recurrent embryonal tumor with abundant neuropil and true rosettes (ETANTR).** *Brain Pathol* 2014;24:45–51 CrossRef Medline
 10. Gessi M, Demir H, Goschzik T, et al. **MET T992I mutation in a case of ependymoblastoma/embryonal tumour with multilayered rosettes.** *J Clin Pathol* 2014;67:1017–18 CrossRef Medline
 11. Antonelli M, Korshunov A, Mastronuzzi A, et al. **Long-term survival in a case of ETANTR with histological features of neuronal maturation after therapy.** *Virchows Arch* 2015;466:603–07 CrossRef Medline
 12. Sato H, Terakawa Y, Tsuyuguchi N, et al. **Embryonal tumor with abundant neuropil and true rosettes in the brainstem: case report.** *J Neurosurg Pediatr* 2015;16:291–95 CrossRef Medline
 13. Horwitz M, Dufour C, Leblond P, et al. **Embryonal tumors with multilayered rosettes in children: the SFCE experience.** *Childs Nerv Syst* 2016;32:299–305 CrossRef Medline
 14. Tariq MU, Ahmad Z, Minhas MK, et al. **Embryonal tumor with multilayered rosettes, C19MC-altered: report of an extremely rare malignant pediatric central nervous system neoplasm.** *SAGE Open Med Case Rep* 2017;5:2050313X17745208 CrossRef Medline
 15. Wang B, Gogia B, Fuller GN, et al. **Embryonal tumor with multilayered rosettes, C19MC-altered: clinical, pathological, and neuroimaging findings.** *J Neuroimaging* 2018;28:483–89 CrossRef Medline
 16. Nowak J, Seidel C, Berg F, et al. **MRI characteristics of ependymoblastoma: results from 22 centrally reviewed cases.** *AJNR Am J Neuroradiol* 2014;35:1996–2001 CrossRef Medline
 17. Nowak J, Seidel C, Pietsch T, et al. **Ependymoblastoma of the brainstem: MRI findings and differential diagnosis.** *Pediatr Blood Cancer* 2014;61:1132–34 CrossRef Medline
 18. Nowak J, Seidel C, Pietsch T, et al. **Systematic comparison of MRI findings in pediatric ependymoblastoma with ependymoma and CNS primitive neuroectodermal tumor not otherwise specified.** *Neuro Oncol* 2015;17:1157–65 CrossRef Medline
 19. Maiti TK, Arimappamagan A, Mahadevan A, et al. **Rare pathologies in the posterior third ventricular region in children: case series and review.** *Pediatr Neurosurg* 2015;50:42–47 CrossRef Medline
 20. Al-Hussaini M, Abuirmeileh N, Swaidan M, et al. **Embryonal tumor with abundant neuropil and true rosettes: a report of three cases of a rare tumor, with an unusual case showing rhabdomyoblastic and melanocytic differentiation.** *Neuropathology* 2011;31:620–25 CrossRef Medline
 21. Ferri Niguez B, Martínez-Lage JF, Almagro M-J, et al. **Embryonal tumor with abundant neuropil and true rosettes (ETANTR): a new distinctive variety of pediatric PNET—a case-based update.** *Childs Nerv Syst* 2010;26:1003–08 CrossRef Medline
 22. Dangouloff-Ros V, Deroulers C, Foissac F, et al. **Arterial spin labeling to predict brain tumor grading in children: correlations between histopathologic vascular density and perfusion MR imaging.** *Radiology* 2016;281:553–66 CrossRef Medline
 23. Dunham C, Sugo E, Tobias V, et al. **Embryonal tumor with abundant neuropil and true rosettes (ETANTR): report of a case with prominent neurocytic differentiation.** *J Neurooncol* 2007;84:91–98 CrossRef Medline
 24. Manjila S, Ray A, Hu Y, et al. **Embryonal tumors with abundant neuropil and true rosettes: 2 illustrative cases and a review of the literature.** *Neurosurg Focus* 2011;30:E2 CrossRef Medline
 25. Adamek D, Sofowora KD, Cwiklinska M, et al. **Embryonal tumor with abundant neuropil and true rosettes: an autopsy case-based update and review of the literature.** *Childs Nerv Syst* 2013;29:849–54 CrossRef Medline
 26. Govindan A, Vp M, Alapatt JP. **Embryonal tumor with multilayered rosettes in a 3-year-old girl: case report.** *Turk Neurosurg* 2017 Jan 8. [Epub ahead of print] CrossRef Medline
 27. Shih RY, Koeller KK. **Embryonal tumors of the central nervous system: from the radiologic pathology archives.** *Radiographics* 2018;38:525–41 CrossRef Medline
 28. Yeom KW, Mitchell LA, Lober RM, et al. **Arterial spin-labeled perfusion of pediatric brain tumors.** *AJNR Am J Neuroradiol* 2014;35:395–401 CrossRef Medline
 29. Kikuchi K, Hiwatashi A, Togao O, et al. **Correlation between arterial spin-labeling perfusion and histopathological vascular density of pediatric intracranial tumors.** *J Neurooncol* 2017;135:561–69 CrossRef Medline
 30. Morana G, Piccardo A, Tortora D, et al. **Grading and outcome prediction of pediatric diffuse astrocytic tumors with diffusion and arterial spin labeling perfusion MRI in comparison with 18F-DOPA PET.** *Eur J Nucl Med Mol Imaging* 2017;44:2084–93 CrossRef Medline
 31. Morana G, Tortora D, Staglianò S, et al. **Pediatric astrocytic tumor grading: comparison between arterial spin labeling and dynamic susceptibility contrast MRI perfusion.** *Neuroradiology* 2018;60:437–46 CrossRef Medline
 32. Vidyasagar R, Abernethy L, Pizer B, et al. **Quantitative measurement of blood flow in paediatric brain tumours: a comparative study of dynamic susceptibility contrast and multi time-point arterial spin labelled MRI.** *Br J Radiol* 2016;89:20150624 CrossRef Medline
 33. Plaza MJ, Borja MJ, Altman N, et al. **Conventional and advanced MRI features of pediatric intracranial tumors: posterior fossa and suprasellar tumors.** *Am J Roentgenol* 2013;200:1115–24 CrossRef Medline
 34. Dangouloff-Ros V, Varlet P, Levy R, et al. **Imaging features of medulloblastoma: conventional imaging, diffusion-weighted imaging, perfusion-weighted imaging, and spectroscopy—from general features to subtypes and characteristics.** *Neurochirurgie* 2018 Aug 28. [Epub ahead of print] CrossRef Medline
 35. Au Yong KJ, Jaremko JL, Jans L, et al. **How specific is the MRI appearance of supratentorial atypical teratoid rhabdoid tumors?** *Pediatr Radiol* 2013;43:347–54 CrossRef Medline

Convolutional Neural Network–Based Automated Segmentation of the Spinal Cord and Contusion Injury: Deep Learning Biomarker Correlates of Motor Impairment in Acute Spinal Cord Injury

D.B. McCoy, S.M. Dupont, C. Gros, J. Cohen-Adad, R.J. Huie, A. Ferguson, X. Duong-Fernandez, L.H. Thomas, V. Singh, J. Narvid, L. Pascual, N. Kyritsis, M.S. Beattie, J.C. Bresnahan, S. Dhall, W. Whetstone, and J.F. Talbott, TRACK-SCI Investigators



ABSTRACT

BACKGROUND AND PURPOSE: Our aim was to use 2D convolutional neural networks for automatic segmentation of the spinal cord and traumatic contusion injury from axial T2-weighted MR imaging in a cohort of patients with acute spinal cord injury.

MATERIALS AND METHODS: Forty-seven patients who underwent 3T MR imaging within 24 hours of spinal cord injury were included. We developed an image-analysis pipeline integrating 2D convolutional neural networks for whole spinal cord and intramedullary spinal cord lesion segmentation. Linear mixed modeling was used to compare test segmentation results between our spinal cord injury convolutional neural network (Brain and Spinal Cord Injury Center segmentation) and current state-of-the-art methods. Volumes of segmented lesions were then used in a linear regression analysis to determine associations with motor scores.

RESULTS: Compared with manual labeling, the average test set Dice coefficient for the Brain and Spinal Cord Injury Center segmentation model was 0.93 for spinal cord segmentation versus 0.80 for PropSeg and 0.90 for DeepSeg (both components of the Spinal Cord Toolbox). Linear mixed modeling showed a significant difference between Brain and Spinal Cord Injury Center segmentation compared with PropSeg ($P < .001$) and DeepSeg ($P < .05$). Brain and Spinal Cord Injury Center segmentation showed significantly better adaptability to damaged areas compared with PropSeg ($P < .001$) and DeepSeg ($P < .02$). The contusion injury volumes based on automated segmentation were significantly associated with motor scores at admission ($P = .002$) and discharge ($P = .009$).

CONCLUSIONS: Brain and Spinal Cord Injury Center segmentation of the spinal cord compares favorably with available segmentation tools in a population with acute spinal cord injury. Volumes of injury derived from automated lesion segmentation with Brain and Spinal Cord Injury Center segmentation correlate with measures of motor impairment in the acute phase. Targeted convolutional neural network training in acute spinal cord injury enhances algorithm performance for this patient population and provides clinically relevant metrics of cord injury.

ABBREVIATIONS: BASICseg = Brain and Spinal Cord Injury Center segmentation; CNN = convolutional neural network; SC = spinal cord; SCI = spinal cord injury; SCT = Spinal Cord Toolbox

The natural history of recovery after spinal cord injury (SCI) is highly variable and often difficult to predict.^{1,2} Early objective neurologic assessment of injury severity in these patients is challenging due to several confounding factors, such as traumatic brain injury, severe pain, intubation, spinal shock, and sedative

medications, among others.^{2,3} Early and accurate classification of patients with SCI as close to the time of injury as possible is imperative for the guidance of triage, acute management, prognostication, and for patient selection in the design of clinical trials in which novel therapies are tested.^{2,3} MR imaging is the criterion standard imaging technique for evaluation of the injured spinal cord (SC) and has been extensively studied for its ability to assess injury severity and predict outcome.^{2,4-6} However, to date, there are mixed results with respect to the accuracy of MR imaging biomarkers for injury prognostication.^{4,5,7-9}

Recent advances in SC imaging analysis have led to the devel-

Received November 9, 2018; accepted after revision February 11, 2019.

From the Departments of Radiology and Biomedical Imaging (D.B.M., S.M.D., J.N., J.F.T.) and Neurological Surgery (R.J.H., A.F., X.D.-F., L.H.T., N.K., M.S.B., J.C.B., S.D., W.W., J.F.T.), Brain and Spinal Injury Center (D.B.M., R.J.H., A.F., X.D.-F., L.H.T., N.K., M.S.B., J.C.B., S.D., W.W.), and Departments of Neurology (V.S.) and Orthopedic Surgery (L.P.), Zuckerberg San Francisco General Hospital, University of California, San Francisco, San Francisco, California; and NeuroPoly Lab (C.G., J.C.-A.), Institute of Biomedical Engineering, Polytechnique Montreal, Montreal, Quebec, Canada.

This work was supported by the Craig H. Neilsen Foundation and the Department of Defense grant SC120259.

Please address correspondence to Jason F. Talbott, MD, PhD, Zuckerberg San Francisco General Hospital, 1001 Potrero Ave, Room 1X57C, San Francisco, CA 94110; e-mail: jason.talbott@ucsf.edu

Indicates open access to non-subscribers at www.ajnr.org

Indicates article with supplemental on-line tables.

Indicates article with supplemental on-line photos.

<http://dx.doi.org/10.3174/ajnr.A6020>

opment of a robust anatomic template and atlas incorporated into an open-source platform referred to as the Spinal Cord Toolbox (SCT; <https://sourceforge.net/projects/spinalcordtoolbox/>).^{10,11} Similar tools have greatly advanced brain image analysis in recent years, offering accurate and less biased methods for analyzing quantitative and semiquantitative multiparametric MR imaging data.^{12,13} Such tools applied to the SC offer great potential for a unique MR imaging biomarker identification.^{11,14,15} SC segmentation is a first step in atlas-based SC analysis.¹⁶ Manual SC segmentation techniques are not conducive to clinical workflow or high-volume batch analysis because they are time-consuming and have interrater variability. Advances in automated SC segmentation algorithms have been made during the past decade, though currently available algorithms have primarily been tested in healthy controls or nontraumatic pathologies.¹⁶⁻¹⁸ The latest generation segmentation algorithms in acute SCI are challenged by coexisting spinal pathology such as canal stenosis, SC compression, and intrinsic SC signal abnormalities, leading to gross segmentation errors. A model specifically targeted to deal with the challenges of the acute blunt SCI population is needed for application of advanced MR imaging analysis tools in traumatic SCI.

Leveraging a robust, prospectively maintained clinical and radiologic data base of patients with acute blunt traumatic SCI as part of the ongoing prospective clinical trial entitled Transforming Research and Clinical Knowledge in Spinal Cord Injury (TRACK-SCI), we present 3 models using 2D convolutional neural networks (CNNs) to segment the SC from T2-weighted axial images of patients with acute SCI. These networks, named Brain and Spinal Cord Injury Center segmentation (BASICseg1-3), are fully automated and use axial image augmentation and a network architecture. Furthermore, we present preliminary data using the same network architecture to automatically segment intramedullary contusion in patients with acute SCI on T2WI. To assess the clinical validity of injury volumes segmented by this network, we correlated the contusion volumes segmented by BASICseg with lower extremity motor scores. Targeted 2D convolutional neural network training with a cohort of patients with acute SCI, in whom whole-cord and contusion-injury segmentation is particularly challenging, enhances the performance of automated spinal cord and contusion injury segmentation for this patient population compared with currently available state-of-the-art algorithms and also provides clinically relevant metrics of cord injury.

MATERIALS AND METHODS

Study Population

The study population included all consenting patients admitted for an acute traumatic SCI at Zuckerberg San Francisco General Hospital between June 2015 and January 2017. This study was in compliance with the Health Insurance Portability and Accountability Act and was approved by the institutional review board for human research. The medical imaging and clinical records included in this study are compiled as part of the TRACK-SCI research trial conducted under the auspices of the Brain and Spinal Cord Injury Center at Zuckerberg San Francisco General Hospital. This prospective study consecutively enrolled all consenting patients

Table 1: Summary of patient demographics and injury

Patient Demographics and Injury Characteristics (N = 47)	
Age (mean) (SD) (yr)	55 (19)
Sex (M/F)	32:15
Time from injury to MRI (mean) (SD) (hr)	5.4 (4.8)
Admission ASIA Grade	
A	10
B	3
C	5
D	21
Unknown ^a	8
Admission lower extremity motor score (mean) (SD)	25 (23)
Discharge lower extremity motor score (mean) (SD)	29 (21)

Note:—ASIA indicates American Spinal Injury Association.

^a We could not perform full formal ASIA grade assessment at admission.

with acute traumatic spinal cord injury at Zuckerberg San Francisco General Hospital between June 2015 and January 2017, with the collection of imaging, acute neurologic examinations, intraoperative and intensive care unit monitoring, and long-term neurologic and functional outcome assessment. Inclusion criteria were the following: 1) blunt acute cervical or thoracic SCI, 2) 18 years of age or older, 3) presurgical cervical or thoracic spine MR imaging performed within 24 hours after injury, and 4) documented motor score assessment and American Spinal Injury Association Impairment Scale score obtained during first hospitalization. Exclusion criteria were the following: 1) penetrating SCI, 2) surgical decompression and/or fusion before MR imaging, 3) MR imaging that was too degraded by motion or other artifacts so that images were nondiagnostic, 4) pre-existing surgical hardware, and 5) incomplete clinical data for the outcome (American Spinal Injury Association Impairment Scale score) or relevant confounders. We identified 56 patients, of whom 47 met all inclusion criteria and were enrolled in the study. More detailed patient demographics and injury characteristics are summarized in Table 1. Penetrating injuries were excluded due to their unique clinical, imaging, and pathophysiologic characteristics.

MR Imaging Acquisition Parameters

All MR imaging studies were performed on a single 3T Magnetom Skyra scanner with software Version E11 (Siemens, Erlangen, Germany). Only the axial and sagittal T2 fast spin-echo sequences from the routine cervical spine trauma protocol were used for image analysis and were performed with the following parameters: axial T2; TR = 3870 ± 400 ms, TE = 96 ± 4 ms, slice thickness = 3 mm, echo-train length = 16, FOV = 240 × 120 mm, nominal in-plane pixel size = 0.47 mm². Additional sequences performed as part of the routine clinical spine MR imaging protocol were not evaluated for this study.

Image Annotation

Images from patients with SCI were divided into training,¹⁹ validation,⁵ and testing¹⁴ groups for analysis. Because our model is a 2D neural network, 1120 axial slices were used in the training set, 200 axial slices were used in the validation set, and 560 axial slices were used in the test set. Two fellowship-trained neuroradiologists (J.F.T. and J.N.) performed image annotation indepen-

dently and then reached consensus together on manual segmentation in FSL (<http://www.fmrib.ox.ac.uk/fsl>) for both the whole SC and areas of intramedullary T2 signal abnormality related to the cord contusion referred to as the SC lesion. Sagittal T2WI was used only to cross-validate axial annotations.

Image Preprocessing

We used the Optic algorithm¹⁸ from the SCT to first detect the SC centerline and create a 26×26 mm square mask around the centerline. No denoising, smoothing, or inhomogeneity or bias correction was applied. All raw images were resampled at 1×1 mm² to be robust to native image resolution. This mask dimension was sufficient to include the entire spinal cord and spinal canal within the FOV for optimal segmentation. The raw images were then cropped using this mask. Images were then resampled to have a pixel size of 0.2 mm² in the axial plane, with no changes made to slice thickness. Because all images had to be of the same dimensions before entering the network for batch-wise processing, this resampling and mask cropping resulted in an image matrix size of 128×128 voxels.

BASICseg-1 Network Architecture

On-line Fig 1 graphically depicts the deep learning architectures for BASICseg-1 and BASICseg-2. These network architectures were used for both whole SC and intramedullary lesion segmentation and are based on the U-net architecture (<https://lmb.informatik.uni-freiburg.de/people/ronneber/u-net/>).²⁰ The U-net architecture for segmentation consists of contracting and expansive paths. The contracting path follows the standard CNN architecture wherein the image is processed into a series of feature maps. This pathway consists of 4 layers, each involving the following: 1) 3×3 zero-padded convolutions followed by a rectified linear unit,²¹ 2) 20% drop-out²² of the previous convolution, 3) 3×3 zero-padded convolutions followed by a rectified linear unit, and 4) 2×2 max pooling operation (<https://www.quora.com/What-is-max-pooling-in-convolutional-neural-networks>) with Stride 2 for downsampling. At each iteration of the contracting layer, the number of feature maps was doubled (first layer: 8 features; second layer: 16 features; third layer: 32 features; fourth layer: 64 features). The fifth layer consisted of the same processes without drop-out (aforementioned processes 1 and 3) creating 128 feature channels. The expansive path consists of 4 layers to rebuild a mask image to match the dimensions of the input image. Upsampling and concatenation processes were followed by two 3×3 upconvolutions using zero-padding, which halves the number of feature channels each followed by rectified linear unit. A 1×1 convolution with sigmoid activation was used in the final layer to map each 8-component feature vector as either SC tissue (value set to 1) or not SC tissue (value set to 0). In total, the network comprises 19 convolutional layers. Stochastic gradient descent was used with a learning rate of $1e-5$ with an Adam optimizer.²³ All hyperparameters were the same for each of the BASICseg architectures. Programming was performed in Python with the TensorFlow framework (<https://www.tensorflow.org/>). Training was performed on 2 GeForce-1080ti GPUs (NVIDIA, Santa Clara, California) with a combined random-access memory of 22G.

BASICseg-2 Network Architecture

To complement the first network architecture, we created a second architecture to study the impact of integrating batch normalization²⁴ between every convolution and rectified linear unit (<https://www.kaggle.com/dansbecker/rectified-linear-units-relu-in-deep-learning-activation>) layer as shown in On-line Fig 1. Batch normalization involves subtracting each value of the feature map from the feature map mean and dividing by the feature map SD, or

$$\hat{x}_i \leftarrow (x_i - \mu_\beta) \div (\sqrt{\sigma_\beta^2 + \epsilon}).$$

This process helps prevent interval covariate shift. With batch normalization, the distribution of each feature map is the same before activation, which leads to better performance and faster convergence.

We removed the drop-out of the feature maps from the contracting path, replaced them with batch normalization layers, and added them in the expanding path. Additionally, we doubled the number of feature maps created at each layer. All other elements of the architecture remained the same. This network was applied to both spine- and lesion-segmentation tasks.

BASICseg-3 Network Architecture and Noise-Adaption Layer

We expected that in areas of SC compression, where there is notable damage and substantially less signal delineation between the SC tissue and adjacent extramedullary tissues, the labeling mask will be imperfect and therefore prone to label noise. To address potentially erroneous labels, we introduced an additional “noise-adaptation layer” into the network between the final feature maps per pixel (in this case, a tensor of $128 \times 128 \times 16$) and the 1×1 convolution-to-sigmoid activation layer (On-line Fig 2).²⁵ Thus, each pixel feature map (1×16) is augmented by a 16×16 weight matrix. This weight matrix can be thought of as an additional Softmax layer (<https://stats.stackexchange.com/questions/79454/softmax-layer-in-a-neural-network>), which modifies the feature vectors for each pixel before compression to $128 \times 128 \times 1$ and calculation of the loss. The weights of this noise layer are estimated as part of the training process to reduce the overall loss of the system. This process is illustrated in On-line Fig 2.

Data Augmentation

To avoid overfitting, we implemented data augmentation of the images using the Keras framework (<https://keras.io/>). We also augmented T2WI and the corresponding masks pair-wise in batches of 32. Additionally, data are augmented by the drop-out after each convolution in the contracting path by randomly removing feature channels during training.

Model Performance and Statistical Analysis

Spine-segmentation and lesion-segmentation performances were evaluated using the Dice coefficient.^{26,27} The Dice coefficient is a measure of overlapping defined as

$$(2|T \cap P| \div |T| + |P|),$$

Where T is the criterion standard segmentation performed by a fellowship-trained neuroradiologist and P is the predicted segmentation of the SC. The proposed segmentation method (BASICseg) was compared with 2 state-of-the-art methods:

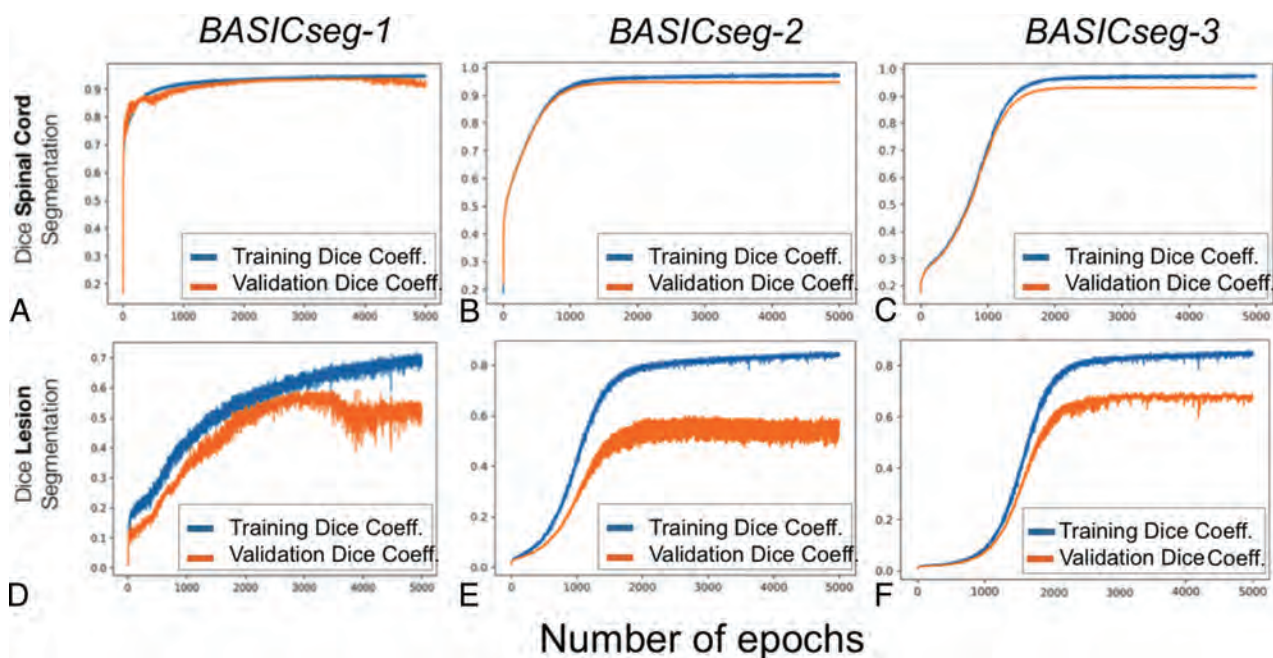


FIG 1. Whole spinal cord and lesion segmentation performance by epoch for BASICseg algorithms for the whole spinal cord (A–C) and the lesion (D–F).

Propseg (https://sourceforge.net/p/spinalcordtoolbox/wiki/sct_propseg/)¹⁶ and Deepseg,²⁸ both included in the SCT.¹¹ Deepseg (sct_deepseg_sc module in SCT; <https://sourceforge.net/p/spinalcordtoolbox/discussion/help/thread/c9972de78a/>) is a recently described deep-learning-based spinal cord segmentation using a succession of 2 CNNs, the first one to detect the SC and the second one to perform the segmentation.²⁸

Dice coefficient results for the 3 evaluated methods (BASICseg, Propseg, and Deepseg) were compared using linear mixed modeling. This initial analysis included all axial images from the test set (including both injured and normal-appearing SC on the T2WI). We restricted the analysis to include injured axial slices only and used the same linear mixed modeling to evaluate differences in segmentation quality based on the Dice coefficient among the evaluated segmentation methods. To determine whether there were relative differences in the models for damaged slice-versus-nondamaged slice segmentation, we used a linear mixed model with an interaction term for model by lesion.

Simple linear regressions were conducted to determine the association between volumes of lesions segmented by the BASICseg and with lower extremity motor scores at day 0 (initial injury) and at a subacute period at the time of patient discharge from the hospital. Data that did not show linearity were appropriately transformed, and R^2 was compared with linear regression; if there was no improvement, a Spearman correlation was used. All statistical analyses were performed in R statistical and computing software (<http://www.r-project.org/>)¹⁹; the significance threshold was $\alpha < .05$. Because our cohort of patients had injuries at a variety of cervical and upper thoracic levels (Table 1), which confounds evaluation of upper extremity motor scores, outcome correlations with injury volume were focused on lower extremity motor scores, which are less likely to be confounded by the level of injury for cervical and upper thoracic spinal cord injuries.

Model Comparison

The 3 models (BASICseg-1 using drop-out, BASICseg-2 using batch normalization, BASICseg-3 using batch normalization and a noise-adaptation layer) were compared for their segmentation performance in the test set data. Models were selected on the basis of the highest validation accuracy, not total completion of epochs; these models were applied to the test sets. For SC segmentation, the model with the highest Dice coefficient was used in statistical analysis to compare with Propseg¹⁶ and Deepseg.²⁸ Propseg is based on iterative propagation of deformable models for SC segmentation, while Deepseg uses a machine learning–based automatic SC segmentation approach with convolutional neural networks. For lesion segmentation, the results for the model with the best performance were modeled with lower extremity motor scores.

RESULTS

Comparison of BASICseg with Existing Models for Traumatic SC Segmentation

The average SC segmentation time for each test patient was 5 seconds. The whole SC Dice coefficient by epoch for each model is plotted and shown in Fig 1A–C. For SC segmentation, BASICseg-1 performed best with a Dice coefficient of 0.93 in the test set versus 0.91 for BASICseg-2 and 0.90 for BASICseg-3. The SC segmentation output at a representative injury level is shown in Fig 2 for 1) the criterion standard manual segmentation, 2) the BASICseg-1 model, 3) Propseg segmentation, and 4) Deepseg segmentation in 5 different subjects from the test set cohort with respective Dice coefficients for each slice. Furthermore, the mean dice coefficients across patients for each segmentation model with corresponding 95% confidence intervals overall and stratified by injury subgroup are presented in On-line Table 1. Linear mixed-effects modeling of Dice coefficients in the test set for segmentation across all axial

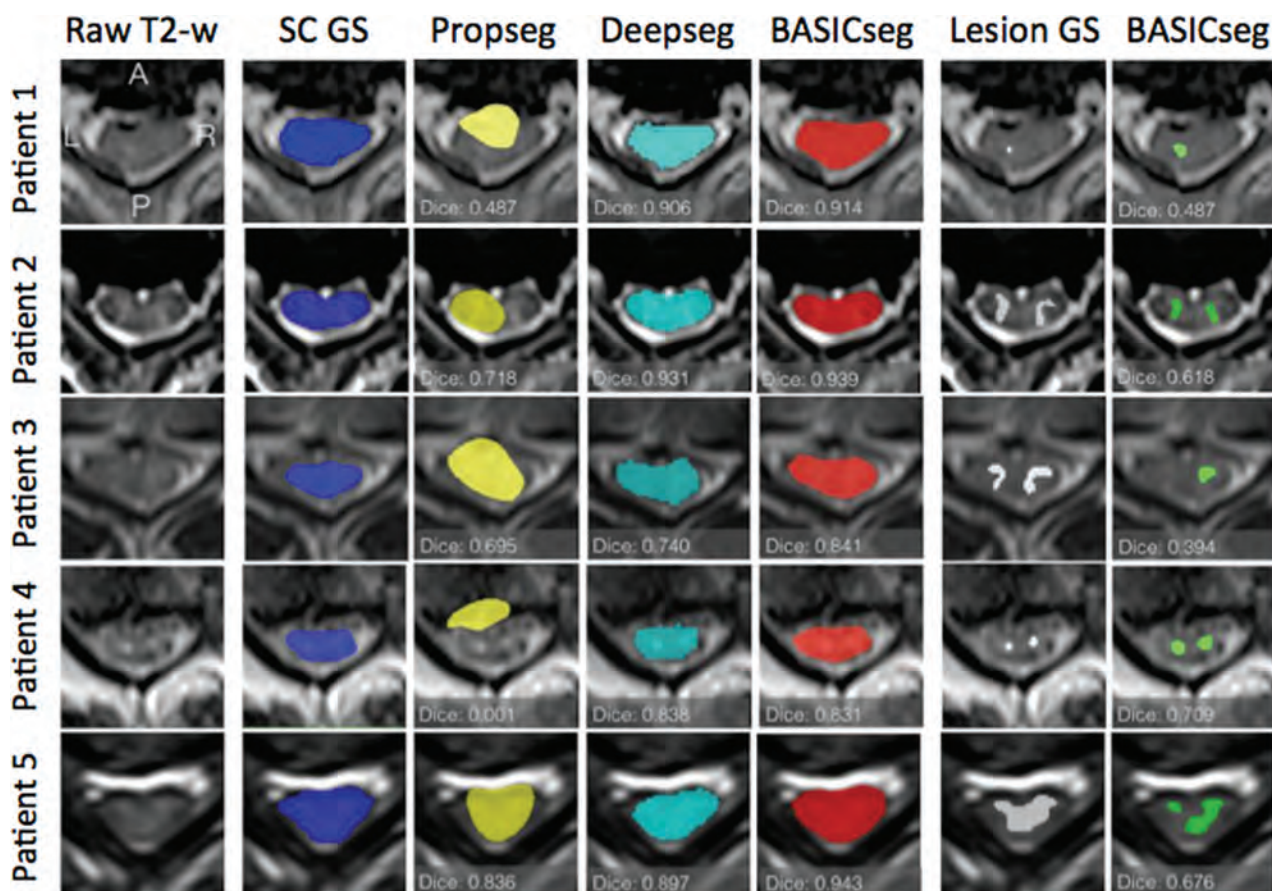


FIG 2. Sample segmentation outputs for the criterion standard manual segmentation and each model for whole spinal cord (columns 2–5) and lesions (columns 6 and 7) in 5 sample patients. The first column contains the sample axial T2WI on which segmentation was performed.

Table 2: Results from linear mixed modeling

Model	Estimate	SE	df	T Value	P Value
Overall spine segmentation					
BASICseg-1 vs Propseg	-0.12166	0.01765	484	-6.893	<.001
BASICseg-1 vs Deepseg	-0.03382	0.01765	484	-1.916	.056
Spine segmentation at levels of lesion					
BASICseg-1 vs Propseg	-0.22028	0.04410	102.62	-4.995	<.001
BASICseg-1 vs Deepseg	-0.10254	0.04347	102.62	-2.359	.020
Spine segmentation at normal-appearing level					
BASICseg-1 vs Propseg	-0.09525	0.01687	367.5	-5.645	<.001
BASICseg-1 vs Deepseg	-0.01338	0.01694	367.5	-0.790	.43
Relative difference in model segmentation between lesion and normal-appearing levels					
Lesion category difference in Propseg compared with BASICseg-1	-0.12249	0.03928	484.4	-3.119	<.001
Lesion category difference in Deepseg compared with BASICseg-1	-0.08689	0.03889	484.4	-2.234	.026

Note:—SE indicates standard error.

slices (both normal-appearing and lesion levels on axial T2WI) showed a significantly higher Dice coefficient for BASICseg-1 compared with Propseg (estimate difference = 0.12, $P < .001$) and borderline significance compared with Deepseg (estimate difference = 0.03, $P < .056$).

When analysis of the SC segmentation was restricted to slices of SC lesions on axial T2WI, the BASICseg-1 had significantly higher Dice coefficients compared with Propseg (difference = 0.220, $P < .001$) and Deepseg (difference = 0.102, $P = .020$; On-line Fig 3). In undamaged regions of the cord, no statistically

significant difference in segmentation performance was found between BASICseg-1 and Deepseg (difference = 0.013, $P = .43$), but there was a significant difference compared with Propseg (difference = 0.0953, $P < .001$; On-line Fig 3). The relative variance in segmentation performance in areas of damage versus no damage among the models showed a significant difference (Deepseg: estimate = 0.087, $P < .026$; Propseg: estimate = 0.122, $P < .001$). Violin plots illustrate the Dice distribution by model and by lesion in On-line Fig 3. Table 2 shows the results from linear mixed modeling.

Intramedullary Lesion Segmentation and Correlation with Motor Impairment

BASICseg-3 demonstrated the best lesion segmentation performance as shown in Fig 1D–F. All models showed overfitting of the training set. Univariate analysis (On-line Table 2) of volumes of intramedullary injury segmented by BASICseg-3 showed significant association with day 0 lower extremity motor scores (estimate = -4.583, $P = .002$), indicating that for each increase in lower extremity motor score, the volume of damage decreases by approximately 6 mm³. Similarly, BASICseg-3 segmented volumes

showed a significant association with lower extremity motor scores at the time of patient discharge: estimate = -4.030 , $P = .009$. Additionally, application of BASICseg-3 to segment lesions from the test set images took approximately 3 seconds per patient.

DISCUSSION

In the present study, we show results for automated whole-SC and traumatic-SC lesion segmentation from axial T2WI performed acutely after blunt SCI. Specifically, we applied a customized image-analysis and processing pipeline integrating 3 different novel 2D-CNN architectures for both whole-SC and traumatic lesion segmentation. Segmentation results from these CNNs were compared with each other and with the criterion standard manual segmentation as well as with current state-of-the-art SC segmentation algorithms.

The BASICseg-1 model, which uses drop-out, showed slightly better performance than models using batch normalization (BASICseg-2) and batch normalization with a noise-adaptation layer (BASICseg-3) for automated segmentation of the SC in this cohort. Because drop-out randomly sets a certain proportion of network weights to zero during training and scales the weight activations by proportion during testing, it may be that better testing segmentation occurs with drop-out because of more distributed learning of the features that map to SC tissue. This result is surprising because many deep learning architectures for image classification have adopted batch normalization; however, our results may be due to the network architecture being comparatively shallow. Additionally, the performance differences between BASICseg-1 and BASICseg-2 and -3 are not large.

BASICseg-1 also demonstrates significantly better performance for overall SC segmentation compared with Propseg and borderline significance compared with Deepseg, the 2 state-of-the-art methods for SC segmentation presently included in the SCT. Additionally, our model shows significantly better SC segmentation in areas of injury and better overall adaptivity as measured by an interaction term using linear mixed-effects modeling. Deepseg, another CNN algorithm developed for automated SC segmentation, was trained primarily with a combination of healthy control subjects in addition to a more heterogeneous cohort of patients with diverse spinal pathologies, primarily including patients with multiple sclerosis, but also those with neuromyelitis optica, amyotrophic lateral sclerosis, degenerative cervical myelopathy, syringomyelia, and 4 patients with traumatic spinal cord injury.²⁸ Our cohort, enhanced with patients with acute traumatic SCIs, is more specifically focused on image analysis in this patient population, and segmentation performance for other SC disease was not tested. SC segmentation for acute SCI is particularly challenging given the high frequency of SC distortion related to compression and associated geometric distortion as well as heterogeneous intramedullary signal abnormality.^{2,29,30} Our targeted, disease-specific approach to network training likely, in part, explains performance differences between BASICseg and Deepseg algorithms for our SCI cohort. All CNN-based algorithms (BASICseg1–3 and Deepseg) outperformed Propseg; this difference highlights the value of CNN applications for SC segmentation.

Current standard of care for MR imaging evaluation of trau-

matic SCI largely relies on subjective and qualitative descriptions of MR imaging findings such as the presence or absence of SC edema and hemorrhage.^{2,4,31} Thus, few validated MR imaging biomarkers for SC injury stratification and prognosis have been described, despite 4 decades of MR imaging clinical application for SCI.^{5,6} In addition to development of improved quantitative imaging sequences, advanced, nonbiased, and automated image-analysis techniques may prove useful to accelerate robust MR imaging biomarker identification.³² As an important step toward achieving this goal, current data show that CNNs can segment the SC in a population with acute SCI with an accuracy close to that of criterion standard manual segmentation by neuroradiologists.

For traumatic SC lesion segmentation, the BASICseg-3 algorithm performed best. The difference in performance for the network using a noise-adaptation layer with batch normalization and the other models may be due to the particularly noisy pixel label data for lesions. During training, a high volume of erroneous label data can impede adequate learning. The noise-adaptation layer can absorb this noise and allows the network to correctly map network features to labeled areas. We show that volumetric measures of SC injury derived from the BASICseg-3 correlate with acute and subacute lower extremity motor scores, validating this approach for injury-severity stratification. Ongoing studies with long-term neurologic assessment and functional outcome measures are currently underway to determine the potential prognostic value of CNN-derived biomarkers for acute SCI.

Similar to SC segmentation, automated injury segmentation based on T2WI is an important advance toward enhanced MR imaging biomarker identification for acute traumatic SCI. Manual traumatic lesion segmentation is a time-consuming process requiring an experienced technician and dedicated software packages. In this study, we have shown that volumetric measures of lesions derived from the BASICseg CNN correlate with acute and subacute lower extremity motor scores. To our knowledge, this is the first demonstration of clinically relevant automated MR imaging biomarker extraction in the context of SCI. Most important, accurate and automated SC and traumatic lesion segmentation from T2WI enables rapid image processing for registration with existing anatomic atlases so that whole-cord and subdomain-specific ROIs (for example, specific white matter tracts or gray matter subregions) can be analyzed. We have recently demonstrated the added value of atlas-based volumetric analysis of traumatic SCI lesions using manual injury-segmentation methods.³³ With rapid and automated SC and injury segmentation using conventional T2WI, atlas-based analysis tools could be feasibly integrated into the radiologist's workflow without the need for time-consuming image postprocessing. Furthermore, large multi-institutional studies incorporating high-volume MR imaging data would potentially benefit from our proposed image-processing pipeline, which is conducive to batch processing with few errors in automated segmentation. Application of radiomic and texture feature-analysis techniques may also potentially benefit from the proposed image-segmentation techniques.³⁴

Limitations of this study primarily relate to the relatively small sample size of patients with SCI, which both lowers the power of statistical tests using biomarkers and precludes the use of 3D convolutional neural networks. Despite application of data-augmen-

tation techniques to ameliorate feature learning particular to the training set, differences in Dice values between training and validation datasets also suggest some degree of data overfitting for lesion segmentation. 3D convolutional networks may improve both lesion and SC segmentation by using features in the z-direction. Despite these limitations, the excellent Dice coefficient of the BASICseg algorithms for SC and traumatic injury segmentation and the correlation of CNN-based lesion volumes with motor scores are reassuring for the application of these tools in the SCI population. As an additional limitation, the current study only evaluates the use of CNNs to segment tissues from T2WI in the axial plane, whereas automated segmentation of the SC and lesions from multiplanar, multiparametric data will allow more robust analysis.²⁸ In addition, our study cohort is derived from a single institution with all imaging performed on a single MR imaging scanner using similar parameters, thus potentially biasing our results. Future multi-institutional studies will be needed with more diverse datasets to validate the current findings. Furthermore, similar to the Softmax layer to correct for possible bias in the labels, clinical data can also be integrated into the final layer infrastructure to modulate segmentation on the basis of clinical variables. These limitations will be addressed in our future work.

CONCLUSIONS

This study demonstrates state-of-the-art performance for SC segmentation after traumatic injury using CNNs. Our model performs favorably in our cohort of patients with acute traumatic SCI compared with currently available algorithms for SC segmentation in areas of damaged cord and shows better overall adaptability with its ability to segment both damaged and undamaged areas. Additionally, we show that training a similar network architecture with the addition of a noise-adaptation layer can successfully segment areas of traumatic SC lesion identified on T2WI. Volumes extracted from lesion segmentation were significantly associated with patient motor scores. Ultimately, the application of these tools will potentially help to advance modernized SC MR image analysis for both research and clinical application. Integration with currently available SC atlases and associated tools as part of the SCT will potentially enhance MR imaging biomarker identification for predictive modeling.

Disclosures: Charley Gros—RELATED: Grant: IVADO Labs.* Adam Ferguson—RELATED: Consulting Fee or Honorarium: University of Texas Medical Branch; Burke Neurological Institute, Weill Cornell School of Medicine, Comments: I have received honoraria for talks at medical schools; Support for Travel to Meetings for the Study or Other Purposes: University of Texas Medical Branch; Burke Neurological Institute, Weill Cornell School of Medicine; European Neurotrauma Summer School; International Symposium on Neural Regeneration; National Neurotrauma Symposium, Comments: I travel to give talks; Fees for Participation in Review Activities such as Data Monitoring Boards, Statistical Analysis, Endpoint Committees, and the Like: National Institutes of Health study section; Swiss National Science Foundation; Wings for Life Foundation; UNRELATED: Grants/Grants Pending: National Institutes of Health; Veterans Administration; Department of Energy; Wings for Life Foundation; Craig H. Neilsen Foundation, Comments: I serve as Principal Investigator or Co-Investigator on grant applications to federal agencies related to this work.* Vineeta Singh—RELATED: Grant: Craig H. Neilsen Foundation grant.* Lisa Pascual—RELATED: Grant: Department of Defense, Comments: "Early Critical Care Decisions and Outcomes after Spinal Cord Injury."* Michael S. Beattie—RELATED: Grant: Department of Defense Congressionally Directed Medical Research Programs Spinal Cord Injury Research Program, Comments: Department of Defense award to support the TRACK-SCI study. I am Principal Investigator.* Jacqueline C. Bresnahan—RELATED: Grant: Department of Defense.* William Whetstone—RELATED: Grant: Depart-

ment of Defense.* Jason F. Talbott—UNRELATED: Expert Testimony: Tindall Bennett & Shoup; RELATED: Grant: Department of Defense Grant SCI20259. Russel J. Huie—RELATED: Grant: Department of Defense Grant SCI20259.* Leigh Thomas—RELATED: Grant: Department of Defense; Craig H. Neilsen Foundation*; UNRELATED: Employment: University of California, San Francisco. Xuan Duong Fernandez—RELATED: Grant: Department of Defense, Craig H. Neilsen Foundation*; UNRELATED: Employment: University of California, San Francisco. *Money paid to the institution.

REFERENCES

- Ahuja CS, Wilson JR, Nori S, et al. **Traumatic spinal cord injury.** *Nat Rev Dis Primers* 2017;3:17018 CrossRef Medline
- Talekar K, Poplawski M, Hegde R, et al. **Imaging of spinal cord injury: acute cervical spinal cord injury, cervical spondylotic myelopathy, and cord herniation.** *Semin Ultrasound CT MR* 2016;37:431–47 CrossRef Medline
- Burns AS, Marino RJ, Flanders AE, et al. **Clinical diagnosis and prognosis following spinal cord injury.** *Handb Clin Neurol* 2012;109:47–62 CrossRef Medline
- Bozzo A, Marcoux J, Radhakrishna M, et al. **The role of magnetic resonance imaging in the management of acute spinal cord injury.** *J Neurotrauma* 2011;28:1401–11 CrossRef Medline
- Kurpad S, Martin AR, Tetreault LA, et al. **Impact of baseline magnetic resonance imaging on neurologic, functional, and safety outcomes in patients with acute traumatic spinal cord injury.** *Global Spine J* 2017;7:151S–74S CrossRef Medline
- Fehlings MG, Martin AR, Tetreault LA, et al. **A clinical practice guideline for the management of patients with acute spinal cord injury: recommendations on the role of baseline magnetic resonance imaging in clinical decision making and outcome prediction.** *Global Spine J* 2017;7:221S–30S CrossRef Medline
- Fehlings MG, Tetreault LA, Wilson JR, et al. **A clinical practice guideline for the management of patients with acute spinal cord injury and central cord syndrome: recommendations on the timing (≤24 hours versus >24 hours) of decompressive surgery.** *Global Spine J* 2017;7:195S–202S CrossRef Medline
- Elizei SS, Kwon BK. **The translational importance of establishing biomarkers of human spinal cord injury.** *Neural Regen Res* 2017;12:385–38 CrossRef Medline
- Farhadi HF, Kukreja S, Minnema A, et al. **Impact of admission imaging findings on neurological outcomes in acute cervical traumatic spinal cord injury.** *J Neurotrauma* 2018;35:1398–406 CrossRef Medline
- Fonov VS, Le Troter A, Taso M, et al. **Framework for integrated MRI average of the spinal cord white and gray matter: the MNI-Poly-AMU template.** *Neuroimage* 2014;102(Pt 2):817–27 CrossRef Medline
- De Leener B, Lévy S, Dupont SM, et al. **SCT: Spinal Cord Toolbox, an open-source software for processing spinal cord MRI data.** *Neuroimage* 2017;145:24–43 CrossRef Medline
- Jenkinson M, Beckmann CF, Behrens TE, et al. **FSL.** *Neuroimage* 2012;62:782–90 CrossRef Medline
- Fischl B. **FreeSurfer.** *Neuroimage* 2012;62:774–81 CrossRef Medline
- Martin AR, De Leener B, Cohen-Adad J, et al. **Clinically feasible microstructural MRI to quantify cervical spinal cord tissue injury using DTI, MT, and T2*-weighted imaging: assessment of normative data and reliability.** *AJNR Am J Neuroradiol* 2017;38:1257–65 CrossRef Medline
- McCoy DB, Talbott JF, Wilson M, et al. **MRI atlas-based measurement of spinal cord injury predicts outcome in acute flaccid myelitis.** *AJNR Am J Neuroradiol* 2017;38:410–17 CrossRef Medline
- De Leener B, Kadoury S, Cohen-Adad J. **Robust, accurate and fast automatic segmentation of the spinal cord.** *Neuroimage* 2014;98:528–36 CrossRef Medline
- De Leener B, Cohen-Adad J, Kadoury S. **Automatic segmentation of the spinal cord and spinal canal coupled with vertebral labeling.** *IEEE Trans Med Imaging* 2015;34:1705–18 CrossRef Medline
- Gros C, De Leener B, Dupont SM, et al. **Automatic spinal cord lo-**

- calization, robust to MRI contrasts using global curve optimization. *Med Image Anal* 2018;44:215–27 CrossRef Medline
19. The R Core Team. **R: a language and environment for statistical computing**. 2013. https://www.researchgate.net/publication/221943918_R_A_Language_And_Environment_for_Statistical_Computing_Reference_Index_2152. Accessed on January 11, 2018
 20. Ronneberger O, Fischer P, Brox T. **U-Net: convolutional networks for biomedical image segmentation**. In: Navab N, Hornegger J, Wells WM, et al, eds. *Proceedings of the International Conference on Medical Image Computing and Computer-Assisted Intervention*, Munich, Germany. October 5–9, 2015;234–41
 21. Nair V, Hinton GE. **Rectified linear units improve restricted Boltzmann machines**. In: *Proceedings of the 27th International Conference on Machine Learning*, Haifa, Israel. June 21–24, 2010; 807–14
 22. Srivastava N, Hinton G, Krizhevsky A, et al. **Dropout: a simple way to prevent neural networks from overfitting**. *Journal of Machine Learning Research* 2014;15:1929–58
 23. Kinga D, Adam JB. **A method for stochastic optimization**. In: *Proceedings of the International Conference on Learning Representations*, San Diego, California. May 7–9, 2015
 24. Ioffe S, Szegedy C. Batch normalization: accelerating deep network training by reducing internal covariate shift. 2015. <https://arxiv.org/abs/1502.03167>. Accessed on January 11, 2018
 25. Sukhbaatar S, Bruna J, Paluri M, et al. Training Convolutional Networks with Noisy Labels. 2014. <https://arxiv.org/abs/1406.2080>. Accessed on January 11, 2018
 26. Dice R. **Measures of the amount of ecologic association between species**. *Ecology* 1945;26:297–302 CrossRef
 27. Zou KH, Warfield SK, Bharatha A, et al. **Statistical validation of image segmentation quality based on a spatial overlap index**. *Acad Radiol* 2004;11:178–89 Medline
 28. Gros C, De Leener B, Badji A, et al. **Automatic segmentation of the spinal cord and intramedullary multiple sclerosis lesions with convolutional neural networks**. *Neuroimage* 2019;184:901–15 CrossRef Medline
 29. Haefeli J, Mabray MC, Whetstone WD, et al. **Multivariate analysis of MRI biomarkers for predicting neurologic impairment in cervical spinal cord injury**. *AJNR Am J Neuroradiol* 2017;38:648–55 CrossRef Medline
 30. Pandit P, Talbott JF, Padoia V, et al. **T1 ρ and T2-based characterization of regional variations in intervertebral discs to detect early degenerative changes**. *J Orthop Res* 2016;34:1373–81 CrossRef Medline
 31. Shah LM, Ross JS. **Imaging of spine trauma**. *Neurosurgery* 2016;79:626–42 CrossRef Medline
 32. Martin AR, Aleksanderek I, Cohen-Adad J, et al. **Translating state-of-the-art spinal cord MRI techniques to clinical use: a systematic review of clinical studies utilizing DTI, MT, MWF, MRS, and fMRI**. *Neuroimage Clin* 2016;10:192–238 CrossRef Medline
 33. McCoy D, Huie R, Dupont S, et al. **Atlas-based volumetric assessment of T2 abnormality in acute spinal cord injury predicts motor outcomes: a transforming research and clinical knowledge in SCI (TRACK-SCI) pilot study**. In: *Proceedings of the International Society of Magnetic Resonance in Medicine*, Paris, France. June 16–21, 2018
 34. Gillies RJ, Kinahan, Hricak H. **Radiomics: images are more than pictures, they are data**. *Radiology* 2016;278:563–77 CrossRef Medline

Spontaneous Intracranial Hypotension: A Systematic Imaging Approach for CSF Leak Localization and Management Based on MRI and Digital Subtraction Myelography

R.I. Farb, P.J. Nicholson, P.W. Peng, E.M. Massicotte, C. Lay, T. Krings, and K.G. terBrugge



ABSTRACT

BACKGROUND AND PURPOSE: Localization of the culprit CSF leak in patients with spontaneous intracranial hypotension can be difficult and is inconsistently achieved. We present a high yield systematic imaging strategy using brain and spine MRI combined with digital subtraction myelography for CSF leak localization.

MATERIALS AND METHODS: During a 2-year period, patients with spontaneous intracranial hypotension at our institution underwent MR imaging to determine the presence or absence of a spinal longitudinal extradural collection. Digital subtraction myelography was then performed in patients positive for spinal longitudinal extradural CSF collection primarily in the prone position and in patients negative for spinal longitudinal extradural CSF collection in the lateral decubitus positions.

RESULTS: Thirty-one consecutive patients with spontaneous intracranial hypotension were included. The site of CSF leakage was definitively located in 27 (87%). Of these, 21 were positive for spinal longitudinal extradural CSF collection and categorized as having a ventral (type 1, fifteen [48%]) or lateral dural tear (type 2; four [13%]). Ten patients were negative for spinal longitudinal extradural CSF collection and were categorized as having a CSF-venous fistula (type 3, seven [23%]) or distal nerve root sleeve leak (type 4, one [3%]). The locations of leakage of 2 patients positive for spinal longitudinal extradural CSF collection remain undefined due to resolution of spontaneous intracranial hypotension before repeat digital subtraction myelography. In 2 (7%) patients negative for spinal longitudinal extradural CSF collection, the site of leakage could not be localized. Nine of 21 (43%) patients positive for spinal longitudinal extradural CSF collection were treated successfully with an epidural blood patch, and 12 required an operation. Of the 10 patients negative for spinal longitudinal extradural CSF collection (8 localized), none were effectively treated with an epidural blood patch, and all have undergone ($n = 7$) or are awaiting ($n = 1$) an operation.

CONCLUSIONS: Patients positive for spinal longitudinal extradural CSF collection are best positioned prone for digital subtraction myelography and may warrant additional attempts at a directed epidural blood patch. Patients negative for spinal longitudinal extradural CSF collection are best evaluated in the decubitus positions to reveal a CSF-venous fistula, common in this population. Patients with CSF-venous fistula may forgo further epidural blood patch treatment and go on to surgical repair.

ABBREVIATIONS: CVF = CSF-venous fistula; DSM = digital subtraction myelography; EPB = epidural blood patch; SIH = spontaneous intracranial hypotension; SLEC = spinal longitudinal extradural CSF collection; SLEC-N = negative for spinal longitudinal extradural CSF collection; SLEC-P = positive for spinal longitudinal extradural CSF collection

The syndrome of spontaneous intracranial hypotension (SIH) is caused by leakage of CSF from the thecal sac within or along the spinal canal.¹⁻⁴ The leakage of CSF causes variable symptoms,

the most characteristic of which is a positional headache and is commonly associated with typical intracranial MR imaging findings or stigmata.⁵⁻¹⁰ We have also noted, as have other authors,^{2,11-13} that while many patients with SIH present with a spinal longitudinal extradural CSF collection (SLEC), some do not.⁵ These SLECs have a typical appearance (Fig 1) and, in our experience, are seen exclusively in patients with SIH with dural mechanical tears along the thecal sac. These dural tears are most commonly seen ventrally.⁵ Conversely, patients with more laterally placed CSF leakage along a nerve root sleeve, from a CSF-venous fistula (CVF) or from a distal nerve root sleeve tear, do not have SLECs. We report here our experience using a strategy predicated on the presence or absence of SLECs to determine the preferred positioning of subsequent digital subtraction myelography

Received January 6, 2019; accepted after revision February 16.

From the Department of Medical Imaging, Division of Neuroradiology (R.I.F., P.J.N., T.K., K.G.t.B.), Department of Anesthesiology (P.W.P.), Department of Surgery, and Division of Neurosurgery (E.M.M.), Toronto Western Hospital, Toronto, Ontario, Canada; and Department of Medicine and Division of Neurology, Women's College Hospital (C.L.) University of Toronto, Toronto, Ontario, Canada.

Please address correspondence to Richard I. Farb, MD, Division of Neuroradiology, Department of Medical Imaging, University of Toronto, University Health Network, Toronto Western Hospital, New East Wing 3MC-430, 399 Bathurst St, Toronto, ON, M5T 2S8 Canada; e-mail: richard.farb@uhn.ca

Indicates open access to non-subscribers at www.ajnr.org

<http://dx.doi.org/10.3174/ajnr.A6016>



FIG 1. Spinal longitudinal extradural collections. *A*, Sagittal T2 FSE. *B*, Reformatted axial T2 SPACE images show SLECs (arrows) and displaced dura outlined by the CSF. *C* and *D*, Images similar to *A* and *B* of the same patient show similar findings in the lower thoracic region.

Table 1: Prevalence of intracranial stigmata of hypotension

	VDS	Sag	Hyg	SDH	Gad	Pit
SLEC-P						
No. of patients	17	15	12	9	17	17
%	81	71	57	43	81	81
SLEC-N						
No. of patients	10	10	7	2	8	9
%	100	100	70	20	80	90

Note:—Hyg indicates positive subdural hygromas over the convexity; Pit, pituitary engorgement; Sag, sagging appearance of the brain stem and posterior fossa structures; VDS, positive venous distension sign; Gad, gadolinium enhancement of the pachymeninges; SDH, patients who displayed subdural hemorrhage over the cerebral convexities.

(DSM). Specifically, patients positive for SLEC (SLEC-P) have CSF leaks that are best seen with DSM performed with the patient in the prone position, while those patients who are negative for SLEC (SLEC-N) have CSF leaks best seen with DSM performed with the patient in the lateral decubitus position. This imaging strategy was investigated for its ability to improve the yield for precisely locating the CSF leak and to help guide subsequent management.

MATERIALS AND METHODS

Institutional review board approval at University Health Network was obtained for this retrospective study.

The electronic patient record was reviewed for all patients who underwent MR imaging and DSM evaluation for SIH refractory

to epidural blood patch (EBP) from December 2016 to October 2018. A patient was categorized as SLEC-P if the spinal MR imaging revealed the presence of an SLEC regardless of the intracranial findings. A patient was categorized as SLEC-N if intracranial findings were present without an SLEC on spinal MR imaging.

Patients in whom there was no evidence of intracranial MR imaging stigmata and in whom the spinal imaging was negative for an SLEC have not been consistently offered DSM at our institution and are not included in this report.

All patients positive for SLEC underwent DSM in the prone position. All patients negative for SLEC underwent DSM in the decubitus positions (first in the left lateral decubitus and then the right lateral decubitus position). DSMs were repeated in other remaining positions until a CSF leak was found, the patient's symptoms resolved or a set of 3 myelograms negative a leak was completed.

MR Imaging

All referred patients whose available imaging from outside institutions did not include routine brain and adequate whole-spine imaging within the previous 90 days underwent an MR imaging

protocol at our institution, which included a 2-station (upper and lower) high-resolution sagittal T2 sampling perfection with application-optimized contrasts by using different flip angle evolution sequence (SPACE sequence; Siemens, Erlangen, Germany) (TE/TR = 125/900 ms, flip angle = 150°, matrix = 317 × 320, FOV = 360 × 360 mm, slice thickness = 0.9 mm, echo-train length = 63, NEX = 1.4, reformatted in the axial plane throughout the spine in 2-mm-thick intervals) to document the presence or absence of SLECs. A similarly positioned T1-weighted spin-echo sequence (TE/TR = 8.5/769 ms, flip angle = 150°, matrix = 320 × 256, FOV = 400 × 400 mm, slice thickness = 3.5 mm, echo-train length = 4, NEX = 1) was also performed to help differentiate fluid from fat within the spinal canal. All images were reviewed by 1 neuroradiologist (R.I.F.) for the intracranial MR imaging stigmata of hypotension, including a sagging appearance of the brain and brain stem, venous distension, pituitary gland enlargement, pachymeningeal enhancement, subdural hygromas, and subdural hemorrhages (Table 1).^{6,7,14,15} The spinal images were specifically reviewed to identify the presence or absence of an SLEC.

DSM

All patients positive and negative for SLEC subsequently underwent DSM. All DSM examinations at our institution are currently performed by 1 neuroradiologist (R.I.F.).

Methodology common to all DSM examinations in this study is similar to that previously described¹⁶ with modifications described below.

The DSMs at our institution were performed with local anesthetic without intravenous sedation. All DSM examinations were performed on a biplane neuroangiographic system. Due to limitations of the equipment along with patient positioning, imaging was always performed in a single plane using the larger (40 × 30 cm) intensifier. Iohexol (Omnipaque 300; GE Healthcare, Piscataway, New Jersey) was used for all DSMs. All patients were positioned head down with bolsters and an additional 4°–8° of tilt added by the table-tilt function. For the initial DSM, all patients positive for SLEC were positioned prone and all patients negative for SLEC were in the left lateral decubitus position (left side down). If this initial DSM was negative for a CSF leak, the patient returned in 1–2 weeks for another DSM in differing position.

A 22-ga spinal needle was inserted under fluoroscopic guidance via a direct posterior approach at the L3–4 level. For patients in the prone position, a CSF opening pressure measurement was not attempted because CSF rarely ascended into the hub of the needle. Moreover, a result obtained with patients in this position would clearly be erroneous. For patients in the lateral decubitus position, an accurate CSF opening pressure was recorded. The remainder of the DSM examination was similar for all patients regardless of position. In all patients, a 0.5-mL test injection ensured an intradural position of the needle tip. Following this, 10 mL of preservative-free normal saline was injected slowly for 2–4 minutes to further dilute and send the test dose down the spinal canal. The saline injection also potentially provided slight pressurization of the intradural compartment to encourage leaking. The DSM runs were performed with breath-hold and hand injection of contrast at a rate of 1 mL per second. The contrast was immediately chased with another 5–10 mL of saline to push the contrast through the tubing and down the thecal sac.

Image acquisition was performed at 1 frame per second for a total of 15–25 seconds per run. Each DSM procedure was divided into 2 separate injections (runs) of approximately 6 and 3.5 mL consecutively. The first injection covered the upper FOV and included from C3–4 to the midthoracic region. If it was positive for the site of leakage, then repeat imaging with a smaller FOV was performed with the remaining 3.5 mL of contrast. If the first injection was negative for the site of leakage, the FOV of the second injection was shifted to the lower thoracic and lumbar spine. Further saline (chasing) was usually not required for this lower injection. The multiple alternating injections of contrast and saline were controlled using a system of labeled syringes, 3-way stopcocks, and tubing. Following the second injection, the needle was removed and (if a leak was found) the patient was taken to the CT suite where scanning was typically performed with the patient in the prone or decubitus position from C2 to S3.

RESULTS

We identified 31 consecutive patients with SIH refractory to an initial EBP who underwent MR imaging of the brain and spine as well as DSM at our institution as described above. An SLEC was seen in 21 (68%) of these 31 patients, thus categorizing them as SLEC-P. Conversely, 10 (32%) patients were categorized as SLEC-N.

Patients Positive for SLEC

Of the 21 patients positive for SLEC, 18 (86%) also showed intracranial stigmata of SIH, and the remaining 3 (14%) did not (Table 1).

All 21 patients positive for SLEC underwent DSM in the prone position, which identified the site of CSF leakage in 19 (90%). DSM was initially negative for a leak in 3 (19%) patients positive for SLEC. One of these patients remained symptomatic and SLEC-P and underwent 3 separate DSMs negative for a leak at our institution (prone, right and left decubitus) and eventually underwent myelography at another institution, which demonstrated a ventral dural tear in the cervical spine not evident on initial prone DSM at our institution (personal written communication of 09/24/2018 with Dr Wouter Schievink, Department of Neurosurgery Cedars-Sinai Medical Center, Los Angeles, California). The remaining 2 patients positive for SLEC in whom the initial DSM was negative for a leak did not undergo further imaging because their symptoms resolved before repeat DSM (likely relating to an earlier EBP). In 3 patients positive for SLEC, the initial prone DSM was positive for a leak, which was better visualized with a subsequent repeat DSM (2 cases with repeat magnified view over the suspected ROI and in 1 case in which a decubitus positioning was optimal).

Thus, in 19 of the 21 patients positive for SLEC, a culprit dural tear was definitively identified. A typically appearing ventral hole within the dura related to degenerative disc disease was found in 15 of these 19 patients who were SLEC-P with DSM positive for a CSF leak. This type of CSF leak has been recognized and described by multiple authors, and we refer to this as a type 1 leak (Fig 2). A more lateral proximal nerve root sleeve tear unrelated to degenerative disc disease, which we have termed a type 2 leak (Fig 3), was found in the remaining 4 patients who were SLEC-P with DSM positive for a CSF leak.

A total of 27 DSMs were performed in the 21 patients positive for SLEC.

Patients Negative for SLEC

In 10 of the 31 consecutive patients (32%) evaluated for persistent symptoms of SIH, there was no evidence of SLEC on spinal MR imaging. These patients all demonstrated typical intracranial stigmata of intracranial hypotension to varying degrees.

In 8 of the 10 patients negative for SLEC, lateral decubitus DSM identified a definitive CSF leakage site. These consisted of 7 cases of CVF, which we have termed as a type 3 leak (Fig 4) and 1 case of a distally extravasating nerve root sleeve leak, type 4 (Fig 5). In 2 of the patients negative for SLEC, a CSF leak could not be definitively identified despite the patient having completed the set of 3 complete DSMs. In total, 22 DSMs were performed in these 10 patients.

A total of 49 DSM examinations were performed in 31 patients.

The distribution of all localized CSF leaks is shown in Fig 6.

Aside from occasional mild transient headache, all patients tolerated the DSM procedures well without complications.

CT

CT was performed approximately 10–30 minutes following DSM in patients positive and negative for SLEC. The CT scans proved

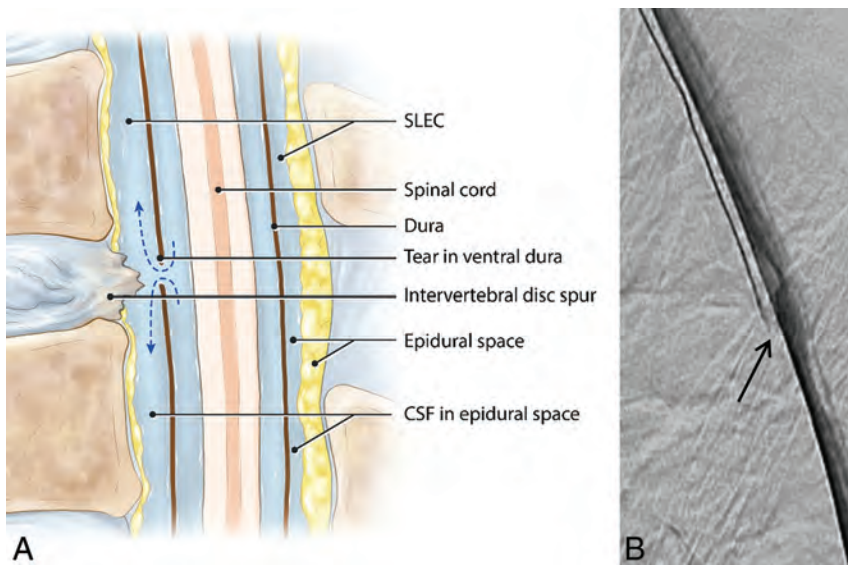


FIG 2. Type 1 CSF leak (SLEC-P). *A*, Schematic drawing shows the relationship of the intervertebral disc spur and a ventral dural tear. *B*, “Shoot through” lateral subtracted image of the thoracic spine DSM with the patient positioned prone on the table. The patient’s head is toward the top of the image and feet at the bottom. The contrast material can be seen escaping from the ventral aspect of the thecal sac at the T7–8 level (*arrow*).

helpful for counting vertebral segments; however, they did not contribute further to the localization of the CSF leak. In patients positive for SLEC, the site of the dural tear demonstrated on the previous DSM could not be demonstrated on CT; however, the continued SLEC was usually evident. In patients negative for SLEC, scanning in this delayed fashion did not reveal evidence of the CVF even when reviewed with knowledge of the location of a CVF seen on the recent DSM.

Intracranial Stigmata

The most common intracranial stigmata were findings of a “positive venous distension sign”,⁶ pachymeningeal enhancement on spin-echo postgadolinium imaging, and pituitary enlargement (Table 1). Three patients positive for SLEC demonstrated no intracranial stigmata on MR imaging. Nonetheless, these patients still

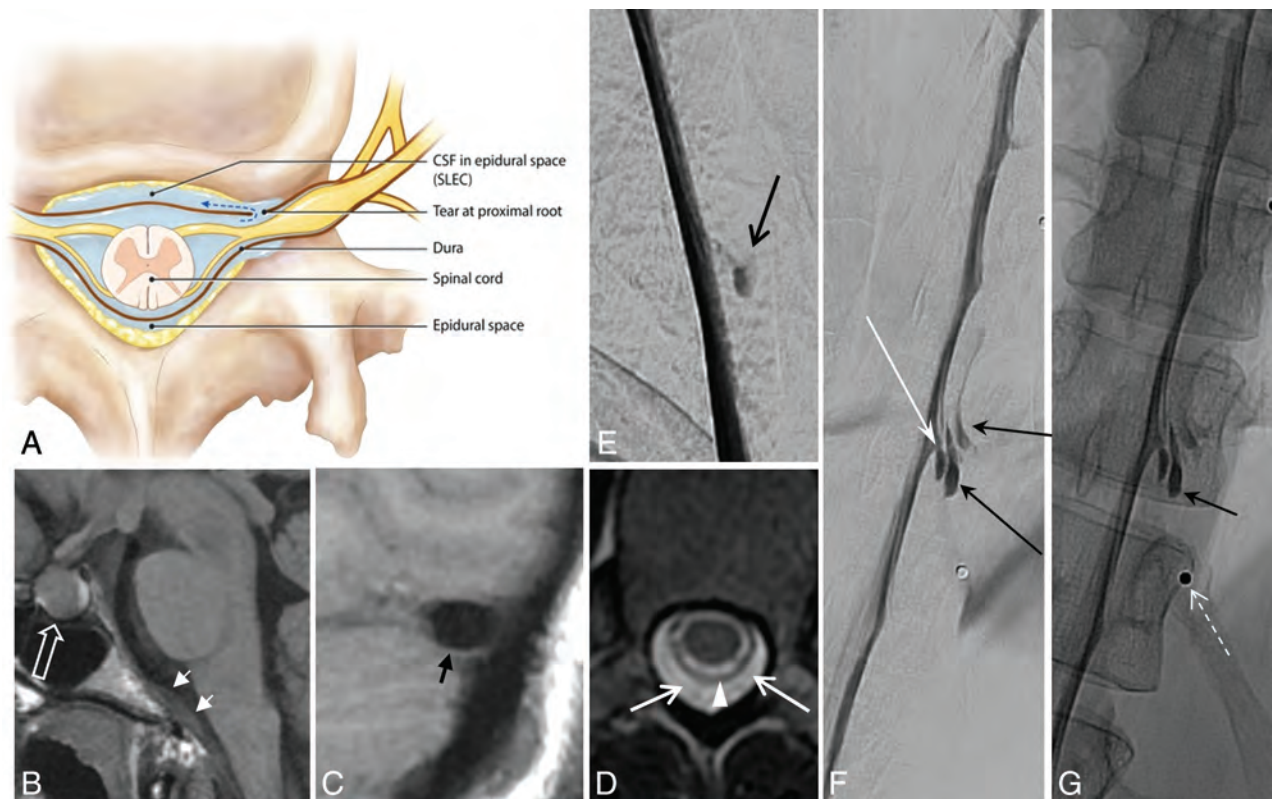


FIG 3. Type 2 CSF leak (SLEC-P). *A*, Schematic depiction of a proximal nerve root sleeve tear bridging the epidural and neural foraminal compartments. *B–G*, From a single patient. *B*, Sagittal T1WI of the brain shows the engorged pituitary gland (*open white arrow*) and dural thickening on the clivus (*short white arrows*). *C*, Sagittal T1WI of the brain shows a “positive venous distension sign” with a convex undersurface of the middle third of the dominant transverse sinus (*short black arrow*). *D*, T2-weighted axial MR image of the thoracic spine shows SLECs (*white arrows*) external to the dura (*white arrowhead*). *E*, Subtracted image from a prone thoracic DSM shows a posterolateral collection of contrast (*black arrow*). *F* and *G*, Subtracted and nonsubtracted images from a repeat right lateral decubitus DSM show contrast leaking into the extradural space (*black arrows*) from a tear along the proximal aspect of the right T11 root sleeve (*long white arrow*). Note the BB (*nipple marker*) placed on the skin for landmarking (*dashed white arrow*).

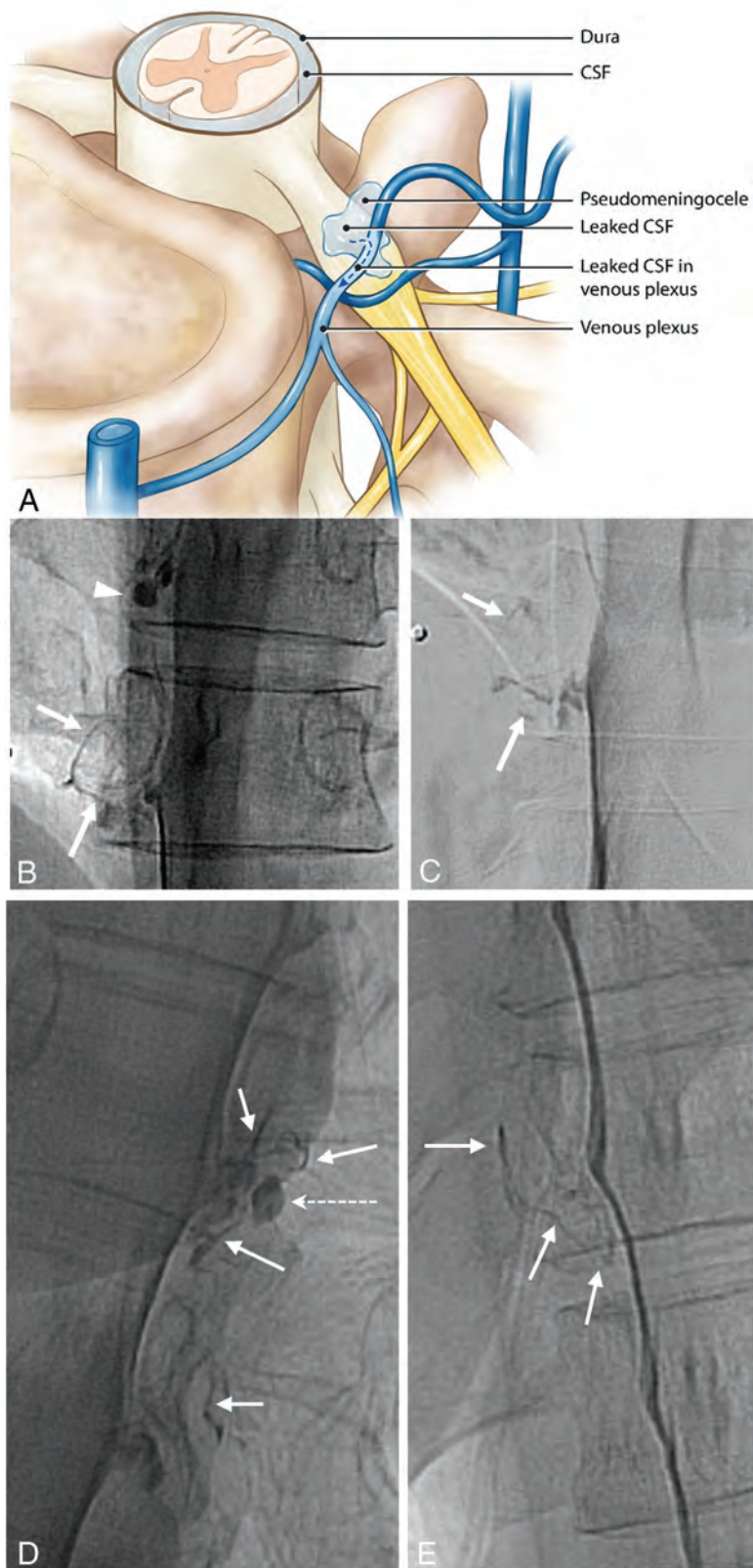


FIG 4. Type 3 CSF leak (SLEC-N). A, Schematic depiction of a CSF-to-venous fistula arising from a dural tear along the nerve root sleeve beyond the epidural compartment (see text). Nonsubtracted (B) and magnified, subtracted (C) images from separate left-side-down DSM runs in a patient negative for SLEC with SIH. A small vascular structure, in keeping with a tortuous vein of a CVF, can be seen coursing away from the root sleeve (arrows). An incidental normal diverticulum is also noted at the level above (arrowhead). D and E, Nonsubtracted images of decubitus DSMs of 2 other similarly presenting patients negative for SLEC demonstrating CVFs. Globular collections of contrast (dashed arrow) are commonly seen near the expected zone of origin of the vein, possibly representing a focal extravasation (pseudomeningocele) of contrast or a diverticulum from which the vein appears to arise.

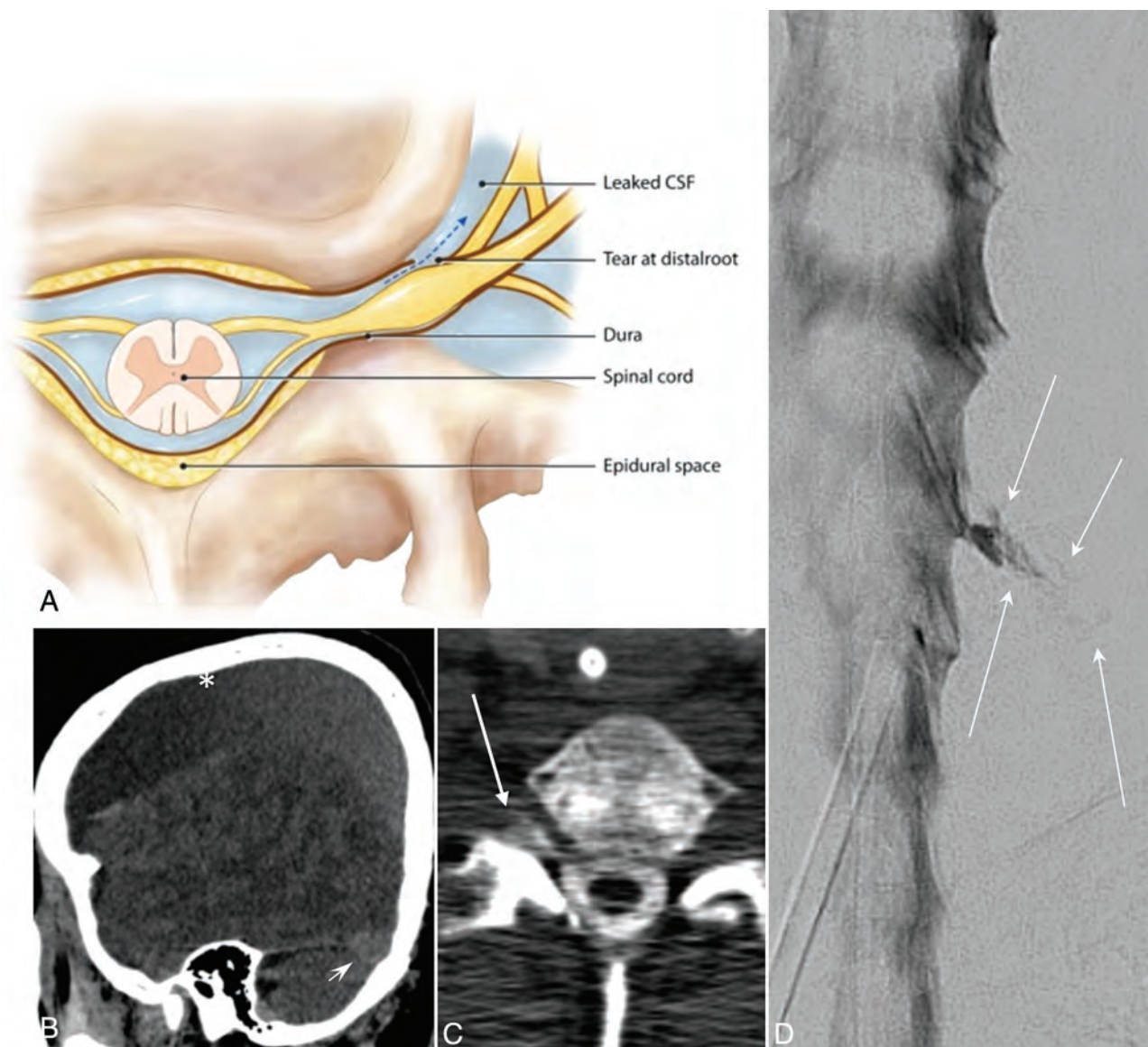


FIG 5. Type 4 CSF leak (SLEC-N). *A*, Schematic depiction of a distal nerve root sleeve dural tear occurring beyond the epidural compartment extravasating into the surrounding fascial planes and loose connective tissue without loculation or fistulization. *B*, CT of the head. Sagittal reformat in a patient negative for SLEC demonstrates large low-density (bilateral) subdural hemorrhages (*asterisk*). Note the prominent “venous distension sign” (*short arrow*) despite the large subdural hemorrhages. *C*, Axial CT image obtained 10–20 minutes post-DSM shows subtle extravasated contrast in the region of the right C8 nerve (*arrow*). Note that on this nondynamic CT (slightly degraded due to beam-hardening artifacts associated with the shoulders), there is little to help distinguish this extravasated contrast from a normal diverticulum. *D*, Subtracted image from a right-side-down decubitus DSM shows extravasation of contrast (*arrows*) into the paraspinal tissues from a leak along the mid-to-distal right C8 nerve root sleeve.

underwent DSM because of their compelling SLECs. A dural tear with an active CSF leak was identified in all 3 patients.

Summary of Management

Of the 31 patients in this series who underwent DSM for SIH, 27 (87%) had their site of CSF leak definitively localized and 26 of these patients have undergone an operation or directed EBP for effective treatment, with complete or near-complete cessation of SIH symptoms (Table 2). One patient is awaiting surgery for an identified CVF at the time of this report. Two of the 31 patients were effectively treated with nondirected EBP (both were SLEC-P with the initial prone DSM negative for a CSF leak). Thus 29 (93%) of the 31 consecutive patients with SIH were effectively

managed with the strategy presented here. However, in 2 patients negative for SLEC, the CSF leak could not be localized despite exhaustive DSM; these patients continue with signs and symptoms of SIH. Follow-up MR imaging was available in 22 of the treated patients, and each showed complete resolution of all MR imaging findings. Four patients continue with some symptoms following treatment, 2 with improved-but-mild headache (beyond typical posttreatment “rebound hypertension”) and 2 with mild back pain. Most interesting, these 4 patients have undergone follow-up MR showing complete resolution of stigmata.

In patients positive for SLEC, EBP was successful in treating 27% and 75% of patients with type 1 and 2 leaks, respectively. In 2 patients positive for SLEC, the type of leak was not defined at

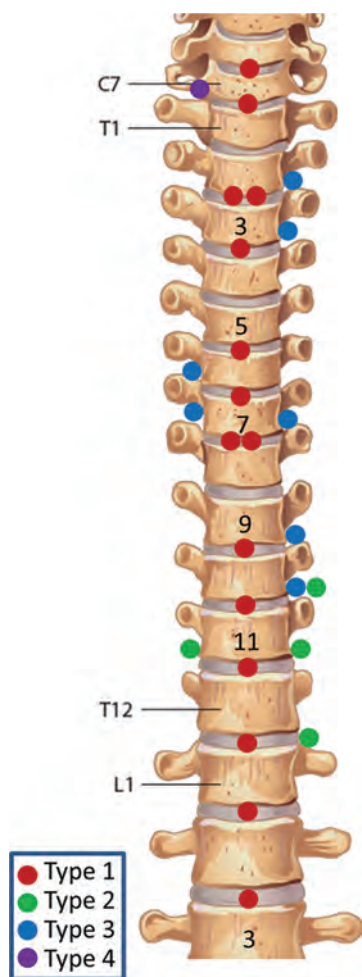


FIG 6. Distribution of CSF leaks.

DSM because it had likely already been slowed or closed by a prior EBP. Thus 9 of 21 (43%) patients positive for SLEC were effectively treated with an EBP alone (usually directed to a region of the spine by leak localization). None of the 10 patients negative for SLEC (8 localized) were effectively treated with an EBP of any kind, and all have undergone or are awaiting surgical repair.

Our limited experience with CT-guided focal fibrin patching of CSF leaks does not parallel that reported by other authors. Following leak localization, CT-guided fibrin injection was performed in 4 patients with a type 1 leak, in 2 patients with a type 2 leak, and in 3 patients with a type 3 leak. In most cases, the fibrin injection failed within 48 hours. One patient with CVF reported some beneficial effect up to 6 months; however, this success was not borne out on follow-up MR imaging and the patient was referred for surgical repair, which resulted in clearing of all MR imaging signs of SIH. Fibrin patching failed to provide durable relief in all 9 injected patients.

DISCUSSION

Until recently, the cause of SIH had been unclear, and several etiologies had been postulated.¹⁰ With evidence presented here as well as that provided by other authors,^{1,2,5,11,17-19} it now appears that these leaks are predominantly, if not exclusively, due to mechanical tears, CVFs, and leaking nerve root sleeves. For guidance

of management and efficiency of discussion, we have categorized the CSF leaks we have encountered into 4 types based on the morphology and distance from the midline. This is similar to a classification scheme previously proposed by Schievink et al.⁵

Type 1 is caused by degenerative disc disease creating a mechanical tear in the ventral dura. Patients with these ventral dural punctures are well-recognized as representing a large segment of patients with SIH (48% in this consecutive series). All patients with type 1 are SLEC-P on MR imaging with or without intracranial findings and show a typical ventral hole in the thecal sac on DSM or dynamic CT myelography.^{5,11,20} The site of CSF leakage is occasionally seen associated with a calcific “microspur” at the site of a degenerated disc.^{11,21} Unless imaged in a dynamic fashion so that the initial flow of contrast agent is captured as it travels down the spine, the site of leakage will be obscured by mixing of contrast in the intradural and extradural compartments above and below the hole.

All type 2 CSF leaks were SLEC-P as well. A type 2 leak due to a more lateral tear in the dura was a less common cause of SLEC-P CSF leakage in our series. The SLECs associated with a type 2 leak may tend to be positioned more in the neural foramina and are not associated with degenerative disc disease. These leaks are thought to arise from the base of the nerve root relating to a pre-existing thinned or dehiscent area of the dura.¹¹ In our experience, these lateral dural dehiscent lesions are more commonly seen in women (4 of 4 in our series) and appear to be more amenable to treatment with multiple EBPs and bedrest, possibly due to the nature of the tear and it not being held open by a disc protrusion or substantiated by continued flow as in a CVF. This lesion was seen in 4 of 31 patients (13%).

The recent discovery of a CVF by Schievink et al¹⁸ provided an extraordinary step forward in the care of patients with SIH. We postulate that the dural defect initiating the formation of a CVF occurs more distally along the nerve root sleeve adjacent to an arachnoid granulation or perhaps where the nerve root sleeve is in close proximity to a venous plexus. In this environment, the extravasated fluid is more likely to find its way into a venous channel. We propose that it is in this manner that an embryonic pseudomeningocele, masquerading as a diverticulum, first insinuates into the venous system and heals, aberrantly creating a 1-way CVF, which we categorize as a type 3 CSF leak (Fig 4). This postulation also accounts for these CVFs being commonly but not invariably seen next to what appears to be a diverticulum. Once established, a CVF will not respond to nondirected EBP because it lies well beyond the epidural compartment. Whether it responds to directed regional EBP remains to be better defined. CT-guided focal fibrin patching may have some success in the hands of other authors; however, in our experience, it has not provided a durable cure. Surgical ligation of a CVF as described by Schievink et al,^{5,22} in our experience, is the most efficacious treatment of these lesions.

The least common form of CSF leak we encountered in our series we have termed a type 4 leak. This results from a distal nerve root sleeve leak that does not fistulize into the venous system but rather tracks into and dissipates into the adjacent facial planes (Fig 4). A type 4 leak, because of its distal location, will present as a SLEC-N leak and will not be amenable to EBP. Whether this can

Table 2: Stratification of patients with SIH by type, management, and outcome and demographics

	No. of Patients	M	F	Avg Age (yr)	OP Avg	OP Range	Effectively Treated with EBP	No. of Patients to Surgery	Continued Symptoms
SLEC-P									
Type 1	15	8	7	46	NA	NA	4	11	1 Back pain
Type 2	4	0	4	31	NA	NA	3	1	1 Mild headache, 1 back pain
Not defined	2	2	0	53	NA	NA	2	0	
SLEC-N									
Type 3	7	2	5	52	8.4	0–12	0	7	1 Awaiting surgery
Type 4	1	1	0	56	0	0	0	1	
Not found	2	0	2	58	10	10	0	0	Continue unchanged

Note:—Avg indicates average; OP Avg, average CSF opening pressure; OP Range, the range of CSF opening pressures seen; NA, not applicable; M, male; F, female.

be treated with CT-guided focal fibrin patching remains to be defined.

Our observations regarding the association of SLECs with differing types of CSF leaks is similar to experiences of other authors. Dobrocky et al¹¹ used DSM as well as conventional and dynamic CT myelography to locate the site of leakage in 14 patients. Their study included only patients with SLECs; thus, the authors did not identify any patients with CVFs in their series. Conversely, Schievink et al⁵ recently reported 14 cases of CVF, none of which were associated with SLEC. Kranz et al¹⁹ have reported their success in using dynamic CT myelography and DSM to identify 22 cases of CVF. In that study, the authors also noted that CVFs “often occur without epidural leak.” The 7 cases of CVF in our series were all seen in the thoracic region, were not associated with SLEC, were all paravertebral extending laterally from the neural foramen, were inconsistently associated with small diverticula (3 of 7), and, in our experience, were more prevalent on the left (5 of 7). These findings are similar to recently reported experience with CVF.^{18,19,22}

The relatively high prevalence of CVF (type 3 leak) in our series presented here is most likely due to the use of lateral decubitus DSM. Lateral DSM optimizes the visualization of the CVF by flooding the lateral gutters of the thecal sac with high-density contrast agent and profiling those gutters with direct frontal high-spatial and high-temporal-resolution myelography. Prone DSM is not optimal for detecting these laterally located CVFs and will commonly result in a false-negative DSM. Spinal MR imaging identified all of these patients as SLEC-N; thus, all were initially in the decubitus position for DSM, substantially increasing the yield of the DSM to identify the leak. This same strategy can no doubt be applied to dynamic CT myelography at those centers where that technique is favored over DSM.

Despite the foregoing, there still are a small number of patients who continue to have SIH in whom a CSF leak cannot be localized. There were 2 such patients in this report. Both patients were negative for SLEC, and both continue to show intracranial MR imaging stigmata. We suspect that these patients have a type 3 or perhaps type 4 leak, which our DSMs failed to identify.

A major question in the SIH arena is what to offer the rapidly growing population of patients with headache with brain and spine MR imaging negative for stigmata of CSF leak in whom a possible diagnosis of SIH continues to be considered. Such patients may still harbor a CSF leak despite normal findings on CSF manometry.^{1,2,23} In this report, 3 symptomatic patients positive for SLEC with no intracranial findings under-

went DSM (mandated by their SLEC) and were proved to have a leak. Therefore, we must allow the corollary to be true—that is, there must be a percentage of patients negative for SLEC (types 3 and 4) who are leaking slowly and thus not attaining the threshold to display intracranial MR imaging stigmata but are still nonetheless leaking and having symptoms. MR imaging, like CSF manometry, is not an adequate screening test for this disease. Moreover, as awareness of the syndrome of SIH increases the population of headache patients inferred to have a positional quality to their headache will undoubtedly grow while the low prevalence a true CSF leak in this population will further decline. A better screening test for SIH is needed. It is inefficient to offer exhaustive DSM with its discomfort, mildly invasive nature, radiation dose, and lack of disseminated expertise to this population of patients as the screening test for SIH.

There is clearly a role for EBP in patients positive for SLEC with SIH. Nine of 21 (43%) of all patients positive for SLEC were treated successfully with EBP (nondirected and directed) and did not require an operation. Determining early which patients positive for SLEC will do well with nondirected-versus-directed EBP and how many times EBP should be attempted before surgical referral is an area for further investigation. Conversely, in this report, 100% of the 10 patients negative for SLEC failed all forms of EBP. This observation is not surprising given the fact that all patients negative for SLEC were shown to have a leak that starts lateral to and beyond the confines of the spinal canal and thus predisposes an EBP to failure.

Once again, the strategy of using MR imaging to divide patients with SIH into SLEC-P and SLEC-N is prescriptive in that it also appears to foreshadow which patients may benefit from EBP before prone DSM and those who should go on to lateral decubitus DSM without further delay.

The limitations of this current report are obvious in that it represents the experience of essentially 1 neuroradiologist at 1 large neurosurgical referral center. A strong selection bias exists because all patients in this study had MR imaging findings of SIH. Despite an increasing awareness of SIH, the syndrome remains relatively uncommon, resulting in a limited number of neuroradiologists, anesthesiologists, and neurosurgeons skilled in the techniques of diagnosis and treatment of these patients. Dissemination of the technique of DSM as well as dynamic CT myelography, pooling of data across multiple centers, and development of a less invasive screening test for SIH

would, no doubt, lead to a more efficient diagnosis and effective treatment of these patients.

CONCLUSIONS

Using spinal MR imaging to dichotomize patients with SIH into SLEC-P and SLEC-N populations accurately determines the nature of their underlying CSF leak (mechanical dural tear versus CVF or nerve root sleeve leak), correctly predicts in whom autologous nondirected and directed EBP may work and in whom it will predictably fail, and finally prescribes the positioning (prone versus decubitus) for subsequent dynamic myelography providing the most efficient pathway to definitive leak localization and subsequent repair. Using this systematic approach, we have been able to identify the exact site of CSF leakage in 27 (87%) of 31 consecutive patients referred to our institution with MR imaging evidence of SIH.

ACKNOWLEDGMENTS

The authors acknowledge the contribution of Wendy Gu, a Biomedical Communicator, for her medical illustrations and help with preparation of the figures for this article.

Disclosures: Philip W. Peng—UNRELATED: Other: equipment support from Fujifilm Sonosite Canada.* Christine Lay—UNRELATED: Consultancy: Novartis, Aralez, Eli Lilly and Company, Allergan*; Payment for Lectures Including Service on Speakers Bureaus: Novartis, Aralez.* *Money paid to institution.

REFERENCES

1. Kranz PG, Gray L, Amrhein TJ. **Spontaneous intracranial hypotension: 10 myths and misperceptions.** *Headache* 2018;58:948–59 CrossRef Medline
2. Kranz PG, Malinzak MD, Amrhein TJ, et al. **Update on the diagnosis and treatment of spontaneous intracranial hypotension.** *Curr Pain Headache Rep* 2017;21:37 CrossRef Medline
3. Schievink WI. **Spontaneous spinal cerebrospinal fluid leaks.** *Cephalalgia* 2008;28:1345–56 CrossRef Medline
4. Schievink WI, Schwartz MS, Maya MM, et al. **Lack of causal association between spontaneous intracranial hypotension and cranial cerebrospinal fluid leaks.** *J Neurosurg* 2012;116:749–54 CrossRef Medline
5. Schievink WI, Maya MM, Jean-Pierre S, et al. **A classification system of spontaneous spinal CSF leaks.** *Neurology* 2016;87:673–79 CrossRef Medline
6. Farb RI, Forghani R, Lee SK, et al. **The venous distension sign: a diagnostic sign of intracranial hypotension at MR imaging of the brain.** *AJNR Am J Neuroradiol* 2007;28:1489–93 CrossRef Medline
7. Forghani R, Farb RI. **Diagnosis and temporal evolution of signs of intracranial hypotension on MRI of the brain.** *Neuroradiology* 2008; 50:1025–34 CrossRef Medline
8. Fishman RA, Dillon WP. **Dural enhancement and cerebral displacement secondary to intracranial hypotension.** *Neurology* 1993;43: 609–11 CrossRef Medline
9. Kranz PG, Amrhein TJ, Choudhury KR, et al. **Time-dependent changes in dural enhancement associated with spontaneous intracranial hypotension.** *AJR Am J Roentgenol* 2016;207:1283–87 CrossRef Medline
10. Mokri B. **Spontaneous intracranial hypotension.** *Continuum (Minneapolis Minn)* 2015;21(4 Headache):1086–108 CrossRef Medline
11. Dobrocky T, Mosimann PJ, Zibold F, et al. **Cryptogenic cerebrospinal fluid leaks in spontaneous intracranial hypotension: role of dynamic CT myelography.** *Radiology* 2018;289:766–72 CrossRef Medline
12. Nakagawa N. **Changes in spinal MRI findings for epidural fluid collection in the treatment of intracranial hypotension [in Japanese].** *No Shinkei Geka* 2016;44:925–33 Medline
13. Verdoorn JT, Luetmer PH, Carr CM, et al. **Predicting high-flow spinal CSF leaks in spontaneous intracranial hypotension using a spinal MRI-based algorithm: have repeat CT myelograms been reduced?** *AJNR Am J Neuroradiol* 2016;37:185–88 CrossRef Medline
14. Kranz PG, Tanpitukpongse TP, Choudhury KR, et al. **Imaging signs in spontaneous intracranial hypotension: prevalence and relationship to CSF pressure.** *AJNR Am J Neuroradiol* 2016;37:1374–78 CrossRef Medline
15. Schievink WI. **Spontaneous spinal cerebrospinal fluid leaks and intracranial hypotension.** *JAMA* 2006;295:2286–96 CrossRef Medline
16. Hoxworth JM, Patel AC, Bosch EP, et al. **Localization of a rapid CSF leak with digital subtraction myelography.** *AJNR Am J Neuroradiol* 2009;30:516–19 CrossRef Medline
17. Dillon WP. **Challenges in the diagnosis and treatment of spontaneous intracranial hypotension.** *Radiology* 2018;289:773–74 CrossRef Medline
18. Schievink WI, Moser FG, Maya MM. **CSF-venous fistula in spontaneous intracranial hypotension.** *Neurology* 2014;83:472–73 CrossRef Medline
19. Kranz PG, Amrhein TJ, Gray L. **CSF venous fistulas in spontaneous intracranial hypotension: imaging characteristics on dynamic and CT myelography.** *AJR Am J Roentgenol* 2017;209:1360–66 CrossRef Medline
20. Thielen KR, Sillery JC, Morris JM, et al. **Ultrafast dynamic computed tomography myelography for the precise identification of high-flow cerebrospinal fluid leaks caused by spiculated spinal osteophytes.** *J Neurosurg Spine* 2015;22:324–31 CrossRef Medline
21. Rosebrock RE, Diehn FE, Luetmer PH, et al. **Penetrating osseous spicules causing high-flow ventral CSF leaks in the setting of relatively low BMI: a preliminary study.** *Clin Neuroradiol* 2018;28: 539–43 CrossRef Medline
22. Schievink WI, Moser FG, Maya MM, et al. **Digital subtraction myelography for the identification of spontaneous spinal CSF-venous fistulas.** *J Neurosurg Spine* 2016;24:960–64 CrossRef Medline
23. Kranz PG, Tanpitukpongse TP, Choudhury KR, et al. **How common is normal cerebrospinal fluid pressure in spontaneous intracranial hypotension?** *Cephalalgia* 2016;36:1209–17 CrossRef Medline

Decubitus CT Myelography for Detecting Subtle CSF Leaks in Spontaneous Intracranial Hypotension

P.G. Kranz, L. Gray, and T.J. Amrhein

ABSTRACT

SUMMARY: Spontaneous intracranial hypotension is caused by spinal CSF leaks, but the site of the leak is not always detected on spinal imaging. We report on the additional value of decubitus positioning during CT myelography in enhancing the detection of subtle leaks.

ABBREVIATIONS: CTM = CT myelography; CVF = CSF venous fistula; SIH = spontaneous intracranial hypotension

Spontaneous intracranial hypotension (SIH) is a condition caused by spinal CSF leaks, either into the epidural space or into an adjacent vein, known as a CSF venous fistula (CVF).^{1,2} Detection of CSF leakage on spinal imaging helps confirm the diagnosis and is critical to guiding treatment.³ Targeted treatment with epidural patching or surgery is important in refractory cases but requires accurate localization of a leak site.⁴ However, spine imaging does not demonstrate the leak site in approximately half of patients with known SIH.^{5,6} These cases with negative findings on imaging are thought to be due to a low-flow CSF leak or occult CVF.²

Imaging techniques that can help improve detection of occult leaks are therefore desirable. We have observed that placing a patient in the lateral decubitus position for CT myelography (CTM) facilitates the detection of CSF leaks in some patients with SIH.

MATERIALS AND METHODS

Subjects

This is a retrospective series of 5 patients with SIH treated between February 2016 and February 2018 in which an etiology of CSF leak was identified on CTM performed with the patient in the lateral decubitus position. The leak was not seen on previously performed prone or supine CTM. The work in this study was approved by the Duke University Medical Center institutional review board and is compliant with the Health Insurance Portability and Accountability Act.

All subjects met International Classification of Headache Disorders, 3rd ed (<https://www.ichd-3.org/>) criteria for SIH. Brain MR imaging with contrast was performed before spine myelography. In all cases, subjects had undergone at least 1 myelogram with standard prone or supine positioning, which had not definitively localized a leak.

Decubitus Myelogram Technique

Decubitus CTM was performed on the basis of a subtle abnormality seen on the initial nondecubitus CTM in 4 of 5 patients. In these patients, the decubitus CTM was obtained as part of a dynamic myelogram under fluoroscopy.⁷ In a dynamic myelogram, intrathecal contrast is injected with the patient in the decubitus position; in these 4 patients, the abnormality seen on the initial prone CTM determined whether right or left decubitus positioning was used. The patient was not rolled before CTM to maintain a high density of dependently layering contrast material, and the CTM was performed within 10–15 minutes after fluoroscopic imaging was completed.

In the remaining patient, decubitus CTM of the spine was performed because previous prone CT myelograms had been unrevealing. In this case, bilateral decubitus scans were obtained immediately after the initial prone CTM did not show a leak.

For all myelograms (both prone and decubitus), 10 mL of iopamidol containing 300 mg/mL of iodine (Isovue-M 300; Bracco, Princeton, New Jersey) was used. All scans were performed on a single 64–detector row CT scanner (Discovery 750HD; GE Healthcare; Milwaukee, Wisconsin) using the following parameters: helical scan mode, rotation time = 0.8 seconds, pitch = 0.969, tube voltage = 120 kV(peak), automated exposure control, tube current = 300–800 mA, noise index = 19.5, slice thickness = 2.5 mm, interval = 2.5 mm, reconstruction thickness = 0.625 mm. Initial prone myelograms of the entire spine were obtained; when further interrogation of a suspected abnor-

Received November 28, 2018; accepted after revision December 22.

From the Department of Radiology, Duke University Medical Center, Durham, North Carolina.

Please address correspondence to Peter G. Kranz, MD, Department of Radiology, Box 3808, Duke University Medical Center, Durham, NC 27710; e-mail: peter.kranz@duke.edu; @PeterGKranz

<http://dx.doi.org/10.3174/ajnr.A5995>

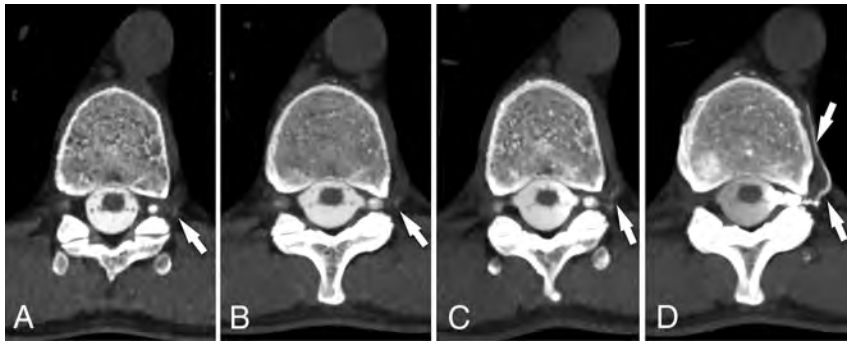


FIG 1. CSF venous fistula visualized best on decubitus CTM. Axial prone CTM image (A) and maximum-intensity-projection image of the same level (B) show subtle linear contrast (arrows) lateral to the T11 nerve root. The patient was turned to the left lateral decubitus position and re-scanned 13 minutes later. Axial MIP image (C) from that scan shows increased intravascular contrast with the patient in the decubitus position, suggestive of a CSF venous fistula (arrow). Axial MIP image (D) from a CTM performed after dynamic myelography on a subsequent day with the patient maintained in the decubitus position after contrast injection shows extensive filling of a paraspinous vein distal to the fistula (arrows).

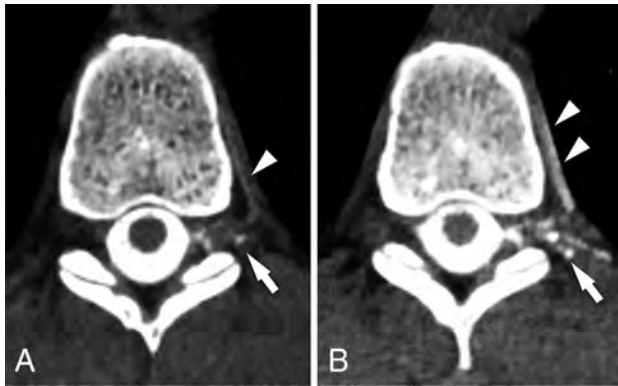


FIG 2. CSF venous fistula visualized best on decubitus CTM. Axial prone CT myelogram (A) shows subtle filling of a network of paraspinous veins (arrowhead) lateral to the nerve root and in the adjacent spinal segmental vein (arrowhead). Axial image (B) from a decubitus CTM performed after dynamic myelography on a subsequent day shows increased filling of the lateral veins (arrow) and segmental vein (arrowheads), making the CVF much more conspicuous.

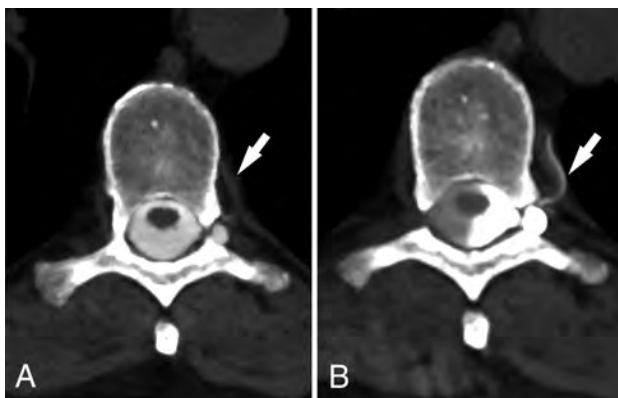


FIG 3. CSF venous fistula visualized best on decubitus CTM. Axial prone CTM image (A) shows possible increased density of a spinal segmental vein (arrow). Axial image (B) from a decubitus CTM performed after dynamic myelography on a subsequent day shows increased filling of the segmental veins (arrow), helping to confirm the diagnosis of CVF. Note the increased density of the left lateral thecal sac due to decubitus positioning.

mality was desired, the scan was limited to the area of interest to decrease the radiation dose.

Image Analysis

The effect of decubitus positioning on the density of intrathecal contrast media was measured by placing an ROI over the thecal sac immediately adjacent to the identified leak. In cases in which a CSF venous fistula was detected, the density of the draining vein was similarly measured, as previously described.⁸

RESULTS

The mean subject age was 54.2 years (range, 31–72 years). Three subjects were women. Pretreatment brain MR imaging showed evidence of SIH in all

cases. Spine MR imaging was performed before myelography in 3/5 subjects and was negative for CSF leak in all cases. The mean number of CTM examinations performed before the decubitus myelogram was 1.6 (range, 1–3).

Decubitus imaging revealed a CVF in the 4 cases in which a subtle abnormality was questioned on a prior CTM (Figs 1–4). The fistulas in each of these 4 cases were located at the T7, T8, T10, or T11 nerve roots, respectively, all on the left. All 4 CVFs were associated with nerve root sleeve diverticula, a common association reported in other series.⁷ In the case in which bilateral decubitus CTM was performed, a low-flow CSF leak into the epidural space was detected at T10–11, which was not seen on the prior CTM (Fig 5).

On decubitus CTM, the mean density of intrathecal CSF at the leak site was 1944 HU (range 834–2960 HU), compared with 729 HU (range, 395–1253 HU) on the prior nondecubitus CTM, representing a mean increase of 301% on decubitus imaging.

For the cases of CVF, the mean density of the draining paraspinous veins on the decubitus CTM was 294 HU (range, 111–514 HU), compared with 104 HU (range, 28–288 HU) on prior nondecubitus CTM, a mean increase of 507%.

DISCUSSION

This investigation demonstrates the additional yield of CTM performed with the patient in the lateral decubitus position in some patients with SIH when initial prone or supine CTM has not been revealing. In most patients in this series, the decision to perform decubitus imaging was prompted by an initial suspicion of a subtle abnormality on prior CTM, and decubitus myelography confirmed an abnormality at the initially suspected level in these cases. In at least 1 patient, however, decubitus CTM detected a leak that was not visible even in retrospect on prior imaging. Moreover, in the cases in which a CVF was suspected on prior CTM, the initial findings were often very subtle and decubitus myelography greatly increased diagnostic confidence. This increased confidence was a critical factor in committing the patient to surgery.⁷

Two factors may contribute to the increased detection of CSF

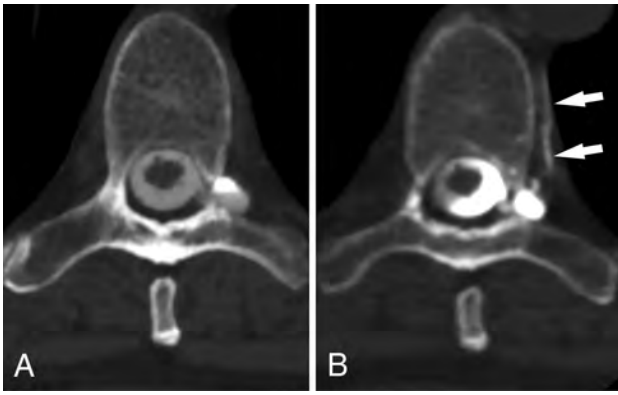


FIG 4. CSF venous fistula visualized best on decubitus CTM. Axial prone CTM image (A) shows a perineural diverticulum, but no clear leak. Axial image (B) from a subsequent CTM obtained with the patient in the decubitus position after dynamic myelography shows clear filling of a segmental vein (arrows), confirming a CVF.

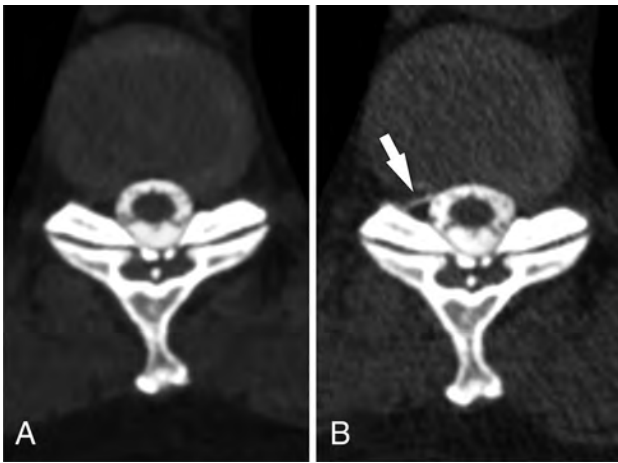


FIG 5. Low-flow CSF leak seen only on decubitus myelography. Axial prone CTM image (A) shows no CSF leak at the T10–T11 level. The patient was turned into the left lateral decubitus position and re-scanned, again with the scan showing no leak (not shown). The patient was then turned to the right lateral decubitus position. An axial CTM image from the decubitus myelogram (B) obtained 6 minutes later shows a low-flow CSF leak not seen on prone myelogram (arrow).

leaks with the patient in the decubitus position. First, when intrathecal contrast is injected and the patient is allowed to remain in the decubitus position, the contrast concentration over the leak site is higher than if the patient is rolled. This is evident from our series, in which the mean density of the intrathecal contrast at the level of the leak increased by 301% with the patient in the decubitus position compared with the prone position.

Second, there appears to be an effect of gravity that promotes the flow of contrast through a leak or into a CVF that is on the dependent side of the thecal sac. In the patient with the low-flow leak, the contrast concentration in the thecal sac only increased slightly between the prone and decubitus scans (778 versus 835 HU), but the leak was only visible when the patient was in the decubitus position (Fig 5).

This investigation does not establish the sensitivity for decubitus CTM in leak detection because only cases positive for CSF leak were included in this initial report. Furthermore, it does not determine the overall additional diagnostic yield for decubitus CTM among all patients with SIH with initial negative findings on prone or supine CTM. Performing additional decubitus scans will necessarily increase the radiation dose; therefore, further investigation is needed to clarify when additional decubitus imaging is justified.

CONCLUSIONS

Decubitus CTM demonstrates CSF leaks not seen on conventional prone or supine CTM in some patients with SIH.

Disclosures: Linda Gray—UNRELATED: Board Membership: medical advisory membership for CSF Leak Association.

REFERENCES

1. Mokri B. Spontaneous low pressure, low CSF volume headaches: spontaneous CSF leaks. *Headache* 2013;53:1034–53 CrossRef Medline
2. Schievink WI, Moser FG, Maya MM. CSF-venous fistula in spontaneous intracranial hypotension. *Neurology* 2014;83:472–73 CrossRef Medline
3. Kranz PG, Luetmer PH, Diehn FE, et al. Myelographic techniques for the detection of spinal CSF leaks in spontaneous intracranial hypotension. *AJR Am J Roentgenol* 2016;206:8–19 CrossRef Medline
4. Cho KI, Moon HS, Jeon HJ, et al. Spontaneous intracranial hypotension: efficacy of radiologic targeting vs blind blood patch. *Neurology* 2011;76:1139–44 CrossRef Medline
5. Kranz PG, Tanpitukpongse TP, Choudhury KR, et al. Imaging signs in spontaneous intracranial hypotension: prevalence and relationship to CSF pressure. *AJNR Am J Neuroradiol* 2016;37:1374–78 CrossRef Medline
6. Schievink WI, Maya MM, Jean-Pierre S, et al. A classification system of spontaneous spinal CSF leaks. *Neurology* 2016;87:673–79 CrossRef Medline
7. Kranz PG, Amrhein TJ, Gray L. CSF venous fistulas in spontaneous intracranial hypotension: imaging characteristics on dynamic and CT myelography. *AJR Am J Roentgenol* 2017;209:1360–66 CrossRef Medline
8. Kranz PG, Amrhein TJ, Schievink WI, et al. The “hyperdense paraspinous vein” sign: a marker of CSF-venous fistula. *AJNR Am J Neuroradiol* 2016;37:1379–81 CrossRef Medline

Paranasal Sinus CT Is of Variable Value in Patients with Pediatric Cancer with Neutropenic Fever

When patients with pediatric cancer are found to have a fever without a source, CT of the paranasal sinuses, chest, abdomen, and pelvis has often been used as a screening tool. I question the role of sinus CT in this protocol.

It is commonly understood among radiologists that most children have some degree of paranasal sinus mucosal thickening, yet clinicians often use CT for answers when the result is almost always equivocal in the absence of symptomatology suggesting complicated sinus disease.¹ To assess this, I looked at 19 children presenting to a desert-climate facility in southern Arizona for trauma without a history of sinusitis, and the average modified Lund-MacKay (mLM) score was 6.88 (95% CI, 5.21–8.55). A same-site sample of patients with pediatric neutropenic fever assessed during the same period yielded a mean mLM of 4.67 (95% CI, 3.38–5.96). A different sample of controls in northern Texas (humid subtropical climate) yielded an average mLM of 4.00 (95% CI, 2.70–5.30). Simply put, mucosal thickening is a normal finding in children which likely depends to some degree on the environment in which they reside. While none of these children had signs or symptoms of complicated sinusitis, several of the pediatric cancer patients with neutropenic fever were subjected to specialty consultations based on the sinus findings, none of which resulted in additional therapy or continued concern for invasive fungal disease.

It is generally accepted that paranasal sinus CT is useful in

patients subject to hematopoietic stem cell transplantation, but the American College of Radiology Appropriateness Criteria assigns this a rating of 4,² the lower limit of “may be appropriate.” The Children’s Oncology Group position is to consider not routinely performing CT of the sinuses in patients without localizing signs or symptoms.³ My hope is that radiologists will do a better job of educating ordering providers regarding the utility of this test in this setting. Bedside sinus endoscopy is an effective alternative approach⁴ that offers the opportunity for sampling and avoids radiation.

REFERENCES

1. Tekes A, Palasis S, Durand DJ, et al; Expert Panel on Pediatric Imaging. **ACR Appropriateness Criteria® Sinusitis-Child.** *J Am Coll Radiol* 2018;15:S403–12 CrossRef Medline
2. Westra SJ, Karmazyn BK, Alazraki AL, et al; Expert Panel on Pediatric Imaging. **ACR Appropriateness Criteria Fever Without Source or Unknown Origin-Child.** *J Am Coll Radiol* 2016;13:922–30 CrossRef Medline
3. Children’s Oncology Group. COG Supportive Care Endorsed Guidelines. January 31, 2019. https://www.childrensoncologygroup.org/downloads/COG_SC_Guideline_Document.pdf. Accessed February 1, 2019
4. Cohn SM, Rokala HR, Siegel JD, et al. **Application of a standardized screening protocol for diagnosis of invasive mold infections in children with hematologic malignancies.** *Support Care Cancer* 2016;24:5025–33 CrossRef Medline

 C.M. Pfeifer

Department of Radiology
University of Texas Southwestern Medical Center
Dallas, Texas

<http://dx.doi.org/10.3174/ajnr.A6007>